Environmental Science and Engineering

Han-Yong Jeon *Editor*

Sustainable Development of Water and Environment

Proceedings of the ICSDWE2022

Springer

Environmental Science and Engineering

The ultimate goal of this series is to contribute to the protection of our environment, which calls for both profound research and the ongoing development of solutions and measurements by experts in the field. Accordingly, the series promotes not only a deeper understanding of environmental processes and the evaluation of management strategies, but also design and technology aimed at improving environmental quality. Books focusing on the former are published in the subseries Environmental Science, those focusing on the latter in the subseries Environmental Engineering.

Han-Yong Jeon
Editor

Sustainable Development of Water and Environment

Proceedings of the ICSDWE2022

Springer

Editor
Han-Yong Jeon
Department of Chemical Engineering
Inha University
Incheon, Korea (Republic of)

ISSN 1863-5520 ISSN 1863-5539 (electronic)
Environmental Science and Engineering
ISBN 978-3-031-07499-8 ISBN 978-3-031-07500-1 (eBook)
https://doi.org/10.1007/978-3-031-07500-1

This Springer imprint is published by the registered company Springer Nature Switzerland AG
The registered company address is: Gewerbestrasse 11, 6330 Cham, Switzerland

Preface of ICSDWE2022

The 5th International Conference on Sustainable Development of Water and Environment (ICSDWE2022) was successfully held online via ZOOM on March 17, 2022.

The aim of ICSDWE2022 is to present the latest research and results of scientists (professors, students, Ph.D. students, engineers, and postdoc scientists) related to sustainable development of water and environment. The key goal of the conference provides opportunities for academic scientists, engineers, and industry researchers to exchange and share their expertise, experience, new ideas, or research result and discuss the challenges and future in their expertise.

ICSDWE2022 had a technical program consisting of 2 international keynote speeches, 18 oral presentations, and 5 poster presentations. Details are as below:

Two international keynote speeches were delivered separately by the Conference Chair Prof. Han-Yong Jeon from Inha University (South Korea) and Prof. Rosemary M. Gutierrez from the University of the Philippines Baguio (Philippines); each keynote speech lasted for 35 min including questions and answers.

Eighteen oral presentations and 5 poster presentations were delivered by experts and scholars, such as Prof. Eusébio Z. E. Conceição from Science and Technology Faculty of the University of Algarve (Portugal), Dr. Ekaterina Bogomilova, University of National and World Economy (Bulgaria), Prof. Yang Yunan, College of Space and Environment, Beihang University (China), Prof. Aihong Gai, College of Resources and Environmental Sciences, Gansu Agricultural University (China), Dr. Hidekazu Yoshioka, Shimane University (Japan), etc.

ICSDWE2022 has received 156 abstracts and full papers. After a preliminary review of the scope, originality, and language, ICSDWE2022 has sent those 134 full papers to reviewers to conduct a single-blind peer review. ICSDWE2022 has been able to accept papers only after reviewers double-checked the revised manuscripts and give their consent to accepting them; as a result, only 32 papers were accepted to be published in Springer Conference Series Environmental Science and Engineering [ISSN: 1863-5520].

On behalf of the conference chair, I would like to thank all the authors who contributed to ICSDWE2022 and the Technical Program Committee Members and

reviewers who gave their valuable comments and suggestions for improving the manuscripts. I also want to thank the publisher for publishing the proceedings. May the readers could enjoy the gain some valuable knowledge from it.

We are expecting more and more experts and scholars from all over the world to join the 6th ICSDWE2023.

Incheon, Korea (Republic of) Prof. Han-Yong Jeon

Contents

1 Salinity Intrusion in the Vietnamese Mekong Delta, a Threat: Possible Causes, Effects on People's Life and Production, and Temporary Solutions and Adaptable Strategies 1
Nguyen Van Tho

2 Improved Stochastic Fractal Search Algorithm for Joint Optimal Operation of Cascade Hydropower Stations 11
Zhanxing Xu, Jianzhong Zhou, Yuqi Yang, and Zhou Qin

3 Regional Hydrological Model with Global Climate Change of Mean Annual Flows of the Santa River Basin, Applying the Fokker–Planck–Kolmogorov Equation 27
Erick Vladimir Castilla Chanco and Samuel Quisca Astocahuana

4 Numerical Modeling of Tsunami in the City of Chorrillos, Lima—Peru 41
Julio César Martínez Herrera
and Samuel Ismael Quisca Astocahuana

5 Evaluation and Correction of Rainfall Forecast by WRF Model in the Upper Reaches of the Yangtze River 61
Wei Fang, Jianzhong Zhou, Xin Yang, Benjun Jia, and Yurong Wang

6 Research and Application of Spatio-temporal Data Model of Water Supply Network Inspection System 69
Fuchen Ban, Xiaoyi Tong, and Zhitong Guo

7 Rapid Development of Online Hydraulic Model Calculation System Based on EPANET Source Code and ArcObjects 77
Fuchen Ban, Ke Xu, and Yueming Hei

8 Sprinkler Irrigation Atomization in Relation to Water Surface Tension: A New Laboratory Technique to Investigate Pesticides and Fertilizers Effect on Irrigation Drop Size 85
Azam Keneti, Davood Farsadizadeh, and Yadollah Bahramian

9 A Volterra Process Model for River Water Temperature 95
Hidekazu Yoshioka, Yumi Yoshioka, and Ayumi Hashiguchi

10 Solubilization of Polycyclic Aromatic Hydrocarbon Mixtures in Conventional and Gemini Surfactant Solutions 107
Jianfie Liu, Zhiyuan Zhao, and Yongsheng Zhang

11 A Sustainable Strategy for Petrochemical Wastewater Treatment via Anaerobic Co-Digestion 117
Anita Atukunda, Mona G. Ibrahim, Manabu Fujii, Shinichi Ookawara, and Mahmoud Nasr

12 Coagulation/Flocculation Treatment of Carwash Wastewater Using Natural-Based Material: A Sustainable Development Approach 129
Derrick Dadebo, Mahmoud Nasr, Manabu Fujii, and Mona G. Ibrahim

13 Phytoremediation of Textile Wastewater Using Water Hyacinth (*Eichhornia Crassipes*): A Sustainable Development Approach 141
Gelasius Gregory Msemwa, Mahmoud Nasr, Manabu Fujii, and Mona G. Ibrahim

14 Synthesis of Carbonized Bagasse and Orange Peel Wastes as Adsorbents for Dye Removal from Aqueous Solution: A Sustainable Approach 153
Bwambale Roice Kalengyo, Mona G. Ibrahim, Manabu Fujii, and Mahmoud Nasr

15 An Economic Evaluation of Integrated Desalination Systems Using Pressurized Water Reactor (PWR) 165
Thaqal Alhuzaymi and Meshari ALQahtani

16 A Cost Analysis Study of Nuclear Reactor Powered Desalination Process by DEEP Analysis—A Case Study of Saudi Arabia 179
Meshari ALQahtani and Thaqal Alhuzaymi

17 The Correlation between Water Eutrophication and Sediment Pollution in the Process of Black Odors Water Treatment: A Case Study of the Ximing River and Keli River in Nanning, China 191
Yang Yunan, Zhang Congcong, Liu Xinyu, Xiong Lin, Zhu Hongxiang, and Chen Yongli

18 The Research of Correlation Between Distribution of Bacteria and Removal of N, P in EHYBFAS 207
Y. N. Yang, H. J. Gong, Y. S. Chen, W. B. Jin, and B. Z. Wang

19 Hybrid Membrane-Thermal Seawater Desalination Engineering: Typical Technology Development and Future Prospects 221
Jianmei Xu, Jianbo Ren, Chungang Xie, Chunhua Qi, and Min Wang

20 Spatial Characteristics and Influencing Factors of Soil and Water Conservation Function in Xixia County of Henan Province 231
Aihong Gai, Xueliang Wang, Xiaoping Wang, Zhengwen Zhang, and Jinke Wei

21 Experiment on Vegetation Grass Blanket Bank Slope Protection Material for Scour Resistance and Soil Conservation 243
Li Ming, Yang Yanhua, Hong Houbing, Wang Lulu, Zhang Jing, Guan Zhenya, and Liu Weibin

22 Development Trend Analysis of Industrial Wastewater Treatment Based on Patent Analysis and Bibliometrics 251
Ma Jiahong, Wang Yang, Zheng Chunxiao, and Yu Jian

23 Intelligent Water Resources Management 263
Desislava Botseva, Nikola Tanakov, and Georgi Nikolov

24 Sustainable Cities via Smart Development Strategies: Bulgarian Case 275
Elka Vasileva, Veselina Lyubomirova, and Georgi Tsolov

25 Policy of the Republic of Bulgaria in the Field of Natural and Environmental Disasters 287
Dimitar Dimitrov, Elenita Velikova, and Ekaterina Bogomilova

26 Innovative Approaches to Reduce the Level of Environmental Pollution from Bus Transport in Sofia, Bulgaria 299
Elenita Velikova and Iliya Gatovski

27 Applications of DSF as Renewable Source Energy Savings in a Small Detached Family House Prototype 309
Eusébio Conceição, João Gomes, Mª Inês Conceição, Mª Manuela Lúcio, and Hazim Awbi

28 Thermal Engineering Applications in Forest Fire Environments 319
Eusébio Conceição, João Gomes, Mª Manuela Lúcio, Jorge Raposo, Domingos Xavier, and Mª Teresa Viegas

29 Airflow Inside of a Virtual Room Integrating a Vertical Confluent Jets Ventilation System 329
Eusébio Conceição, João Gomes, Mª Inês Conceição, Mª Manuela Lúcio, and Hazim Awbi

30 Integration Selective Lithium Exchange Membrane and Diffusion Dialysis to Recover Lithium Ions in Brine Water 337
Jih-Hsing Chang, Keng-Chi Wan, Mohanraj Kumar, and Shan-Yi Shen

31 Using Thermal Desorption Technique to Treat Real Field Diesel Oil-Contaminated Soils 347
Jih-Hsing Chang, Ching-Hsiang Tseng, Mohanraj Kumar, and Shan-Yi Shen

32 Experiment and Simulation of Mobile Underwater Dredger Fill in- Layers Technology in Open Water 357
Hui Sun, Jiaming Qu, Ran Tao, Qinze Chen, and Yuchi Hao

Chapter 1
Salinity Intrusion in the Vietnamese Mekong Delta, a Threat: Possible Causes, Effects on People's Life and Production, and Temporary Solutions and Adaptable Strategies

Nguyen Van Tho

Abstract The Vietnamese Mekong Delta is the most important agricultural production area in Vietnam. Most of this deltaic plain has an extremely low mean elevation of about 0.8 m above sea level and dissected by an inter-linked system of natural rivers and man-made canals connected to the sea. It is recognized as one of the areas worldwide most vulnerable to the impacts of climate change. In recent years, saline intrusion into the Vietnamese Mekong Delta has become increasingly serious due to a combination of factors, including the low topography, a dense system of rivers and canals connected to the sea, drought, low flow rates in the Mekong River during the dry season, growing competition for rapidly depleting water resources, sea level rise, and land subsidence. In 2020 saltwater intruded further inland than ever before and affected 10 out of 13 provinces of the Vietnamese Mekong Delta, causing severe damage to millions of hectares of farming land and the livelihoods of thousands of households. Solutions and adaptation strategies include storage of fresh water in ponds, shifting to farming systems and varieties that are more resilient to high salinity, changing cropping schedules, and building sluices to regulate saltwater intrusion. This paper discusses the main causes of salt intrusion, its effects on people's life and production, and adaptation strategies to mitigate its impacts.

Keywords Salinity intrusion · Vietnamese Mekong Delta · Climate change

1.1 Introduction

The Vietnamese Mekong Delta (VMD) is in the lower section of the Mekong River, adjacent to the sea. It covers an area of around 40,816 km^2 with a total population of over 17 million, accounting for more than 18% of the population in the country (GSO

N. Van Tho (✉)
Mien Tay Construction University, 20B, Pho Co Dieu Street, Ward 3, Vinh Long City, Vinh Long Province, Vietnam
e-mail: nguyenvantho@mtu.edu.vn

H.-Y. Jeon (ed.), *Sustainable Development of Water and Environment*,
Environmental Science and Engineering,
https://doi.org/10.1007/978-3-031-07500-1_1

2020). The VMD consists of 13 provinces/cities: Long An, Tien Giang, Dong Thap, Vinh Long, Tra Vinh, Hau Giang, Soc Trang, Ben Tre, An Giang, Kien Giang, Bac Lieu, Ca Mau and Can Tho city, the central city of the region (Fig. 1.1). The VMD is characterized by a tropical monsoon climate with two distinct seasons: dry season and rainy season. The dry season usually starts from November of the previous year until April of the following year. The rainy season is from May to October.

The VMD is quite flat (Fujihara et al. 2016); most of this deltaic plain has an extremely low mean elevation of about 0.8 m above sea level (Minderhoud et al. 2019) and dissected by an inter-linked system of natural rivers and man-made canals connected to the sea. Vietnam is among the five countries most likely to be most affected by climate change, in large part due to its location, the economy's dependence on sectors such as agriculture in flood-prone areas (WB 2018), and especially to the extreme vulnerability of the VMD to natural disasters and climate change (Clark et al. 2016). The VMD is the key agricultural production and aquaculture area of Vietnam, contributing half of Viet Nam's rice output, 65% of aquatic products and

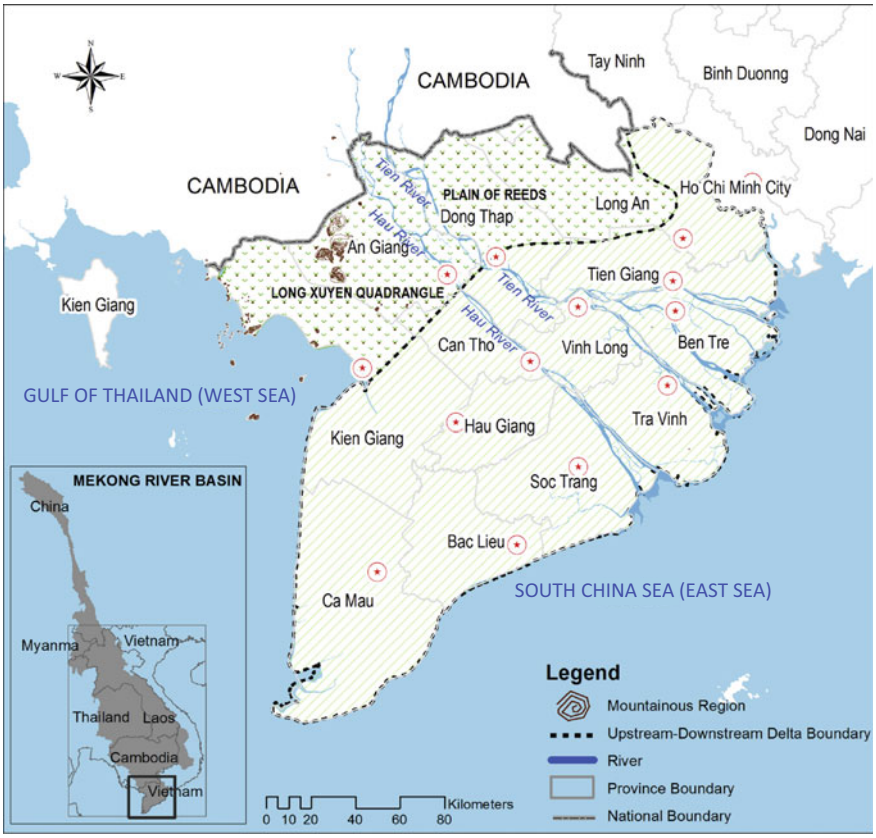

Fig. 1.1 Vietnamese Mekong Delta map and its provinces (Tran et al. 2019a)

70% of fruit. It also accounts for 95% of the country's rice exports and 60% of total overseas shipment of fish (Besset et al. 2019). In recent years, salt intrusion into the VMD has become increasingly serious. This paper discusses the causes of salt intrusion, its effects on production and livelihoods, and adaption strategies to mitigate its impacts.

1.2 Causes of Saline Intrusion in the Vietnamese Mekong Delta

There are many causes for salt intrusion. First, low topography combined with a dense system of rivers and canals allow saline water to penetrate into the delta, especially those parts near to the coast, which are usually affected by saltwater intrusion during the dry season. The VMD has an inter-linked system of natural rivers and man-made canals connected to the sea which facilitate the movement of saltwater inland (Fig. 1.2).

A second major contributor to saltwater intrusion is low flow rates in the Mekong River during the dry season. Flow rates during the dry season are barely 2% of those in the wet season, and are insufficient to prevent extensive and sustained saline

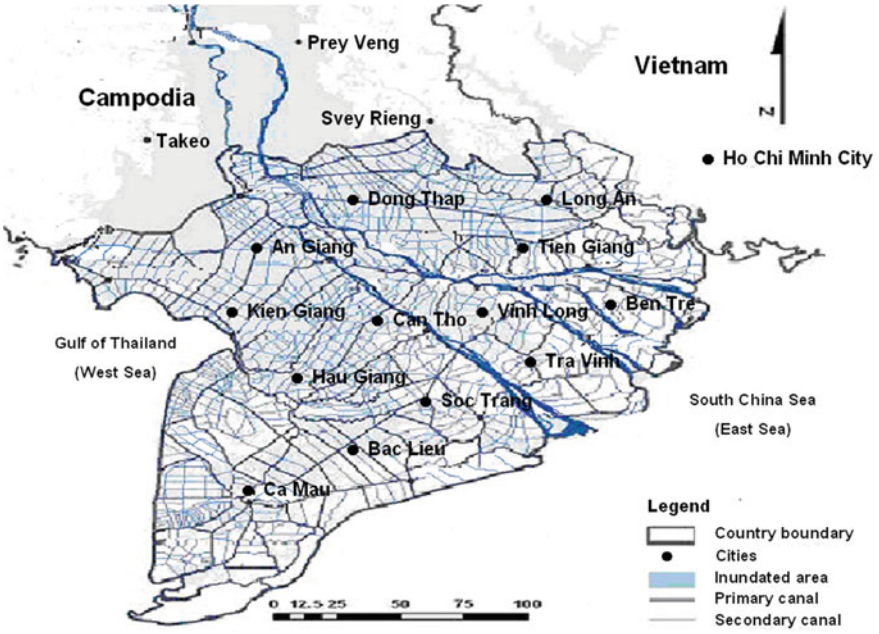

Fig. 1.2 Map showing the dense inter-linked system of natural rivers and man-made canals in the Vietnamese Mekong Delta (Adapted from MRC 2005)

intrusion (WB 2018). The overall hydrological regime in the VMD is directly affected by the upstream river flow, rainfall and the (differing) tidal regimes of the East Sea (South China Sea) and the West Sea (Gulf of Thailand). The low upstream flow period (December to May) occurs during the dry season and the earliest stages of the wet season. One reason for this is that the demand for hydropower has led upstream countries to construct series of dams on the main stream and tributaries of the Mekong River (Fig. 1.3). According to Bussi et al. (2021), a total of 284 dams have been built or are planned for construction on the Mekong River and its tributaries. Of these, 30 dams (seven already completed) are located on the main stem of the Mekong River, and the rest of them are on tributaries. There is evidence to show that existing dams already reduce the flow of water into the lower delta in the dry season (Cosslett and Cosslett 2014; Hecht et al. 2019; Binh et al. 2020). The seasonal discharge regime in the lower Mekong River is also expected to be affected directly by climate change; dry season discharges are predicted to decrease by 2% and the wet season discharges to increase by 5% over the next 30 years (Trieu and Phong 2015). Lower river flows, the lack of rain, and high evaporation during the annual dry season limit freshwater discharge rates which are unable to offset tidally driven salt intrusion. Consequently, salt intrusion often occurs in the Mekong River mouths and extends upstream inland from around December to May, with a peak at the end of April and early May every year.

Third, the VMD is facing growing competition for rapidly depleting water resources (WB 2018), mainly for agriculture and aquaculture. With an area of about 1.5 million ha of rice, including the late Winter-Spring (around January–February) and Summer-Early Autumn crops (sown around April–May), together with about 800,000 ha of aquaculture (670,000 ha of saline/brackish water and 130,000 ha of freshwater), the demand for fresh water for irrigation and aquaculture is very large (Anh 2019). Changes in rice cropping from 1–2 crops per year to 2–3 crops per year has increased the demand for water from about 400 m^3/second in April to 600–700 m^3/second (Anh 2019). Moreover, the construction of flood prevention dykes in the upstream areas of the VMD for agricultural cultivation, especially in two large low-lying areas, namely Dong Thap Muoi (Plain of Reeds) and the Long Xuyen Quadrangle has reduced the capacity of fresh water storage in upstream areas (Hoang et al. 2016). This has also contributed to a decrease in freshwater flows during the dry season. So, fresh water in the deltaic inland is not enough to prevent salt intrusion in this period, exacerbating saltwater intrusion into inland freshwater areas.

It has also been reported that the over-exploitation of ground water resources and land uses leading to land subsidence (Erban et al. 2014; Minderhoud et al. 2018), together with sea level rise induced by global climate change (Clark et al. 2016) have added to the threat of salinity intrusion in the VMD, and will continue to exacerbate the problem in the future.

In addition to the causes mentioned above, strong onshore winds from the east during the Northeast Monsoon or “Chuong Wind” (a local name) also contribute to salt intrusion by pushing saline water deeper into the rivers.

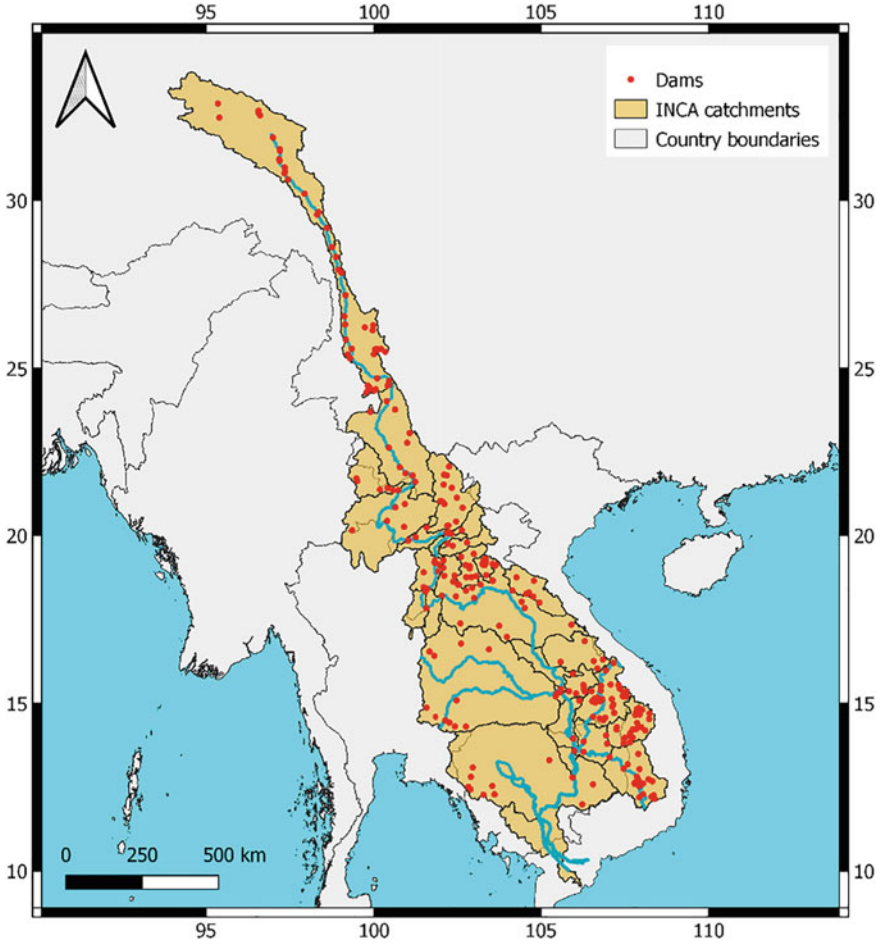

Fig. 1.3 Spatial distribution of dams within the Mekong River catchment (Bussi et al. 2021)

1.3 Effects of Saline Intrusion on People's Life and Production

One of the most severe cases of saline intrusion in the VMD occurred in 2016, when the rainy season in 2015 started late and ended early, resulting in a much lower than average rainfall. This, together with the reduction in water flow in the Mekong River in the early months of 2016, led to elevated salinities extending as far as 93 km upstream in the Mekong Delta (on the Vam Co River, and up to 50–70 km in other estuaries (MARD 2016). This had severe adverse impacts on many economic sectors and people's lives in 10 of the 13 provinces in the region (Long An, Tien Giang, Ben

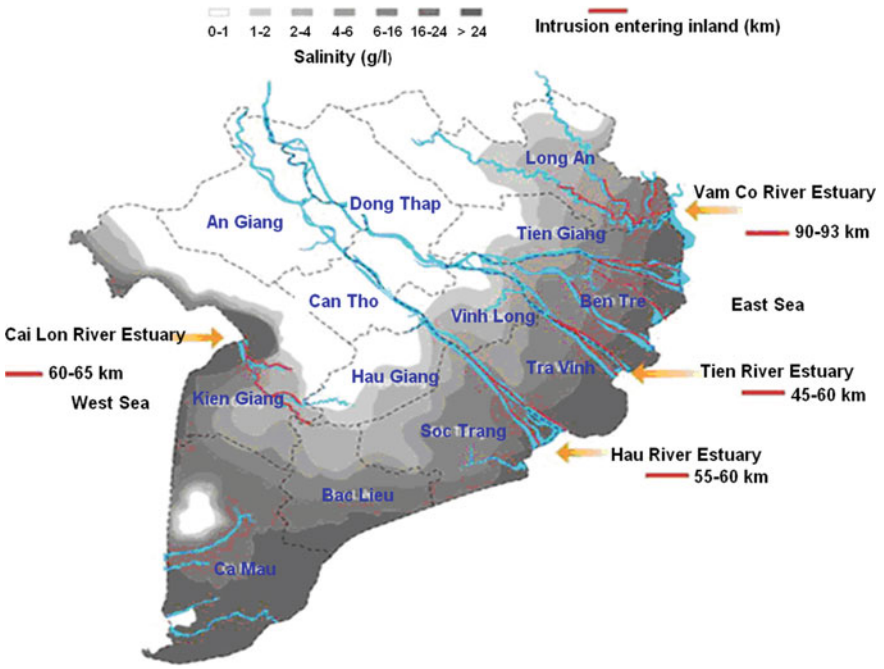

Fig. 1.4 Saltwater intrusion affected many provinces in the Mekong Delta until March 2016 (MARD 2016)

Tre, Tra Vinh, Soc Trang, Bac Lieu, Kien Giang, Ca Mau, Hau Giang and Vinh Long) (Fig. 1.4).

Saline intrusion also affected the availability of freshwater for domestic consumption and agricultural use, especially in many parts of Ca Mau, Kien Giang, Ben Tre, Tra Vinh, and Soc Trang which rely on groundwater for these purposes. Around 208,400 households (about 800,000 people), and many schools, clinics, hotels and factories experienced water shortages and salt intrusion (MARD 2016). According to Rentschler et al. (Rentschler et al. 2020), 22% of rice paddies in the VMD were exposed to salinity intrusion in 2016, leading to loss of 12% in national rice production and 8% in national agricultural GDP, directly affecting the livelihoods of some 3 million rice farmers.

The saltwater intrusion event of 2020 was even more serious than that of 2016, and it is the worst case of saltwater intrusion in the VMD until now. Saltwater intruded deeper inland than ever before and affected agricultural cultivation, aquaculture and livelihoods in 10 out of 13 provinces in the VMD. As an example of this, four villages, Dong Phu, Hoa Ninh, Binh Hoa Phuoc and An Binh, on a small island in the Tien River near Vinh Long city of Vinh Long province which had been in a fresh water area all year round for the past century, experienced a salinity of 4 g/l in the saltwater intrusion disaster of 2020. According to Phong (2020), water with a salinity of 4 g/liter affected 42.5% of the natural area of the whole VMD region,

equivalent to 1,688,600 ha, 50,376 ha more than in 2016. Ca Mau was the most affected province with damage to 16,500 ha of the crop area (including about 85% completely damaged, equivalent to 14,000 ha). For the 2019–2020 winter-spring rice crop, drought and saltwater intrusion affected about 41,900 ha, almost half of which (26,000 ha) experienced complete crop failure, in six provinces (Tra Vinh, Tien Giang, Soc Trang, Kien Giang, Long An and Ca Mau). Tra Vinh was the most severely affected province, with damage to 14,300 ha of rice. Drought and saltwater intrusion also damaged about 6,650 ha of fruit trees in six provinces (Long An, Tien Giang, Ben Tre, Vinh Long, Tra Vinh and Soc Trang), mainly due to a lack irrigation water, resulting in the complete loss of fruit production in 355 ha, and lower productivity elsewhere. More than 8,715 ha of aquaculture area in Ben Tre, Tien Giang, Kien Giang, Bac Lieu and Ca Mau also suffered damage. Altogether, a total of about 96,000 households, equivalent to about 430,000 people were affected by drought and saline intrusion in seven coastal provinces (Ben Tre, Soc Trang, Kien Giang, Ca Mau, Bac Lieu, Long An and Tra Vinh).

1.4 Mitigation and Adaptation Strategies

Because of the agricultural and aquacultural significance of the VMD, local and central government authorities, and farm households have employed a range of engineering and land use strategies to adapt to or mitigate the impacts of saline intrusion. With respect to land use strategies, many farmers who live in areas affected by salt intrusion, have switched from a rice only or rice plus fish farming system to an integrated rice-shrimp farming system where they raise shrimp such as *Penaeus monodon* and *Litopenaeus vannamei* during the dry season and grow rice in the rainy season. This relatively new and very innovative solution carried out by farmers to adapt to saline intrusion helps both to increase farm productivity and to address the shortage of freshwater in the dry season. Another strategy to minimize the impacts of salinity dig an internal ditch system across the rice field to drain out saltwater and store freshwater, which has proven effective to maintain soil moisture and prevent salt deposition (Tran et al. 2019b). Farmers also pump freshwater into canals or small ponds lined with plastic or canvas, or in the case of orchards and vegetable gardens, in long tubular plastic bags which can be rolled up and reused in the future. This provides a better means to store and use freshwater for crop irrigation in conditions of prolonged heat or freshwater scarcity. Many farmers have converted their inefficient coastal rice farming areas, often threatened by saltwater intrusion, to aquaculture. They have also used more salinity-tolerant rice varieties, changed irrigation schedules, and altered rice-planting times to deal with salt intrusion.

Local and central governments have implemented many interventions to deal with saline water intrusion. At a community level, before salinity intrusion occurs, local authorities usually carry out community extension programmes to inform people on measures and tools to store fresh water, in order to ensure sufficient fresh water to sustain daily life and agricultural production during the period of drought or saline

water intrusion. A network of salinity monitoring stations has already been established throughout the VMD. The government has also built sluice gates at many strategic locations in the VMD to control the intrusion of saline water. Under current policy these are closed when salt levels reach 1.5 parts per thousand. Saline monitoring stations in the VMD have now been added by the government in accordance with the Prime Minister's Decision No. 16/QD-TTg issued on January 29, 2007, on the overall planning of monitoring network of National Natural Resources and Environment by 2020. The Prime Minister issued Directive No. 09/CT-TTg dated 12 March 2016 on the implementation of urgent measures to respond to saline intrusion in the VMD. The central government has provided financial support to communities and provincial authorities to mitigate the consequences of salt intrusion and reduce damage to agriculture and other economic sectors (Prime Ministerial Directive No. 09/CT-TTg dated 12 March 2016), committing a total of 523,700 million VND for the first phase (MARD 2016). According to a UNDP Disaster Management Unit Project (VIE/97/002) managed by the General Department of Land Administration, a sea dike of about 1,469 km in length is required to protect the VMD from saltwater intrusion and water level rise (Khong et al. 2018). The cost for a concrete sea dike 2 m high is about 1.16 million USD per km, rising to 2.8 million USD per km for height of 4 m (Khong et al. 2018). Thus the cost of building a 1,469 km long sea dike to protect the whole VMD is prohibitively expensive. Consequently, the central government has focused on supporting the construction of over 450 km of sea dikes, 1,290 km of river dikes and about 7,000 km of intra-field canals to reduce salinity intrusion and flooding in the most vulnerable parts of the VMD. In addition, the Government has recently built large sluice gates at the mouths of the Cai Lon (455 m in width) and Cai Be (85 m in width) Rivers in An Bien and Chau Thanh districts in Kieng Giang province on the west coast of the VMD, at an investment cost of over 3,300 billion VND. These replace a number of smaller, temporary sluice gates and control sea water and fresh water for agriculture and aquaculture in four provinces, Kien Giang, Hau Giang, and some parts of Ca Mau and Bac Lieu.

The Government of Vietnam has strengthened international cooperation with countries in the Mekong Committee and with China to reach agreement on common interests in the development and prosperity of the region in accordance with the 1995 Mekong Agreement, and has signed bilateral or multilateral agreements with each country, especially related to the use of Mekong River water. An example of this is that on March 7, 2016, the Ministry of Foreign Affairs of Vietnam issued a diplomatic note (No. 128/NG-ĐBA) to the Embassy of the People's Republic of China in Vietnam requesting China to increase water discharge from China's hydropower dams to the Lower Mekong River to help prevent salt intrusion. In response, Chinese authorities authorized emergency water discharge during the period from March 15, 2016 to April 10, 2016 (MOST 2016). This fresh water reached Vietnam in early April 2016 and helped to partly push the salt water wedge seawards. However, as more dams along the Mekong River come online, the lack of freshwater flow in the lower arms of the Mekong River will present an ever increasing challenge for dealing with salt intrusion into the VMD.

1.5 Conclusions

The VMD plays an important role in providing food and seafood not only for the region but also for the country, and for export. The delta is located at the end of the Mekong River, with relatively low terrain, along with the dense system of rivers and canals connecting to the sea. The pressure to use water in the region, the competition to exploit water from upstream countries especially in the dry season and rise level sea due to the effects of global climate change are the main causes leading to saline intrusion for the region. Saline intrusion has seriously affected the lives and production of thousands of households, and impacted on millions of hectares of farming soil in the region in recent years, especially in 2016 and 2020. Although a number of strategies have been employed to mitigate and adapt to the consequences of salt intrusion, current strategies may be ineffective in the longer term, because the problem is likely to become more serious in the future, mainly as a result of further reduction in fresh water flow due to dam construction, and because of rising sea levels. Therefore, the long-term delta wide strategy to adapt with saltwater intrusion should focus on "living with and adapting to saline intrusion". This requires careful land use planning to develop and maintain salt-free upstream zones to grow food crops such as rice and fruit trees, and to cultivate freshwater aquaculture. Areas vulnerable to salinization can be converted to saltwater aquaculture (e.g. shifting ineffective rice-planting areas affected by saline intrusion to tiger shrimp cultivation) and areas at less risk of saline intrusion can switch to a combination of brackish water aquaculture and agricultural cultivation. These strategies could help people in the VMD to adapt to saline intrusion in the future while ensuring food security, stabilizing livelihoods, and maintaining economic development. Some farmers have already applied these alternative land use strategies, apparently with some success, but so far there have been no formal studies of their benefits and drawbacks, and over what time frames they might continue to be effective as adaptations to deal with the adverse impacts of salinity intrusion. Further studies of these and other potential options are needed to ensure that they are effective and they can bring cost-effective long-term benefits to the region.

References

Anh NN (2019) Causes of increased saline intrusion in the Mekong Delta and management solutions. http://www.tongcucthuyloi.gov.vn/Tin-tuc-Su-kien/Tin-tuc-su-kien-tong-hop/catid/12/item/2671/nguyen-nhan-xam-nhap-man-tang-cao-o-dong-bang-song-cuu-long-va-giai-phap-quan-ly (in Vietnamese language). Last accessed 25 July 2021

Besset M, Gratiot N, Anthony EJ, Bouchette F, Goichot M, Marchesiello P (2019) Mangroves and shoreline erosion in the Mekong River delta, Viet Nam. Estuar Coast Shelf Sci 226:1–9

Binh DV, Kantoush SA, Saber M, Mai NP, Maskey S, Phong DT, Sumi T (2020) Long-term alterations of flow regimes of the Mekong River and adaptation strategies for the Vietnamese Mekong Delta. J Hydrol Reg Stud 32:1–21

Bussi G, Darby SE, Whitehead PG, Jin L, Dadson SJ, Voepel HE, Vasilopoulos G, Hackney CR, Hutton C, Berchoux T, Parsons DR, Nicholas A (2021) Impact of dams and climate change on suspended sediment flux to the Mekong delta. Sci Total Environ 75:1–12

Clark PU, Shakun JD, Marcott SA, Mix AC, Eby M et al (2016) Consequences of twenty-first-century policy for multi-millennial climate and sea-level change. Nat Clim Chang 6:360–369

Cosslett TL, Cosslett PD (2014) Major threats to Mekong Delta: climate change and mainstream dams. In: Water resources and food security in the Vietnam Mekong Delta. Natural resource management and policy, vol 44. Springer, Cham, pp 75–96

Erban LE, Gorelick SM, Zebker HA (2014) Groundwater extraction, land subsidence, and sea-level rise in the Mekong Delta, Vietnam. Environ Res Lett 9:1–6

Fujihara Y, Hoshikawa K, Fujii H, Kotera A, Nagano T, Yokoyama S (2016) Analysis and attribution of trends in water levels in the Vietnamese Mekong Delta. Hydrol Process 30:835–845

GSO (General Statistics Office of Viet Nam) (2020) Statistical Yearbook of Vietnam 2019. Statistical Publishing House, Ha Noi

Hecht JS, Lacombe G, Arias ME, Dang TD, Piman T (2019) Hydropower dams of the Mekong River basin: a review of their hydrological impacts. J Hydrol 568:285–300

Hoang LP, Lauri H, Kummu M, Koponen J, van Vliet MTH, Supit I, Leemans R, Kabat P, Ludwig F (2016) Mekong River flow and hydrological extremes under climate change. Hydrol Earth Syst Sci 20:3027–3041

Khong TD, Young MD, Loch A, Thennakoon J (2018) Mekong River Delta farm-household willingness to pay for salinity intrusion risk reduction. Agric Water Manag 200:80–89

MARD (Ministry of Agriculture and Rural Development) (2016) Drought, saline intrusion in the Mekong Delta. http://mtnn.mard.gov.vn/5/chi-tiet-tin-tuc-229/han,-man-tien-cong-dong-bang-song-cuu-long (the paper in Vietnamese). Last accessed 25 July 2021

Minderhoud PSJ, Coumou L, Erban LE, Middelkoop H, Stouthamer E, Addink EA (2018) The relation between land use and subsidence in the Vietnamese Mekong delta. Sci Total Environ 634:715–726

Minderhoud PSJ, Coumou L, Erkens G, Middelkoop H, Stouthamer E (2019) Mekong delta much lower than previously assumed in sea-level rise impact assessments. Nat Commun 10(3847):1–13

MOST (Ministry of Science and Technology of Vietnam) (2016) Saline intrusion in the Mekong Delta—effective solutions dealing with climate change conditions (in Vietnamese). https://www.most.gov.vn/vn/tin-tuc/7039/xam-nhap-man-tai-dong-bang-song-cuu-long---nhung-giai-phap-ung-pho-hieu-qua-trong-dieu-kien-bien-doi-khi-hau.aspx. Last accessed 25 July 2021

MRC (Mekong River Commission) (2005) Overview of the hydrology of the Mekong Basin. Mekong River Commission, Vientiane

Phong T (2020) The most severe drought and salinity in the history of the Mekong Delta (in Vietnamese language). https://nhandan.vn/chuyen-lam-an/dot-han-man-nghiem-trong-nhat-trong-lich-su-dbscl-475180/. Last accessed 30 July 2021

Rentschler J, de Vries Robbé S, Braese J, Huy Nguyen D, van Ledden M, Pozueta Mayo B (2020) Resilient shores: Vietnam's coastal development between opportunity and disaster risk. The World Bank, Washington, DC

Tran DD, Halsema GV, Hellegers PJGJ, Hoang LH, Ludwig F (2019a) Long-term sustainability of the Vietnamese Mekong Delta in question: an economic assessment of water management alternatives. Agric Water Manag 223:1–12

Tran TA, Nguyen TH, Vo TT (2019b) Adaptation to flood and salinity environments in the Vietnamese Mekong Delta: empirical analysis of farmer-led innovations. Agric Water Manag 216:89–97

Trieu TTN, Phong NT (2015) The impact of climate change on salinity intrusion and Pangasius (Pangasianodon Hypophthalmus) farming in the Mekong Delta, Vietnam. Aquac Int 23:523–534

WB (World Bank) (2018) Vietnam-Mekong Delta water management for rural development project. The World Bank, Washington, DC

Chapter 2
Improved Stochastic Fractal Search Algorithm for Joint Optimal Operation of Cascade Hydropower Stations

Zhanxing Xu, Jianzhong Zhou, Yuqi Yang, and Zhou Qin

Abstract The joint optimal operation of cascade reservoirs can not only improve the overall capacity of flood control and disaster reduction, but also increase the power generation benefit of hydropower stations, which is conducive to the efficient utilization of water resources in the basin. Long-term joint operation of hydropower stations is a typical multi-stage constrained optimization problem, which has the characteristics of high dimension, nonlinear and strong coupling. To solve this problem effectively, this paper proposes an improved stochastic classification algorithm (ISFS) based on the stochastic fractal search (SFS) algorithm and the disruption operator. The simulation results of 13 benchmark functions show that the algorithm can effectively improve the optimization performance of SFS. The calculation results of the joint operation of four cascade hydropower stations in the upper reaches of the Yangtze River show that the proposed algorithm is superior to the comparison method in terms of convergence speed and solution quality, and the overall power generation of cascade hydropower stations is significantly increased, which proves the advantages of the proposed algorithm in solving the joint operation problem of reservoir groups.

Keywords Improved stochastic fractal search algorithm · Cascade hydropower stations · Joint optimal operation

2.1 Introduction

In the context of "emission peak, carbon neutrality" policy, clean energy such as hydro energy, wind energy and solar energy are gradually highlighting their advantages

Z. Xu (✉) · J. Zhou (✉) · Y. Yang · Z. Qin
School of Civil and Hydraulic Engineering, Huazhong University of Science and Technology, Wuhan 430074, People's Republic of China
e-mail: zhanxing@hust.edu.cn

J. Zhou
e-mail: jz.zhou@hust.edu.cn

Hubei Key Laboratory of Digital Valley Science and Technology, Wuhan 430074, China

H.-Y. Jeon (ed.), *Sustainable Development of Water and Environment*,
Environmental Science and Engineering,
https://doi.org/10.1007/978-3-031-07500-1_2

of renewable and low emission, and vigorously developing clean energy will be the main direction of world energy strategy development in the future. Due to the inherent intermittence and fluctuation of wind power and photovoltaic, its extensive grid connection will directly affect the safe and stable operation of the power grid, and hydropower energy will play a more important role in the future power system with the characteristics of rapid start and stop, strong regulation performance and low operation cost (Sun et al. 2021).

Hydropower dispatching is a necessary means for space–time regulation of hydropower energy. Scientific optimal dispatching is beneficial to improve the utilization rate of hydropower energy and is of great significance for the full play of water resources in the basin (Yang et al. 2016). Mathematically, hydropower dispatching involves multiple decision variables and physical constraints, which is a complex constrained optimization problem. In order to solve this problem effectively, researchers all over the world have successfully developed various optimization methods. It mainly includes linear programming, nonlinear programming, dynamic programming, and other deterministic algorithms, but with the increase of computational dimension, this kind of algorithm has a disadvantage in computational efficiency (Feng et al. 2020). With the development of artificial intelligence and system theory, intelligent optimization algorithm has been deeply studied and widely used in hydropower optimal operation.

Genetic algorithm (GA), individual swarm optimization (PSO), differential evolution algorithm (DE), gravitational search algorithm (GSA), and other swarm intelligence methods have stronger adaptability and higher efficiency than traditional optimization algorithms (He et al. 2019). In recent years, they have been widely studied in solving reservoir optimal operation problems. However, swarm intelligence methods are usually limited by premature convergence and unstable solutions. Therefore, researchers try to develop more effective optimization tools to solve hydropower dispatching problems. Stochastic fractal search (SFS) is a new swarm intelligence method, which is inspired by fractal theory in geometry and has better global search ability and solving efficiency (Salimi 2015). In order to explore the feasibility of a stochastic fractal search algorithm in the optimal operation of cascade reservoirs, we developed the long-term optimal operation model of XLD, XJB, TGR, and GZB cascade hydropower stations, and proposed an improved stochastic fractal search algorithm to improve the optimization performance of standard SFS. Numerical experiments and real-world simulation results show the effectiveness and robustness of the method.

The main contributions of this study are as follows: (1) the generation scheduling optimization model is developed for cascade hydropower stations; (2) An ISFS algorithm combined with disruption operator is proposed to improve the performance of SFS; (3) Compared with the existing methods, this method achieves better results in numerical experiments and practical simulation, and provides a practical method for complex engineering optimization problems. The rest of this paper is organized as follows. Section 2.2 gives the operation optimization model of cascade hydropower stations. Section 2.3 presents the ISFS method. Section 2.4 tests the feasibility of

ISFS in 13 benchmark functions. Section 2.5 gives the application of ISFS to cascade hydropower station scheduling problem. The conclusions are summarized in the end.

2.2 Optimization Model for Cascade Hydropower Stations

2.2.1 Objective Function

In this research, taking the maximum total output of cascade hydropower stations as the optimization criterion, the objective function is described as follows:

$$E = \max \sum_{i=1}^{M} \sum_{t=1}^{T} K_i \cdot H_{i,t} \cdot Q_{i,t} \cdot \Delta t \tag{2.1}$$

where E is the total power generation of cascade hydropower stations; M is the total number of power stations; T is the total number of dispatching periods; K_i is the comprehensive output coefficient of the ith power station; $H_{i,t}$ and $Q_{i,t}$ is the average generating head and generating flow of the ith power station in tth period, respectively; Δt is the length of each period.

2.2.2 Constraints

(1) Water level constraint:

$$\underline{Z}_{i,t} \leq Z_{i,t} \leq \overline{Z}_{i,t} \tag{2.2}$$

where $\overline{Z}_{i,t}$ and $\underline{Z}_{i,t}$ represent the maximum water level limit and minimum water level limit of the ith power station in tth period respectively.

(2) Initial and final water level constraints

$$Z_{i,0} = Z_{i,\text{Begin}}, Z_{i,T} = Z_{i,\text{End}} \tag{2.3}$$

where $Z_{i,\text{Begin}}$ and $Z_{i,\text{End}}$ are the water level limits at the beginning and end of the dispatching period of the ith power station.

(3) Output constraint:

$$\underline{N}_{i,t} \leq N_{i,t} \leq \overline{N}_{i,t} \tag{2.4}$$

where $\overline{N}_{i,t}$ and $\underline{N}_{i,t}$ are the maximum output system and minimum output limit of the ith power station in tth period.

(4) Discharge constraint:

$$\underline{Q}_{i,t} \leq Q_{i,t} \leq \overline{Q}_{i,t} \tag{2.5}$$

where $\overline{Q}_{i,t}$ and $\underline{Q}_{i,t}$ are the maximum and minimum discharge limits of the ith power station in tth period.

(5) Equation of water balance:

$$V_{i,t+1} = V_{i,t} + (I_{i,t} - Q_{i,t}) \cdot \Delta t \tag{2.6}$$

where $V_{i,t}$ and $V_{i,t+1}$ are the initial and final storage capacity of the ith power station period respectively; $I_{i,t}$ and $Q_{i,t}$ are the inflow flow and discharge flow of the ith power station period respectively, and Δt is the period length.

(6) Water level amplitude constraint:

$$\Delta \underline{Z}it \leq \Delta Zit \leq \Delta \overline{Z}it \tag{2.7}$$

where $\Delta \overline{Z}it$ and $\Delta \underline{Z}it$ respectively represent the upper and lower limits of the fluctuation amplitude of the water level of the ith power station in tth period.

(7) Hydraulic connection between cascade hydropower stations:

$$I_{i,t} = Q_{i-1,t} + q_{i,t} \tag{2.8}$$

where $I_{i,t}$ is the inflow of the ith power station in tth period, $Q_{i-1,t}$ is the outflow of the upstream power station, and $q_{i,t}$ is the interval inflow of the upstream and downstream power stations.

2.3 Improved Stochastic Fractal Search Algorithm

2.3.1 Overview of Stochastic Fractal Search Algorithm (SFS)

Stochastic fractal search algorithm (SFS) searches the optimal solution by the diffusion property of fractal. The algorithm mainly includes two processes, diffusion process and update process. In diffusion process, the Gaussian distribution is selected as the random walk mode, in which each individual is diffused around its current position to generate a new generation. This step can be regarded as the exploitation phase of SFS algorithm. For each individual that diffuses, the position of each new individual is created through Gaussian walking and find the best individual among

all individuals (Fig. 2.1). The Gaussian walking function can be expressed as one of the following two equations:

$$GW_1 = Gaussian(\mu_{BP}, \sigma) + (\varepsilon \cdot BP - \varepsilon' \cdot P_i) \tag{2.9}$$

$$GW_2 = Gaussian(\mu_P, \sigma) \tag{2.10}$$

where ε and ε' are random numbers between [0, 1], BP is the optimal individual, P_i is the position of the ith individual, μ_{BP} and σ are Gaussian distribution parameters.

After that is the update process of the SFS, which can be considered as the exploration stage of the algorithm. The process consists of two updates. The first update is for individual components, and the chance of individual component change is determined by sorting individual fitness values and calculating performance indicators. The better the individual fitness, the greater the chance of individual component change, the change formula of performance index and individual component is as follows

$$P_{ai} = \frac{rank(P_i)}{N} \tag{2.11}$$

$$P_i^{'}(j) = P_r(j) - \varepsilon(P_t(j) - P_i(j)) \tag{2.12}$$

where $P_i^{'}$ is the new modified position of P_i, P_r and are random selected individuals in the population.

The second update process aims to change the position of an individual by considering the position of other individuals in the population. This procedure improves the quality of exploration and thus meets the attributes of diversity. Before the second update process begins, all individuals obtained from the first update process need to be sorted again based on Formula 2.10, and then modify the position of $P_i^{'}$ as

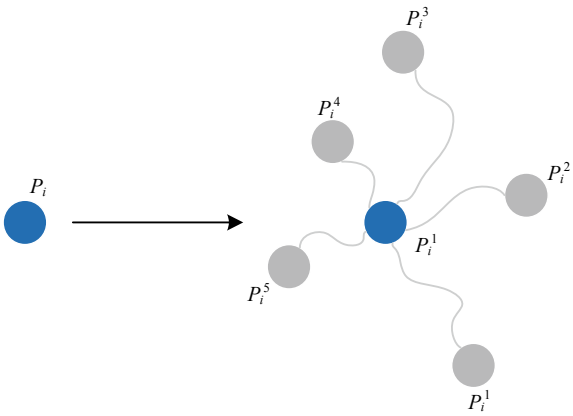

Fig. 2.1 Diffusing a individual in SFS

follows:

$$\begin{cases} P_i^{''} = P_i^{'} - \varepsilon^{'} \cdot (P_t^{'} - BP)\,\varepsilon^{'} \leq 0.5 \\ P_i^{''} = P_i^{'} + \varepsilon^{'} \cdot (P_t^{'} - P_r^{'})\,\varepsilon^{'} > 0.5 \end{cases} \tag{2.13}$$

where $P_i^{''}$ is the position of the individual after the second update, P_r and P_t are two different random points selected from the group, BP is the best point and ε is a random number within the range [0, 1].

2.3.2 *Improved Stochastic Fractal Search Algorithm (ISFS)*

Improved strategy. In practice, it is found that although the SFS algorithm has better global convergence ability than GA, PSO, DE, GSA, and other algorithms, there are still problems of precocity and falling into local optimum when standard SFS algorithm solves some complex optimization problems. In order to improve the performance of the SFS algorithm, a disruption operator is introduced in this section, which is incorporated into the diffusion and update evolution process of the algorithm, an improved stochastic fractal algorithm is proposed.

It is assumed that there is gravitational interaction among individuals in the current system, and other individuals in the system may be disturbed and scattered by the gravitational interaction of the current iterative optimal individual (Fig. 2.2). In order to prevent the divergence of solution and the complexity of the algorithm, the ratio of the distance between each individual and the nearest individual and the distance between the individual and the optimal individual of the system is calculated. If the ratio is less than a certain threshold C, the individual will be destroyed:

$$\frac{R_{i,j}}{R_{i,best}} < C \tag{2.14}$$

where $R_{i,j}$ and $R_{i,best}$ represent the Euclidean distance between the ith individual and the nearest individual in the decision space and the Euclidean distance between the individual and the optimal solution individual in the system, respectively. When the individuals disperse, the threshold C must be large enough to provide more exploration ability. When the individuals gather, the threshold C needs to be small to increase the development ability of the algorithm.

For the individuals that meet the conditions, the position information of each individual is adjusted according to Eq. (2.15):

$$\begin{cases} X_i(new) = X_i(old) + R_{i,j} \cdot U(-0.5, 0.5) \text{ if } \mathrm{R}_{i,best} \geq 1 \\ X_i(new) = X_i(old) \times U(-0.5, 0.5) \text{ otherwise} \end{cases} \tag{2.15}$$

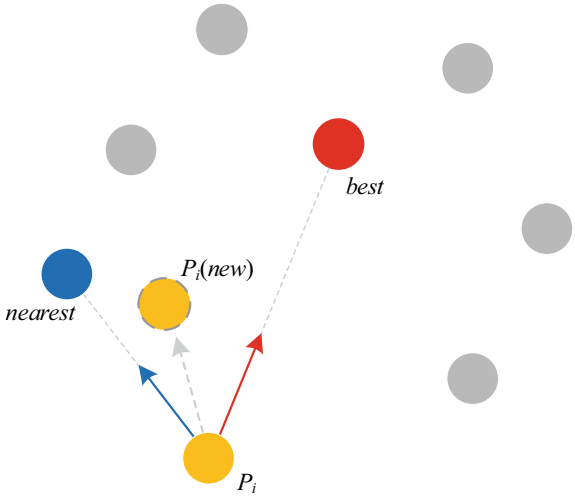

Fig. 2.2 Sketch map of the disruption operator

where $R_{i,j}$ is the distance between the ith individual and the nearest jth individual, and $U(-0.5, 0.5)$ is a random number in the range of $[-0.5, 0.5]$. The formula shows that when $R_{i,best} \geq 1$, the algorithm increases the ability of exploration and tries to explore the better solution in the search space. When $C < 1$, the development ability of the algorithm is gradually enhanced to improve the local optimization performance, which can improve the flexibility of solving more complex problems.

Execution procedure of the proposed method. Taking the standard SFS algorithm as the parent algorithm, by introducing the above disruption operator, we embed it into the diffusion update program of the SFS algorithm, and then propose an improved SFS algorithm, as shown in Fig. 2.3.

The overall procedure used by the proposed ISFS algorithm can be described as following steps.

Step 1: Set the parameters of the algorithm and initialize the population.
Step 2: Calculate the fitness value of each individual in the population and find the global optimal individual.
Step 3: Each individual in the population is diffused by Gaussian walk, and the individual is replaced by the optimal individual generated in the process of each split diffusion, and the global optimal individual is found.
Step 4: Execute the disruption operator to update the position of the individuals satisfying Eq. (2.14).
Step 5: Execute the first update.
Step 6: Execute the second update.
Step 7: Determine whether the number of iterations reaches the maximum number of iterations. If the maximum number of iterations has been reached, the algorithm ends and outputs the result; Otherwise, execute step 3.

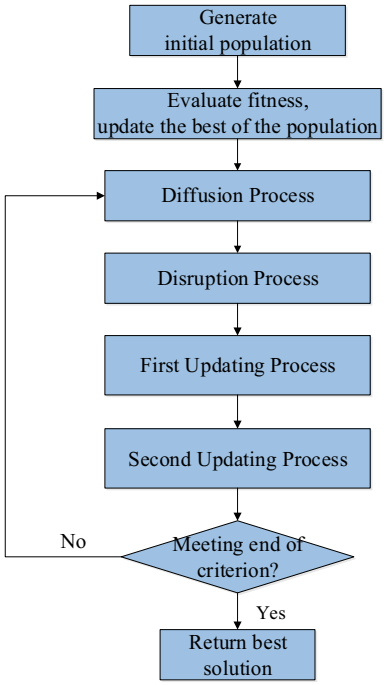

Fig. 2.3 A block diagram of the proposed ISFS algorithm

2.4 Numerical Experiments to Verify the ISFS Performance in Benchmark Functions

To test the optimization performance of the improved algorithm proposed in this paper, 13 benchmark functions in Tables 2.1 and 2.2 are used to test the optimization performance of the ISFS and the SFS. In the simulation experiment, the dimension of the benchmark function is set as 30, the number of individual population is set as 50, and the total number of iterations is set as 1000. The test function is tested 30 times by ISFS and SFS. Then the results and convergence curves are compared and analyzed.

2.4.1 Benchmark Functions

Tables 2.1 and 2.2 are benchmark functions used to test the algorithm, where n is the dimension of benchmark function, S is the definition space of each benchmark function, and is a subset of real number set R^n. The minimum values of benchmark functions in Tables 2.1 and 2.2 in the definition space are all zero, except for F_8 which has a minimum value of $-418.9829 \times n$. Except for F_5, F_{12}, F_{13} and F_8, the

Table 2.1 Unimodal test functions

Test function	S	f_{opt}
$F_1(X) = \sum_{i=1}^{n} x_i^2$	$[-100, 100]^n$	0
$F_2(X) = \sum_{i=1}^{n} \lvert x_i \rvert + \prod_{i=1}^{n} \lvert x_i \rvert$	$[-10, 10]^n$	0
$F_3(X) = \sum_{i=1}^{n} (\sum_{j=1}^{i} x_j)^2$	$[-100, 100]^n$	0
$F_4(X) = \max_i \{\lvert x_i \rvert, 1 \le i \le n\}$	$[-100, 100]^n$	0
$F_5(X) = \sum_{i=1}^{n-1} [100(x_{i+1} - x_i^2)^2 + (x_i - 1)^2]$	$[-30, 30]^n$	0
$F_6(X) = \sum_{i=1}^{n} ([x_i + 0.5])^2$	$[-100, 100]^n$	0
$F_7(X) = \sum_{i=1}^{n} i x_i^4 + random[0, 1)$	$[-1.28, 1.28]^n$	0

Table 2.2 Multimodal test functions

Test function	S	f_{opt}
$F_8(X) = \sum_{i=1}^{n} -x_i \sin(\sqrt{\lvert x_i \rvert})$	$[-500, 500]^n$	$-418.9829 \times n$
$F_9(X) = \sum_{i=1}^{n} [x_i^2 - 10\cos(2\pi x_i) + 10]$	$[-5.12, 5.12]^n$	0
$F_{10}(X) = -20\exp(-0.2\sqrt{\frac{1}{n}\sum_{i=1}^{n} x_i^2}) - \exp(\frac{1}{n}\sum_{i=1}^{n} \cos(2\pi x_i)) + 20 + e$	$[-32, 32]^n$	0
$F_{11}(X) = \frac{1}{4000}\sum_{i=1}^{n} x_i^2 - \prod_{i=1}^{n} \cos(\frac{x_i}{\sqrt{i}}) + 1$	$[-600, 600]^n$	0
$F_{12}(x) = \frac{\pi}{n}\{10\sin^2(\pi y_1) + \sum_{i=1}^{n-1} (y_i - 1)^2[1 + 10\sin^2(\pi y_{i+1})] + (y_n - 1)^2\} + \sum_{i=1}^{n} u(x_i, 10, 100, 4)$, $y_i = 1 + \frac{x_i + 1}{4}$, $u(x_i, a, k, m) = \begin{cases} k(x_i - a)^m & x_i > a \\ 0 & -a < x_i < a \\ k(-x_i - a)^m & x_i < -a \end{cases}$	$[-50, 50]^n$	0
$F_{13}(X) = 0.1\{\sin^2(3\pi x_1) + \sum_{i=1}^{n} (x_i - 1)^2[1 + \sin^2(3\pi x_1 + 1)] + (x_n - 1)^2[1 + \sin^2(2\pi x_n)]\} + \sum_{i=1}^{n} u(x_i, 5, 100, 4)$	$[-50, 50]^n$	0

optimal positions of other test functions are all $[0]^n$, in which the optimal positions of 5, 12 and 13 are all $[1]^n$, and the optimal positions of F_8 are $[420.96]^n$.

2.4.2 Experimental Results

For the unimodal benchmark function in Table 2.1, the ISFS and the standard SFS are used to optimize F_1–F_7 for 30 times respectively. The statistics of the calculation results (optimal value, worst value, and mean value) are listed in Table 2.3. It can be seen from the table that the search effect of the ISFS algorithm is obviously better than that of the standard SFS algorithm except for F_5.

For high-dimensional unimodal function, the optimal convergence curves of ISFS and SFS for F_1, F_2, F_3 and F_4 are shown in Fig. 2.4. It can be seen that the convergence process of the standard SFS algorithm is relatively smooth, while the optimization process of the ISFS algorithm is steeper and faster, and it can be seen from F_3 and F_4, The convergence process of the ISFS algorithm has an obvious inflection point in about 400 iterations, which shows that the algorithm has good performance of jumping out of local convergence, and the disruption operator effectively enhances the global exploration ability of the algorithm, which is better than the standard SFS algorithm.

Table 2.3 Statistical indexes of two algorithms for unimodal functions in 30 independent runs

		SFS	ISFS
F_1	Best best-so-far	6.81×10^{-84}	0
	Average mean fitness	2.55×10^{-70}	0
	Std best-so-far	1.79×10^{-70}	0
F_2	Best best-so-far	1.1×10^{-52}	3.3×10^{-207}
	Average mean fitness	6.7×10^{-49}	5.3×10^{-200}
	Std best-so-far	6.3×10^{-49}	0
F_3	Best best-so-far	3.3×10^{-24}	0
	Average mean fitness	1.3×10^{-15}	7.6×10^{-177}
	Std best-so-far	5.5×10^{-16}	0
F_4	Best best-so-far	3.5×10^{-17}	3.4×10^{-174}
	Average mean fitness	4.6×10^{-11}	1.1×10^{-79}
	Std best-so-far	4.2×10^{-11}	9.6×10^{-80}
F_5	Best best-so-far	26.3	26.7
	Average mean fitness	26.8	27.5
	Std best-so-far	0.11	0.2
F_6	Best best-so-far	1.89	0.94
	Average mean fitness	2.69	1.16
	Std best-so-far	0.1	0.04
F_7	Best best-so-far	1.6×10^{-4}	4.4×10^{-7}
	Average mean fitness	0.001	5.5×10^{-6}
	Std best-so-far	3.1×10^{-4}	2.1×10^{-6}

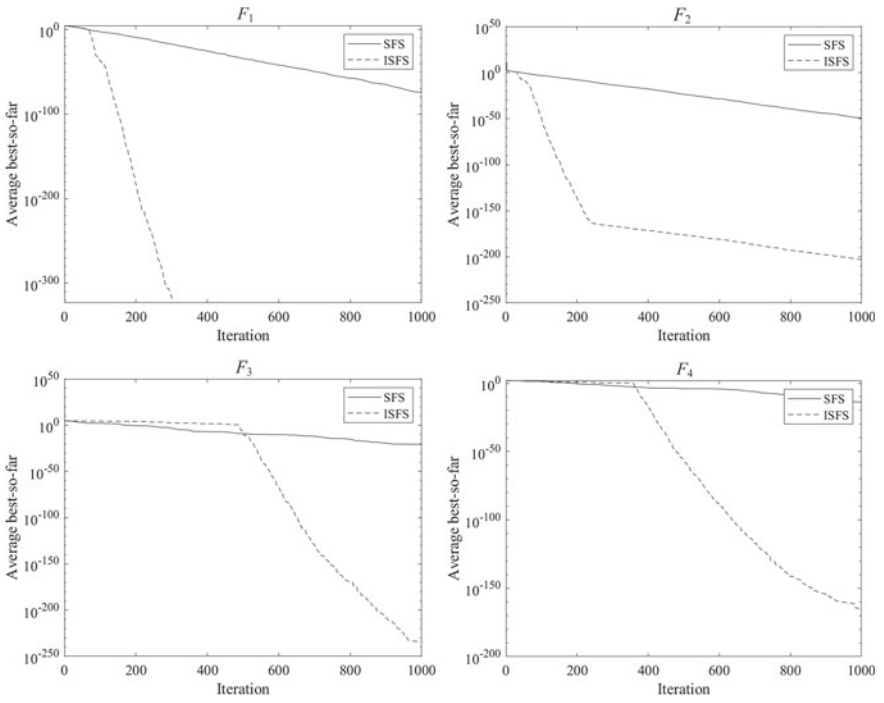

Fig. 2.4 Convergence process of objective functions by two methods for different unimodal test functions

Similarly, the ISFS and the SFS are used to optimize $F_8 \sim F_{13}$ for 30 times for the multimodal benchmark function in Table 2.2, and the calculation results are shown in Table 2.4. As can be seen from the table, in addition to 9 and 11 can find the optimal solution, the optimization effect of the ISFS algorithm is also significantly better than the standard SFS algorithm.

For the high-dimensional multimodal benchmark function, Fig. 2.5 shows the optimization process comparison of ISFS and SFS for 8 and 10, respectively. It can be seen that in the optimization of high-dimensional multimodal function, ISFS converges faster, and the optimization results are closer to the global optimal solution, which has better global optimization performance than SFS.

Table 2.4 Statistical indexes of two algorithms for multimodal functions in 30 independent runs

		SFS	ISFS
F_8	Best best-so-far	-5.3×10^3	-1.2×10^4
	Average mean fitness	-4.4×10^3	-8.9×10^3
	Std best-so-far	136.1	552.9
F_9	Best best-so-far	0	0
	Average mean fitness	0	0
	Std best-so-far	0	0
F_{10}	Best best-so-far	3.9×10^{-15}	4.4×10^{-16}
	Average mean fitness	7.9	4.4×10^{-16}
	Std best-so-far	3.1	0
F_{11}	Best best-so-far	0	0
	Average mean fitness	0	0
	Std best-so-far	0	0
F_{12}	Best best-so-far	0.15	0.05
	Average mean fitness	0.23	0.11
	Std best-so-far	0.02	0.01
F_{13}	Best best-so-far	1.2	0.7
	Average mean fitness	1.7	0.86
	Std best-so-far	0.07	0.04

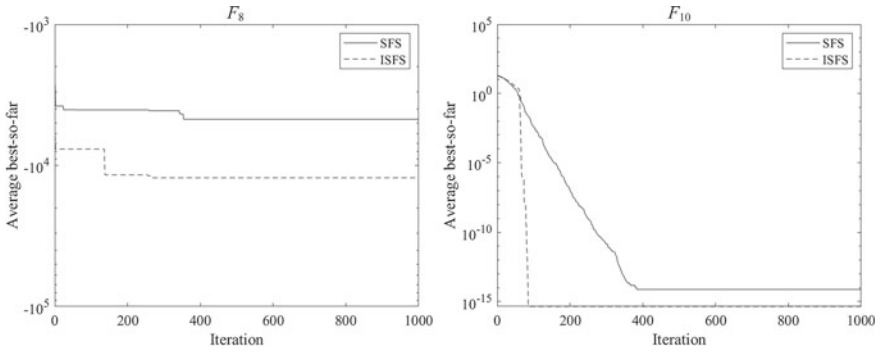

Fig. 2.5 Convergence process of objective functions by two methods for different multimodal test functions

2.5 ISFS for Solving Multiple Hydropower Stations Operation Optimization Problem

2.5.1 Study Area

In this paper, Xiluodu (XLD), Xiangjiaba (XJB), Three Gorges (TGR), Gezhouba (GZB) four cascade hydropower stations as the research object, for the cascade hydropower stations in the long-term power generation optimization scheduling research. The control basin area of the XLD hydropower station is about 4.54×10^5 km^2, accounting for 96% of the total area of the Jinsha River Basin. The control basin area of the XJB hydropower station is about 4.59×10^5 km^2, accounting for 97% of the total area of the Jinsha River Basin. The development tasks of XLD and XJB hydropower stations are mainly power generation, taking into account other functions such as flood control, sediment retention, and navigation. XJB hydropower station is located downstream of XLD, which has a re-regulation effect on XLD. The drainage area of the TGR-GZB cascade hydropower stations is about 1 million km^2, accounting for 56% of the total area of the Yangtze River Basin. The development tasks of the Three Gorges cascade hydropower stations are mainly flood control and power generation, taking into account the functions of navigation and ecology. The GZB hydropower station is located 38 km downstream of the Three Gorges hydropower station, which is the re-regulation reservoir of the Three Gorges.

2.5.2 Coding Strategy

In the process of solving the joint optimal operation model of cascade hydropower stations, the generation flow $Q_{i,t}$ or the water level $Z_{i,t}$ in front of the dam are often used as decision variables. In this paper, the water level of each period of cascade reservoirs is used as decision variables to code the individuals in the algorithm. The individual can be described as

$$X_i = \{z_{11}, z_{12}, \ldots, z_{1T}; z_{21}, z_{22}, \ldots, z_{2T}; \ldots z_{N1}, z_{N2}, \ldots, z_{NT}\} \tag{2.16}$$

where N is the number of cascade power stations and T is the total number of dispatching periods, $z_{1t}(t = 1, 2, ..., T)$, $z_{Nt}(t = 1, 2, ..., T)$ represents the water level process of cascade hydropower stations in each operation period.

2.5.3 Result and Discussion

In this section, the improved stochastic fractal search (ISFS) algorithm is used to solve the joint optimal generation scheduling model of XLD, XJB, TGR, and GZB

reservoirs. In order to verify the effectiveness and performance advantages of the improved algorithm, this paper introduces Differential evolution (DE) algorithm, Gravitational search algorithm (GSA), and Stochastic fractal search (SFS) algorithm to solve the model for comparison experiments.

Taking the inflow process of the lower Jinsha River in 2018 as an example, the above four famous evolutionary methods are used to solve the cascade joint optimal generation scheduling problems of XLD, XJB, TGR, and GZB cascade hydropower stations. The iterative optimization process of each algorithm is shown in Fig. 2.6. It can be seen from the figure that the DE algorithm converges prematurely and falls into the local extremum after about 80 iterations, and the GSA algorithm has good performance of gradual convergence when iterating to 250 times, it gradually loses the ability of global search, which is significantly improved compared with DE algorithm. The convergence process of the standard SFS algorithm is obviously ladder-shaped, which shows that the algorithm has a good ability to jump out of the local optimal value, and the optimization effect is better than the GSA algorithm. By contrast, the disruption operator strategy added in ISFS increases the exploration ability and development ability of the algorithm and makes the ISFS algorithm have better global search ability and faster convergence performance. From the final optimization results, ISFS is significantly better than the standard SFS algorithm and improves the total power generation of cascade hydropower stations.

Using DE, GSA, SFS, and ISFS to solve the joint optimal scheduling model independently for 30 times. Table 2.5 shows the statistical results of 30 times optimization calculations. The results show that the average value, the optimal value, and the worst value of the cascade total power generation by ISFS are better than those by DE, GSA, and SFS, and the standard deviation is the smallest, which indicates that ISFS has better results and better stability in solving the model. The mean value of the total power generation calculated by the ISFS algorithm is 81.1, 43.7, and 3.42

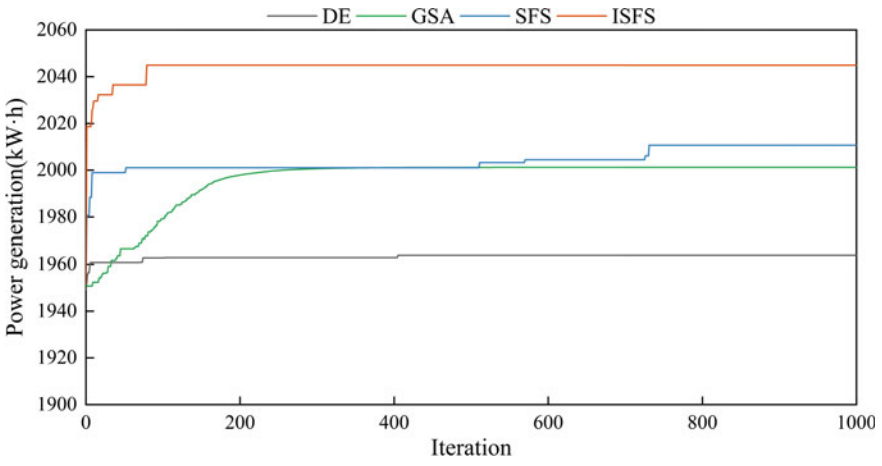

Fig. 2.6 Convergence trajectories of different methods for optimal operation of cascade reservoirs

Table 2.5 Results of 30 independent simulations on power production (10^8 kW h)

Method	Mean	Max	Min	Std
DE	1963.8	1972.4	1958.1	4.27
GSA	2001.2	2004.9	2000.2	1.83
SFS	2010.7	2011.3	2009.8	0.37
ISFS	2044.9	2045.5	2043.1	0.32

$\times 10^8$ kW h higher than that of DE, GSA, and SFS respectively, and the standard deviation is 3.95, 1.51, and 0.05 lower than that of three methods. It shows that the proposed ISFS has better global optimization performance and robustness.

In addition, in order to compare the application advantages of ISFS compared with standard SFS in the joint optimal operation of cascade hydropower stations in detail, Fig. 2.7 shows the water level and output process of XLD, XJB, TGR, and GZB cascade hydropower station joint optimal operation in 2018 solved by the above two methods. It can be seen that the total power generation of the ISFS algorithm are higher than those of the SFS algorithm, which indicates that the ISFS algorithm can easily find the optimal water level process within the scope of meeting the safety constraints of reservoir water level operation so that each reservoir can maintain a higher power generation head and increase the overall power generation benefit of cascade hydropower stations. In addition, it can be seen from the figure that the water level change process of each reservoir and the output process of the power station are more gentle, which is also conducive to reducing the damage of reservoir erosion and ensuring the safe and stable operation of the power system.

2.6 Conclusions

In this paper, an improved random fractal search algorithm that added disruption operator is proposed. The improved algorithm is tested by 13 benchmark functions of high-dimensional unimodal and high-dimensional multimodal. For most functions, the improved ISFS algorithm is obviously better than the standard ISFS, which shows that the disruption operator can effectively enhance the exploration and development ability of the algorithm, and increase the global search ability of the algorithm. In addition, the long-term joint optimal operation model of XLD, XJB, TGR, and GZB cascade hydropower stations is developed, and the ISFS algorithm is used to solve the problem. Compared with DE, GSA, and standard SFS algorithms, the ISFS algorithm has the best calculation results and stability, which shows that the ISFS algorithm has good optimization performance and robustness in solving the joint optimal operation problem of cascade hydropower stations.

Further research is needed on the robustness and adaptability of the ISFS algorithm for the optimal operation problem solving of cascade hydropower stations in other basins.

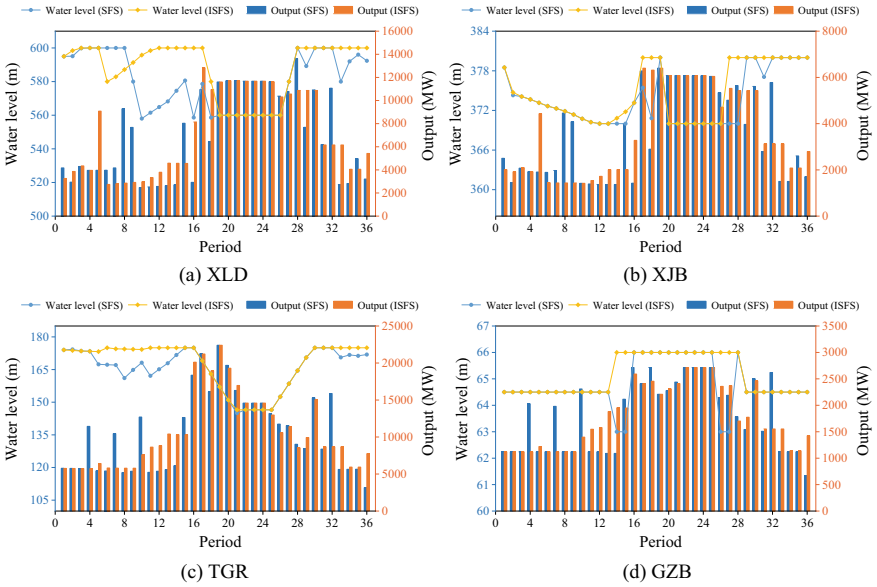

Fig. 2.7 Water level and output process of each power station optimized by SFS and ISFS

Acknowledgements This study is supported by the National Natural Science Foundation Key Project of China (No. 52039004) and National Natural Science Foundation of China (No. U1865202).

References

Feng ZK, Niu WJ, Liu S, Luo B, Miao SM, Liu K (2020) Multiple hydropower reservoirs operation optimization by adaptive mutation sine cosine algorithm based on neighborhood search and simplex search strategies. J Hydrol 590

He Z, Zhou J, Qin H, Jia B, Lu C (2019) Long-term joint scheduling of hydropower station group in the upper reaches of the Yangtze River using partition parameter adaptation differential evolution. Eng Appl Artif Intell 81

Salimi H (2015) Stochastic fractal search: a powerful metaheuristic algorithm. Knowl-Based Syst 75

Sun L, Niu D, Wang K, Xu X (2021) Sustainable development pathways of hydropower in China: interdisciplinary qualitative analysis and scenario-based system dynamics quantitative modeling. J Clean Prod 287

Yang T, Gao X, Sorooshian S, Li X (2016) Simulating California reservoir operation using the classification and regression-tree algorithm combined with a shuffled cross-validation scheme. Water Resour Res 52(3)

Chapter 3
Regional Hydrological Model with Global Climate Change of Mean Annual Flows of the Santa River Basin, Applying the Fokker–Planck–Kolmogorov Equation

Erick Vladimir Castilla Chanco and Samuel Quisca Astocahuana

Abstract Global climate change generates a variation in precipitation and temperature throughout the planet, consequently altering the average, maximum and minimum values of river flows in various parts of the world, causing floods and droughts. Between 1932 and 1994, the glaciers of the tropical Andes in Peru suffered a setback due to the increase in temperature, causing an increase in flow rates. Commonly, hydrological studies applied to the development of hydraulic works consider a stationary hydrological regime; however, with the development and research on global climate change, the need to evaluate the hydrological regime as a non-stationary one arises. This non-stationarity approach can foresee hydraulic projects of maximum and minimum flows not expected determined by current methodologies. The objective of the research was to develop a regional hydrological model of annual mean flows under the influence of global climate change (climate change scenario estimated by SENAMHI for the year 2030) in the Santa River basin. This research used as data the mean annual flow series of the following hydrometric stations: Querococha, Olleros, Quillcay, Chancos, Llanganuco, Parón, Colcas, Los Cedros and Quitaracsa; applying the methodology of linear stochastic models and the Fokker–Planck–Kolmogorov equation, for the development of a regional hydrological model designed to predict future mean annual flows. A regional hydrological model is presented that depends on the basin area with and without snowfall; in addition, it was identified that the model that best describes the stochastic behavior of the mean annual flows is the AR model (1), and that due to the influence of climate change the estimated mean flow decreased by 10%.

Keywords Fokker–Planck–Kolmogorov · Mountain basins with tropical glaciers · Hydrological model · Flow forecasting with climate change

E. V. Castilla Chanco
Universidad Nacional Mayor de San Marcos, Lima, Peru

S. Quisca Astocahuana (✉)
School of Civil Engineering, Universidad Nacional Mayor de San Marcos, Lima, Peru
e-mail: squiscaa@unmsm.edu.pe

H.-Y. Jeon (ed.), *Sustainable Development of Water and Environment*,
Environmental Science and Engineering,
https://doi.org/10.1007/978-3-031-07500-1_3

3.1 Introductions and Antecedents

According to reports by numerous researchers such as Earls (2008), the impact of global warming is very evident in areas close to the planet's polar circles, as well as in tropical highlands (tropical Andes of South America). Likewise, Rodríguez (2011) reports that in 2010 there was a climatic anomaly that affected several Latin American countries, causing droughts and forest fires.

Vuille (2013) indicates that studies on the future of climate change are very limited, focusing mainly on temperature variation and precipitation by the end of the twenty-first century, according to the consensus of scenarios of the Intergovernmental Panel on Climate Change (IPCC).

Kovalenko et al. (2020) mention that the assumption of self-sufficiency of the actual discharge series (under the assumption of statistical stationarity) is of concern. At present, these assumptions are supported under the climate change scenario, as watershed surfaces show a change in their flow formation factors due to deforestation, plowing, etc. Therefore, not only do we need real runoff series on which to build empirical probabilistic density curves and approximate analytical distributions, but we also need to generate long-term mathematical models of river runoff that include climate change scenarios and changing watershed surface characteristics. Also, Quisca (2019), indicates that the reliability of the hydraulic works designed with the existing international technical guidelines and regulations, are based on the assumption that the hydrological regime (of the catchment basin where the project is located) does not change statistically, before design and during its useful life. However, concrete evidence of global climate change and changes in the characteristics of the watershed surfaces demonstrate the opposite. In fact, the records of the flow series may be statistically stable, but become unstable due to climate change, causing changes in precipitation. If the climate system is currently in disequilibrium, we should no longer consider stationary flow series but enter the new field of unstable hydrology, and redefine reliability based on the concept of design flow security. This involves reconciling the concept of the useful life of the hydraulic work and the time it takes for the unbalanced climatological system to return to its equilibrium state.

To this end, we must consider the climatic imbalance and the statistical variability of river flows.

Given the scenario of global climate change that we are experiencing, hydrology and the design of large hydraulic works require the development of new conceptual approaches, methodologies and calculation procedures that allow us to estimate with the necessary reliability the water supply and the hydrological parameters for the design of hydraulic works under the scenario of global climate change.

3.2 Methodology

Weber et al. (2010) mention that a hydrological model aims to represent the various factors involved in the distribution of precipitation and flow formation in a given watershed. Hydrological models can be physical, where the basin can be represented by a small-scale model, or a mathematical model, which is characterized by estimating hydrological responses by means of empirical or conceptual equations, varying parameters and hydrometeorological conditions. Chow et al. (1994) also indicate that a hydrological model can be classified as: physical models and abstract models. Physical models are the scaled representation of reality while an abstract model describes a system by means of a set of equations that relate hydrological variables and responses. The input variables can be functions located in a given space and time, and they can also be random or probabilistic, which do not have a specific value in space and time, but are described by a probabilistic distribution curve.

The purpose of the research consists of the analysis and generation of linear stochastic models (ARIMA), the determination of the basin area with and without snowfall, the obtaining of distribution parameters with climate change and regionalization of ARIMA parameters due to the influence of climate change.

3.2.1 ARIMA Model

Gujarati and Porter (2010) mention that in the publication of George E. P. Box and Gwilym Jenkins (Time Series Analysis: Forecasting and Control), they proposed a new tool for the generation of forecasts, called ARIMA methodology and popularly known as the Box-Jenkins methodology.

González (2009) mentions that ARIMA models aim to generate a time series based on the interrelation of its elements. This model was proposed by Yule and Slutzky in the 1920s, and they proposed that a model can be characterized by sum, difference, weighted or not, of stochastic variables, being the antecedent of the autoregressive processes and moving averages of the ARIMA model, which was published in Box-Jenkins' book in 1970.

To identify the order p and q, which could have generated the stationary series, the FAC and FACP instruments are used, which have the following characteristics (Table 3.1).

Pindyck and Rubinfeld (1998) mention that the weighted averages of the stochastic variable evaluated in q or p periods can explain the observed yt values. The equation that explains the MA(q), AR(q) and ARMA (p, q) and ARIMA (p, d, q) process are as follows:

$$MA\,(q) \quad y_t = \mu + \varepsilon_t - \theta_1 \varepsilon_{t-1} - \theta_2 \varepsilon_{t-2} - \cdots - \theta_q \varepsilon_{t-q} \tag{3.1}$$

$$AR(P) \quad y_t = \phi_1 y_{t-1} + \phi_2 y_{t-2} + \cdots + \phi_p y_{t-p} + \delta + \varepsilon_t \tag{3.2}$$

Table 3.1 Structure of FAC and FACP

Process	FAC	FACP
MA(q)	It cancels out for j > q	Rapidly decreasing, does not cancel out
AR(p)	Rapidly decreasing, does not cancel out	It cancels out for j > q
ARMA(p, q)	Rapidly decreasing, does not cancel out	Rapidly decreasing, does not cancel out

$$ARMA(p,q) \quad y_t = \phi_1 y_{t-1} + \cdots + \phi_p y_{t-p} + \delta + \varepsilon_t - \theta_1 \varepsilon_{t-1} \tag{3.3}$$

After differentiating "y", so that it can be modeled as an ARMA (p, q) stationary series, then it can be said to be an integrated autoregressive moving average process of order (p, d, q) or ARIMA (p, d, q).

3.2.2 Fokker–Planck–Kolmogorov Equation

Alexandrovich (1999) indicates that the solution to the stochastic equation of the Fokker–Planck–Kolmogorov equation is a Markovian process, since it states that future values do not depend only on the present and past. Kovalenko (1993) indicates that the FPK model is based on the mass balance relationship in a control volume.

$$X - E - I = kX \tag{3.4}$$

where X = precipitation intensity, E = evaporation, I = infiltration y K = runoff coefficient.

Considering the effective runoff time τ, which characterizes the inertial properties of the watershed, transforms into the differential equation (Eq. 3.5).

$$\frac{\partial Q_{max}}{\partial t} + \frac{Q_{max}}{k\tau} = \frac{X}{\tau} \tag{3.5}$$

where Q_{max} is the liquid flow rate, $-\frac{1}{k\tau} = C_{(t)}$, $\frac{X}{\tau} = N_{(t)}$. If $C_{(t)}$ and $N_{(t)}$ are non-random functions, then the solution of this equation is non-random, but a dynamic process $Q = f_{(t)}$. Considering that $C_{(t)}$ and $N_{(t)}$ are Random parameters, it is assumed that $C = \overline{C} + \widetilde{C}_{(t)}$ y $N = \overline{N} + \widetilde{N}_{(t)}$, where $\widetilde{C}_{(t)}$ and $\widetilde{N}_{(t)}$ are the Random processes of white noise.

The solution to this stochastic equation is a Markovian process, whose future state depends only on the present (not on the past).

The equation describing the probability density curve was strictly derived by A. I. Kolmogorov, hence the name Fokker–Planck–Kolmogorov equation. In this case, the evolution of the probability density of water discharge is described by the equation

(Eq. 3.6).

$$\frac{\partial p_{(Q,t)}}{\partial t} = -\frac{\partial}{\partial Q}\left[A_{(Q,t)}\, p_{(Q,t)}\right] + 0.5\frac{\partial^2}{\partial Q^2}\left[B_{(Q,t)}\, p_{(Q,t)}\right] \tag{3.6}$$

where the functions A (Q, t) and B (Q, t) are the translation and diffusion coefficients, defined by the following expressions:

$$A_{(Q,t)} = -\left(\overline{C} - 0.5C_{\widetilde{G}}\right)Q - 0.5G_{\widetilde{G}\widetilde{N}} + \overline{N} \tag{3.7}$$

$$B_{(Q,t)} = C_{\widetilde{G}}Q^2 - 2G_{\widetilde{G}\widetilde{N}}Q + G_{\widetilde{N}} \tag{3.8}$$

where $C_{\widetilde{G}}$, $G_{\widetilde{N}}$ *y* $G_{\widetilde{G}\widetilde{N}}$ he mutual intensities and intensities of "white noise".

Since the purpose is to analyze the hydrological regime in a stationary case, the transient regimes are excluded, so from Eq. 3.6 we consider $\frac{\partial p_{(Q,t)}}{\partial t} = 0$, transforming the Fokker–Planck–Kolmogorov equation into the Pearson equation.

$$\frac{\partial p}{\partial Q} = \frac{Q - a}{b_0 + b_1 Q + b_2 Q^2}p \tag{3.9}$$

where depending on the coefficients b_0, b_1 and b_2 different distributions of the Pearson family of curves will be obtained and determined from the following expressions.

$$a = \frac{G_{\widetilde{G}\widetilde{N}} + 2N}{2\overline{C} + C_{\widetilde{G}}} \tag{3.10}$$

$$b_0 = -\frac{G_{\widetilde{N}}}{2\overline{C} + C_{\widetilde{G}}} \tag{3.11}$$

$$b_1 = \frac{G_{\widetilde{G}\widetilde{N}}}{2\overline{C} + C_{\widetilde{G}}} \tag{3.12}$$

$$b_2 = -\frac{G_{\widetilde{C}}}{2\overline{C} + C_{\widetilde{G}}} \tag{3.13}$$

Due to the short length of the historical series being counted, it is possible to solve Eq. 3.10 with a system of algebraic equations with 4 unknowns based on the first centered statistical moments.

$$\alpha_{n-1}nb_0 + \alpha_n[(n+1)b_1 - a] + \alpha_{n+1}[(n+2)b_2 + 1] = 0 \tag{3.14}$$

Being, n = statistical moments not centered (0, 1, 2, 3).

To evaluate the variation of the flow due to climate change as a function of its non-central moments, we proceed as follows.

Paso 1: Knowing the non-central moments of the historical flow record, Eq. 3.14 is solved by obtaining the current climate parameters a, b_0, b_1 and b_2.

Paso 2: Once the current climate parameters are obtained, the future climate scenario parameters (white noise intensities) are obtained from Eqs. 3.10 to 3.13. Replacing the parameters of the future climate scenario in Eq. 3.14 will give the non-centered moments of the future climate.

3.2.3 Application of the Quasi-Stationary Fokker–Planck-Kolmogorov Equation to Determine the Variation of the Flow Rate Due to Climate Change

The determination of the effect of climate change on flows will be evaluated as follows. From Eq. 3.9 which represents a family of Pearson Probabilistic Density Curves, which due to the short length of historical data to be evaluated (which are the annual flow records), the Pearson parameters can be determined in terms of their statistical moments as shown in Eq. 3.14. These statistical moments of current and future climate are generally represented in isovalue maps, as shown in the research of Dominguez (2004). Solving Eq. 3.14 with the current climate moments, the stabilized values of a, b_0, b_1 and b_2 will be obtained and then replaced in Eqs. 3.10 to 3.13 to determine the current climate white noise intensities, which will be assumed constant, to solve again Eqs. 3.22 to 3.24 with the values of white noise and precipitation of the future scenario.

With this information, isoline maps will be constructed to characterize the corresponding hydrological scenario. Considering the short length of the hydrological data collected and available, the values a, b_0 and b_1 solving Eq. 3.14 as follows, it is considered that the anthropic noise.

$$b_1 - a = -\alpha_1 \tag{3.15}$$

$$2\alpha_1 b_1 + b_0 - \alpha_1 a = -\alpha_2 \tag{3.16}$$

$$3\alpha_2 b_1 + 2\alpha_1 b_0 - \alpha_2 a = -\alpha_3 \tag{3.17}$$

Solving the Eqs. 3.15, 3.16 and 3.17 in terms of the unknowns a, b0 and b1 gives the following expressions

$$a = \frac{0.5\left(-\alpha_3 - 4{\alpha_1}^3 + 5\alpha_1\alpha_2\right)}{\left(\alpha_2 - {\alpha_1}^2\right)} \tag{3.18}$$

$$b_0 = \frac{0.5\left(-2{\alpha_2}^2 - \alpha_2{\alpha_1}^2 + \alpha_1\alpha_3\right)}{\left(\alpha_2 - {\alpha_1}^2\right)} \tag{3.19}$$

$$b_1 = \frac{0.5\left(3\alpha_1\alpha_2 - 2{\alpha_1}^3 - \alpha_3\right)}{\left(\alpha_2 - {\alpha_1}^2\right)} \tag{3.20}$$

By solving the white noise parameters of Eqs. 3.10 to 3.13 as a function of the parameters a, b_0 and b_1, they are represented as follows:

$$\overline{C} = \frac{N}{(a - 0.5b_1)} \tag{3.21}$$

$$G_{\widetilde{G}\widetilde{N}} = \frac{Nb_1}{(a - 0.5b_1)} \tag{3.22}$$

$$G_{\widetilde{N}} = -\frac{2Nb_0}{(a - 0.5b_1)} \tag{3.23}$$

where N is the average precipitation of the current climate.

To identify the parameters of the future scenario, the N_{pr} will be used, which represents the average precipitation of the future climate scenario, estimated by the National Meteorology and Hydrology Service of Peru. The magnitudes of the white noise intensities for the future scenario will be estimated as follows, for $\overline{C}_{pr}$ is considered equal to $\overline{C}$ o $\overline{C} = \frac{1}{K}$ (K is the runoff coefficient that can be determined as a function of precipitation, temperature or agroindustrial activities). Regarding the parameters of $G_{\widetilde{G}\widetilde{N}_{pr}} = G_{\widetilde{G}\widetilde{N}}$ and $G_{\widetilde{N}_{pr}} = G_{\widetilde{N}}$. There is currently insufficient information available to estimate these future scenario parameters.

Solving Eqs. 3.10 to 3.13 without considering anthropogenic noise is determined as follows:

$$a_{pr} = \frac{G_{\widetilde{G}\widetilde{N}_{pr}} + 2N_{pr}}{2\overline{C}_{pr}} \tag{3.24}$$

$$b_{0pr} = -\frac{G_{\widetilde{N}_{pr}}}{2\overline{C}_{pr}} \tag{3.25}$$

$$b_{1pr} = \frac{2G_{\widetilde{G}\widetilde{N}_{pr}}}{2\overline{C}_{pr}} \tag{3.26}$$

where a_{pr}, b_{0pr}, b_{1pr} are future climate parameters.

Solving the equation system of Eqs. 3.15 to 3.17 for future scenario generates:

$$\alpha_{1_{pr}} = q_{pr} = a_{pr} - b_{1_{pr}} \tag{3.27}$$

$$\alpha_{2_{pr}} = \alpha_{1_{pr}} a_{pr} - 2\alpha_{1_{pr}} b_{1_{pr}} - b_{0_{pr}} \tag{3.28}$$

$$\alpha_{3_{pr}} = \alpha_{2_{pr}} a_{pr} - 3\alpha_{2_{pr}} b_{1_{pr}} - 2\alpha_{1_{pr}} b_{0_{pr}} \tag{3.29}$$

$$C_{V_{pr}} = \sqrt{\frac{\alpha_{2_{pr}} - q_{pr^2}}{q_{pr^2}}} \tag{3.30}$$

$$C_{S_{pr}} = \left(\frac{\alpha_{3_{pr}} - 3\alpha_{2_{pr}}\alpha_{1_{pr}} + 2\alpha_{1_{pr^3}}}{C_{V_{pr^3}} q_{pr^3}} \right) \tag{3.31}$$

$$\beta = \frac{C_{V_{pr}}}{C_{S_{pr}}} \tag{3.32}$$

From the values q_{pr}, C_{Vpr} and β isovalue maps are constructed for a given climate change scenario. Likewise, by applying the Monte Carlo method, the evolution of the probabilistic density curve for the future scenario is generated.

3.2.4 Study Watershed

The study was carried out in the Santa river basin, which is located on the central coast of Peru, between parallels 8°4′ and 10°8′ south latitude and meridians 77°12′ and 78°38′ west longitude. It includes the regions of Ancash and La Libertad, and belongs to the Pacific Ocean basins, limited to the east by the Cordillera Blanca, formed by the glacier chain, and to the west by the Cordillera Negra, a group of mountain chains without glaciers; it has a basin area of 11,661.53 km^2 of which 10,400.5 km^2 is above 2000 masl, and has a basin length of 316 km to its mouth in the Pacific Ocean, with an average width of 38 km, as shown in Table 3.2.

The data used to generate the regional model in the Santa river basin with climate change are the historical and completed records of the mean annual flow of the Querococha, Olleros, Quillcay, Chancos, Llanganuco, Parón, Colcas, Los Cedros and Quitaracsa hydrometric stations (see Fig. 3.1). As well as the area of

Table 3.2 Glacier surface distribution in the Santa river basin

Station	Sub-basin surface area (km^2)	Surface area with snow (km^2)	Surface area without snow (km^2)
Querococha	62.70	4.10	58.6
Olleros	174.30	25.10	149.2
Quillcay	249.50	29.00	220.5
Chancos	209.90	69.50	140.4
Llanganuco	84.00	37.50	46.5
Parón	53.30	29.00	24.3
Colcas	234.30	45.90	188.4
Cedros	114.50	23.05	91.45
Quitaracsa	384.90	33.32	351.58

snowed and non-snowed basin in the study basin. For the application of the Fokker–Planck–Kolmogorov methodology, we used the total multiannual precipitation and percentage variation of precipitation due to climate change, presented in the report on climate scenarios in Peru for the year 2030 by SENAMHI, indicating a 10% decrease in precipitation.

3.3 Results

Applying the Box-Jenkins methodology in RStudio to generate and estimate the best ARIMA model to represent the mean annual flow values, we began with the evaluation of the stationarity of the hydrometric stations.

Using the adf.test function (Es.ts, alternative = "stationary") on the data series of each hydrometric station, a p-value <5% is obtained, thus testing the stationarity of the series, as shown in Table 3.3.

In order to select the possible ARIMA models to represent the time series, the ACF and PACF diagrams were evaluated. Selecting as the possible models AR(1), MA(1) and ARMA(1, 1), as shown in Table 3.4.

The reliability of the model was determined by the Ljung-Box test since the p-values are greater than 0.05, therefore, the null hypothesis is rejected and it is concluded that the residuals are independent of each other. In conclusion, it is said that the AR(1) model does represent the series of annual mean flows.

The equations of the AR(1) models without climate change are shown in Table 3.5.

Due to the non-stationarity of the values, the Fokker–Planck–Kolmogorov methodology will be applied to estimate the statistical values of the maximum flows considering the effect of climate change.

To estimate future statistical values, the historical data on mean annual flows, predicted precipitation and determination of the climate scenario to be considered will be analyzed. For the study, the 2030 scenario estimated by SENAMHI was considered, which indicates that the percentage variation in precipitation will be −10%. These will be the input data for the generation of future statistical values obtained by applying the quasi-stationary solution of the Fokker–Planck–Kolmogorov equation. Once the future climate statistical values have been determined, we will proceed to estimate the distribution function that best fits the current climate flows, which will be used to readjust the distribution parameters to the new future climate parameters, as shown in Table 3.6.

The regionalization of the parameters ϕ, standard deviation of error and mean annual discharge with snowed and non-snowed basin area yields the following equations

$$\phi_r = 0.2239 + 0.0045N - 0.000496A \tag{3.33}$$

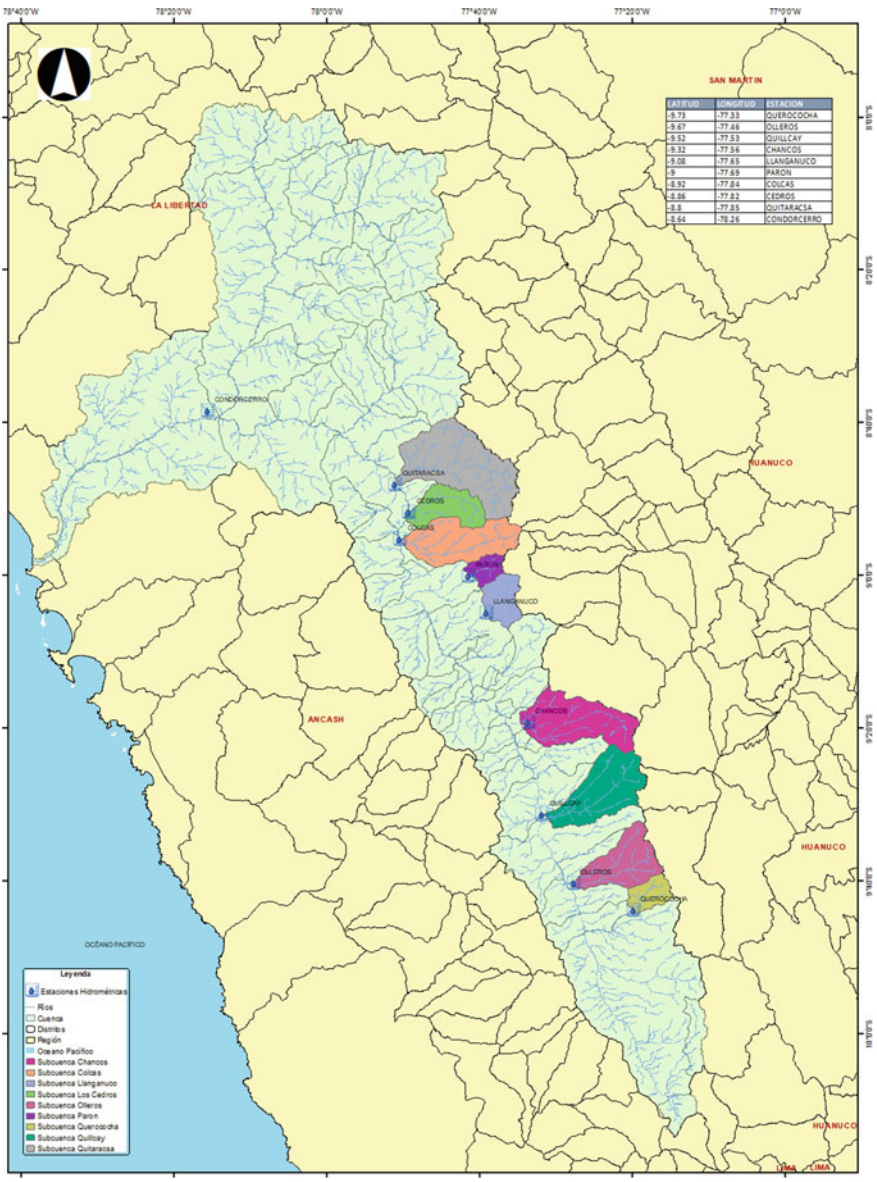

Fig. 3.1 The location of the hydrometric stations and delimitation of the Santa river basin and sub-basins are shown

Table 3.3 Summary of statistical values of instantaneous peak flow rates for current weather

Station	Parameter (ϕ)	$\phi < 1$?	Does it comply with stationarity?
Querococha	0.2772	No	Yes
Olleros	0.3104	No	Yes
Quillcay	0.2310	No	Yes
Chancos	0.4402	No	Yes
Llanganuco	0.3407	No	Yes
Parón	0.3701	No	Yes
Colcas	0.4784	No	Yes
Cedros	0.1178	No	Yes
Quitaracsa	0.1600	No	Yes

Table 3.4 Selected models and modified Schwarz values

Station	AR(1)	MA(1)	ARMA(1, 1)
Querococha	−38.68	−37.94	−35.19
Olleros	30.19	29.83	33.53
Quillcay	43.55	43.86	47.26
Chancos	69.71	69.15	72.57
Llanganuco	−38.59	−40.61	−36.96
Parón	−21.03	−18.56	−19.79
Colcas	43.40	43.72	46.84
Cedros	−13.00	−12.95	−9.32
Quitaracsa	88.62	88.97	91.90

Table 3.5 Model AR(1) equations

Station	AR(1)
Querococha	$y_t = 1.252 + 0.277y_{t-1} + \varepsilon_t$
Olleros	$y_t = 3.282 + 0.310y_{t-1} + \varepsilon_t$
Quillcay	$y_t = 5.453 + 0.231y_{t-1} + \varepsilon_t$
Chancos	$y_t = 4.639 + 0.44y_{t-1} + \varepsilon_t$
Llanganuco	$y_t = 1.998 + 0.3407y_{t-1} + \varepsilon_t$
Parón	$y_t = 1.272 + 0.37y_{t-1} + \varepsilon_t$
Colcas	$y_t = 2.931 + 0.478y_{t-1} + \varepsilon_t$
Cedros	$y_t = 2.984 + 0.118y_{t-1} + \varepsilon_t$
Quitaracsa	$y_t = 8.859 + 0.16y_{t-1} + \varepsilon_t$

$$\sigma_\varepsilon = -0.0155 + 0.0099N + 0.0037A \tag{3.34}$$

$$\mu_p = -0.2826 + 0.0568N + 0.0216A \tag{3.35}$$

Table 3.6 Statistical parameters of future climate

Station	μ	C_{Vpr}	C_{Spr}
Querococha	1.5584	0.242	−0.0122
Olleros	4.2854	0.2025	0.1254
Quillcay	6.3678	0.1742	−0.5087
Chancos	7.4747	0.1898	0.4539
Llanganuco	2.7326	0.1274	0.5148
Parón	1.8207	0.2557	0.3045
Colcas	5.0514	0.2284	−0.2129
Cedros	3.0402	0.1743	−0.3662
Quitaracsa	9.4925	0.1823	−0.0022

$$Q_{t+1} = \mu_p(1 - \phi_r) + \phi_r Q_t + \varepsilon_t \tag{3.36}$$

where

Q_{t+1} estimated flow
μ_p regional average flow
ϕ_r ϕ regional
t time in years
ε_t white noise process with mean 0 and standard deviation $\sigma_{\varepsilon r}$
$\sigma_{\varepsilon r}$ standard deviation of regional error.

3.4 Conclusions

The regional hydrological model of the mean annual flow, considering the 2030 climate change scenario, depends on the value of the basin area with and without snowfall to determine the value of the regional parameters.

The parameters of basin area with snowfall and without snowfall explain 93% of the mean annual mean flow with climate change in the Santa river basin.

The regional hydrological model of the sub-basins analyzed shows an average future mean flow value lower than the historical mean flow, with the exception of the Colcas sub-basin, which shows an increase of 13.9%.

The regional hydrological model determined and the stochastic models do not allow for simulating a precise behavior of the mean annual flows over time, however, they are a good tool for predicting maximum and minimum flood events.

According to the climate change scenario for the year 2030, it is estimated that precipitation would decrease by 10%, which generates an approximate 10% decrease in the value of the mean annual flow, which was obtained by applying the Fokker–Planck–Kolmogorov methodology.

Applying the Fokker–Planck–Kolmogorov methodology, the distribution parameters with climate change are obtained, providing the relevant information to estimate

the probabilistic distribution curve of future mean flows, which indicate a decrease to the mean value, variation of the bias coefficients and coefficient of variation.

Applying the Fokker–Planck–Kolmogorov equation, the probabilistic density curves can be determined with the influence of global climate change, to estimate the design flow values for different return periods, and apply them to various hydraulic engineering projects.

References

Alexandrovich J (1999) Estabilidad de la probabilidad de las características de la escorrentía anual por la acción antrópica. Universidad Estatal Hidrometeorológica de Rusia, San Petersburgo, Federación de Rusia, 1999, 155 pág

Chow V, Maidment D, Mays L (1994) Hidrología aplicada. McGraw-Hill

Domínguez E (2004) Predicción estocástica del ingreso del flujo de agua a los embalses de las centrales hidroeléctricas de la República de Colombia. Universidad Estatal Hidrometeorológica de Rusia. Federación de Rusia, San Petersburgo, 231 pág

Earls J (2008) Manejo de cuencas y cambio climático. Los Andes y las poblaciones altoandinas en la agenda de la regionalización y la descentralización 1:113–126

González M (2009) Análisis de series temporales económicas: Modelos ARIMA

Gujarati D, Porter D (2010) Econometría (quinta edición). Editorial Mc. Graw Hill, México

Kovalenko VV (1993) Modelación de procesos hidrológicos, San Petersburgo, Editorial Hidrometeoizdat, Rusia, 256 pág

Kovalenko VV, Viktorova NV, Gaidukova EV Khaustov VA, Devyatov VS (2020) Resultados de las investigaciones de los procesos hidrológicos probabilísticos en RHSMU, Universidad Hidrometeorológica Estatal de Rusia 60:255–268

Pindyck R, Rubinfeld D (1998) Econometric models and econometric forescast, McGrawHill, New York

Quisca SI (2019) Apunte de clases del curso de Ingeniería de Recursos Hidráulicos, Capítulo 4, Escuela de Ingeniería Civil de la FIGMMG, Universidad Nacional Mayor de San Marcos. Lima, Perú

Rodríguez A (2011) Cambio climático, precipitaciones, sociedad y desastres en América Latina: relaciones y necesidades. Revista Peruana de Medicina Experimental y Salud Publica 28(1):165–166

Vuille M (2013) El cambio climático y los recursos hídricos en los andes tropicales. Banco Interamericano de Desarrollo 21

Weber J, Dasso C, Jorquera E (2010) Desarrollo y calibración de un modelo hidrológico de simulación mixta. Mecánica Computacional 29(39):4013–4037

Chapter 4
Numerical Modeling of Tsunami in the City of Chorrillos, Lima—Peru

Julio César Martínez Herrera and Samuel Ismael Quisca Astocahuana

Abstract Peru is located in a region of tectonic plate interaction, subduction of the Nazca plate underneath the South American plate, originating many earthquakes. Peru has endured the effects of large tsunamis, in some cases very large and destructive (Martínez, Dinámica y modelado numérico de un tsunami en el terminal portuario del Callao y zonas adyacentes, 2014). On October 28, 1746, an earthquake of estimated magnitude 8.8 Mw, generated a large tsunami that affected the central coast of Peru causing destruction in the port of Callao, with waves greater than 20 m and flooding of approximately 5 km, the victims of the earthquake and tsunami reached 4000 people (Silgado, Historia de los sismos más notables ocurridos en el Perú 1513–1974, República de Perú Sector Energía y Minas, Instituto de Geología y Minería, Boletín N°3 Serie C, Geodinámica e Ingeniería Geológica, 1978). In such a scenario, the district of Chorrillos, located in the department of Lima, would be severely affected. This study simulates the most probable scenario, using the homogeneous seismic source model, topographic and bathymetric data with a spatial resolution of 10 m, applying the TUNAMI-N2 algorithm, developed by the Disaster Research and Control Center of Tohoku University. The main results obtained show that the inundation occurs 20 min after the earthquake and reaches 1 km, with heights exceeding 9 m. The hydrodynamic parameters confirm a high level of hazard, because the flood depth is high (>2 m) and the flow velocities exceed 1.5 m/s, signifying high levels of danger to people.

Keywords Tsunami · Numerical modeling of the tsunami · Tsunami floods · Flooding of the Lima coastline

J. C. Martínez Herrera
Geophysical Institute of Peru, Lima, Peru
e-mail: jmartinez@igp.gob.pe

Agrarian National University La Molina, Lima, Peru

S. I. Quisca Astocahuana (✉)
School of Civil Engineering of the San Marcos National University, Lima, Peru
e-mail: squiscaa@unmsm.edu.pe

H.-Y. Jeon (ed.), *Sustainable Development of Water and Environment*,
Environmental Science and Engineering,
https://doi.org/10.1007/978-3-031-07500-1_4

4.1 Introduction

Peru is one of the countries with the greatest seismic potential because it is part of the "Pacific Ring of Fire". Seismic activity is associated with the subduction of the Nazca plate under the South American plate with an average speed of 6–7 cm per year (Norabuena et al. 1998; Villegas et al. 2016). This velocity is considered one of the highest worldwide, hence the high occurrence of tsunami-generating seismic events.

The word "tsunami", of Japanese origin, comes from two words: tsu (port) and nami (wave). It literally means big waves in the harbor. It does not cause damage on the high seas, but is destructive in coastal areas.

The term tsunami is defined as a wave or series of waves produced in a volume of water when it is violently propelled by a force that displaces it vertically, originating a train of long waves, with a period ranging from several minutes to hours, and propagating at high speed in all directions from the area of origin. As the waves approach the coasts, they reach great heights, discharging their energy with great power, causing flooding and destruction of coastal populations (Wiegel 1970; Iida and Iwasaki 1983; SHOA 2018; ITSU 1999).

Tsunamis recorded in Peru from 1500 to the present have seismic origin, meeting the following characteristics (i) epicenter in the sea, (ii) depth less than 60 km, and (iii) magnitude $\geq$6.8 Mw. If an earthquake meets these three conditions, the occurrence of a tsunami is very likely.

4.1.1 Description of the Study Area

The study area comprises the city of Chorrillos; located in the department and province of Lima, at an approximate distance of 20 km from the center of the city of Lima, capital of Peru (Fig. 4.1). According to the 2017 national census conducted by the National Institute of Statistics and Informatics (INEI), the district of Chorrillos has a population of 314,000 population, being 49% female and 51% male, settled over an area of 37 km^2. The approximate population density is 8,798.60 population per square kilometer.

4.1.2 Objective

Define the characteristics of the water flows of a tsunami generated by a great magnitude earthquake (8.8 Mw). The scenario is built from the numerical simulation and will allow knowing the arrival times of the water flows, their speed and the heights

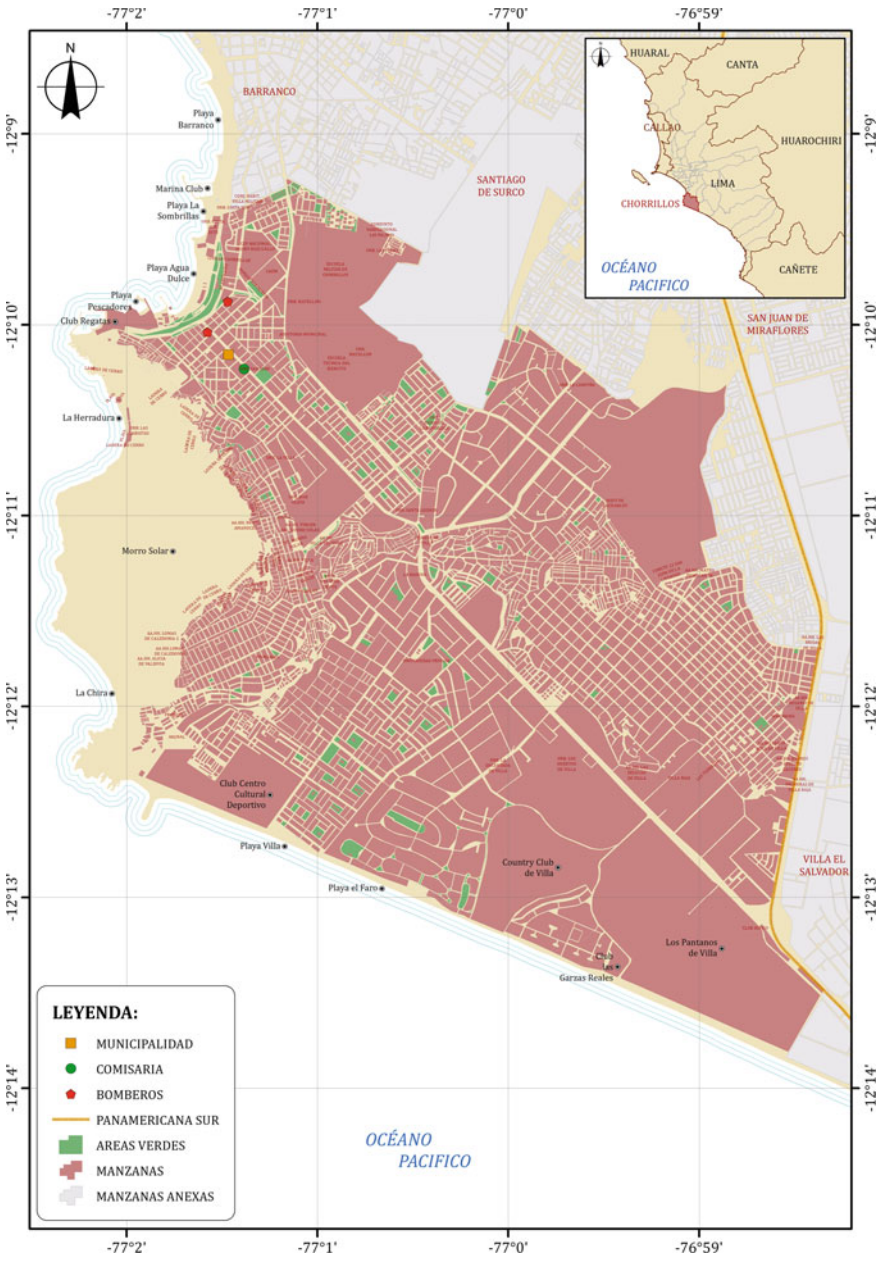

Fig. 4.1 Map of the study area (Chorrillos city)

of the various volumes of water along the coastal coastline of the district of Chorrillos. This information is of great importance to establish early warning systems and generate scenarios to reduce the risk of exposure in urban areas.

4.2 Methodology

In order to perform the numerical modeling of the tsunami generated by a great magnitude earthquake (8.8 Mw) it is necessary to follow the following methodology:

- Collection of data in situ or from available internet databases on the bathymetry of the seabed and the topography of the terrain. The bathymetry will allow estimating the propagation of the waves from the rupture area generated by the earthquake to the coastline; the topography will allow characterizing the interaction of the waves with the coastal zone and how urban areas would be affected.
- To have technical information on the characteristics and seismic parameters of the rupture area such as: magnitude (Mw), strike angle, dip angle, slip angle, length (km), width (km), slip length (m) and depth (km).
- Qualitative and quantitative analysis of possible triggers for tsunami generation. Based on historical information of the events that affected the district of Chorrillos to propose seismic scenarios that could generate a tsunami on the coastal coast.
- Numerical modeling and generation of inundation scenarios of water flow from the ocean, using the computer tool TUNAMI-N2, which is a two-dimensional mathematical model for hydraulic simulation of tsunamis in its three phases: seismic generation, oceanic propagation and coastal inundation.
- Analysis and evaluation of the scenarios that occur after the occurrence of an earthquake of great magnitude as areas affected by the volume of water coming from the ocean. Also, the heights and velocities of flooding in these areas.
- Availability of cadastral maps of urban areas and seaside resorts distributed along the coastal coastline that could be affected by the flow of water from the ocean.
- Construction of hazard scenarios in urban areas due to tsunami inundation.
- Analysis and evaluation of the results obtained in this technical study.

4.3 Data Used

4.3.1 Seismic Data

In order to know the parameters of the seismic source to be used in the numerical model, it was necessary to document the information related to historical and instrumental earthquakes, as well as the macro-seismic and tsunamigenic data of the study area (Silgado 1978; Dorbath et al. 1990; Carpio and Tavera 2002).

The publications by Villegas et al. (2016) and Chlieh et al. (2011) propose seismic scenarios of magnitude equal to 8.8 Mw, with epicenter in the sea, in front of Callao, which corresponds to the most probable earthquake that could occur in front of Lima.

The present study considers the generation of a tsunami by the occurrence of a great magnitude earthquake (8.8 Mw) with a depth of less than 60 km and with epicenter in the subduction zone (Fig. 4.2). An earthquake of these characteristics would generate high levels of deformation of the seafloor, which would be transferred to the mean sea level, generating waves that would form the tsunami upon reaching the coast (Mansinha and Smylie 1971). Table 4.1 describes the characteristics of the proposed earthquake.

4.3.2 Bathymetric Data

To make the bathymetric map of the study area, data from the bathymetric charts of the Directorate of Hydrography and Navigation of the Peruvian Navy (DHN) were used; also, data from global maritime depth models, the model used is GEBCO. These data were converted to a Digital Terrain Model (DTM) considering values of altitude (z), longitude (x) and latitude (y), expressed in the geographic projection system for spatial referencing with a bias of ± 1 and ± 1 m in its vertical and horizontal component respectively.

With the final database, the bathymetric surface of the study area has been elaborated with a spatial resolution of 5 m, sufficient to adequately characterize the bathymetric relief (Fig. 4.3). According to the bathymetric map, the beaches found on the coastline of the Chorrillos district have depths of less than 5 m, being shallower in the north–south direction. Likewise, it is notorious that the direction of the waves will have a W-E direction, in the event of a tsunami in front of the Chorrillos city.

Finally, the water flows coming from the sea in a possible seismic scenario of great magnitude are propagated homogeneously through the maritime relief of the study area with speeds of approximately 800 km/h, decreasing proportionally with the decrease in depth, but would generate an increase in the heights of the tsunami waves along the coastal coastline, affecting all areas susceptible to flooding, including the coasts of the district of Chorrillos.

4.3.3 Topographic Data

The topographic map of the study area was made using contour line and geodetic point data obtained from the National Geographic Institute (IGN), as well as satellite elevation data from the ALOS PALSAR sensor. These data were converted to a digital terrain model (DTM) considering altitude (z), longitude (x) and latitude (y),

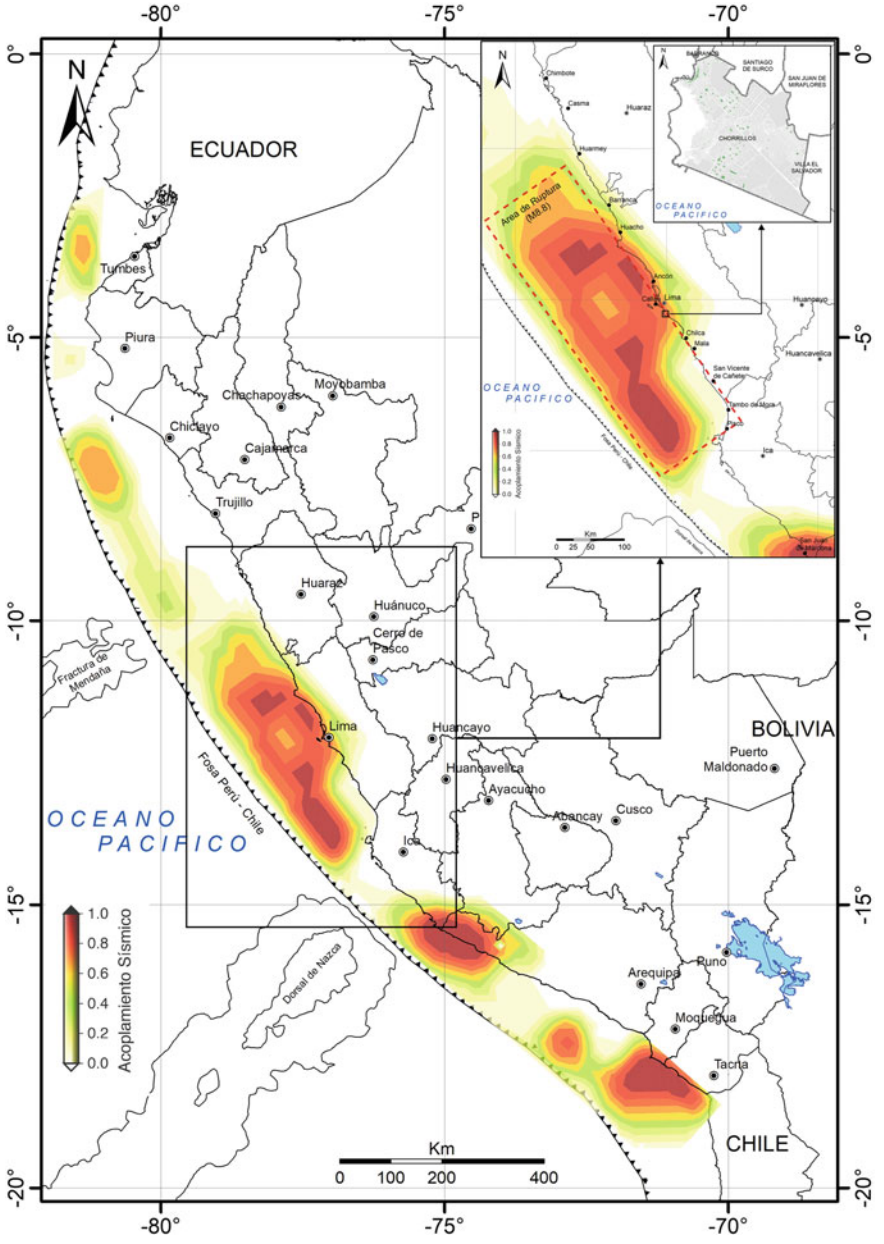

Fig. 4.2 Seismic coupling area, modified from Villegas et al. (2016)

Table 4.1 Seismic source parameters

Magnitude	8.8 Mw	Angle azimuth	325°
Depth	30 km	Angle dip	20°
Length	450 km	Angle slip	90°
Width	125 km	Slip	7 m

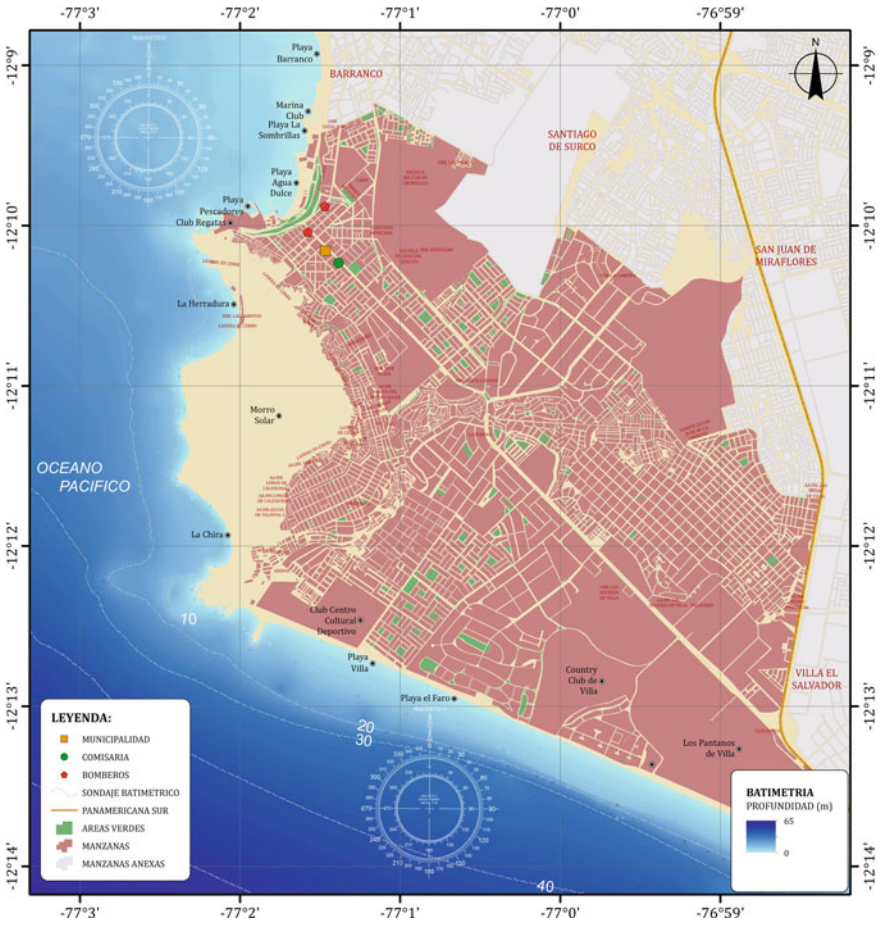

Fig. 4.3 Bathymetric map of the study area

expressed in the geographic projection system for spatial referencing with a bias of ±2 and ±3 m in its vertical and horizontal components, respectively.

With the final database, the topographic surface of the study area has been created with a spatial resolution of 5 m, which is sufficient to adequately characterize the topographic relief (Fig. 4.4). According to the topographic map, the urban zone of the city of Chorrillos is at an average altitude of 35 m above sea level, while the

area of the beach resorts is at an altitude of about 5 m above sea level. Likewise, it is notorious that from the coastline to 1 km inland, the relative unevenness of the terrain does not exceed 10 m in height, enough to allow water flows from the ocean to circulate at high speeds, posing a danger to people who are in the resorts and the urban area located on the coastal coast of the city of Chorrillos.

Finally, water flows from the sea due to a possible seismic scenario of great magnitude are channeled through low-lying areas along the coastal coast, affecting all areas susceptible to flooding, including the coasts of the city of Chorrillos.

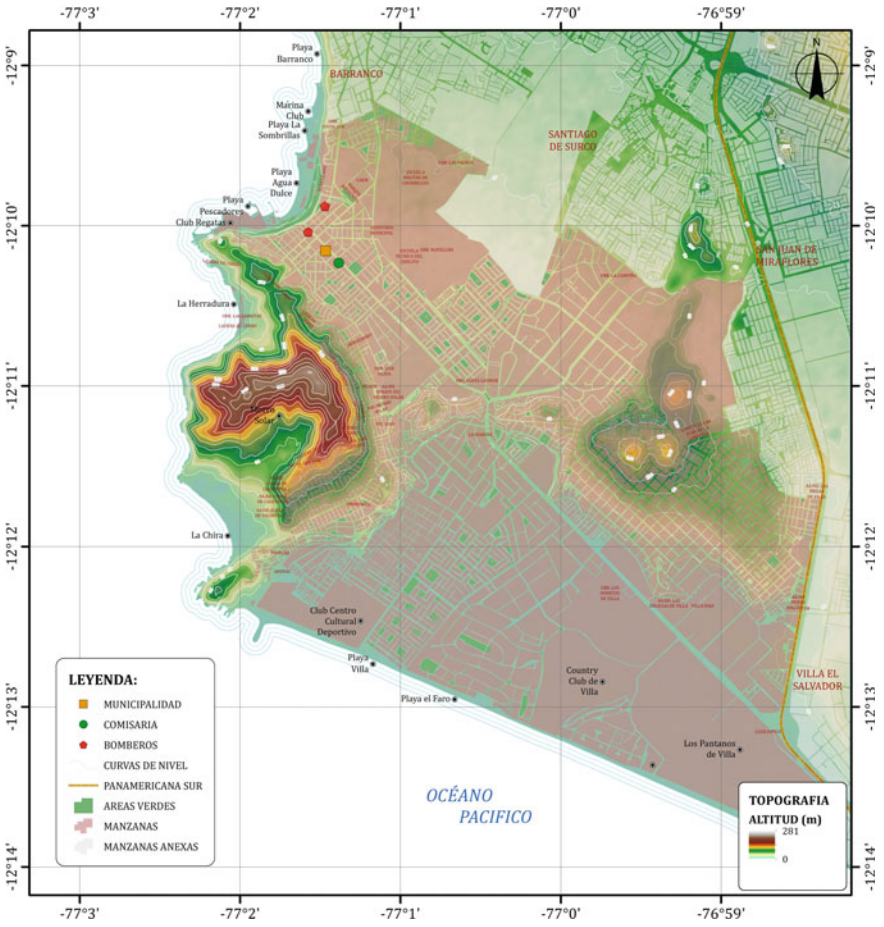

Fig. 4.4 Topographic map of the study area

4.3.4 Cadastral Data

The cadastral data were obtained from the National Institute of Statistics and Informatics (INEI), with information on the number of stories of the lots in the study area (Fig. 4.5). This information made it possible to generate a field of heights to characterize the buildings as if they were topographic elevations, which were added to the existing topographic database in order to increase the spatial resolution of the digital elevation model.

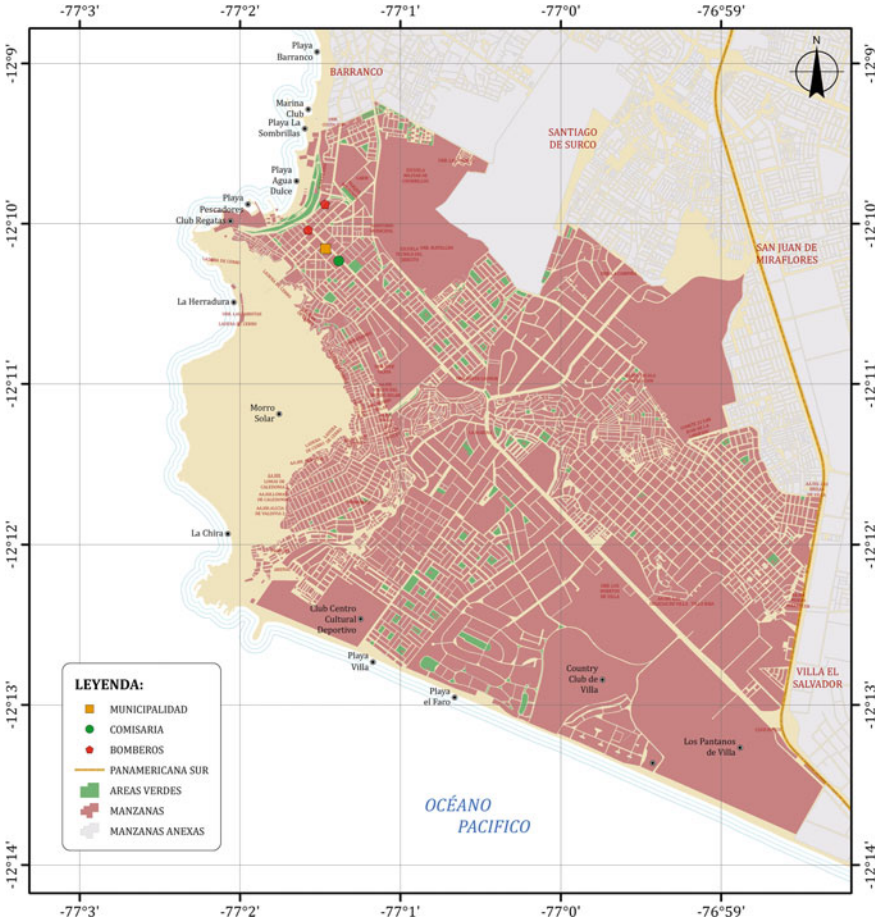

Fig. 4.5 Cadastral map of the study area

4.4 Numerical Modeling

Numerical modeling techniques were used, based on the vertically integrated nonlinear shallow water equations of motion (4.1) and the continuity Eq. (4.2), without the Coriolis effect term.

$$\frac{\partial M}{\partial t} + \frac{\partial}{\partial y}\left(\frac{M^2}{D}\right) + \frac{\partial}{\partial y}\left(\frac{MN}{D}\right) = -gD\frac{\partial \eta}{\partial x} - \frac{gn^2}{D^{7/3}}M\sqrt{M^2+N^2}$$

$$\frac{\partial N}{\partial t} + \frac{\partial}{\partial x}\left(\frac{MN}{D}\right) + \frac{\partial}{\partial y}\left(\frac{N^2}{D}\right) = -gD\frac{\partial \eta}{\partial y} - \frac{gn^2}{D^{7/3}}N\sqrt{M^2+N^2} \tag{4.1}$$

$$\frac{\partial \eta}{\partial t} + \frac{\partial M}{\partial x} + \frac{\partial N}{\partial y} = 0 \tag{4.2}$$

where η is the vertical displacement of the water surface above the quiescent level, M and N are the vertically integrated components of the transport between horizontal and vertical unit width (flow), g is the gravity acceleration and D is the total depth.

The tsunami initial condition was determined using a model that assumes an instantaneous deformation of the ocean surface identical to the vertical deformation of the seafloor (4.3).

$$\frac{\partial h}{\partial t} = \mu U \iint \left[\left(\frac{\partial {u_i}^2}{\partial \xi_2} - \frac{\partial {u_i}^2}{\partial \xi_3}\right)\sin(2\delta) - \left(\frac{\partial {u_i}^2}{\partial \xi_2} + \frac{\partial {u_i}^2}{\partial \xi_3}\right)\cos(2\delta)\right] d\xi_2 d\xi_3 \tag{4.3}$$

where μ is Lamé elastic constant $\approx 5 \times 10^{11}$ dynas/cm^2, U is the slip of the failure plane, u_i is the dislocation magnitude component, δ is the slip angle of the failure plane and $\xi_2 y \xi_3$ are the horizontal spatial coordinates of the failure plane.

Tsunami propagation was simulated using the finite difference method that numerically integrates the shallow water equations. Coastal zone inundation was determined using a moving boundary condition. The integration domain was discretized using a set of nested grids of different spatial resolution, being the most detailed where the tsunami inundation is determined (Goto and Ogawa 1992; Imamura 1989; Koshimura 2009).

4.5 Results

Numerical modeling allowed us to know the physical characteristics of tsunami water flows in the district of Chorrillos, obtaining information on flood zones, maximum heights, water flow velocity and synthetic tide diagrams showing the dynamics of tsunami waves on the coastal coastline.

4.5.1 Maximum Inundation Area

The estimation of the maximum inundation area on the coast is the first approximation for sizing the tsunami hazard in the city of Chorrillos. For the seismic scenario, the maximum tsunami inundation area recorded over a 6-h period at one-minute intervals was analyzed.

For the scenario (8.8 Mw), tsunami lengths fluctuating between 0.3 and 1.0 km are estimated along the coasts of the study area (Fig. 4.6), with maximum inundation occurring in the southern sector of the city of Chorrillos, in areas close to the border with the city of Villa el Salvador.

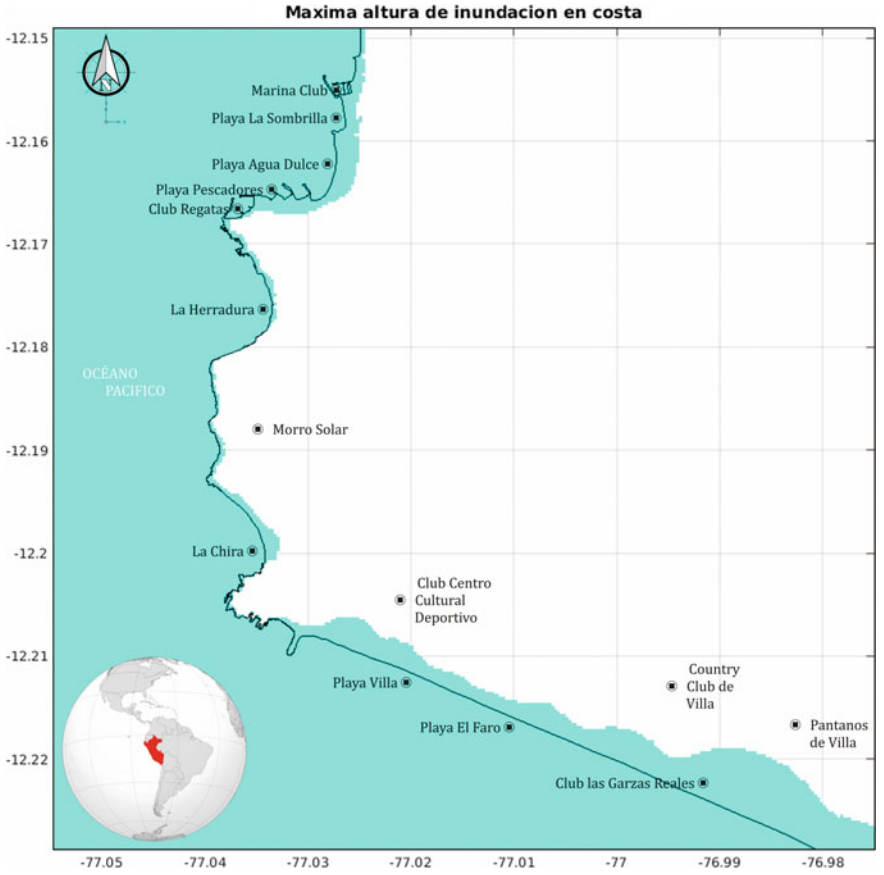

Fig. 4.6 Areas of maximum tsunami inundation (8.8 Mw)

4.5.2 Maximum Flood Heights.

The different heights of the water flow that will flow along the coastline of the city of Chorrillos were calculated for a time period of 6 h after the earthquake occurred. The estimation of the maximum tsunami heights along the coast are the second approximation for sizing the hazard scenarios.

The scenario (8.8 Mw) presents maximum water columns in the northern sector of the city of Chorrillos with values fluctuating between 5 and 9 m, heights that are quickly attenuated in inland areas, while the towns located to the south of the city such as Villa, El Faro and Club las Garzas Reales beaches have inundation depths between 3.0 and 5.0 m (Fig. 4.7).

The maximum flood heights considering the existing buildings in the study area are shown below. Figure 4.8 shows the northern area of the city of Chorrillos, showing the fishing terminal flooded by the tsunami waves. Figure 4.9 shows the southern

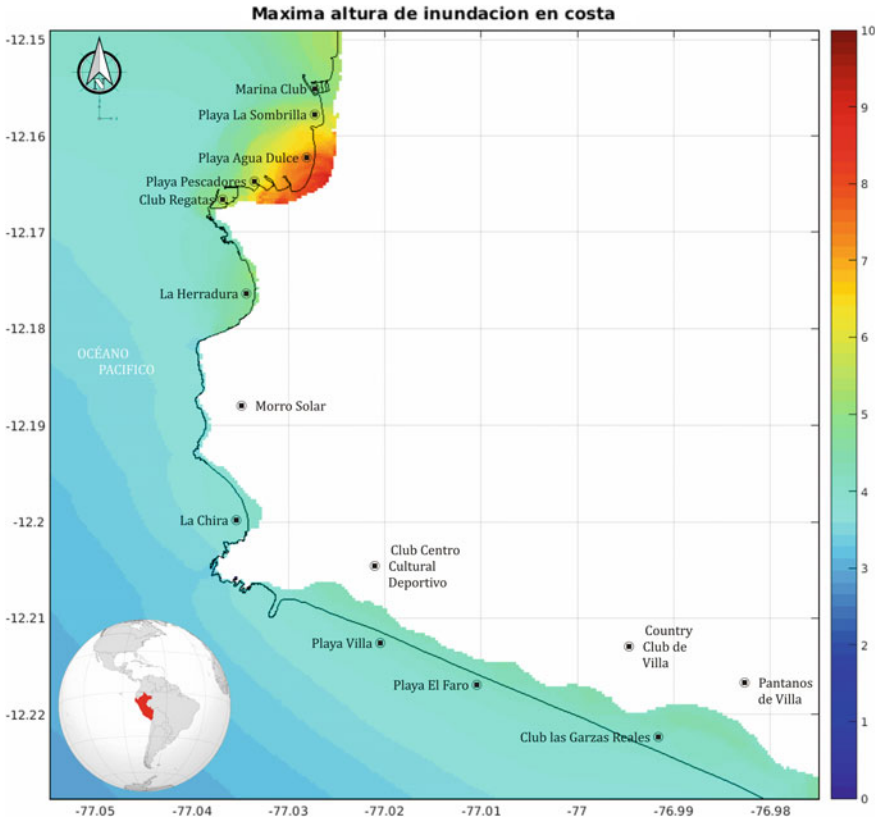

Fig. 4.7 Maximum tsunami inundation height (8.8 Mw)

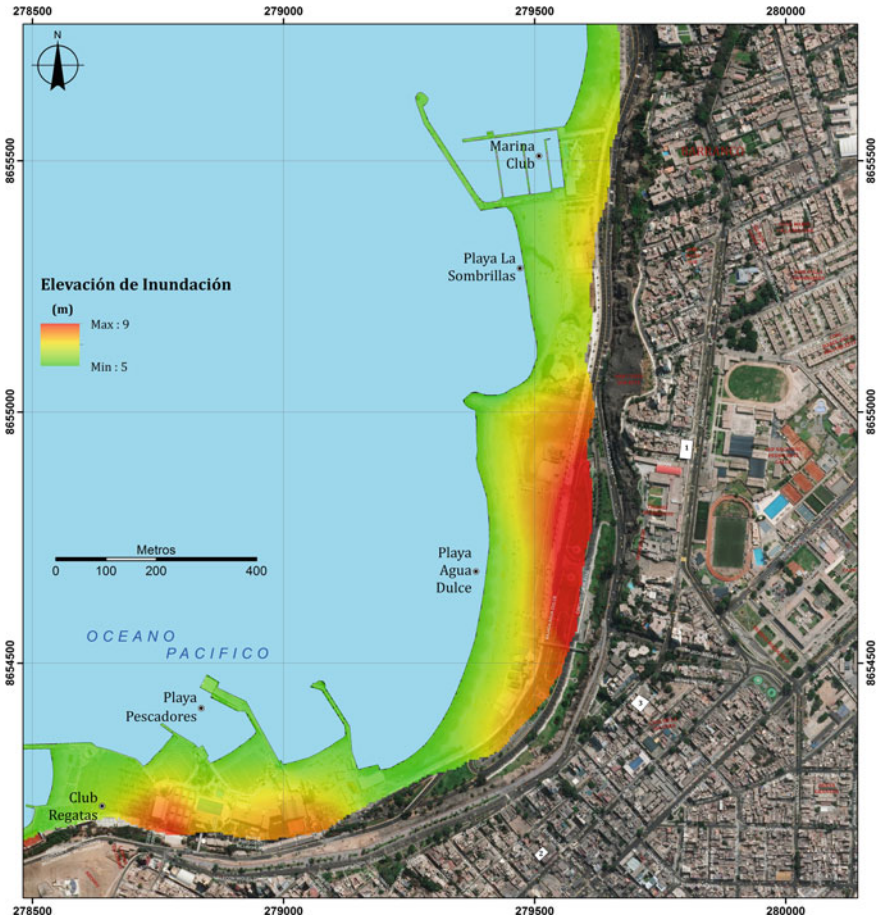

Fig. 4.8 Maximum flood height considering dwellings—north zone

area of the city of Chorrillos, showing some houses that are not covered by the flood, which could be used for vertical evacuation plans.

4.5.3 Maximum Water Flow Velocities

Knowing the velocity of water flow from the sea after a large magnitude earthquake is vital to know the force with which the flow can carry loose materials along its coastal propagation where it travels and that upon reaching urban areas will increase the danger and the dimensions of the affected areas. Therefore, knowing this parameter is important to improve the evaluation of the danger to which urban areas and the population are exposed.

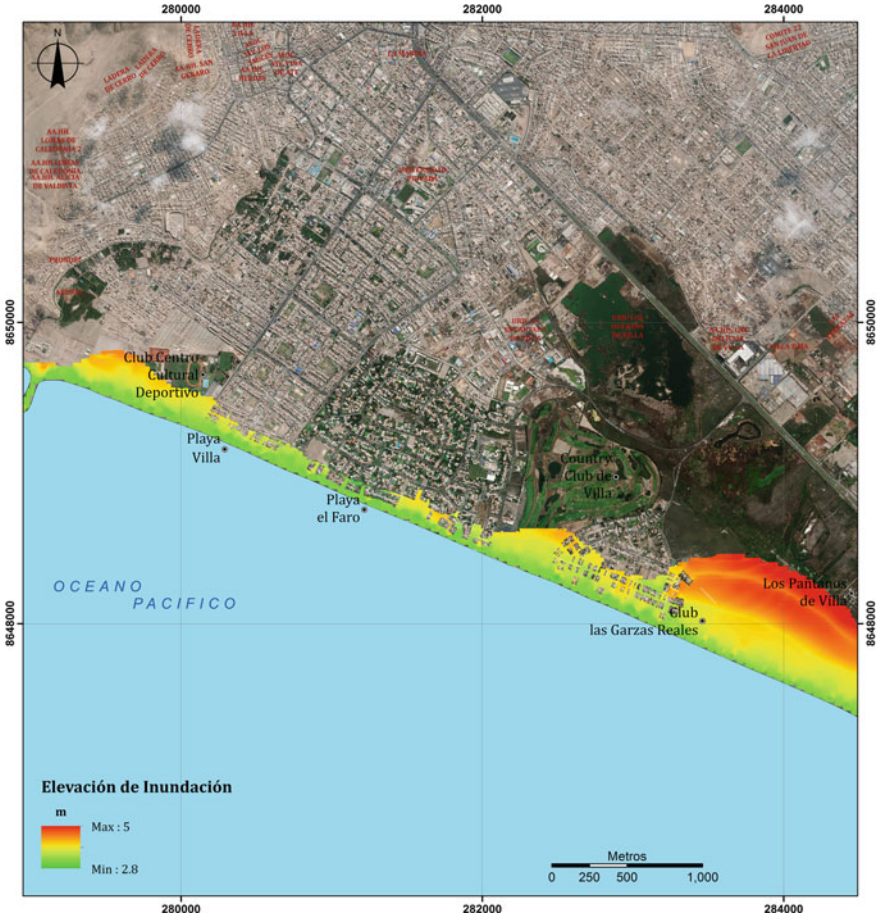

Fig. 4.9 Maximum flood height considering dwellings—south zone

The maximum water flow velocities in the flooding areas are dangerous for people's lives, except for the sectors near the maximum flood limits (run-up). The maximum flood velocities were in the order of 24 and 30 km/h (Fig. 4.10).

The maximum inundation velocities considering the existing buildings in the study area are shown below. Figure 4.11 shows the northern area of the district of Chorrillos, showing the fishing terminal impacted by tsunami waves of 10 m/s. Figure 4.12 shows the southern area of the district of Chorrillos, showing some houses impacted by 6 m/s waves; the presence of buildings generates increased velocities in the streets where the flooding propagates.

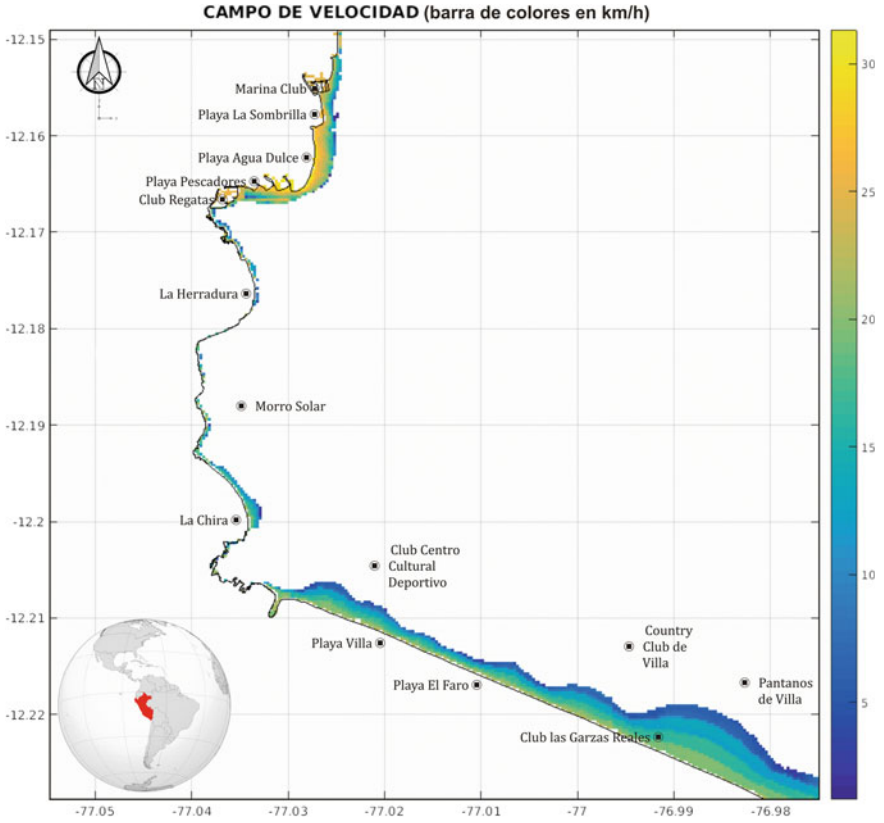

Fig. 4.10 Maximum water flow velocity of the tsunami (8.8 Mw)

4.5.4 Sea Variation Due to the Tsunami

To evaluate the sea level behavior, six tide diagrams were modeled (Fig. 4.13); the first one in front of Agua Dulce Beach (S12.16°–W77.03°), the second one in front of La Herradura (S12.17°–W77.04°), the third in front of Morro Solar (S12.18°–W77.04°), the fourth in front of Playa La Chira (S12.12°–W77.03°), the fifth in front of Playa Villa (S12.21°–W77.02°), and the sixth in front of the Villa Country Club (S12.22°–W77.00°).

The first sea level anomaly occurs before 20 min, with increasing amplitudes fluctuating between 2 and 6 m. Seventy-five minutes after the earthquake, the maximum tsunami amplitude is recorded, reaching 6 m at the synthetic tide gauge at Agua Dulce Beach. Sea level anomalies are maintained for about 6 h, gradually decreasing in magnitude (Figs. 4.14, 4.15, 4.16, 4.17, 4.18 and 4.19).

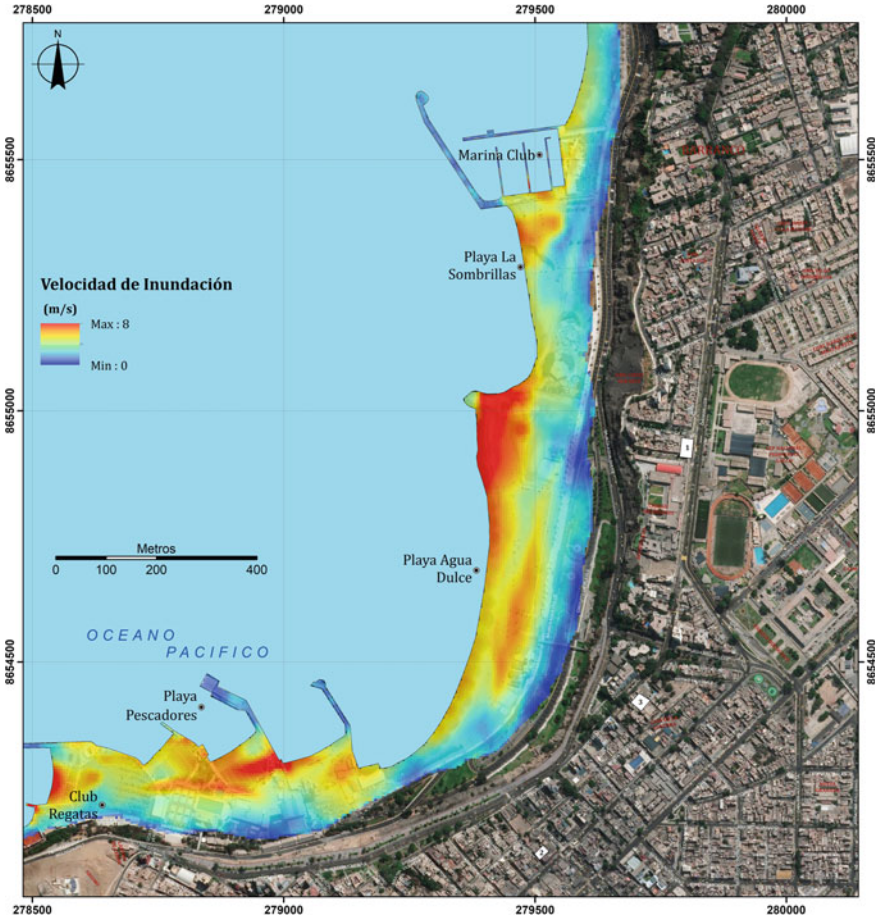

Fig. 4.11 Maximum velocity considering houses—northern zone

4.6 Conclusions

The tsunami hazard scenario evaluated in the city of Chorrillos allows us to understand the potential magnitude of the danger to which the population is exposed. On the coasts of the department of Lima, tsunami heights fluctuating between 3 and 11 m were obtained.

The tsunami inundation areas obtained for the city of Chorrillos have inundation surfaces greater than 1 km without exceeding a height of 10 m. The maximum inundation lengths were in the southern part of the city.

The hydrodynamic parameters of the resulting inundation confirm the high level of danger. The tsunami hazard due to inundation depth is high (>2 m) along the entire

Fig. 4.12 Maximum velocity considering housing—south zone

coastal edge affected by inundation. Meanwhile, current velocities exceed 1.5 m/s, which translates into high levels of danger to people.

For the scenario evaluated, the near-field tsunami rises within minutes. The first sea level anomaly occurs before 20 min, with increasing amplitudes fluctuating between two and five meters.

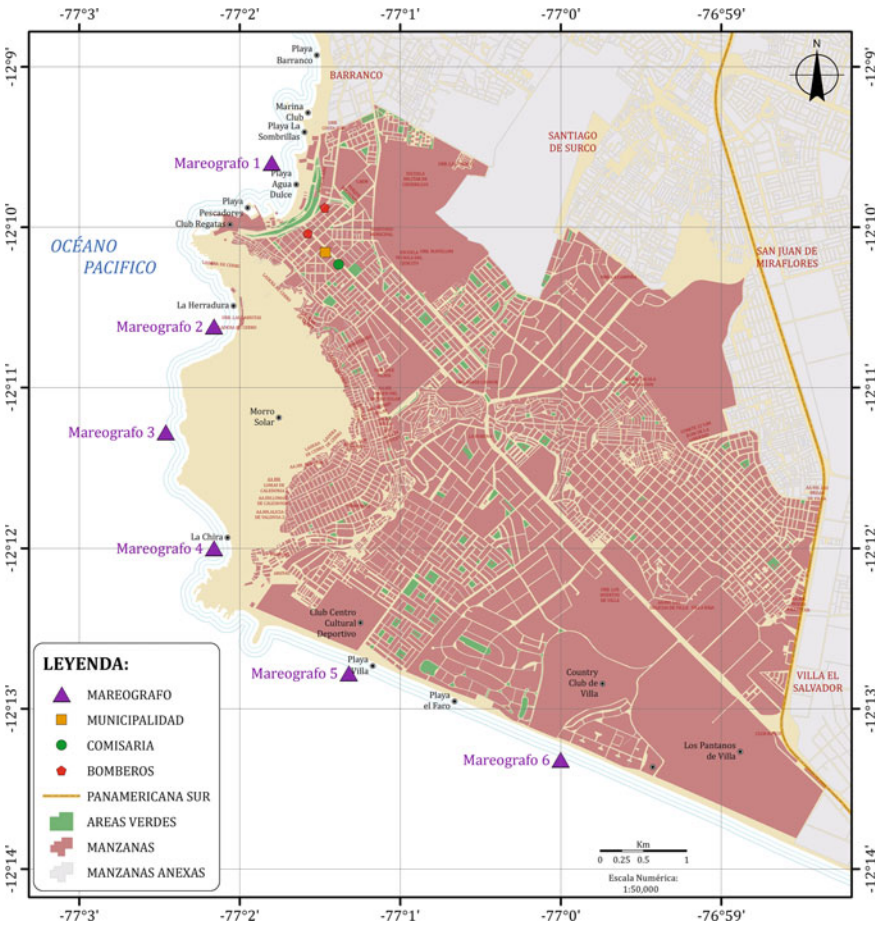

Fig. 4.13 Location of modeled tide gauges

Fig. 4.14 Synthetic tide diagrams in Agua Dulce beach

Fig. 4.15 Synthetic tide diagrams in La Herradura

Fig. 4.16 Synthetic tide diagrams in front of Morro Solar

Fig. 4.17 Synthetic tide diagrams in La Chira beach

Fig. 4.18 Synthetic tide diagrams in Villa beach

Fig. 4.19 Synthetic tide diagrams in Villa Country Club

References

Carpio J, Tavera H (2002) Estructura de un Catálogo de Tsunamis para el Perú, basado en el Catálogo de Gusiakov. Instituto Geofísico del Perú

Chlieh M, Perfettini H, Tavera H (2011) Interseismic coupling and seismic potential along the Central Andes subduction zone. J Geophys Res 116

Dorbath L, Cisternas A, Dorbath C (1990) Assessment of the size and great Historical Earhquakes in Peru. Bull Seismol Soc Am 80(3):551–576

Goto C, Ogawa Y (1992) Numerical method of Tsunami simulation with the leapfrog scheme. Tohoku University

Iida K, Iwasaki T (1983) Tsunamis their science and engineering. Terra Scientific Publishing Company, Tokyo

Imamura F (1989) Tsunami numerical simulation with the staggered leap-frog scheme (Numerical code of TUNAMI-N1). Japón

ITSU (1999) Master plan. Tsunami warning system in the Pacific, 2nd edn. Intergovernmental Oceanographic Commission, UNESCO 32 pp

Koshimura S (2009) Tunami–Code Tohoku University's numerical analysis model for investigation of Tsunami. Japón

Mansinha L, Smylie E (1971) The displacement field of inclined faults. Bull Seismol Soc Am 61(5):1433–1440

Martínez J (2014) Dinámica y modelado numérico de un tsunami en el terminal portuario del Callao y zonas adyacentes

Norabuena E, Leffler-Griffin L, Mao A, Dixon T (1998) Space geodetic observations of Nazca-South America Convergence. Science 279:358–362

SHOA (2018) Servicio Hidrográfico y Oceanográfico de la Armada de Chile. https://www.snamchile.cl

Silgado E (1978) Historia de los sismos más notables ocurridos en el Perú 1513–1974, República de Perú Sector Energía y Minas, Instituto de Geología y Minería, Boletín N°3 Serie C, Geodinámica e Ingeniería Geológica, 130 pp

Villegas J et al (2016) Active tectonics of Peru: heterogeneous interseismic coupling along the Nazca megathrust, rigid motion of the Peruvian Sliver, and Subandean shortening accommodation. J Geophys Res: Solid Earth

Wiegel R (1970) Tsunamis. In: Wiegel R (ed) Earthquake engineering. Prentice-Hall, pp 253–306

Chapter 5
Evaluation and Correction of Rainfall Forecast by WRF Model in the Upper Reaches of the Yangtze River

Wei Fang, Jianzhong Zhou, Xin Yang, Benjun Jia, and Yurong Wang

Abstract The upper reaches of the Yangtze River is an important part of the Yangtze River Basin, which concentrates most of the water energy resources. It is meaningful to carry out high-accuracy rainfall forecast in the basin, which can help extend forecast lead time, improve the forecast accuracy of runoff forecast, and provide important decision information for flood control and disaster reduction. To improve the accuracy of rainfall forecast in the watershed, different combination schemes of microphysical processes, boundary layers, and cumulus convection parameterization scheme combinations in the WRF model were evaluated by *TS* score, mean absolute error and Brier score. AR model was introduced to correct the rainfall prediction results. The results show that the WRF model has the highest accuracy of rainfall forecast when the microphysical process scheme, boundary layer parameterization scheme and cumulus convection parameterization scheme are WRF single-moment 3-class scheme, Yonsei University scheme and New Kain-Fritsch scheme respectively. The corrected rainfall forecast can partially correct the phenomenon of "staggered peak", which make forecast accuracy better.

Keywords The upper reaches of the Yangtze River · Rainfall forecast · Weather Research and Forecasting (WRF) · AR model and correction

5.1 Introduction

The Yangtze River is the longest river in China, with abundant rainfall and hydropower resources. Due to the combined effects of global warming and human activities, floods in the basin have been frequent, which cause serious economic losses and casualties in recent years (Shi et al. 2021). Therefore, it is urgent to

W. Fang · J. Zhou (✉) · X. Yang · B. Jia · Y. Wang
School of Civil and Hydraulic Engineering, Huazhong University of Science and Technology, Wuhan 430074, People's Republic of China
e-mail: jz.zhou@hust.edu.cn

Hubei Key Laboratory of Digital Valley Science and Technology, Wuhan 430074, China

H.-Y. Jeon (ed.), *Sustainable Development of Water and Environment*,
Environmental Science and Engineering,
https://doi.org/10.1007/978-3-031-07500-1_5

combine hydrological forecasting with flood control operation to provide scientific guidance for water resources operation. As the basic input of forecast flood control operation, forecast precipitation has an important influence on the accuracy and forecast lead time of forecast flood control operation. In the past research on short-term rainfall forecast in the basin, artificial prediction, empirical regression or statistical forecasting methods were usually used to predict future precipitation. With the rapid development of computer technology, numerical weather prediction has been rapidly developed, whose effectiveness in rainfall forecast has been widely recognized (Lei et al. 2018).

Numerical weather prediction is based on the actual conditions of the atmosphere and takes large computers as tools to solve the differential equations of the weather evolution process to predict the weather state in the future (Shen et al. 2020). At present, numerical weather prediction systems have been established at home and abroad, and a number of widely used numerical forecast products such as Weather Research and Forecasting (WRF) model, T639 model, and ECMWF model have emerged (Chen and Xue 2004). Among them, the WRF model, favored by many scholars, independently developed by the United States has the characteristics of flexible and efficient calculation and a wide range of platforms. So it is widely used in weather forecasting. The WRF model includes a series of physical processes: cloud microphysics, cumulus, boundary layer, etc. It is classified according to regional conditions, and multiple sets of parameters with different values are configured for each physical process. Then the configuration of hundreds or thousands of various parameters can be simplified to the configuration of several sets of parameterization schemes. Studies have shown that the WRF model has a good precipitation forecasting effect, but it's necessary to select appropriate parameterization schemes according to different watershed characteristics, and make further correction (Liao et al. 2012).

In the study, the upper reaches of the Yangtze River was taken as the study area. Firstly, WRF model's parameterization combination schemes that was suitable for the study region was analyzed. Secondly, the optimal parameterized combination scheme was selected by the evaluation system. Finally, the optimal parameterized combination scheme was used to make a test forecast and the results were corrected.

5.2 Data and Methods

5.2.1 Research Area and Dataset

The Yangtze River is the largest hydropower river in the world and the longest river in Asia. It has a total length of 6,387 km and a total area of 1.8 million km2, which accounts for about 20% of the total area of Chinese mainland. Among them, the upper reaches of the Yangtze River is the area from the source of the Yangtze River to Yichang City, Hubei Province. It is located at 100°–112°E, 23°–35°N, about

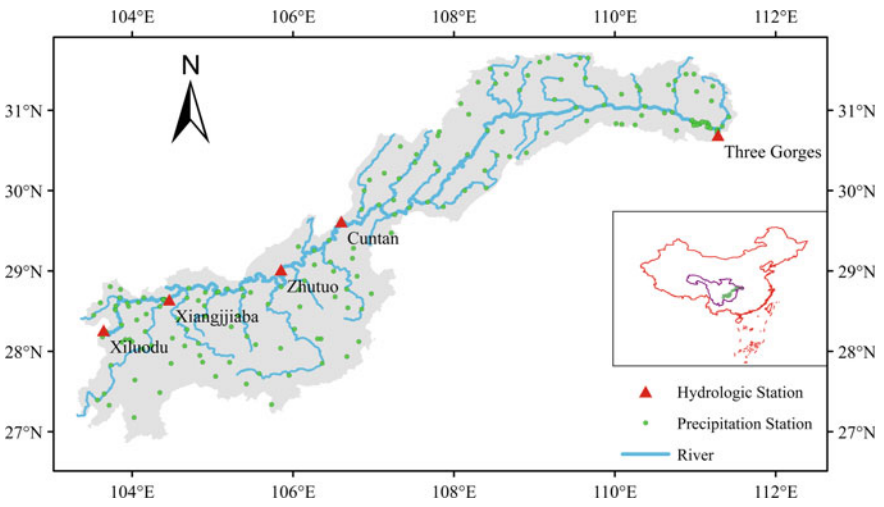

Fig. 5.1 The upper reaches of the Yangtze River

4,500 km long, and the control area of the basin is 1 million km2. It passes through 6 provinces and cities including Qinghai, Tibet, Sichuan, Yunnan, Chongqing and Hubei. The upper reaches of the Yangtze River from the Xiluodu to the Three Gorges in was our study area (see Fig. 5.1).

Due to data limitation and to ensure consistent availability of NCEP-FNL data, the three rainfall processes with daily average rainfall exceeding 30 mm in the basin were selected, which were September 18, 2014, July 15, 2015, and July 1, 2016, respectively. Model was built by the three typical precipitation processes and corrected using the rainfall data from June to September 2018.

5.2.2 The WRF Model

The WRF model is a numerical weather prediction system, designed for atmospheric research and weather forecasting. It is jointly developed by a number of American research and development institutions. WRF mode mainly consists of four modules: drive data, data preprocessing, main program of calculation and mode product post-processing. Firstly, the watershed topographic data and meteorological data should be downloaded to drive the operation of the WRF model. Secondly, the downloaded data should be processed by the preprocessor in WRF mode to make them into the format required by WRF mode. Then, the weather forecast can be made in the main program of calculation. Finally, the weather forecast information of the basin can be extracted through the post-processing program of model products such as NCL, ARWpost and so on.

In the study, five sensitive cloud microphysical parameterization schemes, three sensitive boundary layer parameters schemes and three sensitive cumulus convection parameterization schemes were selected to form 45 alternative parameterization scheme combinations. Sensitive cloud microphysical parameterization schemes included WRF Single-Moment 3-class scheme, WRF Single-Moment 5-class scheme, Ferrier scheme, Kessler scheme, and Lin et al. scheme. Sensitive boundary layer parameters schemes included Yonsei University scheme, Mellor-Yamada-Janjic scheme, and Asymmetric Convective Model version 2 scheme. Sensitive cumulus convection parameterization schemes included New Kain-Fritsch scheme, Betts-Miller-Janjic scheme, Grell-Devenyi Ensemble scheme. In addition, the RRTM scheme and the Dudhia scheme were selected as the long-wave and short-wave radiation schemes, respectively. The Jimenez scheme was selected as the near-surface layer scheme, and the Noah scheme was selected as the land surface layer scheme. The initial test drive data was composed of $1^\circ \times 1^\circ$ FNL data provided by NCEP, and the boundary replacement time was 6 h. Besides, the Lambert projection was selected as the projection method, the horizontal resolution was 10 km, and the number of grids was 113×105.

5.2.3 The AR Model

Limited by people's cognitive ability and technological level, the existing meteorological knowledge is not specific and accurate enough. There is no equation or model that can accurately simulate the atmospheric change of a region. We can only simplify the regional meteorological change through numerical analysis and other means to calculate their approximate value. Therefore, existing rainfall forecasting models are uncertain, and we need to correct their results. In the study, the autoregressive (AR) model was introduced to correct the results of rainfall forecast.

The AR model is a linear prediction model, which can analyze the shown law of prediction error. So it can reveal the change and development law of the error sequence so that the future state of error is analyzed and predicted. As it only reflects the influence and effect of relevant factors on the prediction target through the historical sequence of the variables themselves, it will not be constrained by the assumption that variables are independent of each other.

The mathematical expression of AR model is as follows:

$$X_t = b_1 X_1 + b_2 X_2 + \ldots + b_n X_n + \xi \tag{5.1}$$

where, X_t is a series of observations, b_i is the parameter of AR model, ξ is the Random error value.

5.2.4 Performance Evaluation

In this study, threat score(*TS*), brier score (*BS*) and mean absolute error (*MAE*) were adopted to select the optimal parameterized combination scheme of WRF model. The specific index formula is as follows:

$$TS = \frac{N_c}{N_f + N_o + N_c} \tag{5.2}$$

$$BS = \frac{1}{n}\sum_{k=1}^{n}(P_{Fi} - P_{Oi})^2 \tag{5.3}$$

$$MAE = \frac{1}{n}\sum_{i=1}^{n}|P_F - P_O| \tag{5.4}$$

where, N_f is the number of missed rainfall forecast, N_o is the number of empty forecast, N_C is the number of accurate rainfall forecast, P_F is the forecast value, P_O is the observed value, and n is the forecast times. The closer *TS* is to 1, the closer *BS* and the *MAE* are to 0, the better the forecast results are.

5.3 Results

The evaluation index system was used to evaluate the effect of 45 combination schemes of WRF model on rainfall simulation, and the five parameterized combination schemes with the best comprehensive ranking were selected. Five optimal parameterized combination schemes were shown below in the Table 5.1.

According to Table 5.2, the microphysical process scheme, boundary layer parameterization scheme and cumulus convection parameterization scheme are WRF

Table 5.1 Five optimal parameterized combination schemes

Combination	Microphysical process scheme	Boundary layer parameterization scheme	Cumulus convection parameterization scheme
1	WRF single-moment 3-class	Yonsei University	New Kain-Fritsch
2	WRF single-moment 3-class	Asymmetric convective model version 2	New Kain-Fritsch
3	Lin et al.	Yonsei University	Betts-Miller-Janjic
4	Lin et al.	Asymmetric convective model version 2	Grell-Devenyi ensemble
5	Lin et al.	Mellor-Yamada-Janjic	Grell-Devenyi ensemble

single-moment 3-class scheme, Yonsei University scheme and New Kain-Fritsch scheme respectively. At this time, The *TS* is higher, while *BS* and the *MAE* are smaller, which generally accord with the variation law of flood season weather in the study area. In addition, it can be seen from Table 5.2 that in the case of the same single index value, the multi-index system is more conducive to selecting the most suitable parameterized combination scheme for the basin. Yonsei University and New Kain-Fritsch have been applied to the upper reaches of the Yangtze River with better simulation results. Although Lin et al. appeared more frequently in the best five combinations, the scheme don't have great outstanding advantages in terms of combination results. So combination 1 can effectively improve the rainfall accuracy of WRF model, and make the distribution process of forecast rainfall and measured rainfall more consistent in the standard magnitude of rainfall, which can provide important hydrometeorological data for hydrological forecast of the basin.

The optimal scheme selected above was used to make a trial forecast of rainfall in the basin from May to September 2018 to further verify the applicability of the optimal scheme in the basin, and the AR model was used to calibrate the long-term rainfall forecast series. According to《Grade of valley area precipitation》, daily area precipitation in river basins can be divided into four grades, namely light rain, moderate rain, heavy rain and torrential rain, with 0.1, 6, 15 and 30 mm as the critical precipitation. The result is shown in Table 5.3 and Fig. 5.2.

The accuracy of WRF rainfall forecast decreases with the increase of rainfall grade. When the rainfall is more than 0.1 mm, *TS* is the highest with above 0.9, *BS*

Table 5.2 Evaluate index of five optimal parameterized combination schemes

Scheme	Time	*TS*	*MAE*	*BS*	Rank
1	2014/9/18	0.910	14.82	0.06	1
	2015/7/15	0.899	16.49	0.11	
	2016/7/1	0.934	7.8	0	
2	2014/9/18	0.895	15.36	0.11	2
	2015/7/15	0.866	17.82	0.15	
	2016/7/1	0.914	11.96	0.06	
3	2014/9/18	0.887	15	0.13	3
	2015/7/15	0.866	20.4	0.15	
	2016/7/1	0.921	11.25	0.05	
4	2014/9/18	0.879	13.91	0.15	4
	2015/7/15	0.866	20.61	0.15	
	2016/7/1	0.928	10.79	0.05	
5	2014/9/18	0.887	15.95	0.13	5
	2015/7/15	0.866	19.8	0.15	
	2016/7/1	0.907	13.25	0.09	

Table 5.3 Evaluate index before and after correction

Scheme	Evaluate index	≥0.1 mm	≥6 mm	≥15 mm	≥30 mm
Uncorrected-WRF	*TS*	0.918	0.31	0	0
	BS	0.08	0.69	1	1
	MAE	5.13	6.35	11.25	\
Corrected-WRF	*TS*	0.948	0.464	0.2	0
	BS	0.05	0.54	0.8	1
	MAE	3.53	4.51	7.06	\

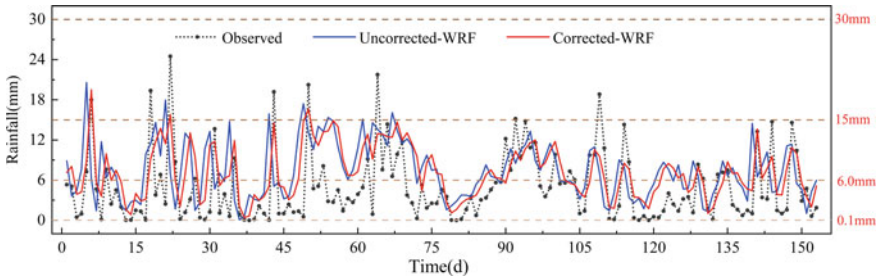

Fig. 5.2 Forecast effect before and after correction

score is the lowest, and *MAE* is the lowest. This indicates that the selected combination scheme has a good effect for the rainfall forecast above the grade of light rain. When the rainfall is more than 6 mm, the accuracy of rainfall forecast decreases obviously. However, when the rainfall is more than 15 mm, the fitting effect of rainfall forecast is even worse. So the selected WRF combination scheme has a good fitting effect on the spatial distribution of light rain and moderate rain levels, but there is a certain deviation in the prediction of heavy rain levels and above.

In addition, the results of corrected-WRF are better than those of uncorrected-WRF. When the rainfall is more than 0.1 mm, *TS* increases by 0.03, *BS* decreases by 0.03, and *MAE* decreases by 1.6, indicating that the results of corrected-WRF narrow the difference in the magnitude of rainfall When the rainfall is more than 6 mm, all indices are all significantly improved, and the prediction accuracy of grade above moderate rain is greatly improved. When the rainfall is more than 15 mm, *TS* of uncorrected-WRF is 0, *TS* of corrected-WRF is 0.2, which greatly improves the prediction accuracy. So corrected-WRF model is superior to uncorrected-WRF model.

5.4 Conclusions

45 different parameterized combination scheme were built to select optimal combination scheme in the upper reaches of the Yangtze River. And results were evaluated by *TS* score, mean absolute error and Brier score. Finally, the AR model was used to correct the prediction results of WRF model. The following conclusions are drawn:

(1) When the microphysical process scheme, boundary layer parameterization scheme and cumulus convection parameterization scheme are WRF single-moment 3-class scheme, Yonsei University scheme and New Kain Fritsch scheme respectively, The measured rainfall is more consistent with the spatial distribution and rainfall grade of the forecast rainfall, and the combined scheme has obvious forecast effect on rainfall above light rain grade.
(2) In order to verify the suitability of the selected optimal combination scheme in the upper reaches of the Yangtze River, a rainfall trial report was carried out for the basin, and rainfall correction was carried out through AR model. The results show that this combination scheme can reflect the characteristics of long series of rainfall time series, and the corrected rainfall forecast can not only improve the numerical difference between the measured series and the forecast series, but also partially correct the phenomenon of "staggered peak" between the two series, making the effect better.

Acknowledgements This study is supported by the National Natural Science Foundation Key Project of China (No. 52039004) and National Natural Science Foundation of China (No. U1865202).

References

Chen DH, Xue JS (2004) An overview on recent progresses of the operational numerical weather prediction models. Acta Meteor Sin 62(05):623–633

Lei XH, Wang H, Liao WH et al (2018) Advances in hydro-meteorological forecast under changing environment. J Hydraul Eng 49(01):9–18

Liao JB, Wang XM, Xia BC et al (2012) The effects of different physics and cumulus parameterization schemes in WRF on heavy rainfall simulation in PRD. J Trop Meteorol 28(04):461–470

Shen XS, Wang JJ, Li ZC et al (2020) China's independent and innovative development of numerical weather prediction. Acta Meteor Sin 78(03):451–476

Shi DM, Jiang GY, Peng XD et al (2021) Relationship between the periodicity of soil and water loss and erosion-sensitive periods based on temporal distributions of rainfall erosivity in the Three Gorges Reservoir Region, China. CATENA 202:105268

Chapter 6
Research and Application of Spatio-temporal Data Model of Water Supply Network Inspection System

Fuchen Ban, Xiaoyi Tong, and Zhitong Guo

Abstract The research, focusing on water supply network inspection system (WSNI), refines the inspection object, conceptually defines the inspection elements as well as completely presents the space–time expressions of the water supply network inspection system and eventually develops the data-based space–time model. This could be achieved via detailed analysis of the space–time features of the WSNI system. The result shows that the WSNI system, which is based on the space–time model, enables the orderly organization of the point, the line and the surface elements on space–time dimensions and are much better organized compared to the traditional water supply system. With an optimized business structure, it is better suited to the operation and management of the water supply enterprises. The well function of the pipe network is ensured through the highly-efficient and low-failure operation of the water supply network.

Keywords Water supply inspection system · Space–time features and objects and elements · Spatio-temporal model

6.1 Introduction

Urban water supply network is a critical part of municipal infrastructure constructions as well as the foundation of urban survival and development. In order to prevent accidents during production process caused by piping system, conducts regular inspections of the outlet ensuring underground pipe network and auxiliary facilities are maintained at all times (Zou 2016). Therefore, the establishment of an intelligentialized water supply network inspection system is an inevitable trend in water supply industry. Prof. Chen (Ting and Liu 2011; Liu et al. 2016; Chen 2012) and other teams had paid a lot attention on the spatial data and text information of pipeline inspection while Lee (Zhang et al. 2016) and his team members have spent time on the

F. Ban · X. Tong (✉) · Z. Guo
School of Municipal and Environmental Engineering, Shenyang Jianzhu University, Shenyang 110168, Liaoning, China
e-mail: 1320060040@qq.com

H.-Y. Jeon (ed.), *Sustainable Development of Water and Environment*,
Environmental Science and Engineering,
https://doi.org/10.1007/978-3-031-07500-1_6

processing method and the law of movement activity in aspect of the tracking inspection. However, there are still not enough study in temporal and spatial characteristics of combined inspection, in turn leading to some disadvantages.

Focusing on the issues, according to the spatio-temporal characteristics of the patrol objects, this paper comprehensively considers the time, space and attribute information along with the inherent correlation between spatio-temporal data to analyze the spatio-temporal characteristics of the patrol objects. In next stage, a more scientific spatio-temporal data model of the patrol inspection system of water supply network will be constructed in order to achieve the multi-dimensional and stereoscopic analysis of the spatio-temporal objects of water supply network.

6.2 Space–Time Data Model of the WSNI Based on Object-Oriented Method

6.2.1 Proposed Conceptual Model

In data models of geospatial research field, the prominent research direction is "object oriented" method. The spatial "geographical ontology" is embodied into "geographical entity" to express complex geographic dynamic phenomena (Chen 2013). With the above referential study, we establish conceptual model of space–time data shows in Fig. 6.1. We apply object-oriented method to time by analogy method to space and combining with time factors. The conceptual model of the WSNI is divided into "inspection objects", "patrol inspection events" and "patrol inspection process". With the time-axis and space-axis, the expression of "point, line and surface" is used to clarify the internal relationship between pipe network and the inspection service to abstract the WSNI, through conceptually visual definition elements as well as completely presenting the space–time expressions.

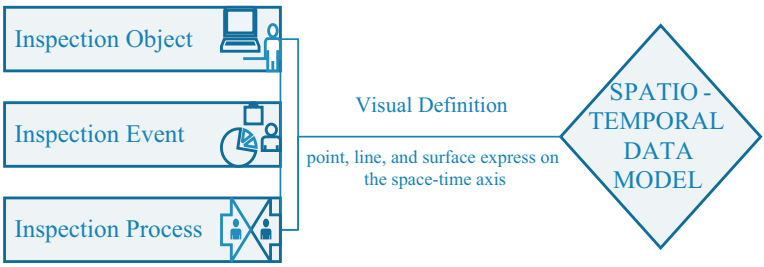

Fig. 6.1 Spatio-temporal data conceptual model

6.2.2 Visual Definition of Elements of the WSNI

The space–time objects of the WSNI are abstract assemblage including time objects and space objects (Zhang 2014). First, spatial object is the abstraction of the spatial entity, which is associated with geographic position. Second, time objects are abstract base classes and cannot be instantiated. In the WSNI service, time objects can be defined by effective time.

Spatial object of the WSNI is set S, and any pipe network space element "s" is a subset of S. And the geographic coordinates of spatial object on space-axis is $S = \{X, Y, Z\}$. Time object of the WSNI is visualized as $T = \{StartingTime, TerminalTime\}$. The effective time T represents one-dimensional data axis, and any time node t is on the t-axis. The time data t extracted by the WSNI including historical period of time and current time. The time of the period from start time *ts* to end time *te* is effective time $V_S = \{ts, te\}$, which is a subset of the complete set T. For a space element s, during its effective time changing, represents temporal change of the space element. Within the space–time dimension, there is also a patrol attribute object (an abstraction of non-spatial entities), which is defined as set of $F = \{F_1, F_2, ..., F_n\}$. The attribute object and the time object form a temporal object, which expresses the characteristic change of the WSNI within a specific time, and defines the temporal object as $Temporal = \{V_{S_1}, \{F_1, F_2, ..., F_n\}\}$. The collection of inspection objects of the same spatial element s at different times is a spatio-temporal feature class, defined as $Temporals = \{S_1, V_S, F\}$. On the class of space element s, the tenses of space and time element are expressed and formalize the space–time object as $ST = \{S, T, F\}$ to express the complete change of the spatio-temporal characteristics of the inspection object.

6.2.3 Characteristics and Relationship of Spatio-temporal Elements of the WSNI

In the construction of the spatio-temporal data model, the attribute features of the refined point, line and surface elements of the WSNI include some characteristics as follows: Uniqueness, Particularity, Immediacy and Relevance.

According to the characteristics of spatio-temporal features, the multi-dimensional spatio-temporal relationship map is constructed as shown in Fig. 6.2. The spatio-temporal relationship is divided into three categories, time relationship, space relationship and network inspection properties.

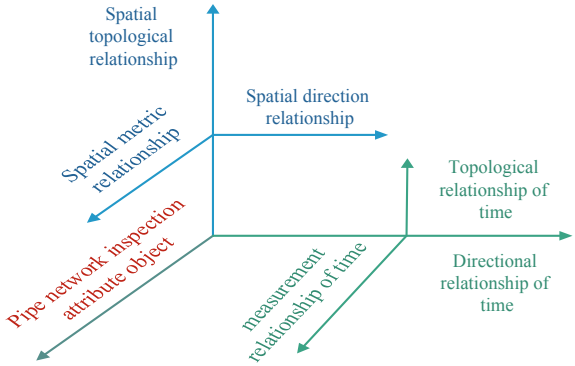

Fig. 6.2 Multidimensional spatio-temporal relation graph

6.2.4 Spatio-temporal Data Model of the WSNI

The spatio-temporal data model of the WSNI is a model which is based on the "point, line and surface" elements that are formally defined, and takes time and space as variables to cover multi-dimensional spatio-temporal topological relations. The model is shown in Fig. 6.3.

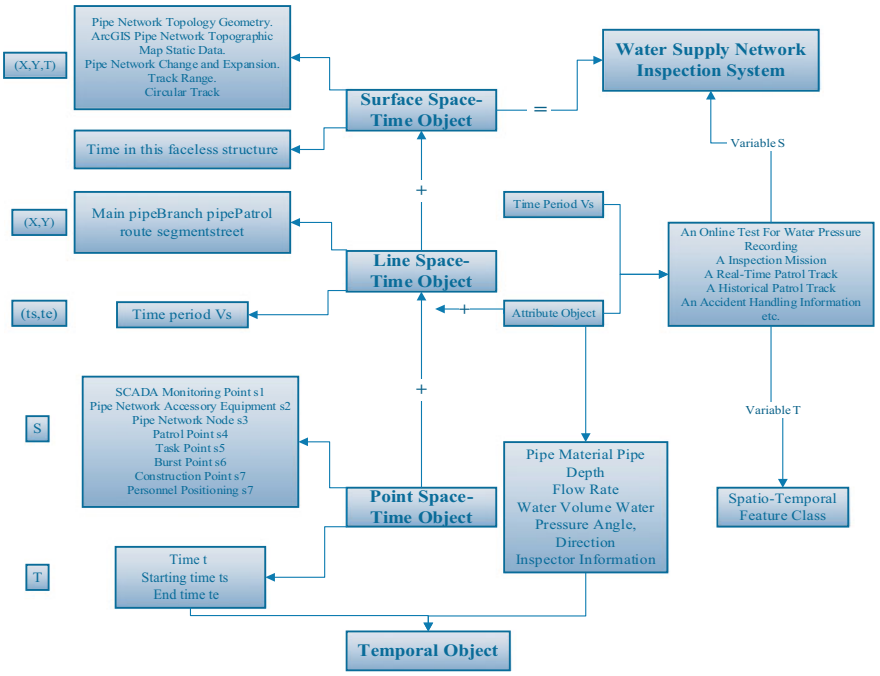

Fig. 6.3 Data model of the WSNI

6.3 Application of Spatio-temporal Data Model in the WSNI

The existing WSNI is mainly limited to the analysis of space and the present situation as shown in Fig. 6.4. It is a system which is mainly based on GIS spatial data, and supplemented by SCADA technology to monitor key points. The inspection work is carried out by the inspection staff according to the key points of the pipe network. After they finish inspection task, system will update some spatial data such as inspection mileage and other spatial data.

However, in the face of complex and ever-changing space–time information of the WSNI, it is difficult for the existing system to support requirements of operation and macro-regulation. According to the proposed spatio-temporal data model, we optimize the existing WSNI with spatio-temporal characteristics as shown in Fig. 6.5.

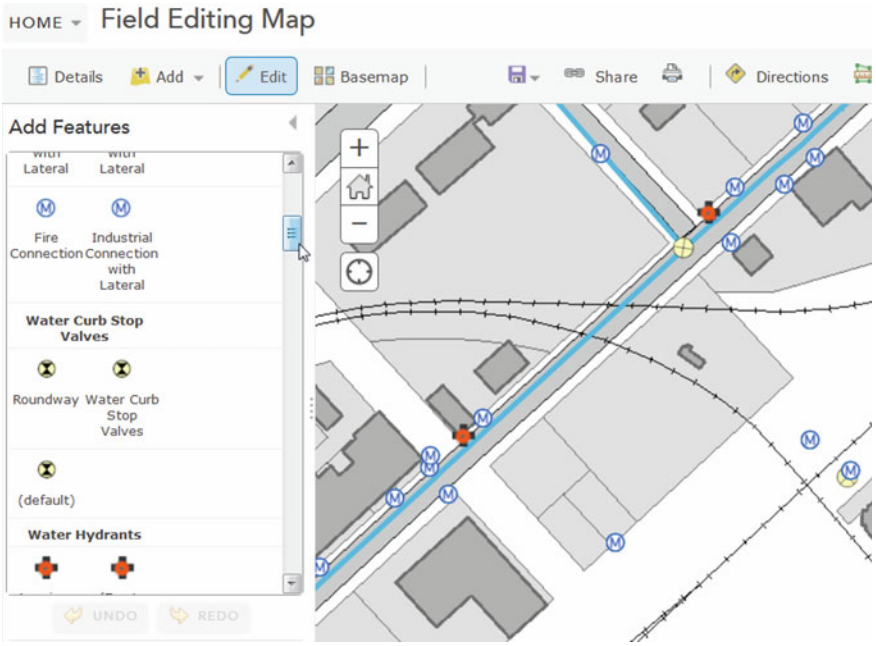

Fig. 6.4 Interface of the existing WSNI

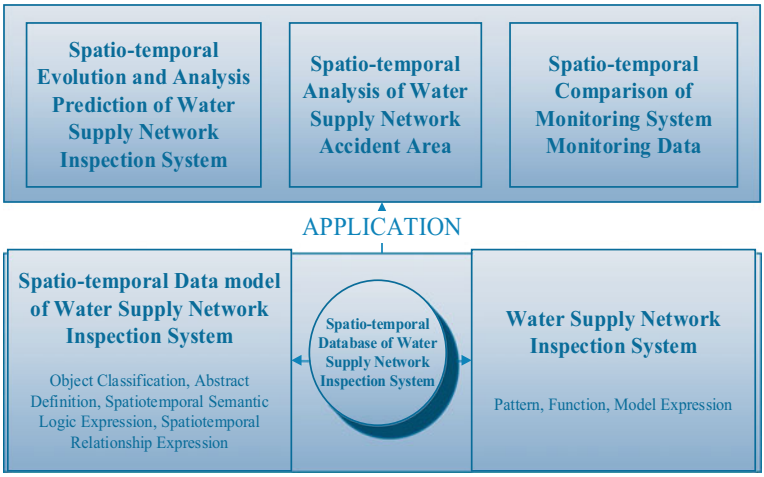

Fig. 6.5 Application system of the WSNI

6.3.1 Spatial–Temporal Evolution and Forecasting Analysis of the WSNI

Based on the spatial–temporal data model of the WSNI, the system expresses change of each inspection element in the dynamic system. Therefore, the initial spatio-temporal evolution of a single element can be obtained by querying the temporal object which constitutes the spatio-temporal feature class. In order to get a more comprehensive and detailed overall evolution (such as expansion, alteration, merger, disappearance, replacement, etc.), we do some works in response. All the works aim to grasp the historical dynamic trend of the municipal pipe network data effectively.

Compared with analyzing in microcosmic point of view, the changes of a certain inspection point and an accident point of the pipe network, especially the problems that are difficult to grasp for the pre-emptive maintenance and expansion of the pipe network. The spatio-temporal data model has it's advantage. The spatial and temporal evolution map shows overall operation status of the WSNI in a macroscopic and visual perspective. It can provide data support for pipe network's plan. This is convenient to study the macroscopic evolution of water supply pipe network, and it has important and practical significance in inspection planning, operation direction design, operation management and evaluation.

6.3.2 Spatial–Temporal Analysis of the Water Supply Network Accident Area

Analyze the causes of pipe network accidents, taking the explosion accident as an example, different qualities of pipes in the same batch, different construction qualities of the same pipe network, different ground load and the pressure may cause the spatial agglomeration of pipe burst (Zhang et al. 2010). Therefore, based on the spatio-temporal data model of the WSNI, method of spatio-temporal analysis for the accident area is carried out. Value range of time measurement is used as the division standard, the accident occurrence period is analyzed according to the time series data of the explosion accident. Combine with the accident point, space area and pipe network attribute data in a certain period. Determine radius and range of the point-space–time object feature and density threshold of the neighborhood space. Combine with the complaints such as squib, water leakage, water pressure anomaly, odor, etc., to obtain a burst time–space scatter plot which is used to assist managers take targeted measures to strengthen scientific network inspections in the key areas to reduce the frequency of accidents.

6.3.3 Spatio-temporal Analysis of Monitoring Data

Based on the spatio-temporal relationship between time, space and inspection attribute objects, upstream and downstream scales of the SCADA monitoring points and patrol points in the adjacent, are retrieved in the spatio-temporal relationship. According to the operation monitoring information of the spatio-temporal relationship, detection data of the relevant inspection points and SCADA online monitoring points in the same time period (such as month, season, etc.) are extracted. And the data are summarized by system. Then calculate the deviation rate of the two indicators in the same detection attribute. Mutually confirm the spatio-temporal monitoring data according to different time scales. The deviation rate of the two in the same detection attribute index is calculated. And the enterprise will obtain detection data with large output deviation rate (customizable configuration). The compared results are used for scheduling reference to ensure the accuracy and authenticity of data.

6.4 Conclusion

We rely on the characteristics of spatio-temporal data in the WSNI, proposed an object-oriented method spatio-temporal data model. To realize the orderly organization of the basic space–time objects (points, lines, and surfaces) in spatio-temporal dimension, we make full use of the data information of the spatio-temporal object as shown. And the spatio-temporal data model is used to develop functional application

in the WSNI, and is used to lay the design foundation for the development of the WSNI. It is conducive to the establishment of a stable and scalable inspection data system structure as well as corresponding functions of the development system. Then it can solve series of problems mentioned in the paper caused by the lack of time and space factors in the existing system. This makes the optimized system closer to the needs of water supply enterprise management and integrated operations.

Acknowledgements I would like to thank the teachers in the school and laboratory for their help in my research and writing with my co-authors. We would also like to thank the Social Governance Science and Technology Special project of Shenyang Science and Technology Plan in 2021 (21-108-9-33) and the Basic Research Project of Higher Education Institutions of Liaoning Province in 2021 (LJKZ0576) for their joint help in providing financial support for our research.

References

Chen GM (2012) Application and effect of pipeline network patrol inspection system in urban water supply. Urban Water Supply 1:44–45

Chen XB (2013) Time-space data model based on object-event-process and its application. Geogr Geogr Inf Sci 29:10–11

Liu MC, Wang J, Zou D (2016) Realization of inspection and maintenance system of water supply network based on GIS&GPS technology. Geo-Spat Inf 14:104–106

Ting X, Liu HJ (2011) Innovation and practice of inspection of water supply network. Water Supply Drain 37:106–107

Zhang ZG (2014) Research on integrated management technology of municipal infrastructure spatio-temporal information. China University of Geosciences

Zhang HY, Tian YM, Pei L (2010) Establishment and application of spatial analysis model of pipe burst in water supply network based on GIS. China Water Supply Drain 19:71–73

Zhang ZG, Wu XC, Wang YL (2016) Spatial and spatial data model of water supply network for integrated management. Water Supply Drain China 32:71–75

Zou JH (2016) Design and implementation of intelligent inspection system based on Android. Donghua University of Technology, Nanchang

Chapter 7
Rapid Development of Online Hydraulic Model Calculation System Based on EPANET Source Code and ArcObjects

Fuchen Ban, Ke Xu, and Yueming Hei

Abstract In recent years, many water companies have proposed to establish an online dynamic hydraulic calculation model of the water supply pipe network to improve the scientific and technical level and service management level of the water supply industry. The model establishment is roughly divided into data collection, pipe network computing, and release services. In this paper, an online water supply network computing system is developed based on the information needs of water companies, which effectively combines EPANET, ArcGIS and database, and then passes through. The NET framework encapsulated as the service is eventually released to the Web platform. The system has strong functionality and low development cost, and can calculate the operation status of the water supply pipe network in real time by connecting the SCADA monitoring data, to provide guidance for the real-time operation scheduling of the water supply pipe network model, and meets the current needs of the water supply industry.

Keywords EPANET · ArcObjects · Water supply network · Online computing system

7.1 Introduction

At present, there are many more mature modeling software on the market, such as WaterGEMS, InfoWorks and other modeling software, which have the conditions of secondary development, but if using these commercial modeling software as the core computing engine will be bound to increase the overall cost of the later secondary development. In this case, the advantage of using the code open source EPANET as the core computing engine is very obvious, and can meet the actual needs of the water companies. Therefore, the method to develop the online dynamic hydraulic

F. Ban · K. Xu (✉) · Y. Hei
Shenyang Jianzhu University, Shenyang 110168, LN, China
e-mail: 1169158075@qq.com

H.-Y. Jeon (ed.), *Sustainable Development of Water and Environment*,
Environmental Science and Engineering,
https://doi.org/10.1007/978-3-031-07500-1_7

calculation model system for the core engine is economical and feasible and has high practical significance.

7.2 System Architecture Introduction

The overall system architecture is shown in Fig. 7.1. The ArcGIS base data stores the static data of the water supply pipe network, It is the basis for building a hydraulic model; The EPANET computing engine uses the ArcGIS water supply pipe network basic data for hydraulic calculation, Results tain hydraulic calculation; The Oracle database stores the basic data and calculation data of the water supply pipe network; The data in the Oracle database were collated and analyzed through ArcObjects development, The output is stored in the ArcSDE for a geographic database; ArcSDE has powerful geographic data management capabilities and enables multi-user concurrent operations; The SCADA database stores the monitoring data, It is mainly used for the verification of the later hydraulic model.

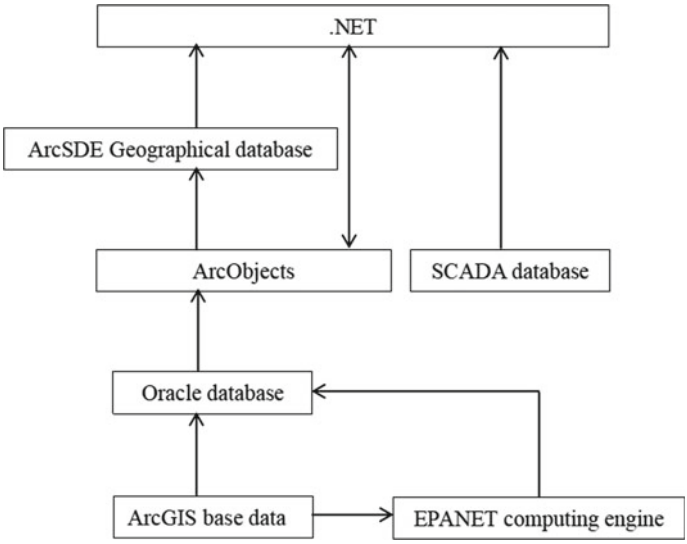

Fig. 7.1 System architecture diagram

7.3 Online Hydraulic Model System Establishment

7.3.1 Engineering Background

The water supply pipe network of Z High-tech Zone in Henan Province is more than 200 km, mainly using water Wells of water companies. Z High-tech Wutong Water Plant is responsible for the water supply in the area. The total scale of Wutong Water Plant is a daily water supply of 200,000 tons, the water plant adopts modern management, and there are more than 70 pressure monitoring points in the area.

7.3.2 EPANET Data and Geodatabase Pipe Network Model Establishment

By collecting and sorting out the water supply data in Z city, the hydraulic model is established in the EPANET modeling software and exporting the hydraulic model into the EPANET input file to facilitate the secondary development of the hydraulic model later. The input file of EPANET is an INP type input file and supports custom modification, and developers can customize the actual pipe network data according to the actual data (Li 2011), as shown in Fig. 7.2.

The INP file contains five types of model data: pipe network component data, system operation data, water quality data, report data, and pipe network marker data, as shown in Table 7.1.

This system first stores the INP data in the Oracle database to store the pipe network data. The data stored in Oracle does not have geographic attributes. The data in Oracle needs to be transferred to the geographic database before the hydraulic model system is released. The created geographic database is shown in Fig. 7.3.

Pipe network components	System operation	Water quality	Options and reports
[TITLE]	[CURVES]	[QUALITY]	[OPTIONS]
[JUNCTIONS]	[PATTERNS]	[REACTIONS]	[TIMES]
[RESERVOIRS]	[ENERGY]	[SOURCES]	[REPORT]
[TANKS]	[STATUS]	[MIXING]	
[PIPES]	[CONTROLS]		
[PUMPS]	[RULES]		
[VALVES]	[DEMANDS]		
[EMITTERS]			

Fig. 7.2 The main attribute tags in the INP file

Table 7.1 Model data contained in the INP file

Data	Detail
Network component data	Property data of each component equipment in the water supply pipe network
System running data	Working parameters and control conditions of the pipe network operation
Water quality data	Parameters that affect the water quality changes in the operation of the pipe networkbold
Report data	Operation results of pipe network
Geographical data of pipe network	The specific coordinate data of pipe network elements are closely related to the topology of pipe network

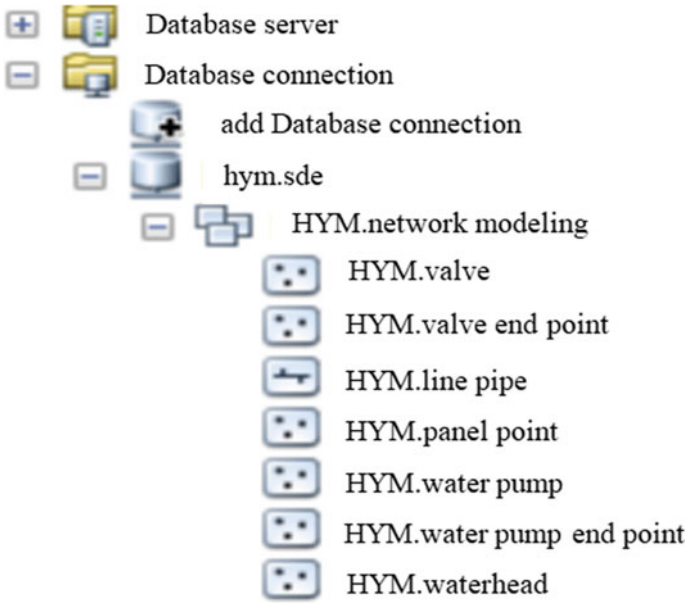

Fig. 7.3 Geographic Database Element Dataset Table Structure

In the EPANET pipe network model, the pipe network is divided into point and line types. EPANET treats pipelines, pumps and valves as line types, which sees pumps and valves as pipelines of length 0 of two overlapping terminals. Since these pipelines of length 0 cannot be identified in Geodatabase, the coordinates of the two overlapping terminals are slightly offset to remove the pipeline of length 0. The two element points are created as the start and termination points of pumps and valves. The display problem of the model data in Geodatabase is solved by the above method to accurately express the model data in Geodatabase.

7.3.3 EPANET Calculation Engine Call

The system development realizes the storage of water supply network data in geographic database by Oracle with INP data and geographic database. The detailed process of this method is as follows: there are many attribute tags in the INP file, regard each tag as a table (Table) in the Oracle database, each tag in the INP contains specific attributes, which are columns in the table, and the INP in the attribute tag downside the row in the table. Pipe network data in the INP is stored in a table into the Oracle database by programming. Similarly, the result data calculated by calling the EPANET calculation engine (node pressure, node flow, segment flow, segment flow, segment flow speed and head loss in the same way) are stored in the Oracle database. This method can standardize the INP data to facilitate Geodatabase reading network data from Oracle database and realize the conversion from Oracle database to Geodatabase.

7.3.4 ArcSDE Manages Geodatabase

ArcSDE is used for users to manage geographic information in data management systems, ArcSDE closely connects Oracle to Geodatabase, ArcSDE provides large spatial database support, and enables multi-user editing operations. There are many ways to call ArcSDE in ArcObjects's API, and through AO (ArcObjects) development, you can connect ArcSDE, create, and manage geographic databases (Yu 2015). The program adopts the development framework provided by ArcGIS SDE for .NET, calls the ArcObjects API to connect the ArcSDE, manage and update the geographic database, to obtain the geographic database meeting the needs of the water supply pipe network model. As shown, Fig. 7.4 is a table view of the pipeline data in the geographic database.

7.3.5 Release of Hydraulic Model System

ArcGIS for Server is a powerful server-side GIS product. After the GIS data is mapped, the GIS service can be deployed on the Web platform through the publishing service function in ArcGIS (Liu et al. 2016). The GIS system has a data analysis function, and users can intuitively understand the real-time situation of the water supply network in the operation process when using the online hydraulic model system (An et al. 2013).

In order to meet the functional demand of the water supply network for the water supply industry, this system has developed the following main functional modules according to the market demand.

OBJECTID *	SHAPE_NUMBE	FROM_NODE	TO_NODE	DIAMETER	ROUGHNESS	LOSSCOEFF	STATUS	PIPE_LENGTH	LINKFLOW
94817	9239	-J-3440	-J-985	100	110	0	Open	.747	.0226550901
94818	11259	-J-1975	-J-1974	100	110	0	Open	.74775	.1696459949
94819	11775	-J-2060	-J-2243	200	110	0	Open	.75095	-. 0000237898
94820	11178	-J-1957	-J-1956	100	110	0	Open	.75204	.0325999909
94821	6665	-J-3439	-J-3440	100	110	0	Open	.75525	.0227016341
94822	7437	29292-B	-J-3383	100	110	0	Open	.75904	.0000724604
94823	7600	-J-3476	-J-3477	600	110	0	Open	.7602	.0000227622
94824	11252	-J-1971	29939-A	100	110	0	Open	.76051	.0000173082
94825	10457	-J-1336	29860-B	200	110	0	Open	.76229	-. 0000243518
94826	7366	-J-3333	29270-A	100	110	0	Open	.76297	.0000207673
94827	10227	-J-1466	-J-1467	100	110	0	Open	.76505	-. 0000229405
94828	6997	-J-3019	-J-3020	100	110	0	Open	.76919	.0000136808
94829	10041	-J-166	-J-1369	100	110	0	Open	.77526	.1227378249
94830	9627	29952-A	-J-1157	100	110	0	Open	.77603	-. 0000274907
94831	11727	-J-1769	28936-B	100	110	0	Open	.77738	-. 0000162991
94832	11570	-J-2153	28888-A	300	110	0	Open	.77824	-26. 3367347717
94833	6579	-J-2727	29876-A	600	110	0	Open	.77927	.0000272054
94834	6455	-J-2654	-J-2655	100	110	0	Open	.77943	.0228950202
94835	7439	29293-B	-J-3384	100	110	0	Open	.77997	.0000321578
94836	11450	-J-1741	-J-1742	100	110	0	Open	.78121	-. 0000299302
94837	8282	-J-200	-J-1285	100	110	0	Open	.78305	.0000354473
94838	8702	-J-566	-J-2338	100	110	0	Open	.7841	.0000189533
94839	7492	-J-3055	29309-A	500	110	0	Open	.78487	.4647617936
94840	11542	-J-2133	28982-A	100	110	0	Open	.78561	.0000356988
94841	11206	-J-2081	-J-2082	100	110	0	Open	.78607	-. 0000170034
94842	8705	-J-569	-J-3348	100	110	0	Open	.78615	.0000281483
94843	9646	29951-B	-J-59	100	110	0	Open	.78628	.9547940803
94844	7108	-J-2122	29173-A	100	110	0	Open	.78975	.0000293191
94845	10049	-J-1392	-J-1391	100	110	0	Open	.78998	.0000291202
94846	10043	-J-1371	-J-1370	100	110	0	Open	.79007	.102602087
94847	11151	-J-1939	29828-B	100	110	0	Open	.79016	-. 0000160517
94848	6407	-J-3105	29162-A	300	110	0	Open	.79409	5. 0629862381
94849	9600	-J-1143	29974-A	100	110	0	Open	.79604	.0000280161
94850	10234	-J-178	29892-A	150	110	0	Open	.79635	.235134093
94851	7575	-J-3460	-J-3461	400	110	0	Open	.79649	.0000136814
94852	9418	29968-B	-J-1126	200	110	0	Open	.79717	1. 7023899555
94853	7386	-J-3348	29275-A	100	110	0	Open	.79833	.0000276683
94854	9294	-J-1003	29760-A	100	110	0	Open	.79996	.0000203371
94855	7874	-J-3660	29464-A	100	110	0	Open	.80107	.7005606294
94856	11378	29874-A	-J-2062	100	110	0	Open	.80298	-. 0000032942
94857	8750	-J-4056	29703-A	100	110	0	Open	.80412	.0000140821
94858	8611	-J-3932	29646-A	100	110	0	Open	.80528	.0000155371
94859	9557	-J-1082	29941-A	100	110	0	Open	.80629	3. 5691790581

Fig. 7.4 Data table view of Z city pipeline in the geodatabase

(1) Data import and export module: the INP data is exported according to the drawn water supply pipe network topology, the INP data is stored and converted into GIS data through Oracle, the hydraulic data obtained by EPANET is stored into GIS data, the data synchronization update mechanism can be realized, and the attribute data of each simulated time point can be exported in the form of a report.

(2) Model editing module: the system supports the users to add, delete and modify the basic data of the pipe network model, and also supports the users to operate the pipe network operation data, such as the water pump switch, water pump operation curve and valve switch. The system has good flexibility.

(3) Model calculation module: this module is the core part of the system, which can conduct the instantaneous calculation and delay calculation of the water supply pipe network, and the calculation results of each time and the GIS diagram display are displayed on the front-end platform.

(4) Calculation result display module: the GIS map through front-end technology generated after model calculation can be marked and rendered, such as color level display pipe network attribute data, dynamic and static water flow, pressure equivalent distribution map and grid rendering.

(5) SCADA module: the pressure and flow monitoring points are distributed in the GIS map, and the system supports the reading of the SCADA data in the monitoring points. It can compare the SCADA data with the simulated and calculated data, and realize the verification function of the pipe network model.

7.4 Conclusion

In view of the current problems in urban water supply network management, this paper presents the first method to quickly develop online hydraulic model calculation system based on EPANET source code and ArcObjects, establish the text data instead of INP, improve the standardization and updating of pipe network data; compile EPANET source code into DLL dynamic link library through COM technology. The hydraulic model system was developed through ArcObjects in the NET platform, and finally the online operation and management of the system were realized through ArcServer, which played a positive guiding role in the planning, management and scheduling of the water supply pipe network.

Acknowledgements I would like to thank the teachers from the school and the laboratory for their help in my research and writing. I would like to thank the Liaoning Provincial Department of Education in 2021 (LJKZ0576) and the Social Governance Science and Technology Special Project of the Shenyang Science and Technology Plan (21-108-9-33) for our research financial support.

References

An SP, Chen ZH, Wang JQ (2013) The construction and application of a water supply enterprise pipe network GIS system. Water Supply Drainage S1:530

Li SP (2011) Development of teaching software for water supply network based on EPANET localization. Water Supply Drainage 7:161

Liu CX, Wang Y, Shen L (2016) Renewal and maintenance management of the hydraulic model of the water supply pipe network in Z city. Water Supply Technol 3:46

Yu ZB (2015) Design and implementation of geographic information system for urban water supply pipe network. Harbin University of Science and Technology, Harbin

Chapter 8
Sprinkler Irrigation Atomization in Relation to Water Surface Tension: A New Laboratory Technique to Investigate Pesticides and Fertilizers Effect on Irrigation Drop Size

Azam Keneti, Davood Farsadizadeh, and Yadollah Bahramian

Abstract The importance of microscopic phenomena such as molecular interactions in water drop formation have been overlooked in the researches about sprinkler irrigation efficiency. It is well known that molecular characteristics of water phase have an influence on droplet size. Similarly, the required energy to make water drops by sprinklers originates from the water jet drag controlled by its surface tension. Thus, dissolved surface-active substances (surfactants) such as pesticides and fertilizers can play a significant role in the performance of the sprinkler systems. In this study, we show that droplet forming rate in atomization is significantly lower than the achievable droplet formation rates in laboratories in spite of the fact that flow rates in a laboratory setting is far below the jet flow rates in sprinkler irrigation systems. Using drop volume method two commercial fertilizer and pesticide have been employed to investigate the mechanisms via which dissolved materials can affect the water drop size during atomization. Experimental results from this study revealed the commercial fertilizers and pesticides can significantly reduce the surface tension of water and, therefore, size of water droplets (up to 60%). Consideration of these outcomes in the design of sprinkler irrigation systems can substantially improve water conservation in the areas adversely affected by the global warming.

Keywords Atomization · Drop size · Surface tension · Irrigation surfactant · Pesticides · Fertilizers · Drop volume method

A. Keneti (✉) · D. Farsadizadeh
Faculty of Agriculture, Tabriz University, Tabriz, Iran
e-mail: aakeneti@gmail.com

Y. Bahramian
Khazar Exploration and Production Company, Tehran, Iran

H.-Y. Jeon (ed.), *Sustainable Development of Water and Environment*,
Environmental Science and Engineering,
https://doi.org/10.1007/978-3-031-07500-1_8

8.1 Introduction

Considering the global warming, it is a key matter in water sensitive agriculture and urban designs to have the optimum droplet size distribution, since it determines the sprinkler's water distribution sensitivity to evaporation, to wind and its impact on soil and crop surface (Edling 1985; Dwomoh et al. 2014; Baifus Manke et al. 2019).

The amount of water that evaporates from a droplet during sprinkler irrigation depends on the surface area of the water droplet and the time the drop remains in the air (Solomon et al. 1985; Tarjuelo et al. 2000). Both of the time available for the drop to remain in air and the droplet surface area are all functions of the drop size. For a unit volume of water, surface area increases by decreasing the droplet size, although this decline in size will extend the drop time suspension in air (Dwomoh et al. 2014). Likewise, distorting effect (i.e. drift loss) of the wind on the sprinkler water distribution is dependent upon the droplet size. In truth, when the droplet sizes are small, the wind distorts the water distribution more strongly (Solomon et al. 1991). For drop sizes lower than a specific size, the total loss of wind draft and evaporation can reach up to 40% (Edling 1985; Tarjuelo et al. 2000). Eventually, the kinetic energy of droplets, which is directly related to the drop size, may lead to erosion or sealing of soil surface (Sun et al. 2008).

Researchers have previously employed different types of methods to study water drop size in order to design efficient sprinkler systems, such as stain method (Solomon et al. 1985; Hall 1970), flour method (Kohl 1974), oil immersion method (Eigel and Moore 1983), and laser optical measurement (Solomon et al. 1991). Based on these studies, there is a correlation between droplet size, which is adversely affected by the flow pressure, and the nozzle size (Kohl et al. 1985; Kohl and Boer 1990; Li 1997). In majority of previous studies related to sprinklers efficiency, however, only mechanical parameters were investigated. Since only mechanical parameters were investigated in majority of previous studies related to sprinklers efficiency, characteristics of the liquid phase (e.g. impurity) and the importance of microscopic phenomena (e.g. molecular interactions and surface tension) in water drop formation have been somewhat overlooked as a result.

It is renowned that molecular qualities of water phase affect the droplet size (Israelachvili 1998). For instance, the surface tension of water controls the size of a hanged droplet (Based on Laplace's equation, a lower surface tension results in a smaller hanged drop size, because of the reduction in the weight compensating the force—after Kryukova et al. (2015). Similarly, the required energy to build water drops by sprinklers originates from the water jet drag (Stevenin et al. 2016), hence the number of droplets is controlled by its surface tension (i.e. a lower surface tension results in more droplets). Here the importance of dissolved surface-active substances (surfactants) such as pesticides and fertilizers in the performance of the sprinkler systems comes into play because surfactants can reduce the size of drop more than 50% (Mandato et al. 2012) which may increase the wind draft and evaporation loss dramatically.

Surface tension is a physical phenomenon resulting from a greater attraction of liquid molecules to each other than to molecules in the air. Prevalent methods of measuring surface tension are: (1) Ring method (Harkins and Jordan 1930), (2) Wilhelmy plate (Biswas et al. 2001), (3) Pendant drop (Stauffer 1965), (4) Capillary pressure method (Javadi et al. 2009, 2010, 2012), and (5) drop/weight volume method (Tornberg 1997). The optimal method to be used for the measurement of surface tension is determined by the nature of phenomenon being investigated. For instance, it is more practical to use capillary or drop volume method for dynamic systems, while methods of ring and plate are preferred for static ones. Forming a drop in atomization is a dynamic process recommending that the methods of capillary or drop/weight volume are more acceptable to study the effect of surface tension on atomized water droplet size. Although there is a limitation for achievable flow rates in a laboratory setting (being far below the jet flow rates in sprinkler irrigation systems in situ), results are strongly related to the flow rate in both of these methods. This restriction might be the reason that why the surface phenomena has been overlooked in the researches which concern the droplet size in sprinkler systems.

In this study, after showing that droplet forming rate in atomization is significantly lower than the achievable droplet formation rates in laboratories, contribution of solutes and the flow rate to the water droplet size have been studied using the droplet volume and surface tension data analysis at the same time. Two commercial fertilizer and pesticide have been used to investigate mechanisms via which common agricultural dissolved materials may change the intermolecular interactions and the water drop size during atomization.

8.2 Materials and Method

As illustrated in Fig. 8.1, the droplet forming rate is completely different from the water jet flow rate. Regarding the Rayleigh equation (Marshall and Marzo 2004), droplet build time in atomization can be calculated as:

$$t = 12\left(\frac{8\rho_l}{\sigma}\right)^{0.5}\left(\frac{d_{lig}}{2}\right)^{1.5} \tag{8.1}$$

where t is the time (in seconds) the droplet is built, ρ_l is liquid density (in kg/cm^3), σ is the surface tension (in Newton/m), and d_{lig} is jet diameter (in meters). The diameter of the water jet can become 200 times of the nozzle diameter in some sections (Stevenin et al. 2016). This means that the droplet formation speed can be as low as one droplet per 4 s when irrigating by sprinklers with 2 mm diameter nozzles which is significantly lower than the achievable droplet formation rates in laboratories.

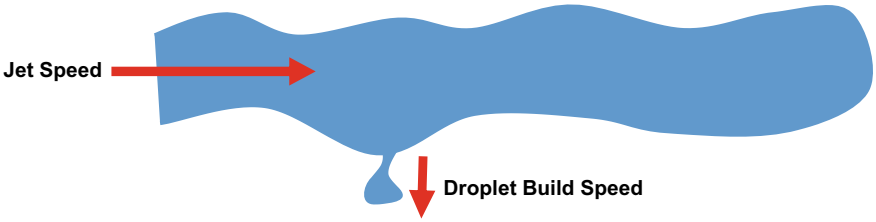

Fig. 8.1 Atomization and the difference between the nature of jet speed and droplet build speed

Table 8.1 Chemical materials used for the experiments

Chemical formula/Systematic name	Concentration (wt%)	Type
(NH_3, HNO_3) (P_2O_5, K_2O, BrO, MoO) (Fe, Cu, Zn, Mn ($C_{10}H_{16}N_2O_8$) $((CH)_n$ (COOH) (NH_2) R) $(H_2O)_n$	1–30	Fertilizer
($C_{17}H_2$) CLN_2O_2S	0.005–1	Pesticide

Using commercial fertilizer and pesticide, the effect of common irrigation dissolved materials on water surface tension and its droplet size have been investigated. It is important to note that deionized water was used to make required solutions for experiments. Table 8.1 presents the detailed information of materials utilized.

For the conducted study, the Profile Analysis Tensiometer (PAT) equipment (Javadi et al. 2009), as an accurate setup, was employed to form a water drop and to measure its maximum volume (i.e. atomization resulted droplet) in different flow rates. This setup is composed of versatile components, for example, an accurate pump, a high resolution camera, several nozzles with various sizes, and the recording and analyzing software. Although PAT cannot be used for measuring the surface tension in this study because of variation in droplet volume, the ability to record data per 0.1 s make it powerful device to fulfill the determination of the maximum droplet size at each flow rate.

Figure 8.2 presents a view of the PAT setup (including its camera, needle, injection/suction lines, light source, and pump) as well as a sample of the recorded data and related interpretation.

As a whole, tested experiments consisted of four steps: loading the pump, adjusting injection rate, injection, and recording the measured droplet volumes. For more accuracy in each experiment, at least 10 consecutive droplets were formed (i.e. steady concentration and flow rate) that the average size of these droplets was recorded as the result of each test.

As previously described, the drop/weight volume technique has been used to measure surface tension. Tornberg (1997), based on the equilibrium of gravity and capillary acting forces on a stable hanging droplet, developed the correlation as given in Eq. (8.2):

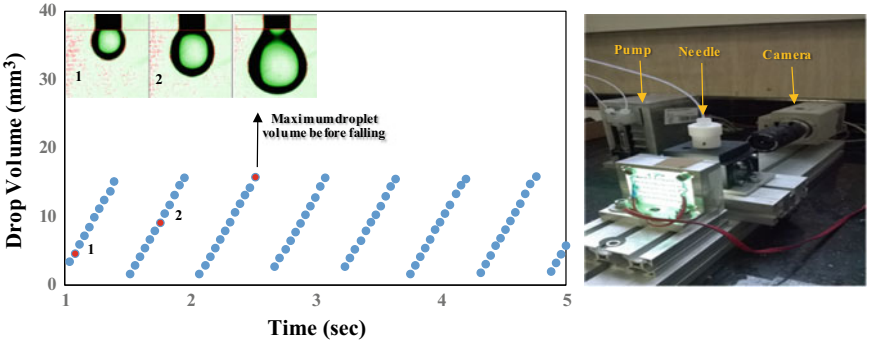

Fig. 8.2 A view of used PAT setup (right) and the way of interpretation of its records to find maximum droplet volume (left)

$$W = V\Delta\rho g = 2\pi r\sigma f\left(\frac{r}{\sqrt[3]{V}}\right) \tag{8.2}$$

where V is droplet volume, r is nozzle diameter, σ is surface tension, and f is the correction factor obtained from the experimental Eq. (8.3):

$$f\left(\frac{r}{\sqrt[3]{V}}\right) = 0.167 + 0.193\left(\frac{r}{\sqrt[3]{V}}\right) - 0.0489\left(\frac{r}{\sqrt[3]{V}}\right)^2 - 0.0496\left(\frac{r}{\sqrt[3]{V}}\right)^3 \tag{8.3}$$

Surface tension was calculated substituting Eq. (8.3) in Eq. (8.2) and re-writing Eq. (8.2) for the surface tension when droplet volume is maximum, as presented in Eq. (8.4):

$$\sigma = \frac{V\Delta\rho g}{2\pi r\left(0.167 + 0.193\left(\frac{r}{\sqrt[3]{V}}\right) - 0.0489\left(\frac{r}{\sqrt[3]{V}}\right)^2 - 0.0496\left(\frac{r}{\sqrt[3]{V}}\right)^3\right)} \tag{8.4}$$

8.3 Results and Discussions

8.3.1 Analyzing the Effect of Solutes Concentration on Droplets Size

Fertilizer effect on droplet volume is shown in Fig. 8.3. As it is evident, fertilizer does not have a noticeable impact on the droplet size in the low concentration of 1% and results are similar to the pure water. However, volumes of produced droplets is significantly reduced at higher concentrations. Changing the fertilizer concentration

from 1 to 30 wt.% resulted in decreasing droplet size from 27 mm^3 to 18 mm^3, respectively. At elevated flow rates, droplet volume becomes approximately comparable to the case of pure water in all fertilizer concentrations which is possibly due to a low adsorption rate of fertilizer molecules owing to their high molecular weight leading to slow diffusion phenomenon. Comparing these results with those obtained for the used pesticide (Fig. 8.4), it is obvious that the surface activity of pesticide is much higher than the fertilizer, leading to smaller droplets at significantly lower concentrations and denoting less dependency of the pesticide surface activity on flow rate at moderate to high concentrations.

In general, from the results presented in Figs. 8.3 and 8.4, it can be inferred that both solutes of pesticide and fertilizer can reduce the size of water drop by 60%. Results showed a variable droplet size trend by flow rate which is in agreement with the importance of dynamic surface tension in forming droplets. It is also noticeable

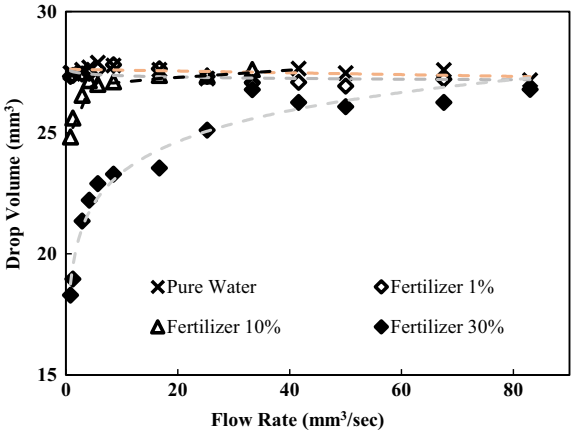

Fig. 8.3 Effect of fertilizer concentration (wt.%) on droplet maximum volume in different flow rates

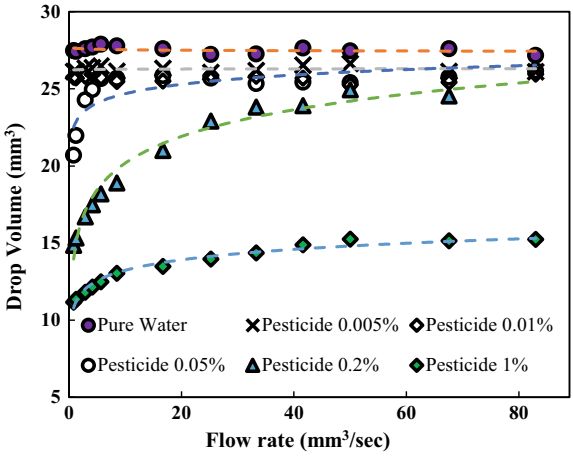

Fig. 8.4 Effect of pesticide concentration (wt.%) on droplet maximum volume in different flow rates

that there is a critical flow rate (approximately 10 mm^3/sec) for fertilizer and pesticide below which the effect of flow rate on droplet size becomes significant.

8.3.2 *Investigation of the Effect of Solutes on the Dynamic Surface Tension*

The measured dynamic surface tension values of the selected fertilizer and pesticide are presenting in Figs. 8.5 and 8.6 for the first time. Slow dynamic behavior of the fertilizer solutions, as presented in Fig. 8.5, suggests that the selected fertilizer is not surface active, particularly at low to moderate concentrations, which tallies well with the variation of droplet sizes with flow rate (Fig. 8.3). An important feature in the Fig. 8.5 is the initial surface tension of about 72 mN/m (surface tension of pure water) for all the investigated concentration, indicating the small diffusivity of the fertilizer towards surface phase supported by the somehow long time required to reach the equilibrium at high concentrations.

Figure 8.6 presents the dynamic surface tensions of the pesticide solutions. For the pesticide concentrations of 0–0.2%, the general trend of experimental data is similar to those of fertilizer samples presented in Fig. 8.5. However, at a high concentration of 1 wt. %, starting point of the surface tension curve is significantly lower than the pure water (72 mN/m). This observation implies that adsorption rate of the pesticide is more than that of the fertilizer. This aspect of the pesticide adsorption rate have conceivably contributed to a more complex effect of flow rate on droplets size. One important finding about the tested pesticide is the low surface tension of 30 mN/m at 1% concentration of the pesticide which is even lower than the lowest achievable reported surface tension by the SDS in pure water (around 38 mN/m) as a well-known surfactant (Xu et al. 2013). This is consistent with the concept of cell destruction by which pesticides kill living beings in some cases (Astiz et al. 2009).

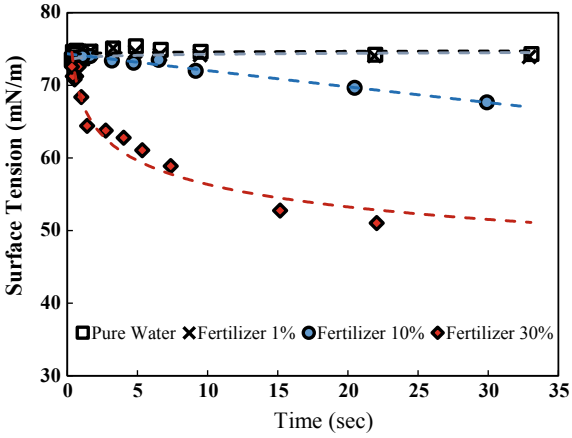

Fig. 8.5 Surface tension of fertilizer solutions at different droplet forming times. Surface tension has been calculated using the measured maximum droplet size before dropping

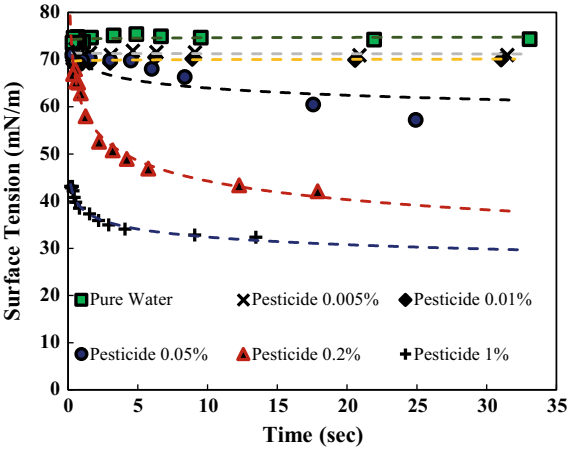

Fig. 8.6 Surface tension of pesticide solutions at different droplet forming times. Surface tension has been calculated using the measured maximum droplet size before dropping

8.3.3 Investigation of the Effect of Flow Rates on Droplets Size

The impact of flow rate on droplet size depends highly on the surface tension (i.e. concentration of the solute) and adsorption rate of the dissolved material. It can be deduced from the results (Figs. 8.3 and 8.4) that in a critical concentration limit of the fertilizer and pesticide the flow rate increases the size of droplets by more than 50%. This is critically important considering the fact that flow rate plays the main role in routine design method of sprinkler irrigation systems, i.e. a way of designing in which the surface tension effect is neglected. On the other hand, when surface tension decreases the risk of critical flow rate (the rate after which no droplet is formed and a continuous stream flows through the nozzle) increases.

8.4 Conclusions

This investigation set out to study the significance of fertilizers and pesticides on the size of water droplets made by irrigation sprinklers. In this study, by showing that droplet forming rate in atomization is significantly lower than the achievable droplet formation rates in laboratories, it has been found that fertilizers and pesticides, like commercial surfactants, affect the surface chemistry of produced droplets and consequently lead to significant change into droplet size (up to 60%). It was also found that dynamic surface chemistry of the droplets and the adsorption rate of the used chemicals, directly affected by the flow rate and the diffusivity of dissolved molecules, had considerable role in the size distribution of formed droplets. The results implied that adsorption rate of the pesticide is more than that of the fertilizer. The selected fertilizer is not surface active, particularly at low to moderate concentrations, but the

tested pesticide can drop the surface tension even lower than the lowest achievable surface tension by the well-known surfactant of SDS. In a critical concentration limit of the fertilizer and pesticide the flow rate increases the size of droplets by more than 50% which is critically important considering the fact that flow rate plays the main role in routine design method of sprinkler irrigation systems. The authors believe that future studies should investigate the effect of solutes on atomizing drag forces to shed more lights on the role of inter-molecular interactions in irrigation systems.

References

Astiz M, Alaniz MJTd, Marra CA (2009) Effect of pesticides on cell survival in liver and brain rat tissues. Ecotoxicol Environ Saf 72:2025–2032

Baifus Manke E, Nörenberg BG, Faria LC, Tarjuelo JM, Colombo A, Chagas Neta MCC, Parfitt JMB (2019) Wind drift and evaporation losses of a mechanical lateral-move irrigation system: oscillating plate versus fixed spray plate sprinklers. Agric Water Manag 225:105759

Biswas SC, Dubreil L, Marion D (2001) Interfacial behavior of wheat puroindolines: study of adsorption at the air-water interface from surface tension measurement using Wilhelmy plate method. J Colloid Interface Sci 244:245–253

Dwomoh FA, Shouqi Y, Hong L (2014) Droplet size characterization of the new type complete fluidic sprinkler. IOSR J Mech Civ Eng 11:70–73

Edling RJ (1985) Kinetic energy, evaporation and wind drift of droplets from low pressure irrigation nozzles. Trans ASAE 28:1543–1550

Eigel JD, Moore ID (1983) A simplified technique for measuring raindrop size and distribution. Trans ASAE 26:1079–1084

Hall MJ (1970) Use of the stain method in determining the drop-size distribution of coarse liquid sprays. Trans ASAE 13:33–37

Harkins WD, Jordan HF (1930) A method for the determination of surface and interfacial tension from the maximum pull on a ring. J Am Chem Soc 52:1751–1772

Israelachvili JN (1998) Intermolecular and surface forces, 2nd edn. Academic Press, California, USA

Javadi A, Bastani D, Krägel J, Miller M (2009) Interfacial instability of growing drop: experimental study and conceptual analysis. Colloids Surf, A 347:167–174

Javadi A, Krägel J, Pandolfini P, Loglio G, Kovalchuk AI, Aksenenko EV, Ravera F, Liggieri L, Miller R (2010) Short time dynamic interfacial tension as studied by the growing drop capillary pressure technique. Colloids Surf, A 365:62–69

Javadi A, Krägel J, Makievski AV, Kovalchuk VI, Kovalchuk NM, Mucic N, Logliod G, Pandolfini P, Karbaschi M, Miller M (2012) Fast dynamic interfacial tension measurements and dilational rheology of interfacial layers by using the capillary pressure technique. Colloids Surf, A 407:159–168

Kohl RA (1974) Drop size distribution from medium-size agricultural sprinklers. Trans ASAE 17:690–693

Kohl RA, De Boer DW (1990) Droplet characteristics of a rotating spray plate sprinkler. Trans ASAE

Kohl RA, von Bemuth RD, Heubner G (1985) Drop size distribution measurement problems using a laser unit. Trans ASAE 28:190–192

Kryukova EN, Sister VG, Rustambekov MK, Ivannikova EM (2015) Effect of surface tension on droplet size during liquid dispersion by a centrifugal atomizer. Chem Pet Eng 50:766–769

Li J (1997) Effect of pressure and nozzle shape on the characteristics of sprinkler droplet spectra. J Agric Eng Res 66:15–21

Mandato S, Rondet E, Delaplace G, Barkouti A, Galet L, Accart P, Ruiz T, Cuq B (2012) Liquids' atomization with two different nozzles: modeling of the effects of some processing and formulation conditions by dimensional analysis. Powder Technol 224:323–330

Marshall AW, di Marzo M (2004) Modelling aspects of sprinkler spray dynamics in fires. Process Saf Environ Prot 82:97–104

Solomon KH, Kincaid DC, Bezdek JC (1985) Drop size distributions for irrigation spray nozzles. Trans ASAE 28:1966–1974

Solomon KH, Zoldoske DE, Oliphant JC (1991) Laser optical measurement of sprinkler drop sizes. In: Automated agriculture for the 21st century, ASAE

Stauffer CE (1965) The measurement of surface tension by the pendant drop technique. J Phys Chem 69:1933–1938

Stevenin C, Vallet A, Tomas S, Amielh M, Anselmet F (2016) Eulerian atomization modeling of a pressure-atomized spray for sprinkler irrigation. Int J Heat Fluid Flow 57:142–149

Sun Z, Kang Y, Jiang S (2008) Effects of water application intensity, drop size and water application amount on the characteristics of topsoil pores under sprinkler irrigation. Agric Water Manag 95:869–876

Tarjuelo JM, Ortega JF, Montero J, de Juan JA (2000) Modeling evaporation and drift losses in irrigation with medium size impact sprinklers under semi-arid conditions. Agric Water Manag 43:263–284

Tornberg E (1997) A surface tension apparatus according to the drop volume principle. J Colloid Interface Sci 60:50–53

Xu H, Li PX, Ma K, Thomas RK, Penfold J, Lu JR (2013) Limitations in the application of the Gibbs equation to anionic surfactants at the air/water surface: sodium dodecylsulfate and sodium dodecylmonooxyethylenesulfate above and below the CMC. Langmuir 29:9335–9351

Chapter 9
A Volterra Process Model for River Water Temperature

Hidekazu Yoshioka, Yumi Yoshioka, and Ayumi Hashiguchi

Abstract Water temperature as a key indicator of river environments evolves dynamically as well as stochastically. We introduce a new mathematical framework for modeling river water temperature at an observation station based on a Volterra process: a non-Markovian model. The non-Markovian nature arises from a non-exponential autocorrelation function, which is effectively captured by a completely monotone kernel. Parameters of the model are identified for a study site in Japan where the water temperature has been measured at a 10-min interval. We show that the observed time series of the water temperature is separated into seasonal and stochastic parts, and that the non-exponential autocorrelation function is fitted well by the proposed model. A brief application of the model to statistical evaluation of the river water temperature subject to misspecification is finally presented.

Keywords River water temperature · Markovian lift · Model identification

9.1 Introduction

Water temperature is a key environmental indicator of surface water bodies as it controls a variety of biological and chemical phenomena. Modeling water temperature has therefore been a fundamental topic in hydrology and related research areas (Kędra and Wiejaczka 2018; Yang et al. 2019).

Water temperature at a fixed point in a surface water body is determined by various factors, such as solar radiation, convection, diffusion, and chemical reaction. Thoroughly describing the processes governing the dynamics of water temperature is

H. Yoshioka (✉) · Y. Yoshioka · A. Hashiguchi
Shimane University, Nishikawatsu-cho 1060, Matsue 690-8504, Japan
e-mail: yoshih@life.shimane-u.ac.jp

Y. Yoshioka
e-mail: yyoshioka@life.shimane-u.ac.jp

A. Hashiguchi
e-mail: hashiguchi@life.shimane-u.ac.jp

H.-Y. Jeon (ed.), *Sustainable Development of Water and Environment*,
Environmental Science and Engineering,
https://doi.org/10.1007/978-3-031-07500-1_9

therefore a challenging task. Conceptual models serve better than fully mechanistic ones in such cases. Among existing conceptual models, stochastic process models that consider water temperature as a time series data driven by noise processes have been used as efficient mathematical tools. Stochastic differential equations (SDEs) and their discrete counterparts have been applied to water temperature dynamics (Dabrowski et al. 2020; Quindala et al. 2021); however, a unified mathematical theory to describe the temporal dynamics of water temperature is still lacking, motivating us to set up such a theory based on stochastic processes.

Focusing on a river as a particular case, we show that the Volterra processes (Barndorff-Nielsen et al. 2018), which have not been well-studied in the context of hydrology, work well in concisely describing the water temperature dynamics. The model is of a non-Markov type that can capture the non-exponential shape of the autocorrelation function of the observed water temperature. Our model assumes a Gaussian distribution of the temperature fluctuation, which is verified in a case study. Furthermore, we show that the Volterra process model combined with the technique of Markovian lift (Abi Jaber 2019) enables us to statistically evaluate the long-run water temperature subject to climate changes having uncertain impacts. We believe that this contribution would open a new door toward stochastic modeling of water temperature dynamics in surface water bodies.

9.2 Volterra Process Model

9.2.1 Formulation

We work with a usual complete probability space. Time is denoted as $t \geq 0$. A 1-D Brownian motion as a Gaussian continuous-time white noise is denoted as W_t at time t. The water temperature at a fixed point in a river is θ_t at time t, which is a continuous-time scalar process. We assume the decomposition of the water temperature:

$$\theta_t = \overline{T}_t + X_t. \tag{9.1}$$

The first term $\overline{T}_t$ is a smooth deterministic part standing for seasonality and X_t the stationary residual responsible for stochasticity. We assume the periodicity $\overline{T}_{t+P} = \overline{T}_t$ $(t \geq 0)$ with the period $P > 0$ (one year in this paper).

The residual X_t is modelled as a stationary Volterra process having a completely monotone kernel $g : \mathbb{R} \to \mathbb{R}_+$ (Barndorff-Nielsen et al. 2018):

$$X_t = \sigma \int_{-\infty}^{t} g(t-s)\mathrm{d}W_s, t \in \mathbb{R} \tag{9.2}$$

with a noise intensity $\sigma > 0$. A completely monotone kernel g is a function such that

$$(-1)^n \frac{\mathrm{d}^n g(t)}{\mathrm{d}t^n} \geq 0, t \geq 0, n = 0, 1, 2, ... \tag{9.3}$$

An example is the exponential function $g(t) = \exp(-\rho t)$ ($\rho > 0$), with which we recover Markovian dynamics X_t of the Ornstein–Uhlenbeck (OU) type as a low-pass filter (Bibbona et al. 2008). This leads to an exponential autocorrelation function $\exp(-\rho\tau)$ with $\tau \geq 0$ the time lag, which is not always satisfactory especially when modeling stochastic processes with non-exponential autocorrelation functions (Resnick 2007). We therefore extend the exponential function in the split of Markovian lift (Abi Jaber 2019):

$$g(t) = \sum_{i=1}^{\infty} w_i \exp(-\rho_i t) \tag{9.4}$$

with constants $\rho_i > 0$ and $w_i \geq 0$ ($i = 1, 2, 3, ...$) such that

$$\sum_{i=1}^{\infty} w_i < +\infty. \tag{9.5}$$

This assumption guarantees convergence of the sum of exponentials (9.4). By appropriately choosing the coefficients, (9.4) approximates a variety of kernels, including the fractional monomials and the exponential one (Barndorff-Nielsen et al. 2018).

The Volterra process (9.2) with the kernel (9.4) cannot be written as one Markovian SDE. Instead, we formally rewrite it as a summation of correlated OU processes:

$$X_t = \sigma \sum_{i=1}^{\infty} X_t^{(i)}, \tag{9.6}$$

where $X_t^{(i)}$ is governed by the classical OU-type SDE

$$\mathrm{d}X_t^{(i)} = -\rho_i X_t^{(i)} \mathrm{d}t + w_i \mathrm{d}W_t. \tag{9.7}$$

A remarkable point is that all $X_t^{(i)}$ ($i = 1, 2, 3, ...$) are driven by the common Brownian motion W_t. We interchangeably use the equivalent formulations (9.2) and (9.6). The Volterra process model is completely specified if the values of σ, $\rho_i > 0$, and $w_i \geq 0$ ($i = 1, 2, 3, ...$) are determined. We end this section with a remark that a sample path of a Volterra process is realized as an advective stochastic partial differential equation (Barndorff-Nielsen et al. 2018), implying its infinite-dimensional nature.

9.2.2 Fitting Procedure

We explain how to fit a Volterra process to real data. Suppose that we have a discrete time series data to be fitted, such as water temperature measured at a small fixed interval.

Firstly, the deterministic component $\overline{T}_t$ is found through the least-squares fitting between the observed and modelled times series, where

$$\overline{T}_t = a_0 + a_1 \cos\left(\frac{2\pi t}{P}\right) + a_2 \cos(2\pi t) + b_1 \sin\left(\frac{2\pi t}{P}\right) + b_2 \sin(2\pi t) \tag{9.8}$$

with real constants a_0, a_1, a_2, b_1, b_2. Namely, we model the deterministic part as a sum of the yearly and daily variations. Here, the dimension of time is (day).

The fitting procedure of the residual X starts from identifying the coefficients $\rho_i > 0$ $(i = 1, 2, 3, ...)$. More specifically, we assume a stationary autocorrelation function of the water temperature with the time lag $\tau \geq 0$:

$$\mathrm{Cor}\big[X_t, X_{t+\tau}\big] = \sum_{i=1}^{\infty} c_i \exp(-\rho_i \tau) \tag{9.9}$$

subject to

$$\sum_{i=1}^{\infty} c_i = 1, c_i \geq 0, (i = 1, 2, 3, ...). \tag{9.10}$$

Again, we can use a least-squares fitting between empirical and modeled autocorrelation functions.

Assume that we identified all ρ_i and c_i. The stationarity of X leads to the explicit formula of the autocorrelation function (Barndorff-Nielsen et al. 2018):

$$\begin{aligned}\mathrm{Cor}\big[X_t, X_{t+\tau}\big] &= \frac{\int_0^\infty g(t)g(t+\tau)\mathrm{d}t}{\int_0^\infty g^2(t)\mathrm{d}t} \\ &= \left(\sum_{i,j=1}^{\infty} \frac{w_i w_j}{\rho_i + \rho_j}\right)^{-1} \sum_{i,j=1}^{\infty} \frac{w_i w_j}{\rho_i + \rho_j} \exp(-\rho_i \tau).\end{aligned} \tag{9.11}$$

Comparing (9.9) and (9.11) yields

$$c_i = \left(\sum_{k,j=1}^{\infty} \frac{w_k w_j}{\rho_k + \rho_j}\right)^{-1} \sum_{j=1}^{\infty} \frac{w_i w_j}{\rho_i + \rho_j} (i = 1, 2, 3, ...). \tag{9.12}$$

The coefficients $w_i \geq 0$ ($n \in \mathbb{N}$) can be determined from (9.12) if it is invertible with respect to them. For this purpose, without any loss of generality we add the constraint $\mathrm{Var}[X_t] = \sigma^2$, which with lengthy calculations leads to

$$\sum_{i,j=1}^{\infty} \frac{w_i w_j}{\rho_i + \rho_j} = 1. \tag{9.13}$$

Consequently, (9.12) simplifies to

$$c_i = \sum_{j=1}^{\infty} \frac{w_i w_j}{\rho_i + \rho_j} (i = 1, 2, 3, ...). \tag{9.14}$$

Inversion of (9.14) is carried out numerically by a common fixed point iteration method with a relaxation. Note that the parameter σ is found as $\sigma = \sqrt{\mathrm{Var}[X_t]}$.

9.3 Application

9.3.1 Study Site and Model Fitting

The study site is an observation station located at 2 km downstream river reach of Obara Dam in the mid-stream Hii River (Length 153 km, Watershed area 2,540 km^2), San-in area, Japan. This is a perennial first-class river in Japan playing a vital role in water resources supply in Shimane Prefecture. Hydrological characteristics of the study site have already been explained in the literature (Tanaka et al. 2021) and is not repeated here.

We have been measuring the water temperature near the riverbed at a dam-downstream observation station (Station O, (Tanaka et al. 2021)) at a 10-min interval (Fig. 9.1, U20: HOBO). The sampling period is from November 16 2020 12:00:00 to July 16 2021 08:40:00 in JST. The data before and after the sampling period was lost due to severe flooding events. The fitted model is also presented in Fig. 9.1, where fitted parameter values are $a_0 = 14.1$, $a_1 = -1.35$, $a_2 = 0.275$, $b_1 = -8.21$, $a_2 = 0.147$, all having the dimension (°C). The fitted model captures the observed data as shown in Fig. 9.1. The stochasticity in the observed data originates from both hydrological processes and flow regulations, which are difficult to separate with each other.

Figure 9.2 shows the empirical and fitted autocorrelation functions of X, where we assumed the simplest non-Markovian case $c_i = 0$ ($i = 3, 4, 5...$). The fitted parameter values are $\rho_1 = 0.0796$ (1/day), $\rho_2 = 8.10$ (1/day), $c_1 = 0.893$ (−), and $c_2 = 0.107$ (−). The identified model captures the gradual decrease of the empirical result. The identified parameter values suggest that the stochasticity of the water temperature dynamics contains the different time scales, which can be partly due to

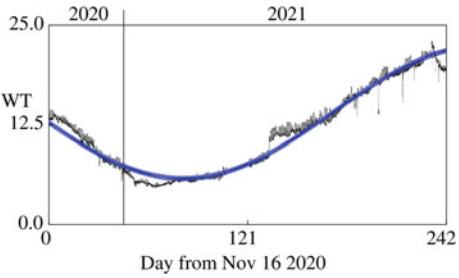

Fig. 9.1 Observed (Black) and fitted (Blue) water temperature

the flow regulations by Obara Dam. Simply assuming the Markovian model $c_i = 0$ ($i = 2, 3, 4...$) results in an overestimation for small τ. A more complex three-term non-Markovian model such that $c_i = 0$ ($i = 4, 5, 6...$) with the corresponding fitted parameters is also plotted in Fig. 9.2 as well, showing that the difference between the two non-Markovian models is visually small. Hence, setting $c_i = 0$ ($i = 3, 4, 5...$) is justified.

By (9.14), we obtain $w_1 = 0.367$ (1/day$^{1/2}$), $w_2 = 1.00$ (1/day$^{1/2}$), and $\sigma = \sqrt{\mathrm{Var}[X_t]} = 0.844$ (°C), suggesting that the stochastic fluctuation has the order of $O\left(10^0\right)$ (°C). Finally, Gaussian property of the residual is verified as demonstrated in a Q-Q plot (Fig. 9.3). Consequently, we completed identification of the Volterra process model at the observation station.

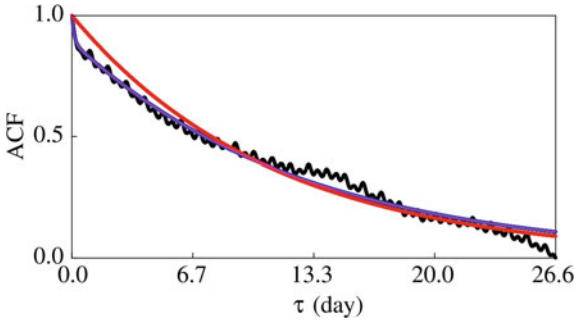

Fig. 9.2 Observed (Black) and fitted non-Markovian (two terms, Blue) autocorrelation functions (ACFs) of the water temperature at the study site. The fitting results with the Markovian model (Red) and another non-Markovian model (three terms, Purple) are also plotted

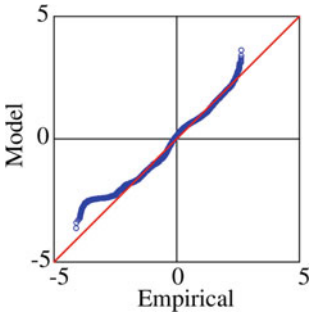

Fig. 9.3 *Q-Q* plot between the empirical and modelled residuals. Blue circles represent the fitted model. The Red line represents the idealized Gaussian model

9.3.2 *Statistical Evaluation of Long-Run River Water Temperature*

We finally present a brief application of the Volterra process model to environmental assessment. Although we successfully identified the model for the water temperature at the observation station, in applications it is usually impossible to avoid misspecification due to a series of theoretical simplifications. Even if the identified model is correct at this stage, it may be distorted in future due to climate changes (Ito and Momii 2021).

We demonstrate that the Volterra process model can be used for evaluation of the worst-case overestimation and underestimation of the annually averaged water temperature based on an ergodic control theory (Yoshioka and Tsujimura 2021). Mathematical details of the theory presented below is complicated, and hence only key points are explained. Interested readers should read the previous research (Yoshioka and Yoshioka 2021).

The misspecification is measured by a relative entropy between the identified and true models, if the latter exists. As in the conventional worst-case optimization (Hansen and Sargent 2001), the misspecification is represented by distorting the Brownian motion as

$$W_t \to W_t + \int_0^t \phi_s \mathrm{d}s \tag{9.15}$$

with a progressively measurable process ϕ. Now, consider the estimation problem of the expectation of the yearly averaged water temperature

$$\frac{1}{P}\mathrm{E}\left[\int_0^P \theta_s \mathrm{d}s\right] = \frac{1}{P}\mathrm{E}\left[\int_0^P \left(\overline{T}_s + X_s\right)\mathrm{d}s\right]. \tag{9.16}$$

If there exists no misspecification ($\phi \equiv 0$), then

$$\frac{1}{P}\mathrm{E}\left[\int_0^P \left(\overline{T}_s + X_s\right)\mathrm{d}s\right] = \frac{1}{P}\mathrm{E}\left[\int_0^P \overline{T}_s \mathrm{d}s\right] = a_0. \tag{9.17}$$

Otherwise, the equality (9.17) is false and there exists some misspecification. The misspecification is evaluated as the relative entropy between the identified and true models, and is given by Hansen and Sargent (2001):

$$r_\phi = \frac{1}{P}\mathrm{E}\left[\int_0^P \frac{\phi_s^2}{2}\mathrm{d}s\right] (\geq 0). \tag{9.18}$$

Assume that we have an upper-bound of the relative entropy; namely,

$$r_\phi \leq R \tag{9.19}$$

with a constant $R > 0$. If the dimension of time is (day), then the dimension of ϕ is (1/day$^{1/2}$), leading to the dimension r_ϕ, R (1/day). The worst-case overestimation of the water temperature is the maximum value of (9.16) with a maximizing ϕ. Similarly, the worst-case underestimation of the water temperature is the maximum value of (9.16) with a minimizing ϕ.

The maximizer and minimizer are found from the corresponding Hamilton–Jacobi–Bellman (HJB) equations having Lagrangian multipliers to deal with the expectation constraint (9.19) (e.g., Jasso-Fuentes et al. 2016). Now, we use the representation formula (9.6) along with the Dynkin's formula and the constraint, and arrive at the HJB equation

$$\begin{aligned} &\frac{\partial \Phi}{\partial s} - \rho_1 x_1 \frac{\partial \Phi}{\partial x_1} - \rho_1 x_2 \frac{\partial \Phi}{\partial x_2} + \frac{w_1^2}{2}\frac{\partial^2 \Phi}{\partial x_1^2} + w_1 w_2 \frac{\partial^2 \Phi}{\partial x_1 \partial x_2} + \frac{w_2^2}{2}\frac{\partial^2 \Phi}{\partial x_2^2} \\ &\pm \frac{\psi}{2}\left(w_1 \frac{\partial \Phi}{\partial x_1} + w_2 \frac{\partial \Phi}{\partial x_2}\right)^2 - H + \overline{T}_s + \sigma(x_1 + x_2) = 0 \end{aligned} \tag{9.20}$$

for $s \in [0, P]$ and $x_1, x_2 \in \mathbb{R}$ with the auxiliary parameter $\psi > 0$ such that

$$R = \frac{1}{P}\mathrm{E}\left[\int_0^P \frac{\psi^2}{2}\left(w_1 \frac{\partial \Phi\left(s, X_s^{(1)}, X_s^{(2)}\right)}{\partial x_1} + w_2 \frac{\partial \Phi\left(s, X_s^{(1)}, X_s^{(2)}\right)}{\partial x_2}\right)^2 \mathrm{d}s\right]. \tag{9.21}$$

A classical solution to the HJB equation is a couple of a constant H and a trivariate function $\Phi = \Phi(s, x_1, x_2)$ having the period P with respect to the first argument. The $+$ sign in the first term of the second line of (9.20) corresponds to the overestimation case, while the minus sign to the underestimation case. The quantity H equals the worst-case overestimation or underestimation of the averaged water temperature (9.16) subject to the constraint (9.19).

The HJB Eq. (9.20) is a degenerate parabolic partial differential equation having a completely degenerating diffusion term: a difficult equation to solve numerically (Øksendal and Sulem 2019; Oberman 2006). Fortunately, owing to the specific form of the Volterra process model, we can guess an affine solution with time-dependent coefficients $A(s)$, $B(s)$, $C(s)$:

$$\Phi(s, x_1, x_2) = A(s) + B(s)x_1 + C(s)x_2. \tag{9.22}$$

Indeed, substituting (9.22) into (9.20) yields the system of time-backward ordinary differential equations that governs the three coefficients A, B, C:

$$\frac{\mathrm{d}B}{\mathrm{d}s} - \rho_1 B + \sigma = 0, \tag{9.23}$$

$$\frac{\mathrm{d}C}{\mathrm{d}s} - \rho_2 C + \sigma = 0, \tag{9.24}$$

$$\frac{\mathrm{d}A}{\mathrm{d}s} \pm \frac{\psi}{2}(w_1 B + w_2 C)^2 + \overline{T}_s - H = 0 \tag{9.25}$$

subject to $A(0) = A(P)$, $B(0) = B(P)$, $C(0) = C(P)$. We get

$$B = \frac{\sigma}{\rho_1} \text{ and } C = \frac{\sigma}{\rho_2} (\text{constant functions}). \tag{9.26}$$

With the help of (9.21), substituting (9.26) into (9.25) yields

$$\frac{\mathrm{d}A}{\mathrm{d}s} \pm \sigma\sqrt{\frac{R}{2}}\left(\frac{w_1}{\rho_1} + \frac{w_2}{\rho_2}\right) + \overline{T}_s - H = 0. \tag{9.27}$$

Integrating (9.27) over $(0, T)$ with respect to s finally yields

$$H = a_0 \pm \sigma\sqrt{\frac{R}{2}}\left(\frac{w_1}{\rho_1} + \frac{w_2}{\rho_2}\right), \tag{9.28}$$

where the + sign in the second term of the right-hand side corresponds to the overestimation case, while the – sign to the underestimation case. The corresponding worst-case distortions, denoted as ϕ^*, are the constants

$$\phi^* = \pm\sqrt{2R}. \tag{9.29}$$

The physical interpretation of the formula (9.28) is clear; the first term in the right-hand side is the averaged water temperature without misspecification and the second term is the worst-case deviation from the identified model. The deviation is proportional to the square root of the maximal relative entropy R and to the standard deviation of the identified model, showing their qualitative impacts on the worst-case

estimations of the average temperature. The interpretation of the formula (9.29) is far simpler and it implies that the distortion of the drift is proportional to the square root of the maximal relative entropy R.

By invoking (9.28)–(9.29), we obtain an explicit linkage between the relative entropy and the uncertainty range due to climate changes. The worst-case increase or decrease of the temperature amounting to the maximal relative entropy R equals $\pm\sigma\sqrt{\frac{R}{2}}\left(\frac{w_1}{\rho_1}+\frac{w_2}{\rho_2}\right)$ (the second term of (9.28)). In our study site, this quantity has the absolute value $2.8\sqrt{R} = O\left(10^0\right) \times \sqrt{R}$ (°C). Assuming climate changes with the temperature increase or decrease of the amount $O\left(10^0\right)$ (°C) during 2021 to 2050 (Piotrowski et al. 2021), as a rough estimate we obtain $\sqrt{R} = O\left(10^0\right)$ (1/day) and hence $R = O\left(10^0\right)$ (1/day). Because the relative entropy may not be easy to intuitively understand in applications, this estimation helps assess how much of the relative entropy, namely the amount of uncertainty, should be assumed when analyzing climate changes. This kind of explicit linkage among climate changes, stochastic processes, and relative entropy is rarely pointed out in the literature.

9.4 Conclusions

A Volterra process was fitted to times series data of the water temperature in a perennial river environment. The non-exponential nature of the autocorrelation of the water temperature was captured by the proposed model. Furthermore, the model was applied to overestimation/underestimation of the averaged water temperature based on an ergodic control theory. The specific form of the model enabled us to explicitly derive a statistical formula connecting the misspecification and climate changes.

In summary, the Volterra process turned out to be a useful tool for analyzing and deeper understanding temperature dynamics of river waters from a stochastic viewpoint. We focused solely on the water temperature in this contribution, while there exist other indicators of river environments, which include but not are limited to discharge, bedload, and water quality indices. We are trying to fit Volterra processes and related stochastic processes to these environmental indicators with a focus on fish migration (Yoshioka 2021).

Currently, analysis of stochastic control theory of non-Markovian models is a prominent issue in mathematical sciences. Our HJB equation serves as a key tractable case arising in an engineering problem. One can extend the HJB Eq. (9.20) to

$$\begin{aligned}&\frac{\partial\Phi}{\partial s}+\sum_{i=1}^{n}\left(-\rho_i x_i\frac{\partial\Phi}{\partial x_i}\right)+\sum_{i,j=1}^{n}\left(\frac{w_i w_j}{2}\frac{\partial^2\Phi}{\partial x_i\partial x_j}\right)\\&\pm\frac{\psi}{2}\left(\sum_{i=1}^{n}w_i\frac{\partial\Phi}{\partial x_i}\right)^2-H+\overline{T}_s+\sigma\sum_{i=1}^{n}x_i=0\end{aligned}\tag{9.30}$$

for arbitrary large $n \in \mathbb{N}$. Its potential $\Phi = \Phi(x_1, x_2, ..., x_n)$ still admits an affine form analogous to (9.22). In this way, our model is extended to a very large-dimensional case without any difficulties if all the coefficients are identifiable. However, convergence of the Eq. (9.30) itself under the limit $n \to +\infty$ is far from being trivial. This point should be addressed in our future research. In this limit, the HJB equation can be defined in a Hilbert space and its solution not as a function but as an operator.

Acknowledgements The following research grants supported this research: Kurita Water and Environment Foundation 19B018, 20K004, 21K018, Grant for Environmental Research Projects from the Sumitomo Foundation 203160, Japan Society for The Promotion of Science KAKENHI 19H03073.

References

Abi Jaber E (2019) Lifting the Heston model. Quant Financ 19(12):1995–2013

Barndorff-Nielsen OE, Benth FE, Veraart AE (2018) Ambit stochastics. Springer, Cham

Bibbona E, Panfilo G, Tavella P (2008) The Ornstein-Uhlenbeck process as a model of a low pass filtered white noise. Metrologia 45(6):S117

Dabrowski JJ, Rahman A, Pagendam DE, George A (2020) Enforcing mean reversion in state space models for prawn pond water quality forecasting. Comput Electron Agric 168:105120

Hansen L, Sargent TJ (2001) Robust control and model uncertainty. Am Econ Rev 91(2):60–66

Ito Y, Momii K (2021) Potential effects of climate changes on evaporation from a temperate deep lake. J Hydrol Reg Stud 35:100816

Jasso-Fuentes H, Escobedo-Trujillo BA, Mendoza-Pérez AF (2016) The Lagrange and the vanishing discount techniques to controlled diffusions with cost constraints. J Math Anal Appl 437(2):999–1035

Kędra M, Wiejaczka Ł (2018) Climatic and dam-induced impacts on river water temperature: assessment and management implications. Sci Total Environ 626:1474–1483

Oberman AM (2006) Convergent difference schemes for degenerate elliptic and parabolic equations: Hamilton-Jacobi equations and free boundary problems. SIAM J Numer Anal 44(2):879–895

Øksendal B, Sulem A (2019) Applied stochastic control of jump diffusions. Springer, Cham

Piotrowski AP, Osuch M, Napiorkowski JJ (2021) Influence of the choice of stream temperature model on the projections of water temperature in rivers. J Hydrol 601:126629

Quindala KI, Cuaresma DC, Mamplata J (2021) Modeling the historical temperature in the province of Laguna using Ornstein-Uhlenbeck process. Eur J Pure Appl Math 14(1):327–339

Resnick SI (2007) Heavy-tail phenomena: probabilistic and statistical modeling. Springer, New York

Tanaka T, Yoshioka H, Yoshioka Y (2021) DEM-based river cross-section extraction and 1-D streamflow simulation for eco-hydrological modeling: a case study in upstream Hiikawa River, Japan. Hydrol Res Lett 15(3):71–76

Yang K, Yu Z, Luo Y, Zhou X, Shang C (2019) Spatial-temporal variation of lake surface water temperature and its driving factors in Yunnan-Guizhou Plateau. Water Resour Res 55(6):4688–4703

Yoshioka H (2021) Fitting a superposition of Ornstein–Uhlenbeck processes to time series of discharge in a perennial river environment, ANZIAM Journal, June 2022, Vol 63:C84–C96. https://doi.org/10.21914/anziamj.v63.16985

Yoshioka H, Tsujimura M (2021) Hamilton–Jacobi–Bellman–Isaacs equation for rational inattention in the long-run management of river environments under uncertainty, Computers & Mathematics with Applications, April 2022, Vol 112:pp 23–54. https://doi.org/10.1016/j.camwa.2022.02.013, arXiv:2107.12526.

Yoshioka H, Yoshioka Y (2021) Designing cost-efficient inspection schemes for stochastic streamflow environment using an effective Hamiltonian approach, Optimization and Engineering, September 2022, Vol 23:1375–1407. https://doi.org/10.1007/s11081-021-09655-7

Chapter 10
Solubilization of Polycyclic Aromatic Hydrocarbon Mixtures in Conventional and Gemini Surfactant Solutions

Jianfie Liu, Zhiyuan Zhao, and Yongsheng Zhang

Abstract Polycyclic aromatic hydrocarbons (PAHs) are common organic compounds, which do great harm to the environment and health. The solubility ability enhancement of three PAHs, phenanthrene (PHE), fluoranthene (FLA), and benzo(a)anthracene (BaA) by two surfactants, TritonX-100 (TX-100) and a gemini surfactant (CG) have been studied and compared. For single-PAH system, molar solubilization ratio (MSR) decreased as increased octanol–water partitioning coefficient of PAHs in two surfactants. As for gemini and conventional surfactant, MSR did not follow the rule that the lower HLB value means the higher solubilization capacity. For mixture PAH systems, the results showed that there was competitive interaction among PAHs in both surfactants. In TX100 or CG surfactant solutions, the solubility of PHE decreased in all co-existing solution. The solubility of FLA was increased at the co-existing solution with PHE but decreased at the co-existing solution with BaA. The solubility of BaA increased in all co-existing solution. This is because more hydrophobic solute displaced the less hydrophobic, which reduced the Km value of PHE at the co-existing solution. Gemini surfactant can ionize in the solution and the free ions may affect the micelle reorganization resulting in the decrease of the apparent solubility significantly.

Keywords Solubilization · Polycyclic aromatic hydrocarbons · Surfactant · Micelles

10.1 Introduction

Polycyclic aromatic hydrocarbons (PAHs) are general include more than 100 different chemicals, which is mostly caused by the incomplete combustion of fossil fuel, or other organic matter (Bzdusek et al. 2004; Wang et al. 2010). One promising method to remediate contaminated soil caused by PAHs is surfactant-enhanced remediation (Khan et al. 2004; Svab et al. 2009). Surfactant can significantly increase the

J. Liu · Z. Zhao · Y. Zhang (✉)
School of Civil Engineer, Henan Polytechnic University, Jiaozuo 454003, P. R. China
e-mail: zhangyongsheng@hpu.edu.cn

H.-Y. Jeon (ed.), *Sustainable Development of Water and Environment*,
Environmental Science and Engineering,
https://doi.org/10.1007/978-3-031-07500-1_10

solubility of lipophilic liquid in water and the dissolution of soil bound aromatic hydrocar-bons.

Most of earlier studies were about the solubility enhancement of PAHs in single or mixed surfactant for an individual PAH system (An et al. 2002; Zhou and Zhu 2005, 2008a, b; Zhao et al. 2005; Mohamed and Mahfoodh 2006). There are some relationships between surfactant and solute structures for the enhancement of lipophilic solubility (Li and Chen 2002; Paria and Yuet 2006). There have numbers research about use conventional surfactant for remediate contaminated soil. Compared with the traditional surfactant, the surface-active substances of gemini surfactant are a type of surface-active substance composed with two hydrophobic tails and hydrophilic heads linked by a relatively small space groups (Zana 2002). There are limited papers about the gemini surfactant properties to PAHs in our knowledge (Kabir-ud-Din et al. 2009; Wei et al. 2011a, b; Panda and Kabir-ud-Din 2011). In recent years, there are some studies on the solubilization ability of PAH in mixed system composed by gemini and conventional surfactants. The result show mixed gemini and conventional surfactant systems have synergistic effect, which indicated the less surfactant can be used for the similar remediation effect (Yadav et al. 2017; Fatma et al. 2020; Manorama et al. 2011; Pandakabir-Ud-Din 2013).

However, there are many researches interested in the single PAH solubilization behavior in the mixed surfactants. Since PAHs exist as mixture in nature, it is of great significance to study the solubilization behavior of PAHs mixture in a surfactant. The micelle-water distribution coefficient is an important solubility property for surfactant, which is widely used in the traditional surfactants for single compound. However, it is might not be suited for the mixture compounds (Chaiko et al. 1984). When different kind PAHs exist, there may be a synergistic, inhibitive, or negligible effect in the solution for hydrophilic chains and properties of surfactants (Masrat et al. 2013; Yang et al. 2015; Liang et al. 2016). Compare with the ionic surfactant, the nonionic surfactants have large size core and low critical micelle concentration value and have better solubilization ability of PAH. Owing to the favorable electrostatic interactions between surfactant electron and positive charge head group, ionic or cationic surfactants also have better solubilization ability. However, the solubilization behavior of mixed PAHs in gemini surfactant solution remains yet to be studied. Competitive solubilization and synergistic effects did not clear during co-solubilization process for the phenomenon of conventional surfactant is not applicable for the gemini surfactant. This research has great meaning for selecting surfactants in remediation for contaminated sites.

The solubilization properties of individual or mixed PAHs in a conventional and gemini surfactant were investigated in this paper. The research goal is to get the solubilization properties of individual PAH and to clarify the synergistic solubilization properties of conventional surfactants and gemini surfactants on mixed PAHs.

10.2 Materials and Methods

10.2.1 Materials

The surfactant Triton X-100 with purity >98% was obtained from J&K Scientific Ltd, China. Gemini surfactant (CG) N_1-dodecyl-N_1,N_1,N_2,N_2-tetramethyl-N_2-octylethane-1,2-diaminium bromide with purity >98% was purchased from Chengdu Organic Chemicals Co., Ltd., China. The molecular structure of CG is $C_{12}H_{25}N + (CH_3)_2(CH_2)_2–N + (CH_3)_2C_{12}H_{25}·2Br–$ and its CMC is 0.85 mM. The molecular structure of TX100 is $C_8H_{17}C_6H_4O(OCH_2CH_2)_{9.5}H$ and its CMC is 0.2 mM.

Phenanthrene (PHE), fluoranthene (FLA), and benzo(a)anthracene (BaA) with more than 99% purity were obtained from Sigma-Aldrich Co. Ltd., USA.

10.2.2 Solubilization Experiments

The solubility of individual or mixed PAHs was determined with different surfactant solutions. For batch tests, a conical flask containing 25 mL both surfactant solution and excess single or mixed polycyclic aromatic hydrocarbons, were sealed with a Teflon lined septum. The solubilization experiments conditions are the same as our previous work (Liu et al. 2016).

10.2.3 Analytical Methods

PAH concentration in water and surfactant was determined by HPLC (Dionex U3000) with a UV detector. The test conditions are the same as our previous work (Liu et al. 2016).

10.2.4 Data Calculation

Molar solubilization ratio (MSR) is an important parameter to evaluate the PAH solubility in surfactant solution, which is determined by:

$$MSR = \frac{S_{ac} - S_{cmc}}{C_{surf} - CMC} \tag{10.1}$$

where S_{ac} is the total PAHs solubility in the surfactant solutions. C_{surf} and S_{cmc} is the solubility of PAHs at surfactant solution in CMC.

Partition coefficient K_m is PAHs fraction between surfactant micelles and the aqueous phase, which is determined by the following formula:

$$K_m = \frac{X_m}{X_a} \tag{10.2}$$

where X_m is the PAH mole fractions in surfactant micelles; X_a is the PAH mole fractions in water.

The values of X_m can be calculated by the following formula:

$$X_m = \frac{MSR}{1 + MSR} \tag{10.3}$$

For mixture PAHs, $X_{m,i}$ can be calculated by the following formula:

$$X_{m,i} = \frac{MSR_i}{1 + \sum_{1}^{n} MSR_i} \tag{10.4}$$

For commercially available surfactants sold by weight unit price, the weight solubilization ratio is intuitive, it indicates that the increased surface activity per unit volume. The relationship between WSR and MSR can be defined as the following:

$$WSR = MSR \times \frac{M_{PAH}}{M_{surf}} \tag{10.5}$$

where M_{PAH} and M_{surf} are the molecular weight of PAH and surfactant, respectively.

The standard free energy change ΔGs can be defined by the following formula:

$$\Delta G_s = -RT \ln K_m \tag{10.6}$$

where R is the general gas constant, T is the absolute temperature, and K_m is the molar partition coefficient between the surfactant micellar and the aqueous phase.

10.3 Results and Discussion

10.3.1 Solubilization of Single Compounds

The solubility ability of CG for three PAHs above the CMC is illustrated in Fig. 10.1 and the solubility enhancement for TX100 have studied in our previous work (Liu

et al. 2016). The solubility amount of single PAH enhanced with the increased surfactant concentration higher than CMC. There was a correlation between the solubilization of PAHs and surfactant solution. The slopes were determined by the least-square regression and the results are displayed in Table 10.1.

As for TX100, MSR for PHE is 0.11 closed to the reported values of 0.13 (Li and Chen 2002). MSR for FLA is 0.08 closed to the reported value of 0.09 (Prak and Pritchard 2002). MSR for BaA is 0.015 and there is no reported value on literature to compare. As for CG, MSR for PHE is 0.15 closed to the reported value of 0.14 (Wei et al. 2011b). The MSR value for FLA is 0.09 and the MSR value for BaA is 0.016. There is no value on literature to compare in our knowledge. For a single-PAH

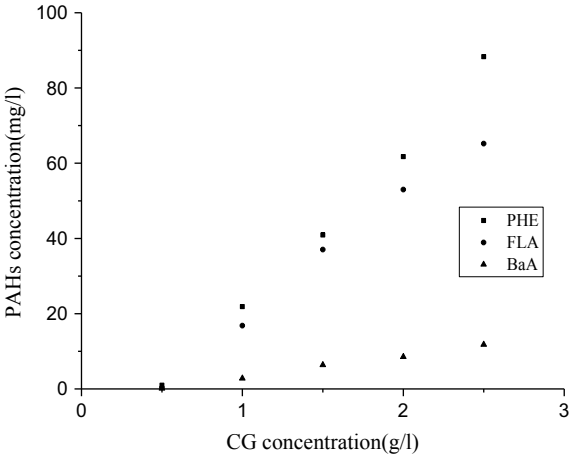

Fig. 10.1 Solubilization ability of single PAH in the gemini CG

Table 10.1 MSR values of PAHs in two surfactants

Surfactant	PAH		Single compound	Binary compound			Three compound
				With-PHE	With-FLA	With-BaA	
TX100	PHE	MSR	0.12		0.11	0.09	0.09
		$\log K_m$	5.65		5.59	5.53	5.51
	FLA	MSR	0.08	0.097		0.067	0.09
		$\log K_m$	6.17	6.2		6.09	6.17
	BaA	MSR	0.015	0.016	0.016		0.017
		$\log K_m$	7.02	7.06	7.03		7.07
CG	PHE	MSR	0.15		0.11	0.12	0.10
		$\log K_m$	5.86		5.71	5.65	5.55
	FLA	MSR	0.10	0.11		0.08	0.10
		$\log K_m$	6.37	6.39		6.16	6.24
	BaA	MSR	0.016	0.016	0.017		0.017
		$\log K_m$	7.01	7.02	7.01		7.02

system, MSR decreased with the increase of the K_{ow} of PAHs. For all surfactants, BaA has higher K_{ow} value than PHE and FLA. Km is linearly related to K_{ow}, which is agree with other research conclusion (Edwards et al. 1991). The increase in apparent solubility of PHE and FLA by CG is much greater that of TX100. As for BaA, MSR is hardly changed. It is expected that PHE with the smallest K_{ow} value, therefore it is more easily for PHE to be partitioned into two surfactants micelles.

As we know, the lower the Hydrophile-Lipophile Balance Number (HLB), the higher the solubilization efficiency of the surfactant. However, the surfactants of TX100 and CG did not follow this rule. The HLB of TX100 is 18.7, less than 23.5 of CG. In fact, MSR of CG is above that of TX100. The difference in solubilizing capacity of surfactants may be related to their structure. CG surfactant has high solubilization ability, which may be due to the wide diffusion interaction between the positive charge double head group of CG surfactant and π-electron of PAHs. The strong hydrophobicity of CG surfactant is also beneficial for the excessive solubilization of PAHs (Wei et al. 2011a). Moreover, CG surfactant with larger shell and micelle bulk than that of TX100, benzene structure of CG surfactant has a certain affinity for aromatic compounds. From the above results, we can know both HLB and the surfactant structure are important parameters for solubilization power towards PAHs. Moreover, the solubilization is more affected by the surfactant structure than by the HLB. From the view of surfactant structure, with the longer alkyl chain, gemini surfactant have larger solubilization capacity.

10.3.2 Solubilization of PAH Mixtures

Table 10.1 lists the respective value of $\log K_m$ and MSR of three PAHs in all possible combination in two surfactants. All of which were calculated using Eqs. 10.2–10.5. The results of three PAH solubility in surfactant solution are shown in Figs. 10.2 and 10.3.

As listed in Table 10.1, the solubility of PHE, FLA and BaA was significantly influenced by a completive effect with each other in TX100. Less hydrophobic solute like PHE was displaced by FLA from surfactant, which increased the Km value of FLA in ternary mixture. The displacement behavior between PHE and BaA is similar. If the solutes compete with each other for internal position of surfactant micelle, the solubility of less hydrophobic solute will decrease in the co-existing solution (Guha et al. 1998). If other more hydrophobic compound displaced PHE from the micelle cores, this would reduce the apparent PHE solubility in the PHE and FLA co-existing solution. Likely, the FLA solubility decreases in the FLA and BaA co-existing solution.

In presence of both PHE and FLA, BaA solubility increases significantly in TX100. At the co-existing solution including PHE, FLA, and BaA, BaA with less hydrophobic can be dissolved in the interface area of hydrophobic core, which usually leads to the decrease of interface tension between surfactant core and water, and then can maintain a large internal space at the same energy (Chen et al. 2002).

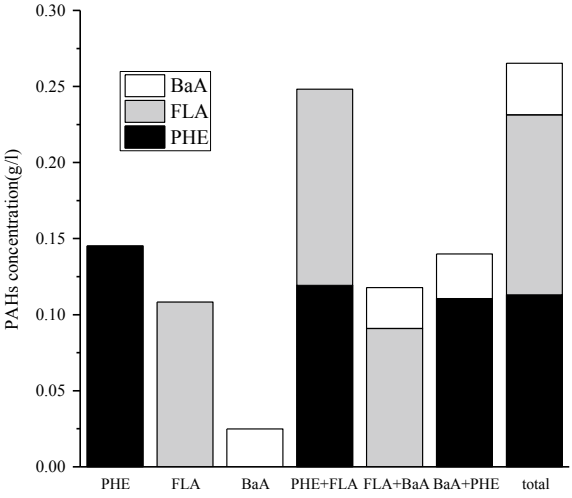

Fig. 10.2 PAH concentration in TX100 (5 g/L)

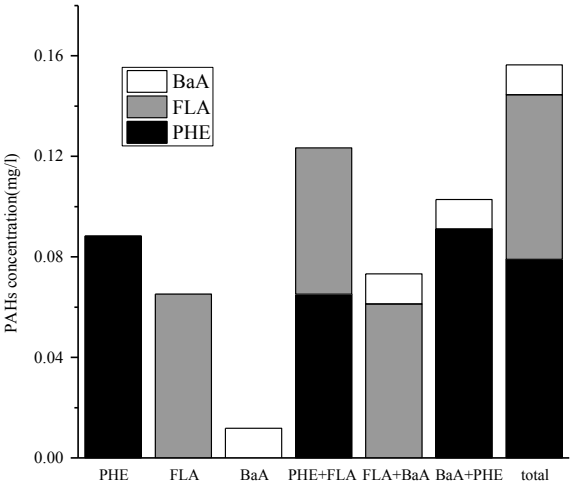

Fig. 10.3 PAH concentration in CG (2.5 g/L)

Atwood summarizes several researches that show surfactant micelles are recombined to contain both solutes and a great number of monomers for certain solutes (Attwood 1983). It can be supposed that in the presence of two solutes, surfactant micelles can further recombination and solutes can be packed, so that the filling degree of two PAHs in micelles is the same as that in a single PAH system (Prak and Pritchard 2002).

As for gemini surfactant, we observed three different results in our experiment with binary and ternary mixture. If the solubility of a solutes increases, which was found for the partition coefficient of FLA at the FLA-PHE co-existing mixture, it could be explained by that the more hydrophobic solute displaces the less hydrophobic solute.

In some case, the solubility of one solute decreased at the co-existing mixture, which was observed for the K_m value of PHE at the binary and ternary mixtures. The maximum reduction of logK_m value of PHE in CG solution (from 5.86 to 5.55) is much higher than that of in the TX100 solution (from 5.65 to 5.51). These results could be explained by that TX100 as a nonionic surfactant, does not ionize in solution and has higher stability in the water. However, CG as a cationic gemini surfactant, can ionize in the solution and the free-ions may affect the micelle reorganization so result in the reduction of the apparent solubility of PHE greatly. No significant change was observed for BaA, where the core volume and Km changed little, it may due to that the micelle has reached its maximum ability and cannot accommodate the PAHs, especially for high molecular weight PAH.

The results indicate that solubilization behavior of PAHs in Gemini surfactant solution covers complicated interactions between PAHs, and between the PAHs and surfactants. Moreover, the results reveals that the PAHs were solubilized in the whole surfactant micelles by nuclear magnetic resonance. Since gemini surfactant has double heads and tails, the solubilization behavior is more complex than the conventional surfactant and should be studied further.

10.3.3 Thermodynamic of Solubilization

Analyzing the thermodynamic parameters of the solubilization process is beneficial to better understand the thermodynamics process. Thermodynamic parameters of solubilization process can be calculated by the standard free energy. ΔGs value would be a negative value from Eq. 10.6, which shows the solubilization process is spontaneous.

10.4 Conclusions

The capacities of conventional surfactant (TX100) and gemini surfactant (CG) on PHE, FLA and BaA were evaluated through MSR and Km. Although the HLB of the studied gemini surfactant is higher than that of TX100, it exhibits excellent solubilization ability towards PAHs. As for gemini and conventional surfactant, MSR did not follow the rule that the lower HLB value means the higher solubilization capacity. Thus, K_m is a more important factor than HLB for solubilization process. The results showed that there was competitive interaction among PAHs in both surfactants. For mixture PAH systems in TX100 or CG surfactant solutions, the solubility of PHE decreased in all co-existing solution. The solubility of FLA was increased at the co-existing solution with PHE bud decreased at the co-existing solution with BaA. The solubility of BaA increased in all co-existing solution.

Acknowledgements This research was supported by Key scientific research projects of colleges of Henan province (21B610006), and the Fundamental research funds for the universities of Henan Province.

References

An YJ, Carraway R, Schlautman A (2002) Solubilization of polycyclic aromatic hydrocarbons by perfluorinated surfactant micelles. Water Res 36(1):300–308

Attwood DA (1983) Surfactant systems: their chemistry, pharmacy, and biology. Chapman & Hall, New York

Bzdusek A, Christensen R, Li A, Zou QM (2004) Source apportionment of sediment PAHs in Lake Calumet, Chicago: application of factor analysis with nonnegative constraints. Environ Sci Technol 38(1):97–103

Chaiko A, Nagarajan R, Ruckenstein E (1984) Solubilization of single-component and binary-mixtures of hydrocarbons in aqueous micellar solutions. J Colloid Interf Sci 99(1):168–182

Chen LC, Lee J, Park J (2002) Solubilization of PAH mixtures by three different anionic surfactants. Environ Pollut 118(3):307–313

Edwards A, Luthy G, Liu ZB (1991) Solubilization of polycyclic aromatic-hydrocarbons in micellar nonionic surfactant solutions. Environ Sci Technol 25(1):127–133

Fatma N, Panda M, Kabir-ud-Din (2020) A study on the solubilization of polycyclic aromatic hydrocarbons in gemini-conventional mixed surfactant systems by 1H NMR spectroscopy. Mater Chem Phys 254(1):123223

Guha S, JafféP R, Peters A (1998) Solubilization of PAH mixtures by a nonionic surfactant. Environ Sci Technol 7(32):930–935

Kabir-ud-Din, Shafi M, Bhat A, Dar A (2009) Solubilization capabilities of mixtures of cationic Gemini surfactant with conventional cationic, nonionic and anionic surfactants towards polycyclic aromatic hydrocarbons. J Hazard Mater 167(1–3):575–581

Khan I, Husain T, Hejazi R (2004) An overview and analysis of site remediation technologies. J Environ Manage 71(2):95–122

Li JL, Chen BH (2002) Solubilization of model polycyclic aromatic hydrocarbons by nonionic surfactants. Chem Eng Sci 57(14):2825–2835

Liang X et al (2016) Cosolubilization synergism occurrence in codesorption of PAH mixtures during surfactant-enhanced remediation of contaminated soil. Chemosphere 144:583–590

Liu J, Zhang Y, Sun X, Hu W (2016) Separation of polycyclic aromatic hydrocarbons from rhamnolipid solution by activated carbon adsorption. Environ Earth Sci 75(22):1453

Masrat R, Maswal M, Dar AA (2013) Competitive solubilization of naphthalene and pyrene in various micellar systems. J Hazard Mater 244–245:662–670

Mohamed A, Mahfoodh A (2006) Solubilization of naphthalene and pyrene by sodium dodecyl sulfate (SDS) and polyoxyethylenesorbitan monooleate (Tween 80) mixed micelles. Colloid Surf A 287(1–3):44–50

Panda M, Kabir-ud-Din (2011) Study of surface and solution properties of gemini-conventional surfactant mixtures and their effects on solubilization of polycyclic aromatic hydrocarbons. J Mol Liq 163(2):93–98

Panda M et al (2011) Study of surface and solution properties of gemini-conventional surfactant mixtures and their effects on solubilization of polycyclic aromatic hydrocarbons. J Mol Liquids 163(2):93–98

Pandakabir-Ud-Din M (2013) Solubilization of polycyclic aromatic hydrocarbons by gemini–conventional mixed surfactant systems. J Mol Liq 187(11):106–113

Paria S, Yuet K (2006) Solubilization of naphthalene by pure and mixed surfactants. Ind Eng Chem Res 45(10):3552–3558

Prak D, Pritchard H (2002) Solubilization of polycyclic aromatic hydrocarbon mixtures in micellar nonionic surfactant solutions. Water Res 36(14):3463–3472

Svab M, Kubala M, Muellerova M, Raschman R (2009) Soil flushing by surfactant solution: pilot-scale demonstration of complete technology. J Hazard Mater 163(1):410–417

Wang W, Massey SL, Xue M, Zhao J, Zhang N, Wang R, Cao J, Tao S (2010) Concentrations, sources and spatial distribution of polycyclic aromatic hydrocarbons in soils from Beijing, Tianjin and surrounding areas. North China, Environ Pollut. 158(5):1245–1251

Wei J, Huang GH, Yu H, An CJ (2011a) Effciency of single and mixed Geminiconventional micelles on solubilization of phenanthrene. Chem Eng J 168(190):201–207

Wei J, Huang GH, An CJ, Yu H (2011b) Investigation on the solubilization of polycyclic aromatic hydrocarbons in the presence of single and mixed Gemini surfactants. J Hazard Mater 190(1–3):840–847

Yadav SK et al (2017) Solubilization potentials of single and mixed oppositely charged gemini surfactants: A case of polycyclic aromatic hydrocarbons. Colloids Surf A Physicochem Eng Aspects 514:47–55

Yang XG et al (2015) Cosolubilization of 4,4′-dibromodiphenyl ether, naphthalene and pyrene mixtures in various surfactant micelles. Chem Eng J 274:84–93

Zana R (2002) Dimeric and oligomeric surfactants. Behavior at interfaces and in aqueous solution: a review. Adv Colloid Interfac 97(1–3):205–253

Zhao BW, Zhu LZ, Li W, Chen BL (2005) Solubilization and biodegradation of phenanthrene in mixed anionic-nonionic surfactant solutions. Chemosphere 58(1):33–40

Zhou WJ, Zhu LZ (2005) Distribution of polycyclic aromatic hydrocarbons in soil-water system containing a nonionic surfactant. Chemosphere 60(9):1237–1245

Zhou W, Zhu LZ (2008a) Enhanced soil flushing of phenanthrene by anionic-nonionic mixed surfactant. Water Res 42(1–2):101–108

Zhou WJ, Zhu LZ (2008b) Influence of surfactant sorption on the removal of phenanthrene from contaminated soils. Environ Pollut 152(2):99–105

Chapter 11
A Sustainable Strategy for Petrochemical Wastewater Treatment via Anaerobic Co-Digestion

Anita Atukunda, Mona G. Ibrahim, Manabu Fujii, Shinichi Ookawara, and Mahmoud Nasr

Abstract Petrochemical manufacturing processes release large amounts of water composed of organic and inorganic compounds, imposing high pollution loads on the receiving environment. Treating this petrochemical wastewater (PCW) using a biological system is essential to protecting the environment and human health, with a dual benefit of bioenergy production. In this study, PCW was mixed with domestic wastewater (DWW) at different PCW: DWW v/v ratios of 0:1, 1:2, 1:1, 2:1, and 1:0, and subjected to anaerobic digestion for eliminating chemical oxygen demand (COD) and recovering methane-rich biogas (CH_4). The highest bio-CH_4 yield of 281.55 mL/g$COD_{removed}$, with COD reduction = 93.8%, was observed at 1:1 (PCW: DWW) under mesophilic conditions for 192 h. Increasing the PCW fraction was associated with the deterioration of the biological activity, where bio-CH_4 yield dropped to 196.02 mL/g$COD_{removed}$ at PCW: DWW of 2:1. The study demonstrated that adding DWW to the industrial effluent could be a reliable strategy for diluting the organic load, thus avoiding methanogenesis inhibition from volatile fatty acids (VFAs) accumulation. Accordingly, the study outputs (dual wastewater treatment and

A. Atukunda (✉) · M. G. Ibrahim · M. Nasr
Environmental Engineering Department, Egypt-Japan University of Science and Technology, Alexandria 21934, Egypt
e-mail: anita.atukunda@ejust.edu.eg

M. G. Ibrahim
Environmental Health Department, High Institute of Public Health, Alexandria University, Alexandria 21544, Egypt

M. Fujii
Department of Civil and Environmental Engineering, Tokyo Institute of Technology, Tokyo 152-8552, Japan

S. Ookawara
Department of Chemical Science and Engineering, Tokyo Institute of Technology, Tokyo 152-8552, Japan

M. Nasr
Sanitary Engineering Department, Faculty of Engineering, Alexandria University, Alexandria 21544, Egypt

H.-Y. Jeon (ed.), *Sustainable Development of Water and Environment*,
Environmental Science and Engineering,
https://doi.org/10.1007/978-3-031-07500-1_11

biogas recovery) would meet the 2030 Agenda for sustainable development related to water resource management and renewable energy generation.

Keywords Co-substrate · Terephthalic acid wastewater · Domestic sewage · Methane-rich biogas · Sustainable Development Goals (SDGs)

11.1 Introduction

Wastewater discharged from petrochemical industries, and manufacturing processes contain elevated phenolic substances, benzene, xylene, and polycyclic aromatic hydrocarbons (Tan et al. 2020). Petrochemical wastewater (PCW) may contain aromatic contaminants like terephthalate, 4-carboxybenzaldehyde (4-CBA), benzoic acid (BA), acetic acid, and p-toluic acid (Macarie et al. 1992; Kleerebezem et al. 1997). Discharge of this type of wastewater into the environment is generally associated with risks for both humans and living organisms (Tan et al. 2020). However, the organic fraction in PWC could be transformed into valuable products (biogas, bio-CH_4, bio-H_2, etc.) under the biological conversion processes. In addition to reducing pollution and generation of bioenergy sources, PCW treatment could maintain multiple environmental, economic, and social benefits.

Recently, anaerobic digestion has been proposed as a reliable and cost-effective process for treating PCW (Tan et al. 2020; Kleerebezem et al. 1997). This technology has the advantages of resisting high organic loads, producing a small amount of sludge, and processing with low operational cost (does not consume aeration energy) (Bhatt and Tao 2020). In addition, electric energy from biogas contributes to reduced greenhouse gas emissions. The biological conversion of organics into beneficial products occurs via four basic mechanisms: hydrolysis, acidogenesis, acetogenesis, and methanogenesis (Bhatt and Tao 2020). The biochemical pathways involved in these mechanisms are controlled by various process factors such as pH of microorganisms, hydraulic retention time (HRT), organic loading rate (OLR), temperature, and substrate type (Bhatt and Tao 2020).

The average PCW has low pH values, providing very acidic conditions that are not conducive to the production of bio-CH_4. During the hydrolysis phase, long-chain fatty acids (LCFA) accumulate in the sludge bed, forming a physical barrier (Tawfik et al. 2021). This pattern would limit substrates and metabolic by-products in the mixed liquor from interfacing with the bacteria enzymes; thus, hindering the utilization of organic metabolites. This delays the initial CH_4 production and can lead to system failure (Tawfik et al. 2021). Co-digestion in anaerobic wastewater treatment is considered an efficient method to reduce inhibition caused by LCFA accumulation (Tawfik et al. 2021). In this process, the cost of operation, maintenance, and heating could be compensated by bioenergy production as substrates are simultaneously degraded in a single digester (Bhatt and Tao 2020). In addition, co-digestion can dilute toxic substances, improve the balance of nutrients and relieve the organic load, thus improving the synergy of microorganisms (Shah et al. 2015). Hence, anaerobic

co-digestion is a sustainable green technology for treating various high-strength industrial effluents (Shah et al. 2015). The addition of domestic wastewater (DWW) to a highly acidic medium, such as PCW, has been reported as a promising approach to attenuate the inhibitory effect of LCFA accumulation and reducing the use of buffer reagents (Tawfik et al. 2021). Moreover, the use of DWW as a co-substrate for treating industrial wastewater has been described to adapt the carbon-to-nitrogen (C/N) ratio to around the optimum value for anaerobic processes 25–30 (Wang et al. 2012).

The application of "waste-to-energy" methods to convert organic compounds into biogas has been noticed for pollution reduction and energy generation; hence, meeting the three pillars of sustainability (Dada and Mbohwa 2018). This strategy is linked to multiple sustainable development goals (SDGs), e.g., SDG3 by protecting human health from waste disposal, SDG6 by treating industrial effluent, SDG7 by investing in clean energy to avoid an energy crisis, SDG13 by greenhouse gas mitigation, and SDG14 by protecting aquatic life (United Nations 2019). However, describing the SDGs relevant to anaerobic co-digestion of PCW: DWW to have higher energy yields is still lacking in the literature. This main objective is covered in the current study through specific points (i) prepare anaerobic co-digestion process with different DWW: PCW ratios of 0:1, 1:2, 1:1, 2:1, and 1:0, (ii) investigate the effect of varying DWW: PCW ratios on COD conversion into biogas, and (iii) highlight the SDGs relevant to the study outputs.

11.2 Materials and Methods

11.2.1 Synthetic Wastewater

Synthetic petrochemical wastewater (PCW) was prepared to simulate purified terephthalic acid (PTA) wastewater (Ma et al. 2020). The major compounds were terephthalic acid 2000 mg/L, benzoic acid 600 mg/L, acetic acid 2000 mg/L, and xylene 400 mg/L, corresponding to a theoretical COD range of 2870–3200 mg/L. Acetic acid was selected as a carbon source. The NH_4CL, KH_2PO_4, and $MgCl_2$ chemicals were added to supply micronutrients and promote the specific methanogenic activity following (Ma et al. 2020). Trace elements were added following as reported elsewhere (Li et al. 2014). DWW used in this study was collected from a wastewater treatment plant (WWTP) located in Borg El-Arab, Alexandria, Egypt. The characteristics of PCW and DWW are listed in Table 11.1. These properties suggest that the chemical oxygen demand (COD) of PCW would be diluted with DWW addition. Moreover, DWW would be a zero-cost nitrogen supplement to anaerobic methanogenesis.

Table 11.1 Shows the feed characteristics for the petrochemical and domestic wastewater used in this study

	PCW	DWW	Unit
COD	2800–3200	360	mg/L
pH	3.3	7.34	pH unit
Ammonia-N	0.84	24.64	mg/L
Total solids (TS)	–	1510	mg/L
Volatile solids (VS)	–	402	mg/L
Volatile fatty acids (VFA)	1391	173	mg/L

11.2.2 Inoculum Sludge

Sewage sludge was obtained from a WWTP, treating domestic wastewater. Sludge as inoculum had total solids (TS) and volatile solids (VS) concentrations of 219.5 g/L and 149.1 g/L, respectively. The inoculum was incubated for 10 days at 37 °C before use (Angelidaki et al. 2009). Prior to incubation, the 50 mL headspace of each bottle was flushed with N_2 gas for 3–5 min to remove traces of oxygen (Ezz et al. 2021).

11.2.3 Co-Digestion Experimental Setup

Anaerobic co-digestion batch assays were conducted in 250 mL volumetric glass bottles with a working volume of 200 mL (Fig. 11.1), following the experimental design procedures in Ezz et al. (2021). Homogenized inoculum (40 mL) was added, representing 20% of the working bottle volume. Different mixing proportions of PCW: DWW = 1:2, 1:1, and 2:1 were used as a substrate in the co-digestion experimentation. The control assays were performed with PCW: DWW of 1:0 and 0:1. The reactors are placed in a water bath at mesophilic temperature (37 °C). The initial pH of all reactors was adjusted to pH 6.5–7.5 using 1 M HCl and 1 M NaOH, forming favorable conditions of methanogenic growth and activity (Tan et al. 2020). All experimentations and measurements were performed in duplicate, and average values were used in the analysis.

11.2.4 Analysis Methods

The concentrations of volatile solids (VS), total solids (TS), total Chemical Oxygen Demand (COD_{total}), volatile fatty acids (VFA), and ammonium nitrogen (NH_4-N) were estimated following the procedures in APHA (2017). Effluent samples were collected from the batch supernatant after every gas measurement for COD_{total} and NH_4-N analysis. A multi-parameter portable colorimeter (DR900, HACH, USA) was

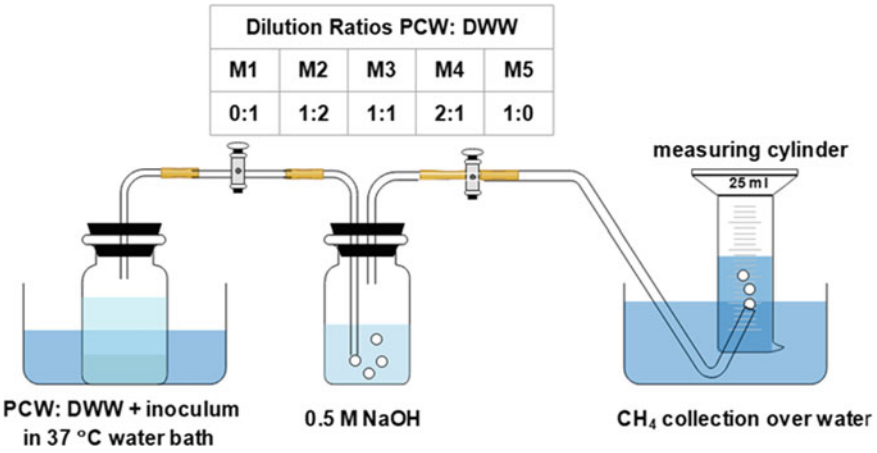

Fig. 11.1 Schematic drawing for the experimental setup of PCW treatment for biogas production using anaerobic co-digestion process

used to measure COD_{total}. The medium temperature and pH were measured with a portable multimeter.

Methane (CH_4) gas was collected as explained by Ezz et al. (2021). An alkaline solution (0.5 M NaOH) was used to eliminate CO_2 in the evolved biogas, leaving CH_4. Biogas production (mainly CH_4) was measured using the water displacement method (Ezz et al. 2021). The modified Gompertz model (Eq. 11.1) was used to calculate the CH_4 potential and maximum production rate (Tawfik et al. 2021):

$$H = Pexp\left\{-exp\left[\frac{R_m e}{P}(\lambda - t) + 1\right]\right\} \tag{11.1}$$

where H: cumulative CH_4 production (mL), t: reaction time (h), P: CH_4 potential (mL), λ: lag phase required to initiate bacterial growth (h), R_m: maximum CH_4 production rate (mL/h), and *e* is the Euler's number (2.71828).

Cumulative biogas yield (CBY) was calculated in terms of COD removed, Eq. (11.2):

$$CBY\ (mL/gCOD\ removed) = \left\{\frac{Cumulative\ biogas\ (mL)}{(CODin - CODfin)\left(\frac{g}{L}\right) * Reactor\ Volume\ (L)}\right\} \tag{11.2}$$

11.3 Results and Discussion

11.3.1 Effect of PCW: DWW Ratios on COD Removal

Figure 11.2d shows the COD removal efficiency for each batch assay with varying feed composition and concentration (PCW:DWW of 0:1, 1:2, 1:1, 2:1, and 1:0). After 192 h of co-digestion, the COD removal efficiencies ranged between 82 and 98% in the same experimental conditions. The highest COD reduction performance (around 98%) was noticed for the PCW: DWW ratios of 0:1 (M1) and 1:2 (M2). This performance could be assigned to the presence of readily biodegradable compounds like proteins, lipids, and fermentable carbohydrates in DWW (Bhatt and Tao 2020). The utilization of 25% PCW in 1:2 (M2) did not significantly affect substrate biodegradation, showing a slight decline to about 97%. However, M5 with 100% PCW showed the least COD removal efficiency (82%) within the same incubation period. The terephthalate compound in PCW wastewater is hardly degraded due to the high stability of its aromatic structures. In particular, the period required for terephthalate degradation could reach up to 100 days of continuous digestion (Kleerebezem et al. 1997). Remarkably, the co-digestion technique enhanced the bacterial activity to degrade PCW. For instance, M3 (1:1) and M4 (2:1) recorded a 12.3 and 7.3% increase in COD removal than M5 (only PWW). Co-digestion offers dilution of the aromatic compounds and a nitrogen source for microbe growth, improving the efficiency of the anaerobic digestion system (Shah et al. 2015).

11.3.2 Effect of PCW: DWW Ratios on Methane Production

Figure 11.2a shows CH_4 production associated with each substrate after 192 h of anaerobic digestion, aiming to improve biogas productivity. M3 recorded the maximum cumulative methane yield of 281.5 mL/g $COD_{removed}$ with a 93.8% COD removal efficiency. This batch bottle contained equal fractions (1:1) of PCW and DWW substrates. In a similar study Siddique et al. (2019) found a maximum methane yield of 321 $\pm$ 5 mL/g from 50:50 co-digestion of PCW and food waste. In another work (Siddique et al. 2014), the co-digestion of PCW with dairy and cattle manure in portions of 50:25:25 produced a maximum CH_4 yield of 99 mL/g. An improvement in CH_4 yield could be assigned to a proper micro and macronutrients balance and increase organic loading, which is attained by co-digestion, as suggested by Fayyaz et al. 2014 (Shah et al. 2015). Accordingly, M3 attained a 30.38% increase in CH_4 yield compared to the digestion of 100% PCW (M5).

Table 11.2 summarizes the performance of each batch reactor on CH_4 production and COD removal. Notably, 100% DWW (M1) digestion produced a higher CH_4 yield than 100% PCW (M5). As previously cited, DWW has a high fraction of fermentable compounds essential for biogas production (Bhatt and Tao 2020), unlike PCW (Tan et al. 2020; Kleerebezem et al. 1997). It is suggested that the results

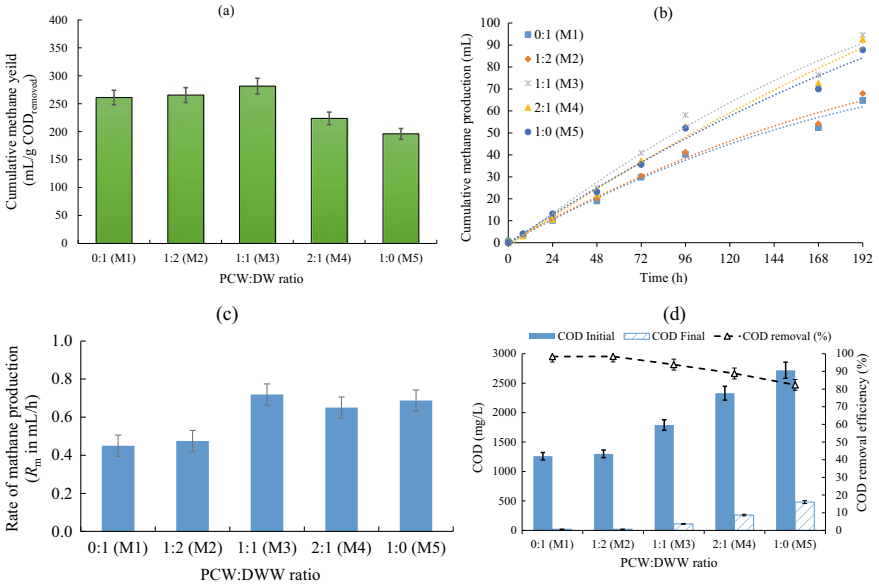

Fig. 11.2 Batch experimental results for anaerobic co-digestion of petrochemical wastewater and domestic wastewater at different PCW:DWW ratios **a** cumulative methane yield, **b** cumulative methane production, **c** rate of methane generation (R_m), and **d** COD concentrations and removal rates

of cumulative biogas from PCW would be enhanced by extending the incubation time. For example, Tan et al. (2020) found that PTA wastewater required 35 d of digestion to have the highest cumulative methane yield of 305.9 ± 2.7 mL/g-COD. Additionally, insufficient biogas production from PCW might be attributed to the unbalanced nutrient composition in the medium, hindering the microbial consortium activity and growth (Shah et al. 2015). Microorganisms would require more time to adapt to the PCW environment, unlike when acting on DWW.

The Gompertz equation showed a fitting accuracy with a coefficient of determination (R^2) of 0.92, implying that the model parameters (P, R_m, and λ) could appropriately describe the CH_4 production process (Fig. 11.2b). The M3 bottle showed the highest methane generation rate, R_m (Fig. 11.2c), corresponding to the maximum P. The CH_4 profile in Fig. 11.2b showed a short λ lag-phase, suggesting that the sludge inoculum adapted to the substrate conditions before conducting the experimentations. Moreover, the data in Fig. 11.2c suggest that additional time would be required to increase the bio-CH_4 productivity, which will be considered in future studies.

Table 11.2 Performance of the batch assays treating petrochemical wastewater and domestic sewage in different mixing PCW:DWW ratios of 0:1 (M1), 1:2 (M2), 1:1 (M3), 2:1 (M4), and 1:0 (M5) under mesophilic condition

PCW:DWW	M1	M2	M3	M4	M5
$COD_{initial}$	1260	1020	1790	2330	2720
COD_{final}	<20	<20	110	260	480
$pH_{initial}$	7.08	7.33	7.44	7.3	7.26
pH_{final}	7.18	6.81	7.07	7.28	7.03
$TS_{initial}$	108.9	85.3	99.6	73.1	121.7
TS_{final}	90.2	52.9	62.2	58.5	66.9
$VS_{initial}$	87.6	55.9	78.7	58.8	62.0
VS_{final}	31.2	39.5	51.1	27.5	22.7
CH_4 (mL/g $COD_{removed}$)	261.09	265.45	281.55	223.82	196.02
Ammonia-N	16.8	11.3	12.3	8.4	14.0

*All values are in mg/L except pH or indicated otherwise

11.3.3 Sustainable Development Goals (SDGs) Associated with PCW Anaerobic Treatment and CH_4 Production

This work shows the feasibility of using PCW and DWW to generate CH_4 via anaerobic co-digestion. The bioconversion of industrial effluents into biofuels would support a true circular green economy (Nasr et al. 2021), establishing multiple SDGs (Fig. 11.3):

Environmental-Related SDGs

Unsafe disposal of industrial effluents into water bodies is dangerous to humans and the aquatic environment. Anaerobic digestion alone does not enable a complete treatment of PCW to reach acceptable discharge standards. However, it effectively degrades complex polycyclic aromatic hydrocarbons (PAHs) in PCW. Secondary treatment methods such as aeration, adsorption, and membrane-based technologies are applied to produce a final effluent complying with the surface water discharge standards (Target 12.4 *Environmental management of all wastes, to agreed international standards*). Tertiary treatment of PCW also guarantees attainment of SDG 6 "*Clean Water and Sanitation*" by safe reuse of wastewater (Target 6.4 *Enhance water use efficiency*) and protection of water-related ecology (Target 6.6 *Ecosystems and water*). Waste management contributes to alleviating the impacts of pollution on human health (Target 3.9 *Reduced mortality from pollution*). Appropriate treatment of PCW also tends to protect marine ecology, emphasizing SDG 14 "*Life Below Water*".

The H_2 and CH_4 produced may be utilized to replace finite fossil fuel-based resources that pollute the atmosphere when burned (United Nations 2019) (Target 9.4 *Clean technologies*). The CO_2 generated in this study is linked to biomass conversions

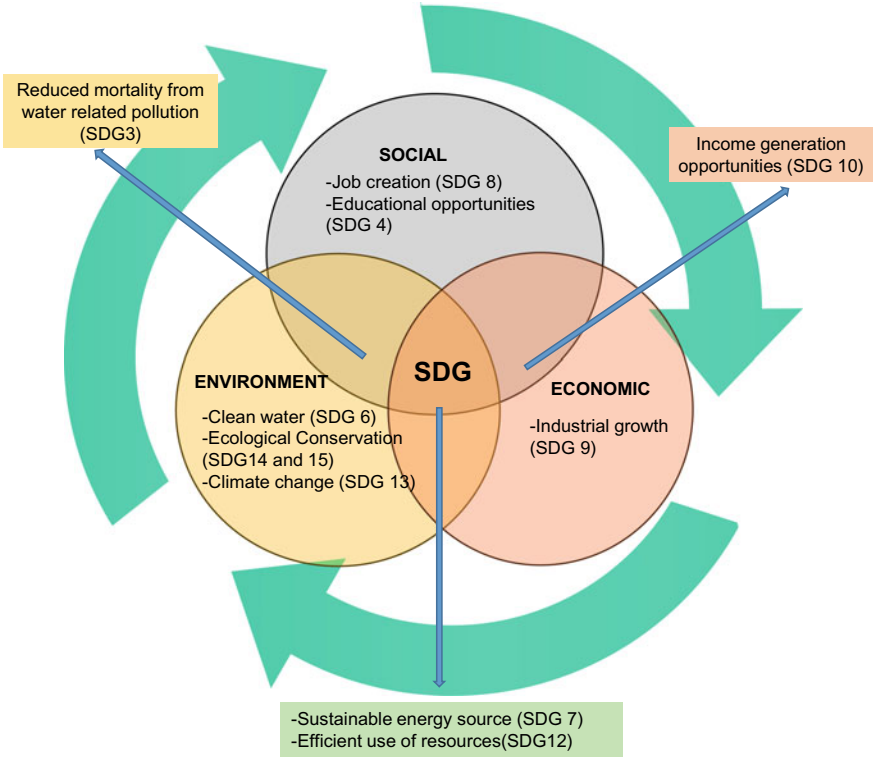

Fig. 11.3 Environmental, economic, and social SDGs relevant to anaerobic digestion for PCW treatment and biogas production

and is considered biogenic carbon emissions "carbon neutral" by the environment (Rodin et al. 2020). Integrating anaerobic digestion of PCW into the industrialized hierarchy will boost renewable energy outputs (Target 7.1 *Access to sustainable energy*), lower the use of fossil fuels and GHG emissions, and reduce related human consequences (Target 13.2 *Climate Change Policy*, Target 3.9 *Reduced mortality from pollution*).

Economic-Related SDG

Literature researches have shown the importance of environmental management in multiple business sectors (Gunarathne and Lee 2019; Giannetti et al. 2020). Environmental management accounting and innovation provide pertinent information for making educated decisions to avoid wasteful resource usage, pollution, and even disasters (Target 12.2 *Efficient use of natural resources*). Educated decisions assist managers in making better and cleaner production commitments and policies (Giannetti et al. 2020), guaranteeing attainment of SDG 12 "*Ensure sustainable consumption and production patterns*." Increasing renewable energy is one of the main objectives of this study by producing a cost-effective and alternative source for heating

and electricity supply to the communities (Target 7.1 *Access to sustainable energy*). Renewable biogas supplies enhance the country's energy security, promoting industrial development and economic growth (Target 9.5 *Enhance scientific research and upgrade industrial sectors' technological capabilities*).

Social Related SDG

The usage of H_2 and CH_4 for power generation improves the country's energy security. Improving the water-energy-food nexus is linked to socioeconomic development, facilitating SDG 1 "*No Poverty*" through improving public utilities, education, health, and employment opportunities (Target 1.2 *Reduce poverty*). Access to low-cost energy sources enables collaboration among stakeholders (community, policymakers, and investors) to create projects/developments. Such projects increase community awareness on global issues related to environmental sustainability (Ansari et al. 2021) and related actions to engage for a collective solution (Target 17.16 *Multi-stakeholder partnerships*). Industrialization creates job opportunities for young men and women in the region (Target 8.3 *Job creation*, Target 10.1 *Income growth*). More importantly, women should be encouraged to participate effectively in various project activities relevant to the "waste-to-energy" concept (Target 5.5 *Women in decision making*).

11.4 Conclusion

The following recommendation can be made based on the study: the effect of nutrients (nitrogen and phosphorus) composition in petrochemical wastewater (PCW) and influence of domestic wastewater (DWW) to the microbial consortium activity and growth should be investigated. The study should be carried out for a longer incubation time to investigate terephthalate decomposition and resultant CH_4 productivity.

In conclusion, this study revealed that adding DWW to PCW improved the methanogenic activity in an anaerobic co-digestion process. Among various co-substrate ratios, PCW: DWW of 1:1 enhanced the bio-CH_4 yield to 281.55 mL/$gCOD_{removed}$, compared to the application of solely PCW. The addition of DWW could have the advantages of diluting the organic load, adapting the C/N ratio, and forming a buffer medium to avoid pH drop from VFA accumulation. The study outcomes were highly linked to the three pillars of sustainability, regarding pollution reduction (environmental goal), bioenergy supply (economic goal), and job creation (social goal). Accordingly, the current study provides essential knowledge to stakeholders (community, policymakers, and investors) for creating projects applicable to the "waste-to-energy" strategy.

Acknowledgements The first author is very grateful to the TICAD7, the cooperation of the Egyptian government and the Japanese government, for providing financial support in the form of an M.Sc. scholarship. Also, thanks to JICA-Japan International Cooperation Agency for providing all facilities and equipment to accomplish this study.

References

Angelidaki I, Alves M, Bolzonella D, Borzacconi L, Campos JL, Guwy AJ, Kalyuzhnyi S, Jenicek P, Van Lier JB (2009) Defining the biomethane potential (BMP) of solid organic wastes and energy crops: a proposed protocol for batch assays. Water Sci Technol 59:927–934

Ansari FA, Nasr M, Rawat I, Bux F (2021) Meeting sustainable development goals (SDGs) through progression of pilot-scale algal system to commercial raceway pond (300,000 L). Biomass Convers Biorefinery

APHA (2017) Standard methods: for the examination of water and wastewater. American Public Health Association

Bhatt AH, Tao L (2020) Economic perspectives of biogas production via anaerobic digestion. Bioengineering

Dada O, Mbohwa C (2018) Energy from waste: a possible way of meeting goal 7 of the sustainable development goals. Mater Today Proc 5:10577–10584

Ezz H, Ibrahim MG, Fujii M, Nasr M (2021) Dual biogas and biochar production from rice straw biomass: a techno-economic and sustainable development approach. Biomass Convers Biorefinery

Giannetti BF, Agostinho F, Eras JJC, Yang Z, Almeida CMVB (2020) Cleaner production for achieving the sustainable development goals. J Clean Prod 271:122127

Gunarathne ADN, Lee K (2019) Environmental and managerial information for cleaner production strategies: an environmental management development perspective. J Clean Prod 237:117849

Kleerebezem R, Mortier J, Pol LWH, Lettinga G (1997) Anaerobic pre-treatment of petrochemical effluents: terephthalic acid wastewater

Li X, Ma K, Meng L, Zhang J, Wang K (2014) Performance and microbial community profiles in an anaerobic reactor treating with simulated PTA wastewater: from mesophilic to thermophilic temperature. Water Res 61:57–66

Ma X, Li X, Wang X, Liu G, Zuo J, Wang S, Wang K (2020) Impact of salinity on anaerobic microbial community structure in high organic loading puri fi ed terephthalic acid wastewater treatment system. J Hazard Mater 383:121132

Macarie H, Noyola A, Guyot JP (1992) Anaerobic treatment of a petrochemical wastewater from a terephthalic acid plant. Water Sci Technol 25:223–235

Nasr M, Tawfik A, Awad HM, Galal A, El-qelish M, Abdul M, Mumtaz M, Khan A, Rehan M, Nizami A, Lee M (2021) Dual production of hydrogen and biochar from industrial effluent containing phenolic compounds. Fuel 301:121087

Rodin V, Lindorfer J, Böhm H, Vieira L (2020) Assessing the potential of carbon dioxide valorisation in Europe with focus on biogenic CO_2. J CO_2 Util 41:101219

Shah FA, Mahmood Q, Rashid N, Pervez A, Raja IA, Shah MM (2015) Co-digestion, pretreatment and digester design for enhanced methanogenesis. Renew Sustain Energy Rev 42:627–642

Siddique MNI, Munaim MSA, Zularisam AW (2014) Mesophilic and thermophilic biomethane production by co-digesting pretreated petrochemical wastewater with beef and dairy cattle manure. J Ind Eng Chem 20:331–337

Siddique MNI, Zaied BK, Kabir MN, Ahmad MF (2019) Progressive two-stage efficient codigestion of food waste and petrochemical wastewater for higher methane and hydrogen production. ASIAN J Chem 31:2575–2578

Tan Y, Zheng C, Cai T, Niu C, Wang S, Pan Y, Lu X (2020) Anaerobic bioconversion of petrochemical wastewater to biomethane in a semi-continuous bioreactor: biodegradability, mineralization behaviors and methane productivity. Bioresour Technol 304:123005

Tawfik A, Ali M, Danial A, Zhao S, Meng F, Nasr M (2021) 2-biofuels (H_2 and CH_4) production from anaerobic digestion of biscuits wastewater: experimental study and techno-economic analysis. J Water Process Eng 39:101736

United Nations (2019) The sustainable development goals report

Wang X, Yang G, Feng Y, Ren G, Han X (2012) Optimizing feeding composition and carbon–nitrogen ratios for improved methane yield during anaerobic co-digestion of dairy, chicken manure and wheat straw. Bioresour Technol 120:78–83

Chapter 12
Coagulation/Flocculation Treatment of Carwash Wastewater Using Natural-Based Material: A Sustainable Development Approach

Derrick Dadebo, Mahmoud Nasr, Manabu Fujii, and Mona G. Ibrahim

Abstract Automobile service stations discharge large quantities of wastewater the contains various organic and inorganic pollutants, causing severe impacts on human health. Hence, experimental work was conducted to treat carwash wastewater (CWW) using the coagulation-flocculation (C/F) process based on a naturally synthesized material, namely *Cicer arietinum* (CA). A standard jar test method supported by a central composite design (CCD) statistical approach was employed to investigate the effects of experimental factors on the removal efficiencies of turbidity and chemical oxygen demand (COD). The optimal process factors were pH of 4, rapid stirring speed of 180 rpm, and coagulant dosage of 1 g/L, achieving turbidity and COD removal efficiencies of 87.3 and 71.3%, respectively. Quadratic regression models were established to predict the removal efficiencies of turbidity and COD with the coefficient of determination (R^2 values) of 0.983 and 0.974, respectively. As supported by the response surface methodology (RSM), the predicted removal efficiencies were 89.7% for turbidity and 68.1% for COD. Based on the experimental data and literature investigation, the application of natural-based coagulants for the treatment of CWW could be eco-friendly and low-cost compared to several inorganic chemical coagulants. The outputs were connected to various social, economic and environmentally-related sustainable development goals (SDGs), suggesting high possibility of scaling up the C/F treatment for real CWW projects.

D. Dadebo (✉) · M. Nasr · M. G. Ibrahim
Environmental Engineering Department, Egypt-Japan University of Science and Technology (E-JUST), New Borg El-Arab City, Alexandria 21934, Egypt
e-mail: derrick.dadebo@ejust.edu.eg

M. Nasr
Sanitary Engineering Department, Faculty of Engineering, Alexandria University, Alexandria 21544, Egypt

M. Fujii
Department of Civil and Environmental Engineering, Tokyo Institute of Technology, Meguro-ku, Tokyo 152-8552, Japan

M. G. Ibrahim
Environmental Health Department, High Institute of Public Health, Alexandria University, Alexandria 21544, Egypt

H.-Y. Jeon (ed.), *Sustainable Development of Water and Environment*,
Environmental Science and Engineering,
https://doi.org/10.1007/978-3-031-07500-1_12

Keywords Carwash effluent · *Cicer arietinum* coagulant · Jar test · Response surface methodology (RSM) · Sustainable development goals (SDGs)

12.1 Introduction

Carwash wastewater (CWW) refers to the effluents of automobile washing services operated either manually or by automation. About 150–1400 L of wastewater is generated per carwash activity, depending on the vehicle size and washing method (Monney et al. 2020). Nevertheless, at least 10 m^3 of water is discharged daily from an automobile washing station (Zaneti et al. 2011). Wastewater discharged from the vehicle cleaning centers encompasses several pollutants, including oil & grease, surfactants, phosphates, organic matter, sand, and dust (Al-Gheethi et al. 2016). Further, these pollutants and associated impurities transfer with domestic wastewater in sewer infrastructure to reach the treatment facilities; or, in some cases, disposed of into waterways without proper treatment. The CWW input imposes significant adverse effects on water bodies, aquatic species, and human health once directly discharged with inappropriate treatment (Rai et al. 2020). To mitigate these human health impacts and environmental risks, appropriate treatment of CWW should be comprehensively investigated, highlighting the environmental sustainability practices.

The coagulation/flocculation (C/F) technique has recently received substantial attention towards CWW treatment and other wastewater sources containing unacceptable concentrations of oil & grease and surfactants. The C/F technique has proved effective in eliminating solids, chemical oxygen demand (COD), and turbidity from CWW (Monney et al. 2019). Although conventional chemical coagulants have shown efficient results in CWW treatment, they generate a large amount of toxic sludge, which forms secondary pollution in the environmental matrix (Veit et al. 2020). Hence, the application of natural-based material seems an eco-friendly alternative to the chemical supplements in CWW treatment by the C/F process (Veit et al. 2020). Recently, natural-based coagulants have been used in the C/F treatment of CWW (Al-Gheethi et al. 2016; Mohamed et al. 2014). *Cicer arietinum* (CA) seed powder contains protein substances that make it a potential candidate for application as a coagulant in wastewater treatment by C/F (Choong Lek et al. 2018).

Several process factors influence the treatment performance of CWW by the C/F technique. Response surface methodology (RSM) has a high ability to demonstrate the relationship between these input attributes and treatment performance. The RSM tool entails statistical and mathematical procedures to develop models, optimize processes, and evaluate the significant inputs (Adesina et al. 2019). Compared to the conventional one-factor-at-a-time (OFAT) approach, central composite design (CCD) integrated with RSM represents a reliable method to address the complex inputs/output interactions (Choong Lek et al. 2018).

Recently, several studies have been reported to treat wastewater coming from car cleaning stations and centers (Zaneti et al. 2011; Veit et al. 2020). However,

the benefits of CWW treatment in relation to the achievable sustainable development goals (SDGs) are still lacking in the literature. These SDGs comprise seventeen goals with 169 targets to balance sustainability's economic, social, and environmental dimensions (United Nations 2021). Because CWW treatment tends to protect the environment and human health, it could maintain the "2030 Agenda" for sustainable development. The interlinkages between the research outputs and SDGs have been previously verified (Ansari et al. 2021; Nasr et al. 2021). Hence, this is an essential study on meeting several SDGs via reducing the pollution associated with CWW. The study objectives are fourfold (i) prepare a natural-based coagulant for treating CWW, (ii) investigate the effects of several process factors on CWW treatment via CCD statistics, (iii) optimize the operational factors to improve the CWW treatment performance, and (iv) generate an interlinkage between study outputs and achievable SDGs. In this investigation, COD was chosen as the main treatment performance because it has been extensively adopted for wastewater monitoring, design, modeling, and operational analysis.

12.2 Materials and Methods

12.2.1 Preparation of Natural-Based Coagulant

Cicer arietinum (CA) seeds were purchased from a local commercial market in Borg El-Arab, Alexandria, Egypt. The plant beans were washed with distilled water and then dried in an oven at 100 °C for 24 h. The seeds were then grinded and sieved through a 425-μm-pore size sieve to prepare a fine powder material.

12.2.2 Preparation of Synthetic Carwash Effluent

Synthetic waster was prepared by adding 224.5 μL of commercial automotive diesel oil (Exxon Mobil, Egypt), 250 mL of 1 g/L sodium dodecyl sulfate, and 200 mL of kaolin suspension (10 g/L) to 500 mL of distilled water in a 1000 mL volumetric flask and after topped up. The resulting aqueous solution was then mixed using a magnetic stirrer at a rate of 500 rpm for 60 min. The COD, turbidity, oil and grease, and surfactants content of the synthetic CWW was 406 mg/L, 940 NTU, 200 and 250 mg/L respectively.

12.2.3 Coagulation-Flocculation (Jar Test) Experiment

The C/F process for treating CWW was performed using a jar test apparatus (Fig. 12.1). The experimentation assays were performed using six 1000 mL beakers with six rotating paddle stirrers (VELP Scientifica JLT 6). A 500 mL of CWW was poured in a 1000 mL beaker per experimental run. The pH values of CWW were recorded before running experiments and adjusted to the desired value using 1 M NaOH and 1 M HCl solution. After coagulant addition, wastewater was agitated faster at 86–254 rpm for 5 min to provide coagulation followed by agitation at 30 rpm for 30 min to provide flocculation. Subsequently, flocs were left to settle. After 3 h' settlement time, the samples from each beaker were withdrawn for subsequent turbidity and COD content analysis. The removal efficiencies of pollutants were calculated by Eq. (12.1).

$$Removal(\%) = \left(1 - \frac{C}{C_0}\right) \times 100 \tag{12.1}$$

where C_0 and C are the concentration values of the parameter before and after treatment, respectively (in mg/L).

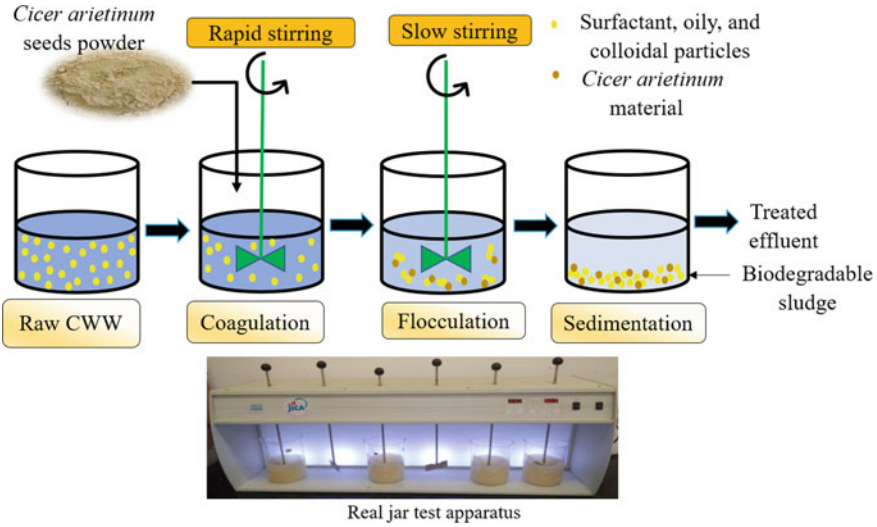

Fig. 12.1 Schematic diagram of jar test to estimate the coagulation/flocculation treatment of carwash wastewater

Table 12.1 Experimental input variables and their coded levels in CCD statistics to optimize the C/F process for CWW treatment

Independent variable	Symbol	Levels of coded variables				
		−1.68 (−α)	−1	0	+1	+1.68 (+α)
pH	A	2.6	4	6	8	9.4
Rapid stirring speed (rpm)	B	86	120	170	220	254
Coagulant dosage (g/L)	C	0.25	1	2.1	3.2	3.95

12.2.4 Design of Experiment

The CCD was used as a reliable statistical approach to optimize the C/F process variables for CWW treatment. Three independent factors, i.e., pH (A), rapid stirring speed (B, rpm), and coagulant dosage (C, g/L), were selected as the model inputs. Table 12.1 lists the coded factors used in the CCD experimental design. The treatment performance was expressed in terms of the elimination efficiencies of turbidity and COD. A total of 20 experimental runs (8 factorial points, 6 axial points, and 6 center points) were generated using CCD in Design-Expert software version 13.0.1.0 (Stat-Ease Inc., Minneapolis, MN 55413, USA).

12.2.5 Statistical Analysis

The CCD input/output experimental variables were employed to generate quadratic curves using the second-degree polynomial equation Eq. (12.2) (Subramonian et al. 2015).

$$Y_r = \beta_o + \sum_{i=1}^{k} \beta_i X_i + \sum_{i=1}^{k} \beta_{ii} X_i^2 + \sum_{i<j}^{k} \beta_{ij} X_i X_j \tag{12.2}$$

where Y_r is the required response (removal of turbidity (%) and COD (%)); β_0 is a constant; β_i, β_{ii}, along with β_{ij} represent the linear, quadratic, and interactive ramification coefficients respectively; k the independent variables optimized in the experiments; X_i and X_j the variable parameters of the C/F operation.

Process factors (A, B, and C) were optimized to maximize turbidity and COD removal efficiencies. To evaluate the significance of a regression model and study of interaction amongst process variables, analysis of variance (ANOVA) and the *F*-test were conducted in the Design-Expert 13 software at a 95% confidence interval.

12.3 Results and Discussion

12.3.1 Regression Model Development and Optimization of C/F Process

The quadratic models used to maximize the C/F treatment of CWW with COD and turbidity removal (%) as responses, expressed as coded factors are depicted by Eqs. (12.3) and (12.4).

$$\text{Turbidity removal}(\%) = 88.07 - 3.82A - 0.66B + 0.42C - 0.67AB - 0.03AC - 0.12BC - 1.31A^2 - 2.35B^2 - 0.36C^2 \quad (12.3)$$

$$\text{COD removal}(\%) = 54.62 - 5.04A - 0.74B - 10.59C - 0.74AB - 2.65AC - 1.54BC + 1.77A^2 - 1.95B^2 - 1.50C^2 \quad (12.4)$$

The relationship between input factors and responses was analyzed by ANOVA. *P*-values and Fisher's F-test determined the statistically significant factors. The results of ANOVA statistics were given in Table 12.2. The F values of 62.38 and 42.35 for the turbidity and COD removal efficiencies, respectively (*P*-values < 0.0001), signify that the predicted models were statistically substantial. The model terms of A, B, AB, A^2, and B^2 regarding turbidity removal were significant (*P*-value < 0.05), while A, C, AC, A^2, B^2, and C^2 were significant (*P*-value < 0.05) model terms for COD removal. Both models' linear and quadratic coefficients were negative except β_3 (turbidity model) and β_{11} (COD model). These results indicate that the impact of pH and CA dosage on the COD elimination efficiency was quadratic-linear concave down, while the influence of stirring speed was quadratic concave.

The lack-of-fit test appraises data variation about the fitted regression model (Subramonian et al. 2015). Lower *F*-values for "Lack of Fit" of 2.21 and 2.54 for the turbidity and COD removal models, respectively, as well as *P*-values >0.05 (Table 12.2), signify that the lack-of-fit is insignificant contrasted to the pure error. The R^2 and R^2_{adj} values were 0.983 and 0.967 for turbidity removal (%) and 0.974 and 0.954 for COD removal (%). For the best fit of any developed regression model, R^2 should be at least 0.80 (Adesina et al. 2019). High R^2 values indicate that both quadratic models for COD and turbidity removals satisfactorily fit the experimental data. These findings reveal the potential of the developed models to predict the responses (turbidity and COD removals) with adequate accuracy. The optimal values of pH, rapid stirring speed, and coagulant dosage that maximize turbidity and COD eliminations from CWW as per this study are given in Table 12.3. The elimination efficiencies (%) for this present study were satisfactory comparable with those of alum (Mohamed et al. 2014) and ferrous sulfate (Al-Gheethi et al. 2016).

Table 12.2 Statistical analysis results of the regression models for CWW pollutant elimination (%)

Source	Turbidity removal (%) model			COD removal (%) model		
	Coefficient (β)	F-value	*P*-value	Coefficient (β)	F-value	*P*-value
Model		62.38	< 0.0001*		42.35	<0.0001*
A	β_1: -3.82	364.73	< 0.0001*	β_1: -5.04	62.99	<0.0001*
B	β_2: -0.66	10.83	0.0081*	β_2: -0.74	1.34	0.2737
C	β_3: 0.42	4.35	0.0636	β_3: -10.59	276.35	<0.0001*
AB	β_{12}: -0.67	6.58	0.0282*	β_{12}: -0.74	0.7853	0.3963
AC	β_{13}: -0.03	0.0102	0.9214	β_{13}: -2.65	10.08	0.0099*
BC	β_{23}: -0.12	0.1924	0.6703	β_{23}: -1.54	3.41	0.0946
A^2	β_{11}: -1.31	46.29	< 0.0001*	β_{11}: 1.77	8.36	0.0161*
B^2	β_{22}: -2.35	143.40	< 0.0001*	β_{22}: -1.95	9.79	0.0107*
C^2	β_{33}: -0.36	3.41	0.0944	β_{33}: -1.50	5.86	0.0360*
Lack of fit		2.21	0.2028		2.54	0.1651

* Statistically significant about 95% confidence interval ($p < 0.05$)

Table 12.3 Validation of experimental results for optimum conditions

Response	pH	Rapid stirring speed (rpm)	Coagulant dosage (g/L)	Predicted value (%)	Experimental value (%)	Error (%)
Turbidity	4	180	1	89.7	87.3	2.4
COD	4	180	1	68.1	71.3	3.2

12.3.2 Effect of Process Parameters

CA dosage: Figure 12.2b, c, e, f depicts the impact of CA dosage on turbidity and COD removal (%) by the C/F process. Although turbidity removal enhanced with dosage, a subsequent increase in dosage from 1 to 3.2 g/L showed no substantial improvement in turbidity removals ($P > 0.05$). The COD removal declined with a rise in dosage from 1 to 3.2 g/L, signifying that the unoptimized biocoagulant dosage had a negative consequence towards COD removal from CWW. Protein(s) in CA seeds powder consisting of the amine functional group acts as a cationic polyelectrolyte that binds to the negatively charged pollutant particles in CWW to form larger flocs that consequently reduce turbidity (Putra et al. 2020).

pH: In the C/F treatment, pH illustrates a critical role in achieving appropriate treatment performance. Figure 12.2a, b, d, e depicts the three-dimensional surface plot regarding the effect of pH on the COD and turbidity removal efficiencies. The C/F process showed a better coagulation activity under acidic conditions (pH 3–5). The possibility for higher performance of the biocoagulant under acidic conditions could be attributed to the reinforced electrostatic attraction between the CA cationic

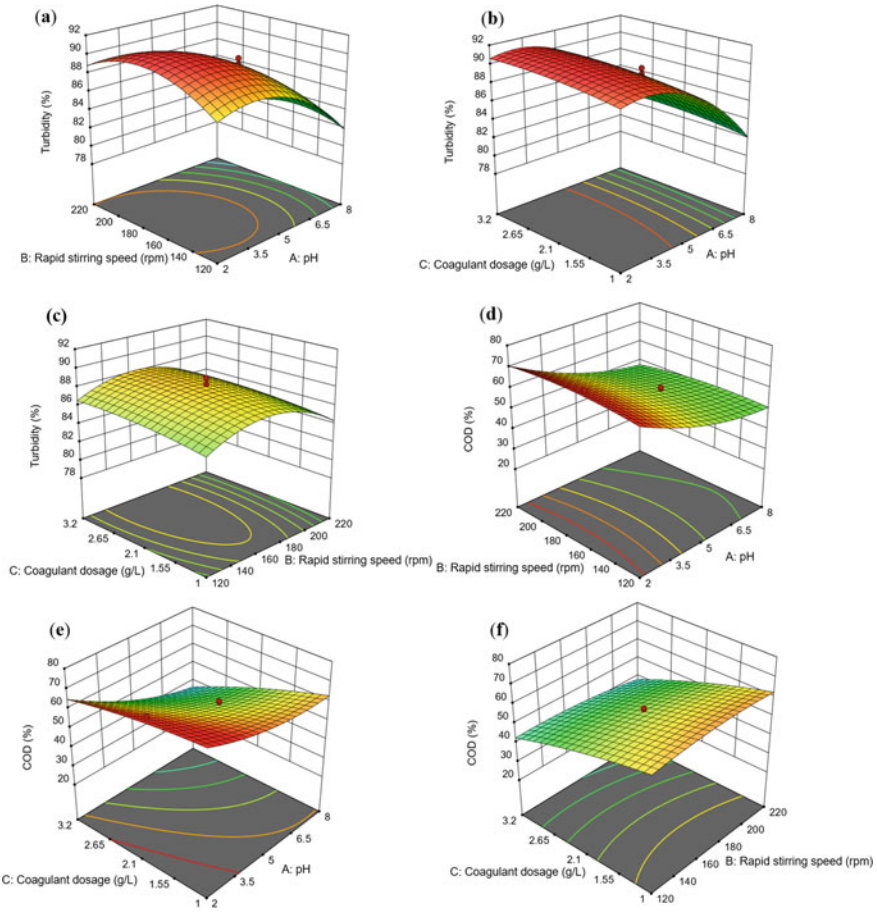

Fig. 12.2 Response surface plots for turbidity elimination (%) in terms of **a** rapid stirring speed and pH; **b** coagulant dosage and pH; **c** coagulant dosage and rapid stirring speed; COD elimination (%) in terms of **d** rapid stirring speed and pH; **e** coagulant dosage and pH; **f** coagulant dosage and rapid stirring speed

polymeric chains and the negatively charged CWW colloidal particles (Putra et al. 2242).

Rapid stirring speed: The variation of rapid stirring speed with turbidity and COD removal (%) is delineated in Fig. 12.2a, c, d, f. The turbidity reduction efficiency declined as the stirring speed was elevated from 180 to 220 rpm. However, the variation of stirring speed from 120 to 220 rpm did not substantially influence COD removal efficiency ($P > 0.05$). Speeds beyond 200 rpm are considered excessive, and they could be associated with the turbulent drag of the polymeric protein chains and colloidal particles in CWW.

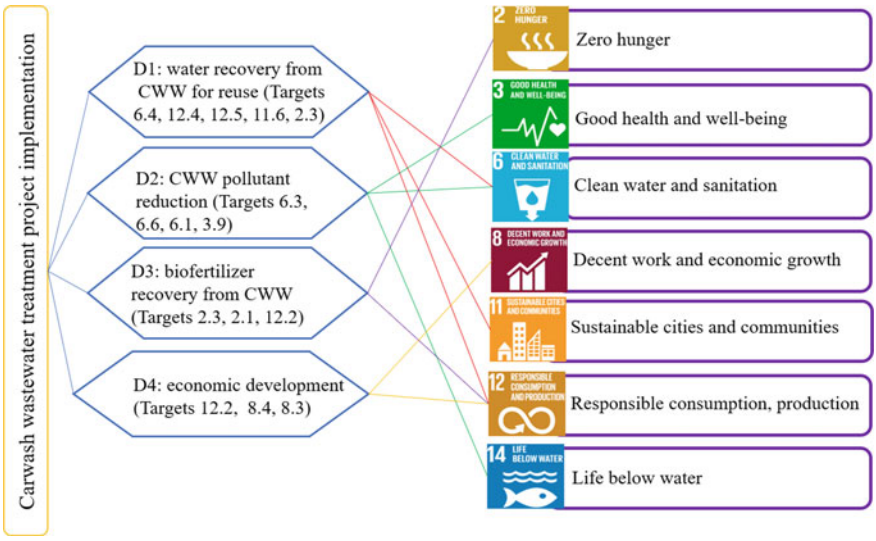

Fig. 12.3 Linkages between attributes of CWW treatment and sustainable development goals (SDGs)

12.3.3 SDGs Associated with Carwash Wastewater Treatment

The attributes associated with the implementation of CWW treatment projects in any economy can be allied to multiple SDGs. Based on the environmental, economic, and social attributes of the CWW treatment projects, four domains relevant to SDGs could be identified (Fig. 12.3).

D1 (water recovery for reuse): CWW treatment by C/F has been considered an efficient strategy to produce reclaimed water that meets the reuse guidelines (Veit et al. 2020). This advantage would reduce withdrawals from rivers, lakes, and groundwater sources to avoid further freshwater scarcity (Target 6.6. Protection and restoration of aquatic ecosystems). Recycling water into the onsite systems may be applicable in the main stages of vehicle washing (Zaneti et al. 2011) to improve annual water savings (Target 6.4. Increased water-use efficiency). The recycling of CWW for onsite reuse (Target 12.4. Environmentally sound management of waste, and Target 12.5. Reduced waste generation) would safeguard towns and cities near carwash bays from environmental impacts associated with carwash activities (Target 11.6. Reduce environmental impact in cities).

D2 (CWW pollutant reduction): In addition to the current study objectives, many researchers have treated CWW to meet the surface water discharge standards. The reduction of CWW pollutant load before discharge protects fresh watercourses from contamination (Target 6.3. Improve water quality) and restores water-related ecosystems (Target 6.6). Consequently, this benefit increases access to clean water (Target 6.1. Universal access to safe water) from surface water bodies (Target 3.9.

Reduce deaths and illnesses from pollution). CWW remediation prior to its discharge into the sea would preserve the coastal and marine ecosystems and biodiversity (Target 14.1. Reduce marine pollution).

D3 (biofertilizer recovery from CWW): Sludge from CWW treatment has elements that make it suitable as compost for soil amendment (Gonder et al. 2019). The addition of sludge to land as a compost would enhance plant growth, consequently increasing agricultural yield (Target 2.3. Double agricultural productivity). High productivity of agricultural lands promotes food security in the country; hence, hunger eradication (Target 2.1. End hunger) (Ezz et al. 2021). Sludge reuse for environmental applications promotes zero liquid discharge (ZLD) (Nasr et al. 2021) (Target 12.2. Sustainable and efficient use of natural resources).

D4 (economic development): CWW treatment investment projects are economically feasible with a payback period of less than a year (Zaneti et al. 2011). Onsite treatment and reuse are efficient ways to conserve freshwater resources (Target 12.2 and Target 8.4. Improvement in global resource efficiency towards consumption). With the burgeoning vehicle population globally, investment in CWW treatment and reuse projects is significant in relation to any country's economic growth and development (Target 10.1. Sustain income growth).

12.4 Conclusion

This study successfully revealed that *Cicer arietinum* (CA) seed powder was an efficient plant-based coagulant for treating carwash wastewater (CWW) by the coagulation/flocculation (C/F) technique. The central composite design (CCD) with response surface methodology (RSM) statistical tool appropriately represented the influence of pH, rapid stirring speed, and coagulant dosage on the C/F treatment performance. At the optimum operating conditions of pH 4, rapid stirring speed 180 rpm, and coagulant dosage 1 g/L, the removal efficiencies of turbidity and COD were 89.7 and 68.1%, respectively. The relative influence of experimental factors on COD removal was coagulant dosage > pH > rapid stirring speed. The predictive models for turbidity and COD elimination efficiencies provided R^2 values of 0.983 and 0.974, respectively; thus, confirming a statistical fit of quadratic regression models to experimental data. The optimum process factors retrieved from this study might thus be scaled up and adopted in the C/F treatment of wastewater from car washing operations. The study benefits were interlinked with SDGs regarding; water recovery for reuse, wastewater pollutant reduction, biofertilizer recovery, and economic development. Further research is needed to evaluate the techno-economic feasibility of using CA powder on real CWW treatment.

Acknowledgements The first author acknowledges the Seventh Tokyo International Conference on African Development (TICAD7) for the M.Sc. scholarship. Further, thanks to the Japan International Cooperation Agency (JICA) for providing equipment used in this research. Also, thanks to Egypt-Japan University of Science and Technology (E-JUST).

References

Adesina OA, Abdulkareem F, Yusuff AS, Lala M, Okewale A (2019) Response surface methodology approach to optimization of process parameter for coagulation process of surface water using Moringa oleifera seed. S Afr J Chem Eng 28:46–51

Al-Gheethi AA, Mohamed RMSRSR, Rahman MAAA, Johari MR, Kassim AHMM (2016) Treatment of wastewater from car washes using natural coagulation and filtration system. In: IOP conference series: materials science and engineering (vol 136, p 012046)

Ansari FA, Nasr M, Rawat I, Bux F (2021) Meeting sustainable development goals (SDGs) through progression of pilot-scale algal system to commercial raceway pond (300,000 L). Biomass Convers Biorefinery

Choong Lek BL, Peter AP, Qi Chong KH, Ragu P, Sethu V, Selvarajoo A, Arumugasamy SK (2018) Treatment of palm oil mill effluent (POME) using chickpea (Cicer arietinum) as a natural coagulant and flocculant: evaluation, process optimization and characterization of chickpea powder. J Environ Chem Eng 6:6243–6255

Ezz H, Ibrahim MG, Fujii M, Nasr M (2021) Dual biogas and biochar production from rice straw biomass: a techno-economic and sustainable development approach. Biomass Convers Biorefinery

Gonder B, Vergili I, Kaya Y, Gönder ZB, Balcıoğlu G, Kaya Y, Vergili I (2019) Treatment of carwash wastewater by electrocoagulation using Ti electrode: optimization of the operating parameters. Int J Environ Sci Technol 16:8041–8052

Mohamed R, Kutty N, Mariam AI, Kassim, Amir H, Radin M, Nadira M, Kutty I, Amir H (2014) Efficiency of using commercial and natural coagulants in treating car wash wastewater. Aust J Basic Appl Sci 8:227–234

Monney I, Buamah R, Donkor EA, Etuaful R, Nota HK, Ijzer H (2019) Treating waste with waste: the potential of synthesized alum from bauxite waste for treating car wash wastewater for reuse. Environ Sci Pollut Res 26:12755–12764

Monney I, Donkor EA, Buamah R (2020) Clean vehicles, polluted waters: empirical estimates of water consumption and pollution loads of the carwash industry. Heliyon 6:e03952

Nasr M, Tawfik A, Awad HM, Galal A, El-Qelish M, Abdul Qyyum M, Mumtaz Ali Khan M, Rehan M, Nizami AS, Lee M (2021) Dual production of hydrogen and biochar from industrial effluent containing phenolic compounds. Fuel 301:121087

Putra RS, Amri RY, Ayu M (2020) Turbidity removal of synthetic wastewater using biocoagulants based on protein and tannin. In: AIP conference proceedings, p 2242

Rai R, Sharma S, Gurung DB, Sitaula BK, Shah RDT (2020) Assessing the impacts of vehicle wash wastewater on surface water quality through physico-chemical and benthic macroinvertebrates analyses. Water Sci 34:39–49

Subramonian W, Wu TY, Chai SP (2015) An application of response surface methodology for optimizing coagulation process of raw industrial effluent using Cassia obtusifolia seed gum together with alum. Ind Crops Prod 70:107–115

United Nations (2021) Sustainable development goals: 17 goals to transform our world. https://www.un.org/sustainabledevelopment/. Accessed 15 Sept 2021

Veit MT, Novais ÍGV, Juchen PT, Palácio SM, da Gonçalves Gilberto C, Zanette JC (2020) Automotive wash effluent treatment using combined process of coagulation/flocculation/sedimentation–adsorption. Water Air Soil Pollut 231

Zaneti R, Etchepare R, Rubio J (2011) Car wash wastewater reclamation. Full-scale application and upcoming features. Resour Conserv Recycl 55:953–959

Chapter 13
Phytoremediation of Textile Wastewater Using Water Hyacinth (*Eichhornia Crassipes*): A Sustainable Development Approach

Gelasius Gregory Msemwa, Mahmoud Nasr, Manabu Fujii, and Mona G. Ibrahim

Abstract Textile industries release large amounts of wastewater containing various organic and inorganic pollutants. This waste should be appropriately treated before reaching the environment to avoid negative impacts on human health. The treatment process must be economically feasible, manageable, and environmentally friendly to meet the concept of sustainability. Hence, this study represents the application of water hyacinth (*Eichhornia crassipes*) for the phytoremediation of the textile effluents, reducing the concentrations of chemical oxygen demand (COD), ammonia nitrogen (NH_3-N), and color. Under the proposed phytoremediation system, the removal efficiencies of COD, NH_3-N, and Color reached up to 98.0, 91.7, and 85.7%, respectively, within 8 days. Quadratic regression models were proposed to demonstrate the influences of treatment duration (2–8 days) and textile wastewater fraction (0–1 v/v) on the phytoremediation process. The models' predictive accuracies were $R^2 = 0.952$; Adj-$R^2 = 0.935$ for COD removal, $R^2 = 0.904$; Adj-$R^2 = 0.869$ for NH_3-N removal, and $R^2 = 0.909$; Adj-$R^2 = 0.876$ for color removal. Based on the study outputs and literature observations, the phytoremediation of textile effluents could meet various sustainable development goals (SDGs) regarding clean and safe water, land protection, ecosystem and biodiversity conservation, climate action, industrialization improvement, and public awareness.

G. G. Msemwa (✉) · M. Nasr · M. G. Ibrahim
Environmental Engineering Department, Egypt-Japan University of Science and Technology (E-JUST), New Borg El-Arab City, Alexandria 21934, Egypt
e-mail: gelasius.gregory@ejust.edu.eg

M. Nasr
Sanitary Engineering Department, Faculty of Engineering, Alexandria University, Alexandria 21544, Egypt

M. Fujii
Department of Civil and Environmental Engineering, Tokyo Institute of Technology, Meguro-ku, Tokyo 152-8552, Japan

M. G. Ibrahim
Environmental Health Department, High Institute of Public Health, Alexandria University, Alexandria 21544, Egypt

H.-Y. Jeon (ed.), *Sustainable Development of Water and Environment*,
Environmental Science and Engineering,
https://doi.org/10.1007/978-3-031-07500-1_13

Keywords Hydroponic water hyacinth · Phytoremediation time · Regression models · Sustainable development · Textile industrial effluent

13.1 Introduction

Textile industries utilize large amounts of water in the bleaching, washing, drying, printing, and dyeing processes. Wastewater released from the textile and dyeing industries contains elevated synthetic dyes, acidic and alkaline reagents, resins, wax, heavy metal, salts, and residual chlorine (Watharkar et al. 2018). The recalcitrant textile compounds cause severe impacts on the environment and human health. Also, textile wastewater forms a floating layer on the water body surface that avoids sunlight penetration, negatively affecting photosynthetic activities (Ceretta et al. 2021). The presence of complex compounds with varying reactivity in the textile effluents can have toxicological properties (mainly mutagenesis and carcinogenesis) (Rather et al. 2018).

Textile wastewater tends to contaminate water bodies and soil matrices and may be further improved by the action of plant biomass. This process is known as phytoremediation, involving the application of plant species to stimulate, transfer, degrade, or stabilize the contaminants from the environment (Kumar and Deswal 2020). An extensive root system can facilitate detoxification, degradation, accumulation, and/or transformation of pollutants. In particular, water hyacinth has been recently employed in the phytoremediation process to efficiently treat different types of wastewater, owing to its fast growth and production of large biomass quantities under severe environments (Khandare et al. 2011).

Recently, the United Nations (UN) have initiated 17 sustainable development goals (SDGs) and 169 targets to maintain socio-economic growth and environmental protection (United Nations 2019). Because phytoremediation protects the environment from organic and inorganic pollutants, it could meet the SDGs relevant to human and aquatic ecosystem health. Moreover, plant biomass has several applications regarding bioenergy, animal feed, fertilization, and medicine preparation; hence, the economic-related SDGs could be demonstrated. Because phytoremediation is eco-friendly and aesthetically attractive, its application could maintain public acceptance to meet social-relevant SDGs.

Although extensive research has been conducted for the phytoremediation of textile wastewater, defining the associated three pillars of sustainability is still lacking. Hence, the current study objectives are fourfold (i) investigate the performance of water hyacinth (phytoremediation) to reduce COD, NH_3-N, and color (represented by methylene blue dye) in textile wastewater, (ii) develop regression models to predict the removal efficiencies based on phytoremediation time, and textile fraction, (iii) understand the research interest in the field of "Textile Wastewater Phytoremediation," suggesting the future scopes of studies, and (iv) find the interlinkage between the study objectives and three pillars of sustainability.

Table 13.1 Characteristics of textile wastewater used for phytoremediation experiment

Parameter	Real textile wastewater	Synthetic textile wastewater	Unit
COD	381–1548	430	mg/L
NH_3-N	5–100	50	mg/L
Color	100–800	391	Pt–Co

13.2 Materials and Methods

13.2.1 Water Hyacinth Preparation

Water hyacinth used for the phytoremediation process was collected from Lake Mariout in Alexandria (29°47.1′ to 29°50.4′ E Longitude and 31°7.5′ to 31°9′ N Latitude) and transferred to the laboratory. The plant was rinsed and washed with tap water followed by distilled water to remove any dirt attached to the biomass surface.

13.2.2 Textile Wastewater Preparation

The composition of textile wastewater used for phytoremediation experiment is given in Table 13.1.

13.2.3 Experimental Setup

A phytoremediation experiment was conducted as a hydroponic system in reactors. Each with a dimension of 40 cm (25 cm), the reactors were made of glass with three ports for sample collection (Fig. 13.1).

The phytoremediation performance of textile wastewater was determined regarding COD, NH_3-N, and color removal efficiencies. The investigated process factors were phytoremediation time (2, 4, 6, and 8 days) and textile wastewater to tap water fraction (R1: 0.5, R2: 0.75, and R3: 1 v/v). A control test (R0) was performed with only tap water.

13.2.4 Analytical Analysis

The chemical oxygen demand (COD) measurement was performed by a HACH calorimeter (digestion reactor DR900, USA) at 150 °C for 120 min. Ammoniacal nitrogen (NH_3-N) was analysed using the Nesslerization method (4500-NH_3),

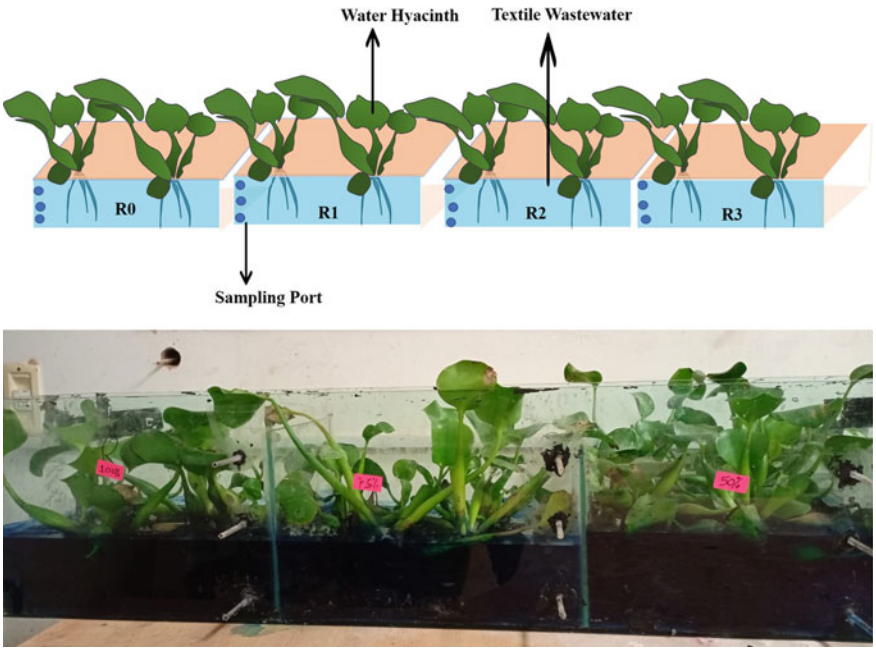

Fig. 13.1 Hydroponic apparatus used for phytoremediation of textile effluent **a** schematic diagram, and **b** real photo

following the procedures of APHA (American Public Health Association). The color was measured following the Platinum-Cobalt Standard Method 8025.

13.2.5 Statistical Analysis

In the form of Eq. (13.1), three quadratic regression models were employed to predict the removal efficiencies of COD, NH_3-N, and color. The model predictive accuracy was assessed using the coefficient of determination (R^2 value) and adjusted R^2 value. All statistical computations were performed using the MATLAB R2015b software and Microsoft Excel. The function of one-way analysis of variance (ANOVA) was used with the level of confidence set below 0.05 ($P < 0.05$).

$$y = \beta_0 + \beta_i(x_i) + \beta_{ii}(x_{ii})^2 \tag{13.1}$$

where y is the predicted removal, β_0 is the model intercept, β_i and β_{ii} are the coefficients related to the linear and quadratic forms of the inputs (x_i and x_{ii}), respectively.

13.3 Results and Discussion

13.3.1 Effect of Time and Textile Fraction on COD Removal

Figure 13.2 shows the effect of phytoremediation time on the removal efficiency of COD at different textile-to-tap water ratios of 0, 0.5, 0.75, and 1 v/v. The results indicated that the hydroponic system was able to achieve the highest COD removal efficiency of 97.96% for the control reactor (0 v/v) at 8 d. Increasing the textile-to-tap water ratio to 1% substantially reduced the COD removal efficiency to 69.77% ($P < 0.05$). Moreover, prolonging the phytoremediation time 0 to 8 d improved COD removal efficiency (Fig. 13.3). The COD reduction profile implied that the hydroponic system could remove organic pollutants from textile wastewater. Increasing the phytoremediation period provides a sufficient contact time for plant and associated micro-organisms to degrade and mineralize organic matters (Mahajan et al. 2019). It is suggested that during photosynthesis in plants, oxygen could be released to provide a suitable aerobic condition for the bacterial activity to reduce COD. Moreover, a high fraction of textile wastewater would negatively influence the phytoremediation performance due to inhibiting the plant and microbes activities (Safauldeen et al. 2019).

A regression model in Eq. 13.2 was developed to establish the linear and quadratic effects of time (d) (x_1) and textile wastewater fraction (v/v) (x_2) on the textile COD removal efficiency (%) (y) as a model response.

$$Y = 22.27 + 20.67(x_1) + 4.31(x_2) - 1.42(x_1)^2 - 32.46(x_2)^2 \quad (13.2)$$

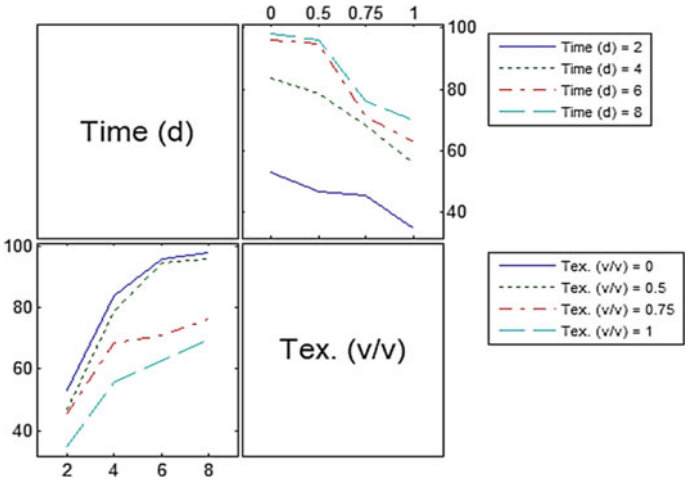

Fig. 13.2 Effect of time and textile fraction on COD removal efficiency for phytoremediation of textile wastewater

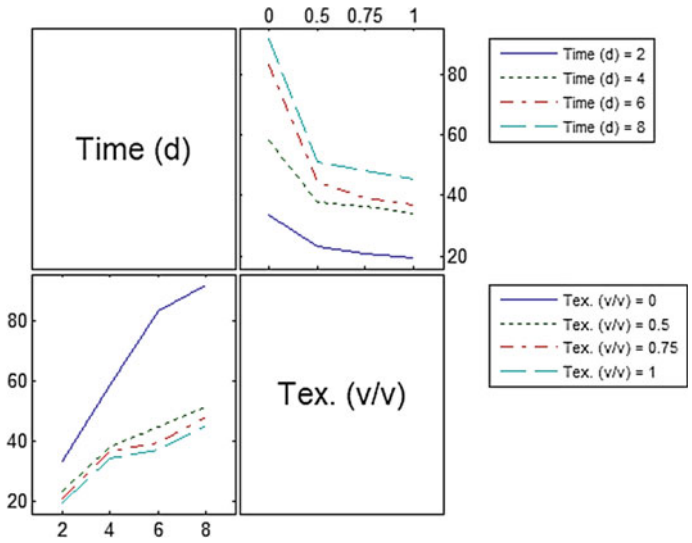

Fig. 13.3 Effect of time and textile fraction on NH_3-N removal efficiency for phytoremediation of textile wastewater

where, y is COD removal efficiency (%), x_1 is time (d), and x_2 is textile fraction (v/v).

The quadratic model developed to predict the COD removal efficiency was statistically significant, owing to the statistical analysis parameters (F-value: 54.8 and P-value < 0.05) (Kriti et al. 2021). The coefficient of determination (R^2) defines the variance of experimental data captured by the model (Kriti et al. 2021). A value of $R^2 > 0.80$ is considered satisfactorily to represent a good fit of the regression model for the phytoremediation experimental data (Kriti et al. 2021). A high Adj-R^2 of 0.935 (close to R^2) showed that the investigated input factors were vital in the phytoremediation of textile wastewater with water hyacinth.

Results of the statistical analysis (Table 13.2) showed that the linear coefficient of time (x_1) had a positive influence ($P < 0.05$) on COD removal. In contrast, the linear term of textile wastewater fraction (x_2) yielded insignificant COD removal efficiency. Moreover, the squared terms of time and textile fraction showed significant adverse effects ($P < 0.05$) on COD removal. The beta coefficients β_{11} and β_{22} of the quadratic term of x_1 and x_2 respectively were negative but statistically significant ($P < 0.05$), signifying that the plot of COD removal (%) versus each of time and textile fraction resulted in quadratic-linear concave up and purely concave curves, respectively.

Table 13.2 Statistical analysis of quadratic regression model for prediction of COD. R^2: 0.952, Adj-R^2: 0.935, SSE: 283, DF: 11, F-value: 54.8, P-value <0.01, and MSE: 25.8

Parameter	Beta	SE	t-stat	P-value	Plot shape	Significance
Constant	β_0: 22.27	7.40	3.01	0.012	–	Significant
x_1	β_1: 20.67	3.22	6.41	0.000	Linear	Significant
x_2	β_2: 4.31	11.57	0.37	0.717	Linear	Insignificant
$(x_1)^2$	β_{11}: −1.42	0.32	−4.48	0.001	Quadratic	Significant
$(x_2)^2$	β_{22}: −32.46	11.45	−2.83	0.016	Quadratic	Significant

13.3.2 *Effect of Time and Textile Fraction on NH_3-N Removal*

Results in Fig. 13.3 depict an increment in NH_3-N removal with prolonging the phytoremediation time. Also, elevating the pollution strength of wastewater by increasing the textile fraction reduced the plant performance to remove NH_3-N. Accordingly, the NH_3-N removal efficiency showed the best value of 91.67% with control (0 v/v) at 8 d. A satisfactory NH_3-N reduction could assign to the utilization of nitrogen as macronutrients for the plant's growth and development (Ezz et al. 2021). Also, the water hyacinth (and other aquatic plants) roots provide a suitable environment for aerobic bacteria to remove NH_3-N via nitrification. Aerobic bacteria would consume nutrients and produce inorganic compounds beneficial for plant metabolism. Accordingly, evaporation, nitrification, and plant uptake processes would be the probable removal mechanisms of NH_3-N in a phytoremediation system. However, increasing the textile fraction to 1 v/v reduced the NH_3-N removal efficiency to only 45.18%. Similarly, Apritama et al. (Apritama et al. 2020) found that at 100% textile effluent, the NH_3-N removal efficiency was unsatisfactory (71.25%) via *Pistia stratiotes* phytoremediation.

A regression model in Eq. (13.3) was developed to predict the NH_3-N removal efficiency by the water hyacinth plant using time and textile fraction as the input factors.

$$y = 26.35 + 11.54(x_1) - 73.09(x_2) - 0.59(x_1)^2 + 41.04(x_2)^2 \quad (13.3)$$

where y is NH_3-N removal efficiency (%), x_1 is time (d), and x_2 is the textile fraction (v/v).

The linear and quadratic impact of each input factor (time and textile fraction) on NH_3-N removal efficiency was determined by t-test. The results are summarized in Table 13.3. The linear and quadratic influence of textile fraction on NH_3-N removal was significant ($P < 0.05$). This trend implied that the plot of NH_3-N removal (%) versus textile fraction produced quadratic-linear convex down curves. Furthermore, the linear effect of time was statistically significant ($P < 0.05$), while its quadratic

Table 13.3 Statistical analysis of quadratic regression model for prediction of NH_3-N removal. R^2: 0.904, Adj-R^2: 0.869, SSE: 581, DF: 11, F-value: 25.8, P-value <0.01, and MSE: 52.8

Parameter	Beta	SE	t-stat	P-value	Plot shape	Significance
constant	β_0: 26.35	10.59	2.49	0.030		Significant
x_1	β_1: 11.54	4.61	2.50	0.029	Linear	Significant
x_2	β_2: −73.09	16.56	−4.41	0.001	Linear	Significant
$(x_1)^2$	β_{11}: −0.59	0.45	−1.29	0.224	Quadratic	Insignificant
$(x_2)^2$	β_{22}: 41.04	16.40	2.50	0.029	Quadratic	Significant

part was insignificant ($P > 0.05$). This result indicated that the plot of NH_3-N removal (%) against time caused linear up curves.

13.3.3 Effect of Time and Textile Fraction on Color Removal

The results in Fig. 13.4 show the removal efficiencies of color (represented by methylene blue, MB, dye) using water hyacinth (*Eichhornia crassipes*) in a hydroponic phytoremediation system. The percentage of color removal improved with increasing the phytoremediation time. In the phytoremediation systems, mechanisms such as adsorption and accumulation have been considered for dye removal. The adsorption of dye through phytoremediation could be supported by (i) the interaction between the functional groups on plant hairy roots and those of dye molecules, and/or (ii) the attraction force between negative charges on plant roots and cationic dye (MB) (Sharma et al. 2021). However, the phytoremediation performance declined at a textile fraction of 1 v/v, suggesting that the plant species could not tolerate long-term exposure to high concentrations of dye/color.

A quadratic model (Eq. 13.4) was used to describe the influence of the time (x_1) and a textile fraction (x_2) on the removal efficiency of color (y).

$$y = 62.26 + 1.92(x_1) - 35.37(x_2) + 0.03(x_1)^2 + 9.49(x_2)^2 \qquad (13.4)$$

where, y is color removal efficiency (%), x_1 is time (d), and x_2 is textile fraction (v/v).

Table 13.4 lists the observations obtained from the statistical analysis, with F-value = 27.4 and P-value < 0.01. The linear form of input "x_2" significantly affected color removal (P-value = 0.003). This correlation means an increase in textile fraction would significantly reduce the plant's ability to remove the color from textile effluents. Moreover, both linear and quadratic statistical forms associated with the input "x_1" were insignificant (P-value > 0.05). Therefore, the plot of color removal against phytoremediation time would result in a flat curve.

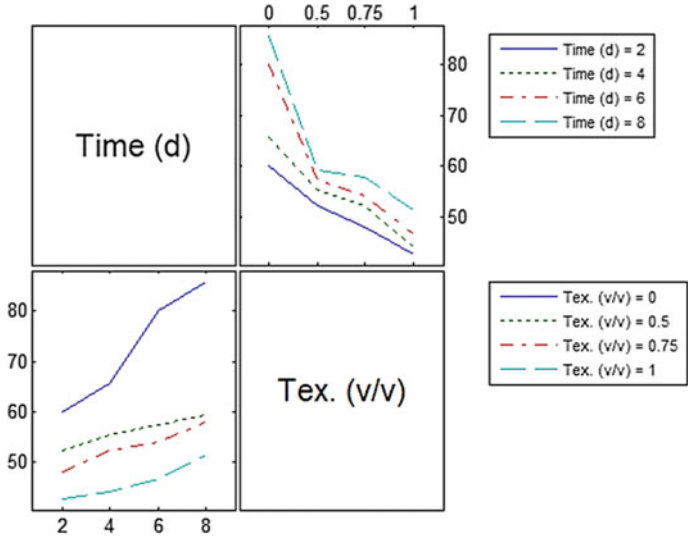

Fig. 13.4 Effect of time and textile fraction on color (methylene blue dye) removal for phytoremediation of textile wastewater

Table 13.4 Statistical analysis of quadratic regression model for prediction of color removal. R^2: 0.909, Adj-R^2: 0.876, SSE: 191, DF: 11, F-value: 27.4, P-value <0.01, and MSE: 17.4

Parameter	Beta	SE	t-stat	P-value	Plot shape	Significance
constant	β_0: 62.26	6.07	10.26	0.000		Significant
x_1	β_1: 1.92	2.65	0.73	0.483	Linear	Insignificant
x_2	β_2: −35.37	9.49	−3.73	0.003	Linear	Significant
$(x_1)^2$	β_{11}: 0.03	0.26	0.10	0.922	Quadratic	Insignificant
$(x_2)^2$	β_{22}: 9.49	9.40	1.01	0.335	Quadratic	Insignificant

13.3.4 Sustainable Development Goals (SDGs) Linked to Textile Wastewater Phytoremediation

Environmental-related SDGs. During phytoremediation, the plant species uptake, degrade, and/or accumulate various elements (e.g., heavy metals and nutrients) in polluted sites (*Target 6.6. Ecosystems and water*). The application of water hyacinth for treating textile wastewater is an essential strategy to protect the water resources by avoiding releasing water-containing chemicals that will protect both surface and groundwater (*Target 6.3 Improved water quality).* Saqr et al. (2021) reported that appropriate methods for water treatment should be adopted to avoid deterioration of groundwater quality. After tertiary treatment, the application of textile wastewater would enable the safe reuse of water and improve water-use efficiency and management (*Target 6.4 Enhance water use efficiency).* Releasing a large volume of untreated

textile wastewater into the environment could cause harm to different types of ecosystems and species of organisms (Velis et al. 2017). Hence, biological diversity would also be protected against pollution by reducing the release of untreated wastewater into the land (*Target 15.5 Protect biodiversity*). Moreover, previous researches have indicated that plant biomass can be harnessed to produce biochar (Ezz et al. 2021). These biochar products could be applied to farmlands, improving soil quality and boosting agriculture productivity (*Target 2.1 End hunger; Target 2.3 Double agricultural productivity*). The use of water hyacinth in fertilizer production has been noted to improve farmland quality (Silva et al. 2021). The efficiency of plants to uptake carbon dioxide (CO_2) for photosynthetic growth is essential for cleaning the atmosphere from industrial gases (*Target 13.2. Climate change policy*). The use of micro-organisms to sequester and fix CO_2 for photosynthetic growth is essential to clean the atmosphere from gaseous pollutants (Ansari et al. 2021). Several plant species could act as an indicator for climate change, hence providing an early warning regarding any anthropogenic and natural causes of climate change (*Target 13.3 Awareness and education on climate change*). Because phytoremediation does not utilize large amounts of chemicals in process operation, it is considered a clean and safe technology for wastewater treatment (*Target 9.4 Clean technologies*).

Economic-related SDGs. After appropriate treatment of textile wastewater, the treated effluent could be reused in the industrial sector, such as an alternative water source for dyeing and finishing processes. Some plants could be utilized as flavouring agents in foods and beverages and the perfume industry. This advantage would maintain the industrial sector to meet (*Target 9.2. Sustainable industrialization).* Because phytoremediation is a simple technology, it could be operated with skilled and unskilled labor, complying with (*Target 8.3. Job creation*).

Social-related SDGs. The existing connection between plant applications for wastewater treatment and SDGs should be included in the educational systems teaching environmental-related courses and topics. The education of these courses would be provided to both men and women (*4.1. Equitable education*). Increasing the use of water hyacinth in textile wastewater treatment would enhance public awareness towards the sustainable treatment of wastewater. People should be aware of the plant applications in wastewater treatment and the associated benefits (advantages to environment, health, and safety), meeting (*Target 13.3. Awareness of climate change*).

13.4 Conclusions

This study demonstrated the interlinkage between phytoremediation and sustainable development goals (SDGs) by treating textile wastewater with a hydroponic (water hyacinth) system. The highest removal efficiencies of COD, NH_3-N, and methylene blue (MB) dye were 97.96, 91.67, and 85.71% at the control test (with tap water), respectively. It is suggested that these parameters were reduced via phytodegradation for COD, uptake/assimilation for NH_3-N, and sorption for color. The use of textile

fraction = 1 v/v was associated with the drop of removal efficiencies to 69.77, 45.18, and 51.41%, respectively, probably due to biomass inhibition. The removal efficiencies of COD, NH_3-N, and MB dye were appropriately predicted using phytoremediation time and textile fraction as the model inputs (ANOVA statistical test: R^2 = 0.90–0.95). The study outputs could be relevant to the three pillars of sustainability; environmental (pollution reduction and biodiversity protection), economic (biomass-based industries), and social (public awareness towards phytoremediation technology).

Acknowledgements The first author acknowledges the Seventh Tokyo International Conference on African Development (TICAD7) for the M.Sc. scholarship. Further, thanks to the Japan International Cooperation Agency (JICA) for providing equipment used in this research. Also, thanks to Egypt-Japan University of Science and Technology (E-JUST).

References

Ansari FA, Nasr M, Rawat I, Bux F (2021) Meeting sustainable development goals (SDGs) through progression of pilot-scale algal system to commercial raceway pond (300,000 L). Biomass Convers Biorefinery

Apritama MR, Koko Suryawan IW, Afifah AS, Septiariva IY (2020) Phytoremediation of effluent textile wwtp for nh3-n and cu reduction using pistia stratiotes. Plant Arch 20:2384–2388

Ceretta MB, Nercessian D, Wolski EA (2021) Current trends on role of biological treatment in integrated treatment technologies of textile wastewater. Front Microbiol 12:1–7

Ezz H, Ibrahim MG, Fujii M, Nasr M (2021) Dual biogas and biochar production from rice straw biomass: a techno-economic and sustainable development approach. Biomass Convers Biorefinery

Khandare RV, Kabra AN, Kurade MB, Govindwar SP (2011) Phytoremediation potential of Portulaca grandiflora Hook. (Moss-Rose) in degrading a sulfonated diazo reactive dye Navy Blue HE2R (Reactive Blue 172). Bioresour Technol 102:6774–6777

Kriti Basant N, Singh J, Kumari B, Sinam G, Gautam A, Singh G, Swapnil Mishra K, Mallick S (2021) Nickel and cadmium phytoextraction efficiencies of vetiver and lemongrass grown on Ni–Cd battery waste contaminated soil: a comparative study of linear and nonlinear models. J Environ Manag 295:113144

Kumar S, Deswal S (2020) Phytoremediation capabilities of Salvinia molesta, water hyacinth, water lettuce, and duckweed to reduce phosphorus in rice mill wastewater. Int J Phytoremediation 22:1097–1109

Mahajan P, Kaushal J, Upmanyu A, Bhatti J (2019) Assessment of phytoremediation potential of Chara vulgaris to treat toxic pollutants of textile effluent

Rather LJ, Akhter S, Hassan QP (2018) Bioremediation: green and sustainable technology for textile effluent treatment. Springer Singapore

Safauldeen SH, Hasan HA, Abdullah SRS (2019) Phytoremediation efficiency of water hyacinth for batik textile effluent treatment. J Ecol Eng 20:177–187

Saqr AM, Ibrahim MG, Fujii M, Nasr M (2021) Sustainable development goals (SDGs) associated with groundwater over-exploitation vulnerability: geographic information system-based multi-criteria decision analysis. Nat Resour Res 30:4255–4276

Sharma R, Saini H, Paul DR, Chaudhary S, Nehra SP (2021) Removal of organic dyes from wastewater using *Eichhornia crassipes*: a potential phytoremediation option. 7116–7122

Silva IAA, de Macedo OFL, Cunha GC, Oliveira RVM, Romão LPC (2021) Using water hyacinth (*Eichhornia crassipes*) biomass and humic substances to produce urea-based multi-coated slow release fertilizer. Cellulose 28:3691–3701

Ugya AY, Hua X, Ma J (2019) Phytoremediation as a tool for the remediation of wastewater resulting from dyeing activities. Appl Ecol Environ Res 17:3723–3735

United Nations (2019) The sustainable development goals report 2019. United Nations Publ. issued by Dep. Econ. Soc. Aff. 64

Velis M, Conti KI, Biermann F (2017) Groundwater and human development: synergies and trade-offs within the context of the sustainable development goals. Sustain Sci 12:1007–1017

Watharkar AD, Kadam SK, Khandare RV, Kolekar PD, Jeon BH, Jadhav JP, Govindwar SP (2018) Asparagus densiflorus in a vertical subsurface flow phytoreactor for treatment of real textile effluent: a lab to land approach for in situ soil remediation. Ecotoxicol Environ Saf 161:70–77

Wickramasinghe S, Jayawardana CK (2018) Potential of aquatic macrophytes Eichhornia crassipes, Pistia stratiotes and Salvinia molesta in phytoremediation of textile wastewater. J Water Secur 4:1–8

Chapter 14
Synthesis of Carbonized Bagasse and Orange Peel Wastes as Adsorbents for Dye Removal from Aqueous Solution: A Sustainable Approach

Bwambale Roice Kalengyo, Mona G. Ibrahim, Manabu Fujii, and Mahmoud Nasr

Abstract Dyes and pigments are released into the environment through various industrial, domestic, and municipal pathways, causing ecological disturbances and serious environmental and health concerns. Although several studies have investigated the removal of the methylene blue (MB) dye from aqueous solutions, comprehensive studies are still required to understand the correlation between dye-based wastewater treatment and sustainable development. Hence, this study represents the preparation of adsorbent from natural material and zero-cost waste to eliminate MB from synthetic solutions, providing an ecofriendly treatment approach. Box Behnken statistical design was employed to find the effects of three process factors, i.e., time, adsorbent dosage and solution pH, on the MB removal efficiency. It was found that bagasse-based carbon (BBC) and orange peel (OP) powder had a high ability to adsorb MB with a removal efficiency of 86.4% under time = 15.4 min, dosage = 1.28 g/L, and pH = 7.63. A quadratic model was developed to predict the MB removal efficiency with a coefficient of determination (R^2) of 0.836 and adjusted R^2 of 0.737. The study outputs were highly correlated to ecosystem safety (e.g., pollution reduction), resource utilization (e.g., biosorbent preparation from natural substances), and industrialization (e.g., application of BBC and OP powder in the industrial sector).

B. R. Kalengyo (✉) · M. G. Ibrahim · M. Nasr
Environmental Engineering Department, Egypt-Japan University of Science and Technology (E-JUST), New Borg El-Arab City, Alexandria 21934, Egypt
e-mail: roice.bwambale@ejust.edu.eg

M. G. Ibrahim
Environmental Health Department, High Institute of Public Health, Alexandria University, Alexandria 21544, Egypt

M. Fujii
Department of Civil and Environmental Engineering, Tokyo Institute of Technology, Meguro-ku, Tokyo 152-8552, Japan

M. Nasr
Sanitary Engineering Department, Faculty of Engineering, Alexandria University, Alexandria 21544, Egypt

H.-Y. Jeon (ed.), *Sustainable Development of Water and Environment*,
Environmental Science and Engineering,
https://doi.org/10.1007/978-3-031-07500-1_14

Accordingly, the study outputs would meet multiple environmental, economic, and social related sustainable development goals (SDGs).

Keywords Textile dye adsorption · Response surface methodology · Sustainable treatment

14.1 Introduction

The synthetic dye manufacturing and textile industries, in addition to several commercial elements (e.g., plastic, clothes, and paper) utilize large amounts of dyes during production (Jawad et al. 2020). Wastewater released from these industries carries various dyes such as methylene blue (MB), azo dyes, and methyl orange recognized as the main pollution source (Cheng et al. 2021). The disposal of dyes-laden wastewater into the environment has been associated with severe impacts on aquatic culture, human health, and terrestrial animals (Gadow and Li 2020). An excessive discharge of dye effluents into water bodies significantly deteriorates the biological quality and characteristics of the ecosystems by increasing the biodegradable oxygen demand (BOD) levels (Georgin et al. 2019). Additionally, dyes, forming a colored top-layer on the water surface, tend to limit light penetration to marine phytoplankton; hence, inhibiting the photosynthetic activities (Jiang et al. 2021). Accordingly, the removal of dyes from textile effluents before reaching the aquatic and land environments is an essential point of research, requiring comprehensive studies.

Previous studies have shown the application of various physical, biological, and chemical-based treatment methods (or their combinations) for eliminating dyes from aqueous solutions (Moosavi et al. 2020). However, a sustainable treatment approach should provide significant advantages such as design simplicity, flexibility, cost-effectiveness, and insensitivity to toxic compounds, whilst avoiding the formation of secondary pollutants. These advantages fit well to the adsorption process, which entails multiple complexation and/or ionic exchange mechanisms to eliminate any anionic, cationic, or organic contaminants from aqueous solutions (Liu et al. 2020). Moreover, the "Sustainability" concept of wastewater treatment by adsorption should be linked to the utilization of adsorbent material prepared from chemical-free additives (Ajayi and Ogunbayio 2012). For instance, various non-living biomass-based material, such as sawdust, eggshell, seed shells, potato and citrus peels, sugarcane bagasse, and rice husk, have found successful applications for treating wastewater laden with dyes and heavy metals (Khaled et al. 2009). This adsorbent material would not cause substantial secondary pollution when discarded into the environment due to its ability to degrade within the soil matrix. Moreover, this adsorbent substance is prepared from almost zero-cost biomass, resulting in a cheap adsorption process towards contaminants removal. Accordingly, employing a wastewater treatment process based on natural adsorbents would meet various environmental, economic, and social related sustainable development goals (SDGs).

Recently, the United Nations (UN) has passed a number of goals to achieve the three pillars of sustainability by 2030 (Ajayi and Ogunbayio 2012). The SDGs cover several aspects relevant to pollution reduction, waste management, utilization of non-toxic substances (natural resources), human health protection, and public awareness towards sustainability (Sawaf and Karaca 2018). Accordingly, providing a highly effective and economical process for dye removal from wastewater effluents to clean up the polluted environment would meet multiple SDGs (Hamdy et al. 2017). However, there is a lack of studies to define the achievable SDGs associated with the removal of dyes from the environment by adsorption process.

Hence, this study attempts to represent a reliable and cost-efficient adsorption process for removing MB dye from aqueous solutions, highlighting the tangible SDGs achieved. The study objectives are fivefold (1) synthesize and prepare an environmentally friendly adsorbent from bagasse-based carbon (BBC) and orange peel (OP), (2) investigate the adsorption performance of the adsorbent material towards MB, (4) represent a predictive model for the MB removal efficiency using three process factors, i.e., adsorption time, adsorbent dosage, and solution pH, and (5) find the interlinkages between the study objectives and the three pillars of sustainability.

14.2 Methodology

14.2.1 Adsorbent Preparation

Fresh sugarcane bagasse (SB) was collected from a juice-service store located in Alexandria city, Egypt. The SB biomass was washed and rinsed with tap water, and the resultant clean material was cut into small pieces and dried overnight (100 °C for 24 h). Further, the product was inserted into a muffle furnace operated at 600 °C for 2 h to form bagasse-based carbon (BBC). The orange peels (OP) waste was obtained from a restaurant in Egypt-Japan University of Science and Technology. The raw OP waste was washed to remove any traces of sand particles and other dirt, dried in an oven at 100 °C for 24 h, and then ground by mechanical grinder. Further, the resultant peels were crushed to have a fine powder of 40#-mesh size according to ASTM (American Standards for Testing and Materials). Afterward, the two fine materials (BBC and OP) were mixed in a ratio of 1:1 and treated with NaOH to remove natural fats, waxes, silica, lignin, and hemicelluloses.

14.2.2 Methylene Blue (MB) Solution Preparation

The methylene blue (MB) cationic dye (molecular formula of C16H18N3SCl and molecular weight of 319.85 g/mol) purchased from Oxford Lab Fine Chemicals LLP was selected as a model contaminant in this study. An amount of 1.0 g MB was

Fig. 14.1 Schematic diagram for application of BBC: OP powder (adsorbent) to remove MB from aqueous solutions

dissolved in 1 L of distilled water to obtain a stock solution of 1000 ppm. The flask containing MB was placed on a magnetic stirrer for 2 h to establish a homogeneous dye aqueous solution. The absorbance of MB dye was detected at the wavelength of 664 using JASCO V-630 UV–Vis–NIR spectrophotometer.

14.2.3 Experimental Design for Adsorption of Methylene Blue Dye onto OP:BBC Biosorbent

A series of batch scale assays were performed in Erlenmeyer flasks (250 mL-capacity) to examine the performance of the adsorbent towards MB removal (Fig. 14.1). A total of 17 experimental runs, with five center points, were carried out based on Box-Behnken design (BBD). This batch experimentation was conducted to understand the correlation between MB removal efficiency with pH, time, and adsorbent dosage. Generation and evaluation of the experimental design was executed using MATLAB and Design Expert® (Stat-Ease Inc., Minnepolis) software (Tripathi et al. 2009). All experimentations were performed at the room temperature (about 25 °C).

14.3 Results and Discussion

14.3.1 Results of Box–Behnken Design for Optimizing MB Removal

Table 14.1 lists the removal efficiencies of MB under different adsorption conditions, i.e., time (A: 10–30 min), adsorbent dosage (B: 0.5–1.5 g/L), and medium pH (C: 5–9).The matrix of these three factors with three levels was prepared according to the Box–Behnken statistical design. The input–output relationship is further demonstrated by interaction plot (Fig. 14.2a) and main-effects-plot (Fig. 14.2b).

An increase in adsorption time from 10 to 20 min caused a slight improvement in the MB removal efficiency (around 80%), which dropped to about 76%, further

Table 14.1 Experimental runs proposed by BBD design to optimize the MB removal efficiency based on three process factors, namely; time, adsorbent dosage, and solution pH

Run	Time, A, (min)	Dosage, B, (g/L)	pH, C	MB removal (%)
1	20	1.0	7	86.00
2	20	1.5	5	78.12
3	20	1.0	7	85.06
4	30	1.0	9	82.00
5	20	1.5	9	80.00
6	20	1.0	7	84.17
7	20	1.0	7	83.73
8	30	0.5	7	73.00
9	10	0.5	7	79.91
10	30	1.5	7	82.10
11	30	1.0	5	66.85
12	10	1.5	7	83.00
13	20	1.0	7	84.91
14	20	0.5	5	67.00
15	10	1.0	9	78.39
16	20	0.5	9	77.84
17	10	1.0	5	78.00

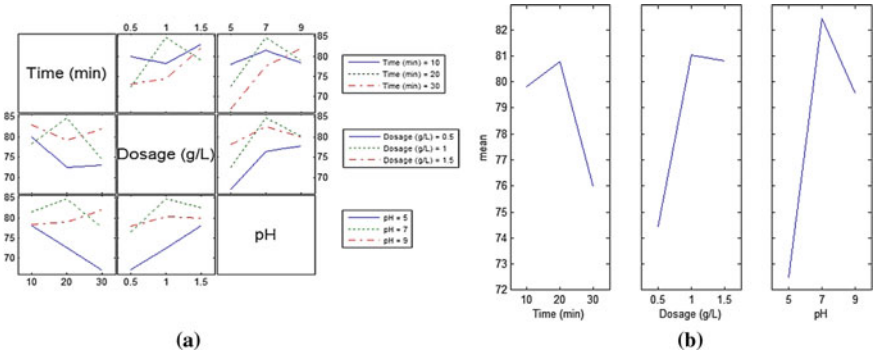

Fig. 14.2 **a** Interaction plot for the effects of three adsorption factors, i.e., time (min), adsorbent dosage (g/L), and solution pH, on the MB removal efficiencies statistical design **b** Mean values of MB removal efficiencies estimated at different time (min), adsorbent dosage (g/L), and solution pH proposed by the Box–Behnken

prolonging the time to 30 min. During the initial stage, this fast adsorption performance was possibly due to the available number of vacant sites to uptake more MB molecules. Further, the adsorption rate declined at time over 20 min. Moreover, increasing the adsorbent dosage over 1 g/L had insignificant ($p > 0.05$) impact on MB removal, probably due to the overlap of the pore structure of the BBC: OP powder adsorbent. This pattern would also reduce the effective surface area of adsorbent; hence, the adsorbent access for the cationic dye decreased. A better MB removal efficiency at pH of 7 suggests that the negatively charged sites formed a robust, attractive force with the positively charged MB molecules.

14.3.2 Quadratic Model Development for MB Removal Prediction

Table 14.2 summarizes the results of t-test used to predict MB removal using three adsorption inputs (time, adsorbent dosage, and solution pH). This test revealed an R2: 0.836, Adj-R2: 0.737, SSE: 87.774, DF: 10, F-value: 8.479, P-value < 0.01, and MSE: 8.777. The results of Table 14.2 also revealed that the input "A" had insignificant ($p > 0.05$) effects hence, the correlation between MB removal-time relationship was a "Flat" curve. Moreover, the plot of MB removal against dosage showed a "Linear Up" curve. The "C" input had significant ($p < 0.05$) effects for both the linear and quadratic effects. Hence, the plot of MB removal versus solution pH resulted in a "Quadratic concave Linear Up" curve (Tripathi et al. 2009).

An equation of the second-order polynomial model for MB dye removal was derived and described in Eq. (14.1). This quadratic model is significant (F-value: 8.479, P-value < 0.01) and could describe 83.6% of the MB removal efficiency data. A is Time (min), B is Dosage (g/L) and C is pH;

$$MB\,removal\,(\%) = -26.09 + 0.75A + 29.73B + 23.16C - 0.02(A)^2 - 11.68(B)^2 - 1.53(C)^2 \quad (14.1)$$

14.3.3 Optimization of Adsorption Factors

Figure 14.4 shows the optimum values for the three inputs, representing time = 15.4 min, adsorbent dosage = 1.28 g/L, and solution pH = 7.63. Under this condition, the highest removal efficiency of the MB dye was 86.53%. This value was confirmed and validated with an experimental efficiency value of 86.4%, hence a reliable model (Vyavahare et al. 2018) (Fig. 14.3).

Figure 14.4 shows the response surface plots as function of time, adsorbent dosage, and medium pH on MB removal, with their mutual interaction. At constant time and

Table 14.2 t-statistic of regression quadratic model used for the prediction of MB removal using three adsorption inputs (time "A", adsorbent dosage "B", and solution pH "C")

	Beta	SE	*t*-value	*p*-value	Significance
Constant	β_0: −26.09	18.52	−1.41	0.19	Insignificant
(A)	β_1: 0.75	0.59	1.27	0.23	Insignificant
(B)	β_2: 29.73	11.74	2.53	0.03	Significant
(C)	β_3: 23.16	5.08	4.56	0.00	Significant
$(A)^2$	β_{11}: −0.02	0.01	−1.63	0.13	Insignificant
$(B)^2$	β_{22}: −11.68	5.78	−2.02	0.07	Insignificant
$(C)^2$	β_{33}: −1.53	0.36	−4.23	0.00	Significant

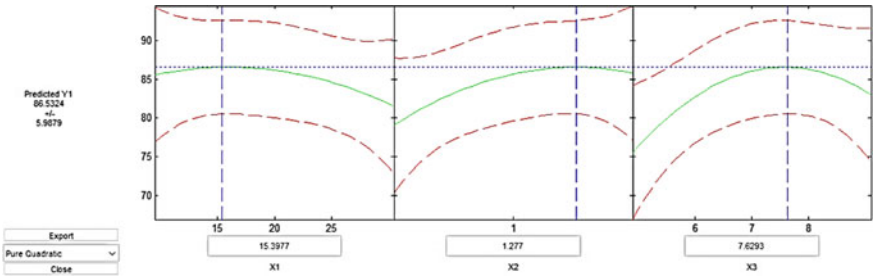

Fig. 14.3 Interactive response surface methodology for optimizing the adsorption inputs, maximizing the MB removal efficiency

pH, a positive relationship between MB removal and adsorbent dosage was manifested. This correlation possibly suggests that the number of adsorbent sites increased with dosage, causing larger specific surface area to capture the MB contaminant. The adsorption rate seems to be fast (around 15 min) to deliver a high MB removal percentage. A comparable trend was reported by Sadaf et al. (2014) to eliminate direct violet 51 dye by adsorption onto lignocellulosic sugarcane bagasse waste.

14.3.4 Sustainable Development Goals (SDGs) Relevant to Dye-Laden Wastewater Treatment

Recently, the exponential increase in demand for textile products has been associated with the release of various organic and inorganic contaminants into the environment. Although there can be improved economic development of the country, the released amounts of wastewater constitute dye compounds. This wastewater affects the aquatic biota and human health; hence, its treatment is essential for (a) ecosystem safety, (b) natural resource utilization, and (c) economic development (Fig. 14.5).

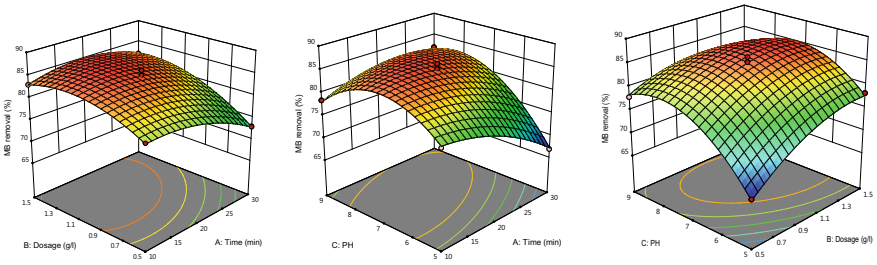

Fig. 14.4 Three-dimensional 3D response surface and contour plot showing the effects of time, adsorbent dosage, and solution pH, and their mutual interaction, on MB removal

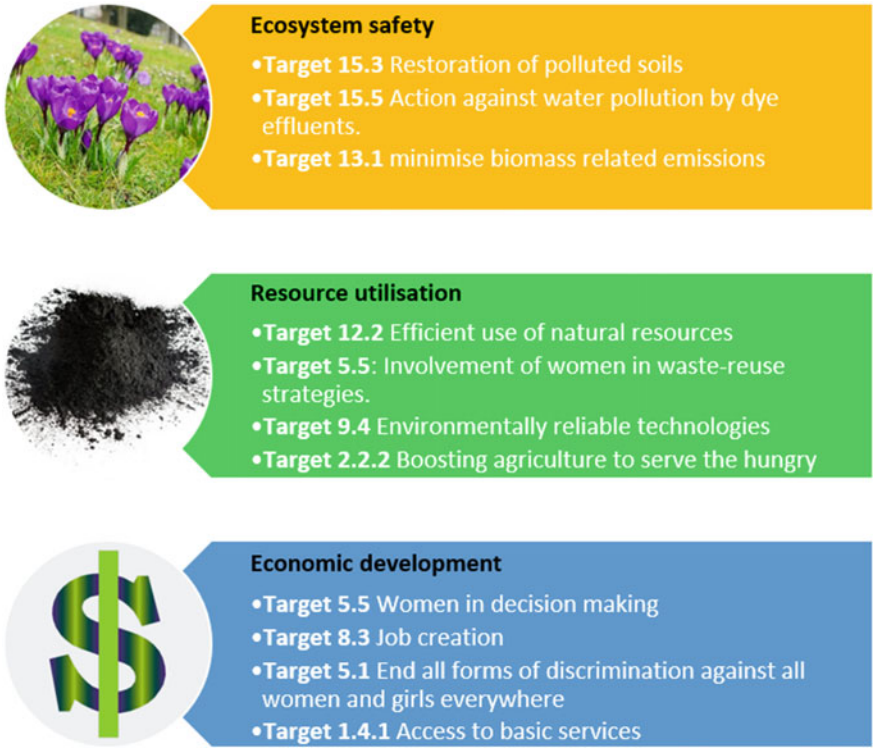

Fig. 14.5 SDGs targets associated with the treatment of textile wastewater relevant to the current study outputs

Ecosystem safety

The current study provides a reliable strategy for minimizing the release of elevated dye concentrations into the aquatic environment. This benefit would protect the aquatic animals and plants and maintain their survival and growth rates (Target 15.5 Action against water pollution). The study also showed the preparation of natural-based adsorbent material, which could be further employed to reduce soil pollution (Target 15.3 restoration of polluted soils). For instance, Zubair et al. (2021) was able to reduce cadmium (Cd) mobility in soil using chitosan-coated textile waste biochar. This biochar could be further characterized and evaluated for its application as a soil amendment, enhancing the agricultural sector (Target 2.2.2 Boosting agriculture to serve the hungry). Soil amendments could also enable the cultivation of non-crop plants like flowers for sale. Moreover, the re-utilization of biomass wastes could limit unwise waste disposal (Target 13.1 minimise biomass related emissions).

Resource utilization

The current study represents a sustainable approach for reutilizing waste orange peels and sugarcane bagasse to ensure full exploitation of the natural biomass resource (Target 12.2 Efficient use of natural resources). Whilst there's a need to utilize resources optimally and efficiently, women leadership in controlling biowaste is key (Target 5.5: women empowerment) (Nasr et al. 2021). A further utilization of natural-based adsorbents for biofuel and biochar productions (Ezz et al. 2021) would enable the achievement of the cleaner energy production agenda (Target 9.4 Clean technologies). The utilization of textile effluents after tertiary treatment and membrane-based technologies for irrigating particular types of crops would be a feasible strategy to mitigate impacts on freshwater ecosystems (Target 1.4.1 Access to basic services).

Socio-economic development

The current study provides a system that could be simply operated by skilled and unskilled laborers (Target 8.3 Job creation). After dye adsorption, the carbonized adsorbent material would be subjected to multiple regeneration cycles to extract the adsorbed dye. This dye is further utilized in the textile factories for printing, coloring, and finishing, providing a great economic value (Meneses et al. 2022).The treatment of dye polluted wastewater provides a well sanitated environment thus allowing the majority to enjoy the comfortable public services.

Conclusion and future aspirations

This study succeeded in providing a reliable and cost-effective adsorbent material prepared from bagasse-based carbon (BBC) and orange peel (OP). A quadratic model was developed and used to predict the MB removal, showing the highest value of 86.4% efficiency under the optimum condition (time = 15.4 min, dosage = 1.28 g/L, and pH = 7.63). The conducted study achieved several UN targets relating to; (ecosystem safety and pollution reduction), economic (e.g., industrialization and trading), and social (e.g., job creation and gender equality) as pillars of sustainability.

Further studies are required to synthesize novel adsorbent material for textile wastewater treatment under real scale conditions. Moreover, artificial intelligence tools and internet of things can be incorporated into the adsorption process during industrial wastewaste treatment.

Acknowledgements The first author acknowledges the Seventh Tokyo International Conference on African Development (TICAD7) for the M.Sc. scholarship. Further, thanks to the Japan International Cooperation Agency (JICA) for providing equipment used in this research. Also, thanks to Egypt-Japan University of Science and Technology (E-JUST).

References

Ajayi TO, Ogunbayio AO (2012) Achieving environmental sustainability in wastewater treatment by phytoremediation with water hyacinth (eichhornia crassipes). J Sustain Dev 5:80–90

Al Sawaf MB, Karaca F (2018) Different stakeholders' opinions toward the sustainability of common textile wastewater treatment technologies in Turkey: A Case study Istanbul province. Sustain. Cities

Cheng H, Yuan M, Zeng Q, Zhou H, Zhan W, Chen H, Mao Z, Wang Y (2021) Efficient reduction of reactive black 5 and Cr(VI) by a newly isolated bacterium of Ochrobactrum anthropi. J Hazard Mater 406:124641

Ezz H, Ibrahim MG, Fujii M, Nasr M (2021) Dual biogas and biochar production from rice straw biomass: a techno-economic and sustainable development approach. Biomas Conver Biorefinery

Gadow SI, Li YY (2020) Development of an integrated anaerobic/aerobic bioreactor for biodegradation of recalcitrant azo dye and bioenergy recovery: HRT effects and functional resilience. Bioresour Technol Reports 9:100388

Georgin J, Alves E, Drumm F, Tonato D, Grassi P, Piccin JS, Oliveira MLS, Dotto GL, Mazutti MA (2019) Application of Beauveria bassiana spore waste as adsorbent to uptake acid red 97 dye from aqueous medium. Environ Sci Pollut Res 26:36967–36977

Hamdy A, Mostafa MK, Nasr M (2018) Zero-valent iron nanoparticles for methylene blue removal from aqueous solutions and textile wastewater treatment, with cost estimation. Water Sci Technol

Jawad AH, Mohammed IA, Abdulhameed AS (2020) Tuning of fly ash loading into chitosan-ethylene glycol diglycidyl ether composite for enhanced removal of reactive red 120 Dye: optimization using the box-behnken design. J Polym Environ 28:2720–2733

Jiang R, Yu G, Ndagijimana P, Wang Y, You F, Xing Z, Wang Y (2021) Effective adsorption of Direct Red 23 by sludge biochar-based adsorbent: adsorption kinetics, thermodynamics and mechanisms study. Water Sci Technol 83:2224–2236

Khaled A, Nemr AE, El-Sikaily A, Abdelwahab O (2009) Removal of Direct N Blue-106 from artificial textile dye effluent using activated carbon from orange peel: adsorption isotherm and kinetic studies. J Hazard Mater 165:100–110

Liu L, Yang C, Tan W, Wang Y, Wang Y (2020) Degradation of acid red 73 by activated persulfate in a heat/Fe_3O_4@AC system with ultrasound intensification. ACS Omega 5:13739–13750

Meneses IP, Novaes SD, Dezotti RS, Oliveira PV, Petri DFS (2022) CTAB-modified carboxymethyl cellulose/bagasse cryogels for the efficient removal of bisphenol A, methylene blue and Cr(VI) ions: Batch and column adsorption studies. J Hazard Mater 421:0–3

Moosavi S, Li RYM, Lai CW, Yusof Y, Gan S, Akbarzadeh O, Chowhury ZZ, Yue XG, Johan MR (2020) Methylene blue dye photocatalytic degradation over synthesised fe3o4 nano-catalyst: degradation and reusability studies. Nanomaterials 10:1–15

Nasr M, Tawfik A, Awad HM, Galal A, El-Qelish M, Abdul Qyyum M, Mumtaz Ali Khan M, Rehan M, Nizami AS, Lee M (2021) Dual production of hydrogen and biochar from industrial effluent containing phenolic compounds. Fuel 301:121087

Sadaf S, Bhatti HN, Nausheen S, Noreen S (2014) Potential use of low-cost lignocellulosic waste for the removal of direct violet 51 from aqueous solution: equilibrium and breakthrough studies. Arch Environ Contam Toxicol 66:557–571

Tripathi P, Srivastava VC, Kumar A (2009) Optimization of an azo dye batch adsorption parameters using Box-Behnken design. Desalination 249:1273–1279

Vyavahare GD, Gurav RG, Jadhav PP, Patil RR, Aware CB, Jadhav JP (2018) Response surface methodology optimization for sorption of malachite green dye on sugarcane bagasse biochar and evaluating the residual dye for phyto and cytogenotoxicity. Chemosphere 194:306–315

Zubair M, Adnan Ramzani PM, Rasool B, Khan MA, ur-Rahman M, Akhtar I, Turan V, Tauqeer HM, Farhad M, Khan SA, Iqbal J, Iqbal M (2021) Efficacy of chitosan-coated textile waste biochar applied to Cd-polluted soil for reducing Cd mobility in soil and its distribution in moringa (Moringa oleifera L.). J Environ Manage 284

Chapter 15
An Economic Evaluation of Integrated Desalination Systems Using Pressurized Water Reactor (PWR)

Thaqal Alhuzaymi and Meshari ALQahtani

Abstract Desalination is a process of getting potable water by treatment of highly saline brackish or sea water. The techniques are being adopted to treat sea water (67%), brackish water (19%), river water (8%) and waste water (6%) which can further help to cope up with the condition of water crisis. Global desalination techniques (i.e. reverse osmosis (RO), multistage flash (MSF), multi-effect distillation (MED)) are currently utilizing around 75.2 TWh of energy per year. These techniques need a continuous supply of power for their proper functioning. In remote areas renewable energy resources are used as power supply for smooth working of plants. Among these energy resources nuclear energy is found to be highly efficient energy that can be used to treat sea water. The energy produced from nuclear reactors can be coupled with thermal desalination units and can further used to treat water. The pressurized water reactor (PWR) is highly cost efficient and reliable technology that is being coupled with desalination unit for the treatment of highly saline water. Results from DEEP analysis showed that reverse osmosis system (RO) coupled with nuclear reactor are proved to be highly cost efficient and can provide high quality freshwater. The average cost for such type of unit is found to be 0.787 $/m^3. The study concluded that coupling desalination units with nuclear reactors can provide clean water at comparatively lower cost.

Keywords Desalination · Pressurized water reactor (PWR) · Nuclear reactor · Renewable energy (RE) · Cost analysis

15.1 Introduction

Water, a sign of life, is going through situation of extreme crisis worldwide. These crisis are resulting due to increased industrialization, population explosion, high living standards, agriculture activities and uneven distribution of water (Woo 2018;

T. Alhuzaymi · M. ALQahtani (✉)
King Abdulaziz City for Science and Technology, Kingdom of Saudi Arabia, Nuclear Science Research Institute, P.O. Box 6086, Riyadh 11442, Saudi Arabia
e-mail: mmalqahtani@kacst.edu.sa

H.-Y. Jeon (ed.), *Sustainable Development of Water and Environment*,
Environmental Science and Engineering,
https://doi.org/10.1007/978-3-031-07500-1_15

Rezaei 2017). According to an estimate around 70% of earth surface is covered with water in the form of seas, oceans, lakes, rivers, glaciers etc. Out of this 70% around 2.5% is fresh water. Major portion of this fresh water is being locked in the form of cryosphere and permafrost and eventually only 0.008% is available as potable water that makes around 70,000 km^3 (Park 2014; Naserbegi 2019). As currently the concept of sustainable development is considered to be a vital parameter that includes some fundamental approaches like economic, environmental and social. There is a firm need to develop some alternative ways to overcome the situation of water crisis (Rezaei 2017). Hence to cope up with such drastic condition of continuously increasing water crisis, desalination is found to be an effective technique (Ali 2018).

Desalination is a process of getting potable water by treatment of highly saline brackish or sea water (Ali 2018; Eke 2020). Studies have shown that the desalination techniques are being adopted to treat sea water (67%), brackish water (19%), river water (8%) and waste water (6%) (Ali 2018). The technique was introduced in middle of twentieth century and till now a larger number of countries including Middle East, North and South Africa have adopted this technique to deal with situation of water scarcity (Elsaid 2020). Recently, due to development in desalination technology, it is found to be a promising technique worldwide which has been adopted with exponential rate worldwide. According to global statistics about desalination, in 2005 round about 35 m^3 MCM/day (million cubic meter per day) water was being desalinated which became 95 MCM/day in the same year. This treated water was being used for municipal as well as for industrial purpose (Elsaid 2020; Jones 2019). The desalination capacity data of various countries is being shown in Table 15.1.

The desalination of saline water is done in two major types of processes named as thermal desalination process which includes some major technologies such as multi-stage flash evaporation (MSF), multi-effect distillation (MED) and vapor compression (VC). While the other is membrane desalination process that includes reverse osmosis (RO), forward osmosis (FO) and electro-dialysis (ED) (Ahmed 2014).

Table 15.1 Some major countries practicing desalination technique

Country	Desalination capacity (%)	References
Middle East and North Africa	47.5	Elsaid (2020), Jones (2019)
East Asia	18.4	Elsaid (2020), Jones (2019)
Saudi Arabia	15.5	Jones (2019)
North America	11.9	Elsaid (2020), Jones (2019)
USA	11.2	Jones (2019)
United Arab Emirates	10.1	Jones (2019)
China	7.5	Jones (2019)
Spain	5.7	Jones (2019)
Kuwait	3.1	Jones (2019)

Currently technologies have been developed to couple desalination units with various renewable energy resources to deal with cost and energy crisis of desalination process. Global desalination techniques are currently utilizing around 75.2 TWh of energy per year (Wakil 2017). These thermal desalination process and membrane desalination process. techniques need a continuous supply of power for their proper functioning. In remote areas renewable energy resources are used as power supply for smooth working of plants. The renewable energy resources can be geothermal, wind energy, solar energy or nuclear energy (Al-Othman 2019).

Nuclear energy is found to be a major source of efficient energy that can be used to treat sea water especially in nuclear power plants. The energy produced from these power plants can be coupled with thermal desalination units and can further used to treat water. The technique has found to be environment friendly as it can reduce greenhouse gas emission and is also a cost efficient. As the production of electricity with the help of nuclear energy is also increasing during past years, it is also facilitating the desalination practices and its dependence on nuclear resources (Sanchez-Cervera 2013). There are few techniques which are currently working as nuclear reactor techniques to treat sea water which are; pressurized water reactor (PWR), boiling water reactor (BWR), pressurized heavy water reactor (PHWR), gas cooled reactor (GCR) and fast breeder reactor (FBR) (Al-Othman 2019; Alemberti 2014). Studies have revealed that in 2016 approximately 441 nuclear reactors were working in thirty countries for desalination of water which were accounting 382.9 GW(e) (Giga-watt (electrical)). This capacity is expected to be 511 GW(e) in 2030 (IAEA 2016). The current scenario of nuclear energy usage for producing potable water is considered to show a promising future to deal with energy crisis as well as water crisis.

The aim of study is to review the effectiveness of nuclear reactors for the production of potable water by treating highly saline water. The study is being conducted to access that how nuclear energy resources can be effective in dealing with water crisis and can provide clean energy without causing any environmental deterioration. Furthermore, it is also aimed to find out most effective technique used for desalination resulting in high cost benefit as well as providing better results of providing high quality water that can be used as potable water, or also can be used for industrial or agricultural purpose.

15.2 Desalination Techniques

The desalination process is used to remove excessive amount of salts from sea water to make it healthy for consumption. Studies have revealed that normally brackish water has approximately 10,000 ppm of salts whereas sea water possess approximately 35,000–45,000 ppm of salts which is known as total dissolved salts (TDS). The world health organization (WHO) claims that the TDS level for potable water must range between 500 and 1000 ppm (Ali 2018; Miller 2010). Desalination process is being divided into two major techniques;

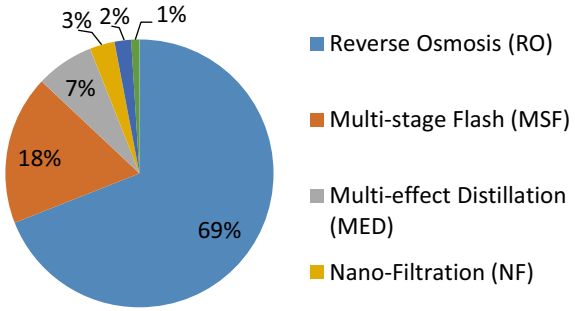

Fig. 15.1 Desalination Techniques and their role in water treatment (Jones 2019)

1. Thermal desalination technique,
2. Membrane desalination technique.

The thermal desalination technique basically works on the process of evaporation and condensation. During these processes salts are being separated from water by providing high amount of heat (Al-Othman 2019). The energy in the form of electricity is being provided to the water to create fluid flow which helps to provide an effective desalination process (Polat 2018). Thermal desalination is further divided into processes such as multi-effect distillation (MED), multi-stage flash distillation (MSF) and vapor compressor distillation (VCD) (Okampo 2021).

While membrane desalination process works on the principle of ion adsorption or semi permeability membranes having unique chemical and physical properties. Feed water enters in membrane through pressure pumps and brine is being treated based on concentration gradient. Some major techniques used in membrane desalination are reverse osmosis (RO), forward osmosis (FO) and electro-dialysis (ED) (Okampo 2021; Abdelkareem 2018). Studies have showed that reverse osmosis is found to be most practiced desalination technique followed by MSF and MED. Statistical analysis showed that RO is accounts for 65% of total desalination (Okampo 2021). Other process and their contribution in worldwide desalination practices are being shown in Fig. 15.1 given bellow.

15.3 Nuclear Reactors for Desalination

The coupling of desalination plants with renewable energy (RE) resources is becoming a highly practicing technique from last couple of decades. The reason behind this surge of increasing using of renewable resources is that these resources possess low to no carbon footprints which makes them environment friendly techniques. On the other hand, RE is found to be highly suitable to combat with water crisis in remote areas with less consistent or no supply of electricity (Khan 2018a, b). The common types of RE are wind energy, geothermal energy, solar energy and tidal energy. Nuclear energy itself is also classified as renewable and cleaner source of energy but concern of waste disposal is still there. Hence to cope up the problem

of production of excessive amount of nuclear wastes or waste disposal, the nuclear reactor based desalination plants are commonly installed on nuclear power plants where they utilizes wasted heat from power plant to run their turbines. On the other hand some medium/small nuclear reactor devices are also being introduced that uses lesser amount of nuclear material as fuel and can run desalination unit for longer time span (Khan 2018a, b).

As desalination is being carried out by providing a supply of heat or electricity to thermal or membrane desalinizing units, hence in the case of nuclear desalination units, a plant is being coupled with nuclear reactors where it utilizes waste heat from plants to produce electricity and run desalination plant. The process is generally known as cogeneration as two various types of processes (generation of electricity and desalination) are being carried out by using single type of energy source. The technique provides a clean energy sources with lower consumption of maintenance cost with a longer life span of plant (Ahmed 2014; Ali 2018). As nuclear power works on the principle of fission reaction hence it is found to be second largest source of CO_2 free source of energy. Due to its lowest carbon footprints nuclear energy is also categories as "Green Technology". As this type of energy provides a consistent power supply hence this feature has made it more reliable source of energy to power various systems worldwide. Globally it is found that nuclear energy accounts around 1% of total production of electricity. The dependence of global need of power on nuclear resources is increasing day by day. Currently 67 nuclear reactors are producing approximately 64,000 MW of electricity in 15 countries. The statistical studies have revealed that during current scenario of energy crisis and limited availability of fossil fuel reservoirs, there is strong need to encourage production of electricity through nuclear energy resources (Ali 2018).

A general description of a nuclear reactor driven desalination unit is being discussed in Fig. 15.2.

Nuclear reactors convert thermal energy into electrical energy that helps to power desalination units directly. On the other hand the thermal energy can be converted to electrical energy in the form of electricity that can be sold to power grids Some major types of desalination units are enlisted below:

1. Pressurized Water Reactor (PWR),
2. Boiling Water Reactor (BWR),
3. Heavy Water Reactor (PHWR),
4. Gas Cooled Reactor (GCRs),
5. Liquid metal cooled reactor (LMCR) (Mansouri 2017).

Nuclear reactors works on different principles, a brief discussion about working of these reactors is being discussed below.

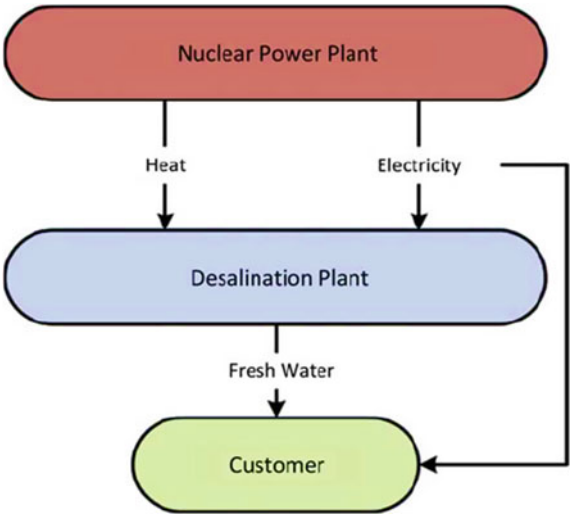

Fig. 15.2 Flow chart showing nuclear desalination process (Dincer 2018)

15.3.1 Pressurized Water Reactor (PWR)

The pressurized water reactors (PWR) generally works with light water i.e. the coolant is in the form of H_2O. In this system nuclear heat is generated and is further transferred with the help of steam generators in secondary power circuit (Dincer 2018). In this type of reactor controlling pressure is found to be a key feature of reactor for its safety as well as functioning. This pressure is being controlled by a pressurizer in the pressure vessel (El-Sefy 2019). Some major types of PWRs are AP1000 (Alonso 2012), The AP-600, The French PWR-900 (Nisan 2003) and HPR1000 (Xing 2016). An AP1000 reactor is shown in Fig. 15.3.

15.3.2 Boiling Water Reactor (BWR)

A boiling water reactor (BWR) is a reactor that performs its function similar to PWR but with an exception that a BWR has no steam generator in it. In this type of reactor light water is being used for the purpose of cooling and moderating. The system operates at lower pressure and thus water is being boiled within the pressure vessel that eventually runs the turbine and produce electricity. The energy conservation of the system is evaluated with the help of Rankine Cycle which is basically a saturated steam condensation cycle. This system doesn't have any primary or secondary loop. As stated earlier the BWRs are the second largest globally applied nuclear reactors with 21% of operating units (Ahmed 2014). The common example of BWR is VK-300. The reactor has ability to produce thermal or electrical power up to 750 MWth/250 MWe by using UO_2 as fuel (Ahmed 2014).

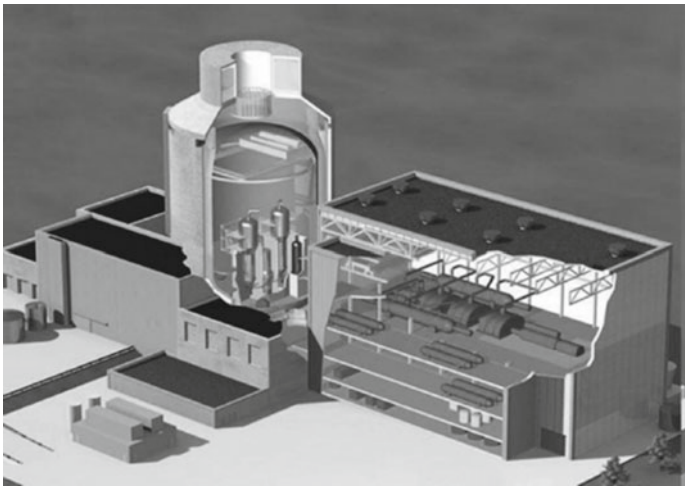

Fig. 15.3 An AP1000 nuclear reactor (Alonso 2012)

15.3.3 Heavy Water Reactor (HWR)

A heavy water reactor (HWR) works on the principle of using isotope of water. These reactors use heavy water as coolants and are moderated with the help of pressurized water reactor, hence can be called as pressurized heavy water reactors (PHWR). In these reactors fuel is places in hundreds of pressure tubes instead of a single pressure vessel. HWRs represent around 10.5% of the total operating systems. Furthermore, in this type of reactor natural uranium is being used as fuel which can also be refilled (Ahmed 2014).

15.3.4 Gas Cooled Reactor (GCRs)

Gas cooled reactors are one of the initially adopted technologies that uses gases like helium and carbon dioxide as coolant. In this type of reactor graphite blocks are being used as moderators. During the cooling process with the help of gas heat is either extracted through it which is indirectly be used to generate electricity and to run turbines. This reactor performs with 50% of efficiency on high temperature i.e. at 1000 °C (Ahmed 2014; Rowinski 2015).

15.3.5 Liquid Metal Cooled Reactor (LMCR)

A liquid metal cooled reactor works on the concept of using liquid metals, instead of water, as a coolant. This technique utilizes neutron fast spectrum hence there is no need of a moderator in this system. The reactor is built on the concept of two main approaches i.e. loop and pool concept. In the former type of LMCR sodium is being used and reactor has two loops of liquid metal. That's why it uses two heat exchanging units for the production of heat. In the later type of reactor heat exchangers or steam generators are being used i.e. in lead cooled reactors (Rowinski 2015).

15.4 Pressurized Water Reactor (PWR) a Best Technique

A pressurized water reactor works on the concept of two loops such as primary coolant system which removes energy resulted from fission reaction in the reactor. This loop works at high pressure ranging up to 15 bar to sustain the physical form of water at high pressure. After this energy is being transferred to secondary coolant where water is being treated by keeping pressure up to 7 bar to boil water and make steam. The exchanger of heat in this system is known as steam generator (SG). Hence later this steam is used to run turbine and produce electricity (Rowinski 2015). In a general pressurized water reactor (PWR) there are following major parts:

1. A pressure vessel for nuclear fuel,
2. Control rods,
3. Moderator,
4. Coolants.

A pressurized water reactor is considered to be highly efficient and more reliable technology to treat sea water and produce potable water (Ahmed 2014). Figure 15.4 shows the schematic diagram of PWR coupled desalination unit.

Currently PWR technique is one of the most practicing nuclear reactors. Studies have explained the efficiency of the technique. Current analysis declared that there are approximately 434 operational nuclear reactors worldwide with a ratio of PWR 68%, BWR 20%, PHWR 6%, LWGR 3%, GCR 2% and FBR 1% (Mansouri 2017). Mansouri (2017) conducted a study based on comparison between nuclear desalination and desalination coupled with other energy resources. The major aim of their study was to evaluate the effectiveness of nuclear desalination at Saudi Arabia, a fossil fuel enriched country. Their results revealed that nuclear desalination can be proved as highly cost efficient technique in Saudi Arabia and can combat with two major crisis including water scarcity and energy crisis (Mansouri 2017). Bazedi (2019) stated the global scenario of nuclear plant coupled desalination units. Their study showed that Kazakhstan desalination plant which is working on the principle of MED coupled with LMFR power plant possess capacity of 80,000 m^3/day. China has developed a NHR-PWR reactor which works on desalination of seawater with reverse

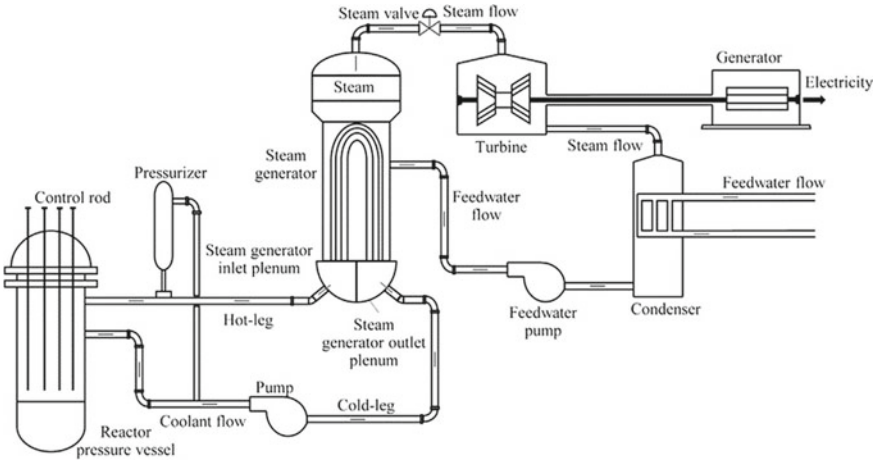

Fig. 15.4 Schematic diagram of a pressurized water reactor plant (PWR) (El-Sefy 2019)

osmosis. The reactor has capacity of treating up to 80,000–120,000 m^3/day (Bazedi 2019). A desalination unit in Pakistan which is basically a MED nuclear desalination unit treats 1600 m^3/day. Japan is rigorously working on nuclear desalination and had installed eight nuclear desalination units coupled with BWR reactors. These units have capacity to treat approximately 1000–2000 m^3/day per unit (Dincer 2018; Park 2014). Dong (2019) conducted a study on integrated pressurized water reactor (iPWR) coupled with MED-TVC. The results showed that the coupling proved to be highly efficient and cost effective (Dong 2019). Al-Othman (2019) stated a survey and concluded the capacity of pressurized water reactor in the production of electricity and production of treated water (Al-Othman 2019). A summary is being stated in Table 15.2.

Table 15.2 PWR nuclear reactor desalination and their capacity (Al-Othman 2019)

Reactor type and desalination process	Net electricity production (MW)	Net water production (m^3/day)
AP1000 RO	957.25	1,100,000
AP1000 MSF	1568.83	1,000,000
AP1000 MED	1919.75	1,040,000
IRIS RO	1188.80	1,040,000
IRIS MSF	1028.08	1,000,000
IRIS MED	1348.50	1,100,000
IRIS MSF-RO	1180.80	1,040,000
IRIS ED-RO	1389.00	1,100,000

15.5 Economic Evaluation of PWR with a Desalination System

The analysis based on cost (capital and maintenance cost) showed that nuclear energy is one of the highly cost efficient technique. Figure 15.5 shows the comparison of different types of energy resources and their cost on desalination process. A feasibility study conducted by Schmidt (2021) concluded that a reverse osmosis plant powered by nuclear power plant can produce potable water at lowest cost (Schmidt 2021). A desalination economic evaluation program (DEEP) in Qeshm Island was done by considering six different energy programs based on fossil fuel, PWR, PBMR, and CC. results showed that fossil fuel based desalination unit consumed approximately 97.72 $/kWh which is around 30% higher than PWR, PBWR and CC. On the other hand comparison between CC and PWR showed that the annual cost of desalination as 1.78 and 1.49 $/m^3 (Rezaei 2017). The DEEP analysis showed that the fuel and maintenance cost in the case of PWR is found to be extremely low as compared to other techniques which make it highly suitable technology to be used in desalination (Abdallah 2018).

15.5.1 Model Verification

In this study a desalination Economic Evaluation Program (DEEP) analysis was conducted to carry out economic analysis for PWR reactor for power level of 1000 MW(e). For this purpose the water production cost was estimated for three commonly used desalination techniques which are MED, MSF, RO, MED + RO, and MSF + RO. DEEP analysis verified the capital and marginal costs used in analysis which is being shown in Table 15.3.

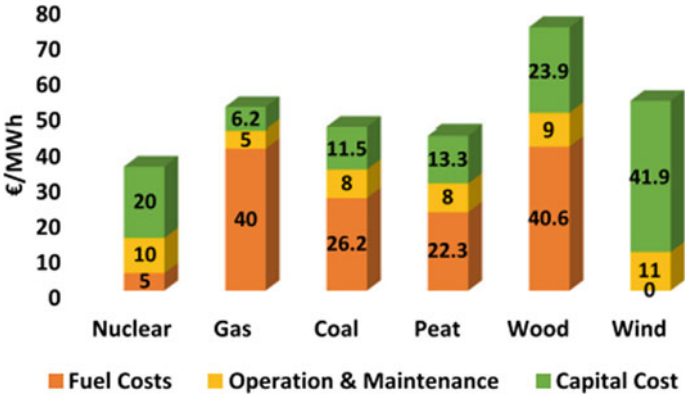

Fig. 15.5 Cost analysis of various energy resources (Eke 2020)

Table 15.3 Results of PWR coupled desalination system

Desalination technologies	Unit	MED	MSF	RO	MED + RO	MSF + RO
Total capital cost	M$	209	245	147	179	179
Total operation cost	$/m^3	0.61	1.09	0.45	0.59	1.04
Total electricity cost	$/m^3	0.48	0.96	0.23	0.46	0.92
Total water cost	$/m^3	1.065	1.595	0.787	1.053	1.508

The above table shows that the cost of reverse osmosis system (RO System) coupled with PWR can produce water at cheaper rates as compared to other technique which is 0.787 $/m^3. On the other hand a hybrid desalination unit using MSF + RO technique will cost approximately 1.508 $/m^3. The results clearly exhibit that the coupled desalination unit is proved to be highly economical unit for power generation as well as for the production of potable water which is quite healthy for human consumption and other uses such as agriculture. As stated in previous section, PWR are designed on the concept of Rankine cycle which is energy efficient cycle. This cycle in power plants work on closed loop system in which steam is reused for power generation yet a lot of heat is being wasted in the process of condensation. The wasted heat is being released into atmosphere and nearby reservoirs which are using this heat for plant cooling purpose. In nuclear desalination process the extra heat produced by some nuclear plant is being used by desalination plant and hence brackish or sea water can be utilized and treated to get fresh water.

As it is clear from above results that during current time of water scarcity, a reverse osmosis system is proved to be highly cost efficient and easy to operate facility which can help to cope up with stress condition. The facility is highly cost efficient and the major cost that is in the form of power supply can be managed by coupling it with renewable energy resources which needs a comparatively high capital cost but low maintenance or running cost (as shown in Fig. 15.5) which makes it cumulatively energy and cost efficient technique. On the other hand other distillation plants also shows some promising positive impacts in the form of being reliable and longer working life span which make technique, ore suitable to overcome water stress in arid or semiarid areas. A hybrid technique of MED + RO is second highly practiced technique worldwide after RO. The technique has found to be highly cost efficient and furthermore can treat highly saline water (i.e. in the form of produced water). Furthermore, data has revealed that the hybrid technique of MED + RO is highly cost efficient in the case of energy consumption (as shown in Table 15.3), easy to installed and simple to operate. On the other hand a currently rising practice of hybrid desalination is found to be effective to deal with highly polluted or saline water. In this technique RO plant is being coupled with distillation plant (i.e. MSF or MED). Both techniques by working together can produce high quality fresh water on lower and reasonable cost which is also being shown in above DEEP analysis.

Apart from this, as we have already discussed and DEEP analysis is also based on coupling of desalination units with some nuclear reactors. It is being noted that a medium size desalination unit coupled with nuclear reactor can start working within

cost range of 0.33–1.89 $/m^3. The cost also depends on type of nuclear reactor. Furthermore, cost benefit analysis of a nuclear reactor coupled desalination unit showed that production of fresh water from a dual purpose desalination unit is more cost efficient as compared to a unit independently installed for this purpose.

15.6 Conclusion

It is being concluded from current study that during the rising water scarcity issues desalination has found to be highly effective technique in all possible scenarios. The analysis has clearly shown that MED + RO, a hybrid desalination technique, is the second most effective process after RO. The process has ability of co-generation by producing electricity as well as desalinizing water. The technique is highly effective in areas with arid and semi-arid conditions. Hence installation of desalination units is a best strategy. Furthermore, by taking into account the power crisis, coupling of desalination unit with some renewable energy resource is found to be a best technique. Nuclear energy termed as green energy, is found to be the best technique to power desalination plants, with a position impact of being cost efficient in the case of fuel and maintenance. In the case of nuclear reactors, the major cost is found to be the capital cost which can also be minimized in reactors that are installed at power plants. The best working technology for this purpose is pressurized water reactors (PWR) that are also most practiced technique. Results from DEEP analysis showed that reverse osmosis system (RO) coupled with nuclear reactor are proved to be highly cost efficient and can provide high quality freshwater. There is further need to develop these reactors to effectively reduce the nuclear waste as it is an environmental concern.

Based on detailed study of desalination processes coupled with nuclear reactor, reverse osmosis technique has found to be most efficient in terms of cost and benefit analysis. The major reason behind its effectiveness is both process needs high capital cost but lower maintenance cost and effort. On the other hand the technique also possesses best desalination of wastewater, brackish water, saline water as well as produced water. Due to its wider applicability and results reverse osmosis has found to be most adoptable and versatile technique which can cope up water scarcity issues by utilizing lower amount of electricity.

Recommendations

Reviewing the current energy crisis and enhanced environmental impacts of fossil fuel burning, usage of clean energy and renewable energy resources has found to be an effective technique. As MENA countries are located in arid and semi-arid regions and are facing water scarcity. Hence, by taking in view the scenario of water scarcity in the region it is recommended to further conduct DEEP analysis of installation of desalination units coupled with nuclear energy resources to cope up with energy crisis as well as to find the feasibility of using nuclear power in regions enriched with fossil fuel reservoirs.

References

Abdallah AAHA (2018) Innovative development of nuclear desalination technologies and cost improvement approaches. Ann Fac Eng Hunedoara Int J Eng 16(2)
Abdelkareem MA (2018) Recent progress in the use of renewable energy sources to power water desalination plants. Desalination 435:97–113
Ahmed SA (2014) Small/medium nuclear reactors for potential desalination applications: mini review. Korean J Chem Eng 31(6):924–929
Alemberti A (2014) Overview of lead-cooled fast reactor activities. Prog Nucl Energy 77:300–307
Ali A (2018) Membrane technology in renewable-energy-driven desalination. Renew Sustain Energy Rev 81:1–21
Alonso G (2012) Alternatives of seawater desalination using nuclear power. Nucl Eng Des 245:39–48
Al-Othman A (2019) Nuclear desalination: a state-of-the-art review. Desalination 457:39–61
Bazedi GAA (2019) Coupling pressurised water reactor to large scale SWRO desalination plants: an economic assessment. Int J Nucl Governance Econ Ecol 4(3):198–211
Dincer S (2018) Comparative evaluation of possible desalination options with various nuclear power plants. In: Exergetic, energetic and environmental dimensions, pp 569–582
Dong Z (2019) Dynamical modeling and simulation analysis of a nuclear desalination plant based on the MED-TVC process. Desalination 456:121–135
Eke J (2020) The global status of desalination: an assessment of current desalination technologies, plants and capacity. Desalination 495:114633
Elsaid K (2020) Environmental impact of desalination technologies: a review. Sci Total Environ 748:141528
El-Sefy M (2019) System dynamics simulation of the thermal dynamic processes in nuclear power plants. Nucl Eng Technol 51(6):1540–1553
International Atomic Energy Agency (2016) Nuclear technology review. Vienna
Jones E (2019) The state of desalination and brine production: a global outlook. Sci Total Environ 657:1343–1356
Khan MA (2018a) A hybrid renewable energy system as a potential energy source for water desalination using reverse osmosis: a review. Renew Sustain Energy Rev 97:456–477
Khan SUD (2018b) Nuclear energy powered seawater desalination. In: Renewable energy powered desalination handbook, pp 225–264
Mansouri NY (2017) Does nuclear desalination make sense for Saudi Arabia? Desalination 406:37–43
Miller FP (2010) International atomic energy agency: nuclear technology, nuclear weapon, United Nations, United Nations General Assembly, United Nations Security Council, Mohamed ElBaradei, Nobel Peace Prize, Yukiya Amano, IAEA Areas. Alphascript Publishing
Naserbegi A (2019) Energy management of nuclear desalination plant by efficient coupling a pressurized water reactor and a multi-effect distillation system-thermodynamic evaluation. Desalination Water Treat 151:34–46
Nisan S (2003) Sea-water desalination with nuclear and other energy sources: the EURODESAL project. Nucl Eng Des 221(1–3):251–275
Okampo EJ (2021) Optimisation of renewable energy powered reverse osmosis desalination systems: a state-of-the-art review. Renew Sustain Energy Rev 140:110712
Park MY (2014) Thermodynamic evaluation on the integrated system of VHTR and forward osmosis desalination process. Desalination 337:117–126
Polat MF (2018) Comparative evaluation of possible desalination options for Akkuyu nuclear power plant. In: Exergetic, energetic and environmental dimensions, pp 583–596
Rezaei A (2017) Economic evaluation of Qeshm island MED-desalination plant coupling with different energy sources including fossils and nuclear power plants. Desalination 422:101–112
Rowinski MK (2015) Small and medium sized reactors (SMR): a review of technology. Renew Sustain Energy Rev 44:643–656

Sánchez-Cervera IG (2013) DE-TOP: a new IAEA tool for the thermodynamic evaluation of nuclear desalination. Desalination 321:103–109
Schmidt JM (2021) Nuclear cogeneration for cleaner desalination and power generation–A feasibility study. Cleaner Engineering and Technology 2:100044
Wakil M (2017) Energy-water-environment nexus underpinning future desalination sustainability. Desalination 413:52–64
Woo CH (2018) Research trend of membranes for water treatment by analysis of patents and papers' publications. Desalin Water Treat 10:201–220
Xing J (2016) HPR1000: advanced pressurized water reactor with active and passive safety. Engineering 2(1):79–87

Chapter 16
A Cost Analysis Study of Nuclear Reactor Powered Desalination Process by DEEP Analysis—A Case Study of Saudi Arabia

Meshari ALQahtani and Thaqal Alhuzaymi

Abstract Desalination is highly suitable technique in current era of water crisis especially in arid and semiarid regions. The techniques are being adopted worldwide with a capacity to treat sea water (67%), brackish water (19%), river water (8%) and waste water (6%) which can further help to cope up with the condition of water crisis. Global desalination techniques (i.e. reverse osmosis (RO), multistage flash (MSF), multi-effect distillation (MED)) are currently utilizing around 75.2 TWh of energy per year. These techniques need a continuous supply of power for their proper functioning. In remote areas renewable energy resources are used as power supply for smooth working of plants. Among these energy resources nuclear energy is found to be highly efficient energy that can be used to treat sea water. The energy produced from nuclear reactors can be coupled with thermal desalination units and can further used to treat water. Results from DEEP analysis showed that PHWR-600 nuclear reactor coupled with reverse osmosis system (RO) is proved to be highly cost efficient and can provide high quality freshwater. The coupled process can provide fresh water at even more lowest cost as compared with nuclear reactors coupled with MED and MSF technologies.

Keywords Desalination · Pressurized water reactor (PWR) · Nuclear reactor · Renewable energy (RE) · Cost analysis

16.1 Introduction

During current era of water crisis, desalination is found to be highly suitable technique to deal with water scarcity. Some areas, especially arid and semiarid regions, which receive low rainfall, are more prone to desertification and lower availability of water for potable purposes. To deal with such drastic conditions, practicing desalination coupled with renewable energy resources has found to be a highly practicing

M. ALQahtani · T. Alhuzaymi (✉)
King Abdulaziz City for Science and Technology, Kingdom of Saudi Arabia, Nuclear Science Research Institute, P.O. Box 6086, Riyadh 11442, Saudi Arabia
e-mail: talhuzaymi@kacst.edu.sa

H.-Y. Jeon (ed.), *Sustainable Development of Water and Environment*,
Environmental Science and Engineering,
https://doi.org/10.1007/978-3-031-07500-1_16

technique. The technique was initially practiced in mid 1950s for the production of freshwater to be used in industries. During current rise in population, industrialization and metropolization the need of freshwater is also rising day by day. Hence desalination is being widely adopted to provide freshwater to industrial purposes, agriculture purpose and also for water supply as potable water (Ghazaie 2019).

Desalination is basically a technique of getting fresh water by treating highly saline water in the form of brackish or sea water (Ali 2018; Eke 2020). Studies have shown that the desalination techniques are being adopted to treat sea water (67%), brackish water (19%), river water (8%) and waste water (6%) (Ali, 2018). The global statistics about desalination claims that, in 2005 round about 35 m3 MCM/day (million cubic meter per day) water was being desalinated which became 95 MCM/day in the same year (Jones 2019; Elsaid 2020). On the basis of technical aspects, desalination is being divided into two major categories which are thermal distillation and membrane separation. The most commonly practiced thermal distillation techniques are multi-stage flash distillation (MSF), multi-effect distillation (MED) and vapor compression (VC). While reverse osmosis (RO), electro-dialysis (ED) and forward osmosis (FO) are major examples of membrane separation technology. Studies have shown that reverse osmosis (RO) is the most practicing technique worldwide with a share of around 60% of desalination followed by MSF which accounts 25%, MED 8% and ED which accounts 4% of total desalination (Mansouri 2017; Al-Othman 2019). As all these techniques utilize energy for their working which is being provided by some external resource. Recently coupling of desalination techniques with some renewable energy resources are getting more recognition.

Renewable energy resources are highly in practice for the production of fresh water through desalination process in areas with inconsistent or no supply of electricity. Such techniques are found to be effective in arid and semiarid areas like Saudi Arabia, UAE, Morocco and other countries with comparatively lower rainfall. Renewable energy techniques use solar, wind, geothermal and tidal energy for production of electricity. Nuclear energy is a source of clean energy as it does not produce any greenhouse gas (Ali 2018). Apart from disposal issue rising from nuclear waste, practice of nuclear technology for desalination is rising due to being a cost efficient technique with no environmental pollution. During oil crisis era ranging from 1970s−1980s, nuclear desalination was highly practiced due to being a lower cost technique. A survey conducted in 2016 revealed that 441 nuclear desalination reactors were operating in 30 countries during that years and were producing around 382.9 GW (e) (Giga Watt (electricity). The capacity is estimated to reach around production of 511 GW (e) in 2030. According to a report presented by the world energy council in 2016, the production of Uranium (a nuclear fuel) has reached around 70% in recent one decade which has capacity to provide electricity for more than 100 years (Al-Othman, 2019). A socio economic cost analysis of the desalination units coupled with nuclear reactors is being shown in Fig. 16.1.

The study is aimed to conduct a comparison of cost of various desalination techniques powered by nuclear reactors. On the other hand it was also being considered the feasibility of nuclear desalination in Saudi Arabia, a country enriched with fossil fuels.

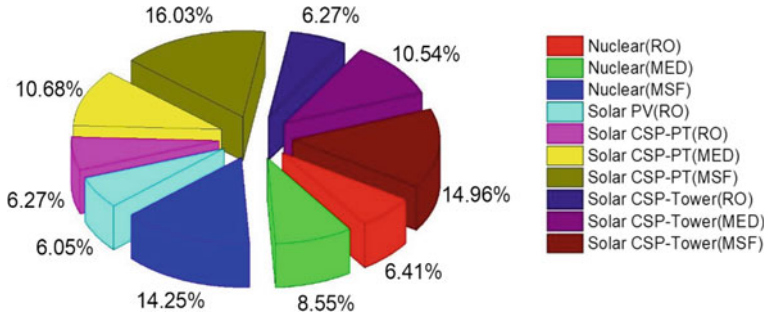

Fig. 16.1 Cost of water desalinating units coupled with nuclear and solar energy resources (Khan 2021)

16.1.1 Area of Study

The kingdom of Saudi Arabia (KSA) is located in Arabian Peninsula and is neighbored by Red Sea and Arabian Gulf. The country is stretched from 15.5−32.5 °N in latitude and 32−55 °E in longitude and is covering a larger surface area of about 2,250,000 km2. KSA shares a complex topography of being arid and semi-arid region hosting a wider desert region. The climate of region is being affected by surface as well as atmospheric circulations. The rainfall of region is being affected by North Atlantic Oscillation (NAO) and El-Niño Southern Oscillation (ENSO). The seasonal and low average rainfall is majorly responsible for the arid nature of region (Hasanean 2015). Some areas of Saudi Arabia are experiencing extremely lower rainfall ranging up to <60 mm making area sand deserts. Spring and winter are among seasons with highest rainfall 38.93% and 32.51% respectively. While summer and autumn are among most dry seasons with annual rainfall of 11.46% and 17.09% respectively (Hasanean 2015).

The water resource study of area revealed that KSA has lower groundwater reservoirs and is exploiting non-renewable groundwater reservoir known as "fossil water" from sandstone aquifer of Mesozoic era. The country has around 103,360 MCM of groundwater reservoir. It is being estimated that the country is among highest per capita user of fresh water with an annual withdraw of about 20 billion m3 of groundwater. On the other hand the annual recharge of aquifer is calculated as 2.4 billion m3. This water is being utilized in industrial, agricultural and for drinking purpose (Chandrasekharam 2018). Furthermore, the water reservoir analysis has shown that the contribution of renewable groundwater is only 2.8 BCM/year (National Water Strategy 2030, 2018). The thickness of non-renewable or fossil water is 300 m at the depth of 500−1500 m. The capacity of this water table has been estimated as 259−761 BCM (Fanak Water 2021).

Another water resource of Saudi Arabia is desalinated water which accounts around 70% of national water supply. KSA is among countries practicing desalination

Fig. 16.2 Map of study area—Kingdom of Saudi Arabia (Google Maps 2021)

at higher extent. The total capacity of desalinated water is estimated as 7.4 BCM/day in 2020 (Fanak Water 2021, Fig. 16.2).

16.2 Methodology

16.2.1 Desalination Processes

Chandrasekharam, D. (2018) in his study stated that due to excessive withdrawal of water from groundwater in Saudi Arabia, the water table is lowered about 60 m till the date (Chandrasekharam 2018). Such condition can lead to more drastic conditions in the form of desertification in area. Hence there is need to adopt and practice desalination techniques. As stated in Sect. 1, the technique is being divided into two major categories given bellow;

1. Thermal distillation
2. Membrane separation.

The thermal desalination technique basically works on the process of evaporation and condensation. During these processes salts are being separated from water by

providing high amount of heat (Al-Othman 2019). The energy in the form of electricity is being provided to the water to create fluid flow which helps to provide an effective desalination process (Polat 2018). Thermal desalination is further divided into processes such as multi-effect distillation (MED), multi-stage flash distillation (MSF) and vapor compressor distillation (VCD) (Okampo 2021).

While membrane desalination process works on the principle of ion adsorption or semi permeability membranes having unique chemical and physical properties. Feed water enters in membrane through pressure pumps and brine is being treated based on concentration gradient. Some major techniques used in membrane desalination are reverse osmosis (RO), forward osmosis (FO) and electro-dialysis (ED) (Okampo 2021; Abdelkareem 2018). Studies have showed that reverse osmosis is found to be most practiced desalination technique followed by MSF and MED. Statistical analysis showed that RO is accounts for 65% of total desalination (Okampo 2021). The working of some majorly practiced technique is discussed below.

Multi-stage flash distillation (MSF). Multi-stage flash distillation (MSF) is a thermal distillation technique works on the principle of distillation in multistage chambers. In this process pressure is being reduced at each stage to carry out distillation process. The technique is found to be second most practiced technique worldwide. MSF is highly reliable with a distinction of being easy to operate and having longer life span.

A conventional MSF plant works on the principle of heating feed water with the help of brine heater with reduction of pressure. Here around 10−30 stages are being involved in which temperature is being dropped up to 2 °C on each stage. During this process evaporation is carried out. Furthermore vacuumed ejectors, chemical addition pumps and feed screen are installed to carry out the process. The thermal performance of a high capacity MSF desalination system was evaluated with the help of three scale inhibitors named as polymaleic, polyphosphonate and polycarboxylates, all of which were effective for both inhibiting alkaline scale formation and improving the top brine temperature. Figure 16.3 shows a schematic diagram of a MSF desalination unit coupled with some power plant (Al-Othman 2019).

Some major advantages of process are that due to recent technological development MSF has become one of the cost efficient processes which can be coupled with various renewable energy resources. Studies have shown that the cost of process has decreased up to 10 folds since 1960s when the process was being introduced (Al-Othman 2019; Gude 2018).

Multi-effect distillation (MED). Multiple effect distillation (MED) is one of the oldest desalination techniques. The system basically consists of pre-heaters, distillation units and condensers in which saline water is being evaporated by preheated multiple tubes surface. The preheating of brine in MED is same as in MSF. The resultant stream is being condensed in tubes at reduced pressure and temperature. Figure 16.4 shows a schematic diagram of MED.

MED technique is also third most adopted technique which has undergone immense developments in past one decade. These improvements include the significant increase in the capacity up to 22,700 m3/day, reduction in the tube scaling through prope2019r design, and improvement of the heat transfer with aluminum for

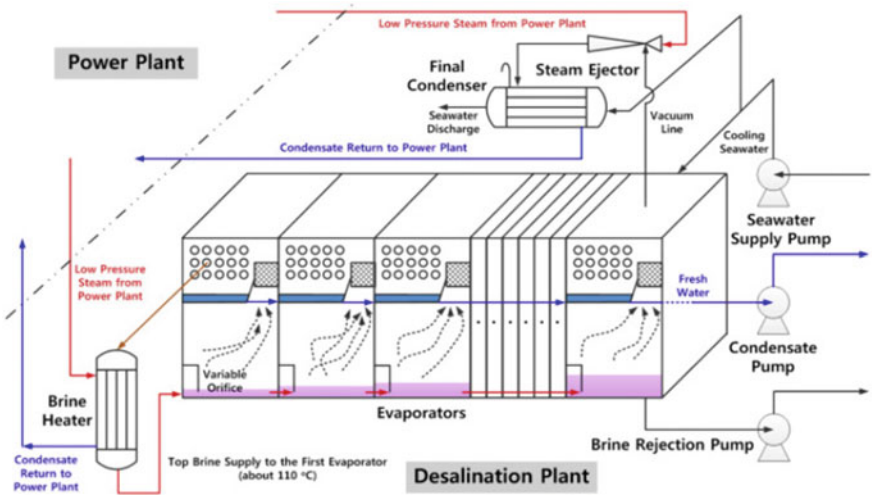

Fig. 16.3 A schematic diagram of MSF Unit (Al-Othman 2019)

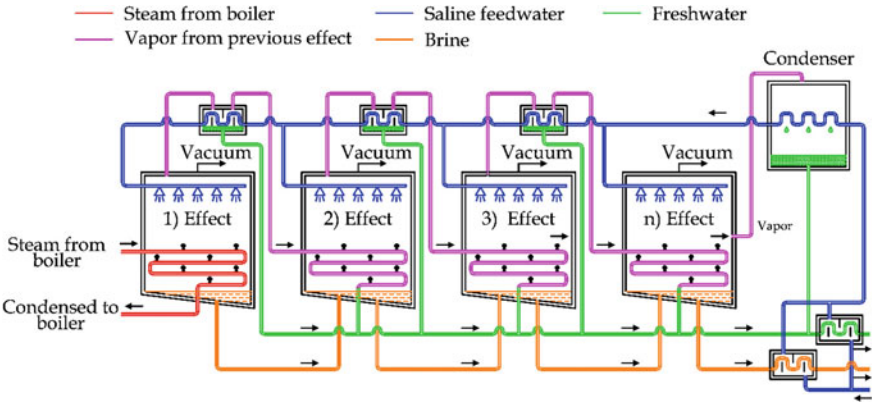

Fig. 16.4 Multi-effect distillation Unit (Curto 2021)

surfaces. Furthermore MED can also be coupled with renewable energy resources as power supply (Al-Othman).

Reverse osmosis (RO). Reverse osmosis is a process of separation salts by using semi-permeable membrane from feed water due to osmotic pressure. Reverse osmosis is the most practicing desalination technique worldwide accounting for 65% of total desalination process. In this process high pressure of 50−80 bar is being applied to separate salts through membrane. RO is one of the most cost efficient techniques for production of potable water which costs 1 USD/m3. The cost of process also depends on the source of energy. A RO system coupled with nuclear energy source has found to be most cost efficient with a cost 0.787 $/m3 (Al-Othman 2019, Fig. 16.5).

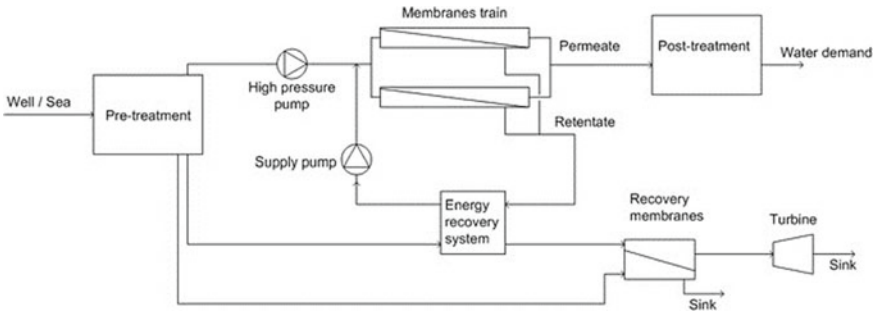

Fig. 16.5 A schematic diagram of Reverse Osmosis desalination plant (Abdallah 2018)

16.2.2 Desalination and Nuclear Energy Resource

Nuclear energy is found to be a major source of efficient energy that can be used to treat sea water especially in nuclear power plants. The energy produced from these power plants can be coupled with thermal desalination units and can further used to treat water. The technique has found to be environment friendly as it can reduce greenhouse gas emission and is also a cost efficient. As the production of electricity with the help of nuclear energy is also increasing during past years, it is also facilitating the desalination practices and its dependence on nuclear resources (Sanchez-Carvera 2013). There are few techniques which are currently working as nuclear reactor techniques to treat sea water which are; pressurized water reactor (PWR), boiling water reactor (BWR), pressurized heavy water reactor (PHWR), gas cooled reactor (GCR) and fast breeder reactor (FBR) (Al-Othman 2019; Alemberti 2014).

Pressurized water reactor (PWR). The pressurized water reactors (PWR) generally works with light water i.e. the coolant is in the form of H2O. In this system nuclear heat is generated and is further transferred with the help of steam generators in secondary power circuit (Khan 2018). In this type of reactor controlling pressure is found to be a key feature of reactor for its safety as well as functioning. This pressure is being controlled by a pressurizer in the pressure vessel (Ahmad 2014). Some major types of PWRs are AP1000 (Alonso 2012), The AP-600 (Nisan 2003), The French PWR—900 (Nisan 2003) and HPR1000 (Xing 2016).

Heavy water reactor (HWR). A heavy water reactor (HWR) works on the principle of using isotope of water. These reactors use heavy water as coolants and are moderated with the help of pressurized water reactor, hence can be called as pressurized heavy water reactors (PHWR). In these reactors fuel is places in hundreds of pressure tubes instead of a single pressure vessel. HWRs represent around 10.5% of the total operating systems. Furthermore, in this type of reactor natural uranium is being used as fuel which can also be refilled (Ahmad 2014, Table 16.1).

Table 16.1 PWR nuclear reactor desalination and their capacity (Al-Othman 2019)

Reactor type and desalination process	Net electricity production (MW)	Net water production (m3/day)
AP1000 RO	957.25	1,100,000
AP1000 MSF	1568.83	1,000,000
AP1000 MED	1919.75	1,040,000
IRIS RO	1188.80	1,040,000
IRIS MSF	1028.08	1,000,000
IRIS MED	1348.50	1,100,000
IRIS MSF-RO	1180.80	1,040,000
IRIS ED-RO	1389.00	1,100,000

16.2.3 DEEP Analysis

The desalination economic evaluation program (DEEP Code) was initially developed in 1980s by IAEA to evaluate desalination plant. The earliest version of DEEP code was called "the Co-generation and Desalination Economic Evaluation spreadsheet". DEEP code is a user friendly approach that has ability to approach multipart excel module which can evaluate three different power plants i.e. power plant, desalination plant and coupling system. The economic feasibility of a power plant working can be evaluated by various criteria including "Levelized Cost of Electricity (LCOE)". LCOE is often used to compare the generations of electricity generating technologies. It involves several parameters such as the capital costs, operating and maintenance cost, fuel cost, and carbon tax. A general process of LCOE is being discussed in equation given below;

$$LCOE = \frac{Life\ cycle\ cost\ (\$)}{Lifetime\ energy\ production\ (kWh)} \tag{16.1}$$

As shown in Table 16.2, nine major parameters are being assessed to evaluate total capital cost, operating cost and maintenance cost of unit. The capital cost includes expenditure during construction and start of processing of unit. While operating and maintenance cost includes carbon taxes, maintenance cost and fuel cost (either renewable or nonrenewable energy resource). A pressurized water reactor possesses higher capital while lowest maintenance and fuel cost.

The DEEP analysis was being carried out by assuming basing cost involved in the process based on cost and capacity of plant. The parameters assumed of DEEP analysis shown that RO system possesses lowest cost of 800$/ m3/day to desalinate 60,000 m3/day water. On the other hand MED and MSF are respectively high cost desalination processes as shown in Table 16.3.

Table 16.2 Input parameters for nuclear power plants comparison by using DEEP code

DEEP Item	Unit	PWR-600	PWR-900	PHWR-600	PHWR-900
Power plant output	MW€	600	900	676	875
Net thermal efficiency	%	31.5	33	23.8	32.2
Availability	%	90	90	95	95
Construction lead time	Months	60	72	52	50
Specific O&M cost	$/MW.h	11	9	6.8	6.3
Fuel cost	$/MW.h	5	8.5	2.4	2.3
Lifetime	Year				
Discount/interest rate	%	8	8	8	8
Seawater temp	°C	30	30	30	30
TDS	ppm	45,000	45,000	45,000	45,000
Management cost	$/year	60,000	60,000	60,000	60,000
Labour cost	$/year	30,000	30,000	30,000	30,000

Table 16.3 Desalination processes assumption for DEEP calculation

Desalination process	Base unit cost US $/(m3/d)	Desalination plant capacities m3/d
RO	800	60,000
MED	900	60,000
MSF	1800	60,000

16.3 Results

In this study a desalination Economic Evaluation Program (DEEP) analysis was conducted to carry out economic analysis for the reactors (PWR-600, PWR-900, PHWR-600 and PHWR-900) to generate power of up to 1000 MW(e). For this purpose the water production cost was estimated for three commonly used desalination techniques which are MED, MSF and RO. DEEP analysis verified the capital and marginal costs used in analysis which is being shown in Table 16.2.

As discussed in Sect. 1, nuclear energy coupled desalination power plants are among most cost efficient techniques which is being proved by DEEP analysis of the study. The results have shown that a PHWR-600 powered nuclear plant showed the consumption of lowest power cost that is 0.018 ($/kWh) followed by PHWR-900, PWR-600 and PWR-900 respectively. The DEEP analysis study of water cost also showed that PHWR-600 powered RO plant is most cost efficient technique among all other as shown in Table 16.4.

Table 16.4 Results of DEEP calculation

Power source	Water cost ($/m3)			Power cost ($/kWh)
	MED	MSF	RO	
PWR-600	0.87	1.08	0.79	0.032
PWR-900	0.91	1.17	0.82	0.039
PHWR-600	0.69	0.93	0.63	0.018
PHWR-900	0.71	1.04	0.64	0.023

16.4 Conclusion

The study clearly showed that desalination through nuclear power supply is one of the most environmental friendly technique. Despite of the production of hazardous waste (which can be properly disposed of) nuclear desalination is found to be best technique to deal with water crisis of Saudi Arabia and other arid regions. Another positive impact of technique is that it has ability to produce clean power with no carbon foot prints. For this purpose the water production cost was estimated for three commonly used desalination techniques which are MED, MSF and RO. The DEEP analysis of MED, MSF and RO coupled with various nuclear power reactors has shown that PHWR-600 coupled RO unit is one of the most cost efficient technologies with a longer time span.

As it is clear from results that during current time of water scarcity, a reverse osmosis system coupled with nuclear power reactor is proved to be highly cost efficient and easy to operate facility which can help to cope up with stress condition. The facility is highly cost efficient and the major cost that is in the form of power supply can be managed by coupling it with renewable energy resources which needs a comparatively high capital cost but low maintenance or running cost which makes it cumulatively energy and cost efficient technique. On the other hand other distillation plants also shows some promising positive impacts in the form of being reliable and longer working life span which make technique,ore suitable to overcome water stress in arid or semiarid areas. Multi-effect distillation (MED) is second highly practiced technique worldwide after RO. The technique has found to be highly cost efficient and furthermore can treat highly saline water (i.e. in the form of produced water). The technique is found to be a cost efficient in the case of energy consumption, easy to installed and simple to operate. On the other hand a currently rising practice of hybrid desalination is found to be effective to deal with highly polluted or saline water. In this technique RO plant is being coupled with distillation plant (i.e. MSF or MED). Both techniques by working together can produce high quality fresh water on lower and reasonable cost which is also being shown in above DEEP analysis.

Recommendations

The current study was conducted to find out cost analysis of installing nuclear desalination units in Kingdom of Saudi Arabia, a land rich with fossil fuel reservoirs. As the area study explained that the region is going through immense water stress due to

its arid and semi-arid nature, hence it is recommended to conduct further cost benefit analysis of coupling desalination units with smaller/medium nuclear desalination units to cope up energy crisis and also to provide continuous supply of fresh water. The feasibility study based on safe installation of nuclear energy based power plant which can better deal with water scarcity in the region.

References

Abdallah AAHA (2018) Probability of nuclear desalination for the usage with economical incentives and future prospects. Am J Constr Build Mater 2(1):1–9

Abdelkareem MA (2018) Recent progress in the use of renewable energy sources to power water desalination plants. Desalination 435:97–113

Ahmed SA (2014) Small/medium nuclear reactors for potential desalination applications: Mini review. Korean J Chem Eng 31(6):924–929

Alemberti A (2014) Overview of lead-cooled fast reactor activities. Prog Nucl Energy 77:300–307

Ali A (2018) Membrane technology in renewable-energy-driven desalination. Renew Sustain Energy Rev 81:1–21

Al-Othman A (2019) Nuclear desalination: a state-of-the-art review. Desalination 457:39–61

Alonso G (2012) Alternatives of seawater desalination using nuclear power. Nucl Eng Des 245:39–48

Chandrasekharam D (2018) Water for the millions: focus Saudi Arabia. Water-Energy Nexus 1(2):142–144

Curto D (2021) A review of the water desalination technologies. Appl Sci 11(2):670

Eke J (2020) The global status of desalination: An assessment of current desalination technologies, plants and capacity. Desalination 495:114633

Elsaid K (2020) Environmental impact of desalination technologies: A review. Sci Total Environ 748:141528

Fanak Water Homepage, https://water.fanack.com/saudi-arabia/water-resources-in-ksa/, last accessed 2021/11/29.

Ghazaie, S.H. (2019). Nuclear desalination in Iran, current status and perspectives. In E3S Web of Conferences 140, 04001

Google Maps https://www.google.com/maps/place/Saudi+Arabia/@23.9552296,36.0327705,5z/data=!3m1!4b1!4m5!3m4!1s0x15e7b33fe7952a41:0x5960504bc21ab69b!8m2!3d23.885942!4d45.079162, last accessed 2021/11/29.

Gude VG (2018) Use of exergy tools in renewable energy driven desalination systems. Therm Sci Eng Prog 8:154–170

Hasanean H (2015) Rainfall: features and variations over Saudi Arabia, a review. Climate 3(3):578–626

Jones E (2019) The state of desalination and brine production: A global outlook. Sci Total Environ 657:1343–1356

Khan SUD (2018) In renewable energy powered desalination handbook, nuclear energy powered seawater desalination. Butterworth-Heinemann.

Khan SUD (2021) Socio-Economic and environmental impact of nuclear dsalination. Water 13(12):1637

Mansouri NY (2017) Does nuclear desalination make sense for Saudi Arabia? Desalination 406:37–43

National Water Strategy (2030) Ministry of environment, water and agriculture. last accessed 2021/11/29.

Nisan S (2003) Sea-water desalination with nuclear and other energy sources: the EURODESAL project. Nucl Eng Des 221(1–3):251–275

Okampo EJ, Nwulu N (2021) Optimisation of renewable energy powered reverse osmosis desalination systems: A state-of-the-art review. Renew Sustain Energy Rev 140:110712
Polat MF, Dincer I (2018) Comparative evaluation of possible desalination options for Akkuyu nuclear power plant. In: Exergetic, Energetic and Environmental Dimensions 583–596
Sánchez- IG, Kavvadias KC, Khamis I (2013) DE-TOP: A new IAEA tool for the thermodynamic evaluation of nuclear desalination. Desalination 321:103–109
Xing J, Song D, Wu Y (2016) HPR1000: advanced pressurized water reactor with active and passive safety. Eng 2(1):79–87

Chapter 17
The Correlation between Water Eutrophication and Sediment Pollution in the Process of Black Odors Water Treatment: A Case Study of the Ximing River and Keli River in Nanning, China

Yang Yunan, Zhang Congcong, Liu Xinyu, Xiong Lin, Zhu Hongxiang, and Chen Yongli

Abstract Water body black odor is an extreme manifestation of water eutrophication. Phosphorus and nitrogen in sediment are important sources of water eutrophication. In order to evaluate the correlation between eutrophication degree of urban river water body and sediment pollution in the process of black and odorous water treatment in Nanning, eutrophication index method and nitrogen and phosphorus comprehensive pollution index method are used to evaluate the water body and sediment of only 15 monitoring sections in research area. The results show that after three years of treatment, there is a strong correlation between the eutrophication degree of water body and the pollution status of sediment, that is, the eutrophication of water body is mesotrophic section, the sediment is clean or slightly polluted, and the consistency between the area with severe eutrophication and the area with severe or moderate sediment pollution is 100%. On the other hand, it shows that water pollution will bring sediment pollution. With the implementation of treatment engineering measures, the improvement of water quality will also reduce sediment pollution, the water bodies of Ximing River and Keli River are mainly nitrogen pollution, but the pollution degree of Keli river is more serious than that of Ximing River. We should strengthen the treatment of nitrogen and phosphorus pollution in the Keli River. The measures include the construction of onshore rainwater run off reduction and control facilities and coastal aquatic plant planting.

Y. Yunan (✉) · Z. Congcong · L. Xinyu
School of Space and Environment, Beihang University, Beijing 100191, China
e-mail: yangyn@buaa.edu.cn

X. Lin
CAUPD Planning & Design Consultants CO, Beijing 100044, China

Z. Hongxiang
Institute of Environmental Science, Guangxi University, Nanning 530004, China

C. Yongli
Guangxi Bossco Environmental Protection Technology Co. Ltd., Nanning 530007, China

H.-Y. Jeon (ed.), *Sustainable Development of Water and Environment*,
Environmental Science and Engineering,
https://doi.org/10.1007/978-3-031-07500-1_17

Keywords Black odors water treatment · Water etrophication index method · Sediment comprehensive pollution index method · TN · TP

17.1 Introduction

River water eutrophication is a phenomenon that human activities lead to excessive input of pollutants into the river, resulting in deterioration of water body, decline of aquatic biodiversity and destruction of the stability of water ecosystem. Sediment is an important part of river ecosystem. Sediment is not only the destination of some water pollutants, but also an important source of water eutrophication. Studying the content of phosphorus and nitrogen in river sediment and its pollution evaluation has important guiding significance for controlling black odor, eutrophication and ecosystem restoration (Cooper 1993; Smith et al. 1999; Zhao et al. 2018).

In this study, the section of Ximing River and Keli River of Guangxi University for Nationalities in the black and odorous water treatment demonstration area of Nanning, Guangxi Province is selected as the research area. Ximing River is a tributary of Yongjiang river and a flood discharge channel of the city. As a natural ecological element in Nanning, it forms a public and Open Waterfront Landscape Belt in combination with the river section where the water body meets Yongjiang river. Keli River is the second largest tributary in the North West embankment on the North Bank of Yongjiang river. Its functions are mainly flood discharge, flood storage and landscape rest, taking into account the functions of transportation and shipping. Before the treatment in 2017, the water quality of Ximing River and Keli River was seriously polluted, which had always been inferior to class V water body, and the main pollution sources were domestic sewage and aquaculture wastewater. In this study, TN, TP and COD_{Mn} in water bodies and TP and TN contents in sediment of Ximing River and Keli River in December 2019 and October 2020 were monitored, and water eutrophication, nitrogen and phosphorus pollution in sediment and their correlation in the study area were evaluated, so as to provide basis for the evaluation of urban black and odorous water treatment effect.

17.2 Materials and Methods

17.2.1 Sampling Section Setting and Sample Collection

Based on the previous water area data investigation, this study fully investigates and theoretically analyzes the geographical situation of the study area, and determines the monitoring location and section after comprehensively considering the location of the sewage outlet and the type of wastewater discharged. Ten sampling sections are set in the Ximing River of Nanning, Guangxi, and five sampling sections can be selected in the section of Keli River of Guangxi University for Nationalities

Fig. 17.1 Sampling Section Distribution of Ximing River (Left) and Keli River of Guangxi University for Nationalities Section (Right). *Note* (Left): L1 Luowen Reservoir, L2 Ring highway, L3 University for Nationalities, L4 University Road south side, L5 the north of Changtaixicheng, L6 Jiangbei entrance, R1 Hewu Reservoir, R2 Luowenpoguxiaopu, R3 Luowenxiangsi Lake North Intersection, R4 the northeast of Changtaixicheng. *Note* (Right): 1. Background point, 2. Start point 1, 3. Turning point 1, 4. Turning point 2, 5. East gate of Guangxi University for Nationalities

section. The specific locations of sampling sections are shown in Figs. 17.1 and 17.2. DEM data comes from Google Earth data with a spatial resolution of 10 m. In addition, according to the implementation of the project of Nanning black odors water treatment demonstration area and the impact of local climate factors in dry and rainy seasons, and considering the continuity of sampling period, the sampling time is December 2019, and water samples and sediment samples are collected at each monitoring section at the same time.

17.2.2 Monitoring Methods for Physical and Chemical Properties of Water Quality

Water samples shall be collected in accordance with water quality technical regulation on the design of sampling programmes (HJ495-2009) and with reference to Water quality sampling-technical regulation of the preservation and handling of samples (HJ493-2009). When collecting water samples from the river, it is generally taken 0.2~0.5 m below the water surface in the middle of the river section. When the section is open, the monitoring section shall be added, and the bank monitoring section shall be set at the place where the water flow is unobstructed. Select appropriate and clean sampling equipment for water sample collection and storage. The sampling volume of each monitoring section is more than 500 ml, indicating the number, sampling place and sampling time. After cryopreservation, it shall be transported back to the laboratory as soon as possible for sample analysis and testing. Water

Table 17.1 Water quality monitoring items and methods

Monitoring indicators	Monitoring methods and sources	Instrument and model used
TN	Water quality alkaline potassium persulfate digestion ultraviolet spectrophotometry	Ultraviolet spectrophotometer uv-1800
TP	Ammonium molybdate spectrophotometry	Ultraviolet spectrophotometer uv-1800
COD_{Mn}	Water quality determination by COD_{Mn} method	

quality monitoring items include TN, TP and COD_{Mn}. The monitoring methods of each index are shown in Table 17.1.

17.2.3 Determination of Physical and Chemical Properties of Sediment

According to the technical specification for soil environmental monitoring (HJ/T166-2004) to collect samples and preserve soil samples. When collecting the river sediment, take the surface sample, with the sampling amount of about 500 g, and put it into a clean sampling bag, indicating the number, sampling place and sampling time. Conical sampler, drill sampler and suspension sampler can be used in the sampling process. The sediment samples are brought back to the laboratory for pretreatment, including air drying, grinding, screening, mixing and preservation. The specific operation is to lay a thin layer of sediment samples on tin foil and place them in the drying room for ventilation and air drying. The air-drying time is about 3 days. After the samples are air dried, plant residues and stones are removed, and the samples are ground with a ceramic mortar to make them all pass the sieve with an aperture of 1 mm, clean sample bags shall be packed and sealed, and labels shall be affixed to indicate the sample number, sampling place, mud sample name, sampling date and other information for subsequent experiments.

The main determination items of sediment are TP, TN and moisture. The determination method is shown in Table 17.2. In order to ensure the accuracy of data, two parallel tests are made for each sample, and the data is taken as the average value.

17.2.4 Evaluation Method

Evaluation method of water eutrophication index The water eutrophication assessment method realizes the continuous classification of the nutritional status of river water quality through a number of indicators comprehensively affecting the

Table 17.2 Determination method of physical and chemical properties of sediment

Monitoring indicators	Method name	National standard no./instrument used
TP	Alkali fusion molybdenum antimony resistance Spectrophotometry	HJ632-2011
TN	Ultraviolet spectrophotometry	
Dry matter and moisture	Gravimetric method	HJ613-2011

water environment. The specific index calculation formula and classification standards are as follows (Technical specification requirements for environment quality assessment of surface water 2011).

$$\mathrm{TLI}(\Sigma) = \Sigma(\mathrm{j} = 1)\text{^}\mathrm{mWj} \cdot \mathrm{TLI(j)} \tag{17.1}$$

where, TLI (Σ) comprehensive nutritional status index of polluted areas; In this study, the correlation weights of TN, TP and COD_{Mn} were 0.33, 0.34 and 0.33 respectively; TLI (j) is the nutritional status index of the j-th parameter. The nutritional status index formula of TP, TN and COD_{Mn} is: W_j

$$\mathrm{TLITP} = 10(9.436 + 1.624\ \ln \mathrm{TP}) \tag{17.2}$$

$$\mathrm{TLTN} = 10(5.453 + 1.694\ \ln \mathrm{TN}) \tag{17.3}$$

$$\mathrm{TLI(COD)_{Mn}} = 10(0.109 + 2.66\ \ln \mathrm{COD_{Mn}}) \tag{17.4}$$

The grading judgment of water nutritional status evaluation is shown in Table 17.3.

Comprehensive pollution index evaluation method The pollution status of nutrients *i* in sediment was evaluated by single pollution index *Pi*. The calculation formula of *Pi* is

$$\mathrm{Pi} = \mathrm{Ci/Coi} \tag{17.5}$$

Table 17.3 TLI evaluation grade of water nutritional status

TLI (∑)	<30	30~50	50~60	60~70	>70
Index grade	Oligotro-phic	Mesotrophic	Mild eutrophication	Middle eutrophication	Severe eutrophication

Table 17.4 Comprehensive pollution assessment and classification of sediment

Grade	PTN	PTP	F_{co}	Grade
1	<1.0	<0.5	<1	Clean
2	1.0~1.5	0.5~1	1~1.5	Light pollution
3	1.5~2	1~1.5	1.5~2	Moderate pollution
4	>2	>1.5	>2	Severe pollution

where, $Pi > 1$ indicates that the evaluation factor i exceeds the evaluation standard value, Ci is the measured concentration of nutrients i in sediment samples, Coi is the standard value of environmental assessment. The standard values of TN and TP are 670 m/kg and 440 mg/kg respectively (Zhang 2019).

The calculation formula of comprehensive pollution index evaluation method is:

$$F_{co} = \sqrt{(((F_i)\text{^}2 + (F_{\text{imax}})\text{^}2)/2)} \tag{17.6}$$

where, F_{co} is the comprehensive pollution index, Fi is the average value of single pollution index, F_{imax} is the largest single pollution index. Table 17.4 shows the classification of comprehensive pollution assessment of sediment (Wu and Gu 2019).

17.3 Results and Analysis

17.3.1 Engineering Measures for Black and Odorous Water Treatment

In order to eliminate black odor, the dredging project of Ximing River was carried out in 2018, and a sewage treatment station with a daily treatment capacity of 15000 m^3/d by SBR process was built at the downstream of R3 Luowenxiangsi Lake North Intersection of the right branch of Ximing River at the end of December of the same year, Sewage is collected at 1 monitoring section at the upstream of Guangxi University for Nationalities section of Keli River by building sewage interceptors. AO + ACM and ACM + denitrification filter processes are used for treatment between monitoring Sects. 17.1 and 17.2 respectively, with a treatment capacity of 2500 t/d, and the effluent quality meets the class I B standard. At the same time, the river sediment will be desilting in April 2018 and the clean water will be replenished in early 2019.

17.3.2 Evaluation Method of Water Eutrophication Index

River water eutrophication is a phenomenon that human activities lead to excessive input of pollutants into the river, resulting in deterioration of water body, decline of aquatic biodiversity and destruction of the stability of water ecosystem. Therefore, the evaluation method of water eutrophication index is applied to the treatment and monitoring of Ximing River and Keli River of Guangxi University for Nationalities section, so as to judge and warn the degree and trend of river eutrophication in time. According to the monitoring values of TP, TN and COD_{Mn} sampled from different sections, the results of water nutritional status of Ximing River and Keli River of Guangxi University for Nationalities section in the black and odorous water treatment demonstration area calculated by the water eutrophication index evaluation method are shown in Tables 17.6, 17.7 and 17.8.

The monitoring results from December 2019 to October 2020 show that the Ximing River is mainly nitrogen pollution, and the TN of all monitoring sections exceeds the standard, the left branch exceeds the standard by 1.58–3.22 times and 1.33–4.18 times respectively, and the right branch exceeds the standard by 1.38–7.25 times and 1.28–5.64 times respectively. The content range of total phosphorus in the left branch of Ximing River is 0.03~0.20 mg/L and 0.05~0.15 mg/L respectively, and all sections meet class III standards, the contents of total phosphorus in the right branch of Ximing River are 0.08~0.55 mg/L and 0.05~0.38 mg/L respectively. Except that the northeast of Changtaixicheng exceeds the standard, other sections

Table 17.6 Assessment results of water eutrophication in the left branch of Ximing River

Time	No	TP	TLI_{TP}	TN	TLI_{TN}	COD	TLI_{COD}	Eutrophi-cation index	Eutrophication degree
2019.12	L1	0.12	59.38	1.58	62.28	7.57	54.93	59.06	Mild eutrophication
	L2	0.20	68.22	1.62	62.70	7.57	54.93	62.02	Middle eutrophication
	L3	0.03	37.41	2.28	68.49	0.61	-12.06	31.34	Mesotrophic
	L4	0.03	37.41	2.84	72.21	0.78	-5.42	34.73	Mesotrophic
	L5	0.13	61.23	2.56	70.45	2.00	19.53	50.51	Mild eutrophication
	L6	0.12	59.93	3.22	74.34	1.65	14.41	49.66	Mesotrophic
2020.10	L1	0.08	53.34	1.33	59.36	3.42	33.80	48.88	Mesotrophic
	L2	0.15	63.55	1.44	60.71	3.39	33.56	52.72	Mild eutrophication
	L3	0.05	45.71	1.94	65.76	2.23	22.42	44.64	Mesotrophic
	L4	0.05	45.71	2.03	66.52	1.35	9.07	40.49	Mesotrophic
	L5	0.07	51.17	4.18	78.76	1.85	17.45	49.15	Mesotrophic
	L6	0.10	56.97	3.14	93.91	1.09	3.38	44.88	Mesotrophic

Table 17.7 Eutrophication evaluation results of right branch of Ximing River

Time	No	TP	TLI_{TP}	TN	TLI_{TN}	COD	TLI_{COD}	Eutroph-ication index	Eutrophication degree
2019.12	R1	0.08	53.34	1.38	59.99	7.39	54.29	55.85	Mild eutrophication
	R2	0.16	64.60	1.39	60.11	7.74	55.52	60.12	Middle eutrophication
	R3	0.55	84.65	7.25	88.09	7.91	56.10	76.36	Severe eutrophication
	R4	0.16	64.60	6.39	85.95	2.52	25.68	58.80	Mild eutrophication
2020.10	R1	0.05	45.71	1.28	58.71	4.77	42.65	48.99	Mesotrophic
	R2	0.12	59.93	1.48	61.17	5.77	47.71	56.31	Mild eutrophication
	R3	0.38	78.65	5.64	83.83	7.06	53.08	71.92	Severe eutrophication
	R4	0.12	59.93	1.53	61.73	1.87	17.74	46.60	Mesotrophic

Table 17.8 Evaluation results of water eutrophication in Keli River of Guangxi University for nationalities section

Time	No	TP	TLI_{TP}	TN	TLI_{TN}	COD	TLI_{COD}	Eutrophication index	Eutrophication degree
2019.12	1	3.62	115.25	44.47	118.81	22.00	83.31	105.89	Severe eutrophication
	2	0.43	80.65	23.56	108.05	8.96	59.42	82.69	Severe eutrophication
	3	0.28	73.69	10.75	94.76	6.70	51.69	73.38	Severe eutrophication
	4	0.40	79.48	9.74	93.09	5.65	47.15	73.30	Severe eutrophication
	5	0.51	83.42	11.78	96.31	10.70	64.14	81.31	Severe eutrophication
2020.10	1	2.98	112.09	35.80	115.14	10.88	64.58	97.42	Severe eutrophication
	2	0.23	70.49	14.53	99.87	6.39	50.43	73.56	Severe eutrophication
	3	0.20	68.22	11.74	96.25	6.87	52.35	72.24	Severe eutrophication
	4	0.20	68.22	7.62	88.93	4.99	43.85	67.01	Severe eutrophication
	5	0.17	65.58	6.32	85.76	2.98	30.14	60.54	Severe eutrophication

are within class III standard. The monitoring results of COD_{Mn} show that in October 2020, except that the northeast of Changtaixicheng, the right branch, exceeded the standard, the water quality of the two tributaries of Ximing River reached the class III standard of surface water. In terms of time, after nearly three years of treatment, the water quality of the black odor water treatment demonstration area in Nanning, Guangxi has improved, and the eutrophication degree of the left branch of the Ximing River has changed from moderate and mild eutrophication to mild and moderate eutrophication. The right branch of Ximing River is heavily eutrophic, and the monitoring section is R3 Luowenxiangsi Lake North Intersection, and the eutrophication index decreases from 76.36 to 71.92, and the two slightly eutrophic sections turn to mesotrophic state, indicating that the content of nutrients in the water body of these monitoring sections decreases. Based on the monitoring results and the investigation of pollution sources, it is analyzed that the excessive TN and TP in the sediment is mainly caused by the deposition of non-point source pollutants around the section after entering the water body. In terms of space, the increasing trend of pollution is obvious, In December 2020, except R3 section of Ximing River except for heavy pollution (Luowen Xiang Si Lake North Intersection), the sediment of other river sections is in the state of medium nutrition or light pollution. Section R4 is in the state of medium nutrition, which is related to the sewage treatment plant with a daily treatment capacity of 15000 m^3/d by SBR process built downstream of section R3 Luowenxiangsi Lake North Intersection. The sewage treatment plant reduces the point source and non-point source pollution around section R3.

The monitoring results of Keli River of Guangxi University for Nationalities section in December 2019 and October 2020 show that the pollution is mainly N and P pollution, and the N pollution is more serious. Therefore, controlling nitrogen and phosphorus in the river is the main goal to avoid the deterioration of water quality. TN of all monitoring sections exceeds class III standard, and the exceeding multiple is 9.74–44.47 and 6.32–35.80 times respectively. Total nitrogen includes dissolved nitrogen in water and nitrogen in suspended solids. It is mainly composed of dissolved ammonia, inorganic ammonium salt, nitrite, nitrate and nitrogen in organic nitrogen-containing compounds. It is one of the important indicators to characterize the degree of water eutrophication. Total nitrogen is the main limiting factor of eutrophication, according to the internationally recognized critical concentration of eutrophication proposed by Qing (TN is 0.20 mg/L) it can be seen that the Keli River can provide sufficient nitrogen for algae growth. If the hydrodynamic conditions are poor, temperature and light are appropriate, it can promote the growth and reproduction of algae, and the water body is at risk of eutrophication, the total phosphorus content ranges from 0.28 to 3.62 mg/L and 0.17 to 2.98 mg/L respectively, and 90% of the sections exceed the class III standard of surface water, the monitoring results of COD_{Mn} show that in 2020 October, except that the background point exceeded the standard, COD_{Mn} in the section of Keli River of Guangxi University for Nationalities section reached or approached 6.00 mg/L of class III standard for surface water. At the same time, it shows that after nearly three years of treatment, although the section of Keli River of Guangxi University for Nationalities section is still highly eutrophic, the eutrophication index shows a downward trend and the water quality is improved.

17.3.3 Analysis of Comprehensive Pollution Index Evaluation Results

The calculation results of comprehensive pollution index of nitrogen and phosphorus in sediment of Ximing River and Keli River of Guangxi University for Nationalities section are shown in Tables 17.9, 17.10, 17.11. By comparing with the pollution assessment classification in Table 17.4, it can be seen that the bottom mud pollution of Ximing River is better than that of Keli River of Guangxi University for Nationalities section as a whole.

According to the monitoring results twice in December 2019 and October 2020, the variation range of W (TP) in the sediment of the left branch of Ximing River is 307~620 mg/kg and 236~411 mg/kg respectively. The variation range of W (TN) was 382~1220 mg/kg and 193~944 mg/kg, respectively. The single pollution index of TP and TN ranges from 0.5 to 1.4 and 0.3 to 1.9. The variation range of W (TP) in the sediment of the right branch of Ximing River is 307~941 mg/kg and 263~612 mg/kg respectively. The variation range of W (TN) was 566~1456 mg/kg and 106~1243 mg/kg respectively. The single pollution index of TP and TN ranges from 0.60 to 2.14 and 0.16 to 2.17.

The results show that in December 2019, the sediment of the left and right branches of the Ximing River is heavily polluted only by nitrogen and phosphorus at the Luowenxiangsi Lake North Intersection, the rest of the total phosphorus is moderately and slightly polluted, and most of the total nitrogen is clean or slightly polluted. The pollution level of TP in sediment is higher than that of TN, indicating that phosphorus pollution is more serious than nitrogen pollution. The comprehensive pollution index evaluation results show that after nearly three years of treatment, the sediment pollution of Ximing River is consistent with the water body, and shows a better trend in time change. Along the way, the increasing trend of pollution is obvious, In December 2020, except R3 section of Ximing River except for moderate pollution, the sediment of other river sections is clean or slightly polluted. R4 section is clean because a sewage treatment station with a daily treatment capacity of 15000 m^3/d using SBR process has been built at the downstream of R3 Luowenxiangsi Lake North Intersection, which reduces the pollution of domestic sewage from the periphery of R3 section.

It can be seen from Table 17.11 that according to the monitoring results twice in December 2019 and October 2020, the variation range of w(TP) in the sediment of Guangxi University for Nationalities section of Lijiang River is 821~1846 mg/kg and 647~1078 mg/kg respectively, variation range of w(TN) was 1327~2464 mg/kg and 1579~2087 mg/kg, respectively. The single pollution indexes of TP and TN range from 1.47 to 4.20 and 1.98 to 3.68. The results show that the TN and TP in the sediment of Guangxi University for Nationalities section of Keli River are seriously polluted except that Sect. 5 is moderately polluted, and the nitrogen pollution is more serious than phosphorus pollution.

Table 17.9 Evaluation results of comprehensive pollution index of sediment in the left branch of Ximing River

Time	No	TP	P_{TP}	Class of pollution	TN	P_{TN}	Class of pollution	F_{co}	Comprehensive pollution of sediment
2019.12	L1	307	0.70	Light	412	0.61	Clean	0.68	Clean
	L2	503	1.14	Moderate	784	1.17	Light	1.16	Light
	L3	540	1.23	Moderate	549	0.82	Clean	1.13	Light
	L4	620	1.41	Moderate	1220	1.82	Moderate	1.72	Moderate
	L5	387	0.88	Light	382	0.57	Clean	0.81	Clean
	L6	467	1.06	Moderate	823	1.23	Light	1.19	Light
2020.10	L1	236	0.54	Light	193	0.29	Clean	0.48	Clean
	L2	368	0.84	Light	262	0.39	Clean	0.73	Clean
	L3	410	0.93	Light	629	0.94	Clean	0.94	Clean
	L4	363	0.83	Light	753	1.12	Light	1.05	Light
	L5	391	0.89	Light	944	1.41	Light	1.29	Light
	L6	411	0.93	Light	823	1.23	Light	1.16	Light

Table 17.10 Evaluation results of comprehensive pollution index of sediment in the right branch of Ximing River

Time	No	TP	P_{TP}	Class of pollution	TN	P_{TN}	Class of pollution	F_{co}	Comprehensive pollution of sediment
2019.12	R1	307	0.70	Light	566	0.84	Clean	0.81	Clean
	R2	508	1.15	Moderate	1033	1.54	Moderate	1.45	Light
	R3	941	2.14	Severe	1456	2.17	Severe	2.16	Severe
	R4	631	1.43	Moderate	689	1.03	Light	1.34	Light
2020.10	R1	263	0.60	Light	106	0.16	Clean	0.50	Clean
	R2	480	1.09	Moderate	944	1.41	Light	1.33	Light
	R3	612	1.39	Moderate	1243	1.86	Moderate	1.75	Moderate
	R4	439	1.00	Moderate	658	0.98	Clean	0.99	Clean

Table 17.11 Evaluation results of comprehensive pollution index of Keli River of Guangxi University for nationalities section

Time	No	TP	P_{TP}	Class of pollution	TN	P_{TN}	Class of pollution	F_{co}	Comprehensive pollution of sediment
2019.12	1	1354	3.08	Severe	2464	3.68	Severe	3.53	Severe
	2	1462	3.32	Severe	2061	3.08	Severe	3.26	Severe
	3	1846	4.20	Severe	2139	3.19	Severe	3.95	Severe
	4	1644	3.74	Severe	2370	3.54	Severe	3.69	Severe
	5	821	1.87	Severe	1327	1.98	Modera-te	1.95	Moderate
2020.10	1	1078	2.45	Severe	2087	3.11	Severe	2.95	Severe
	2	928	2.11	Severe	1637	2.44	Severe	2.36	Severe
	3	937	2.13	Severe	1596	2.38	Severe	2.32	Severe
	4	912	2.07	Severe	1738	2.59	Severe	2.47	Severe
	5	647	1.47	Moderate	1579	2.36	Severe	2.15	Severe

The evaluation results of sediment comprehensive pollution index show that after nearly three years of treatment, the sediment pollution of Ximing River is consistent with that of water body. Although the pollution state is severe pollution, the comprehensive pollution index in October 2020 shows an obvious downward trend compared with December 2019, indicating that the degree of sediment pollution is reduced. The water monitoring data of Keli River show that although the sewage treatment station adopts AMC main process, the treatment effect is obvious, so that the total nitrogen concentration in the water body of Guangxi University for Nationalities section of Keli river is reduced by 47~59.4% and TP is reduced by 88.1~92.3%, all monitoring sections after the effluent from the sewage treatment station are still in a state of severe eutrophication. In the field pollution source investigation of Keli River of Guangxi University for Nationalities section, it is found that there are multiple rainwater and sewage outlets in this river section. Therefore, the low control rate of non-point source pollution sources and rainwater overflow are the main causes of nitrogen and phosphorus pollution in Keli River of Guangxi University for Nationalities section, and nitrogen and phosphorus mainly come from external input, In the later stage, the treatment of black and odorous water body in the section of Keli River of Guangxi University for Nationalities section focuses on the control of onshore pollution sources, the adjustment of existing treatment processes, parameter commissioning and the recovery of aquatic plants. At the same time, artificial oxygenation, water replenishment and other measures can also improve the pollution situation of Keli River.

17.3.4 Correlation Analysis Between Eutrophication Degree and Sediment Pollution

Due to the long-term high nutrient load pollution of the black odor river sediment, the sediment can continuously release nutrients to the overlying water, which has become an important external input of the river, and the river that is already in the state of eutrophication continues to deteriorate. Therefore, relevant measures must be taken to treat the heavily polluted sediment. After nearly three years of treatment, the degree of water eutrophication and sediment pollution of Ximing River and Keli River show a high degree of consistency in time and space. The pollution of water and sediment at the bottom of Ximing River is better than that of Keli River of Guangxi University for Nationalities section as a whole. On the one hand, the water eutrophication degree and sediment pollution degree of Ximing River and Keli River are reduced in time. On the other hand, the water eutrophication degree and sediment pollution degree along Ximing River show an obvious increase trend in space, while the water eutrophication degree and sediment pollution degree along Keli River show a gradual decrease. The eutrophication of water body is mesotrophic, and the sediment in the section is clean or slightly polluted. The consistency between the area with severe eutrophication and the area with severe sediment pollution is 90%.

On the other hand, it shows that water pollution will bring sediment pollution, and the improvement of water quality will also reduce sediment pollution.

17.4 Conclusions

The black and odorous river has become the main water environment problem faced by China. The main feature of the black and odorous river is high nitrogen and phosphorus pollution, and the appearance of black and odorous. In this study, the eutrophication index method and comprehensive pollution index method are used to evaluate the correlation between the eutrophication degree of river water body and the nitrogen and phosphorus pollution degree of sediment. The results show that after nearly three years of treatment, the eutrophication degree of Ximing River and Keli River is consistent with the sediment pollution in time and space, the eutrophication of water body is mesotrophic, and the sediment in the section is clean or slightly polluted. The consistency between the area with severe eutrophication and the area with severe sediment pollution is 90%. On the other hand, it shows that water pollution will bring sediment pollution. With the implementation of engineering measures, the improvement of water quality will also reduce sediment pollution.

The water body and sediment of Ximing River are clean or slightly polluted except that the section at the Luowenxiangsi Lake North Intersection is heavily polluted. The pollution degree of water body and sediment in Keli River of Guangxi University for Nationalities section is more serious than that in Ximing River, and the sampling section with severe pollution reaches 90%. In the later treatment, we should strengthen the treatment of nitrogen and phosphorus pollution in the Keli River of Guangxi University for Nationalities section. The measures include the construction of onshore rainwater runoff reduction and control facilities, and nitrogen and phosphorus pollution control technologies such as coastal aquatic plant planting.

Acknowledgements We would like to express our gratitude to the Guangxi Innovation-driven Development Special Fund Project, Research and development of key technologies for pollution control of black and odorous water bodies and improvement of water environment quality (AA17202032).

References

Cooper CM (1993) Biological effects of agriculturally derived surface water pollutants on aquatic systems-a review. J Environ Qual 22(3):402–408

Smith VH, Tilman GD, Nekola JC (1999) Eutrophication: impacts of excess nutrient inputs on freshwater, marine, and terrestrial ecosystems. Environ Pollut 100(1–3):179–196

Technical specification requirements for environment quality assessment of surface water (2011 Trial Version)

The technical specification for soil environmental monitoring (HJ/T166–2004)

Water quality sampling-technical regulation of the preservation and handling of samples (HJ493–2009)
Water quality technical regulation on the design of sampling programmes (HJ495–2009)
Wu XF, Gu J (2019) Characteristics and evaluation of nutrient pollution in the bottom sediment of Qingcao Sha reservoir. Water Purification Technol (Chinese) 38(12):70–73+104
Zhang RG (2019) Distribution and pollution evaluation of nitrogen, phosphorus and organic matter in urban river sediment in Zigong City. Environ Protect Sci Technol (Chinese) 25(05):28–32
Zhao YF, Xu M, Liu Q et al (2018) Study of heavy metal pollution, ecological risk and source apportionment in the surface water and sediments of the Jiangsu coastal region, China: a case study of the Sheyang Estuary. Mar Pollut Bull 137:601–609

Chapter 18
The Research of Correlation Between Distribution of Bacteria and Removal of N, P in EHYBFAS

Y. N. Yang, H. J. Gong, Y. S. Chen, W. B. Jin, and B. Z. Wang

Abstract Pure culture technique was used to analyze the amount, distribution and variation of specifically functional bacteria in enhanced hybrid biofilm-activated sludge biological process (EHYBFAS) of a reconstructed project of Buji Stream in Shenzhen. The level and conversion laws of nutrients were also analyzed combined with water quality. The results showed that the number of bacteria in activated sludge was ten times higher than that in biofilm, and the former dominated the degradation of pollutants in the anoxic phase in EHYBFAS. In the aerobic phase, the function of activated sludge was gradually weakened, and biofilm dominated the final degradation of low concentration pollutants, the bacterial number at the end of biofilm was 10^9–10^{10} cfu/g; in composite reactor pond, the amounts of Phosphorus Accumulating Organisms (PAOs) was 10^5–10^6 cfu/mL. It was better to use EHYBFAS to remove phosphorus than single biofilm. Efficient bacteria dosing helped the system run the quick start. When influent phosphorus concentration was 2–5 mg/L, the system ran stably, and it was positive correlation among the amounts of PAOs, the total phosphorus removal, and the phosphorus content in sedimentation sludge; The amounts of ammonifiers and denitrifying bacteria were much higher than that of nitrobacteria in this system, so they were not the restrictive factor to denitrification; The amounts of nitrobacteria were 102–103 cfu/mL, which caused weak nitrosification and nitrification. Nitrosobacteria and nitrate bacteria alternate between the partial benefit made that the growth of nitrate bacteria was restrained by not enough nitrite substrate, so the nitrosobacteria was the restrictive factor to denitrification of the system.

Keywords Functional bacteria · EHYBFAS · Pure culture · Removal of NP · Buji stream · PAOs · Ammonifiers · Denitrifying bacteria · Nitrosobacteria · Nitrate bacteria

Y. N. Yang (✉) · H. J. Gong · Y. S. Chen
School of Space and Environment, Beihang University, Beijing, China
e-mail: yangyn@buaa.edu.cn

W. B. Jin · B. Z. Wang
Department of Municipal Engineering, Shenzhen Graduate School, Harbin Institute of Technology, Harbin, China

H.-Y. Jeon (ed.), *Sustainable Development of Water and Environment*,
Environmental Science and Engineering,
https://doi.org/10.1007/978-3-031-07500-1_18

18.1 Introduction

Activated sludge and biofilm method were two important types of wastewater biological treatment. For the existing contradictions in single-sludge process, it caused great concern in using composite activated sludge and biofilm process (Liu et al. 2006; Fadi 1999). Enhanced hybrid biofilm-activated sludge biological process (shortened form: EHYBFAS, Patent Number: 200620017991.5) was developed in view of the design which got the good results under the condition of 6 ~ 8 h residence time (Wang et al. 2003; Wang and Wang 2004) in sewage treatment plants using previously submerged biofilm-activated sludge composite process, but had no operation experience under the condition of 3 ~ 4 h residence time. The process was applied to $10^5 m^3/d$ reconstruction project of Buji Stream in Shenzhen. It combined the advantages of activated sludge and biofilm method, which made its micro-ecosystem more complex. If the bacteria in eco-system were studied according to different physiological populations (Wang et al. 2007), it would be clearer about the function of the microbes in aquatic ecosystems, as bacteria and other microbes had irreplaceable places in the process of material cycle, energy flow and information transmission in the ecosystem and different bacterial populations implemented different functions in a variety of ecosystem processes that were composed by a variety of bacterial populations and environmental conditions together. It had important guiding significance for engineering applications to study the ecological distribution, quantity, inter-relationship, role and status of different functional bacteria in the ecosystem process.

In this paper, the traditional pure culture technique was used to research the correlation between the removal efficiency of N, P in water and the number, distribution and variation of the specifically functional bacteria (ammonifiers, nitrobacteria, denitrifying bacteria and poly-P bacteria) which can remove nitrogen and phosphorus. Combined water quality characteristics and transformation rules, the ecological relationship of functional bacteria was preliminary studied in the system. It is designed to provide a theoretical foundation to new process and reference to optimization of operating parameters in practical engineering.

18.2 Materials and Methods

18.2.1 The Introduction of EHYBFAS Wastewater Treatment System

EHYBFAS, with size of 10^5 m^3/d, was applied to water purification technology of Buji Stream in Shenzhen. The total residence time of composite reactor pond was 3.5 h (anoxic phase HRT = 0.5 h, aerobic phase HRT = 3 h). The effluent water quality indicators were needed to meet 1A–1B standard of "The Pollutants Discharge Standards of Municipal Wastewater Treatment Plants" (GB18918-2002).

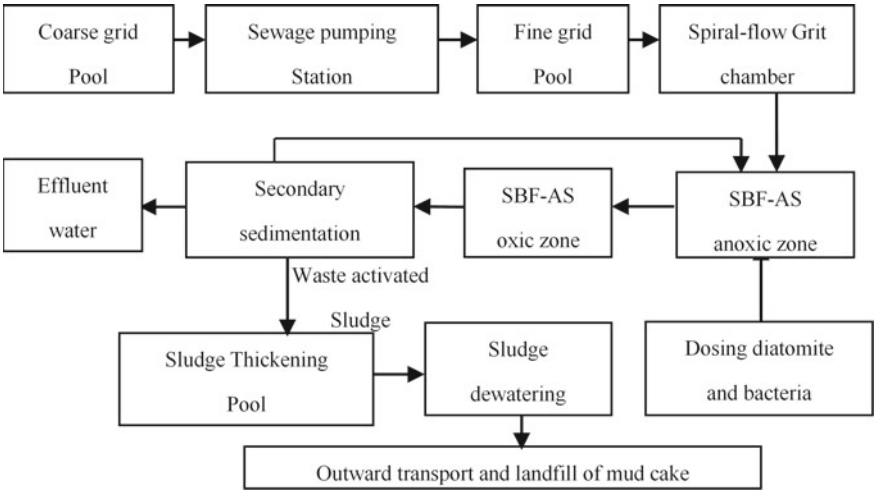

Fig. 18.1 Technological flow chart of EHYBFAS processing system

The process after reform consulted reference (Ma et al. 2002). When the system started running, efficient functional bacteria with nitrogen and phosphorus removal capabilities were dosed to improve the efficiency of wastewater treatment, including the nitrogen cycling bacteria (ammonifiers, nitrobacteria and denitrifying bacteria) and poly-P bacteria, etc. These bacteria added to the anoxic phase after culturing with fermenters were screened in Buji Stream in Shenzhen. The dosage was 10t (10^8–10^9 cfu/mL) for each bacterium. Technological flow chart of EHYBFAS processing system was as Fig. 18.1.

18.2.2 Sampling and Sample Processing

Samples came from ten samplingsites including water samples and biofilm samples. The specific distribution was shown in the Fig. 18.2: 1#: water samples after Fine screen Pool; 2#:activated sludge samples in front of SBF-AS anoxic phase; 3#: biofilm samples in front of SBF-AS anoxic phase; 4#: activated sludge samples at the end of SBF-AS anoxic phase; 5#: biofilm samples at the end of SBF-AS anoxic phase; 6#: activated sludge samples in front of SBF-AS oxic phase; 7#: biofilm samples in front of SBF-AS oxic phase; 8#: activated sludge samples at the end of SBF-AS oxic phase; 9#: biofilm samples at the end of SBF-AS oxic phase; 10#: Water samples after secondary sedimentation pond.

Water samples were obtained by conventional methods. Biofilm samples were chosen from better growth filler which was clipped about 15 cm with scissors. In the laboratory, the filler was washed by sterile water and biofilm was stripped, then diluted 500-fold for standby. Washed filler were weighed after drying by oven (75

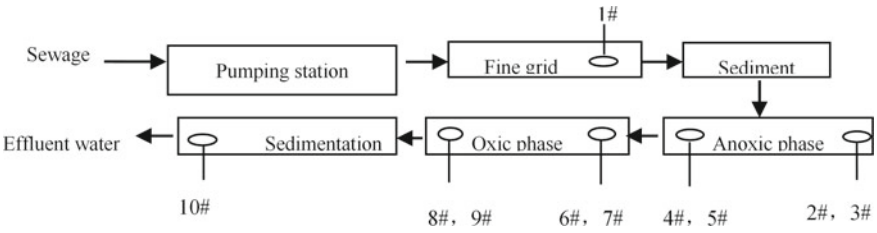

Fig. 18.2 Distributions of samplingsites

°C, 5 h). The sampling date was: the 29th day, the 48th day, the 62th day, the 93th day, the 105th day, and the 120th day. That was two samples and interval was about 2 weeks. Systems were operating normally when sampling.

18.2.3 Culture and Counting of Microbes

It used plate count method to count PAOs (National Environmental Protection Agency 2002) and MPN (most probable number) method (Hu et al. 2002) to assay nitrogen cycling bacteria in activated sludge-biofilm.

18.2.4 Targets and Methods for Water Quality Analysis

National standards promulgated by SEPA were used to determine NH_3-N, TN, TP and so on (Hu et al. 2002).

18.2.5 Unit Conversion

In the same reaction tank, the quantity unit of microbes in biofilm was cfu/g dry filler, while in activated sludge was cfu/mL water. To convert microbe contained in per gram filler into that contained per milliliter volume, conversion relationship could be calculated through the pool capacity and filler density. The relationship was: per gram filler was equal to 500 mL volume.

18.3 Results and Discussion

18.3.1 The Correlation Between Distribution of PAOs in Biofilm or Activated Sludge and Phosphorus Removal

PAOs was the organism which absorbed more phosphorus than it needed for normal growth. PAOs played a decisive role in the biological phosphorus removal. The spatial distribution and changes over time of PAOs in SBF-AS aerobic pond were showed in Table 18.1.

In the same reaction tank, the numbers of PAOs had little difference in biofilm and activated sludge. It was 10^5–10^6 cfu/mL in activated sludge, 10^4–10^6 cfu/mL in biofilm, and 10^5–10^6 cfu/mL in composite reactor pool. This showed uniform spatial distribution of PAOs in different systems, so it could be speculated that both activated sludge and biofilm in EHYBFAS system had contribution to phosphorus removal. The final removal of phosphorus was depended on PAOs absorbed excessive phosphate and released it under anaerobic conditions, and then activated sludge system settled sludge with plenty of phosphorus down; the aerobic environment on the surface of biofilm was suitable for PAOs to absorb phosphorus and biofilm was washed off into sludge by aeration. Both of these could remove phosphorus finally by sludge discharge or right recycle. So, the EHYBFAS with both activated sludge and biofilm was more favorable for biological phosphorus removal, avoiding low efficiency of phosphorus removal in single biofilm and having incomparable advantages compared with single biofilm.

Because PAOs played the decisive role in phosphorus removal and had few differences in the spatial distribution in aerobic pond, the average number of PAOs in the front and at the end of aerobic pond could represent the level of PAOs in the pond, which meant the amount of PAOs both in biofilm and activated sludge. In order to further analyze relationship between the amounts of PAOs and capacity of absorbing phosphorus, the variation of influent and effluent TP was determined in this study. The relationship between TP removal rate and the amounts of PAOs in aerobic

Table 18.1 Distribution of PAOs in the aerobic pond (unit: cfu/mL)

Date	Water samples in front of aerobic pond	Water samples at the end of aerobic pond	Biofilm samples in front of aerobic pond	Biofilm samples at the end of aerobic pond
Sep. 25	2.1×10^5	6.2×10^5	2.6×10^5	8.3×10^5
Oct. 14	1.3×10^6	5.9×10^5	1.7×10^6	7.7×10^4
Oct. 28	1.2×10^6	4.4×10^5	1.6×10^6	6.6×10^5
Nov. 28	6.1×10^5	5.3×10^5	2.5×10^5	1.1×10^5
Dec. 10	8.2×10^5	4.3×10^5	6.8×10^5	2.7×10^5
Dec. 24	2.5×10^6	8.1×10^5	1.5×10^6	3.2×10^5

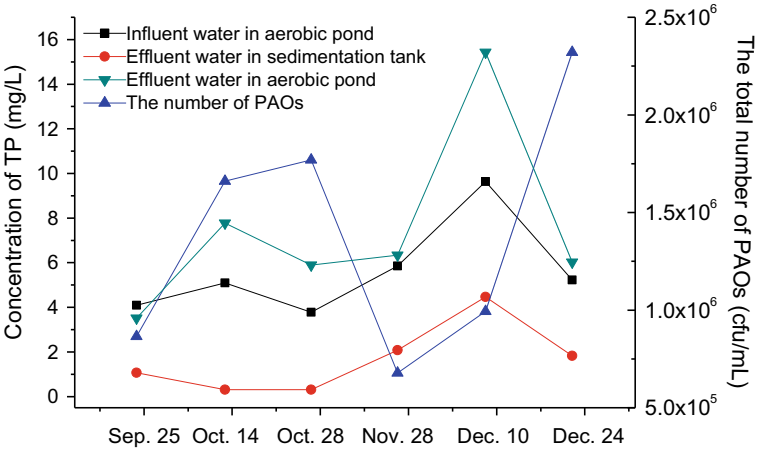

Fig. 18.3 Variation of the amount of PAOs and the concentration of Influent and effluent TP

pond was shown in Fig. 18.3. Figure 18.3 showed, at the prior period of system commissioning, biological phosphorus removal system stabilized soon and maintained a very good treatment effect. The effluent phosphorus concentration remained at 0.5–1 mg/L before the October 28, which met "The Pollutant Discharge Standards of Municipal Wastewater Treatment Plants" (GB18918-2002) 1A–1B standard; in addition, effluent phosphorus concentration was higher than the influent concentration in aerobic pond, the reason might be the anaerobic sludge released phosphorus incompletely. The results determined after November 28 showed that deterioration of the system phosphorus removal with the influent TP concentration increased dramatically, effluent phosphorus concentration was high, and the results of last three times were significantly higher than the first three times, even the influent phosphorus concentration of December 10 was up to 9.68 mg/L. The system was running a serious overload.

The theory was that the change of influent phosphorus concentration affected the growth and multiplication of PAOs, thereby affected the absorption of phosphate, while the amount of phosphorus in the sedimentation tank sludge was closely related to phosphorus that PAOs absorbed.

In order to further analyze the specific relevance, Table 18.2 listed influent TP content, TP utilization, the amounts of PAOs, and changes of TP concentrations in recycle sludge under different times; Table 18.3 analyzed the Correlation coefficient between the amount of PAOs and the water quality characteristics in the entire stage in Tables 18.2 and 18.4 analyzed the correlation coefficient between the amount of PAOs and the water quality characteristics in stable stage (before November 28th) in Table 18.1.

From the correlation of entire stage, there was no substantial correlation between the amounts of PAOs and influent phosphorus concentration, the amount of TP

Table 18.2 Variation of the amount of PAOs and the concentration of influent and effluent TP under different time

Data	Sep. 25	Oct. 14	Oct. 28	Nov. 28	Dec. 10	Dec. 24
Average number of PAOs in aerobic pool (cfu/mL)	9.60×10^5	1.83×10^6	1.95×10^6	7.50×10^5	1.10×10^6	2.57×10^6
TP concentrations in recycle sludge (mg/L)	235.9	466.9	487.3	229.4	577.4	316.9
Influent TP concentrations (mg/L)	4.1	5.1	3.9	5.9	9.7	5.3
TP utilization (mg/L)	2.9	4.7	3.7	3.9	5.2	3.4

Table 18.3 Correlation coefficient between the amount of PAOs and the water quality characteristics in the entire stage

Correlation coefficient	The amount of PAOs	TP concentrations in recycle sludge	Influent TP concentrations	TP utilization
The amount of PAOs (cfu/mL)	1			
TP concentrations in recycle sludge (mg/L)	0.2373	1		
Influent TP concentrations (mg/L)	−0.3121	0.5039	1	
TP utilization (mg/L)	−0.1084	0.7682	0.7705	1

Table 18.4 Correlation coefficient between the amount of PAOs and the water quality characteristics in the stable stage

Correlation coefficient	The amount of PAOs	TP concentrations in recycle sludge	Influent TP concentrations	TP utilization
The amount of PAOs (cfu/mL)	1			
TP concentrations in recycle sludge (mg/L)	0.9993	1		
Influent TP concentration (mg/L)	0.2456	0.2824	1	
TP utilization (mg/L)	0.7301	0.7556	0.8417	1

removal (respectively, −0.3121, −0.1084), but a low correlation with TP concentrations in recycle sludge (0.2373). This was contrary to theoretical speculation, but in fact no contradiction. It could be seen from Table 18.4 that in the period when system was running stably, the amounts of PAOs and TP concentrations in recycle sludge was highly correlated (0.9993), and was also closely related to TP removal rate (0.7301), which fully verified the PAOs' function on the absorption of phosphorus from a macroscopical view; but for a low correlation (0.2456) between PAOs and influent phosphorus, this showed that the change of influent phosphorus concentration affected PAOs less during stable period and the system had a certain resistance to shock load. In practical engineering applications, microbe growth and multiplication were not a stable process, which changed along with nutrient levels change. When the nutrient levels and the amounts of micro-organisms were coupled coordination, the amounts of micro-organisms could reflect the levels of certain substances, but it could not directly reflect the level of pollutants while external conditions changed largely and the micro-ecological environment where micro-organisms lived in was damaged. For the water quality, the influent TP after Nov. 28 was significantly higher than pre-period. This meant phosphorus concentration exceeded the peak load of PAOs. Due to the competitive relationship among microbial populations, PAOs could not multiply indefinitely. PAOs continuously adjusted to adapt to changes in nutrients, so the amounts of PAOs of the latter part was volatile, phosphorus removal system was instable, which was also a direct impact on effluent quality. In addition, it could be seen from Table 18.4 that the amounts of PAOs, the phosphorus concentration in recycle sludge and the amount of TP removal by system were highly correlated, which also verified that the PAOs was the main role to remove phosphorus in EHYBFAS system.

18.3.2 The Correlation Between Distribution of Denitrification Bacteria in Biofilm or Activated Sludge and Nitrogen Removal

The number and distribution of ammonifiers The number, distribution and changes over time of ammonifiers in EHYBFAS technology system were showed in Table 18.5. It could be seen from the table that the amounts of ammonifiers in activated sludge in the anoxic pond and the aerobic pond was kept 10^6–10^7 cfu/mL. Regardless of in front or at the end of the biofilm in aerobic pond, ammonifiers were counted relatively stable at 10^9 cfu/g, but 10^8–10^9 cfu/g in the anoxic pond. The amounts of ammonifiers in the anoxic pond fluctuated in a magnitude over time, while less fluctuations in the aerobic pond, it's almost stable.

It could be seen from the amounts of ammonifiers that the amounts of ammonifiers was always high, whether in activated sludge or biofilm and whether in anoxic pond or aerobic pond. It could be speculated that ammoniation function of ammonifiers was stronger. From the NH_3-N/TN of influent and effluent water in Fig. 18.4, we could

Table 18.5 Distribution of ammonifiers (units: cfu/mL, cfu/g)

Date	Sep. 25	Oct. 14	Oct. 28	Nov. 28	Dec. 10	Dec. 24
Water samples in front of anoxic pond	9.5×10^6	2.5×10^7	4.5×10^7	7.5×10^6	2.5×10^7	2.5×10^7
Biofilm samples in front of anoxic pond	5.1×10^8	9.7×10^7	5.6×10^8	2.3×10^8	3.5×10^9	1.6×10^9
Water samples at the end of anoxic pond	1.5×10^6	1.5×10^7	4.0×10^7	2.5×10^7	2.5×10^7	4.5×10^6
Biofilm samples at the end of anoxic pond	7.4×10^8	1.5×10^9	3.6×10^8	4.3×10^8	2.2×10^9	4.8×10^8
Water samples in front of aerobic pond	9.5×10^6	1.1×10^8	9.5×10^6	2.5×10^7	9.5×10^6	2.5×10^6
Biofilm samples in front of aerobic pond	2.8×10^9	1.8×10^{10}	3.3×10^9	2.5×10^9	4.0×10^9	1.6×10^9
Water samples at the end of aerobic pond	9.5×10^5	4.5×10^7	2.5×10^7	9.5×10^6	9.5×10^6	9.5×10^6
Biofilm samples at the end of aerobic pond	1.6×10^9	4.4×10^8	8.7×10^9	1.1×10^9	7.0×10^9	3.2×10^9

see that NH_3-N/TN in effluent water was significantly higher than that in influent water, which verified that the system had stronger ammoniation function, and it was more than nitrification. For the spatial location and time changes of ammonifiers, fluctuations were not widespread, and that indicated ammonifiers' ecosystem was stable. Location and time changes of ammonifiers in biofilm in aerobic pond were almost keep stable. The main reason of that was that the biofilm's own resistance capacity to shock load, so it's able to adapt to a range of water quality change. Another reason was that the degradation of organic nitrogen in anoxic pond eased impact on the aerobic pond by water quality changes.

Quantity and distribution of nitrobacteria Nitrobacteria, including nitrosobacteria and nitrate bacteria, belonged to the autotrophic bacteria. In EHYBFAS process, the main place to complete the nitrification process was aerobic phase, so this study measured distribution of nitrosobacteria and nitrate bacteria in aerobic phase in SBF-AS composite reactor, as shown in Table 18.6. From Table 18.6 we could see that the amounts of nitrosobacteria in aerobic pond was about 10^3–10^4 cfu/mL in activated sludge, and was about 10^5–10^6 cfu/g in biofilm; the amounts of nitrate bacteria in aerobic pond was about 10^2–10^3 cfu/mL in activated sludge with higher in the front than the end, and was about 10^5–10^6 cfu/g in biofilm.

Compared to the microbe number of other microbial community, the amounts of nitrosobacteria and nitrate bacteria was less, the main reason was that nitrobacteria was autotrophic bacteria, had long generation time, slow growth and multiplication, and there was competition in the system which also had a large number of heterotrophic bacteria. From the influent and effluent quality in Fig. 18.5 we could see that the system was running under a high concentration of NH_3-N; NH_3-N and TN concentration in effluent water was always high which was difficult to

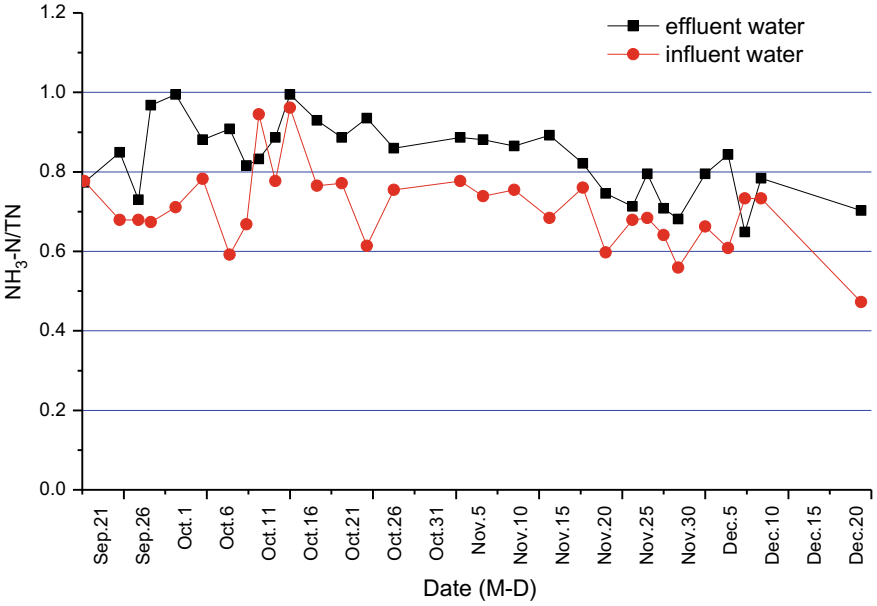

Fig. 18.4 Variation of influent and effluent NH_3-N/TN

achieve primary standard of municipal wastewater treatment plants. This indicated that the system had not complete denitrification, which was also verified by the low number of nitrate bacteria. As the change of time, concentration of NH_3-N and the water temperature should have some change, while nitrosobacteria were not showed regular changes. Three possible reasons: Firstly, as Shenzhen's sub-tropical climate, temperature maintained above 20 °C generally, the changing range was not much, which had little impact on nitrate bacteria; Secondly, the system had very adequate nitrogen source, so the changes of nitrogen source did not directly affect the growth of nitrate bacteria; the most likely reason might be that the competition between nitrate bacteria and heterotrophic bacteria inhibited the growth of nitrate bacteria.

As the nitrosobacteria was inhibited, the ability of ammonia oxidizing into nitrite reduced greatly. It also limited the growth of nitrate bacteria because nitrite was the nutrient source to nitrate bacteria and made the low number of nitrate bacteria and even lower than the amounts of nitrosobacteria; because of weak nitrification in anoxic pond, the NO_2^- accumulated invisibly in the front was higher than the end in aerobic pond, so this made the nitrate bacteria number in the front is slightly higher than the end in aerobic pond.

Quantity and distribution of denitrifying bacteria Denitrifying bacteria was heterotrophic, facultative anaerobes. The final step of denitrification was the nitrate reducing into nitrogen gas by denitrifying bacteria under hypoxic condition. In the EHYBFAS process, denitrification might exist in activated sludge in SBF-AS anoxic phase on the one hand, on the other might exist in the biofilm both in the anoxic

Table 18.6 Distribution of the nitrosobacteria and the nitrate bacteria in the aerobic pond

Date	Water samples in the front of aerobic pond (cfu/mL)		Biofilm samples in the front of aerobic pond (cfu/g)		Water samples at the end of aerobic pond (cfu/mL)		Biofilm samples at the end of aerobic pond (cfu/g)	
	Nitroso bacteria	Nitrate bacteria	Nitroso bacteria	Nitrate bacteria	Nitroso bacteria	Nitrate bacteria	Nitroso bacteria	Nitrate bacteria
Oct. 14	9.5×10^4	9.5×10^3	2.5×10^6	2.5×10^5	4.5×10^4	4.5×10^3	7.8×10^6	7.8×10^6
Oct. 28	7.5×10^4	1.5×10^3	6.0×10^5	1.3×10^5	9.5×10^3	9.5×10^2	1.8×10^6	1.8×10^6
Nov. 28	1.5×10^3	7.5×10^3	2.5×10^6	1.6×10^5	4.5×10^2	9.5×10^2	1.1×10^6	5.1×10^5
Dec. 10	1.5×10^4	9.5×10^3	2.4×10^5	7.2×10^5	2.5×10^3	4.5×10^3	2.3×10^5	1.5×10^6
Dec. 24	1.5×10^4	1.5×10^4	1.6×10^6	2.6×10^6	9.5×10^3	4.5×10^4	5.3×10^6	2.0×10^7

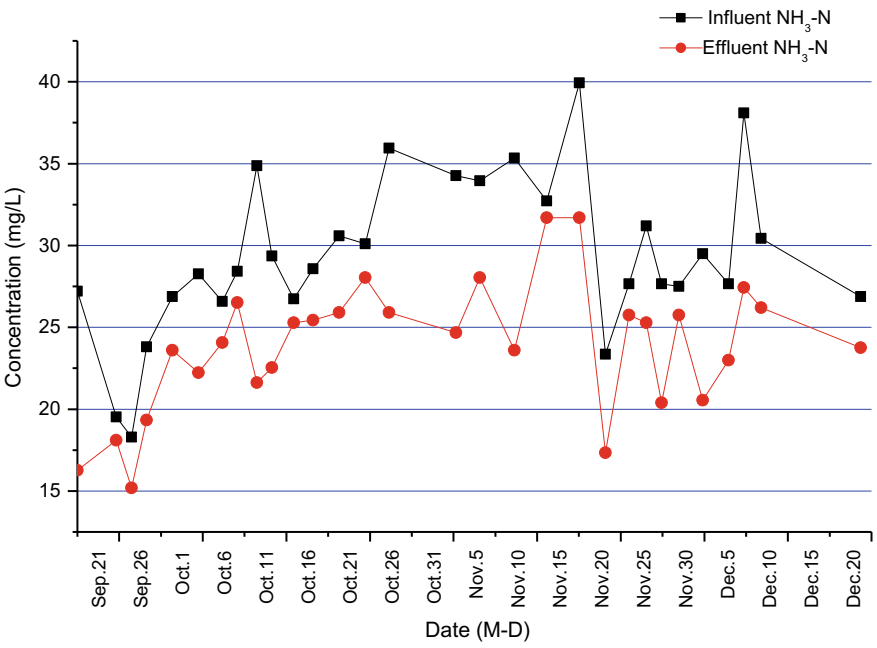

Fig. 18.5 Variation of influent and effluent NH_3-N

pond and aerobic pond. So, the amounts of denitrifying bacteria were determined before and after the aerobic pond and in raw water. Results showed that the amounts of denitrifying bacteria before and after aerobic pond were 10^4 cfu/mL, equal to the quantity in raw water, which described the weak denitrification in sludge in aerobic pond. The distribution of denitrifying bacteria in activated sludge and biofilm in anoxic phase was determined, as shown in Table 18.7. As could be seen from Table 18.7, the denitrifying bacteria quantity in activated sludge in anoxic pond was 10^4–10^5 cfu/mL; it was 10^6–10^8 cfu/mL in biofilm both in anoxic pond and aerobic pond. The number of denitrifying bacteria was significantly higher than nitrobacteria's, mainly because denitrifying bacteria were heterotrophic bacteria, which was easier growth and multiplication than nitrobacteria. At the same time, denitrifying bacteria were also facultative bacteria. They grew under aerobic conditions with oxygen as electron acceptor. This also indicated that the denitrification was better than nitrification in the system.

Generally speaking, denitrifying bacteria changed in a less extent. Because of the restrictions on the amounts of nitrobacteria in system, nitrate content in water was low, with concentration of about 0.3–0.5 mg/L. So, the reducing action of denitrifying bacteria with nitrate as the electron acceptor was relatively small, while they were easier to maintain their own growth and degradation of organic matter with oxygen as an electron acceptor under the aerobic conditions. Therefore, due to the lack of oxygen in anoxic pond, denitrifying bacteria were more inclined to use nitrate as

Table 18.7 Distribution of the denitrifying bacteria

Date	Influent water samples in anoxic phase (cfu/mL)	Effluent water samples in anoxic phase (cfu/mL)	Biofilm samples before anoxic phase (cfu/g)
Oct. 14	2.5×10^5	2.5×10^5	9.7×10^6
Oct. 28	2.5×10^5	4.5×10^4	1.2×10^6
Nov. 28	9.5×10^5	2.5×10^5	7.0×10^6
Dec. 10	4.5×10^5	7.5×10^4	1.3×10^7
Dec. 24	2.5×10^5	1.5×10^5	1.6×10^7
Average	4.3×10^5	1.5×10^5	9.4×10^6
	Biofilm samples after anoxic phase (cfu/g)	Biofilm samples before aerobic phase (cfu/g)	Biofilm samples after aerobic phase (cfu/g)
Oct. 14	2.4×10^6	7.6×10^7	7.8×10^6
Oct. 28	1.4×10^6	1.3×10^7	1.8×10^6
Nov. 28	4.3×10^6	7.4×10^6	2.3×10^7
Dec. 10	3.5×10^6	7.2×10^6	2.3×10^7
Dec. 24	4.8×10^6	4.3×10^7	3.2×10^7
Average	3.3×10^6	2.9×10^7	1.8×10^7

electron acceptor for breeding, while the nitrate content was limited, which restricted denitrifying bacteria to multiply indefinitely. In aerobic pool, biofilm had both aerobic environment and anoxic environment, so denitrifying bacteria had two parts: one grew with nitrate as the electron acceptor, and another grew with oxygen as an electron acceptor. Organic matter had a greater impact on growth of denitrifying bacteria. Water quality in the front of aerobic pool changed a lot, so the amounts of denitrifying bacteria changed greatly, too. But at the end of the aerobic pond, organic matter was relatively stable, and the relative shortage of carbon source, so the change was relatively small.

Table 18.7 showed that the amounts number of denitrifying bacteria in the biofilm in aerobic pond was significantly higher than that in anoxic pond, for two main reasons: Firstly, nitrate accumulates as nitrification occurred in aerobic pond so that denitrification worked in inner layer of anoxic biofilm; secondly, denitrifying bacteria didn't do total denitrification and part of them did aerobic respiration under aerobic conditions. The number of denitrifying bacteria in the biofilm in aerobic pond was higher than that in anoxic pond. In anoxic pond, nitrate was the main electron acceptor for denitrifying bacteria due to anoxic environment. The amount of nitrate in the front of anoxic pond was higher than that at the end because of back flow, and denitrifying bacteria grew more easily, so the amounts of denitrifying bacteria both in activated sludge and biofilm in the front of anoxic pond were all higher than that at the end, which also showed that growth of denitrifying bacteria at the end of anoxic pond was inhibited due to the lack of nitrate.

18.4 Conclusion

In composite reactor pond, the amounts of PAOs were 10^5–10^6 cfu/mL. It was better to use EHYBFAS to remove phosphorus than single biofilm. Efficient bacteria dosing helped the system run the quick start. When influent phosphorus concentration was 2–5 mg/L, the system ran stably with a certain resistance to shock load, and it was positive correlation among the amounts of PAOs, the total phosphorus removal, and the phosphorus content in sedimentation sludge; while influent phosphorus concentration increased to 6–10 mg/L, the system deteriorated.

The amounts of ammonifiers and denitrifying bacteria were not the restrictive factor to denitrification, the nitrosobacteria was the restrictive factor to denitrification of the EHYBFAS system. In anoxic pond of EHYBFAS system, nitrate was the main electron acceptor for denitrifying bacteria to do denitrification. Because of the lack of nitrate, the amounts of denitrifying bacteria had small changes over time; denitrification was better in front than that in the end. Part of denitrifying bacteria did denitrification, and part of them did aerobic respiration in the biofilm in aerobic pond, which made the amounts of denitrifying bacteria in the biofilm in aerobic pond be significantly higher than them in the biofilm in anoxic pond. The lack of nitrate was a key factor for denitrifying bacteria to do denitrification.

Acknowledgements We would like to express our gratitude to the Guangxi Innovation-driven Development Special Fund Project, Research and development of key technologies for pollution control of black and odorous water bodies and improvement of water environment quality (AA17202032).

References

Fadi G (1999) Activated sludge biofilm wastewater treatment system. Water Res 33(1):230–238

Hu ZR, Wentzel MC, Ekama GA (2002) Anoxic growth of phosphate-accumulating organisms (PAOs) in biological nutrient removal activated sludge systems [J]. Water Res 36(19):4927–4937

Liu S, Wang BZ, Wang L et al (2006) Full scale application of combined SBF-AS process for municipal wastewater treatment in small towns and cities in China. J Harbin Inst Technol 3:51–55

Ma F, Ren NQ, Yang JX (2002) Microbiology experiments of pollution control [M]. Harbin Institute of Technology Press (in Chinese), Harbin

National Environmental Protection Agency (2002) Monitoring and analysis methods of water and wastewater [M], 4th edn. China Environmental Science Press (in Chinese), Beijing

Wang BZ, Wang D, Li GQ et al (2003) Water and environment series [M]. IWA Publishing, USA

Wang SM, Wang BZ, Cao XD et al (2007) Reconstruction of coagulation and sedimentation system of Bujihe wastewater treatment plant in Shenzhen City [J]. China Water Wastewater (in Chinese) 23(6):23–27

Wang BZ, Wang L (2004) Novel technologies on water pollution control-new concept, new processes and new theories [M]. Beijing Science Publishing House

Chapter 19
Hybrid Membrane-Thermal Seawater Desalination Engineering: Typical Technology Development and Future Prospects

Jianmei Xu, Jianbo Ren, Chungang Xie, Chunhua Qi, and Min Wang

Abstract Hybrid desalination systems are usually defined as combining two or more desalination technologies in order to achieve combined features of these technologies. Due to the high plant availability, good operational flexibility and water matching ability with lower specific energy consumption, hybrid configurations have attracted growing attention in recent years. Various hybrid systems have been developed, such as thermal distillation/membrane desalination hybrid system, and desalination/electricity co-generation system. In this review, it surveys several typical hybrid membrane-thermal desalination systems, including blending the products of the thermal and membrane process, reverse osmosis (RO) feeding by brine reject of the thermal desalination process, integrating system of nanofiltration (NF) as water pre-treatment method for thermal desalination processes, and hybrid FO membrane/thermal desalination systems, etc. In addition, pervaporation (PV) and membrane distillation (MD) as novel hybrid membrane-thermal technology are introduced.

Keywords Hybrid systems · Thermal desalination · Membrane desalination

19.1 Introduction

Water crisis has become one of greatest issues facing all over the world. As the accessible fresh water on earth continues to decline, it is imperative to find ways to produce fresh water from natural water resources (Zhu et al. 2019; Cosgrove and Loucks 2015; IDA 2020; World Health Organization (WHO) 2011; Haddad 2018; Singh 2015). In some places of the world that are surrounded by seas and oceans, seawater desalination has offered a promising strategy to alleviate the water shortages and meet the growing water demand from human activities (Thimmaraju et al. 2019; Gude 2016; Shatat and Riffat 2014; Ekea et al. 2020). However, desalinating seawater

J. Xu (✉) · J. Ren · C. Xie · C. Qi · M. Wang
The Institute of Seawater Desalination and Multipurpose Utilization, Ministry of Natural Resources (MNR), NO. 55 Hanghai Road, Nankai District, Tianjin, PR China
e-mail: xujianmei_0402@126.com

H.-Y. Jeon (ed.), *Sustainable Development of Water and Environment*,
Environmental Science and Engineering,
https://doi.org/10.1007/978-3-031-07500-1_19

comes at a high cost. The research trend is seeking low-cost technologies to reduce the cost and promote the development and industrialization of desalination.

Desalination techniques are mainly categorized into membrane desalination technology and thermal desalination technology. In the thermal desalination system, firstly, saline water is heated to produce water vapor by phase separation method, and then condensed to produce freshwater. This technology mainly includes multi-effect distillation (MED), multi-stage flash distillation (MSF), and vapour compression evaporation (VC).Compared with other desalination technologies, thermal desalination offers significant savings in operational and maintenance costs.

The quality of desalinated water could be in a high-level purification. Generally, the total dissolved solids (TDS) of the desalinated water reaches $\leq$10 mg/L. The plants are normally operated at higher temperatures for improving efficiency. However, it also has some disadvantages. If the excessive salts such as calcium sulphate and calcium carbonate precipitate on the tubes surfaces, the mechanical problems like tube clogging will happen. The residual heat generated during the distillation process ended up being taken away by the cooling water.

The membrane processes mainly consist of reverse osmosis (RO), nanofiltration (NF), and forward osmosis (FO). Since membrane systems are compact, smaller spaces for installation required comparing with other desalination systems (Bruggen 2018). Meanwhile, there is no a phase change in the membrane processes involve the separation, the energy requirements are relatively low (Misdan et al. 2012; Ahmad 2020). Due to their modular design, the maintenance and expansion of these systems are simple. Furthermore, many membrane systems are fully automated, and the start-up and shutdown procedure controlled by interlocks automatically. However, there are some shortcomings of the membrane desalination. On the one hand, the TDS of the RO product water is about $\leq$500 mg/L (Awerbuch 2011), for some special needs, it is not clean enough. On the other hand, the performance of the RO membrane is sensitive to the temperature of the feed water. Besides, nanofiltration has limited applications for separating divalent ions.

Considering the advantages and disadvantages of thermal and membrane methods, the advanced and integrated hybrid membrane/thermal systems could be a good way to provide a lower water cost and more efficient system by increasing the seawater recovery, decreasing energy wasted of thermal desalination, and improving the productivity of membrane desalination etc.

19.2 Typical and Novel Hybrid Desalination Systems

19.2.1 Blending the Products of the Thermal and Membrane Processes

For eliminating the requirement of a second-pass RO process, the early hybrid desalination was suggested as combine higher-salinity desalinated water of first-pass RO process with the better-quality desalinated water from thermal plant. The hybrid MSF/RO desalination power process is the simplest and most widely application (Bloushi et al. 2018). The combination of seawater RO plant with either a new or existing dual-purpose thermal/power plant, offers the following advantages: (1) Blending technology can meet the highest TDS and chloride concentration of drinking water standards due to higher salinity of SWRO plant products. (2) Blending membrane with distillate desalinated water could reduce requirements on Boron removal by RO. (3) The blending water quality can maintain at a suitable and stale level. (4) Blending of RO permeate can reduce temperature of distillate from MSF/MED plants. (5) The RO membrane life can be extended effectively. Besides, some thermal desalination plants were built together with power plants (Hamed 2005; Almulla et al. 2005). Excess power production from the desalting complex can be reduced significantly, or the power-to-water ratio can be drastically decreased. Compared with thermal-only or RO-only option, this kind hybrid systems offers significant savings of energy costs. The example diagram of this kind hybrid desalination system is shown in Fig. 19.1.

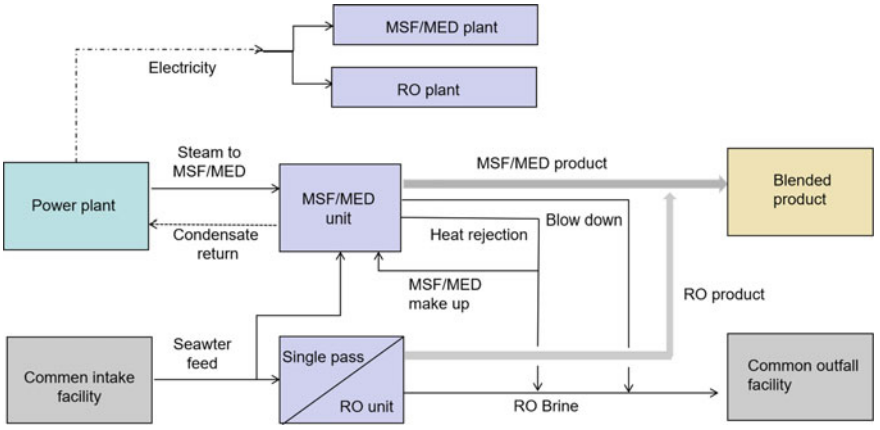

Fig. 19.1 Schematic diagram of commercially RO and MSF/MED hybrid desalination plants with power plant (Ekea et al. 2020)

19.2.2 RO Feeding by Brine Reject of the Thermal Desalination Process

Another important hybrid membrane-thermal desalination system involves using the rejected brine from the thermal desalination process as feed water for RO process. Examples include using all or partial of the preheated cooling seawater discharged from the heat-reject section of the MSF/MED or power plant condenser, blending brine reject of the thermal desalination process, as feed to a SWRO plant (Bloushi et al. 2018). As the temperature of preheated seawater leaving the heat rejection of the MSF distiller or the last effect of the MED plant increased, the operating temperature of the RO plant could be elevated and controlled at its optimal value (Marcovecchio et al. 2005; Farsi and Dincer 2019). For most of the membranes, water flux could be influenced by feed temperature. With the feed water increasing one degree, the water flux/production will improve 1.5–3% at a constant feed pressure (Darre and Toor 2018). On the condition that maintain being given permeate capacity, the number of RO membrane modules will be reduced, and the service life of membrane could be extended (Bloushi et al. 2018; Cardona and Piacentino 2004). As a result, investment will be cut down. Moreover, recovery ratio is one of the key RO design parameters. It determines the size of the feed water handling system. High water flux enables recovery ratio to be higher for reducing consumption of energy and chemicals. On the other hand, the low-pressure steam from the MSF/MED plant is used to de-aerate or use de-aerated brine as a feedwater to the RO plant to minimize corrosion and reduce residual chlorine. In addition, some parts of seawater pre-treatment process and post-treatment system can be integrated. This is also a way for reducing the cost (Fig. 19.2).

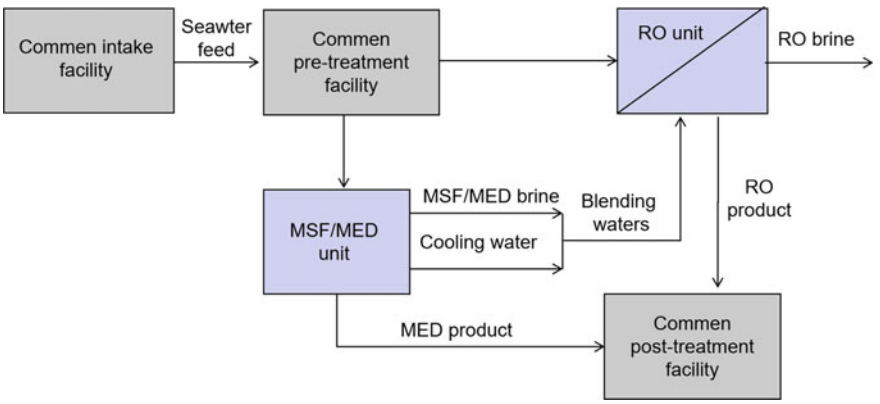

Fig. 19.2 Schematic diagram of the typical RO feeding by brine reject of the thermal desalination process

19.2.3 Integrating System of NF as Water Pre-treatment Method for Thermal Desalination Processes

NF membrane has the feature of high rejection for divalent ions (Ca^{2+}, $Mg^{2+}$and SO_4^{2-}). The hybridization of NF membrane as softening membrane process for feed of distillation plants could improve the productivity and reduce cost of the desalination plants effectively (Zhou et al. 2015). Compared with feed water containing a higher concentration of hardness ions, the hardness concentration of softened stream by NF membrane treatment is sufficiently reduced. As a result, the risk of scaling and fouling could be eliminated significantly. By that means, the top brine temperature (TBT) of the distillation desalination process can be raised. Higher operating temperatures improves productivity, recovery and performance with lower energy and chemical consumption (Turek 2003). Thus, the cost of desalinated water production consist of operation and maintenance could be drastically decreased.

Extensive evaluation tests of 20 m^3/d MSF pilot plant coupled with NF pretreatment system were carried out by the Research & Development Center (RDC) in Al-Jubail (Hamed 2005). Their result showed that the TBT could reach 130ºC, without injection of scale control additive over a period of 1200 h and the product recovery ratio was up to 70%, twofold than that of the conventional operated MSF desalination plants (Hamed et al. 2003).

Compared with MSF, the major potential advantage of the MED process is the ability to produce a significantly higher gain output ratio (GOR) in excess of 16 pounds of the product per pound of steam, where MSF limits GOR to 11 (Awerbuch 2011). Thus, the MED system possesses a great potential for water cost reduction (Fig. 19.3).

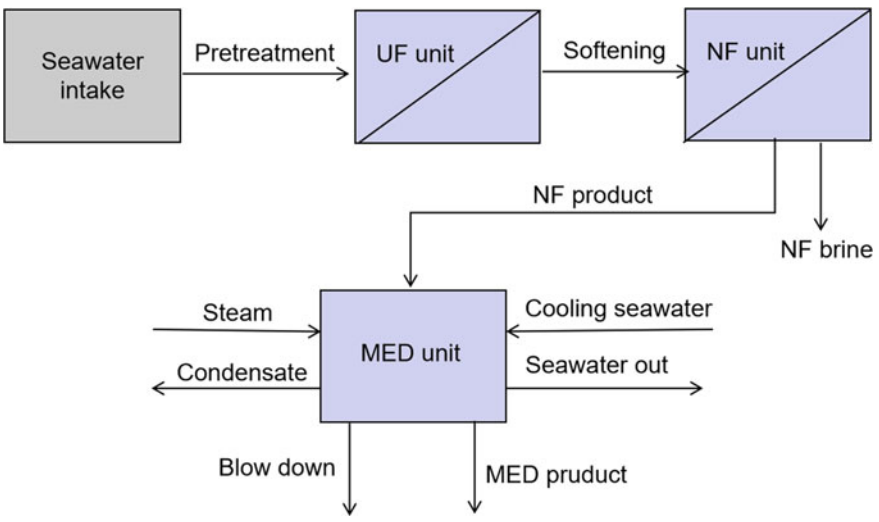

Fig. 19.3 Schematic diagram of hybrid NF/MED desalination system

19.2.4 Hybrid FO Membrane/Thermal Desalination Systems

As a mature low-energy desalination method, the FO process can hybridize the existing desalination technologies, especially thermal desalination systems. Being able to remove divalent ions from MSF/MED feeding water, FO membrane process has also been widely applied as a pre-treatment technique. In this process, seawater as extraction liquid passing though the FO system, it will be diluted as MSF feed water. As the divalent ions have been reduced, the evaporation temperature of the thermal desalination plants will be increased. Some researches show that, using FO to remove $CaSO_4$ from the MSF feed which will allow the desalination temperature to be greater than 110 °C (Jain 2021; Arjmandi 2020). There are many advantages of FO-MED/MSF hybrid systems. Firstly, the productivity of the thermal plants will increase, which will reduce the desalination cost of the entire system and save energy. Meanwhile, the chemical additives dosing will decrease effectively Ang (2019a, b). Another hybrid strategy between FO and MSF/MED is using the concentrated brine of MED/MSF as extraction liquid of the FO system. By the heated extraction liquid, the water flux of the FO process will increase (Ndiaye and Bounahmidi 2019; Darwish and Hassan 2016). Furthermore, the concentrated brine of the MSF/MED process could be reused, and the treatment cost will be cut down.

19.2.5 Novel Hybrid Membrane-Thermal Desalination Systems

Traditional membrane processes are driven by pressure. However, with the development of membrane technology, membrane processes which driven by thermal have become attractive in seawater desalination treatment, such as pervaporation (PV) and membrane distillation (MD). Especially, as the novel kinds of hybrid membrane-thermal technology, MD and PV make the most of waste heat from industrial processes or renewable heat from solar or geothermal energy to separate water from seawater at 40–75 °C (Deka 2021; Lu 2019; Deshmukh 2018). MD, as a thermally-driven separation process, has been extensively studied for desalination (Afsari et al. 2021; Boo et al. 2016). The MD membrane is a type of porous-medium membrane, it can allow the water vapor passing through and reject other substances. In MD plant, the water vapor is fully hold in a chamber. Increasing the vapor pressure to drive the molecules passing through the MD membrane. And then, the vapor encounters a cool space or device surface and condenses into liquid. The driving force in the MD process is the vapor pressure difference induced by the temperature difference across the membrane. Differently, in a typical PV process, a liquid mixture contacts with the pervaporation membrane and desorbs at the permeate side (Warsinger et al. 2014; Mejia Mendez 2018). The chemical potential between the feed side and permeate side of the PV membrane is the mass transfer of permeate

by thermal driven. Thus, the membranes properties including materials, affinity, nanostructure and charge density is important.

MD and PV are suitable for processing the source water with high TDS and they are more resistant to membrane fouling (Xue 2020; Liang et al. 2015). With the incorporation of MD and PV membranes with high water flux, the generation of brine can be effectively suppressed (Wang et al. 2016) Thus, MD and PV can be used for desalination brine treatment. Therefore, MD and PV technologies can be fully utilized to treat the brine from thermal desalination and membrane desalination in the future.

19.3 Conclusions

This review analyzed the characteristics of thermal and membrane technologies, and outlined the typical hybrid desalination systems based on membrane and thermal distillation processes. In the future, further advancements of hybrid systems involving thermal desalination processes (MSF and MED) and reverse osmosis process with nanofiltration/forward osmosis pretreatment should be initiated. Especially, MD and PV as the novel kinds of membrane-thermal hybrid systems are worth more attention to develop.

Acknowledgements This work was supported by Central-Level Research Institutes Fundamental Research Team Project (K-JBYWF-2019-T03); Science and Technology Assistance Project for National Key Research and Development Project (2018YFC040800204).

References

Afsari M, Shon HK, Tijing LD (2021) Janus membranes for membrane distillation: recent advances and challenges. Adv Colloid Interface Sci 289:102362

Almulla A, Hamad A, Gadalla M (2005) Integrating hybrid systems with existing thermal desalination plants. Desalination 174:171–192

Arjmandi M, Chenar MP, Altaeec A, Arjmandid A, Peyravid M, Jahanshahid M, Binaeian E (2020) Caspian seawater desalination and whey concentration through forward osmosis (FO)-reverse osmosis (RO) and FO-FO-RO hybrid systems: experimental and theoretical study. J Water Process Eng 37:101492

Awerbuch L (2011) New advances and future needs in thermal-membrane hybrids for water desalination. In: World congress/Perth Convention and Exhibition Centre (PCEC), Perth, Western Australia. REF: IDAWC/PER11-378

Al Bloushi A, Giwa A, Mezher T, Hasan SW (2018) Chapter 3-environmental impact and technoeconomic analysis of hybrid MSF/RO desalination: the case study of Al Taweelah A2 plant. In: Sustain desalin handbook, pp 55–97

Ang WL, Mohammada AW, Johnson D, Hilal N (2019a) Forward osmosis research trends in desalination and wastewater treatment: A review of research trends over the past decade. J Water Process Eng 31:100886

Ang WL, Mohammada AW, Johnson D, Hilal N (2019b) Forward osmosis research trends in desalination and wastewater treatment: A review of research trends over the past decade. J Water Process Eng 32:100886

Ahmad NA, Goh PS, Yogarathinam LT, Zulhairun AK, Ismail AF (2020) Current advances in membrane technologies for produced water desalination. Desalination 493:114643

Boo C, Lee J, Elimelech M (2016) Engineering surface energy and nanostructure of microporous films for expanded membrane distillation applications. Environ Sci Technol 8:1–24

Van der Bruggen B (2018) Microfiltration, ultrafiltration, nanofiltration, reverse osmosis, and forward osmosis. Fundam Model Membr Syst 25–70

Cardona E, Piacentino A (2004) Optimal design of cogeneration plants for seawater desalination. Desalination 166:411–426

Cosgrove WJ, Loucks DP (2015) Water management: current and future challenges and research directions. Water Resour Res 51(6):4823–4839

Deka BJ, Guo J, An AK (2021) Robust dual-layered omniphobic electrospun membrane with anti-wetting and anti-scaling functionalised for membrane distillation application. J Membr Sci 624:119089

Darre NC, Toor GS (2018) Desalination of water: a review water pollution. Curr Pollut Rep 4:104–111

Darwish M, Hassan A, Mabrouk AN, Abdulrahim H, Sharif A (2016) Viability of integrating forward osmosis (FO) as pretreatment for existing MSF desalting unit. Desalin Water Treat 57(31):14336–14346

Deshmukh A, Boo C, Karanikola V, Lin S, Straub AP, Tong T, Warsinger DM, Elimelech M (2018) Membrane distillation at the water-energy nexus: limits, opportunities, and challenges. Energy Environ Sci 5:1–52

Ekea J, Yusuf A, Giwa A, Sodiq A (2020) The global status of desalination: an assessment of current desalination technologies, plants and capacity. Desalination 495:114633

Farsi A, Dincer I (2019) Development and evaluation of an integrated MED/membrane desalination system. Desalination 463:55–68

Gude VG (2016) Desalination and sustainability—an appraisal and current perspective. Water Resour 89:87–106

Haddad B, Heck N, Paytan A, Potts D (2018) CHAPTER 14: social issues and public acceptance of seawater desalination plants. In: Sustainable desalination handbook, pp 505–525

Hamed OA (2005) Overview of hybrid desalination systems-current status and future prospects. Desalination 186:207–214

Hamed OA, Alshail K, Bamardouf K (2003) Performance of an integrated NF/MSF desalination pilot plant, process. In: IDA world congress on desalination and water reuse. Bahamas

IDA (2020) IDA desalination yearbook 2019–2020. Media Analytics Ltd., Oxford

Jain H, Garg MC (2021) Fabrication of polymeric nanocomposite forward osmosis membranes for water desalination—a review. Environ Technol Innov 23:101561

Liang B, Zhana W, Qi G, Lin S, Nan Q, Liu Y, Cao B, Pan K (2015) High performance graphene oxide/polyacrylonitrile composite pervaporation membranes for desalination applications. J Mater Chem A 3:5140–5147

Lu KJ, Chen Y, Chung T-S (2019) Design of omniphobic interfaces for membrane distillatioe review. Water Res 162:64–77

Mejia Mendez DL, Castel C, Lemaitre C, Favre E (2018) Membrane distillation (MD) processes for water desalination applications. Can dense selfstanding membranes compete with microporous hydrophobic materials? Chem Eng Sci 188:84–96

Marcovecchio MG, Mussati SF, Scenna NJ, Aguirre PA (2005) Optimization of hybrid desalination processes including multi stage flash and reverse osmosis systems. Desalin, Trends Technol 182:311–134

Misdan N, Lau WJ, Ismail AF (2012) Seawater Reverse Osmosis (SWRO) desalination by thin-film composite membrane—current development, challenges and future prospects. Desalination 287:228–237

Ndiaye I, Vaudreuil S, Bounahmidi T (2019) Forward osmosis process: state-of-the-art of membranes. Sep Purif Rev 0:1–21

QinzhuoWang NL, Bolto B, Hoang M, Xie Z (2016) Desalination by pervaporation: a review. Desalination 387:46–60

Shatat M, Riffat SB (2014) Water desalination technologies utilizing conventional and renewable energy sources. Int J Low-Carbon Technol 9:1–19

Singh R (2015) Membrane technology and engineering for water purification, 2nd edn. Elsevier Ltd., USA

Thimmaraju M, Sreepada D, Babu GS, Dasari BK, Velpula SK, Vallepu N (2019) Desalination of water. Desalin Water Treat 16:333–337

Turek M (2003) Seawater desalination and salt production in a hybrid membrane-thermal process. Desalination 153:173–177

Warsinger DM, Swaminathan J, Guillen-Burrieza E, Arafat HA, Lienhard JH (2014) Scaling and fouling in membrane distillation for desalination applications: a review. Desalination 356:294–313

World Health Organization (WHO) (2011) Safe drinking-water from desalination. WHO

Xue YL, Huang J, Lau CH, Cao B, Li P (2020) Tailoring the molecular structure of crosslinked polymers for pervaporation desalination. Nat Commun 11:1461

Zhou D, Zhu L, Fu, Yinyi, Zhu M, Xue L (2015) Development of lower cost seawater desalination processes using nanofiltration technologies—a review. Desalination 376:109–116

Zhu Z, Peng D, Wang H (2019) Seawater desalination in China: an overview. J Water Reuse Desalin 9(2):115–132

Chapter 20
Spatial Characteristics and Influencing Factors of Soil and Water Conservation Function in Xixia County of Henan Province

Aihong Gai, Xueliang Wang, Xiaoping Wang, Zhengwen Zhang, and Jinke Wei

Abstract Xixia County of Henan Province is the water source area of the Danjiangkou Reservoir area of Middle route project of South to North Water Transfer. This study used the Universal Soil Loss Equation (USLE) and INVEST Models to analyze the spatial characteristics and influencing factors of soil conservation function of ecosystem in 2017. The results showed that: (1) In 2017, the total amount of soil conservation in Xixia County was 1.90×10^8 t, and the average amount of soil conservation was 554.16 t/hm^2. The forest ecosystem was the main body of soil conservation function, and the cropland ecosystem still played a considerable role in soil conservation; (2) The areas with high soil conservation capacity were mainly distributed in Dinghe Town, Miping Town, Shuanglong town and other towns, with less sloping land, high vegetation coverage, and large topographic relief. The areas with low soil conservation capacity were mainly distributed in Danshui Town, Huihe Town, Tianguan Township and other densely populated areas, with more urban construction land and vegetation coverage Low areas; (3) Natural and human factors were the main causes of soil and water loss, among which climate and topography are the main factors affecting the spatial pattern of soil conservation, and land-use mode and other factors are also the main factors of soil and water loss in the

A. Gai (✉) · J. Wei
College of Resources and Environmental Sciences, Gansu Agricultural University, Lanzhou 730070, China
e-mail: gaiah@gsau.edu.cn

X. Wang
School of Resources, Environment and Chemistry, Chuxiong Normal University, Chuxiong 675000, China

X. Wang
Lanzhou Institute of Arid Meteorology ChinaMeteorological Administration, Key Laboratory of Arid Climate Change and Disaster Reduction of Gansu Province/China Meteorological Administration, Lanzhou 730000, China

Z. Zhang
Surveying and Mapping Engineering Institute Department of Natural Resources of Gansu Province, Lanzhou 730070, China

H.-Y. Jeon (ed.), *Sustainable Development of Water and Environment*,
Environmental Science and Engineering,
https://doi.org/10.1007/978-3-031-07500-1_20

study area. The results can provide scientific guidance for the ecological protection and erosion control of Xixia County.

Keywords Ecological protection · Soil erosion · Spatial pattern · Influencing factors · USLE · Xixia County

20.1 Introduction

Soil erosion is one of the global environmental problems, which seriously threatens national and regional ecological security. China is one of the countries with the most serious soil erosion in the world, and the soil erosion is widespread and serious. According to the national soil erosion remote sensing survey, the water erosion and wind erosion area in China is about 3.569 million km^2, accounting for 37.6% of the total land area (Li et al. 2008; Ministry of Water Resources, PRC 2015). Ecosystem services are the frontier and hotspot of ecology and geography research, the resource and environment foundation on which human beings rely for survival and development, and the bridge and link between natural processes and human processes (Costanza et al. 1999). Land use and land cover change (LUCC) directly affects ecosystem service functions by changing ecosystem types, patterns and ecological processes, and is an important driving force for ecosystem service changes (Swetnam et al. 2011). Quantitative assessment of the relationship between LUCC and ecosystem service changes has become a hot topic of current ecological research (Wang et al. 2014).

Soil conservation function is an important component of ecosystem services, which plays an important role in soil formation, water conservation, soil control and sand fixation, and reduction of soil and water loss. Current studies on soil conservation function mainly use the Universal Soil Loss Equation (USLE) (Wischmeier et al. 1971; Xiao et al. 2003), but the USLE model does not consider the ability of the plot itself to intercept upstream sediments, and there are some problems in the soil conservation amount calculated by the USLE model (Hu et al. 2014).With the rapid development of "3S" technology, models and methods based on USLE and GIS have been produced accordingly (Huang et al. 2013).The value of ecosystem services and the trade-off comprehensive evaluation model (InVEST), based on the USLE model, consider the land's own ability to intercept upstream sediments. Therefore, the rationality and accuracy of soil conservation function assessment have been improved (Wang et al. 2014). At present, the InVEST model is relatively mature in terms of soil conservation function, which not only promotes the quantitative research on soil conservation function at regional scale, but also provides a solid guarantee for the integrated management and decision-making of ecosystem services.

Xixia County is located in the upper reaches of Danjiangkou Reservoir in the middle route of South-to-North Water Diversion Project. Soil erosion is the main ecological problem in the upper reaches of Danjiangkou Reservoir. With complex

terrain and crisscross rivers and ravines, the county is generally located in the mountainous area of mild loss, which has caused serious harm to the water quality of Danjiangkou reservoir area (Li et al. 2018). In this paper, soil erosion and soil conservation distribution in Xixia County were calculated based on InVEST model and 3S technology, and the ecological soil conservation function in Xixia County was evaluated. The research results can provide scientific basis for ecological protection and erosion control in Xixia County.

20.2 Materials and Methods

20.2.1 Overview of the Study Area

Xixia County is the water source area of Danjiangkou Reservoir Region in Henan Province. It is located in the southwest border of Henan Province, the southern foot of Funiu Mountain and the northwest edge of Nanyang Region, bordering Lu Shi and Luanchuan in the north, Xichuan in the south, Neixiang and Song County in the northeast, and Shangnan County in Shaanxi Province in the west. The geographical coordinates are between 111°01'–111°46' E and 33°05'–33°48' N. It is 78 km long from east to west and 79.3 km wide from north to south, with a total land area of 3443.8 km^2. It is the second largest county in Henan Province. The region is dominated by middle and low mountains. The main vein of Funiu Mountain in the north is connected with the east–west structural belt of Qinling Mountains in Shaanxi Province. It is a high and steep mountain in the direction of northwest to southeast, with an elevation of about 1500 m (http://www.xixia.gov.cn/sitesources/xxxrmzf/page_pc/zjxx/xxgk/article9ddec58ea6084976b720ae903e76e373.html).

The soil in the study area belongs to the northern subtropical soil. There are 5 soil types including aquic soil, yellow brown soil, brown soil, paddy soil and purple soil, which are divided into 9 subtypes and 26 soil genera. As an important water source conservation area in the upper reaches of the Danjiangkou Reservoir Region, forest vegetation covers a large area, widely distributed and diverse, with a vegetation coverage rate of 83% (Fig. 20.1).

20.2.2 The Data Sources

The data used in this study mainly include: land use type data obtained through interpretation of TM, ETM, MODIS and other remote sensing images; Digital elevation model for calculating slope and slope length; Soil data products formed by the second national soil census; The average annual rainfall erosivity data of Xixia County and its surrounding meteorological stations were calculated by the daily rainfall model. County-level administrative boundary data (Table 20.1).

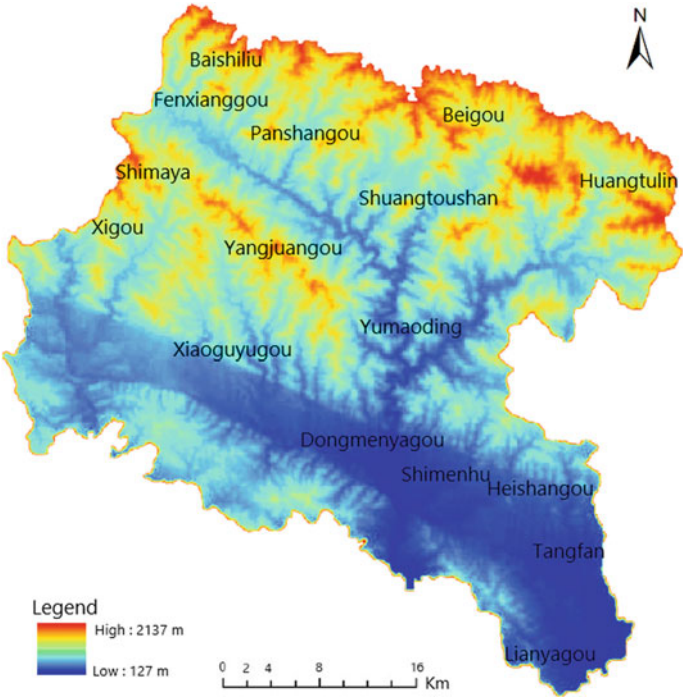

Fig. 20.1 Location of Xixia County

Table 20.1 Principal data sources for soil conservation assessment

Data type	Resolution	Sources
Land cover	30 m	Institute of Remote Sensing and Digital Earth, Chinese Academy of Sciences
Vegetation coverage	250 m	Institute of Remote Sensing and Digital Earth, Chinese Academy of Sciences
Radar topography mission	90 m	International Scientific Data Mirror Network, Chinese Academy of Sciences
Administrative boundary	1:10,000	Satellite Environmental Application Center, Ministry of Environmental Protection
Rainfall erosivity factor	Weather stations	Henan Meteorological Bureau

20.2.3 Soil Conservation Evaluation Models

Soil conservation function of ecosystem was characterized by the difference between potential soil erosion and actual soil erosion. Considering the scale, model complexity and data availability, soil erosion was estimated using the Universal Soil Loss Equation (USLE). The model form is as follows:

Table 20.2 Classification table of ecosystem service function important area

Functional division	Generally important	Important	Very important
Soil retention (t/hm^2)	<50%	50–100%	>100%

Potential soil erosion: $RKLS = R \times K \times LS$.

Actual soil erosion: $USLE = R \times K \times LS \times C \times P$.

Soil conservation: $SC = RKLS - USLE$.

Where, RKLS and USLE represent potential soil erosion intensity ($t\ hm^{-2}a^{-1}$) and actual soil erosion intensity ($t\ hm^{-2}a^{-1}$), SC represents soil retention intensity ($t\ hm^{-2}a^{-1}$), R represents rainfall erosivity factor ($MJ\ mm\ hm^{-2}\ h^{-1}a^{-1}$), K is the soil erodability factor ($T\ hm^2h\ hm^{-2}mj^{-1}\ mm^{-1}$), LS is the topographic factor, and C is the vegetation cover factor. In this paper, it mainly refers to the role of ecosystem in protecting soil. The calculation and assignment methods of each parameter are referred to Rao et al. (2000), Zhang et al. (2008), Rao et al. (2014), Pimentel et al. (1995).

20.2.4 Classification of Soil Conservation Importance

Under the influence of regional topography, climate, soil and vegetation spatial pattern, soil conservation function of ecosystem in Xixia County has obvious spatial heterogeneity. In order to clarify the guarantee effect of soil conservation function of ecosystem in different regions on regional ecological security, and then identify the important soil conservation areas, according to their importance to regional ecological security, they can be divided into three grades: very important, important and generally important (Table 20.2).

The specific dividing steps are as follows: (1) Based on soil conservation intensity data, the proportion of each grid soil conservation in the total soil conservation in the study area was calculated; (2) Calculate the cumulative proportion of soil conservation of each grid according to the order of soil conservation intensity from large to small; (3) The grids with accumulated soil retention ratio between 0 and 50% are generally important for soil conservation, those between 50 and 100% are important, and those greater than 100% are very important.

20.2.5 Statistical Analysis

The spatial pattern of soil conservation function is the result of the comprehensive action of climate, soil, topography and vegetation. In order to reveal the influencing factors and acting characteristics of the spatial differences of soil conservation at

the regional scale, the stepwise regression method was adopted for analysis. The independent variable was rainfall erosivity factor, soil erodibility factor, topographic factor and vegetation cover factor at the county scale, and the dependent variable was soil conservation intensity at the county scale. The analysis process was completed in SPSS 25.0.

20.3 Results and Analysis

20.3.1 General Characteristics of Soil Conservation Function

Using the USLE model, the total amount of soil conservation in the ecosystem of Xixia County in 2017 was 1.90×10^8 t, and the average amount of soil conservation was 554.16 t/hm^2.

Under different land use types, the soil conservation per unit area of woodland was the highest (613.05 t/hm^2), and the soil conservation per unit area of grassland was the lowest (205.76 t/hm^2), with a difference of 407.29 t/hm^2 (Table 20.3). The total amount of soil conservation (SUM) under different land use types was the largest, accounting for 92.1% of the total amount of soil conservation, followed by farmland. The soil conservation amount of woodland is much higher than that of other land use types. This is because the area of woodland, shrub land and other woodland accounts for more than 80% of the total area of the study area. The large vegetation coverage can effectively reduce the impact of rainfall on the soil and make the soil have strong stability and corrosion resistance. Can retain a large amount of sediment, thus improving the ability of soil and water conservation.

Table 20.3 Soil conservation service in various ecosystems in Xixia County

Land use type	Area (hm^2)	Max (t)	Mean (t)	Std	Uat (t/hm^2)	Sum (t)
Other land	297.18	1199.58	54.46	80.05	605.57	1.80×10^5
Water body	4834.71	2267.23	44.48	83.21	494.34	2.39×10^6
Construction land	8961.48	2993.46	24.16	63.45	268.93	2.41×10^6
Grassland	12,052.79	3115.55	19.86	52.53	205.76	2.48×10^6
Arable land	29,435.61	2509.78	24.14	52.71	257.17	7.57×10^6
Woodland	285,459.34	5581.90	57.83	88.01	613.05	1.75×10^8

20.3.2 Spatial Characteristics of Soil Conservation Function

In order to clarify the soil conservation function of each region and the distribution of soil conservation important areas, the soil conservation intensity and soil conservation important areas in Xixia County were analyzed and compared through regional statistics. The areas with high soil conservation capacity in Xixia County are relatively scattered, mainly distributed in the eastern part of the middle part of Xixia County, including: In the middle and eastern part of Dinghe Town, Miping Town, Zhaigen Town, Shuanglong Town, Shijiehe Town and the north part of Wuliqiao Town, the distribution of sloping farmland in these areas is less, the vegetation coverage rate is high, and the topography-relief degree is large. The main reason for the high soil conservation ability is that these areas are mainly alpine woodland, and the proportion of commercial construction land in towns is relatively small. The high forest vegetation coverage rate, to a large extent, has a protective effect on soil solidification ability and vegetation consolidation ability, thus improving soil conservation ability (Fig. 20.2).

The areas with low soil conservation capacity were concentrated, mainly located in Danshui Town, Huizhou Town, Tianguan Township, Lianhua Sub-district and Baiyu Sub-district Office, the middle and eastern part of Xiping Town and the south part of Yangcheng Township. The main reason for the low soil conservation capacity

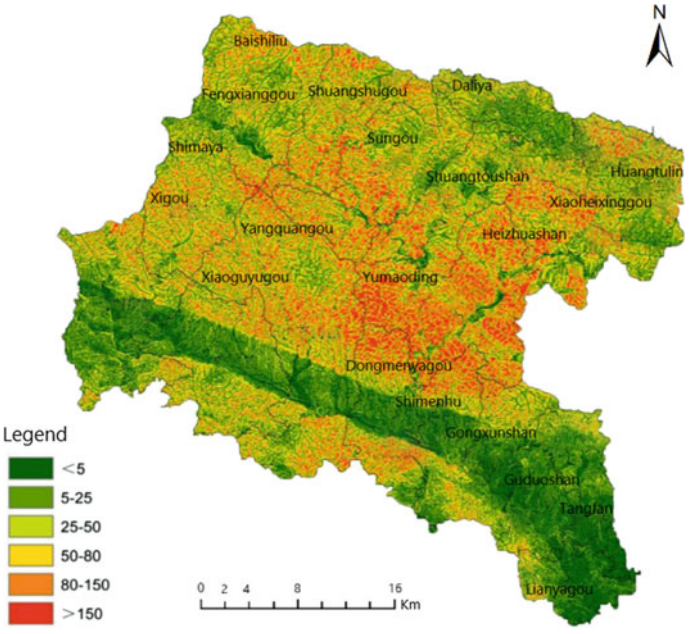

Fig. 20.2 Soil conservation distribution of Xixia County

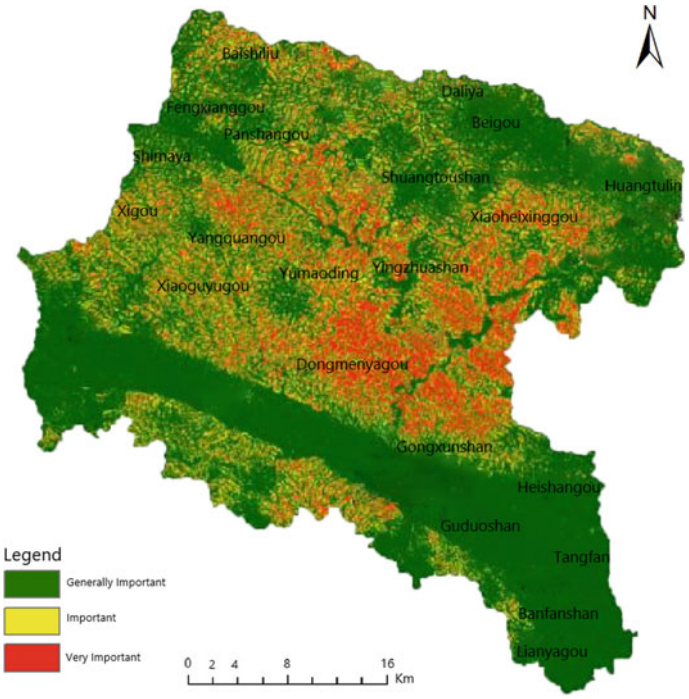

Fig. 20.3 Zoning map of soil conservation function in Xixia County

is that these areas are densely populated areas with more urban construction land and relatively low vegetation coverage rate.

The areas with important soil conservation function were mainly distributed in Dinghe Town and Shuanglong Town, with an area of 47,568.33 hm^2, accounting for 13.82% of the total area. The important areas of soil conservation function were scattered with an area of 67,040.88 hm^2, accounting for 19.48% of the total area. Generally important areas of soil conservation function are concentrated in Xiping Town, Chongyang Town, Huiche Town, Danshui Town and Tianguan Township (Fig. 20.3), with an area of 229,599.01 hm^2, accounting for 66.70% of the total area.

20.3.3 Influencing Factors of Soil Conservation Function

The spatial pattern of soil conservation function is the result of the comprehensive action of climate, soil, topography and vegetation. Stepwise regression analysis showed that the ground form, climate and soil factors on the ecological system in the study area has a significant impact on soil conservation function ($P < 0.01$), including terrain and climate factors contribution is bigger, can explain the spatial variability of soil conservation by 32.5 and 37.5%, the influence of soil factors are relatively small

Table 20.4 Result of stepwise regression

Predictors	Standardized coefficients	R2	P
LS_township	1.311	0.325	0.000
R_township	0.743	0.706	0.000
K_township	0.342	0.757	0.000

SC_township: soil conservation capacity_township); LS_township: topographic factor_township; R_township: rainfall erosivity factor_township; K_township: soil erodibility factor_township

(variance contribution rate of about 4.9%). In contrast, the influence of vegetation factors on this scale is not significant ($P < 0.05$) (Table 20.4).

20.4 Results and Discussion

20.4.1 Discussion

Soil conservation is the reduction of soil erosion in the ecosystem, which plays an important role in maintaining soil nutrients, preventing land degradation and alleviating river sediment deposition. In 2017, the total amount of ecosystem soil conservation was 190 million t, and the average soil conservation intensity was about 554.16 t/hm^2 t hm^{-2}a^{-1}, much higher than the national average level (224.42 t hm^{-2}a^{-}1) (Rao et al. 2000). The ecosystem was inhibiting soil erosion. It has played an important role in ensuring the ecological security of the upper reaches of Danjiangkou Reservoir in the middle route of the South-to-North Water Diversion Project.

Affected by the spatial differentiation of topography, climate, soil and vegetation, the ecosystem soil conservation function in Xixia County presents a high degree of spatial heterogeneity. Due to the special geographical location of Xixia County, and the comprehensive influence of topography, geomorphology, rainfall and human activities, soil and water flow in Xixia County has a large area, wide distribution and high harm. The distribution characteristics are as follows: the damage of soil and water loss is more serious in the middle and lower reaches where the population is concentrated and the transportation is convenient, the urban set up land is more, and the cultivated land and barren mountain reclamation are concentrated. However, the water and soil loss is relatively weak in the upper reaches where there are few population, inconvenient roads, less residential land and high vegetation coverage. Natural factors and human destruction are the main causes of soil and water loss, among which the natural factor is the objective condition of soil and water loss, while the human destruction of natural environment is the dominant factor of soil and water loss.

Agricultural land has always been considered as the main source of erosion and sediment yield (Lin et al. 2008). It is estimated that about 3/4 of the global soil erosion comes from farmland, but it plays an irreplaceable role in providing food, vegetables, oil and other agricultural products for human beings and ensuring regional food security (Wang et al. 2015).The study showed that the soil conservation amount of cultivated land in Xixia County was 7.57×10^6 tons, accounting for about 3.98% of the total soil conservation amount in the study area, ranking first after woodland, indicating that cultivated land played a certain role in soil conservation while providing various products for human beings.

The areas with relatively severe soil erosion in Xixia County are scattered, mainly involving the central and western parts of Wuliqiao Town and the central and eastern parts of Dinghe Town, the southern part of Yangcheng Town, the central and northeastern parts of Shuanglong Town, the northeastern part of Chongyang Town and the eastern part of Xiping Town. There are two main reasons for the relatively high degree of soil erosion in these areas. On the one hand, there are natural factors including: (1) Topography. These areas are mainly mountainous and hilly areas, and the large slope and elevation difference is easy to cause soil erosion; (2) Soil-forming parent material. In these areas, the parent material is mainly weathered residual slope deposits of granite, calcareous rock and many other rocks. The soil layer is thin and the soil viscosity is poor. (3) the vegetation coverage, because these areas are mainly two earth class residents land and construction land, the vegetation coverage rate is low, prone to the surface of the water loss and soil erosion, residents to agricultural development at the same time, the large-scale destruction of forest land, forest land, the grass to the surface of naked severe leakage, which again adds to the degree of soil erosion. On the other hand, due to the weak awareness of environmental protection, the early residents blindly carried out urban expansion and industrial construction for the sake of social and economic development, resulting in the destruction of forests and grasslands and serious soil loss. Residents more farmers in the mountain areas, mountainous land is not flat, less arable land per capita, the residents' needs for survival on the local natural resources is wanton for destroyed the land resource, constantly cut down trees, land to forest area reducing, the low vegetation coverage on soil consolidation ability, surface runoff increase reduced precipitation of seep into the soil, Resulting in extensive soil erosion; At the same time, in the process of industrial production and construction, excessive development will destroy the soil composition to a certain extent, thus causing soil erosion.

Stepwise regression analysis showed that climate factors and terrain factors were the main factors affecting soil conservation function in the study area, and soil factors also showed a certain effect, while vegetation factors played an insignificant role. That on the one hand, the scale of the soil conservation function may have similar characteristics, Xixia climate, topography, macroeconomic factors such as spatial difference is obvious, for regional soil conservation spatial pattern showed significant control effect, the vegetation factors or work on local scale, the space for the macroeconomic factors such as climate, reduce; On the other hand, suggests that there may be multiple collinearity between variables, the vegetation itself is the product of the regional climate, topography, soil conditions, and the effect of vegetation on

soil conservation function not only with its own ability of soil conservation, more affected by its environment condition is determined by the climate, topography, soil potential soil erosion influence (Wei et al. 2002), the greater the potential of soil erosion, The greater the effect of vegetation on soil conservation.

20.4.2 Results

(1) The total amount of ecosystem soil conservation in Xixia County in 2017 was 1.90×10^8 t, and the average amount of soil conservation was 554.16 t/hm^2. Forestland was the main body of soil conservation function, while cultivated land still played a considerable role in soil conservation. However, attention should be paid to soil and water conservation measures in agricultural activities.
(2) In the whole study area, the areas with high soil conservation capacity are mainly distributed in the central and eastern part of Dinghe Town, Miping Town, Zhaigen Township, Shuanglong Town, Shijiehe Township and the north part of Wuliqiao Town, where the distribution of sloping farmland is less, the vegetation coverage rate is high and the topographic relief degree is large.The low soil conservation capacity is mainly distributed in Danshui Town, Huizhou Town, Tianguan Township and other populated areas, where the urban construction land is more and the vegetation coverage rate is low.
(3) Natural factors and human factors are the main causes of soil and water loss. Climate and topography are the main factors affecting the spatial pattern of soil conservation in the study area. Soil factors also have a certain influence on the regional scale, and human factors such as land use patterns are the main factors for soil and water loss.

Acknowledgements This project was support by Discipline Construction Fund Project of Gansu Agricultural University (GAU-XKJS-2018-216) and National Natural Science Foundation of China (42075120).

References

Costanza R, D'Arge R, Groot RD (1999) The value of the world's ecosystem services and natural capital. World Environ 387(1):3–15

http://www.xixia.gov.cn/sitesources/xxxrmzf/page_pc/zjxx/xxgk/article9ddec58ea6084976b720ae903e76e373.html. Accessed 25 Nov 2020

Hu S, Cao M, Liu Q, Zhang T, Qiu H, Liu W (2014) Comparative study on the soil conservation function of InVEST model under different perspectives. Geogr Res 33(12):2393–2406

Huang C, Yang J, Zang W (2013) Development of ecosystem services evaluation models: research progress. Chin J Ecol 32(12):3360–3367

Li Z, Cao W, Li B, Luo Z (2008) Current status and developing trend of soil erosion in China. Sci Soil Water Conserv 6(1):5–62

Li X-M, Wen L, Liu C, Wei P-F, Wang L-X, Tian W-T (2018) Spatial distribution characteristics and influencing factors of soil and water loss in Danjiangkou reservoir area and surrounding area. Hunan Agric Sci 9:54–59

Lin WT, Tsai JS, Lin CY, Huang PH (2008) Assessing reforestation placement and benefit for erosion control: a case study on the Chi-Jia-Wan Stream, Taiwan. Ecol Model 211(4):444–452

Ministry of Water Resources, PRC (2016) China river sediment bulletin 2015. China Water Resources and Hydropower Press, Beijing

Pimentel D, Harvey C, Resosudarmo P, Sinclair K, and etc (1995) Environmental and economic costs of soil erosion and conservation benefits. Science 267(5201):1117–1123

Rao EM, Xiao Y, Ouyang ZY, Zheng H (2016) Changes in ecosystem service of soil conservation between 2000 and 2010 and its driving factors in southwestern China. Chinese Geograph Sci 26(2):165–173

Rao EM, Ouyang ZY, Yu XX, Xiao Y (2014) Spatial patterns and impacts of soil conservation service in China. Geomorphology 207:64–70

Swetnam RD, Fisher B, Mbilinyi BP (2011) Mapping socio-economic scenarios of land cover change: a GIS method to enable ecosystem service modelling. J Environ Manag 92(3):563–574

Wang M, Ruan J, Yao J, Sha C, Wang Q (2014) Study on soil conservation service of ecosystem based on InVEST model-a case study of Ningde City, Fujian Province. Res Soil Water Conserv 21(4):184–189

Wang L-Y, Xiao Y, Rao E-M, Jiang L (2015) Spatial characteristics of food provision service and its impact factors in China. J Nat Resour 30(2):188–196

Wang WJ, Guo HC, Chuai XW (2014) The impact of land use change on the temporospatial variations of eco-systems services value in China and an optimized land use solution. Environ Sci Policy 44(2):62–72

Wei H, Li R, Yang Q (2002) Research advance of vegetation effect on soil and water conservation in China. Acta Phytoecol Sin 26(4):489–496

Wischmeier WH, Johnson CB, Cross BV (1971) Soil erodibility nomograph for farm land and construction site. J Soil Water Conserv 26(5):189–193

Xiao Y, Xie G, An K (2003) The function and economic value of soil conservation of ecosystems in Qinghai–Tibet Plateau. Acta Ecol Sin 23(11):2367–2378

Zhang KL, Shu AP, Xu XL, Yang QK, Yu B (2008) Soil erodibility and its estimation for agricultural soils in China. J Arid Environ 72(6):1002–1011

Chapter 21
Experiment on Vegetation Grass Blanket Bank Slope Protection Material for Scour Resistance and Soil Conservation

Li Ming, Yang Yanhua, Hong Houbing, Wang Lulu, Zhang Jing, Guan Zhenya, and Liu Weibin

Abstract The anti-current scour mode and the erosion characteristics of the underlying soil body of the vegetation grass blanket bank slope protection material under the combined conditions of typical flow and water level were studied in indoor water flume experiment. The results of the study show that the damage of the vegetation grass blanket material mainly occurs under the condition of large flow, and the lower the water level is, the greater the possibility of material damage will be, mainly reflected by the pulled-out fixed steel nails and the floating materials. Compared with the bare soil bank slope, the vegetation grass blanket material has a certain protective effect on the underlying soil. Soil erosion starts at the point of initial contact between the grass blanket and the soil, and gradually spreads to a larger area in the shape of a fan in the point-to-area mode.

Keywords Vegetation grass blanket · Water flow · Scouring · Soil retention · Destruction

21.1 Introduction

Vegetation grass blanket is made from rice straw, wheat straw, etc. (as raw materials), plus grass, shrub, flower seeds, water retention agent, nutrient soil, etc. on the carrier layer (Qin et al. 2012; Huang et al. 2017; Huang et al. 2016). Two structural forms can be adopted according to the needs of use: one structure is divided into five layers: upper net, plant fiber layer, seed layer, wood pulp paper layer, and lower net; the other structure is divided into three layers: upper net, plant fiber layer, and lower net. The specific structure is shown in Fig. 21.1. The plant fiber layer is made of pure natural material coconut fiber which are punched, needled and processed into a base

L. Ming · H. Houbing · W. Lulu · Z. Jing · G. Zhenya · L. Weibin
Anhui Provincial Group Limited for Yangtze-to-Huaihe Water Diversion, Tianjin, China

Y. Yanhua (✉)
Tianjin Research Institute for Water Transport Engineering, Tianjin, China
e-mail: yyh200@163.com

H.-Y. Jeon (ed.), *Sustainable Development of Water and Environment*,
Environmental Science and Engineering,
https://doi.org/10.1007/978-3-031-07500-1_21

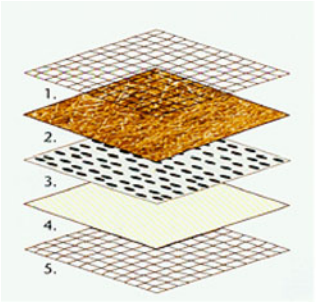

1 net 2 plant fiber layer 3 seed 4 paper 5 net
(a) Ecological vegetation blanket structure with seed

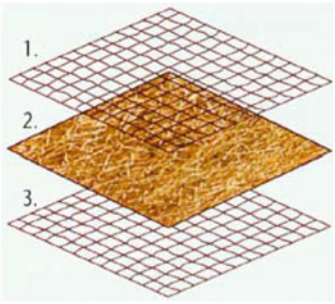

1 net 2 plant fiber layer 3 net
(b) Ecological vegetation blanket structure without seed

Fig. 21.1 Structure diagram of vegetation grass blanket

belt for plant growth in a rectangular parallelepiped mesh structure. The ecological vegetation blanket is 8–10 mm in thickness, with moderate fiber thickness (fiber diameter of 0.3–0.8 mm) and reasonable length range (fiber length of 10–20 cm). Fertilizers, nutrients, water-retaining agents, various grass species, etc. can be added as needed.

As a kind of flexible and ecological material, vegetation grass blanket can play the role of soil consolidation and protection when laid on the bank slope, which have been used for bank slope protection of highways or water conservancy projects in recent years (Chen et al. 2015; Ping et al. 2020; Xie et al. 2016). Compared with traditional gray slope protection such as stone masonry and concrete, the vegetation grass blanket slope protection project has the advantages of green ecology, simple construction and low maintenance cost (Liu et al. 2019; Chen et al. 2017; Chen 2017). In order to study the erosion resistance of vegetation grass blankets as bank slope protection material against water erosion and the soil conservation effect on the underlying soil, this paper carried out a flume experiment to study the erosion resistance and soil conservation of vegetation grass blankets.

21.2 Flume Experiment

In order to analyze the anti-scouring performance of vegetation grass blankets, a sink scour test was carried out. Firstly, a clear water scour test was carried out under bare soil conditions, and then an erosion test was carried out on the slope protection of vegetation grass blankets.

The experiment flume adopts a triangular section, with 24 m in total length, 1.5 m in width, and 0.5 m in inner height. One side of the sink is a vertical wall, and the other side is a side slope with a slope gradient of 1:3. The 6 m long area at the inlet

section of the flume is the test section. In order to increase the flow rate of the water, the inlet and outlet of the flume were modified, and a bottom slope with a slope gradient of 0.05 was laid at the bottom of the flume in the test section to increase the flow rate in the experiment (Fig. 21.2).

Before the experiment, soil was laid on the 1:3 side slope of the flume in the test section and compacted and leveled to produce a slope with slope gradient of 1:3. The bank slope protection materials used for the experiment were placed on the upper part of the soil in blocks, with each piece of material of 1.3 m in length. And 5 pieces were laid along the upstream direction from the end of the test section of the flume. The upstream materials overlapped the downstream material that had been laid, and at the laps on both sides of the material, the slope top and the slope toe, and the center of the material pad, U-shaped steel nails were driven into to fix. That is, 9 U-shaped steel nails were driven into each material pad for fixing, as shown in Fig. 21.3.

In this experiment, the slope surface water flow velocity and the degree of material inundation when the bank slope protection material is laid, as well as the bare soil

Fig. 21.2 Test materials of vegetation grass blanket

Fig. 21.3 Experiment flume

Fig. 21.4 Soil erosion at the entrance of the test section

bank slope and the vegetation grass blanket bank slope under the combined condition of two flow rates and two water levels, have been considered to carry out the scour test. The two flow rates used are 300 m^3/h (hereinafter referred to as small flow condition) and 1000 m^3/h (hereinafter referred to as large flow condition); the water level control section is the end of the test section, and the two water levels are respectively 33.67 cm (hereinafter referred to as low water level condition) and 45.76 cm (hereinafter referred to as high water level condition), forming four test conditions: small flow and low water level, small flow and high water level, large flow and low water level, and large flow and high water level.

21.3 Experimental Study on Scouring and Soil Conservation Characteristics of Vegetation Grass Carpet

In this bare soil scour test and the erosion test of bank slope protection materials, the soil erosion at the entrance of the test section and the bank slope toe is relatively large, and the scour phenomenon is more obvious, as shown in the figure below. This is mainly because that the topography and roughness of the bed surface changed greatly after the water flow entered the test section, and the combination of the two resulted in a strong local turbulence. In order to minimize the soil erosion at the entrance of the test section and the bank slope toe, it is recommended to set an anchor groove at the joint of the entrance section when carrying out such type of test, fix the material pad carefully on the entrance section, and to further reinforce the bank slope protection material pad at the slope toe.

Under the conditions of small flow and low water level, small flow and high water level, large flow and low water level, and large flow and high water level, the average velocity distribution of the slope surface of the bare soil erosion test with only soil on

the bank slope and the test with vegetation grass blanket on the bank slope are shown in Figs. 21.5, 21.6, 21.7 and 21.8. Specifically, under the condition of small flow and low water level, the average flow velocity U of the bare soil and the vegetation grass blanket slope surfaces was 0.589 m/s and 0.472 m/s, respectively. During the 40 h of scouring process, the vegetation grass blanket had not been damaged. Under the condition of small flow and high water level, the average velocity U of the bare soil and the vegetation grass blanket slope surfaces was 0.052 m/s and 0.045 m/s, respectively. During the 40 h of scouring process, the vegetation blanket had not been damaged. Under the condition of large flow and low water level, the average velocity U of the bare soil and the vegetation grass blanket slope surfaces was 1.907 m/s and 1.724 m/s, respectively, and the vegetation grass blanket was damaged after 2 h of scouring. Under the conditions of large flow and high water level, the average flow velocity U of the bare soil and the vegetation grass blanket slope surfaces was 1.205 m/s and 0.927 m/s, respectively, and the vegetation grass blanket was damaged after 4.25 h of scouring. The damage of vegetation grass blanket is mainly reflected by the ejection of U-shaped steel nails and the floating of materials, as shown in Fig. 21.9.

It can be seen from the soil loss rate Δ of bare soil and vegetation grass blanket bank slopes after 40 h of water scouring in Tables 21.1 and 21.2 that under the conditions of small flow and low water level, small flow and high water level, large flow and low water level, and large flow and high water level conditions, the loss rate of the eroded soil is lower in the case of vegetation grass blanket than that in the case of bare soil. Compared with the bare soil scour test under the same current conditions, the eroded soil volume percentage is reduced by 6.555%, 7.074%, 0.377%, and 6.273%, respectively.

Volume loss rate of bank slope soil:

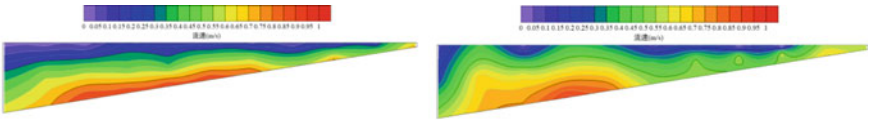

(a) Bare soil (b) Vegetation blanket

Fig. 21.5 Distribution of average velocity on slope surface under the condition of small flow and low water level

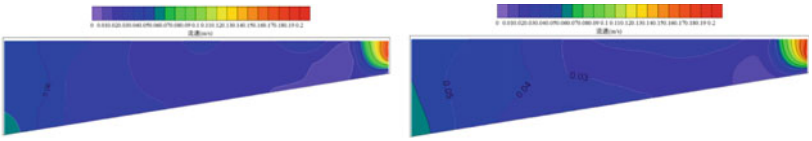

(a) Bare soil (b) Vegetation blanket

Fig. 21.6 Distribution of average velocity on slope surface under the condition of small flow and high water level

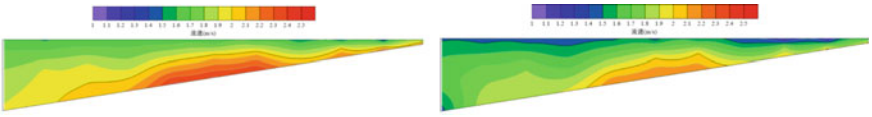

(a) Bare soil (b) Vegetation blanket

Fig. 21.7 Distribution of average velocity on slope surface under the condition of large flow and low water level

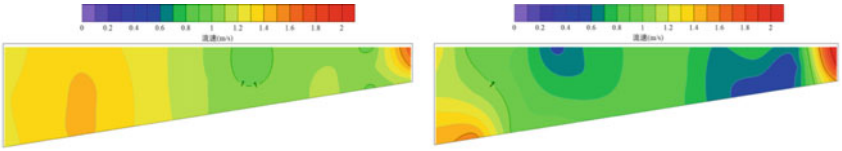

(a) Bare soil (b) Vegetation blanket

Fig. 21.8 Distribution of average velocity on slope surface under the condition of larger flow and high water level

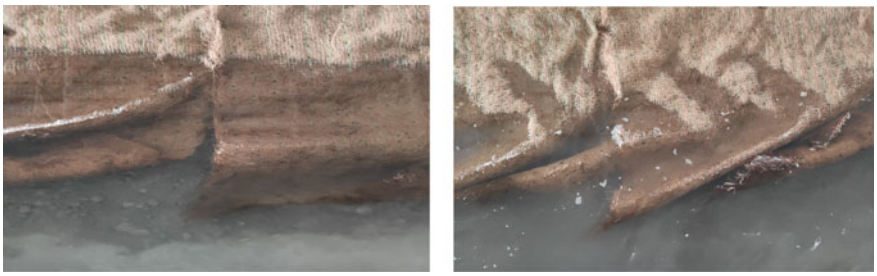

Fig. 21.9 Damage of vegetation grass blanket materials

Table 21.1 Statistics of slope erosion under bare soil condition

Water flow conditions	V_0 (cm^3)	V_1 (cm^3)	ΔV (cm^3)	Δ (%)	U (m/s)
SFLL	283,200	215,208.18	67,991.817	24.008	0.372
SFHL	283,200	107,131.47	176,068.524	62.171	0.045
LFLL	283,200	165,816.08	117,383.913	41.449	1.687
LFHL	283,200	85,249.43	197,950.565	69.898	0.954

Table 21.2 Statistics of slope erosion under the condition of vegetation grass blanket

Water flow conditions	V_0 (cm^3)	V_1 (cm^3)	ΔV (cm^3)	Δ (%)	U (m/s)
SFLL	283,200	218,393.583	64,806.417	22.884	0.472
SFHL	283,200	108,167.310	175,032.690	61.805	0.045
LFLL	283,200	165,817.950	117,382.050	41.448	1.724
LFHL	283,200	82,563.875	200,636.125	70.846	

$$\Delta = \frac{V_0 - V_1}{V_0} = \frac{\Delta V}{V_0} \tag{21.1}$$

where Δ is the soil volume loss rate of the bank slope, %; V_0 is the volume of the soil laid on the bank slope before water flow erosion, cm^3; V_1 is the volume of the remaining soil on the bank slope after water flow erosion, cm^3; ΔV is the soil loss volume before and after water flow erosion, cm^3. In Tables 21.1 and 21.2, SFLL means small flow and low water level, SFHL means small flow and high water level, LFLL means large flow and low water level, LFHL means large flow and high water level.

21.4 Conclusion

(1) In order to minimize the degree of soil erosion at the entrance of the test section and the toe of the bank slope, it is recommended to set up anchor grooves at the joints of the entrance section during the erosion test of such bank slope protection materials as vegetation grass blankets, fix the material pad carefully on the entrance section, and to further strengthen the material pad at the slope toe.
(2) Vegetation grass blanket material damage mainly occurs under high flow conditions, and the lower the water level is, the greater the possibility of material damage will be. Due to the complex flow pattern at the slope toe and the greater intensity of water turbulence, the U-shaped steel nails fixed at the slope toe tend to pop out first, and then the material floats.
(3) In the bare soil scour test, the soil is directly washed by water and eroded to a greater degree. The soil on the slope surface generally erodes gradually along the direction of the streamline of the water, and the shape of the erosion section is relatively regular; the vegetation grass blanket material has a certain soil retention effect on the soil, and the soil erosion starts from the initial contact point between the grass blanket and the soil and gradually spreads to a larger area in a fan shape in the point-to-area mode.

References

Chen Z (2017) Application of plant fiber blanket in high speed side slope protection. Henan Sci Technol 6:132–134
Chen W, Tan S, Baiyinbaokigao, Jin Z (2015) Study on anti-erosion characteristics of KLD grass carpet. Water Resour Hydropower Eng 46(4):152–155
Chen X, Jian L, Jia X, Li H, Liu L (2017) Effect of plant fiber blanket coverage on revegetation of highway side slope. J Highw Transp Res Dev 34(2):143–148
Huang X, Xu Z, Yang Y (2016) Application of straw plant blanket in highway slope protection. J China Foreign Highway 36(4):11–17

Huang X, Cheng J, Yang Y (2017) Application of straw plant blanket in highway slope protection. Highway (1):220–225

Liu H, Liu L, Liu X, Zhang K, Luo J, Wang J (2019) Comprehension benefit evaluation on the protection technique of pant fiber blanket on the road side slope. J Soil Water Conserv 33(1):345–352

Qin F, Ge H, Ge Q, Yang F (2012) A new slope protection technology for expressway in Mountainous area-vegetation grass blanket bioengineering technique. J Suzhou Univ 27(5):50–53

Xie Z, Xiang Z, Xiao H (2016) Study on the production of soilless grass blanket with plant waste. Crop Res 30(1):67–72

Zhang P, Wang S, Ma Y, Xu J, Li G (2020) Effects of plant fiber blankets of different herbaceous plant growth stages on runoff and sediment rield in the loess hilly and gully region. J Soil Water Conserv 34(5):49–55

Chapter 22
Development Trend Analysis of Industrial Wastewater Treatment Based on Patent Analysis and Bibliometrics

Ma Jiahong, Wang Yang, Zheng Chunxiao, and Yu Jian

Abstract Today the world is facing a major problem of getting rid of industrial wastewater safely so that it does not disrupt the environment. The random discharge of industrial wastewater will have a huge impact on the water environment and threaten human health due to the characteristics of heavy pollution, deep harm and large impact of industrial wastewater. In order to gain an access to the research status and the developing trend of industrial wastewater treatment (IWT), In this study, the global research trends through IWT technologies based on the Web of Science (WOS) and patent literature, using bibliometric statistics and visualization methods, research indicators of IWT were analyzed, including the amount of papers, publication date, publication countries, publication institutions, publication journals, authors, inventors, International Patent Classification and keywords. The research results we have gained indicate: China is the country that publishes the most papers and patents related to IWT technology. The paper research hotpots are wastewater treatment based on biological process, wastewater treatment by adsorption, activated carbon and methylene blue method, as well as wastewater treatment by photo catalysis and oxidation. The hot spots of patent layout are water purification through filtration process, adsorption, activated carbon, etc., and scale inhibition or corrosion prevention of water treatment (composition) using polymers. The above analysis revealed the IWT technological gap between China and other countries, so valuable suggestions were be made for sustainable development.

Keywords Wastewater treatment · Bibliometric analysis · Patent analysis

M. Jiahong · W. Yang (✉) · Z. Chunxiao
National Science Library, Chinese Academy of Sciences, Beijing 100190, China
e-mail: wangyang@mail.las.ac.cn

W. Yang · Y. Jian
School of Economics and Management, University of Chinese Academy of Sciences, Beijing 100049, China

Y. Jian
Institute of High Energy Physics, Chinese Academy of Sciences, Beijing 100049, China

H.-Y. Jeon (ed.), *Sustainable Development of Water and Environment*,
Environmental Science and Engineering,
https://doi.org/10.1007/978-3-031-07500-1_22

22.1 Introduction

Under the background of increasing global energy consumption and increasingly serious environmental pollution, mining resources from industrial wastewater has proved to be an excellent source of secondary raw materials i.e., proficient for providing economic and financial benefits, clean and sustainable resilient environment, and achieving sustainable development goals (SDGs) (Dutta et al. 2021; Adetunji and Olaniran 2021; Lefebvre and Moletta 2006).

Bibliometric is an indicator that helps to measure the impact of the research, journals, institutes on the society through mapping, visualizing, and understanding of various scientific fields and citations in a particular area (Price 2014; Wouters et al. 2001). In recent years, bibliometric has been widely used in the statistical research of published academic papers in various research fields, so as to have a specific understanding and understanding of the current research and future research direction (Chiu and Ho 2005; Wang et al. 2010; Fu et al. 2010, 2013).

Although some researchers have conducted valuable bibliometric analysis on industrial wastewater (Mao et al. 1998; Raji and Mirbagheri 2021; Fang et al. 2019; Zheng et al. 2015), these studies mainly analyze published papers or analyze one of the technical directions, there are still some limitations. Based on patent analysis and literature measurement methods, this paper studies the global IWT technology trend from the aspects of development trend, key technical fields, regional distribution and advantageous institutions, so as to provide support and reference for relevant scientific research institutions and industries.

22.2 Methodology

22.2.1 Data Sources and Search Strategy

In order to analysis the development trend of global IWT technology, we used two types of data, patents and papers. We worked out the search formula of IWT technology in July 2021, 56,196 patents were searched in the Derwent Innovations Index (DII) database and 59,896 Science Citation Index (SCI) papers were searched in the Web of Science (WOS).

22.2.2 Bibliometric Analysis

We used many bibliometric tools like Derwent Data Analyzer (DDA), VOSViewer and Excel to analysis the data of patents and SCI papers. Research indicators of IWT were analyzed, including the amount of papers, publication date, publication

countries, publication institutions, publication journals, authors, inventors, International Patent Classification and keywords. We compared the technology strength of countries in the world, especially China and the USA. The analysis also includes a comparison of the technology strength of global research institutions, an analysis of the annual trend and comparison of the overall level of publications and the research institutions. The keywords of the papers were detailed analyzed, and a visual image showed the world IWT research priority clearly.

22.3 Results and Discussion

22.3.1 Analysis of Time Trend

The output trend of papers and patents can reflect the research and development in specific fields to a certain extent and capture the change of focus in research and applications in each period at a macro level.

Figure 22.1 shows the annual output of papers related to IWT technology, which shows the output trend can be divided into three periods. The first period was before 1990. The earliest SCI papers of IWT technology was published in 1945. During this period, the annual number of papers and patents about IWT technology was very small (less than 50). The second period was from 1991 to 2013. During this period, the number of SCI papers grew slowly, which did not exceed the number of 3000 each year. The third period is from 2014 to the present. In 2014, the number exceeded 3000. In 2015, the number exceeded 4000. In 2019, the number exceeded 6768. It can be clearly shown that the growth period of IWT SCI papers began and maintained stable growth.

Figure 22.2 shows the annual output of patents related to IWT technology, which shows that the output trend can be divided into three periods.

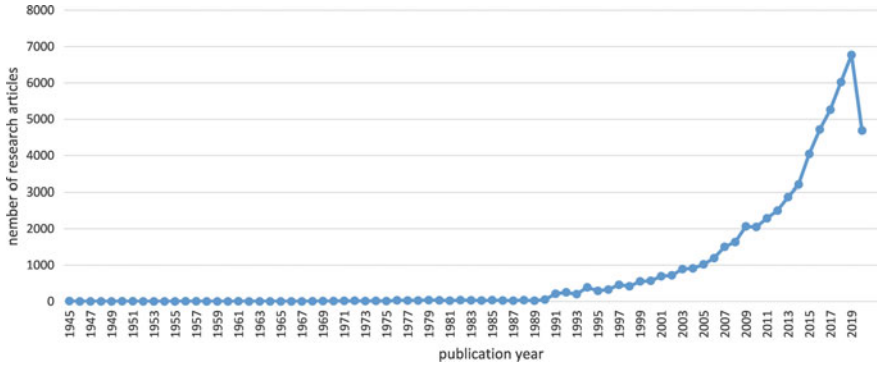

Fig. 22.1 Annual output of SCI papers related to IWT technology

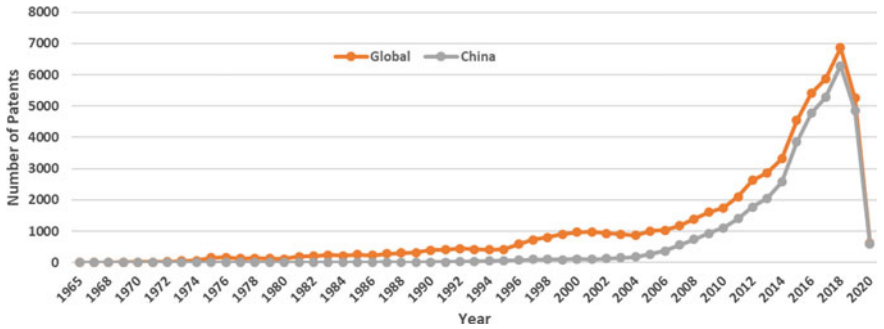

Fig. 22.2 Annual output of patent related to IWT technology

The first period was before 1995. During this period, the number of SCI papers grew slowly, which did not exceed the number of 600 each year. The second period was from 1996 to 2015, the number of SCI papers grew faster which did not exceed the number of 4500 each year. The third period is from 2016 to the present, the number of patents increased very rapidly. In 2016, the number of patents exceeded 4500. And the number of patent applications reached a peak of 6980 in 2018. The IWT patent of China was born in 1985 which 20 years late from the world. But the number of patents of China grew very fast. In 2018, it reached a peak of 6288.

Furthermore, the patent data are incomplete after 2019 for the patents' confidentiality period (18 months), and there was a delay in adding data to the database. So the paper and the patent data are incomplete in 2019 and 2020.

22.3.2 Performance of Countries and Regions

By analyzing the number of papers in different countries and regions, we were able to understand the major countries and regions in which research on IWT technology has been conducted. Figure 22.3 shows the 10 countries with the largest numbers of papers are China, India, the USA, Iran, Spain, Turkey, Brazil, South Korea, the UK and Germany. The output of the ten countries accounts for 65.7% of the global IWT papers. China is far ahead of other countries in terms of paper output, ranking first in the world with 14,901 papers, while India and the US are second and third with 5,956 and 5,242 papers, respectively.

The USA and Germany began to research IWT in the 1970s, but for China, SCI papers were first published in 1985, and its growth trend is in line with the global growth trend, with a significant increase since 2005 and a surge in the number of publications since 2013, showing a strong momentum of development. India has the same earliest date of publication in IWT as China, also with a significant increase in the rise since 2005, although its rise is lower than China (Fig. 22.4).

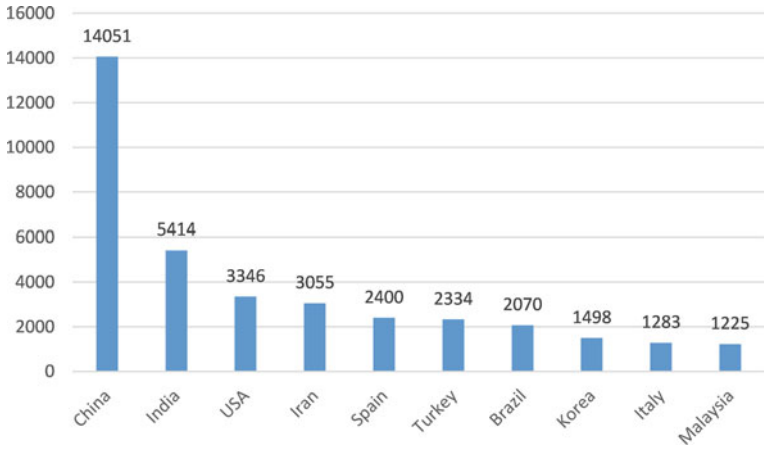

Fig. 22.3 Top 10 countries output of IWT papers

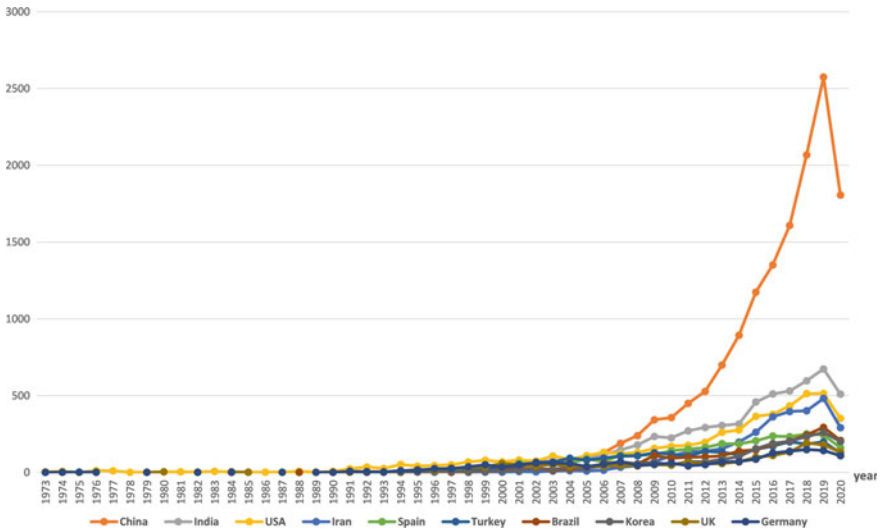

Fig. 22.4 Annual output of IWT papers of TOP10 countries

By analyzing the number of patent applications of specific fields in different countries and regions, we discovered the important target markets of technology applications. Figure 22.5 shows the main countries and regions that accepted IWT technology patents. The global leader of IWT is China, the number of IWT patents accepted in China accounted for 51% of the global IWT patents.

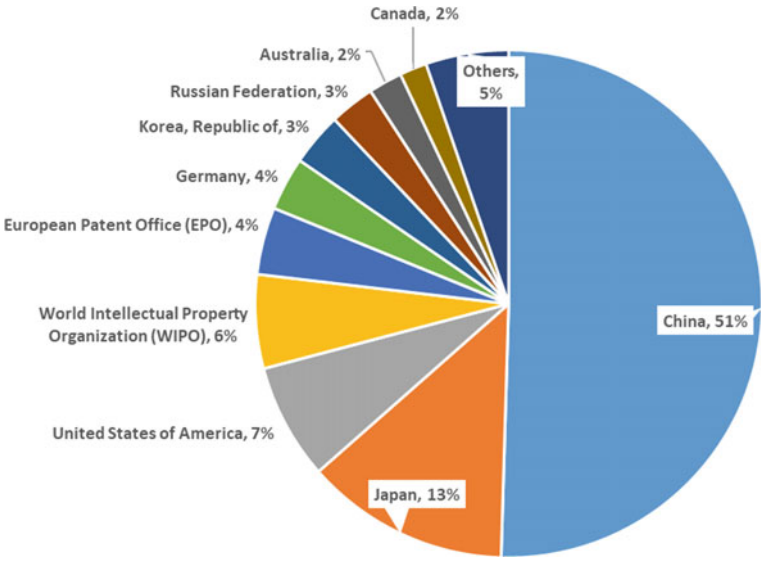

Fig. 22.5 TOP 10 countries/regions of IWT patents

22.3.3 Analysis of Organizations

The main organizations producing IWT papers are shown in Fig. 22.6. There are 11 Chinese institutions among the TOP20 institutions, namely, the Chinese Academy of Sciences, Tsinghua University, Harbin Institute of Technology, Zhejiang University, University of Chinese Academy of Sciences, Tongji University, Dalian University of Technology, Nanjing University, Shandong University, Tianjin University and Sichuan University, accounting for 53.90% of the total publications of the TOP20 institutions. There are nine foreign institutions, including three from India and one each from Iran, Singapore, Spain, Saudi Arabia, Brazil and Turkey.

Figure 22.7 shows the main applications for IWT patents. China Petroleum and Chemical Corporation filed the highest number of patents at 411. Japan Watering

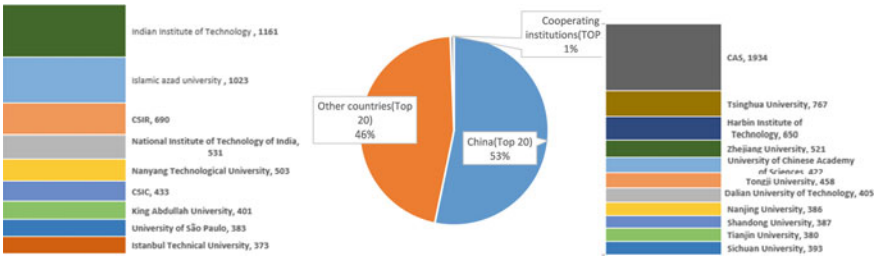

Fig. 22.6 Overview of the top 20 institutions IWT papers

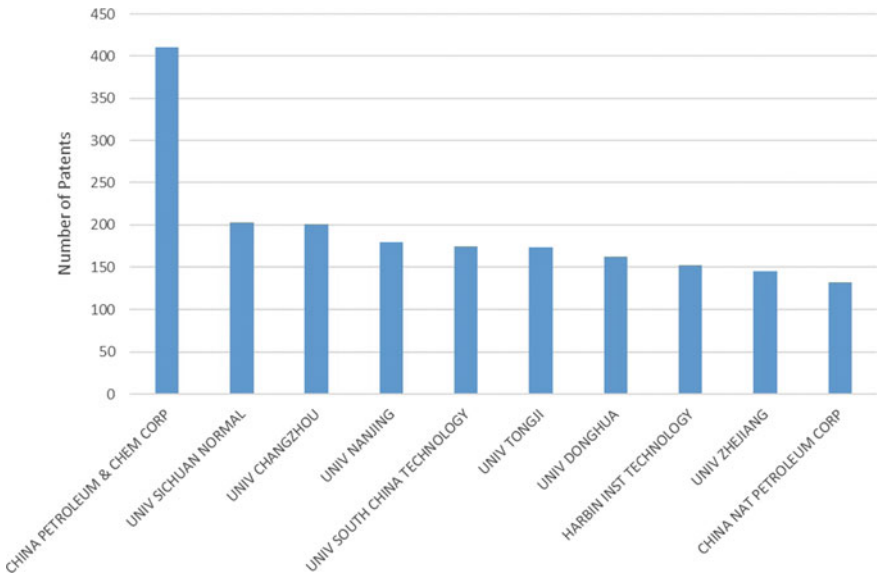

Fig. 22.7 Key global patent holder

Co., Ltd. and Japan Kurita Water Industry Co., Ltd. also filed more than 400 patent applications, 405 and 402, respectively, in second and third place.

Figure 22.8 shows a visualization of the top 50 patent holder cooperating in patent applications. According to the degree of close cooperation of the patentees, they can be divided into two parts, namely, the Chinese cooperation camp and the Japanese cooperation camp. The Chinese camp includes seven university institutions. The Japanese cooperation camp involves 18 institutions, namely, Mitsubishi Chemical Corporation, Mitsubishi Rayon Corporation, Hitachi Group, Kurita Water Industry Corporation, etc. The closest cooperation is between Hitachi Group, Kurita Water Industries and Nippon Steel Corporation, all of which are world-renowned multinational conglomerates.

22.3.4 Analysis of Research Themes

In this study, VOSViewer, as a scientific mapping tool, was used to analyze the keyword clustering of SCI papers published in the past five years (2015–2019) in the field of IWT and to build a knowledge map (network) based on the word co-occurrence matrix, which is shown in Fig. 22.9. Each node represents a keyword, with a larger node representing a keyword with a higher frequency. An edge between two nodes represents the co-occurrence frequency of keywords, with a thicker line corresponding to a higher frequency. The distance between two nodes represents

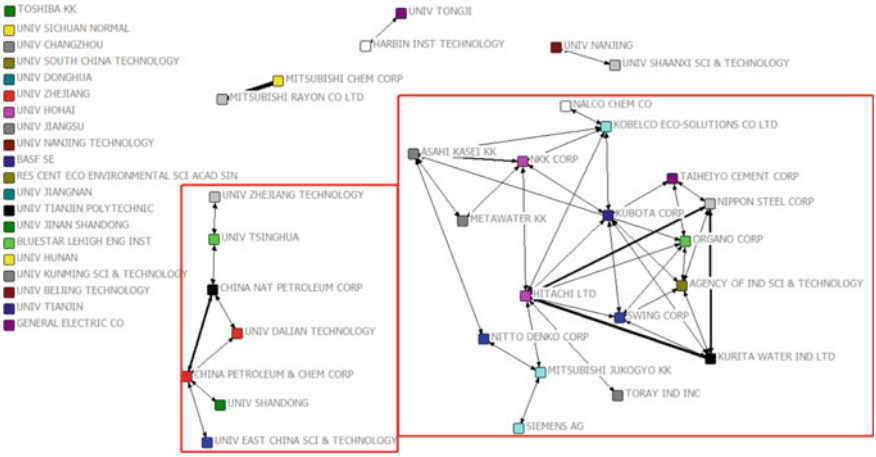

Fig. 22.8 Cooperation network of TOP50 patent holder

the relationship between keywords, with a shorter distance representing a higher similarity. The colors were assigned through clustering based on the occurrence of words describing the topics, and each color represents a topic cluster (Colares et al. 2020).

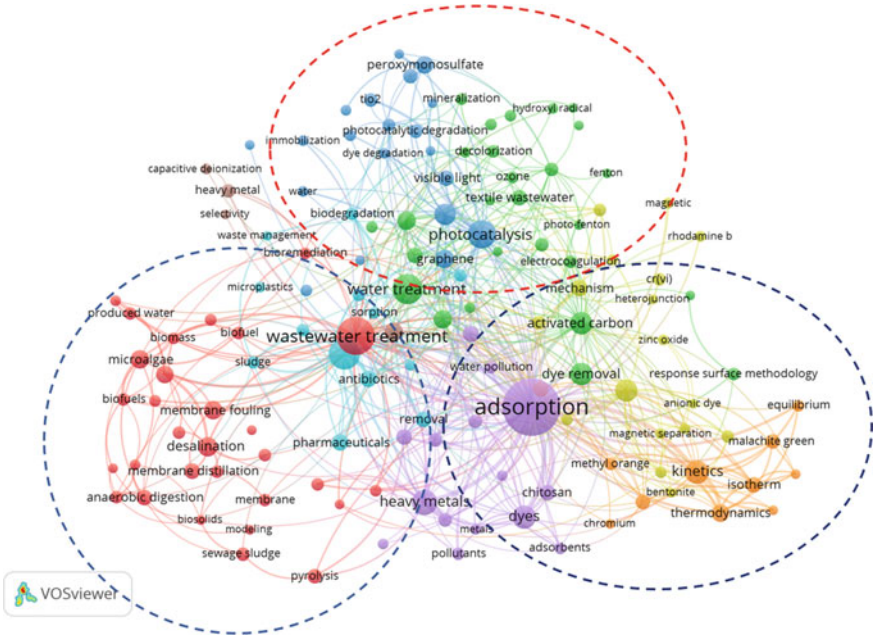

Fig. 22.9 Research topics of IWT papers

As we can see from Fig. 22.9, the topic clustering analysis of SCI paper keywords in the IWT field shows that IWT technology research has focused on three major research categories. We painted different colors to distinguish them. The blue circles are the hot topics of research on IWT based on biological processes. The purple circles are the hot topics of research on IWT by adsorption, activated carbon and methylene blue methods. And the red circles are the hot topics of research on IWT in terms of photo catalysis and oxidation.

Patents are important outputs of technology innovation, and the distribution of patents reflects the technology application field. International Patent Classification (IPC) is an international general patent classification and searching tool, which is necessary for all countries in the world. IPC defines categories according to the technology topics and forms a complete stepwise classification system, according to departments, divisions, large categories, small categories, large groups, and small groups. Different IPC numbers represent different types of technical topics. Figure 22.10 shows the distribution of technical subjects of patent applications in major countries/regions. China and Japan are rising through active investment and are becoming the most active zone for IWT patents. The IWT patents of China focus on the application in water purification through adsorption, activated carbon and others technologies. Japan had a high presence in water purification through biological processes. And USA had advantages in water purification by biological processes and the application of polymers for water treatment (compositions) for scale and corrosion inhibition.

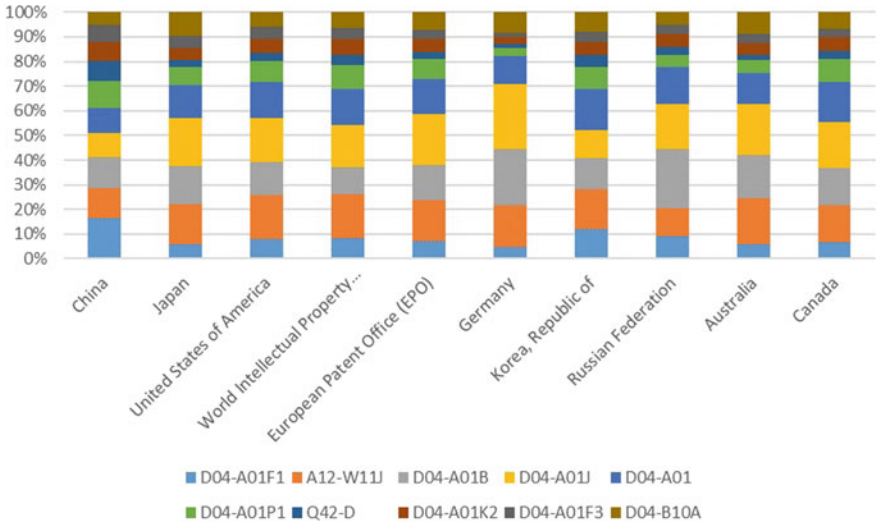

Fig. 22.10 Distribution of technical subjects of patent applications in major countries/regions

22.4 Conclusion

In this paper, topic discovery and clustering were studied using bibliometric, social network analysis, and information visualization technology, based on the WOS database and the DII global patent database. The technology searched for papers and patents related to IWT technology to reveal the development trends of IWT technology and provide the references for related technical layout and hotspot tracking.

Through bibliometric analysis and topic clustering of papers and patents in the IWT field, some trends of IWT technology research and development are evident:

1. It can be observed, from the annual publication trends of IWT papers, that the out-put of SCI papers has maintained stable growth in the past decade, and there is a trend of continuous growth in the future, with a high development momentum.
2. In terms of national research strength, China ranks first in the number of published papers and patent applications.
3. Both Japanese and Chinese patent holder prefer to cooperate with domestic institutions and to some extent lack foreign exchange and cooperation, so they may need to expand overseas technology partners in the future.
4. The global research hotspot in IWT are biological processes; adsorption, activated carbon and methylene blue methods; photo catalysis and oxidation.
5. Different countries have different performances in technology layout: China focus on the application in water purification through adsorption, activated carbon and others technologies. Japan had a high presence in water purification through biological processes. And USA had advantages in water purification by biological processes and the application of polymers for water treatment (compositions) for scale and corrosion inhibition.

It should be pointed out that the conclusions of this paper come from two databases—WOS and DII—which do not fully include papers published in all forms and languages around the world. Therefore the conclusions are similarly representative but have certain limitations.

Acknowledgements This study was supported by the Information Monitoring of Water Treatment, National Science and Technology Library (No. 2021XM56-1).

References

Adetunji A, Olaniran O (2021) Treatment of industrial oily wastewater by advanced technologies: a review. Appl Water Sci 11(6):98(2021)

Chiu WT, Ho YS (2005) Bibliometric analysis of homeopathy research during the period of 1991 to 2003. Scientometrics 63(1):3–23

Colares G, Wiesel PG, Oliveira GA, Lemos PZ, Lutterbeck CA, Kist LT, Machado ÊL (2020) Floating treatment wetlands: a review and bibliometric analysis. Sci Total Environ 714(Apr.20):136776.1–136776.17

Dutta D, Arya S, Kumar S (2021) Industrial wastewater treatment: current trends, bottlenecks, and best practices. Chemosphere 285:131245–131245

Fang Y, Zheng T, Wu Y, Wang Y, Li F (2019) Global trends of coagulation for water and wastewater treatment by utilizing bibliometrics analysis. Desalin Water Treat 151:93–105

Fu HZ, Ho YS, Sui YM, Li ZS (2010) A bibliometric analysis of solid waste research during the period 1993–2008. Waste Manag 30(12):2410–2417

Fu HZ, Wang MH, Ho YS (2013) Mapping of drinking water research: a bibliometric analysis of research output during 1992–2011. Sci Total Environ 443(Jan.15):757–765

Lefebvre O, Moletta R (2006) Treatment of organic pollution in industrial saline wastewater: a literature review. Water Res 40(20):3671–3682

Mao G, Hu H, Liu X, Crittenden J, Huang N (2021) A bibliometric analysis of industrial wastewater treatments from 1998 to 2019. Environ Pollut 275

Price D (2014) A general theory of bibliometric and other cumulative advantage processes. J Am Soc Inf Sci 27(5):292–306

Raji M, Mirbagheri SA (2021) A global trend of Fenton-based AOPs focused on wastewater treatment: a bibliometric and visualization analysis. Water Pract Technol 16(1):19–34

Wang MH, Yu TC, Ho YS (2010) A bibliometric analysis of the performance of water research. Scientometrics 84(3):813–820

Wouters P, Ding Y, Chowdhury G, Foo S (2001) Bibliometric cartography of information retrieval research by using co-word analysis. Inf Process Manag 37(6):817–842

Zheng T, Wang J, Wand Q, Nie C, Smale N, Shi Z, Wang X (2015) A bibliometric analysis of industrial wastewater research: current trends and future prospects. Scientometrics 105(2):863–882

Chapter 23
Intelligent Water Resources Management

Desislava Botseva, Nikola Tanakov, and Georgi Nikolov

Abstract In the current research, the authors' team considers water as a primary resource for the protection of human life and health, but also as a generator of socio-economic growth and healthy environment. Rationally managed water resources are an essential component of urban development, which reduces poverty and morbidity and improves the quality of life. Conventional water system management maximizes existing water flows to fulfill the necessities of society. Another aspect taken into account is the impact of climate change on the sustainability of water resources. On the one hand, such a thought line considers the risk of water scarcity, on the other, the possibility of generating new innovative solutions, dictated by such a challenge. Sustainable water management is essential for ensuring Earth's life and future. The challenges in environmental planning for sustainable water development are stochastic dynamics and hydraulic constraints. This document proposes adaptive intelligent, diligent water resources planning to maintain the urban water environment (AIDWRP). The adaptive smart approach is a subset of artificial intelligence (AI) technology that effectively models environmental planning for sustainable water development. Artificial intelligence modeling improves water efficiency. It transforms information and lays the foundation for a more cost-effective process, improving data-based decision-making. The technology combines digital tools for artificial intelligence and human intellectual skills.

Keywords Sustainability · Regional · Development · Urban · Artificial intelligence

23.1 A Few Introductory Words

Water resources are considered an essential factor in economic and social growth for effective environmental management and planning. The need to design sustainable water resources management is vital to preserving their ecological, economic

D. Botseva (✉) · N. Tanakov · G. Nikolov
University of National and World Economy, Sofia 1000, Bulgaria
e-mail: d_botseva@unwe.bg

H.-Y. Jeon (ed.), *Sustainable Development of Water and Environment*,
Environmental Science and Engineering,
https://doi.org/10.1007/978-3-031-07500-1_23

and hydrological integrity for the current society and future generations (Ali et al. 2019). Researchers apply artificial intelligence methods in planning urban water resources, mainly due to their powerful capacity for analysis, flexibility, modeling, and forecasting of water capacity. Water resources must be allocated appropriately and utilized. It is necessary to assess the impact of their operation on the environment, which is a specific challenge in designing ecological systems (Lin et al. 2019; Li et al. 2019).

Increasing water demand is due to climate change, urbanization, and population growth. There is a need for these processes to be effectively researched and modeled for the diversified and complex urban water resources using modern technology platforms (Mrówczyńska et al. 2019; Liu et al. 2019). Technological solutions contributing to the development of a sustainable environment can allow progressive socio-economic changes for sustainability (Cazorla-Montero et al. 2019; Bazan-Krzywoszańska et al. 2019). Traditionally established water management approaches should go beyond their standardized frameworks. This modernity, in turn, requires the measurement and modeling of stability. The researchers use the sustainability index of water policies and related solutions. The Sustainability Index (SI) analyzes the effectiveness of different water policies on the environment and the system's water capacity. The main goal is to reduce the vulnerability of water resources using new generation technologies and artificial intelligence (Prabakaran et al. 2019; Wang et al. 2019). Such a methodology is in line with the dynamically increasing Smart City concept, which should meet the needs of modern societies in the perspective of the sustainability of all its systems.

The SI integrates performance standards that consider the ability to manage the sustainability of water basins and the environment with the help of AI (Zhang et al. 2019). The index makes it possible to compare effective environmental planning and management policies through modernized criteria (Qian et al. 2019; Sachs et al. 2018). The index should measure the adaptability of the proposed approach to sustainability and environmental friendliness, thus making the most appropriate decisions (Goralski and Tan 2020).

Current water availability requires an effective resource management solution to meet the life-cycle supply and demand ratio. In many regions, water demand is growing. That arises several water management challenges. Water basins exceed their capacity, contributing to an imbalance between supply and demand. Climate change further accelerates this process (Abdo and Zeadally 2020). Activating water protection and management mechanisms at the regional level will create a prerequisite for achieving sustainable cities. They would become much safer, more efficient, socially and economically active urban structures. Water management must be responsible.

The socio-economic and environmental dimensions are also not clearly expressed in the quantitative principles needed for planning, management, decision-making, monitoring, and evaluation. Assessment models include potential indicators of environmental sustainability used when comparing management strategies in different ecosystems as an object of modeling analysis. The aim is to assist the decision-making process scientifically and measure progress towards sustainable development (Tsolov et al. 2020).

Sustainable economic and environmental development has led to over-exploitation of groundwater (Di Baldassarre et al. 2019), another powerful generator of imbalances between water supply and demand (Aina et al. 2019) that further increases the need to explore opportunities for rational use of water resources and achieve their sustainability. There are many reasons why most of them are not active due to improperly unified management of water resources, primarily due to excessive water consumption and waste (Hameed 2019).

One of these studies optimizes several methods of intelligent planning (Lozano et al. 2019). According to the study's results, integrated water resources management (IWRM) might be one of the solutions. IWRM is a mechanism that supports integrated development and management of land (Li et al. 2019), water, and interconnected resources to optimize social and economic conditions for sustainable, exploitable ecosystems in the future. IWRM focuses on promoting coordination and integration to sustain water resources.

The present study considers adaptive intelligent, diligent water resources planning (AIDWRP), a subset of AI proposed for sustainable water management in urban areas. A stochastic approach to water network modeling lies on Markov Decision processes to optimize the allocation of system resources following many uncertainties. The Markov chain describes the serial correlation for water frame optimization using artificial intelligence techniques integrated into AIDWRP. This study shows a method for optimizing the limited water resources of the basin for effective environmental management and planning. The main goal of this study is to develop a framework for modeling artificial intelligence for water resources management to increase the efficiency of their control. Artificial intelligence formulates the optimal water distribution to minimize costs, subject to improved sustainable environmental management. One of the main achievements of the model is saving water costs by controlling the water reserve of the basin.

The significant contribution of this study can be summarized as follows:

• Design and development of AIDWRP, the subset of AI for sustainable water resources management in urban regions;

• Design of a statistical model for seasonal water needs, local discharge limits, and annual consumption limits;

• Performed simulation analysis to confirm the accuracy of forecasting energy demand for sustainable environmental planning and management.

The adaptive intelligent approach consists of artificial intelligence (AI) technologies that effectively model environmental planning for sustainable water production. Artificial intelligence modeling improves water quality by making knowledge more specialized and enhancing decision-making based on data, analysis, and evidence-based on a combination of AI and computational intelligence methods. Markov's decision-making process (MDP) at AIDWRP deals with complex water management annually. It recognizes local weaknesses that identify sensitivity-oriented approaches to optimizing multiple policy areas to allow for environmental management and effective environmental planning.

The present study is influential as it contributes to the modernization of science, education, and practice in regional development. In turn, this is a must to meet

current and future challenges through integrated educational training to make the right decisions in building smart cities and regions of the future.

23.2 Problems in the Search for the Sustainability of Water and the Environment

The effects of human socioeconomic activity and climatic factors—global warming, natural disasters, risk areas, and zones—significantly impact regional and spatial planning approaches. These changes and the consequences of their action should be addressed in the overall governance concepts of all countries and have an impact on the developed strategies for spatial planning, water management, land, and natural values. However, crisis and disaster modeling and analysis and the construction of appropriate defense facilities require extensive knowledge and experience. Such a level of expertise is difficult to provide at all times, especially at the district and municipal levels of administration (Dimitrov et al. 2017). Adapting regional and spatial development approaches to global warming will ensure environmental comfort in urban areas and reduce the risk of natural disasters. The United Nations Risk Reduction Strategy classifies the risks as hydrological, meteorological, geophysical, and biological natural phenomena and disasters.

The strategic documents in the environment and water must set and integrate common goals and several requirements related to climate change, adaptation to climate change, and water management into regional and spatial development planning. They must consider the specificities and problems of each country and each region. The main goal is to determine to what extent and in what way the processes of regional and spatial development affect the state of the environment and the security and quality of water in a specific territory; what are the main problems and possible measures to solve them; what will be the required activities and resources during the relevant planning period. However, such a thought-line should not be merely conceptual. The preparation of management decisions and their transformation into strategies should align with programs and measures for river basin management, flood risk management, drought risk management and ensure coherence with environmental protection or adaptation to climate change. The overall concept should be developed at the supranational and national levels and recognized and implemented at the regional level. Environmental issues should be an integral part of each country's goals and priorities and find concrete expression in the measures included in the individual implementation programs. There is a growing need for precise environmental planning to achieve sustainability. Territory exploitation must not harm the rights of future generations (Velikova 2021).

23.3 Modern Water Management Modeling. Reality or Chimera?

Modern planning and management of water resources and the environment should involve the possibilities for intelligent modeling. Traditional approaches to water exploitation will be increasingly unsuitable in the present and the near future. This challenge requires the commitment of a new system to achieve the optimal intelligent mechanism to overcome future obstacles. The most convenient and effective models should adapt to the specific regional reality. In this way, considering the regional socio-economic system as a living organism that is actively and dynamically evolving could be harnessed to the much-needed concept of sustainability. When we talk about efficient and effective use of resources, including water resources, the most optimal model is the one that applies the regional approach. Knowledge of the typical regional (local) specifics, the exhaustive advantages, and disadvantages create the basis for building the overall management of regional systems in their optimum. The research team has selected, characterized, and summarized the following models and adapted them to the regional aspect to meet the current needs of regional and sustainable development and effective and efficient management and exploitation of water and the environment. A particular focus here should be the water supply network's quality and the possibility of diversification and decentralization of water basins. In this process, the specific significance and importance of the regional approach manifest.

The water supply model is satisfactorily optimized and validated. It offers various model simulations, and in almost all conditions, the water potential is sought to achieve the necessary indicators for productivity and operation. The research team proves that the best balance between demand and water supply must be conducive to sustainable water management in future uncertainty and change. For example, Ajay Gajanan Bhave et al. (Fritz et al. 2019) took a significant step by introducing the Uncertainty Decision Approach (DMUU) for water planning in 2019. A considerable contribution to his models is changing the adaptation processes according to the stakeholders' priorities. For example, prioritizing controlling agricultural demand increases sustainability and trade-offs between water quality within the basin and the availability of water throughout the basin.

The following proposed model is offered by Qiang Wang et al. (Osorio-Cano et al. 2019), known as the PressureState-Response and Matter-Element Extension (PSR-MEE), to assess water sustainability. The method of variance coefficient is used to estimate the weight of the indices. It quantifies sustainable water supply based on data quality. The results show that on a large scale, in different regions of the world, the sustainability of water supply is relatively low and cannot provide satisfactory use in the long run. The assessment results are designed to guide decision-makers in developing water policy.

Manuela Carini et al. (Bierbaum et al. 2020) propose the lowest cost optimization model (LCOM) for multi-source and consumer water distribution networks. This model considers a realistic situation that would compensate for the maximum allowable flow for existing source-user relationships. According to the authors, sustainable

water supply use at the national and regional levels is strategically essential. Sustainable water supply use leads to economic and social change and contributes to the proper process of sustainable development of the environment.

David Haro-Monteagudo et al. (Modgil et al. 2020) build a Cascade Modeling Approach (CMA) for the long-term sustainability of water resources in climate change. Therefore, indices based on the duration, frequency, and size of water deficits assess the productivity and resilience of the system. The results demonstrate the future challenges that current management scenarios generate, especially for irrigated agriculture. The study calls into question the future viability of the system. These results indicate that current water strategies in this area need to be reviewed based on climate change.

Water is an essential resource for maintaining socio-economic stability and sustainable ecosystems in the modern era. Its importance and significance will increase over the coming years. Conventional water management is challenging to optimize current flows to meet all conflicting needs. Climate change will also exacerbate problems in water supply control, leading to instability.

23.4 AIDWRP and the Possibilities for Regional Application in Uncertainty and Change

Based on the study, the sustainable development of water management in urban areas for environmental management and planning is essential for today's challenges. By researching AIDWRP, we could search for opportunities to overcome some of the challenges at the regional level.

In essence, AIDWRP uses a subset of AI with high reliability without compromising hydrological, environmental, and physical integrity. Sustainable water resources, policies, and integrated resource management are essential characteristics that can combine all water problems and appropriate solutions and their socio-economic and environmental aspects. The challenges and opportunities for designing an effective model for sustainable water management with the help of AIDWRP and MDP in urban areas are defined below, and the findings show that decision-makers in urban water management can use the modeling system. A necessary clarification for the present study is that the mechanisms and approaches of regional development are fully utilized concerning urban areas, considering them as urban regional structures.

In this document, AIDWRP is the subset of AI. It should propose a mechanism for sustainable planning, programming, development, and management of water resources and the environment, based on data algorithms generated in urban areas. The broader scope of using artificial intelligence algorithms in the water supply is to increase the overall productivity of water infrastructure activities such as controlling and repairing assets, energy-saving, and reducing the carbon and water footprint, thus increasing the quality and the cost of services provided. Such an interpretation aligns with the adopted UN Sustainable Development Goals, their European context and

reading, the Green Deal, the Knowledge Economy, the Carbon–Neutral Economy, and others.

Artificial intelligence aims to develop water infrastructure to implement climate protection strategies, water safety strategies, disaster risk management plans, and improved water management. Sustainable Water Resources Management (SWRM) involves allocating financial and social services needed to maintain water systems for sustainable planning and environmental management. Urban water management aims to build sustainability, vitality, productive and sustainable cities, and towns. The SWRM assessment requires accountability for the actual costs of water management overheads.

Evaluation models include future environmental sustainability indicators to compare management practices with site modeling analyses that allow individual managers and governments to assess progress toward sustainable practices. The proposed model also considers socio-economic and environmental aspects, which often do not easily translate into quantitative values needed for planning, decision-making, monitoring, and evaluation. The constraints for sustainable water resources management in urban areas are analyzed and presented in the Fig. 23.1.

The following figure shows the proposed AIDWRP approach in urban waters. Water supply in the region includes the primary urban economic substructures such as social and natural characteristics. Water has its natural presence in nature and the geographical environment. The artificially improved water management network is the urban aquatic environment. The natural water cycle significantly impacts the urban climate, including restoring water resources. Rainfall is one of the most critical aspects of the city's water supply network and plays a vital role in restoring water supply to the environment.

Precipitation reaches the river network and groundwater, significantly affecting their slope, permeability, soil structure, and rainfall intensity (Fig. 23.2).

Urban water systems have revolutionized large, highly engineered systems in which extensive pipeline networks bring water from surrounding watersheds and aquifers. In large irrigation systems, the water used will be mainly collected and processed to remove pollutants and nutrients recovered in rivers and the sea. These systems provide the population and industry with reliable, clean water and protect society, but there are suggestions that water services can be much more efficient than simply importing water, discharging wastewater, and collecting rainwater. The regional community should effectively use available local water sources, especially in dynamic urbanization processes. When the population grows and scatters in different settlements, it is necessary to study the possibilities for using local water resources from watersheds and aquifers, which have not been thoroughly researched and exploited. The artificial intelligence modeling system applies to this process and flood risk control. It could overcome the challenge of water supply from traditional water sources and catchments, obsolete sewerage networks, and the exploitation of water resources with exhausted reserves and quality.

The ability of the internal (local) and external (centralized) water supply systems influences water supply reliability through Artificial Intelligence. Water depletion and component damage affect the efficiency of the water supply system. The quality

Fig. 23.1 Functions of urban water management

of the local system is crucial for water supply. Water scarcity in the primary water source and damage to the water supply system affect the efficiency of the water supply. Here, the different uses of the pre-planned water system further complicate its efficiency. TPPs evolved much later than the water supply network; however, it uses the same network that now has to satisfy various functions, which further questions the efficiency of water supply. Any water supply system aims to reduce water losses and increase reliability, as this will improve economic and environmental performance and will certainly provide consumers with more exceptional service.

23.5 Conclusion

The environment needs to be recognized both as a legitimate water user and as a source of water resources. In this sense, it is necessary to look for opportunities to achieve water management's ecological and hydrological integrity. The effects on

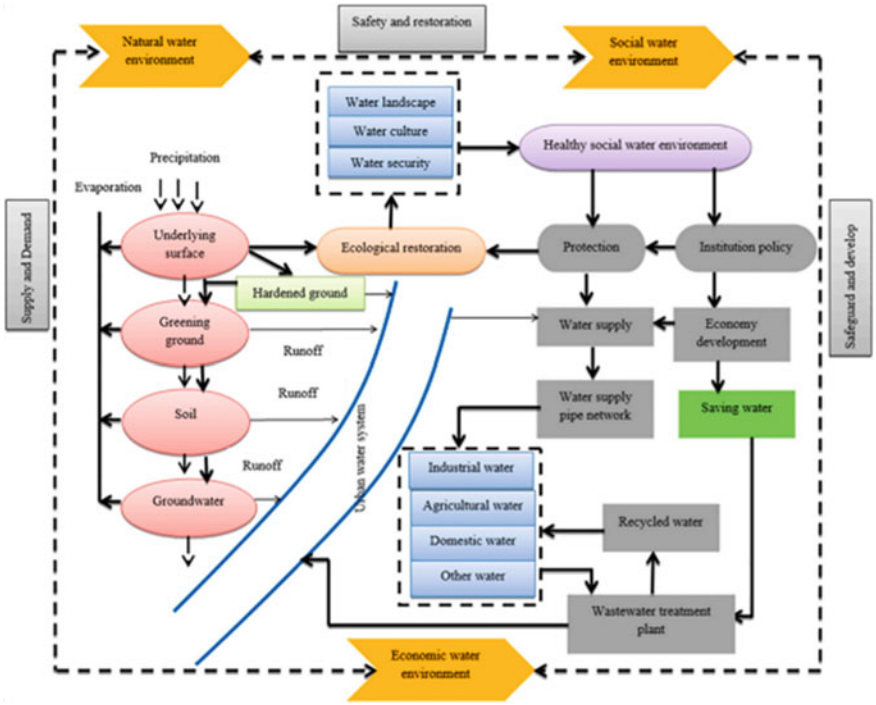

Fig. 23.2 The proposed AIDWRP method in an urban water environment

the development of water resources could be mitigated. The present study offered the AIDWRP's water management capabilities in urban areas.

Markov's approach to the decision-making process for planning and managing water resources explores the possibilities of different water horizons. The planning and development of water resources must include future climate scenarios to ensure their sustainable development. Such a development should carry out the relevant environmental assessments and meet the pre-defined criteria and standards. The model achieves optimization by reducing water supply costs. Groundwater drainage can continue without regulation as long as the cost of pumping exceeds the value of the user's limit.

The proposed AIDWRP method improves the ratio between supply and demand of water resources compared to other existing methods. The findings show that the artificial intelligence modeling system can be used for decision-making in urban water management. Markov's decision-making process (MDP) in AIDWRP deals with complex water management. It recognizes local weaknesses that identify sensitivity-oriented approaches to optimizing multiple policy areas to allow for environmental management and effective environmental planning. Accordingly, the commitment to water management supply and demand has been eased, and significant increases in local economic performance have been simulated with observed effects.

The future searches of the author's team will focus on creating a system for monitoring the effective management of water resources through the LoRa-network. Such research is needed to link modern regional development education with the construction of smart cities and regions of the future.

Acknowledgements The paper is part of a research project titled НИ-14/2020, "Modernizing regional development in the context of digital transformation," financed by the University of National and World Economy via the program for Scientific and research activities.

References

Ali R, Kuriqi A, Abubaker S, Kisi O (2019) Hydrologic alteration at the upper and middle part of the yangtze river, China: towards sustainable water resource management under increasing water exploitation. Sustainability 11(19):5176

Bazan-Krzywoszańska A, Mrówczyńska M, Tront S (2019) GIS technology, 3D models and mathematical models as a tool for assessing development capabilities of flood risk land to make arrangements of municipal planning documents. J Ecol Eng 20(1)

Bierbaum R, Leonard SA, Rejeski D, Whaley C, Barra RO, Libre C (2020) Novel entities and technologies: environmental benefits and risks. Environ Sci Pol 105:134–143

Cazorla-Montero A, de los Ríos-Carmenado I, Pasten JI (2019) Sustainable development planning: master's based on a project-based learning approach. Sustainability 11(22):6384

Cernev T, Fenner R (2020) The importance of achieving foundational sustainable development goals in reducing global risk. Futures. 115:102492

Di Baldassarre G, Sivapalan M, Rusca M, Cudennec C, Garcia M, Kreibich H, Konar M, Mondino E, Mård J, Pande S, Sanderson MR (2019) Sociohydrology: scientific challenges in addressing the sustainable development goals. Water Resour Res 55(8):6327–6355

Dimitrov D, Penchev G, Bogomilova E (2017) GIS application for economic assessment of direct disaster losses. In: 2nd international conference on information technology in disaster risk reduction (ITDRR), Sofia, Bulgaria, pp 123–135. https://doi.org/10.1007/978-3-030-18293-9_11. ⟨hal-02280319⟩

Endl A, Tost M, Hitch M, Moser P, Feiel S (2019) Europe's mining innovation trends and their contribution to the sustainable development goals: blind spots and strong points. Res Policy 10:101440

Fritz A, Haase VG, Rasanen P (Eds) (2019) International handbook of mathematical learning difficulties. Cham Switzerland: Springer

Hameed AA (2019) Smart city planning and sustainable development. In: IOP conference series: materials science and engineering, vol 518, no 2. IOP Publishing, p 022042

Li S, Xiao W, Zhao Y, Xu J, Da H, Lv X (2019b) Quantitative analysis of the ecological security pattern for regional sustainable development: case study of Chaohu Basin in eastern China. J Urban Plan. Dev 145(3):04019009

Lin T, Fan W, Xiao C, Yao Z, Zhang Z, Zhao R, Pan Y, Chen Y (2019) Energy management and operational planning of an ecological engineering for carbon sequestration in coastal Mariculture environments in China. Sustainability 11(11):3162

Liu D, Zhang G, Li H, Fu Q, Li M, Faiz MA, Ali S, Li T, Khan MI (2019) Projection pursuit evaluation model of a regional surface water environment based on an ameliorative moth-flame optimization algorithm. Ecol Indic 107:105674

Lozano R, Barreiro-Gen M, Lozano FJ, Sammalisto K (2019) Teaching sustainability in European higher education institutions: assessing the connections between competences and pedagogical approaches. Sustainability 11(6):1602

LNCS Homepage, http://www.springer.com/lncs. Accessed 21 Nov 2016
Martinezpaz JM, Pellicermartinez F, Colino J (2014) A probabilistic approach for the socioeconomic assessment of urban river rehabilitation projects Land Use Policy, 36:468–477
Mrówczyńska M, Sztubecka M, Skiba M, Bazan-Krzywoszańska A, Bejga P (2019) The use of artificial intelligence as a tool supporting sustainable development local policy. Sustainability 11(15):4199
Modgil V, Id JM, Narayan C, Kalia M (2020) Comparative analysis of virulence determinants, phylogroups, and antibiotic susceptibility patterns of typical versus atypical enteroaggregative E. coli in India. PloS Negl. Trop Dis 14(11):e0008769. https://doi.org/10.1371/journal.pntd.0008769
Osorio-Cano JD et al (2019) Effects of roughness loss on reef hydrodynamics and coastal protection: approaches in latin America Estuaries Coasts 42:1742–60
Prabakaran K, Nagarajan R, Eswaramoorthi S, Anandkumar A, Merlin Franco S (2019) Environmental significance and geochemical speciation of trace elements in Lower Baram River sediments. Chemosphere 219:933–953. https://doi.org/10.1016/j.chemosphere.2018.11.158
Qian J, Law WR, Wei JW (2019) Knowledge mapping in travel website studies: A scientometric review. Scandinavian Journal of Hospitality and Tourism, 19(2):192–209. https://doi.org/10.1080/15022250.2018.1526113
Sachs J, Schmidt-Traub G, Kroll C, Lafortune G, Fuller G (2018) Implementing the goals. SDG index report 2018. Bertelsmann stiftung and sustainable development solutions network, New York
Tsolov G, Vasileva E, Lyubomirova V (2020) Incoming conditions for a green economy building in the Bulgarian regions, International symposium on natural resources management, Pirot, Serbian, ISBN 978-86-7747-624-3, pp 205–210
Velikova E (2021) Sustainable environmental planning of a tourist destination Bulgaria—state and trends. In: Jeon HY (eds) Sustainable development of water and environment. ICSDWE 2021. Environmental science and engineering. Springer, Cham. https://doi.org/10.1007/978-3-030-75278-1_22
Wang W, Chen P, Lee EJ, Mu D (2019) Full-3D seismic tomography for structure of the critical zone. Chapter in earthquake and disaster risk: Decade retrospective of the wenchuan earthquake, 1st Ed. YG Lee (Ed) Higher education press & Springer Nature Singapore. https://doi.org/10.1007/978-981-13-8015-0_8

Chapter 24
Sustainable Cities via Smart Development Strategies: Bulgarian Case

Elka Vasileva, Veselina Lyubomirova, and Georgi Tsolov

Abstract Sustainable development is one of the leading directions of regional policy in Europe. Smart systems implementation for achieving sustainability is a gaining popularity policy-recognized direction for city development. The Smart city strategy index works as a new instrument of city policies following sustainable smart planning. Bulgarian cities are making some smart and sustainable development steps as part of the city plans but still do not work on specific smart city strategies. The authors analyze Bulgarian city policy programs for the Smart city strategy index indicators. The results provide an overview of implemented smart and sustainable development measures. Concluded is how far or near specific smart city strategies are Sofia, Varna, and Burgas as main regional centers in Bulgaria.

Keywords Sustainable city · Smart city strategy · Local development

24.1 Introduction

The transformation of cities via implementing smart products and services is still not mainstream. However, the process is going in that direction with an increasing year rate of examples from different regions worldwide. Smart city development is more an instrument than a goal. It helps cities adapt to the expanding technological reality in all life and well-being areas. Although smart innovations are the way, the goal is a future with more sustainable cities. The sustainable development goals are implemented in the whole philosophy of today's and future EU regional development

E. Vasileva · V. Lyubomirova (✉) · G. Tsolov
University of National and World Economy, Sofia 1000, Bulgaria
e-mail: veselina@unwe.bg

E. Vasileva
e-mail: elvasileva@unwe.bg

G. Tsolov
e-mail: georgi.tsolov@unwe.bg

H.-Y. Jeon (ed.), *Sustainable Development of Water and Environment*,
Environmental Science and Engineering,
https://doi.org/10.1007/978-3-031-07500-1_24

policy (Kalfova 2019). European institutions and policymakers focus more concentrate the Union policy declarations and vision on cities. In the policy papers and supernational political declarations, they recognize cities' role and place as the key actors and main arenas for the sustainable future (Saykova 2020).

Bulgaria has been an EU member state since 2007 and already two strategic periods conduct regional policy regarding the EU methodologies—2007/2013 and 2014/2020. During these periods the national and local authorities organize a whole new structure of strategic documents, including city planning, financing, and development.

According to the Eurostat methodology, Bulgaria is divided into six regions for organizing the European Union in comparable statistical entities. The three central and leading cities have been adopting an increasing number of smart products and services during the last six years. Even so, their practice in smart development is still highly fragmented.

24.2 Sustainable Smart City

In the increasing number of scientific literature about sustainable cities, approaches differ from a research angle and territorial, geographical, natural, administrative, historical, political tradition and factors. Whatever the perspective is, the triangle of leading indicators includes three adjectives—accessible, green, and fair (Simon 2016). These three dimensions have dominated the conceptualization and empirical analysis in the last two decades and are the essence of today's regional development plans in Europe. "Sustainable development occurs only when management goals and actions are simultaneously ecologically viable, economically feasible, and socially desirable" (Campbell and Heck 1997).

Accessibility in cities means a new level of physical and digital accessible urban area for tourists, elderly inhabitants, visitors, etc. For example, a mobile app for the tourist city directions accessible with will chairs, or an application for different able gests in museums and other cultural spots (Nikolov et al. 2021; Velikova 2019). The broadest and most important content of accessibility includes easy public transport access to the city center and whole urban agglomeration, well-organized and provided access to social services including schools, medical facilities, teachers and doctors, etc. Accessibility is in strong relation with a meaning of a fair, socially inclusive city. Accessible is also a city with digital administrative services, a normative and institutional environment welcoming and supporting local start-up entrepreneurs investors.

There are numerous varieties of green cities due to city management vision and conducted policy. Generally, a concept of a green city contains policy recommendations and regulations to increase industrial and public infrastructure investments, taking into account the requirements for the green transition. In the last decade, governments have extended their ideas to green development with soft measures such

as implementing ICT applications and products for measuring different green-related indicators in the urban environment and society (Blewitt 2015).

Back in the 90ties, before the rapid development of smart technologies, the need for a link between technology and sustainable goals and challenges was determined. "Sustainable technologies are those that can reduce environmental pollution through significant technical advances. Because society as a whole benefits from sustainable technologies, they represent appropriate targets for public investment". Underlined is the leading role of governance for adopting sustainable technologies, to invest in technologies for achieving green goals, provide proper normative and local conditions for development and implementation of technologies, and develop public policies and funding in that direction (Shen 1997). Jeffry Sachs stresses the place of sustainable technologies not as an element of development patterns but as a core wave for transition for economy, society, and territories. In his concept "wave of sustainable technologies are ways to produce and mobilize energy and to transport ourselves and transport goods, to relieve the massive human pressures and human-caused destruction of the Earth's ecosystems" (Sach 2015). Furthermore, he sees sustainable technologies as a "core part of achieving sustainable development" (Sach 2015).

In addition, via technologies, "cities were among the first to take advantage of the new open data movement" (Stowers et al. 2018). As a result, local authorities and city management have the new opportunity—to use smart city instruments for achieving accessible, green, and socially fair economic development and well-being for citizens, visitors, investors, and other newcomers.

On the one hand, cities are municipalities with local governments and authorities. On the other side, they are also cities with management bodies. Both governance centers are connected and dependent on delegated national funding by sectors, national law framework, policies, etc. At the same time, the local management has the chance to build a specific portfolio of sustainable measures for the city. In this regard, the challenge of sustainable development includes a shift away from narrow sectoral programs in urban development towards approaches which can both address and build upon these interdependent concerns" (Elliott 2013).

Several cities have already launched smart city strategies. As a sign of a new wave of transformative management in regions and cities, sustainability via smart finds a decent place among other policy-making approaches. "Local governments have found that it is not only a matter of changing approaches of planning and city-making, but also how city-making is practiced—it has had to reinvent its role without overlooking its institutional constraints, and open-up to experimenting" (Frantzeskaki et al. 2018).

Supranational institutions and international organizations have different sustainable development measurement systems. "Sustainable development goals require big-picture thinking and an ability to recognize priorities without losing sight of essential elements of complex socio-ecological systems" (Pinter et al. 2017). Although most recommendations of sustainable policy come from international strategic documents and agendas, national states have the leading role in their

implementation. Sustainable technologies can be seen as implementing sustainable development measures via smart products and instruments in cities.

There are several smart city dimensions. A smart city can be a way of development on a systemic level, including all public areas, policies, and sectors. It remains accurate that "there is a difference between the tempo of the conceptual development of the smart city and its adoption and understanding from the political agenda on a national and local level" (Vasileva et al. 2020).

Smart instruments can enhance cities in different directions, and smart city strategy can work for structuring the local authorities and managers' vision in that area. If we consider the smart transformation an instrument, then the city's future still needs a goal. A sustainable city via smart systems and technologies is a possible fruitful concept in that direction.

The recently developed smart city strategy index provides 12 indicators for measuring the smart city stage and level. The indicators also have 31 sub-criteria. The index creators divine the main indicators in two categories—6 action fields and six enablers with equal weight in the final score (Berger 2019). In the index are considered only cities with complete smart city strategies and evaluate them with the criteria in Table 24.1.

If a city needs smart enhancements to accomplish sustainable sectoral policies, the city's preparedness for smart transformation is first for observation and analysis. In this regard, the smart city strategy index' criteria are a kind of a pathway for policymakers and experts to evaluate different local strategic documents. They can assess what stage of smart transformation a city is. The index's six action fields and their sub-criteria (right column on Table 24.1) are strongly related to sustainable development in cities. Therefore, cities' strategic documents containing the index action filed criteria (Table 24.1) have to be considered closer to sustainable goals.

Table 24.1 Criteria and sub-criteria for smart city strategy evaluation

Enablers (factor from the city environment)	Action fields (areas from investments)
Budget (funding and financing)	Building (facility management, home applications, construction)
Plan (time plan, measurable goals)	Energy and environment (energy management, water management, waste management)
Coordination (executive priority, administrative coordination)	Mobility (traffic management, multi-modality, logistics)
Stakeholders (citizen acceptance, partnership)	Education (education platforms, learning formats, digital skills)
Policy and legal framework (regulation, innovation, and financial support, IT and data security	Health (health information systems, ambient assisted living, telemedicine)
Infrastructure (open data, high-speed internet, connectivity technology)	Government (e-services, digital public administration, civil security)

Source Based on the Smart City Breakaway (Berger 2019)

24.3 Bulgarian Case—Evidence from the Three Main Cities and Regional Centers

24.3.1 Case Study—Bulgarian Cites Burgas, Varna, and Sofia

For Bulgaria, as a current EU member state, sustainable cities are part of balanced regional development. The role of a regions' central cities is to work as a flagman for exogen and endogen economic development. The leading city is responsible for attracting investors and generating an environment for regional economic potential. In fact, in a unitary state with a low level of actual fiscal decentralization (Pavlova-Banova and Aleksandrova 2021), only a few major cities have resources, opportunities for multilevel partnership, administrative capacity, EU grant financing, and other advantages for funding a process of smart systems implementation.

The EU framework for grant financing regarding regional development requires all projects for funding commitment to sustainable development issue and related to that—local problem-solving. In this regard, the Bulgarian regional and municipality strategies and plans contain sustainable development goals. Furthermore, innovations in public services support for local industry and business environment are also an integrated part of the planned cities development measures.

We are using the 12 leading indicators of the Smart city strategy index to outline the Bulgarian case. Focus of analysis are three leading Bulgarian cities: the capital city with a population of over 500 000, and two seacoast cities also unformal regional centers, financially capable of developing city policies and investments. Varna and Burgas are the main seaports industrial and tourism centers for the north and south Bulgarian Black Sea coast. They are also the most significant industrial, administrative, and educational cities for the regions they belong. In addition, the examined cities have several similar strategic documents as part of the national, regional, and local development framework.

They all have new plans for integrated development (2021–2027), according to the national, regional development methodology and the EU framework and requirements for policy funding for that period.

The examined research question in these documents was, are there any smart measures for sustainable development. We outline them with the smart city strategy index criteria—mainly the six from the action field section (right column in Table 24.1). The idea is to define where these cities are in their way to initiate complete smart city strategies with the understanding that such a complex document is a pathway for achieving more sustainable development.

24.3.2 Smart City Strategy Enablers Criteria in the Examined Cities

Budget

In the Bulgarian case, the measured enablers (criteria for the city environment) are similar for the three cities. As belonging to the six leading cities in the country, these three have their financial resources for policies development. However, they depend on the national government in many sectors, where most financing is a delegated budget from the state and their self-financing opportunities. Cities' budgets are based on the local authorities' responsibilities and the ongoing strategic plans. Special budget lines for sustainability are mainly part of external EU project-based financing.

Plan

All the examined cities have their plans for integrated development during the period 2021–2027 and similar plans for earlier periods. These documents are part of the national regional policy and contain EU, national, and local funding projects. The strong dependency on EU funds on these strategies requires most sustainable development goals, innovations, and smart growth projects.

Coordination

The coordination capacity of the local administration was systematically developed, especially regarding EU funding and regional planning governance responsibilities. This is constantly monitored during the assessment of the strategic plan. The sustainable development challenges are recognizable and are often part of the policy debate among local administration and authorities. Still, smart specialization is not a well-known direction for city transformation.

Stakeholders

Sofia, Varna, and Burgas have numerous civil society initiatives, active NGO sector, and working partnerships with the local authorities and other stakeholders—business, social partners, etc. A good illustration of that working relations is the achieved prices for Burgas—as European sport capital in 2015, Varna—European youth capital in 2017, and Sofia—in the innovative cities top 20 for 2020, among other awards. All alwards were achieved in partnership with all stakeholders.

Policy and Legal Framework

The policy supporting the smart development of cities is also related to innovations in regional development, cybersecurity risk, GDPR legal requirements, etc. In Bulgaria, all these issues are maintained and considered on a national level. Cities and municipalities have smaller space for other self-regulations. They can develop local e-governance services, digitalize administrative processes, and train the employed human resources.

Infrastructure

The index is considering the implementation of ICT and smart system systems. The Bulgarian municipalities and the three main cities examined here still do not have systematic results. Smart products and enhancements are fragmented in different policy sectors without a strategic horizon.

24.3.3 Smart City Strategy Action Field Indicators in the Examined Cities

The following table presents results from content analysis of integrated development plans (2021–2027) of three Bulgarian cities, Burgas, Varna, and Sofia. In addition, information of other relevant local strategic documents is used for verification and additional information (Table 24.2).

The table contains information about planned sustainable activities in each policy area—buildings, energy, environment, mobility, education, health, and government. Most important are measured smart initiatives for the achievement of sustainable goals.

In general, the data show that the examined cities are oriented to sustainable development measures in almost all areas. We illustrate some examples for the fulfilled sub-criteria in each category during the period 2021–2027 (Integrated development plan of Burgas, Varna, Sofia) (Integrated development plan of Burgas municipality 2021–2027; Integrated development plan of Varna municipality 2021–2027; Integrated development plan of Sofia 2021–2027):

Buildings

Burgas is planning systems for energy and resource management of public buildings and improving the efficiency of building installations. Similarly, Sofia is thinking of renewable energy sources and service intelligent installations. In addition, both cities are working on green bindings ideas such as a carbon–neutral industrial park (Burgas) and construction and maintenance of "green" roofs and photovoltaic installations (Sofia). Sofia is planning to invest in 'deep renovation' of a public building. Meanwhile, Varna is still on the level of energy efficiency of a public building.

According to the sub-criteria—facility management, home applications, construction—the building's management in the three cities mainly fulfills the sub-criteria about construction and partly about facility management. On the other hand, smart applications for public building facilitation are not included.

Energy and Environment

Burgas is planning investments in circular economy measures—blue growth center, intelligent systems for waste management, including food, water, and industrial waste. Varna is also interested in waste management projects and installation for

Table 24.2 Comparative smart-sustainable performance of chosen cities

Criteria	Burgas		Varna		Sofia	
	Sustainable	Smart-sustainable	Sustainable	Smart-sustainable	Sustainable	Smart-sustainable
Building	✓	✓	✓	✗		✓
Energy and environment	✓	✓	✓	✓	✓	✓
Mobility	✓	✓	✓		✓	✓
Education	✓	✓	✓	✓	✓	✓
Health	–	✓	–	✗	–	✓
Government	–	✓	–	✓	–	✓

Source The authors, based on the Smart City Strategy Index Criteria and the integrated strategies of Burgas, Varna, Sofia (Integrated development plan of Burgas municipality 2021–2027; Integrated development plan of Varna municipality 2021–2027; Integrated development plan of Sofia 2021–2027)
✓ Identified as planned; x identified as not planned; – not applicable

an utilization of obsolete car tires. Sofia is focusing on alternative heating sources and systems and hydro- and geothermal energy use. Biowaste management and city composters are also in the capital sustainable interest. Different smart applications are part of the solutions in Sofia, as well as an intelligent systems for monitoring and management electricity and gas supply.

Shortly the three cities are working and planning investments in all subcriteria from that field—water-, energy- and waste management.

Mobility

Burgas invests in intelligent traffic and mobility management systems electric mobility, incl. new environmentally friendly public transport vehicles. The authorities are working on developing electric bicycle transport, mobile bicycle rental applications, flexible transport models for labor mobility. Also, Varna is planning the optimization of daily labor and urban mobility. Improving noise parameters from heavy traffic and limiting the environmental burden is part of Varna's plan measures.

Sofia, as a capital city, has a more complex mobility strategy. The city management plans electric cars for public, business, taxi, and logistics transport, electrification of urban public transport, etc. Smart systems for digitalization of underground networks, development of information infrastructure and synchronization, building a system for sustainable urban logistics, construction of charging infrastructure for electric vehicles are part of the sustainable technologies in the Sofia strategic documents. Structural support and construction of the Green Ring of the capital, the creation and expansion of a shared bicycle system, and the development of private services for shared cars are also part of the numerous directions of sustainable smart development planned and started in the capital.

According to the index subcriteria, our content analyses show that traffic management, multimodality, and logistics are considered in Sofia planning, on some level in Burgas, too but so far less in Varna.

Education

Burgas's investments are directed to a high-tech academic center for biophysics and biomechanics, a center for virtual reality in partnership with a university, and a regional innovation hub for the digitalization of businesses. Meanwhile, the municipality opened STEM classrooms and a learning environment.

Varna is planning to start the construction of new, innovative educational infrastructure with more STEM equipment in school kindergartens and investments in building IT and high-tech infrastructure. Sofia is working for more technological partnerships with the universities in the capital via an intelligent specialization strategy. The capital city is increasing the number of STEM classrooms, too.

Educational smart solutions are adopted and planned in all examined cities but still need digital skills investments. It is important to underline that the three cities also have their university networks and insufficient partnership with them with significant potential for smart and sustainable initiatives.

Health

Sofia and Varna have medical universities with hospitals and research facilities which is in great use in smart, sustainable solutions planning. Burgas is planning to invest in creating a digitalized municipal health register and a network of virtual doctor's offices. In addition, the city has an idea to develop telemedicine programs and other new medical science investments. Varna falls behind these ideas and is not working on smart services in the health sector. On the other hand, like Burgas, Sofia is planning the development of mobile and remote health services (telemedicine) and smart products in socially important diseases prevention.

The subcriteria—health information system—is considered by Burgas. Both with Sofia are planning to develop telemedicine infrastructure. However, only smart technologies for assisted living are not in the plans of either of the three cities yet.

Government

Burgas plans to implement cloud services and a unified work environment and connectivity in the administration, information system for civic participation in local self-government, and internet platforms and applications for integrated tourism products. Varna will provide new electronic administrative services for citizens and businesses and plan to expand video surveillance in urban environments. The establishment of innovative centers and provision of high-tech apparatus and equipment for the development of key areas such as artificial intelligence, cybersecurity, digitalization of public administration, etc., are also prioritized from the city of Varna. Sofia focuses on an integrated platform for online and offline communication (virtual office work, civic activity, public consultations, etc. The capital city will invest in smart systems for video surveillance and public lighting. The project of digital synchronization of annual investment programs is one of the new steps of better city management of the capital.

The subcriteria for government development include e-services, digital public administration, and civil security. The three cities have planned investment in them according to their needs but considering the tendencies.

24.4 Conclusion

The experiment to use criteria and subcriteria from a new index without the whole methodology have two reasons. First, we find the smart city strategy index a timely relevant initiative. The city management worldwide faces transformation challenges and new requirements. We are interested in the Bulgarian city level of preparation for the upcoming standards for the city environment. With the index' indicators were tested the situation in the Bulgarian city strategies. From the results, it becomes clear that Burgas, Sofia, and Varna have their own smart city development mix, usually connected with sustainable goals and planned for implementation via sustainable

technologies. Sofia and Burgas are more prepared with investment initiatives, but Varna is not far behind.

Our conclusion is that the three cities have a solid base to start with discussing specialized smart city strategies. The local authorizes challenge is the connection between new specialized smart city strategies with the existing integrated development plans as a leading investment document as well as with other local strategies. In further research, there is a space for development of a smart city strategy pathway based on the uses index. Smart transformation stage of other countries and cities can be analyzed and compared via the adopted criteria.

Acknowledgements The paper is part of a research project titled НИ-14/2020, "Modernizing regional development in the context of digital transformation," financed by the University of National and World Economy via the program for Scientific and research activities.

References

Berger R (2019) The smart city breakaway, pp 6–7. https://www.rolandberger.com/en/Insights/Publications/Smart-City-Strategy-Index-Vienna-and-London-leading-in-worldwide-ranking.html

Blewitt J (2015) Understanding sustainable development, 2nd edn, Routledge, NY

Campbell LC, Heck WW (1997) An ecological perspective on sustainable development, p 55. In: Mischett D (eds) Principles of sustainable development. CRS Press, London, UK, pp 47–68

Elliott J (2013) An introduction to sustainable development, 4th edn. Routledge, London, p 299

Frantzeskaki N, Hölscher K, Bach M, Avelino F (2018) Co-creating sustainable urban futures. Springer, p 44

Integrated development plan of Burgas municipality 2021–2027 [План за интегрирано развитие на община Бургас за периода 2021–2027 г]. https://www.strategy.bg/StrategicDocuments/View.aspx?lang=bg-BG&Id=1503. Accessed 5 Feb 2022

Integrated development plan of Sofia 2021–2027 [План за интегрирано развитие на Столична община за периода 2021–2027 г. Програма за София, https://sofiaplan.bg/portfolio/programofsofia/. Accessed 30 Jan 2022, 5 Feb 2022

Integrated development plan of Varna municipality 2021–2027 [План за интегрирано развитие на община Варна за периода 2021–2027 г]. https://www.varna.bg/bg/1612. Accessed 5 Feb 2022

Kalfova E (2019) Regionalno upravlenie I regionalna politika – upravlenie i otsenka, UI – Sv. Kliment Ohridksi, Sofia, p 30 [Калфова, Е.: Регионално управление и регионална политика – управление и оценка, УИ Св. Климент Охридски, София, s. 30, (2019)]

Nikolov G, Lyubomirova V, Tanakov N (2021) Social innovation for the development of accessible tourism in cities, p 29. In: 9th international conference proceedings "Ohrid – Vodici". Center for Advanced Researches, Skopje, North Macedonia, pp 27–38

Pavlova-Banova M, Aleksandrova A (2021) Financial resources of municipalities in Bulgaria and European Union Countries. In: Collection of papers from international scientific conference "Globalism, Regionalism, Security". UNWE, Publishing Complex, Sofia, pp 65–75

Pinter L, Kok M, Almassy D (2017) Measuring progress in achieving the sustainable development goals. In: Kanie N, Biermann M (eds) Governing through goals. The MIT Press, Cambridge, Massachusetts, pp 99–134

Sach J (2015) Columbia University Press, NY, pp 85–86

Saykova E (2020) Gradski politki I mestna demokratsia v nachaloto na XXI vek, New Bulgarian University, Sofia, pp 137–138 [Стайкова, Е.: Градски политики и местна демокрация в началото на XXI век, New Bulgarian University, s. 137–138, Sofia, (2020)]

Shen TTh (1997) Technologies for sustainable development. In: Mischett D (eds) Principles of sustainable development. CRS Press, London, UK, pp 83–129

Simon D (ed) (2016) Rethinking sustainable cities, 1st edn. Policy Press, University of Bristol

Stowers G, Hyde A, Joaquin E (2018) Managing the sustainable city, 1st edn. Routledge, NY, p 126

Vasileva E, Lyubomirova V, Botseva D (2020) The smart city as a policy trend: implementation challenges. In: Noworol A, Jopek D (eds) City and countryside—identity and space in the 21st century. The complexity of mutual interactions in the peri-urban interface. Cracow University of Economics Press, Poland, pp 43–53

Velikova E (2019) Innovation and digitalization in tourism—restriction or development for business in Bulgaria. Med J Trakya Univ 17(1):252–258

Chapter 25
Policy of the Republic of Bulgaria in the Field of Natural and Environmental Disasters

Dimitar Dimitrov, Elenita Velikova, and Ekaterina Bogomilova

Abstract In the last years of the new century, natural disasters are a key threat to the security of the population in the Republic of Bulgaria. National policy is the tool that can outline the problems and causes of natural disasters, as well as make a proposal to ensure the security of the population and its property in the long run. The report provides a critical analysis of the legislative framework for disaster protection in Bulgaria. The strategic documents for protection in case of natural disasters were also commented. As a result of the review of the legislation, a problematic analysis was made in the implementation of the policy on protection against natural disasters in the Republic of Bulgaria. The purpose of the report is based on the critical analysis to provide guidelines for improving the policy of the Republic of Bulgaria in relation to natural and environmental disasters.

Keywords Natural and Environmental disasters · Protection · Bulgaria

25.1 Protection Against Natural Disasters

The first law regulating the issues of protection in case of natural disasters and environmental catastrophes is the Law on the Ministry of Interior. The law regulates the activities and bodies for ensuring safety and protection in case of fires, disasters and emergencies. These activities are carried out through: Preventive activity; state fire control and preventive control; fire-fighting and rescue activities; permitting and control activity of traders performing activities for ensuring the fire safety of sites and/ or maintenance and servicing of devices, systems and equipment related to

D. Dimitrov · E. Velikova (✉) · E. Bogomilova
University of National and World Economy, Sofia 1000, Bulgaria
e-mail: evelikova@unwe.bg

D. Dimitrov
e-mail: dimdim@unwe.bg

E. Bogomilova
e-mail: ebogomilova@unwe.bg

H.-Y. Jeon (ed.), *Sustainable Development of Water and Environment*,
Environmental Science and Engineering,
https://doi.org/10.1007/978-3-031-07500-1_25

fire safety; conformity assessment and control activity of fire extinguishing products; urgent emergency recovery works, operational protection in case of floods and search and rescue operations, and chemical, biological and radiation protection; early warning and notification in case of disasters and air danger to the executive authorities and the population; methodological and expert assistance to the territorial bodies of the executive power regarding the protection in case of disasters and in organizing the activity of the voluntary formations; determination of the fire characteristics of products and the technical and operational indicators of fire-fighting equipment and fire-fighting products (Bulgarian Legal Portal Homepage, Directory, Normative Acts, Laws, Law on the Ministry of Interior, Chapter V 2022).

The scope and content of the individual activities under para. 2 shall be determined by the regulations under art. 37, para. 3. The activity of ensuring the access of the citizens to the emergency response services through the National Emergency Call System with European Emergency Phone Number 112 is carried out by the order of this law and the Law on the National Emergency Call System.

The activity for ensuring access of the citizens to the emergency response services is carried out through:

- Receiving, automatically registering and processing all emergency calls to 112;
- Providing uninterrupted access to a contact line;
- Collecting information on the type, place, time and basic data for the emergency;
- Analysis and transmission of the processed information to the emergency response services, within the meaning of the Law on the National Emergency Call System with a single European number 112, depending on the type of emergency;
- Receiving feedback from the relevant emergency response services, within the meaning of the Law (Bulgarian Legal Portal Homepage, Directory, Normative Acts, Laws, Law on the Ministry of Interior, Chapter V 2022).

The policy on protection against natural disasters is one of the strategic frameworks of the country, which can be said that its improvement is a priority not only for the stakeholders of the state administration, but also part of the public's commitment to these processes.

Currently, this policy is based on the Disaster Protection Act, the National Disaster Risk Reduction Strategy, which outlines the protection tasks for the period 2014–2020, the National Disaster Protection Program 2014–2018 and the National Protection Plan in disasters, which is developed annually. Although it may seem at first glance that disaster protection policy contains most of the elements of strategic management, much of the pre-, during and post-disaster activities are difficult to find a place in the regulation on stakeholder responsibilities and obligations. The main problem of this strategic policy related to the protection of the population is not so much the lack of strategic documents in this area, but the financial security and resource provision of urgent preventive activities in the field of natural disasters.

The protection in case of natural disasters in the Republic of Bulgaria is based on the Disaster Protection Act (Promulgated SG No. 102 of 19 December 2006). It regulates the protection of life and health of the population, protection of the environment and property in the event of a natural disaster. The law regulates the

main activities before, during and after natural disasters. Significant place is given to prevention as part of the overall protection process together with its accompanying elements. In the law the legislator regulates the obligations and responsibilities of the interested parties in the protection against natural disasters.

Preventive activities are carried out in order to reduce the risk of disasters and include: Analysis and assessment of disaster risks, mapping of disaster risks, categorization of settlements according to the number of potentially affected population, identification of critical infrastructures and their sites and assessment risk for them, disaster protection planning, compliance with spatial planning requirements, investment design, construction and operation of buildings, construction and maintenance of monitoring systems, early warning and notification, provision of collective and individual means of protection, training and practical training of the central and territorial bodies of the executive power, the response forces, the voluntary formations and the population, adoption and implementation of the National Disaster Protection Program, preventive control. Disaster protection planning is carried out at the municipal, regional and national levels (Homepage et al. 2022a).

25.2 Legislative Framework for Protection Against Natural Disasters

In the Republic of Bulgaria the need to build a crisis management system arose in the 90 s of the last century. With the adoption of the Disaster Protection Act in 2006, a unified rescue system was established in the country—to manage the forces and resources of the structures of the executive authorities included in the unified rescue system. Moreover, in the country there were practically three non-departmental management systems—when declaring a "state of war", "martial law" or "state of emergency" within the meaning of the Constitution of the Republic of Bulgaria and the Law on Defense and Armed Forces; for crisis management, with the new Law on Defense and the Armed Forces adopted in May 2009, has led to such a situation that in practice there is no legal regulation for the management of national resources in the event of crises, disasters and other emergencies. The issue of the use of the existing staff structures for crisis management at the executive bodies, as well as the situation centers established in most ministries, remains unresolved. The emergency management system should be designed to provide (Milushev and Milusheva 2010): Warning; Implementation of urgent measures to reduce the impact; Disclosure; Rescue operations; Providing medical assistance; Search and rescue operations; Carrying out urgent emergency—restoration works; Other disaster protection operations. The unified rescue system is the organization, coordination and management of the actions of the units, services and structures in preparation for response, in case of emergency and the need to perform both rescue and emergency recovery work of two or more parts or units (Milushev and Milusheva 2010).

The support and rehabilitation activities are important: Payment of contingencies for disaster protection; Providing rehabilitation assistance; Financing of emergency activities; Other benefits. The activities for assistance and reconstruction are carried out by the bodies of the executive power by establishing an Interdepartmental Commission at the Council of Ministers, chaired by the Minister of Interior. This commission includes ministers and heads of departments involved in the disaster situation. The Commission is assisted by the General Directorate "Fire Safety and Protection of the Population in Disasters"—Ministry of Interior.

Resource provision—protection in case of disasters is provided from the budgets of the ministries and departments and the municipal budgets. The financial and material technical provision of disaster protection includes: Current maintenance of forces and means; Design and implementation of capital construction; Development of early warning and warning systems for disasters; Creation and maintenance of crisis stocks to ensure protection (Milushev and Milusheva 2010, Fig. 25.1).

Important for protection in case of disasters is the Law on Territorial Planning, which is in force since 31.03.2001. Prepared by the order of the ordinance under art. 6, para. 2 and the municipal plans under Art. 9, para. 1 of the Disaster Protection Act, as well as the necessary preventive measures and manner of organization and protection. The general development plan of a city with its land or of a settlement formation of national importance shall determine the territories endangered by disasters, determined in accordance with the maps prepared in accordance with the ordinance under Art. 6, para. 2 and the municipal plans under Art. 9, para. 1 of the

Fig. 25.1 Structure of the unified rescue system

Disaster Protection Act, as well as the necessary preventive measures and manner of organization and protection (Legislation et al. 2022).

The Law on Waters in Chap. 9 regulates the protection against the harmful effects of water, which includes the protection of: Floods; from ice phenomena; on the shores of wave impact; from dangerous increase or decrease of the groundwater level; of watersheds from water erosion; from artificial dumping of groundwater; from sea-induced floods in coastal areas. The protection under Art. 137 of the Water Act is operational and permanent. The operational protection is expressed in carrying out the activities under art. 19, para. 1 of the Disaster Protection Act and is carried out by the Unified Rescue System and in accordance with the emergency plans under Art. 138a of the Protection Act and with the plans for protection in case of disasters under Art. 9 of the Disaster Protection Act.

Permanent protection includes:

- Construction and maintenance of dikes, corrections of rivers and ravines and other hydro-technical and protective facilities;
- Creation and maintenance of monitoring, forecasting and warning systems;
- Regulation of the groundwater level in case of their dangerous increase or decrease;
- Activities for protection of watersheds from water erosion;
- Maintaining the conductivity of river beds;
- Construction and maintenance of fortification and / or coastal protection facilities on the sea coast for protection against wave impact;
- Implementation of measures to prevent and limit the damage caused by natural floods, carried out in accordance with the flood risk management plans;
- Implementation of measures for maintaining the dam walls and the facilities to them in good technical condition and ensuring their safe operation;
- Implementation of activities for immediate decommissioning of dam walls and/ or facilities to them, which are in pre-emergency condition, until restoration of their technological and structural safety or liquidation of such dam walls and/ or facilities, if their restoration or reconstruction are inappropriate;
- Maintaining the conditions for navigation on the Danube River (Homepage et al. 2022b).

Regulations for proper and safe operation and maintenance of hydro-ameliorative infrastructure facilities correct and safe operation for maintenance of hydro-ameliorative infrastructure facilities, the conditions of which must meet the facilities, guarantee of operating personnel, population, buildings, agricultural land and others. The regulations regulate the manner of operation of dam walls and their facilities, repair and reconstruction of dam walls and facilities, meteorological, hydrological monitoring and water balance assessments in the operation of dams and facilities and equipment for their monitoring and equipment. dam walls (Homepage et al. 2022b).

In the Energy Act, published in the State Gazette no. 107 of December 9, 2003 regulates the control over the readiness of the energy sites for work in case of disasters and martial law and the activities of the persons under this law for work in case of disasters and in wartime, assigned to them by the Minister of Energy.

In the Regional Development Act, published in the State Gazette No. 50 of May 30, 2008, the legislator envisages activities to reduce the risk of disasters in endangered areas. According to the implementation of this activity, a methodology for geological risk assessment has been developed.

In the event of emergencies (severe traffic accidents, snowstorms, avalanches, icing, landslides, collapses, excavations, destruction of bridge facilities, etc.) emergency recovery work is carried out to ensure traffic safety, restore the minimum level of road maintenance and protection of road elements from more serious damage.

The preventive activity, the coordination and the management of the emergency-recovery works in the disaster area are carried out in accordance with the Disaster Protection Act, the Spatial Planning Act and the by-laws and documents for their implementation (Ministry of regional development and public works homepage 2012).

25.3 Strategic Documents for Protection Against Natural Disasters

The Disaster Risk Reduction Strategy aims to outline a coherent framework for setting strategic priorities for action to reduce disaster risk and to support the implementation of measures for their implementation at national, regional and municipal levels (Disaster Risk Reduction Strategy 2014).

An international document setting out guidelines for disaster risk reduction is the UN Hyogo Framework for Action 2005–2015: "Building the Resilience of Nations and Societies to Disasters".

An important international document for the region of Southeast Europe is the Memorandum of Understanding on the Institutional Framework of the Disaster Preparedness and Prevention Initiative for South-Eastern Europe (DPPI SEE) and the biennial Strategy and an action plan of the Initiative. These documents aim at an effective regional approach to disaster and emergency management through an analysis of the current situation, available capabilities, challenges and opportunities for expanding regional cooperation for preparedness and prevention.

The strategy includes:

1. Analysis of the situation (main natural and man-made hazards, main natural and man-made hazards, legal framework, responsible structures for disaster risk reduction and existing situation for disaster risk reduction
2. Main strategic goal and priorities for action to reduce the risk of disasters. The draft strategy outlines the following three strategic objectives, which define the priority activities:

    - Effectively integrate key disaster risks into sustainable development policies by planning at all levels of prevention, risk and impact reduction, preparedness and response activities.

- Improving institutional capacity and mechanisms at all levels and in particular at local level to achieve lasting resilience to disasters.
- Unification of the approaches in order to reduce the risk in the development and implementation of plans and programs for disaster preparedness, response and recovery and the transformation of the policy for disaster risk reduction into a mass culture of the Bulgarian society.

3. Monitoring and evaluation is expected to be carried out annually in the implementation of disaster risk reduction activities.
4. Financial provision is provided by the State Budget, European Funds and the Interdepartmental Commission at the Council of Ministers.

The National Disaster Protection Program defines the goals, priorities and tasks for disaster protection for a period of 5 years. It is a key policy document in the field of disaster prevention, management and response and outlines guidelines for the establishment of an effective, resource- and technically secure national disaster prevention and response system. The program reflects the level of development of policy, practice and scientific achievements in this field at the national level, with a main focus on disaster prevention. The strategic goal of the National Program and the state policy in disaster protection is prevention, control and overcoming of their consequences, protection of life, health and property of the population, protection of the environment, cultural and material values. The main priority of the National Disaster Protection Program is the establishment of a working system for coordination between the participants in the process of disaster prevention planning.

The main tasks of this program are:

- Introduction and systematic use in practice of methodologies for analysis, assessment and forecasting of the risks of disasters;
- Improving the management and coordination of disaster risk reduction activities and increasing the resilience of critical infrastructure sites;
- Establishment of a National System for Early Warning and Disaster Warning;
- Improving the quality of management, improving the organization and technical security of the unified rescue system;
- Development of systems for seismological observations and monitoring of water basins and rivers;
- Educating the population through the use of modern technologies and mass media in order to form a culture of safe living;

This National Program is prepared on the basis of Art. 6, item 5 and Art. 18 of the Disaster Protection Act. Annual plans are adopted for the implementation of the National Disaster Protection Program (Information site of the General Directorate for Fire Safety and Protection of the Population 2022).

Disaster protection bodies annually develop a National Disaster Protection Plan for the probable situation of a natural disaster in the Republic of Bulgaria, and respectively 28 districts in turn also develop plans that are consistent with the climatic and relief characteristics of the region.

The annual plan includes tasks and activities for planning and response to a negative natural event, and each of the plans contains: Forecast of possible risks, characteristics of possible consequences; the necessary disaster response capabilities and the means and means of preventing, controlling and overcoming natural disasters, accidents and catastrophes.

Disaster protection plans are prepared in parts for each of the hazards specific to the respective territory, and the parts for earthquakes, floods and nuclear and radiation accidents are mandatory.

Disaster protection plans must contain:

1. Analysis and assessment of the risk of disasters;
2. The measures for prevention or reduction of the risk of disasters;
3. The measures for protection of the population;
4. The distribution of the obligations and the responsible bodies and persons for implementation of the envisaged measures;
5. The means and resources necessary for the implementation of the activities under items 2, 3,4;
6. The manner of interaction between the constituent parts of the unified rescue system;
7. The procedure for early warning and notification of the bodies of the executive power, of the constituent parts of the unified rescue system and of the population in case of danger or occurrence of disasters;
8. Information about the teams and the means of the constituent parts of the unified rescue system;
9. Time for readiness for reaction of the constituent parts of the unified rescue system.

The "Flood" part of the disaster protection plans shall be prepared in compliance with the flood risk management plans developed under the terms and conditions of the Water Act.

The measures envisaged in the flood risk management plans under para. 12 are included in the annual plans for implementation of the National Disaster Protection Program (Dimitrov et al. 2019).

When assigning or approving the detailed development plans under the Spatial Planning Act, the bodies preparing disaster protection plans shall provide information on the foreseeable disasters threatening the territories within the scope of the detailed development plans and on the necessary preventive measures for their protection included in the plans. for disaster protection.

The plans, which are the responsibility of legal entities and sole traders, are approved by the competent authorities, in coordination with the line ministries, respectively with the municipal administration, which is authorized to control this process of security and protection not only in natural disasters but also industrial accidents.

Comprehensive disaster protection activities are monitoring, risk analysis and assessment, warning, action planning, response actions, etc.

25.4 Analysis of the Problems in the Implementation of the Policy on Protection Against Natural Disasters in the Republic of Bulgaria

After the changes in the executive branch in 2009 and after the closure of the Ministry of Emergency Situations, there are problems with coordination between the various departments and structures, and in the event of a natural disaster it is not specified who protection of the population. According to the Disaster Protection Act in the Republic of Bulgaria there is a Unified Rescue System, which includes all activities for rescuing the population and repair and restoration works. The analysis shows that the causes of natural disasters occurring in the country are the result of lack of prevention (preliminary control over the operation of facilities and facilities) by the competent authorities. An example of such a weakness in defense is from 2012, when a flood occurred in the village of Biser, Bulgaria. It turned out that there was no warning system for declaring a state of emergency (alarm sound systems, so-called sirens). For example, during the above-mentioned flood, the population had no information that a tidal wave was heading to their homes.

Planning as a process and the accompanying plans as part of prevention in Bulgaria are carried out at the national level. The implementation of local policy in the global market further intensifies the trend (Velikova 2021). Currently, protection in case of natural disasters is organized on the basis of the following normative documents: Disaster Protection Act, National Strategy for Disaster Risk Reduction 2014–2020, National Program for Disaster Protection 2014–2018 and the annual plans for disaster protection. All four documents related to the protection of the population in case of natural disasters highlight several problems: First of all, there is no analysis of the threats, vulnerabilities and risk of disasters in the country. Secondly, the normative documents present a summary picture of natural disasters typical for the country and the bodies involved in their management, but it lacks details of the elements characterizing the specifics of emergencies. Thirdly, the plans drawn up at regional level do not contain measures to be taken on prevention in order to prevent the occurrence of natural disasters or their intensity, but are aimed at the post-disaster response itself.

The lack of threat and risk analysis deprives the whole system of reliability and expediency in the implementation of the set tasks, namely reducing the likelihood of occurrence and limiting the magnitude of the negative effects of natural disasters. Planning as a process must be included in all elements of disaster protection action, which will ensure stability in the management of the crisis itself (Nikolov et al. 2021). The better the risks and threats are analyzed and assessed, the protection resources are planned and the obligations of the participants in the protection process are determined and secured in the performance of the tasks, the smaller the losses for the state and society and the possibility for long-term planning and investment in sites and areas vulnerable to natural disasters.

Another problem of protection in case of natural disasters occurring on the territory of the country is inexpediency and inefficiency in the use of available resources

or funds allocated for emergency prevention. The reason for the inefficient use of resources are the poor design of projects, lack of control (technical and financial) in the implementation of repairs of riverbeds and dams, strengthening of landslides, deforestation, or lack of transparency in the selection of contractors for relevant projects. If the funds allocated for repair and restoration activities are invested in preventive measures, disasters occurring in the Republic of Bulgaria will not be common or the damage they cause to human property will be insignificant.

25.5 Conclusion

In conclusion, in order to improve the protection of the whole system and its accompanying elements in the event of natural disasters, it must ensure the sustainability of development. The state and the population will have a greater capacity to neutralize and counteract the consequences when this goal is achieved. Appropriate actions in the implementation of the activities set out in the strategic documents on protection against natural disasters will lead to a stable and resilient system. In future publications, research interest may focus on developing a model for risk assessment in the event of natural and environmental disasters.

Acknowledgements This work was financially supported by the UNWE Research Programme (Research Grant No. NID NI 5/2020).

References

Bulgarian legal portal homepage, directory, normative acts, laws, Law on the Ministry of Interior, Chapter V, Article 1,2, http://www.lex.bg/laws/ldoc/2136243824, last accessed 2022/02/02

Bulgarian legal portal homepage, directory, normative acts, laws, Disaster Protection Act, http://lex.bg/laws/ldoc/2135540282, last accessed 2022a/02/02

Bulgarian Legal Portal Homepage, Directory, Normative acts, Laws, Law on Waters, http://lex.bg/laws/ldoc/2134673412, last accessed 2022b/02/02.

Dimitrov D, Penchev G, Bogomilova E (2019) GIS application for economic assessment of direct disaster losses. https://doi.org/10.1007/978-3-030-18293-9_11. Retrieved from www.scopus.com

Disaster Risk Reduction Strategy (2014−2020), Sofia, 2014, Republic of Bulgaria, Council of Ministers Homepage, http://www.nspbzn.mvr.bg/NR/rdonlyres/DA55BDC6-488B-4223 -A81E-7BBE41A548D1 / 0 / DRR_Strategy.pdf, last accessed 2022/02/02

Information site of the general directorate for fire safety and protection of the population, reference information, legislation, http://pojarna.com/bg/sections/spravochna_informaciq/normativna_uredba/nacionalnata_programa_za_zashtita_pri_bedstviq_2009_2013/, last accessed 2022/02/02

Milushev L, Milusheva S, (2010) Security strategies and policies, civil security - policies and building a unified rescue management system. In: International Scientific Conference, Sofia, April 9

Ministry of the interior homepage, legislation, laws and regulations, Spatial Planning Act, http://www.nspbzn.mvr.bg/Norm_uredba/default.htm, last accessed 2022/02/02

Ministry of regional development and public works homepage, normative acts, ordinances, ordinance № rd-02–20–19 of 12 November 2012 on maintenance and current repair of roads, http://www.mrrb.government.bg/?controller= articles & id = 483, last accessed 2022/02/02

Nikolov G, Vasileva E, Botseva D (2021) Methodological aspects of strategic regional planning for achieving sustainable development in Bulgaria. In: 2021 4th International Conference on Sustainable Development of Water and Environment, ICSDWE 2021 Bangkok12 March 2021 through 13 March 2021. https://doi.org/10.1007/978-3-030-75278-1_28. Retrieved from www.scopus.com

Velikova, E (2021) Sustainable environmental planning of a tourist destination Bulgaria—State and trends. In: 4th International Conference on Sustainable Development of Water and Environment, ICSDWE 2021 Bangkok12 March 2021 through 13 March 2021. https://doi.org/10.1007/978-3-030-75278-1_22. Retrieved from www.scopus.com

Chapter 26
Innovative Approaches to Reduce the Level of Environmental Pollution from Bus Transport in Sofia, Bulgaria

Elenita Velikova and Iliya Gatovski

Abstract The manuscript examines some of the main factors influencing the level of environmental friendliness of urban bus transport, with an emphasis on the modernization of rolling stock and the use of alternative fuel sources as innovative transport solutions. A 10-year period, from 2010 to 2020, is considered, for which an analysis is made of how much harmful emissions are reduced in buses with a higher Euro standard on the example of an enterprise for providing public transport in the capital of Bulgaria – "Stolichen Avtotransport" EAD. Transport research and innovation are crucial to ensuring fast, safe and clean transport for citizens and businesses in big cities. The transport sector needs innovative solutions more than ever, as the cost of transporting passengers will increase in value and time, especially after rising global fuel prices. Reducing the level of harmful emissions from urban transport will lead to environmental sustainability, which is a goal and priority of all EU countries. That is why the search for innovative approaches in the field of transport is crucial.

Keywords Public transport · Environmental friendliness · Rolling stock · Bulgaria

26.1 Introduction

Research in all economic sectors in recent years has focused on ensuring their sustainable development in order to guarantee the right of future generations to have equal access to available resources. Social and environmental priorities are at the heart of any economic activity. Sustainable development is a universal goal of the EU, including Bulgaria, and it is extremely important that it covers all sectors of the economy and is not an isolated phenomenon only within a certain country.

E. Velikova (✉) · I. Gatovski
University of National and World Economy, Sofia 1000, Bulgaria
e-mail: evelikova@unwe.bg

I. Gatovski
e-mail: gatovski@unwe.bg

H.-Y. Jeon (ed.), *Sustainable Development of Water and Environment*,
Environmental Science and Engineering,
https://doi.org/10.1007/978-3-031-07500-1_26

Sustainable development requires the management not only of human, physical and financial capital, but also of environmental assets that are not substitutable, not unlimited, and without which the application of others would lose its meaning. Sustainable economic development must strive to use natural resources in a way that meets human needs while maintaining the natural balance of the environment. These needs must be able to be met in the future. A sustainable economy develops on the basis of harmony between the use and conservation of resources through the integration of the local community. In all definitions of sustainable development and sustainable transport, the issue of preserving the ecological balance and reducing harmful emissions is central.

Today, the term "sustainable development" is a key concept both in European politics and globally. Uncertainty about what the future holds, both economically and socially, makes governments and citizens around the world think about the current waste of resources, the consequences of harmful emissions into the atmosphere and the way of life of modern man. Numerous measures are being taken, agreements are being signed and countries are being united to build effective strategies aimed at the environment, industry, society and many other areas, giving stable prospects for prosperity and overcoming the painful problems of the present (Vodenicharova 2012).

The main thesis of the study is that the modernization of rolling stock and the use of alternative fuel sources in urban bus transport—natural gas; hydrogen; hybrid buses and powered by electricity will reduce harmful emissions many times over.

26.2 State of the Problem

Transport is a sector of the national economy that covers transport companies providing services for a fee. The sector is one of the most dynamically developing in Bulgaria in recent years, especially after overcoming the financial and economic crisis of 2007 (Христозов 2014). The transport service of mass urban passenger transport together with healthcare and education largely shape the social and economic climate in each city. This transport service is vital for the existence of any settlement. It is a necessary prerequisite for the implementation of other types of services such as: Commercial services, recreation or tourism and moving from place of residence to work and back, etc. The territorial development of cities and their attractiveness are largely determined by the condition and functioning of public transport.

The main polluter of harmful emissions in Sofia is road transport. Emissions are generated mainly by residents' personal vehicles and only 10% of bus transport. However, the main way to reduce emissions is through the development of public transport and the reduction of the use of personal vehicles. Like any large city with a growing population, Sofia is facing the big problem of intensifying road traffic and a significant deterioration in the quality of the environment. Cars are one of the main polluters in the city, releasing more than 200 harmful substances as a result of burning liquid fuels of petroleum origin. Congestion, which is increasingly saturating the

urban environment, not only during the so-called peak hours, significantly contributes to the complication of this problem (Цветкова and Минков 2017). In addition, they are the cause of increased noise, more traffic accidents and loss of time in extended travel from one point to another. All this provokes the need to wrap and modernize the rolling stock of bus transport in the capital. Reducing the harmful impact on the environment from buses in urban areas is important because they perform over 50% of the transport task in Sofia.

The transport operators performing public transport in Sofia are:

- Metropolitan EAD—a company owned by Sofia Municipality, which serves the railways for fast transport—metro in Sofia;
- Stolichen Avtotransport EAD—a sole proprietorship joint stock company with 100% shares owned by the Sofia Municipality, which provides public bus transport in Sofia;
- Stolichen Elektrotransport EAD—a company, a municipal sole proprietorship, which carries out tram and trolleybus traffic in the capital;
- Karat-S AD—a joint-stock company that performs bus transportation of passengers (Sofia Municipality Homepage 2022).

In terms of volume of work performed in km (Table 26.1), it can be seen that Stolichen Avtotransport EAD has the largest share of the total mileage, namely 59.3%. In second place is Stolichen Elektrotransport EAD with 24.3%, followed by other bus carriers with 9% and Metropolitan EAD with a share of 7.3%. Bus transport has the largest share due to its prominent advantages so far.

Table 26.2 shows the change in the structure of rolling stock from 2010 to 2020 by type of fuel used, size and average age. In 2020, the enrolled rolling stock in Stolichen Avtotransport EAD is 590 buses, of which 323 articulated (18-m) and 267 single (12-m), compared to 2017, when it was a total of 522 buses, of which 286 articulated and 236 single. There are a total of 236 Euro 6 buses, 126 of which use fuel—natural gas, which is a quarter of the total. The other buses are powered by diesel engines.

Table 26.1 Work performed in km by the main transport operators in Sofia for public passenger transport for 2020

Transport operators	Mileage (work performed) in thousands of km	Percentage of total work performed
Stolichen Avtotransport EAD	34,500	59,3%
Stolichen Elektrotransport EAD	14,141	24,3%
Metropolitan EAD	4200	7,3%
Other operators	5272	9,1%
Total	58,113	100%

Source Stolichen Avtotransport EAD

Table 26.2 Structure of the rolling stock in Stolichen Avtotransport EAD

Type of bus		Number of buses			Average age		
Size	Engine	2010	2020	%	2010	2020	%
12-meter	Diesel	265	315	18,87	13,5	11,8	−12,66
18-meter	Diesel	366	141	−61,48	19,2	19,5	1,80
12-meter	Natural gas	24	8	−66,67	13,4	9,0	−33,02
18-meter	Natural gas	0	126	–	0,0	2,0	–
Total		655	590	−9,9	16,8	10,5	−37,5

Source Stolichen Avtotransport EAD

According to the indicator "Average age of the rolling stock" in "Stolichen Avtotransport" EAD of 16.8 years in 2010 (289 single buses with an average age of 13.5 years and 366 articulated buses with an average age of 19 years), decreases at 10.5 g in 2020.

For the needs of the analysis, four main categories of harmful emissions are considered in the development: CO—Carbon monoxide; CxHx—Hydrocarbons; Nox—Nitrogen oxides and fine dust particles. Table 26.3 shows that harmful emissions are most reduced in buses using natural gas as fuel, namely:

Table 26.3 Harmful emissions in kg by bus type and fuel used

Type of bus		CO—Carbon monoxide			CxHx—Hydrocarbons		
Size	Engine	2010	2020	%	2010	2020	%
12-meter	Diesel	113 021,42	95 406,33	−16	110 842,74	66 962,17	−40
18-meter	Diesel	194 094,21	48 153,49	−75	144 043,32	60 006,26	−58
12-meter	Gas	10 299,52	197,98	−98	5 682,67	1 113,61	−80
18-meter	Gas	–	24 824,56	–	–	18 700,08	–
Type of bus		Nox—Nitrogen oxides			Fine dust particles		
Size	Engine	2010	2020	%	2010	2020	%
12-meter	Diesel	923 412,22	658 649,17	−29	20 618,90	12 067,46	−41
18-meter	Diesel	1 302 212,64	443 039,66	−66	32 712,07	11 185,46	−66
12-meter	Gas	52 095,49	4 479,20	−91	1 233,26	44,54	−96
18-meter	Gas	–	25 396,17	–	–	1 633,19	–

Source Stolichen Avtotransport EAD

Table 26.4 Reduction of harmful emissions by years

Year	t	Percentage of reduction
2010	2910	
2011	2721	−6.49%
2012	2611	−10.27%
2013	2392	−17.80%
2014	2380	−18.28%
2015	2134	−26.67%
2016	2123	−27.04%
2017	1693	−41.82%
2018	1619	−44.36%
2019	1472	−49.42%
2020	1250	−57.04%

Source Stolichen Avtotransport EAD

- CO—Carbon monoxide 2020/2010—98%;
- CxHx—Hydrocarbons 2020/2010—80.4%;
- Nox—Nitrogen oxides 2020/2010—91.4%;
- Fine dust particles 2020/2010—96.4%.

Of course, there is a reduction in harmful emissions in diesel buses, which is due to the higher environmental standard—Euro 6.

A total of nearly 3 million kg/ year for each year. (3000 tons) in 2010 harmful emissions are decreasing annually at an increasing rate and reach 1250 tons in 2020 (Table 26.4).

26.3 Opportunities to Reduce Harmful Emissions

The aim of European transport policy is to build a sustainable transport system that meets the economic and social needs of society (Velikova 2019). Recent research in the European Union on transport development is structured in four main target areas. Firstly, reducing the harmful effects of transport on the environment, including noise and harmful emissions, improving the safety and security of transport, increasing the mobility of people and goods and increasing the competitiveness of transport (Tzvetkova 2017a). Transport companies must constantly pay more attention to the requirements of consumers for the availability of the necessary vehicles that are well equipped, clean and in good technical condition (Yordanov 2019).

A study of the literature shows that there are six opportunities for sustainable transport design: Development and use of new technologies; improving public transport; stronger environmental orientation of citizens, promotion of sustainable land

use planning, including transport infrastructure; expanding information and communication technologies and the use of market-based tools to influence consumers and businesses (Holden 2007). Ensuring sustainable transport in cities is a prerequisite for improving the quality of life of residents.

In order to be able to determine the extent to which environmental performance indicators have been achieved in the use of urban transport, we need to answer the following questions: Has the transport pressure on the city been reduced? Do citizens travel with more sustainable means of transport? What are the main means of transport used by citizens? (Velikova 2019).

By using the latest technologies with high resource and energy efficiency, the redistribution of travel by different modes of transport, which favors soft mobility and public transport over the private car, it is possible to take measures to reduce resource consumption, which will ensure their preservation for future generations. Sustainable development is still largely linked to ecological balance. This brings to the fore the issues of its provision (Velikova 2019).

Modern innovations in transport are characterized by high technology and complexity, achieved by combining the efforts of research centers supported by business and government agencies. The need to create and implement innovations in transport is explained by the declining productivity of many components of the system and processes, leading to unsatisfactory levels of productivity, low capacity and reliability, loss of resources and time, high operating costs. Another reason for seeking new solutions in transport is the need to improve connections with the outside world, namely: Minimizing the negative environmental effects; ensuring unhindered access to services in time and space and improving the quality of services.

Innovations in road transport are divided into two major groups: Innovations in terms of vehicles and Innovations in road infrastructure. The leading motive for the implementation of the innovation activity is the replacement of the current vehicles with more ecological, more functional and safer ones, which will serve to overcome the observed imbalances in road transport (Ministry of Transport and Communications Homepage 2030).

Two of the fundamental directions in ensuring the sustainable development of cities are the development of new technologies in the provision and organization of transport infrastructure and the change in travel behavior. The idea of sustainable development requires us as citizens to radically rethink our behavior. Clear political will is also needed. In order to overcome the mass of personal transport, it is not enough just to improve public transport. Energy support for innovative solutions in the transport sector can contribute to the economic and tourist attractiveness of cities (Velikova 2019).

The technological breakthrough that will take place in the transport sector in the coming years is the replacement of conventional cars with electric ones. A wide range of innovations concerning vehicles and their equipment are related to new types of propulsion and the use of alternative fuels. The most telling examples in this regard are:

- Electric traction vehicles;

- Fuel cell vehicles;
- Hybrid electric vehicles;
- Compressed air vehicles;
- Automatically controlled vehicles;
- Auto trains (Цветкова and Моноv 2018).

The concept of the electric car has the greatest chance of a technological breakthrough in road transport. The researchers' ambition is for electric cars to have all the useful features of conventional cars and to become an emblem of zero-emission vehicles.

The concept of the hydrogen car is also innovative in its essence. Hydrogen technology ensures a significant reduction in harmful emissions. The global crisis is not preventing the emergence of new generation machines, but is delaying mass production. Despite the fact that the development of hydrogen fuel vehicles has been going on for many years, the initial stage has not yet been overcome and the issue of safe storage of hydrogen has not been resolved.

Fuel cell cars are a technological innovation designed to reduce harmful emissions into the atmosphere. Hydrogen can be used as fuel for traditional internal combustion engines or in fuel cells to generate energy.

Another green alternative to conventional cars are those with hybrid propulsion (electric fuel only, hydrogen only or a combination of both). Internal combustion engines (ICE) and electric motors can operate in alternate mode as needed—electric motors are preferred for urban traffic and internal combustion engines for long distance travel.

In the future, electric cars with batteries and cars with fuel cells will enter the big cities en masse. Hybrid cars will be needed for long-distance transportation (Tzvetkova 2017a).

An important criterion when buying a new bus is the engine. Not only its power but also its ecological norms are extremely important to it. Bus engines must provide maximum power with minimum exhaust emissions, which reduces their impact on the environment. Currently, the highest environmental standard is Euro-6, which began to be implemented by some carmakers in 2011–2012. In most European countries, vehicles with a higher eco-standard are subject to lower eco-taxes. In this regard, Bulgarian transport policy should be aimed at paying lower taxes and fees on cars with a higher environmental standard, which will encourage entrepreneurs in this sector to buy such.

The automated traffic management and control system is also an important part of the innovation process. By integrating into the existing system for territorial positioning and control of public transport vehicles, it can ensure a more even distribution of all vehicles on the road network, and hence the possibility of unimpeded movement of public transport. These two systems will allow flexible and cost-effective development of public urban transport, providing reliable, accurate, timely and comprehensive information on both the processes related to traffic conditions and the activities

performed by transport operators based on the number of passengers carried and traveled mileage, as well as opportunities for effective service pricing policies (Tzvetkova 2017b).

One of the main goals of the future sustainable development of urban passenger transport must be to meet the consumer needs of citizens as much as possible. The aim of the strategy should be to attract more people to public transport services. To this end, its quality must be improved by ensuring quality, regular, safe and reliable transport with convenient and functional connections between the individual lines.

The policy to reduce the harmful impact on the environment and develop socially efficient and high-quality urban passenger transport must consist in building optimal connections and high coordination between different types of urban transport ensuring sustainable urban mobility—reduced travel time, comfort, security and vehicle safety, nature and environmental protection and, in general, improving the quality of life of citizens (Tzvetkova 2017b).

Increasing the environmental friendliness and competitiveness of urban transport companies should be sought with every possible detail of the activity of the transport company. Careful selection when purchasing new vehicles with more innovative solutions, improving and maintaining the available rolling stock, raising the qualification of transport workers are just some of the measures that can be implemented.

Experts point out that the crisis caused by the proliferation of COVID-19 in 2020 opens up new opportunities for people to move around in urban areas, namely cycling and mopeding and walking. All this, combined with the implementation of a new vision for the development of the urban environment with infrastructure oriented to pedestrian traffic and the construction of safe bike lanes, will help us live and work in a safer transport system (Арнаудов 2021).

26.4 Conclusion

The sustainable development of bus transport in Sofia implies the commissioning of modern environmentally friendly vehicles that meet European technical standards. Ensuring reliable and regular transport will reduce the number of accidents and traffic accidents. The new environmentally friendly vehicles will improve the quality of the air in the city of Sofia—reduce harmful emissions and fine dust particles. The renewal of the bus fleet with new vehicles will also be a prerequisite for reducing noise pollution in the capital, which in many places is currently above the permissible norms (Цветкова and Монов 2018).

The specific objectives of sustainable development, in turn, can be summarized as follows: Economic success, environmental protection, sustainable development and local integration, ie. acceptance by the local population. Planning activities must ensure that the systems function in a way that does not harm or destroy the environment (Velikova 2021). In conclusion, it can be noted that the connection made between the younger average age of the rolling stock, the fuel used by buses and

the pollution rates at the same operating capacity will increase the level of their environmental friendliness.

The technical condition of the vehicles and the comfort offered in them is extremely important for improving the quality of transport. Modern environmentally friendly vehicles are a guarantee for the reduction of noise and dust pollution, as well as guarantee the peace of mind of citizens whose habitats are in close proximity to the elements of public transport infrastructure. The introduction of new technologies in electric transport ensures that the released kinetic energy will be converted and reused. This in turn leads to savings and reduced losses.

In this regard, the object of future research may be to study the willingness of consumers to reduce the use of their cars and replace them with alternative modes of transport or public transport. Of interest are also intelligent transport systems, which can significantly facilitate movement, shorten it in terms of duration and thus reduce the harmful effects on the environment.

Acknowledgements This work was financially supported by the UNWE Research Programme (Research Grant No. NID NI 5/2020).

References

Vodenicharova M (2012) Green logistics as a principle of sustainable development. Management and sustainable development 4(35), 128–132

Христозов, Я. „Анализ на платежоспособността в сектор „Транспорт, складиране и пощи (2007–2013), сб. с доклади „Транспортът в променящия се свят – предизвикателства и решения, научно – практическа конференция, УНСС 2014 г., стр.77 – 85

Цветкова, Св. Минков, Т., Анализ и оценка на вредното въздействие на транспорта върху околната среда в градовете, Икономически и социални алтернативи, брой 3, 49–62, (2017)

Sofia Municipality Homepage, https://www.sofia.bg/en/transport-operators, last accessed 2022/02/20

Velikova E (2019) Methodological guidelines for the sustainable development of the Bulgarian touristic resorts through reducing the harmful impact of transport. In: E3S Web of Conferences 101, 01004 (2019) ICESD 2019. https://www.scopus.com/authid/detail.uri?authorId=57209577656, last accessed 2022/02/20.

Tzvetkova, Sv (2017a) Policies for the stable development of automobile transport. management and stable development journal, university of forestry, Year 19, Vol. 65, Issue 4. 48–51

Yordanov D (2019) Consumer assessment of the quality of transport services and guidelines to increase their competitiveness. Economic Alternatives 2019(4):571–581

Holden E (2007) Achieving sustainable mobility: everyday and leisure-time travel in the EU Aldershot: Ashgate.

Ministry of transport and communications homepage, integrated transport strategy until (2030) https://www.mtc.government.bg/bg/category/42/integrirana-transportna-strategiya-v-perioda-do-2030-g, last accessed 2022/02/20.

Цветкова, Св., Монов, С. Анализ на състоянието на автобусния транспорт на територията на Столична община и насоки за устойчивото му развитие. Икономически и социални алтернативи, брой 3, 33–47, (2018)

Tzvetkova Sv (2017b) Reducing the harmful impact of urban passenger transport on the environment, Management and sustainable development 4/2017b (65), 56–72

Арнаудов, Б. Пътната безопасност при уязвимите участници – състояние и насоки за нейното подобряване. Научни трудове на УНСС (3) 2021, ИК – УНСС. http://unwe-research-papers.org/uploads/ResearchPapers/RP_vol3_2021_No09_B%20Arnaudov_Rcd.pdf, last accessed 2022/02/24

Velikova E (2021) Sustainable environmental planning of a tourist destination Bulgaria—State and trends. In: 2021 4th International Conference on Sustainable Development of Water and Environment, ICSDWE 2021 Bang-kok12 March 2021 through 13 March 2021. https://doi.org/10.1007/978-3-030-75278-1_22 Retrieved from www.scopus.com

Chapter 27
Applications of DSF as Renewable Source Energy Savings in a Small Detached Family House Prototype

Eusébio Conceição, João Gomes, Mª Inês Conceição, Mª Manuela Lúcio, and Hazim Awbi

Abstract The applications of DSF (Double Skin Facade) as renewable source energy savings in a small detached family house prototype is developed in this study. The DSF system, utilized in this work in the improvement of the thermal comfort conditions and used as HVAC (Heating, Ventilating and Air Conditioning) system in the ventilation mode, is installed in the south-facing building in two windows. This numerical study, made in winter condition in a Mediterranean typical day, use a Building Thermal Modeling software developed by the authors. The software, that simulate the opaque, transparent and internal bodies and spaces, simulate in this work also the DSF system in detail. The software, using balance equations of energy and mass, evaluates the solar radiation, glass radiative proprieties, convective coefficients, internal airflow, thermal comfort evaluation, in transient conditions. This study assesses the level of thermal comfort without and with DSF system mounted in the south-facing building of the two main windows. According the obtained results is possible to verify that without DSF system the south-facing spaces are uncomfortable by positive PMV values and the north-facing spaces are uncomfortable by negative PMV values. When is used the DSF system, in general, the level of thermal comfort is near the acceptable values, as provided for in intentional standards.

Keywords Energy production · Numerical model · Double skin facade · Energy and mass balance equations

E. Conceição (✉) · M. M. Lúcio
FCT—University of Algarve, Campus de Gambelas, 8005-139 Faro, Portugal
e-mail: econcei@ualg.pt

J. Gomes
CINTAL, Campus de Gambelas, 8005-139 Faro, Portugal
e-mail: jgomes@ualg.pt

M. I. Conceição
Instituto Superior Técnico, Av. Rovisco Pais, 1049-001 Lisboa, Portugal
e-mail: ines.conceicao@tecnico.ulisboa.pt

H. Awbi
School of Built Environment, University of Reading, Reading RG6 6AW, UK
e-mail: h.b.awbi@reading.ac.uk

H.-Y. Jeon (ed.), *Sustainable Development of Water and Environment*,
Environmental Science and Engineering,
https://doi.org/10.1007/978-3-031-07500-1_27

27.1 Introduction

A DSF (Double Skin Façade) system is usually used in the building construction to introduce insulation envelopes. This kind of isolation can improve acoustical and thermal comfort levels to which occupants are exposed. It is also useful in regulating the transmission of solar radiation to the compartments and in allowing high levels of natural lighting inside the compartments. Usually, the DSF system is built in existing windows mainly in spaces turned to south direction. The DSF consists of two glazed surfaces ("skins") divided by an air channel. Natural, forced or hybrid ventilation can be applied in this air cavity. Some devices use Venetian-type blinds. This Venetian-type blinds are used not only to control the solar radiation entrance, as the implementations of photovoltaic cells. Numerical and experimental studies on this subject were developed in the last years (Pasut and Carli 2012; Wang et al. 2019; Hazem et al. 2015; Parra et al. 2015; Luo et al. 2018; Ghaffarianhoseini et al. 2016; Poirazis 2004; Lucchino et al. 2019; Xue and Li 2015; Lee and Chang 2015; Lee et al. 2015; Li et al. 2019).

The numerical work presented in this work was done by own research software based on a numerical model, Building Thermal Response (BTR), whose development has been continuously done by the authors over the years. For more details about its application see (Conceição et al. 2010; Conceição and Lúcio 2010). The numerical simulation of the conductive, convective and radiative model issues can be analyzed, also, in Conceição et al. (Conceição et al. 1999).

Balance integral equations of energy and mass, solved by the Runge–Kutta-Felberg method with error control, are used in BTR. The temperature fields of the DSF system and of opaque and transparent bodies of the virtual building are calculated, in transient conditions, using the energy balance equations. The water and contaminants mass fields of the air within in both DSF and virtual building are evaluated using the mass balance equations.

Phenomena of convection, conduction and radiation are considering by the balance equations of energy. The heat transfers by natural, forced and mixed convection, applied to opaque and glazed surfaces, are evaluated using dimensionless coefficients. The phenomenon of heat transfer by conduction occurs between the various layers existing inside the opaque surfaces. Radiative heat exchanges caused by incident solar radiation, the absorbed and transmitted solar radiation associated to glazed surfaces and the absorbed solar radiation by opaque bodies are also taken into account. The shading devices that are mounted in the air channel of the DSF are also considered by the model that represents the radiation phenomenon.

The equations of energy balance are applied in the calculation of the temperature fields existing in the DSF, namely in their Venetian-type blinds, in their two glazed surfaces (the interior, formed by the window, and the exterior) and in their surrounding structure. They are also applied in the calculation of the air temperature fields inside the DSF and virtual building and in the evaluation of the temperature fields of the remaining transparent (glass), opaque (ceiling, walls, floor, doors) and interior bodies of the virtual building.

The equations of mass balance, based on the phenomena of diffusion and convection, are applied in the calculation of the mass of contaminants and water vapor concentrated inside the virtual building as well as inside the DSF.

The Predicted Mean Vote (PMV) index, presented in the work of Fanger (1970), is applied here to assess the level of thermal comfort as it is proposed in ISO 7730 (2005). Examples of application of this index by BTR are shown, in detail, in numerical works developed by Conceição et al. (2018, 2019).

This work analyses the influence of the implementation of five DSF in the thermal response of the building and in the level of thermal comfort of inhabitants. DSFs with different dimensions are mounted in front of south-facing windows. Each DSF is connected by a duct to a specific compartment of the building. The study compares the numerical results obtained when using or not using the DSF system on a typically very cold day in winter conditions.

27.2 Methodology

This study is developed for a virtual building that represents a small family house (Fig. 27.1a). The numerical simulation considers one outdoor space, five indoor spaces (Fig. 27.2), a loft and five DSF systems (Fig. 27.1b), with the following specifications:

- Space 1—outdoor space: the air temperature, air relative humidity, wind velocity and wind direction obtained here constitute input data for the numerical simulation;
- Space 2—transition space without permanent occupation;

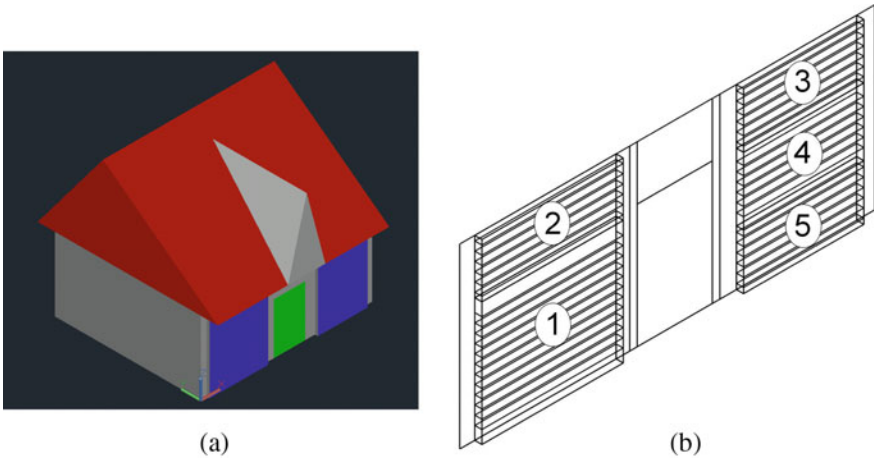

Fig. 27.1 **a** Design of the virtual building; **b** scheme of DSFs and its numeration

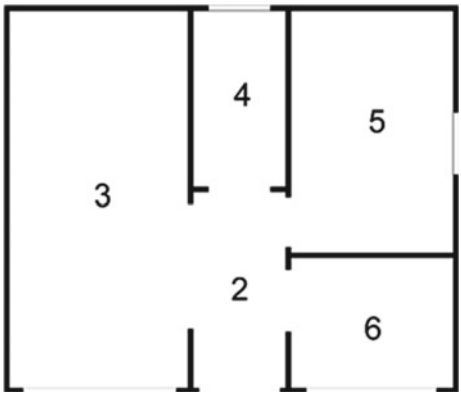

Fig. 27.2 Scheme of the indoor spaces and respective numeration

- Space 3—space occupied by two persons between 7 p.m. (19:00) and 12 p.m. (24:00); it has the largest window facing south;
- Space 4—space occupied by two persons between 12 a.m. (12:00) and 2 p.m. (14:00) and by one person between 6 p.m. (18:00) and 7 p.m. (19:00); it has a window facing north;
- Space 5—space occupied by two persons between 0 a.m. (00:00) and 8 a.m. (08:00); it has a window facing east;
- Space 6—space occupied by one person between 6 p.m. (18:00) and 7 p.m. (19:00); it has the smallest window facing south;
- Space 7—loft: this space is used for regulating the temperature in the building;
- DSF 1—larger DSF system installed in front at the bottom of space 3 window: this system provides heating for space 3 and is not under the effect of shading caused by the roof;
- DSF 2—small DSF system installed in front at the top of space 3 window: this system provides heating for space 2 and is under the partial effect of shading due to the roof;
- DSF 3—small DSF system installed in front at the top of space 6 window: this system provides heating for space 6 and is under the partial effect of shading due to the roof;
- DSF 4—small DSF system installed in front at the middle of space 6 window: this system provides heating for space 5 and is not under the effect of shading caused by the roof;
- DSF 5—small DSF system installed in front at the bottom of space 6 window: this system provides heating for space 4 and is not under the effect of shading caused by the roof.

The scheme of the five DSF and respective numeration are presented in Fig. 27.1b. The scheme of the indoor spaces and respective numeration are presented in Fig. 27.2.

The comparative study was carried out considering the use or not of the DSF systems. Thus, this study is divided into two Cases:

- Case A—non-use of the DSF systems: the space heating process is carried out using only direct solar radiation;
- Case B—use of the DSF systems: the space heating process is carried out using direct solar radiation and transporting the heat produced in the DSFs for spaces 2 to 6 of the building cyclically occupied.

The airflow rate considered in the heating process when using DSF systems is 0.02 m^3/s.

For Case A (non-use of DSF systems), an airflow rate of 35 m^3/h by person, suggested by the standards, was used in the numerical simulation only when the spaces are occupied (Conceição et al. 1997, 2012). Note that it was considered that each space can be occupied by a maximum of two persons.

Each DSF is constructed with two glazed surfaces, divided by an air channel, and a surrounding structure. In the air cavity is mounted a Venetian-type blind system constituted by an adjustable set of aluminium lamellae. The DSF system 1 has a Venetian-type blind system consisting of eleven lamellae. The DSF systems 3 and 5 have a Venetian-type blind system consisting of seven lamellae. The DSF systems 2 and 4 have a Venetian-type blind system consisting of six lamellae.

The virtual building is located in a region characterized by a typically Mediterranean climate. The external environmental data, required as input data for the numerical simulation, were therefore obtained from a meteorological station present in that region. The external input data (wind speed and direction, temperature and relative humidity) were then obtained during the twenty-four hours of a typical winter day (particularly the 21st of December). The evolution of solar radiation was therefore determined by the BTR for that day considering that the sky is clear. Numerical simulation results were obtained over the 24 h of that day. In the numerical simulation the five previous days were considered in order to obtained the real building thermal behaviour.

BTR uses the values of 1.2 met and 1.0 clo as, respectively, the activity and clothing insulation levels of the building occupants in the assessment of the PMV index (ISO 7730 2005).

27.3 Results and Discussion

Figure 27.3 presents the mean air temperature evolution in outdoor space (Outdoor) and in the air channel of the DSFs (DSF1, DSF2, DSF3, DSF4 an DSF5). Figure 27.4 shows the mean air temperature evolution in the internal compartments of the virtual building without the use of DSF (rooms 2a to 6a) and with the use of DSF (rooms 2b to 6b).

As can be seen in the Fig. 27.3, the outdoor temperature varies between around 0 °C and around 8 °C throughout the day. Along the day, the air temperature evolution in the air cavity of the DSF 1 presents the highest values. The temperature evolution is very similar in the DSF 4 and DSF 5 as they are similar in size and, according

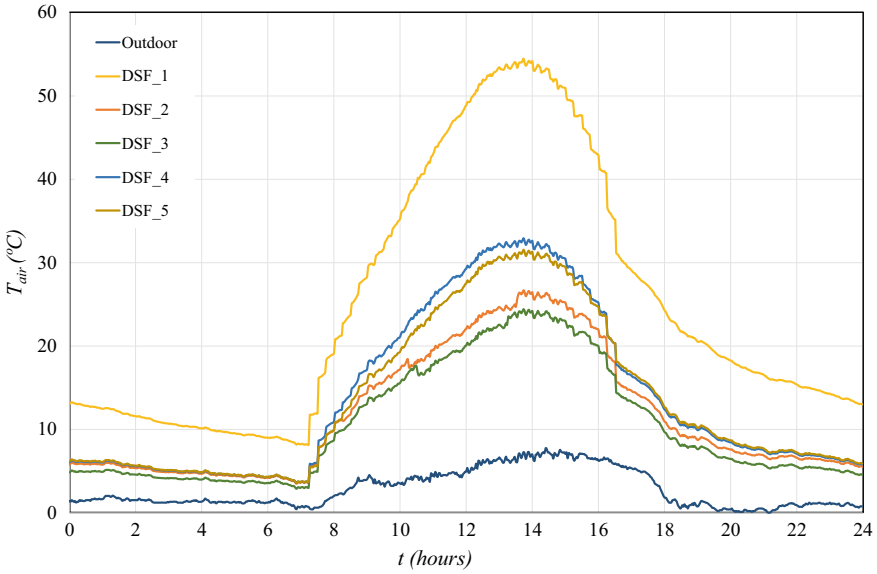

Fig. 27.3 Air temperature evolution in the outdoor space (Outdoor) and in the air channels of the DSFs (DSF1 to DSF5)

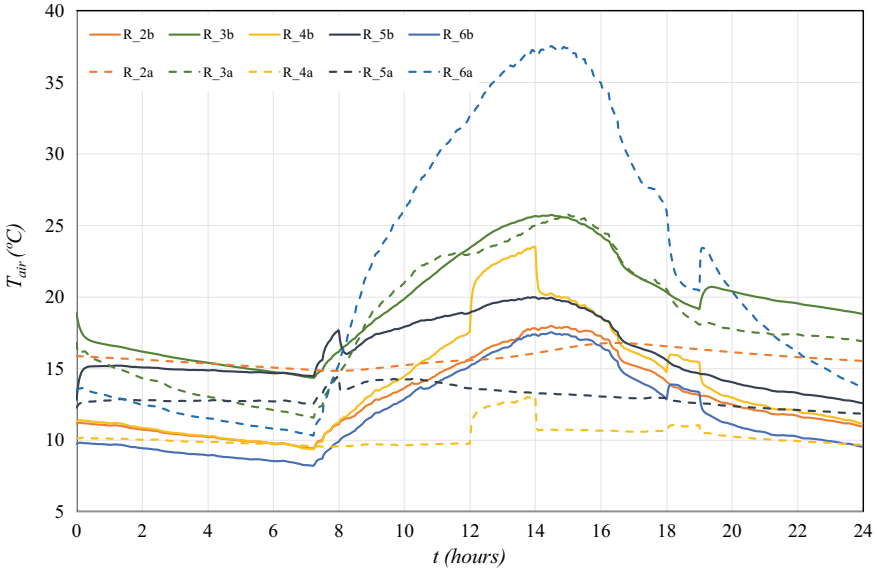

Fig. 27.4 Air temperature evolution in the internal spaces without the use of DSF (rooms R_2a to R_6a) and with the use of DSF (rooms R_2b to R_6b)

to their location in the window of space 6, they are not subject to shading effect due to the roof. The maximum values of temperatures reached in DSF 4 and DSF 5 are around 32 °C. The evolution of lower temperatures can be seen in DSF 2 and DSF 3, essentially due to their location at the top of the windows in spaces 3 and 6, respectively, as they are subject to shading effect due to the roof. The maximum values of temperatures reached in DSF 2 and DSF 3 are around 27 °C and 25 °C, respectively.

Without the use of DSF, the air temperature evolution in compartments 3 and 6 (both with south-facing windows) shows higher values than the air temperature evolution in compartments 4 (with north-facing window) and 5 (with east-facing window). Spaces 3 and 6 reach a maximum air temperature of, respectively, 25.8 °C around 3 p.m. and 37.5 °C around 2.30 p.m. Throughout the day, the air temperature in the space 4 varies between about 9.5 and 13.1 °C. In space 5, the air temperature changes between about 11.9 and 14.5 °C.

Analysing the results obtained, there is a great asymmetry in the distribution of air temperatures in the indoor spaces of the virtual building. Therefore, a set of DSF systems was developed with a connection to a duct system that allows for a better distribution of air temperatures throughout all spaces. To take benefit of the southern location of the windows in compartments 3 and 6, five DSF systems were installed in front of them (as shown in Fig. 27.1b). In this situation, the air temperatures in spaces 4 and 5 have increased, mainly when they are occupied, while the air temperatures in spaces 3 and 6 have decreased.

The level of thermal comfort of the occupants is determined by the PMV index. Figure 27.5 presents the PMV index evolution in the indoor spaces of the virtual building.

When the DSF system is not utilized, the level of thermal comfort in compartments 4 and 5 is uncomfortable due to negative values of the PMV index. In compartment 3, when occupied, the thermal comfort level is uncomfortable, due to PMV index negative values, between 7.30 p.m. and 12 p.m.; this compartment is only comfortable for PMV index negative values between 7 p.m. and 7.30 p.m. When occupied, space 6 is comfortable by positive values of the PMV index between 7 p.m. and 8 p.m.

When the DSF system is used, the level of thermal comfort in compartment 3 is acceptable until 10 p.m. and near acceptable (ISO 7730 2005) the remaining time, by negative PMV values, when the space is occupied. When it is occupied, space 4 presents acceptable thermal comfort levels, by negative PMV values, between 1 p.m. and 2 p.m., and near acceptable, also by negative PMV values, between 12 a.m. and 1 p.m. However, between 6 p.m. and 7 p.m., the thermal comfort level is unacceptable by negative PMV values. Nevertheless, the thermal comfort conditions in this space improve significantly (on average 30.0%) throughout the day with the use of the DSF system. Space 5 presents an unacceptable thermal comfort level, by negative PMV values, throughout all day. When it is occupied, the thermal comfort conditions in space 5 improves, on average, 21.7% compared to not using the DSF system. If we consider the performance of the DSF system throughout the day, the level of thermal comfort conditions improves, on average, 28.8% with its use. Finally,

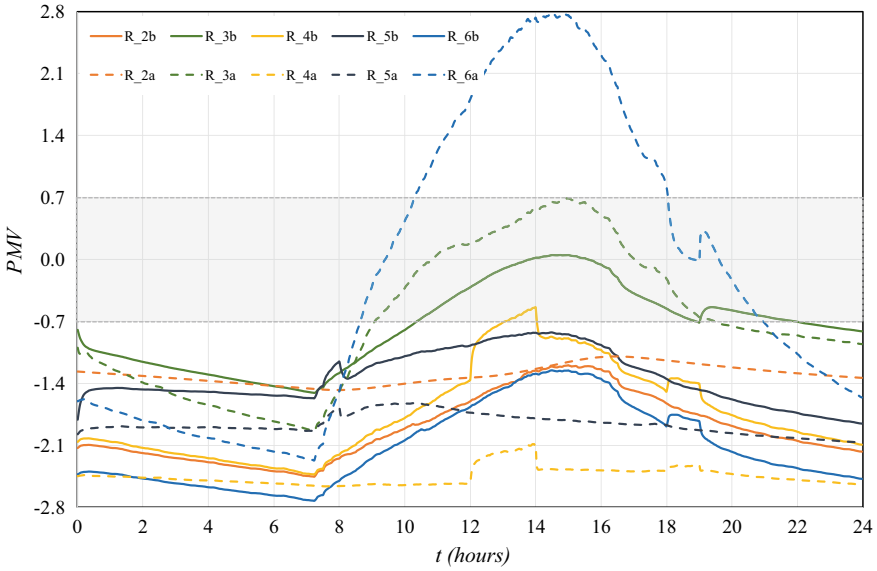

Fig. 27.5 PMV index evolution in the indoor spaces without the use of DSF (rooms R_2a to R_6a) and with the use of DSF (rooms R_2b to R_6b). The gray zone represents the thermal comfort zone

space 6 presents unacceptable thermal comfort conditions, by negative PMV values, throughout the day.

Therefore, for the simulated outdoor temperature conditions, the operating mode of the DSF systems utilized is not the most suitable to obtain acceptable thermal comfort levels for the occupants in all spaces throughout the day. Thus, it is suggested to use a lower airflow rate to ensure that the outside air temperature supplied to the interior compartments is warmer.

27.4 Conclusions

In this paper was presented a numerical work on the contribution of the use of a set of DSF systems to the improvement of the thermal comfort conditions of the occupants of a small virtual family house. The comparative study was developed for cold winter conditions, supposing two situations: the non-use and the use of a set of DSF systems. Five DSF were used in front of the existing windows on the south facade. Each DSF provides air heated by direct solar radiation to a specific space.

In general, without using the DSF systems, when spaces 3, 4 and 5 are occupied, the level of thermal comfort found in them is unacceptable due to PMV index negative values. On the other hand, space 6, when occupied, presents an acceptable thermal comfort level due to PMV index positive values.

With the use of the DSF systems, the thermal comfort level in spaces 4 and 5, when occupied, improves by PMV index negative values close to the acceptable limit; in fact, space 4 manages to present an acceptable thermal comfort level between 12 a.m. and 1 p.m. due to PMV index negative values. Space 3 has an acceptable thermal comfort level between 7 p.m. and 10 p.m. by PMV index negative values and close to acceptable, also by PMV index negative values, between 10 p.m. and 12 p.m. On the other hand, space 6, when occupied, presents an unacceptable thermal comfort level due to PMV index negative values.

It is concluded that the thermal energy provided by the DSF to heat the spaces of this small family building is not enough. Therefore, as a future study, it is proposed to assess the use of a lower airflow rate. This will allow the supplied air to be warmer.

Acknowledgements The authors acknowledge to the project (SAICT-ALG/39586/2018) from Algarve Regional Operational Program (CRESC Algarve 2020), under the PORTUGAL 2020 Partnership Agreement, through the European Regional Development Fund (ERDF) and the National Science and Technology Foundation (FCT). The authors grateful the collaboration of Margarida Conceição on the project design development.

References

Conceição E, Lúcio M (2010) Numerical study of the influence of opaque external trees with pyramidal shape on the thermal behaviour of a school building in summer conditions. Indoor Built Environ 19(6):657–667

Conceição E, Silva M, Viegas D (1997) Air quality inside the passenger compartment of a bus. J Expo Anal Environ Epidemiol 7(4):521–534

Conceição E, Nunes A, Gomes J, Lúcio M (2010) Application of a school building thermal response numerical model in the evolution of the adaptive thermal comfort level in Mediterranean environment. Int J Vent 9(3):287–304

Conceição E, Farinho J, Lúcio M (2012) Evaluation of indoor air quality in a classroom equipped with crossed ventilation. Int J Vent 11(1):53–67

Conceição E, Santiago C, Lúcio M, Awbi H (2018) Predicting the air quality, thermal comfort and draught risk for a virtual classroom with desk-type personalised ventilation systems. Buildings 8:35

Conceição E, Gomes J, Awbi H (2019) Influence of the airflow in a solar passive building on the indoor air quality and thermal comfort levels. Atmosphere 10(12):766

Conceição E, Silva M, André J, Viegas D (1999) A computational model to simulate the thermal behaviour of the passengers' compartment of vehicle. In: Proceedings of 1999 SAE international congress and exposition, Detroit, USA

Fanger P (1970) Thermal comfort: analysis and applications in environmental engineering. Danish Technical Press, Copenhagen, Denmark

Ghaffarianhoseini A, Ghaffarianhoseini A, Berardi U, Tookey J, Li D, Kariminia S (2016) Exploring the advantages and challenges of double-skin façades (DSFs). Renew Sustain Energy Rev 60:1052–1065

Hazem A, Ameghchouche M, Bougriou C (2015) A numerical analysis of the air ventilation management and assessment of the behavior of double skin facades. Energy Build 102:225–236

ISO 7730 (2005) Ergonomics of the thermal environments—analytical determination and interpretation of thermal comfort using calculation of the PMV and PPD indices and local thermal comfort criteria. International Standard Organization, Geneva, Switzerland

Lee J, Chang D (2015) Influence on vertical shading device orientation and thickness on the natural ventilation and acoustical performance of a double skin façade. Proc Eng 118:304–309
Lee J, Alshayeb M, Chang D (2015) A study of shading device configuration on the natural ventilation efficiency and energy performance of a double skin façade. Proc Eng 118:310–317
Li Y, Darkwa J, Su W (2019) Investigation on thermal performance of an integrated phase change material blind system for double skin façade buildings. Energy Procedia 158:5116–5123
Lucchino E, Goia F, Lobaccaro G, Chaudhary G (2019) Modelling of double skin facades in whole-building energy simulation tools: a review of current practices and possibilities for future developments. Build Simul 12:3–27
Luo Y, Zhang L, Liu Z, Xie L, Wang X, Wu J (2018) Experimental study and performance evaluation of a PV-blind embedded double skin façade in winter season. Energy 165:326–342
Parra J, Guardo A, Egusquiza E, Alavedra P (2015) Thermal performance of ventilated double skin façades with venetian blinds. Energies 8:4882–4898
Pasut W, De Carli M (2012) Evaluation of various CFD modelling strategies in predicting airflow and temperature in a naturally ventilated double skin façade. Appl Therm Eng 37:267–274
Poirazis H (2004) Double skin façades for office buildings—literature review. Report EBD-R–04/3. Department of Construction and Architecture, Lund University, Lund, Sweden
Wang Y, Chen Y, Li C (2019) Airflow modeling based on zonal method for natural ventilated double skin façade with Venetian blinds. Energy Build 191:211–223
Xue F, Li X (2015) A fast assessment method for thermal performance of naturally ventilated double-skin façades during cooling season. Sol Energy 114:303–313

Chapter 28
Thermal Engineering Applications in Forest Fire Environments

Eusébio Conceição, João Gomes, Mª Manuela Lúcio, Jorge Raposo, Domingos Xavier, and Mª Teresa Viegas

Abstract This article describes a Hygrothermal Tree Modelling numerical model and a three-dimensional pine tree geometry design. This numerical simulation accounts a modelling of the processes of water circulation and energy transmission in a tree. Here, the design of the pine tree geometry is developed using a Computer Aided Design system. In the mass transmission, namely, the water mass evaluation, the water distribution, diffusion and transpiration processes are bringing into account, while in the energy transmission, namely, the temperature evaluation, the conduction, convection, radiation and transpiration processes are bringing into account. In the calculation of radiation, applying mesh generation, pine tree and fire front geometries are utilized in view factors evaluation. The radiative heat exchanges between the virtual fire surface defined by the flames and the virtual pine tree will be assessed by these view factors. The geometry of the virtual tree pine was constructed from 2289 cylindrical elements. The virtual pine tree, 1.8 m high, consists of 14 trunks, 25 branches and 2250 leaves. The fire surface extends over 10 m with a height of 1 m, being located at a distance of 5 m from the pine tree. The results obtained demonstrate that the proposed numerical model adequately simulates the dynamic behavior of moisture in the leaves of a tree when under the influence of a forest fire.

Keywords Numerical models · Energy and mass integral equations · Design · Tree thermal response

E. Conceição (✉) · Mª. M. Lúcio
FCT - Universidade do Algarve, Campus de Gambelas, 8005-139 Faro, Portugal
e-mail: econcei@ualg.pt

J. Gomes
CINTAL, Campus de Gambelas, 8005-139 Faro, Portugal
e-mail: jgomes@ualg.pt

J. Raposo · D. Xavier · Mª. T. Viegas
FCT - Universidade de Coimbra, Pólo II, Pinhal de Marrocos, 3030-290 Coimbra, Portugal
e-mail: xavier.viegas@dem.uc.pt

Mª. T. Viegas
e-mail: maria.viegas@dem.uc.pt

H.-Y. Jeon (ed.), *Sustainable Development of Water and Environment*,
Environmental Science and Engineering,
https://doi.org/10.1007/978-3-031-07500-1_28

28.1 Introduction

The Thermal Applications in Forest Fire Environments, presented in this work, are associated with the tree thermal response in forest fire environment. The mass (water distribution, diffusion and transpiration performance) and the energy (temperature performance) are considered in this type of phenomenon. Thus, in this work, the mass transmission process and the thermal transmission process will be analyzed in detail.

In the mass transmission phenomena, the work of Janott et al. (2011) proposed a new model concept of water flow in soil–plant systems which takes advantage of the similarity between the way water flows in the plants xylem and in the soil. Porous media equation was used to derive both models of one-dimensional xylem water flow and soil water flow. With this model, Janott et al. (2011) managed to replicate the main mechanisms related to the hydrodynamics of plants, including obtaining water from the soil through their roots. Consequently, they were able to conduct a sensitivity analysis of the process of water uptake by the roots as well as the dynamic process of transpiration of the plants. Wang et al. (2012) developed a model of tree structure and functioning to include biomass production, organ sharing and water availability solutions to simulate plant and environment interaction. This model, validated and calibrated based on experimental measurements, also incorporates soil water dynamics. In the work of Simon et al. (2018), it is presented a model to evaluate leaf temperatures and transpiration rates of trees. The simulation results were compared against monitored leaf temperatures and transpiration fluxes of two urban trees, obtaining a high agreement. It was shown that the tree geometry replication in the model demonstrated to be relevant in the accurate simulation of the transpiration rate of trees. Green et al. (2003) carried out experimental studies to compare with a soil water balance numerical model that utilizes, in the water flow, Richards' equation, and, in the root uptake, a spread macroscopic sink term. Comparing the experimental results with the model results, a good agreement was then reached.

The water transfer model, namely the distribution, diffusion and transpiration processes, involved in the present study is based on models of blood and water transfer processes verified in the human body, developed previously (Conceição and Awbi 2021; Conceição et al. 2007).

The energy transmission phenomena are important to be evaluated in the distribution of temperature in the different elements (trunks, branches and leaves) that make up the tree. In order to evaluate this temperature distribution is important to have the grid generation and to know the thermal phenomena, specially, the conduction, evaporation, radiation and convection, that happen in the tree. The determination of radiative exchanges in forest fire research is relevant to construe the tree and surface fire thermal interaction. The grid generation theory implemented in the presented study is founded on the grid generation theory used to define a vehicle, building or human body geometry, necessary for the calculation of radiative exchanges (Conceição and Lúcio 2010; Conceição et al. 2010).

This work uses a numerical model to create a grid, representing the virtual tree geometry, and calculate the existing view factors between the outer surface of the tree and the plane defined by the flame. The thermal response numerical model will use these view factors to assess the Mean Radiant Temperature (Fanger 1970; Lai et al. 2017; Vorre et al. 2015) and the transient surface temperatures in the different elements of the virtual tree.

The pine tree thermal response model, presented in this work, is founded on thermal and radiative numerical models previously developed and used in the assessment of thermal response of various systems, namely, the application of conduction, evaporation, radiation and convection in buildings (Conceição et al. 2018) and in vehicles (Conceição et al. 1999). The validation of the modeling of the aforementioned phenomena was carried out by Conceição and Lúcio (2001) for the thermal response of the human body. Other studies related with the pine tree thermal response can be seen in Jansen (1994) and Ishak et al. (2021).

This work has as main objective to simulate the Tree Thermal Modelling, namely, the thermal and the mass phenomena verified in a pine tree placed in a forest fire environment. This numerical model is applied in the study of the thermal and mass responses of a pine tree placed close to a surface of fire.

28.2 Numerical Model

This section presents the numerical model utilized to estimate the thermal and mass phenomena existing in a pine tree when it is under the influence of a forest fire. In the transmission of energy, the phenomena of conduction, convection, radiation and transpiration are considered. In the radiative phenomenon, the view factors and the Mean Radiant Temperature determination are evaluated based on the grid generation developed for the tree elements and the fire front. The water mass evaluation, the water distribution, diffusion and transpiration are issues considered in the mass transmission.

The three-dimensional geometry model of the tree, consisting of trunks, branches and leaves, is designed from cylindrical elements. Each cylindrical element is sized by its length and diameter and subdivided into several layers. The tree thermal response numerical model will use the three-dimensional geometry model of the tree as an input.

The tree thermal response numerical model is based on the numerical model of human thermal response numerical model, with a new geometry where the thermoregulatory system was dismissed and new paths were built for the water circulation. It is used to evaluate the thermal response, in steady state and transient regime, of a tree under the influence of a forest fire.

The tree thermal response numerical model is founded on balance integral equations of:

- Energy for body tissues of the pine tree;

- Mass for the water in the pine tree.

The equations systems constituted above are solved by the Runge–Kutta-Fehlberg algorithm with error control.

The thermal response model considers the following phenomena:

- Radiation verified between the external surface of the tree elements and the surface of fire, whose modelling uses the values of Mean Radiant Temperature;
- Conduction verified between the several layers of each tree element;
- Heat convection verified between the outer bodies' surface and the surrounding air environment;
- Heat evaporation, considering simultaneously the mass and heat transfer and the water phase change, verified between the outer bodies' surface and the surrounding air environment.

The following phenomena are considered in the mass transmission:

- Water distribution: the water is transported from the trunk to the branches and leaves;
- Water diffusion: water is transported within the trunk from the internal tissues to the external tissues; in this calculation, the cylindrical elements that form the trunk are divided into several layers (one inner, one outer, and a set of central layers located between them);
- Water transpiration: water is evaporated by convection from the outer layer to the environment, considering evaporative phenomena.

28.3 Numerical Methodology

The virtual pine tree model, with a height of 1.8 m, consists of 2289 cylindrical elements (divided into 14 trunks, 25 branches and 2250 leaves) spread over two levels. Each level has 7 trunks and 12 branches. At the top of the tree there is also a branch. Finally, each branch has 90 leaves.

The fire surface, with a height of 1 m, is distributed over 10 m, remaining static during the simulation time. The tree is located 5 m away from this fire surface, as can be seen in Fig. 28.1.

The input data of the numerical simulation are as follows:

- Flat and rectangular flame with an average temperature of 500 ºC;
- Average ambient air temperature of 20 ºC around the pine tree;
- Average relative humidity of ambient air of 50% around the tree;
- Average wind speed of 5 m/s.

The output data of the numerical simulation are the surface temperature distribution and moisture distribution in the pine tree got in a steady state and in a transient state during a time interval of 900 s.

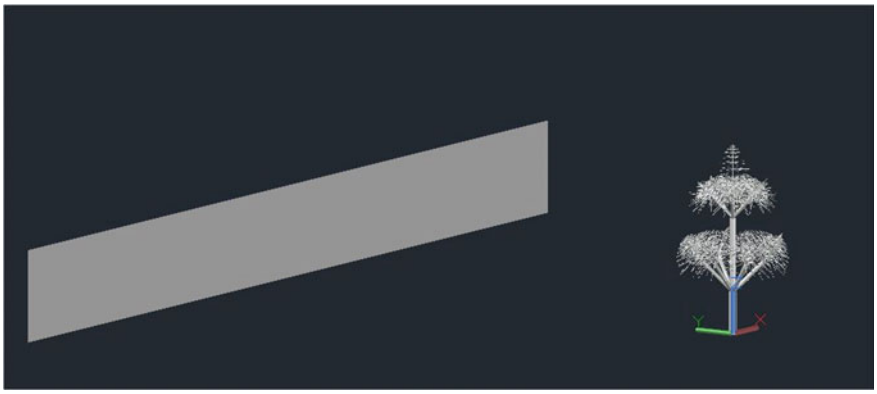

Fig. 28.1 Pine tree location relative to the surface of fire (immobilized)

28.4 Results and Discussion

This section shows the results acquired from the evolution of moisture in the branches (Figs. 28.2 and 28.3) and leaves (Figs. 28.4 and 28.5) of a pine tree. Only some of the leaves elements were selected to be presented. The leaves belonging to the branches, at each of the two levels of the pine tree, most exposed to the fire front were chosen. Pine moisture is obtained as the ratio between the water weight and the total water weight plus dry mass. It should also be noted that the simulation was carried out in such a way that, initially, before the appearance of the fire front, the moisture of the pine tree presented already stabilized values. The value of pine moisture obtained in steady-state regime was 53.46%. This value is in agreement with those obtained experimentally.

The results show that the moisture content in pine branches decreases with exposure to the fire front. The moisture content of pine branches decreases more rapidly in those located on the first level (close to the ground) than in those located on the second level (near the top). By level, it can be seen that the moisture content decreases more rapidly in those facing the fire front than in those facing the opposite direction. The moisture content in the leaves decreases faster than in the branches. By level, it can be seen that the moisture content decreases more rapidly in leaves facing the fire front than in those facing the opposite direction. It is then verified that the exposure of branches and leaves to higher temperatures causes their greater heating and therefore greater evaporation of the water contained in them.

Therefore, the numerical model used represents well the phenomena that occur in a pine tree when exposed to the effects of an intense heat source represented here by a fire surface. The numerical model well simulates the effect of the water evaporation contained in the different elements of the pine tree when they are subjected to an increase in temperature. Furthermore, it also takes into account the type of element (branch or leaf) as well as the levels of reduction in moisture content that are proportional to the increase in temperature.

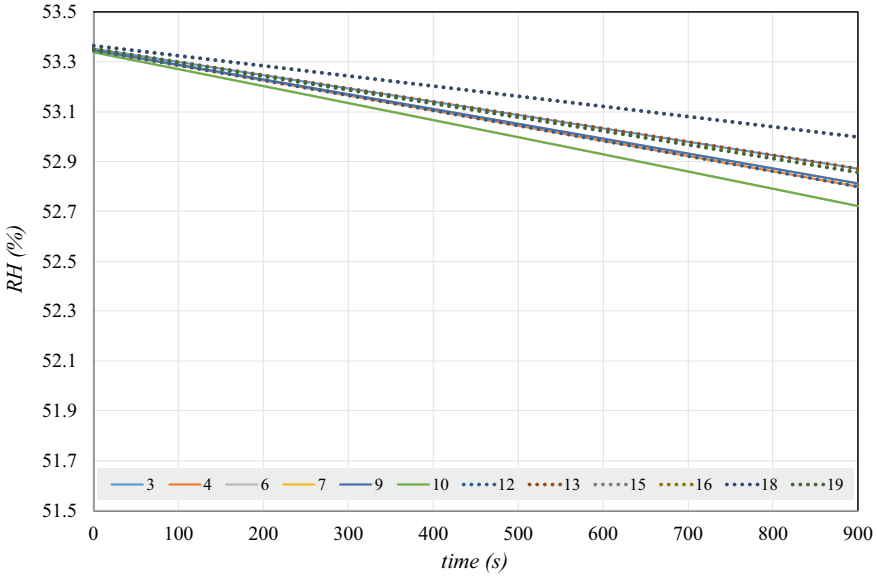

Fig. 28.2 Evolution of moisture content in branches located on the first level (closer to the ground) of a pine tree

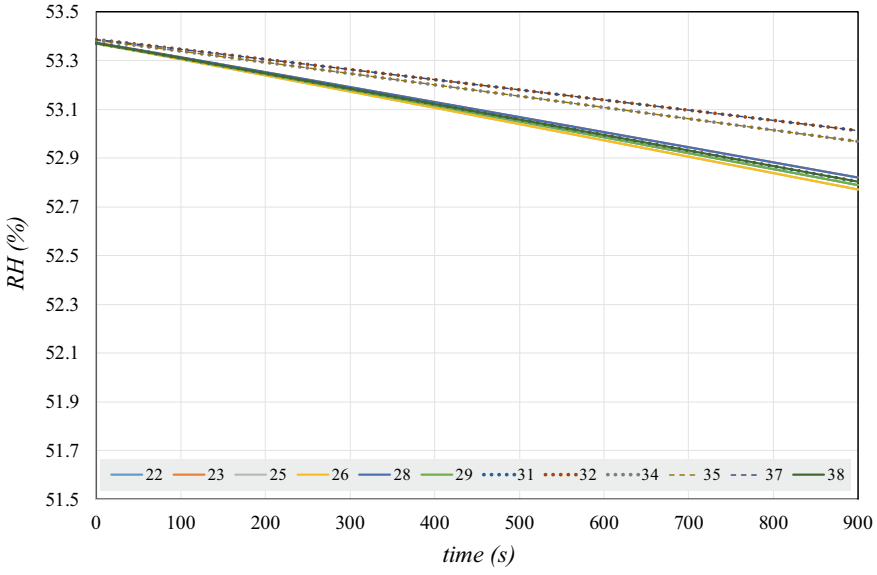

Fig. 28.3 Evolution of moisture content in branches located on the second level (closer to the top) of a pine tree

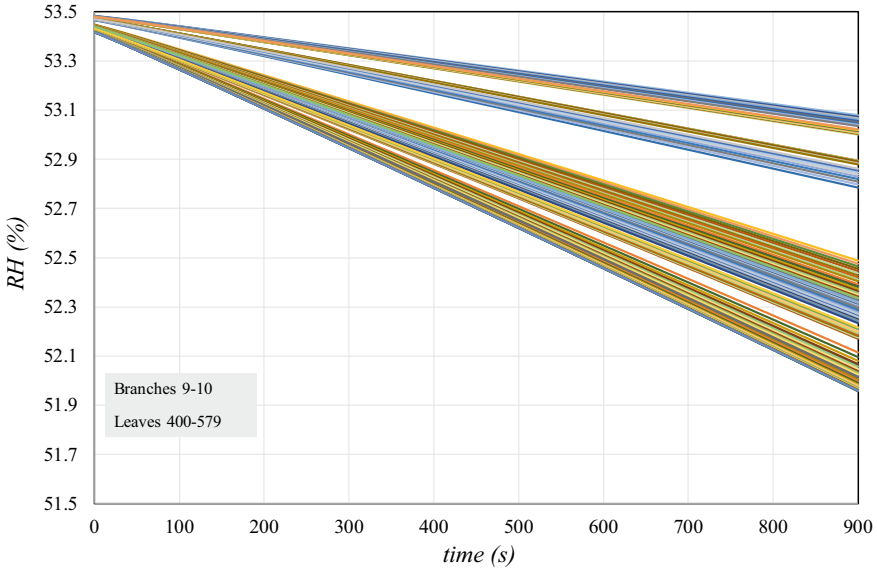

Fig. 28.4 Evolution of moisture content in leaves located on first-level branches most exposed to the fire surface

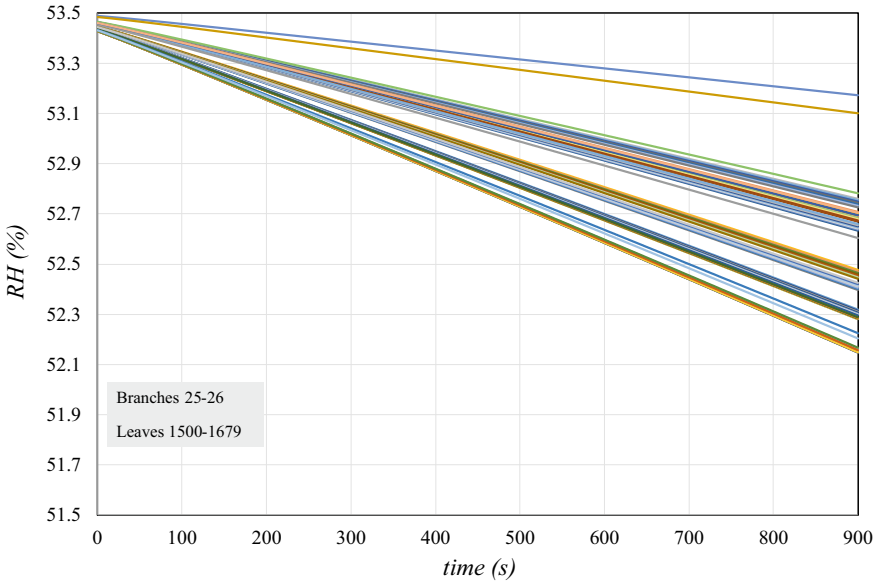

Fig. 28.5 Evolution of moisture content in the leaves located in second-level branches of most exposed to the fire surface

28.5 Conclusions

This article presented a numerical work on the dynamic behavior of heat and mass transmission in a pine tree when under the influence of a fire surface in its vicinity. For this purpose, a numerical model was developed to simulate the pine tree thermal response from a similar model that simulates the human body thermal response. In heat transmission, the phenomena of conduction, convection, radiation and evaporation were considered. In mass transmission, the phenomena of distribution, diffusion and evaporation were considered.

The results show that the moisture content in the various constituent elements of pine decreases, over time, with exposure to increasing temperature. The decrease in moisture content is greater in the leaves than in the branches, greater in the leaves located in the first level (closer to the ground) than in the second level of the pine (closer to the top), and in the branches and leaves that are facing the direction of fire than facing the opposite direction.

Therefore, it can be concluded that the numerical model used makes it possible to reliably represent the thermal response of a tree.

Acknowledgements The authors acknowledge the support of the project reference PCIF/MPG/0108/2017, funded by the FCT.

References

Conceição E, Awbi H (2021) Evaluation of integral effect of thermal comfort, air quality and draught risk for desks equipped with personalized ventilation systems. Energies 14(11):3235

Conceição E, Lúcio M, Farinho J (2007) Experimental and numerical study of personalized of ventilation in classrooms desks. In: Proceedings of 10th international conference on air distribution in rooms, ROOMVENT 2007, Helsinki, Finland, 13–15 July

Conceição E, Lúcio M (2010) Numerical study of the influence of opaque external trees with pyramidal shape on the thermal behaviour of a school building in summer conditions. Indoor Built Environ 19(6):657–667

Conceição E, Nunes A, Gomes J, Lúcio M (2010) Application of a school building thermal response numerical model in the evolution of the adaptive thermal comfort level in the Mediterranean environment. Int J Vent 9(3):287–304

Conceição E, Santiago C, Lúcio M, Awbi H (2018) Predicting the air quality, thermal comfort and draught risk for a virtual classroom with desk-type personalized ventilation systems. Buildings 8(2):35

Conceição E, Silva M, André J, Viegas D (1999) A computational model to simulate the thermal behaviour of the passengers' compartment of vehicle. In: Proceedings of 1999 SAE international congress and exposition, Detroit, USA

Conceição E, Lúcio M (2001) Numerical and subjective responses of human thermal sensation. In: 6th portuguese conference on biomedical engineering, BIOENG'2001, Faro, Portugal, 11–12 June

Fanger P (1970) Thermal comfort: analysis and applications in environmental engineering. Danish Technical Press, Copenhagen, Denmark

Green S, Vogeler I, Clothier B, Mills T, Dijssel C (2003) Modelling water uptake by a mature apple tree. Aust J Soil Res 41:365–380

Ishak M, Zolkepli M, Yunus M, Ali N, Kassim A, Zaini M (2021) Verification of tree induced suction with numerical model. Phys Chem Earth 121:102980

Janott F, Gayler S, Gessler A, Javaux M, Klier C, Priesack E (2011) A one-dimensional model of water flow in soil-plant systems based on plant architecture. Plant Soil 341:233–256

Janssen U (1994) The transpiration rate of a single tree—numerical simulations. Ecol Model 75–76:321–330

Lai A, Maing M, Ng E (2017) Observational studies of mean radiant temperature across different outdoor spaces under shaded conditions in densely built environment. Build Environ 114:397–409

Simon H, Lindén J, Hoffmann D, Braun P, Bruse M, Esper J (2018) Modeling transpiration and leaf temperature of urban trees—a case study evaluating the microclimate model ENVI-met against measurement data. Landsc Urban Plan 174:33–40

Vorre M, Jensen R, Dréau J (2015) Radiation exchange between persons and surfaces for building energy simulations. Energy Build 101:110–121

Wang F, Letort V, Lu Q, Bai X, Guo Y, Reffye P, Li B (2012) A functional and structural Mongolian Scots pine (Pinus sylvestris var. mongolica) model integrating architecture, biomass and effects of precipitation. PLoS ONE 7(8):43531

Chapter 29
Airflow Inside of a Virtual Room Integrating a Vertical Confluent Jets Ventilation System

Eusébio Conceição, João Gomes, Mª Inês Conceição, Mª Manuela Lúcio, and Hazim Awbi

Abstract The airflow inside a virtual room integrating a vertical confluent jets (VCJ) ventilation system is done in this study. The VCJ ventilation system consists of one inlet and one exhaust system, both equipped with independent ventilators and located near the ceiling zone. The inlet system considers two horizontal duct equipped with two group of vertical consecutive nozzles located in opposite walls. The exhaust system considers a vertical duct, placed in the room central area, near the ceiling. The presenting work is carried out using a Computational Fluids Dynamics (CFD) methodology. The three-dimensional velocity of the air components field, the intensity of air turbulence and turbulent variables were obtained in this work. The results present an airflow, promoted by the VCJ ventilation system, with a descendent direction, furthers an ascendant ventilation in the occupation zone. In the inlet area, the air velocity is highest. In the occupation zone, the airflow has an air recirculation characteristic. The velocity of the air decreases, near the wall surface, taking downward direction from the inlet zone to the floor. At this level, the velocity of the air starts by distributing itself along the floor and then takes an upward direction towards the exhaust zone with increasing values.

Keywords Vertical confluents jet system · HVAC · CFD · Indoor airflow

E. Conceição (✉) · Mª. M. Lúcio
FCT - Universidade Do Algarve, Campus de Gambelas, 8005-139 Faro, Portugal
e-mail: econcei@ualg.pt

J. Gomes
CINTAL, Campus de Gambelas, 8005-139 Faro, Portugal
e-mail: jgomes@ualg.pt

Mª. I. Conceição
Instituto Superior Técnico, Av. Rovisco Pais, 1049-001 Lisboa, Portugal
e-mail: ines.conceicao@tecnico.ulisboa.pt

H. Awbi
School of Built Environment, University of Reading, Reading RG6 6AW, UK
e-mail: h.b.awbi@reading.ac.uk

H.-Y. Jeon (ed.), *Sustainable Development of Water and Environment*,
Environmental Science and Engineering,
https://doi.org/10.1007/978-3-031-07500-1_29

29.1 Introduction

In this work the confluent jets ventilation (CJV) system is applied. This kind of ventilation system is utilized in indoor spaces to improve the levels of indoor air quality and thermal. Previous works was analyzed for several authors. For example, in this sense, Arghand et al. (2015) studied the performance of under-floor, CJV and mixing ventilation (MV) systems applied in spaces of an office. Karimipanah et al. (2000) studied different systems used in the air distribution in a classroom space. Cho et al. (2008) analyzed the influence of both wall displacement ventilation (DV) and CJV systems in the thermal and air quality conditions of occupants of an indoor space.

Depending on the type of ventilation system used, internal spaces are able to promote MV, DV, CJV, impinging ventilation, among others.

In the calculation of the internal airflow topology, the velocity, temperature and turbulence intensity of the air, inside the room space, should be measured. Examples of application of several airflows inside spaces were presented for vehicles spaces (Conceição et al. 1997a), and buildings spaces (Conceição et al. 2008).

To calculated the level of thermal comfort, the Mean Radiant Temperature and the air velocity, air temperature, air relative humidity and clothing and activity levels, are used (see Conceição et al. 2010). These parameters were created in Fanger (1970) to be applied in indoor spaces provided by ventilation systems, heating systems and air conditioning systems (as presented also in international standard ISO 7730 2005).

To calculated the air quality inside the spaces, the concentration of the carbon dioxide, used as air quality indicator of the indoor space, ANSI/ASHRAE Standard 62–1 (ANSI/ASHRAE Standard 62-1 2016), is utilized, to calculate the airflow rate and the carbon dioxide, or other gas, concentration evaluation is used (Conceição et al. 1997b).

In the assessment of the Draught Risk level, the velocity, temperature and turbulence intensity of the air, are used. This index, developed in Fanger et al. (1988), is present in standard ISO 7730 (2005). This index was applied, for example, in a virtual room provided with personalized ventilation systems (Conceição et al. 2018).

To estimate the internal airflow, the present work uses a coupling of two software, namely, the CFD and the Human Thermal Modelling (see as example, Conceição and Awbi 2021). The coupling of the two software uses input data from Buildings Thermal Modelling software, see Conceição and Lúcio (2010). Applications of the software applied in this study are shown in Yang et al. (2014), Sailor (2008) and Balagi et al. (2013).

CFD is a numerical methodology used to evaluate environmental variables inside spaces, such as the air velocity, temperature and turbulence intensity fields, among others variables. CFD applications are detailed in the papers of Bhutta et al. (2012), Awbi (1998) and Xing et al. (2001).

In this work is evaluated the airflow inside a virtual room indoor environment, that integrated a Vertical Confluent Jet (VCJ) ventilation system. The VCJ ventilation

system consists of an inlet system, constructed with consecutive nozzles, and an exhaust system, both located near the ceiling.

29.2 Numerical Model Methodology

The study is made in a virtual room, equipped with a ventilation system, based on VCJ ventilation system, with dimensions of $2.7 \times 2.45 \times 2.4\ m^3$ (see Fig. 29.1). The virtual room is equipped with a VCJ ventilation system consisting of one exhaust and one inlet systems.

The inlet system considers two ducts, with a horizontal position, with 0.125 m diameter, placed at 1.8 m high, and two ducts located on each of the opposing walls. Each of these ducts, of equal length, is fed by a fan placed between them. Each horizontal duct is equipped with two group of 50 equally spaced consecutive nozzles. Each nozzle has a diameter of 6 mm and the distance between their centers is 16 mm. Each horizontal duct promotes a vertical jet near the wall.

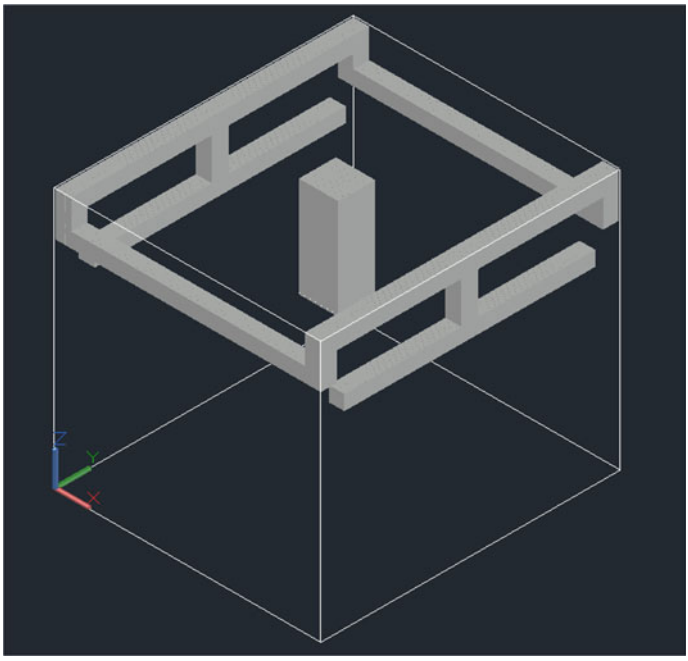

Fig. 29.1 Scheme used in the CFD representing the virtual room and VCJ ventilation system: inlet system represented by the two horizontal ducts and exhaust system represented by the duct at the middle of the space

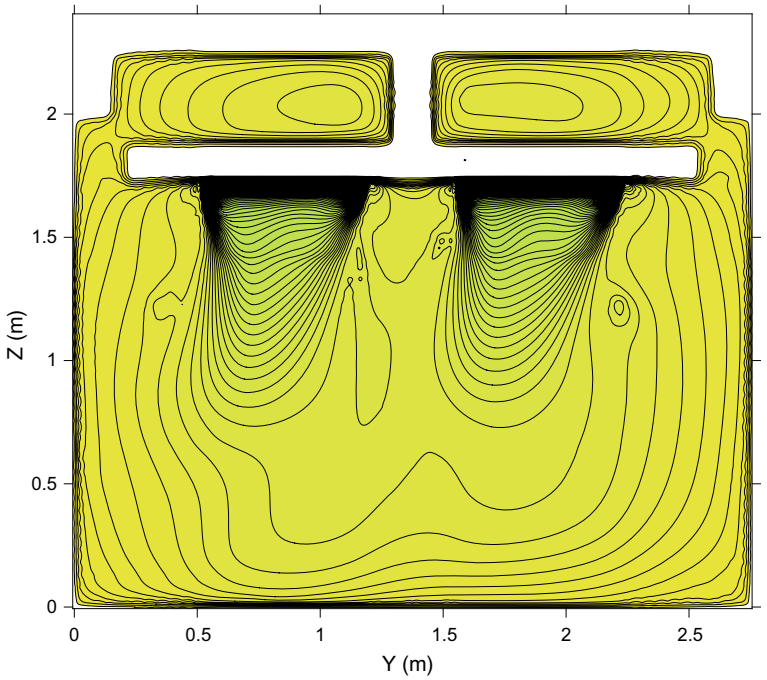

Fig. 29.2 Field of the airflow in a plan placed at 0.076 m in the X direction

The exhaust system is performed with one vertical duct, placed at 1.8 m high in the middle zone of the virtual room. The exhaust system is equipped with a fan placed in the exhaust zone.

The numerical work was made in winter conditions, with the following characteristics:

- Inlet mean temperature of the air of 20 °C;
- Inlet mean velocity of the air of 10 m/s;
- Outdoor temperature of the air of 20 °C.

29.3 Results and Discussion

The distribution of the velocity of the air, are presented in the following pictures:

- Figure 29.2 presents the field of the airflow in a plan placed at 0.076 m in the X direction, located in the inlet zone;
- Figure 29.3 shows the field of the airflow in a plan placed at 0.202 m in the X direction;
- Figure 29.4 presents the field of the airflow in a plan placed at 0.704 m in the X direction;

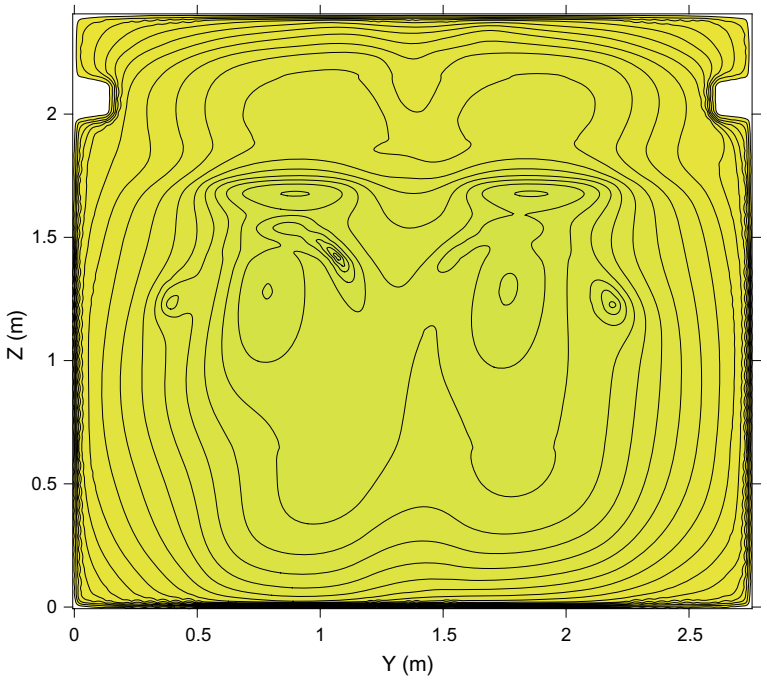

Fig. 29.3 Field of the airflow in a plan placed at 0.202 m in the X direction

- Figure 29.5 shows the field of the airflow in a plan placed at 1.225 m in the X direction, which is placed in the exhaust zone.

In these pictures, the green is associated with highest velocity of the air, while the yellow is associated with lowest velocity of the air.

In accordance with presented results in this work, the following conclusions can be obtained:

- The field of the velocity of the air in a plan placed at 0.076 m, in X direction, is highest in the inlet zone and its values decrease close to the wall until it reaches the floor.
- The field of the velocity of the air in a plan placed at 0.202 m, in X direction, is highest in the central and lower zone. These values are associated with the influence of the inlet airflow.
- The field of the velocity of the air in a plan placed at 0.704 m, in X direction, has highest values in the ceiling central zone. These values are associated with an air recirculation verified in the virtual room central area.
- The air velocity field in a plan placed at 1.225 m, in X direction, presents the highest value above the exhaust level. These values are associated with the air recirculation verified in the central zone of the virtual room and with the exhaust methodology used.

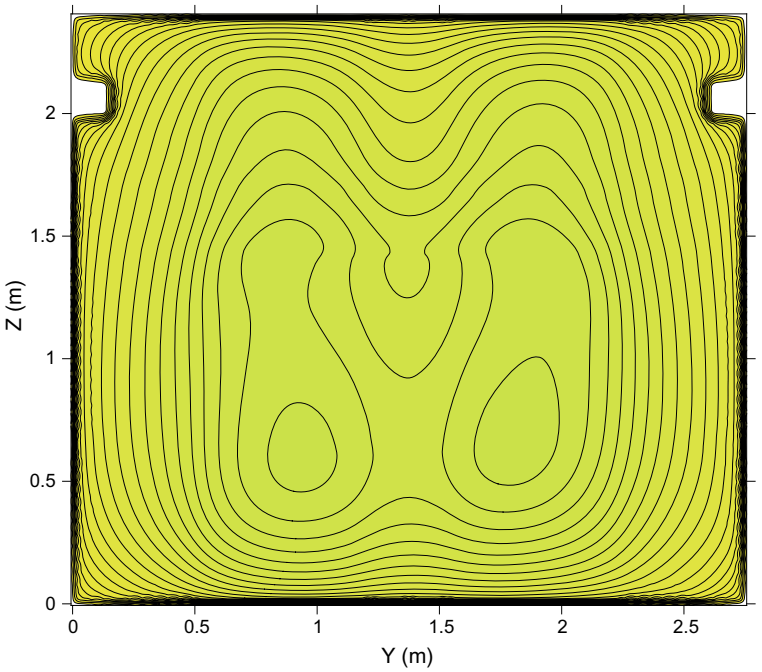

Fig. 29.4 Field of the airflow in a plan placed at 0.704 m in the X direction

Thus, as the results show, the VCJ ventilation system presented in this work produces a descendent vertical airflow. The velocity of the air presents a highest value in the inlet zone. The velocity of the air values decreases, near the wall surface, with descending direction, from the inlet zone to the floor level. In the occupation zone, the airflow presents an air recirculation typology. The velocity of the air is distributed along the floor, then shows increasing values in an upward direction towards the exhaust system.

29.4 Conclusions

In this study the airflow inside a virtual room integrating a VCJ ventilation system is done. Two horizontal ducts, equipped with consecutive vertical nozzles, are considered. The set of vertical nozzles promotes a descendent airflow.

The results present a velocity of the air, promoted by the VCJ ventilation system, present a descendent airflow near the wall surface. The velocity of the air presents a highest value in the inlet zone and the airflow characteristics show that the velocity of the air values decrease when the distance between the inlet and the floor increase. Close to the floor, the velocity of the air is distributed throughout it and then its values

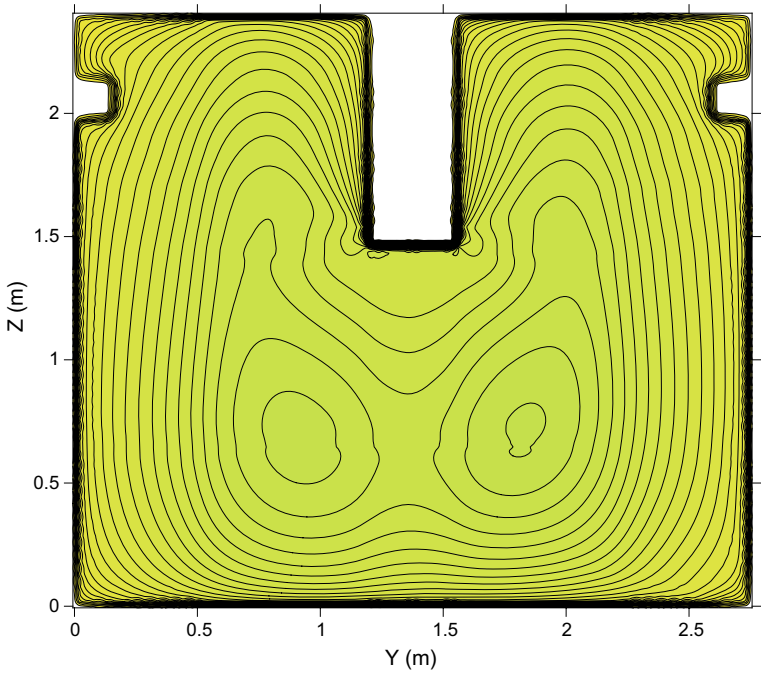

Fig. 29.5 Field of the airflow in a plan placed at 1.225 m in the X direction

increase in an ascending direction towards the exhaust system. The characteristics of the airflow in the occupied zone present an air recirculation typology.

Acknowledgements The authors acknowledge to the project (70156-Safeair) from the CRESC Algarve 2020, PORTUGAL 2020, through the ERDF.

References

ANSI/ASHRAE Standard 62-1 (2016) Ventilation for acceptable indoor air quality, American Society of Heating, Refrigerating and Air-Conditioning Engineers, Atlanta, GA, USA

Arghand T, Karimipanah T, Awbi H, Cehlin M, Larsson U, Linden E (2015) An experimental investigation of the flow and comfort parameters for under-floor, confluent jets and mixing ventilation systems in an open-plan office. Build Environ 92:48–60

Awbi H (1998) Energy efficient room air distribution. Renew Energy 15:293–299

Balaji N, Mani M, Venkatarama B (2013) Thermal performance of the building walls. In: Proceedings of building simulation applications BSA 2013. BU Press, Bozen-Bolzano, pp 151–159

Bhutta M, Hayat N, Bashir M, Khan A, Ahmad K, Khan S (2012) CFD applications in various heat exchangers design: a review. Appl Therm Eng 32:1–12

Cho Y, Awbi H, Karimipanah T (2008) Theoretical and experimental investigation of wall confluent jets ventilation and comparison with wall displacement ventilation. Build Environ 43(6):1091–1100

Conceição E, Awbi H (2021) Evaluation of integral effect of thermal comfort, air quality and draught risk for desks equipped with personalized ventilation systems. Energies 14(11):3235

Conceição E, Lúcio M (2010) Numerical study of the influence of opaque external trees with pyramidal shape on the thermal behaviour of a school building in summer conditions. Indoor Built Environ 19(6):657–667

Conceição E, Silva M, Viegas D (1997a) Airflow around a passenger seated in a bus. HVAC&R Res 3(4):311–323

Conceição E, Silva M, Viegas D (1997b) Air quality inside the passenger compartment of a bus. J Expo Anal Environ Epidemiol 7(4):521–534

Conceição E, Lúcio M, Vicente V, Rosão V (2008) Evaluation of local thermal discomfort in a classroom equipped with crossed ventilation. Int J Vent 7(3):267–277

Conceição E, Nunes A, Gomes J, Lúcio M (2010) Application of a school building thermal response numerical model in the evolution of the adaptive thermal comfort level in the Mediterranean environment. Int J Vent 9(3):287–304

Conceição E, Santiago C, Lúcio M, Awbi H (2018) Predicting the air quality, thermal comfort and draught risk for a virtual classroom with desk-type personalized ventilation systems. Buildings 8(2):35

Fanger P (1970) Thermal comfort: analysis and applications in environmental engineering. Danish Technical Press, Copenhagen, Denmark

Fanger P, Melikov A, Hanzawa H, Ring J (1988) Air turbulence and sensation of draught. Energy Build 12:21–39

ISO 7730 (2005) Ergonomics of the thermal environments—analytical determination and interpretation of thermal comfort using calculation of the PMV and PPD indices and local thermal comfort criteria. International Standard Organization, Geneva, Switzerland

Karimipanah T, Sandberg M, Awbi H (2000) A comparative study of different air distribution systems in a classroom. In: Proceedings of 7th international conference on air distribution in rooms, ROOMVENT 2000. Elsevier, Amsterdam, pp 1013–1018

Sailor D (2008) A green roof model for building energy simulation programs. Energy Build 40(8):1466–1478

Xing H, Hatton A, Awbi H (2001) A study of the air quality in the breathing zone in a room with displacement ventilation. Build Environ 36(7):809–820

Yang L, Yan H, Lam J (2014) Thermal comfort and building energy consumption implications—a review. Appl Energy 115:164–173

Chapter 30
Integration Selective Lithium Exchange Membrane and Diffusion Dialysis to Recover Lithium Ions in Brine Water

Jih-Hsing Chang, Keng-Chi Wan, Mohanraj Kumar, and Shan-Yi Shen

Abstract With the rise of the electronic equipment and electric vehicle industry, a large number of lithium batteries are used, which has caused widespread demand for lithium. Seawater contains abundant lithium resources; thus, a technique to extract lithium from seawater has recently received more attention. In this study, we fabricated two types of lithium selective exchange membrane: ion-sieve membrane and ion-imprint membrane. At the same time, such membranes combined with diffusion dialysis were employed to recover lithium ions in brine water (analogic to seawater). The brine water was prepared at a concentration of 100 mg/L sodium, potassium, magnesium, and calcium ion, respectively, while the lithium concentration was 0.17 mg/L. The adsorption and diffusion dialysis experiments evaluated the separation efficiency of lithium ions for the two exchange membranes. This study explored the effect of the film thickness, pH value, conductivity, and voltage on the extraction efficiency of lithium for the diffusion dialysis process. Moreover, the lithium adsorption capacity of an ion-sieve membrane and ion-imprint membrane were around 2,000 mg/m^2 and 1,800 mg/m^2, respectively, according to adsorption experiments. To consider the selectivity of ions, the results indicated that the ion-sieve membrane possessed higher lithium selectivity than the ion-print membrane; after 54 h of the ion-sieve membrane combined with diffusion dialysis, the recovery efficiency of lithium was 18%, and that was 2.5 times higher than that of the current extraction technique (7%). In addition, the electricity of 0.08 V was produced under such diffusion dialysis conditions.

Keywords Diffusion dialysis · Lithium recovery · Selective ion exchange membrane · Seawater extraction

J.-H. Chang · K.-C. Wan · M. Kumar
Department of Environmental Engineering and Management, Chaoyang University of Technology, Wufeng 41349, Taiwan

S.-Y. Shen (✉)
Department of Environmental Engineering, Da-Yeh University, Changhua 515006, Taiwan R.O.C.
e-mail: shanyi@mail.dyu.edu.tw

H.-Y. Jeon (ed.), *Sustainable Development of Water and Environment*,
Environmental Science and Engineering,
https://doi.org/10.1007/978-3-031-07500-1_30

30.1 Introduction

With the huge changes in the global climate and environment, the world has set a goal of achieving net-zero carbon emissions by 2050. According to the "Net Zero by 2050: A Roadmap for the Global Energy Sector" published by the International Energy Agency (IEA) in 2021, seven key technologies are proposed, which list the possibilities of electrification. Directly reducing the use of fossil fuels and coupled with low-carbon electricity can reduce carbon emissions. For example, 60% of new cars in 2030 will be electric vehicles, which will have varying degrees and dimensions of impact in the global economy, energy industry, and natural resource extraction. As a result, "lithium" is fast becoming a strategically important commodity.

In 2019, the global demand for lithium had reached 269,000 tons, the global annual demand for lithium raw materials will continue to increase under the worldwide carbon reduction policy plan. The total demand is expected to reach 5.11 million tons of lithium by 2050 (Zavahir et al. 2021). The lithium feedstock currently used commercially comes from high-grade ores on land and salt lake brine, which is collected using chemical precipitation techniques, but extracting lithium from ore and salt lake brine can have a significant impact on the environment including water pollution and depletion, soil destruction and air pollution. Moreover, the limited lithium reserves on land with extremely uneven geographical distribution (more than 98% of the total reserves are concentrated in Chile, Argentina, China, and Australia). On the contrary, seawater contains a large number of lithium resources (estimated to be about 230 billion tons) and a wide distribution range that accounts for 71% of the earth's area. Therefore, to effectively solve the above problems, the extraction of lithium from seawater has great potential.

At present, common technologies for extracting lithium from seawater are absorption, solvent extraction, electrodialysis, and diffusion dialysis. The adsorption method is the most common due to the high extraction efficiency. Although most of the powder adsorbents have strong adsorption capacity, the loss of the adsorbent and the difficulty of recovery will be limited in industrial applications (Li et al. 2019). The solvent extraction method mainly has high costs and damage to the environment and other disadvantages. Both the electrodialysis and the diffusion dialysis method use the thin film separation treatment, and the main difference is the use of electric field and diffusion as the driving force of ion migration. The electrodialysis is simple to operate, the environment is friendly and the extraction time is short, but it still has the application of additional electric field, energy consumption and film easy to scale problems (Al-Amshawee et al. 2020; Park et al. 2015). Diffusion dialysis technology has the advantages of zero energy consumption, low cost, and stable operation, as well as pollution-free (Luo et al. 2011). Which through the high concentration difference as the driving force, maintains a good lithium-ion recovery efficiency and generates additional energy benefits. Therefore, this study mainly uses diffusion dialysis technology, supplemented by lithium-ion selective exchange membrane (ion-sieve membrane and ion-imprint membrane, respectively) to explore

the adsorption phenomenon and selectivity of lithium, which to compare the difference between ion-sieve membrane and ion-imprint membrane. Finally, the artificial seawater solution (containing lithium, sodium, magnesium, calcium, and potassium) was tested with an appropriate lithium exchange membrane and diffusion dialysis technology. During the experiment, the changes in selectivity, recovery efficiency, pH value, conductivity, and voltage value were discussed using exchange membranes of different thicknesses.

30.2 Materials and Methods

30.2.1 Fabrication of Selective Ion Exchange Membranes

First, we made two kinds of lithium selective membrane namely ion-sieve film and ion-imprint membrane, followed by adsorption and diffusion dialysis test is carried out. The manufacturing steps of the two membranes are as follows.

The preparation of ion-sieve membrane

(1) Heat the lithium-ion manganese oxide to 400 °C for 4 h, (2) Add polyvinyl chloride as an adhesive and N,N-dimethyl acetamide as a solvent to heat at 80 °C, stir for 6 h, (3) The solution is applied to the glass sheet and rinsed with deionized water to cool to form an exchange membrane, (4) Placed in 0.5 M HCl to remove lithium ions from the exchange membrane.

The preparation of ion-inprint membrane

(1) Adding cellulose acetate, chitosan, polyvinylalcohol, polyvinylpyrrolidone and dimethyl sulfoxide as a solvent to mix evenly, (2) After mixing, glutaraldehyde was added as a crosslinker and stirred at 50 °C for 12 h and let stand for 6 h, (3) taking the solution in a glass slide and soaking with deionized water for 1 h to form a membrane, (4) The membrane and dopamine were mixed with tris (hydroxymethyl) aminomethane to be stirred for 6 h, then rinsed with deionized water, and dried at 50 °C, (5) After drying, 12-crown 4 ether was added as the selective for lithium, lithium chloride as the target ion, 3-aminopropyltriethoxysilane, tetraethyl orthosilicate and ethanol were mixed, (6) After mixing, add ammonia water as a catalyst to stir for 8 h, after which impurities are removed by rinsing with deionization, (7) 0.01 M hydrochloric acid was added to remove the lithium ions from the exchange membrane, and finally rinsed with deionized water and to dried at 50 °C.

30.2.2 Experiment of Adsorption and Diffusion Dialysis

In this experiment, two kinds of lithium ion-selective membranes were prepared. The adsorption capacity of lithium and ions selectivity were discussed by adding different metal solutions. The adsorption experiment process is as follows. (1) Cutting the area of the lithium selective membrane was 1 cm^2 for the adsorption test, (2) Five different kinds of solutions were prepared, namely, 1. pure lithium, 2. lithium + sodium, 3. lithium + sodium + magnesium, 4. lithium + sodium + magnesium + calcium, and 5. lithium + sodium + magnesium + calcium + potassium solution, to explore the competitive relationship for adsorption between ions. The initial concentrations of each ion were lithium (20 mg/L), sodium (40 mg/L), magnesium (60 mg/L), calcium (80 mg/L) and potassium (100 mg/L), respectively, (3) The lithium selective membrane was placed in the above-mentioned prepared solution to be stirred for 24 h with a shake. Finally, the concentration was detected. The capacity of the adsorption equilibrium equation is listed in Eq. 30.1.

$$Q = (C_0 - C_e)V/S \tag{30.1}$$

where,

Q Adsorption capacity (mg/m^2), C_0: Initial concentration (mg/L),

C_e Concentration after equilibrium (mg/L), V: Volume (L),

S Area of lithium exchange membrane (m^2).

The schematic of diffusion dialysis is shown in Fig. 30.1. Here, the lithium selective membrane separates the two ends, which one end is the contains lithium, sodium, magnesium, calcium, potassium solution and another end is a hydrochloric acid solution. Using the diffusion mechanism to make the lithium ions in seawater through the lithium selective membrane to move to the recovery end for extraction and the electricity meter for measuring voltage values. Through every time sampling analysis to explore the recovery efficiency of lithium and the selectivity of other ions. The diffusion dialysis test is as follows. (1) The equipment is made of acrylic, the size is length 10 cm × 8.5 cm width × 8.5 cm height. Place the lithium selective membrane with a size of 7.5 cm × 6.5 cm between the seawater end and the recovery end to separate the two ends, (2) The prepared solution contains lithium chloride, sodium chloride, magnesium chloride, calcium chloride dehydrate, and potassium chloride as the seawater end, and the concentration is 0.17, 100, 100, 100, and 100 mg/L, while recovery end is 0.1 M hydrochloric acid. The two ends are mixed uniformly with an aerator, (3) The seawater end and recovery end are sampled and determined concentration of each metal, pH value, conductivity, and voltage value at 0, 24, 30, 48, and 54 h.

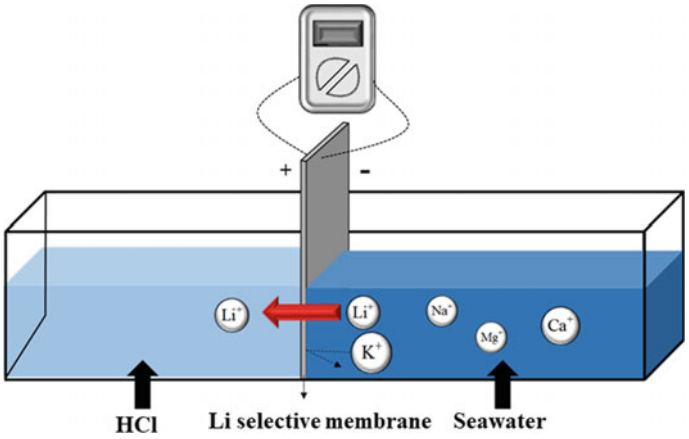

Fig. 30.1 The schematic of diffusion dialysis in this study

30.3 Results and Discussion

30.3.1 Adsorption Capacity and Selectivity of Lithium Ions

The concentration of adsorption equilibrium and the amount of lithium adsorption were plotted on the X and Y axes, respectively. As shown in Fig. 30.2 (left), the equilibrium adsorption of lithium in different ionic solutions of the ion-sieve membrane was more than 1,900 mg/m^2. The trend shows that the amount of lithium adsorption was a variation insignificantly with the increase of other metal elements and has suitable identification of lithium, which can block other metal elements. Hence, the lithium can be selectively adsorbed on the ion-sieve membrane. Figure 30.2 (right) is the adsorption capacity of lithium ions in the ion-imprint membrane. The capacity of equilibrium adsorption is 1,800, 1200, 600, 400, and 400 mg/m^2, respectively. The adsorption capacity decreased with the increase of ion species. The main reason should be that the pore position on the ion-imprint membrane is occupied by other metal elements, resulting in a gradual decrease in the selectivity of the ion-imprint membrane for lithium.

The adsorption capacity of different ions by the ion sieve membrane is 1,960 mg/m^2 with lithium ions, and the others are magnesium 1,600 mg/m^2, calcium 1,200 mg/m^2, sodium 800 mg/m^2, and potassium 800 mg/m^2. The main extraction mechanism of the ion-sieve membrane is to use the hole to identify the target ions and selectively extract the ions by the size of the ion radius. Since the radius of magnesium ions is similar to that of lithium (lithium of 58 pm and magnesium of 72 pm), the pore position of the ion-sieve membrane is occupied. As a result, the adsorption capacity of magnesium ions also reaches a certain degree. Compared with the ion-sieve membrane, the adsorption of each ions by the ion-imprint membranes is low, namely lithium 400 mg/m^2, sodium 200 mg/m^2, magnesium 200 mg/m^2, calcium

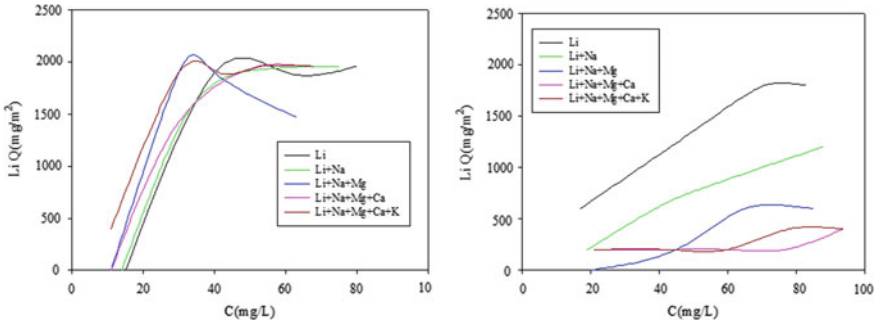

Fig. 30.2 The variation of adsorption capacities of lithium by an ion-sieve membrane (left) and ion-imprint membrane (right)

400 mg/m^2, and potassium 400 mg/m^2. It is mainly speculated that the ion-imprint membrane may have a lower specific surface area and less homogeneous pore size, thus resulting in less obvious adsorption capacity and selectivity for ions.

30.3.2 Characteristics of the Membrane After Adsorption

In this study, X-ray diffraction analysis (XRD) and field emission scanning electron microscopy (FE-SEM) was used to identify the differences in surface microstructure before and after adsorption of the ion-sieve membrane, as shown in Fig. 30.3. According to XRD analysis, $Li_{1.6}Mn_{1.6}O_4$ appeared at 2θ angles of 18.8°, 31.03°, 36.55°, 38.26°, 44.53°, 48.67°, 58.92°, and 64.67°, respectively. According to the JCPSD database atlas comparison, it was confirmed that it was consistent with the ion-sieve membrane before adsorption. After the ion-sieve membrane is adsorbed, another peak can be found at 2θ angles of 25°–30°, and it is estimated that it is sodium and calcium. Figure 30.4 shows the microstructure of the surface at 10,000 magnification using FE-SEM. From the surface morphology, it can be known that the surface of the ion-sieve membrane has a mesh structure and many holes, and the channel is composed of multiple holes and forms a multi-layer structural morphology. In addition, it can be clearly seen that some granular matter appears on the membrane surface, it speculated that metal elements are adsorbed in the membrane after adsorption. Figure 30.5 are the EDS spectra before and after the adsorption experiment of the ion-sieve membrane. Before adsorption, there are oxygen and manganese elements. Because the chemical for making an ion-sieve membrane is manganese oxide, manganese oxide will combine with lithium to form pores of a specific size. After adsorption, sodium, magnesium, calcium, and potassium were estimated to be the main sources of particulate matter. In addition, there is chlorine element present before and after adsorption, mainly because the ion-sieve membrane removes the target ions by using hydrochloric acid during the manufacturing process, resulting in chlorine remaining on the ion-sieve membrane. Lithium does not appear in this

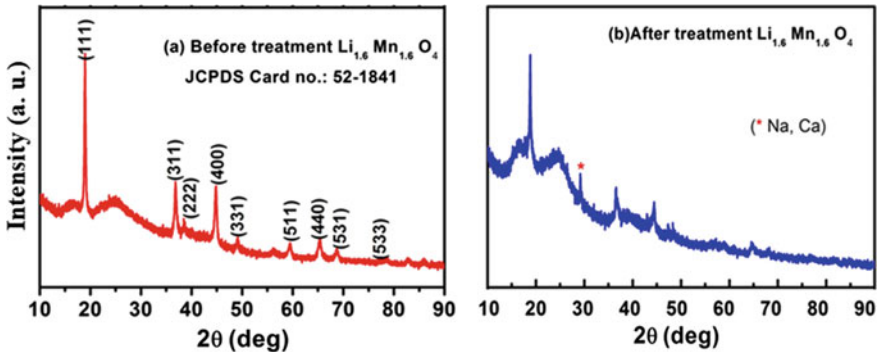

Fig. 30.3 XRD patterns of lithium selective membrane before (red) and after (blue) adsorption

spectrum, it is speculated that due to the small mass of lithium, the resulting signal is weak.

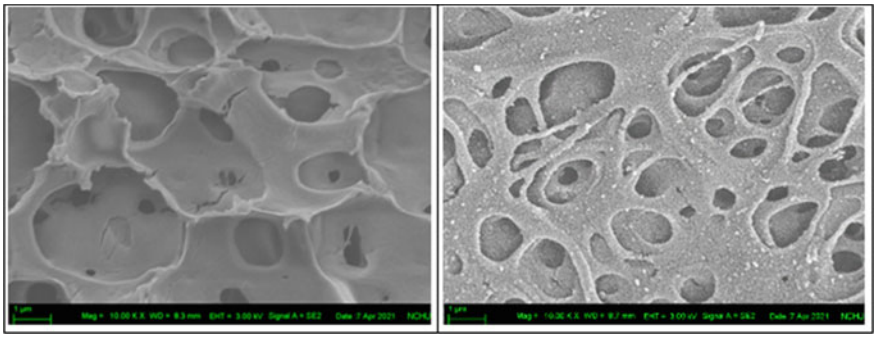

Fig. 30.4 FESEM images of lithium selective membrane before (left) and after (right) adsorption

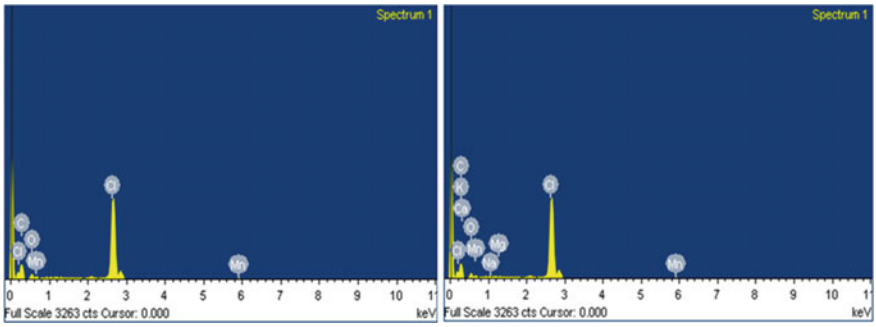

Fig. 30.5 EDS spectra of lithium selective membrane before (left) and after (right) adsorption

30.3.3 The Experiments of Diffusion Dialysis

Since the ion-sieve membrane has better ion selectivity for lithium ions, the diffusion dialysis test was carried out with the ion-sieve membrane. In this study, three ion-sieve membranes with different thicknesses were used for dialysis experiments, and the initial pH values of the seawater end and the recovery end were about 8 and 1.8. After 24 h of operation, the pH value of the seawater end dropped to about 2, and the lithium selective membranes with different thicknesses had similar results. Since the lithium selective membrane contains hydrogen ions, the metal ions in the water pass through the lithium selective membrane, the metal ions will exchange with hydrogen ions in the lithium selective membrane. Meanwhile, the hydrogen ions on the lithium selective membrane will move to the seawater end, causing the pH value of the seawater end to drop.

Figure 30.6 show the variation of the conductivity and voltage of three ion sieve membranes with different thicknesses in diffusion dialysis. The initial conductivities of the seawater end and the recovery end were 2 mS/cm and 42 mS/cm, respectively, and the conductivity of the seawater end increased with time, which may be caused by the hydrogen ions released by the selective exchange membrane. In addition, the system voltage value decreases with the increase of the thickness of the ion-sieve membrane, and the measured maximum voltages are followed by 0.08 V (single layer), 0.06 V (two layers), and 0.05 V (three layers). Due to diffusion dialysis using the concentration difference as the driving force to move the metal ions in the water, the metal ions can penetrate the lithium selective membrane and voltage was obtained. When the thickness of the lithium selective membrane is increased, the resistance of metal ions penetrates is thus increased, resulting in a decrease in voltage.

Figure 30.7 show the variation in the adsorption concentration of lithium, sodium, potassium, magnesium, and calcium using ion-sieve membranes with different thicknesses. The recovery efficiency of lithium, sodium, potassium, magnesium, and

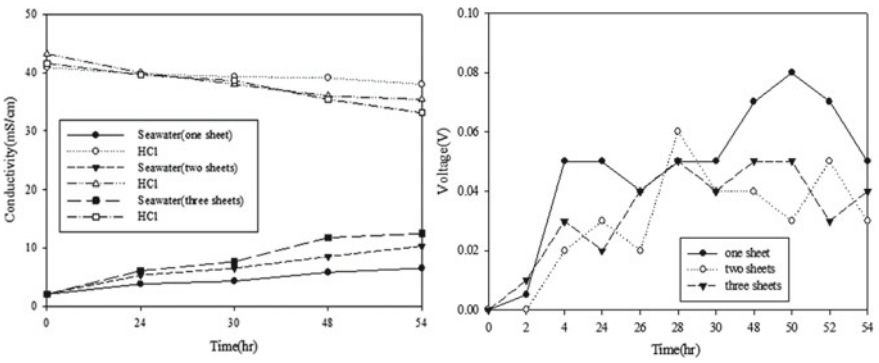

Fig. 30.6 The variation of conductivity and voltage of different thicknesses membrane

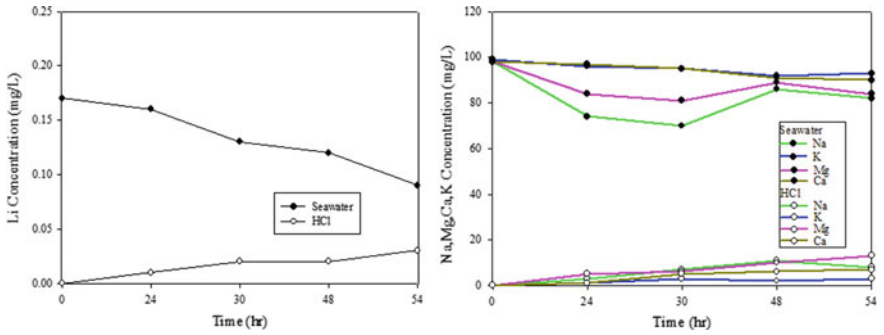

Fig. 30.7 The concentration of lithium and other metals by three layers membranes

calcium were 26%, 15%, 8%, 20%, and 10%, respectively, after 54-h diffusion dialysis using a single ion-sieve membrane. When the number of ion sieve membranes is increased to two layers, although the extraction efficiency of lithium is slightly reduced to 21%, the other ions as sodium, potassium, magnesium, and calcium are significantly reduced to 6, 6, 12, and 9%. The results show that the ion selectivity of the two layers of lithium selective membrane is better, and it can block more metal ions in the seawater. The thickness of the lithium selective membrane was increased to three layers. After 30 h of operation, the concentrations of lithium, sodium, and magnesium ions at the seawater end decreased significantly, but the recovery end had not increased significantly. When the operation time is 54 h, the recovery efficiency of lithium, sodium, potassium, magnesium, and calcium are 18%, 8%, 3%, 13%, and 7%, respectively.

The recovery efficiency of lithium, potassium, and calcium decreased compared to the two layers membrane. Through the selectivity equation as Eq. 30.2, the selectivity of lithium with different thicknesses of ion sieve membranes was compared. Results show that the selectivity values of one, two, and three layers ion-sieve membranes by diffusion dialysis are 0.53, 0.5, and 0.43, respectively. The value of the three layers in ion-sieve membranes is the smallest, which confirms that the three layers can recover the amount of lithium was higher selectivity compared with other metal elements.

$$N = W_0/W \tag{30.2}$$

where,

N Selectivity of lithium selective membrane,
W_0 Proportion in the initial lithium solution (%),
W The ratio of lithium on the membrane (%).

30.4 Conclusion

Based on these research outcomes, the conclusions are given below:

1. When adsorption equilibrium of the ion-sieve membrane for lithium, the adsorption capacity remains greater than 1,900 mg/m^2 with the increase of different metal elements; the adsorption capacity of the ion-imprint membrane was 1,800 mg/m^2, and the adsorption capacity will decrease to 400 mg/m^2 in the presence of different metals.
2. The thickness of the ion-sieve membrane increases to three layers, the recovery efficiency of other metals such as sodium, potassium, magnesium, and calcium can be reduced to 8, 3, 13, and 7%. Improving the selectivity of ion-sieve membranes has a positive effect.
3. Through the selectivity equation, the selectivity values of one, two, and three layers ion-sieve membrane used in diffusion dialysis are 0.53, 0.5, and 0.43, respectively. The selectivity of the ion-sieve membrane to extract lithium is better during three layers.
4. The recovery efficiency of lithium was 18%, and that was 2.5 times higher than that of the current extraction technique (7%). In addition, the electricity of 0.08 V was produced under such diffusion dialysis conditions.

References

Al-Amshawee S, Yunusa MYBM, Azoddein AAM, Hassell DG, Dakhil IH, Hasan HA (2020) Electrodialysis desalination for water and wastewater: a review. Chem Eng J 380:122231

Li X, Mo Y, Qing W, Shaod S, Tang CY, Li J (2019) Membrane-based technologies for lithium recovery from water lithium resources: a review. J Membr Sci 591:117317

Luo J, Wu C, Xu T, Wu Y (2011) Diffusion dialysis-concept, principle and applications. J Membr Sci 366:1–16

Park H, Singhal N, Jho EH (2015) Lithium sorption properties of HMnO in seawater and wastewater. Water Res 87:320–327

Zavahir S, Elmakki T, Gulied M, Ahmad Z, Al-Sulaiti L, Shon HK, Chen Y, Park H, Batchelor B, Han DS (2021) A review on lithium recovery using electrochemical capturing systems. Desalination 500:114883

Chapter 31
Using Thermal Desorption Technique to Treat Real Field Diesel Oil-Contaminated Soils

Jih-Hsing Chang, Ching-Hsiang Tseng, Mohanraj Kumar, and Shan-Yi Shen

Abstract Crude oil may leak in the process of extraction, refining, storage, transportation, and use, which cause the surface to be polluted or seep from the bottom, has received attention to huge environmental impact. Currently, most of the oil-contaminated soil is treated with soil excavation and backfilled method, but the waste contaminated soil is cannot be effectively treated, and it also causes pollution in other areas, resulting in the pollution expanded. In order to effectively solve the soil pollution caused by oil products, direct remediation in the real field contaminated sites is a way can reduce the pollution hazard. Therefore, this research has developed a thermal desorption technique to treat oil-contaminated soil. In this study, the diesel-contaminated soil was treated by thermal desorption to explore its removal efficiency, observing the influence of soil treat amount, combustion temperature, and operation time. Moreover, we also recover the volatilized organic gas during the thermal desorption process to construct an effective diesel oil thermal desorption technique. According to experimental results show, the removal efficiency of diesel oil exceeds 95% based on appropriate operation conditions with a contaminated concentration of 2,000 mg/kg, 300 °C of combustion temperature, and treatment time of 5 min. In addition, the concentration of the exhaust gas collection system shows that the collection efficiency was around 70%. The thermal desorption technique was further applied to the diesel-contaminated soil in the real field, and results found that the highest removal efficiency could reach 90%. The results confirmed that the developing thermal desorption technique can achieve the goal of removing diesel-contaminated soil in this study.

Keywords Diesel oil · Thermal desorption · Real field · Contaminated soils

J.-H. Chang · C.-H. Tseng · M. Kumar
Department of Environmental Engineering and Management, Chaoyang University of Technology, Wufeng 41349, Taiwan

S.-Y. Shen (✉)
Department of Environmental Engineering, Da-Yeh University, Changhua 515006, Taiwan R.O.C.
e-mail: shanyi@mail.dyu.edu.tw

H.-Y. Jeon (ed.), *Sustainable Development of Water and Environment*,
Environmental Science and Engineering,
https://doi.org/10.1007/978-3-031-07500-1_31

31.1 Introduction

Petroleum is one of the main resources worldwide and could be refined into gasoline, diesel, kerosene, asphalt, and so on by fractionation at different temperatures. The products from fractionation are divided into C_4–C_{12} light distillates (LPG, gasoline, naphtha), C_{12}–C_{26} intermediate distillates (kerosene, diesel), and C_{26}–C_{70} heavy distillates (heavy fuel oil, lubricating oil, wax, asphalt). The leakage may cause contamination on the surface or bottom layer of soil during the process of extraction, refining, storage, and transportation (Li et al. 2021). Hence, the impact on the environment is gradual to be paid attention such as the investigation of soil contamination shows that the primary source includes: 1. the leakage during fractionation and refining process; 2. the leakage during transportation, such as the accident of rank truck, corrosion of transfer pipe; 3. the leakage of the oil storage tank under the gas station. Due to the increase of soil contamination problem, this study intends to develop a new technology to solve the puzzle.

In general, the soil excavation and soil vapor extraction methods are the leading technologies for dealing with soil contamination by oil (Liang and Yang 2021; Yu et al. 2019). The most common method of excavation is excavation and backfilled, which is to dig up the contaminated soil in-situ and replace it with clean soil, then transport the contaminated soil to off-site treatment. However, sometimes the contaminated soil could not be treated effectively, even causing the contamination in other sites and spread. The soil vapor extraction method uses vacuum extraction to make pollutants volatilize. Pollutants are transferred from the solid of the liquid phase to the gas phase and the contaminants are pumped out as the soil gas moves towards the suction well and the soil gases that are removed can be recovered or discharged after treatment. However, this method is only suitable for highly volatile pollutants (Liu et al. 2021). Meanwhile, the limitations of oil gas extraction methods have to be carried out with air injection methods and biological aeration methods. In order to effectively and quickly solve the problem of oil-contaminated soil, this study established a set of thermal desorption techniques to deal with oil-contaminated soil. Taking diesel contaminated soil as a test sample, the diesel removal efficiency was discussed under different operating conditions (treatment soil amount, combustion temperature, and treatment time). At the same time, exhaust gas is collected during thermal desorption operation for subsequent recycling. Finally, this thermal desorption technique is applied to the in-situ diesel-contaminated soil to observe the feasibility of the practical application.

31.2 Materials and Methods

This study aims to understand the removal efficiency of diesel contaminated soil under different operating parameters and find the appropriate treatment conditions. A set of treatment systems are designed to collect the gases that volatilize into the

air during heating. Finally, we have conducted tests in the real field to establish a practically feasible diesel desorption technique.

31.2.1 Chemicals and Equipment

The drugs used in this study include commercially available diesel (Source: China oil, purity: 99%) and sodium anhydrous sulfate (Source: Merck, purity: 99%). Commercial diesel is an oil product that simulates leakage from gas stations, and sodium sulfate anhydrous can absorb the un-volatile water in the contaminated soil and finally extract it through n-hexane (Source: Merck, purity: 99%). A thermal desorption test was carried out in a high-temperature furnace (JH-1) to observe the treatment efficiency. In addition, soil heating was carried out by a magnet agitator to simulate the thermal desorption process, and exhaust gas was collected. The contaminated soil is extracted and diesel concentration is detected with a gas phase chromatography/flame ion detector (GC-FID, DB-5 Columns, Varian 3800 GC).

31.2.2 Experiment of Thermal Desorption

During the thermal desorption process, the desorption temperature is selected according to the characteristics of the pollutant, and the higher temperature will cause damage to the soil and make the soil lose its original properties (Falciglia et al. 2011). Since the boiling point of diesel is 170–390 °C, this study is carried out using low-temperature thermal desorption, and the diesel in the soil is volatilized into a gas by heating method to obtain the best combustion temperature and treatment time. The thermal desorption temperature is set at 200, 250, and 300 °C, and the treatment efficiency is observed under 30 min of operation. The soil treatment amount of 0.5, 5, and 10 g was tested to explore the effect of soil treatment amount on the heat desorption temperature rate.

31.2.3 Analysis of Exhaust Gas

In order to capture the exhaust gas concentration during thermal desorption, a treatment system was designed for this study (Fig. 31.1). The primary operation mode is heating the diesel-contaminated soil in the circular flask by oil-proof heating for volatilization and using the condensing device to cool the volatile organic matter, then introducing the produced organic gas into the extraction that the gas can be directly dissolved in n-hexane. Finally, calculate the recovery efficiency. The main operating steps are as follows: set the silicone oil on the magnet mixer for heating to 300 °C, then the contaminated soil is placed in the silicone oil for continuous heating,

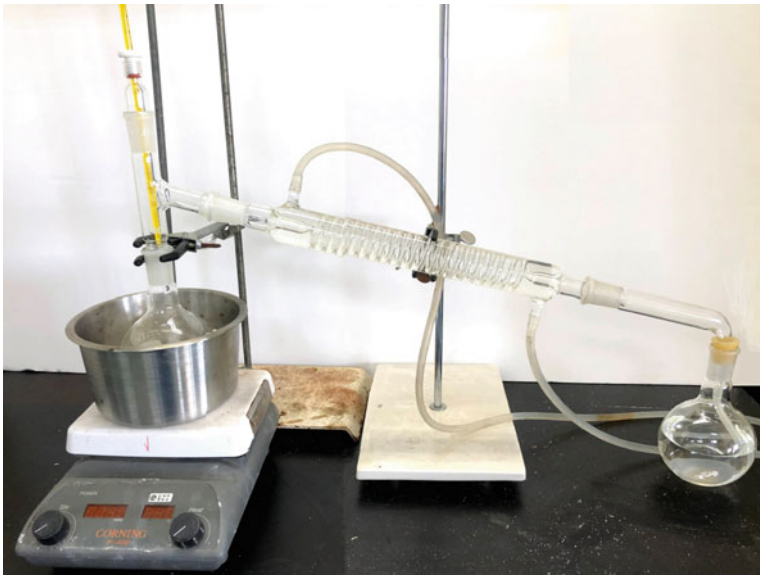

Fig. 31.1 The device of exhaust gas collection in this study

and the gas pipe is placed into the extract; then the two ends of the condensing tube are insulated with insulation to prevent the gas from condensing into a liquid state back into the soil; finally, the concentration of diesel in n-hexane is detected.

31.2.4 Detection of Diesel Concentration

The main steps for the detection of diesel concentration in contaminated soil in this study are as follows: take 5 g of a soil sample by a balance scale in a glass test tube, and when the soil water content is too high, anhydrous sodium sulfate should be added; then, 25 mL of n-hexane was added, and then extracted by shock extraction device for 5 min. Then centrifugation is followed by removal of the upper layer of extract for testing. Finally, concentration detection is performed with GC-FID. During sample testing, the sample is gasified through the injection port (set to 300 °C), and then pushed from the carrier gas into the analysis column, where the temperature is heated in a gradient heating method, maintaining 50 °C for the first 5 min, and then heating up at 12 °C per minute to 300 °C for 10 min. The sample is pushed into the detector by the carrier gas due to the volatilization time of different compounds, and the detector temperature is 300 °C.

The GC-FID detection and analysis figure is shown in Fig. 31.2. Using the characteristics of diesel to obtain the highest peak C15, which is used to calculate C10–C25, and used to calculate the total peak area. According to GC-FID, the C15 shows a

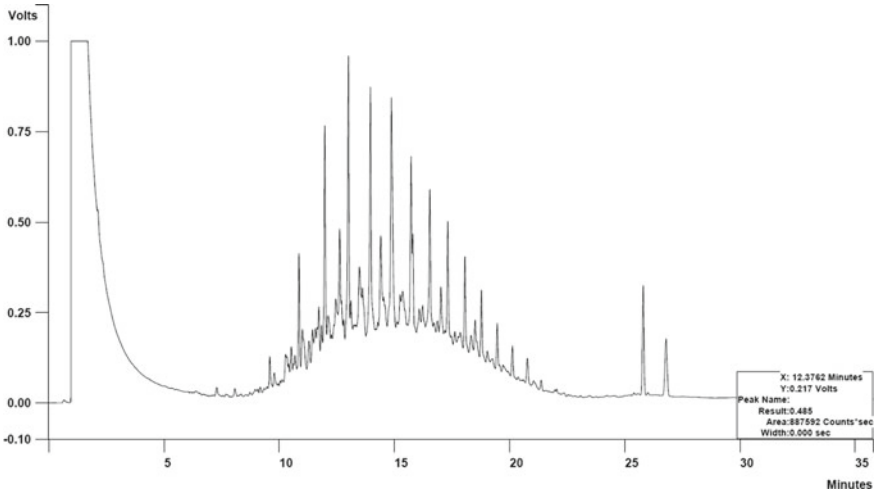

Fig. 31.2 The chromatogram picture of diesel extraction in the n-hexane

peak of about 12.9 min, while C10 shows a peak of about 6.7 min, and C25 shows a peak of about 20.3 min. Bring the data into linear regression Eq. 31.1 to get the slope and intercept formula. This measurement line is shown in Fig. 31.3, the X-axis is the diesel concentration, the Y-axis is the integral area obtained by GC-FID analysis, and the diesel concentration can be obtained through the equation known by the measurement line.

$$y = ax + b \tag{31.1}$$

where,

y Instrument signal (sum of quantitative ion peak areas),
a The slope of the line (also known as the coefficient of x),
x The concentration of the standard,
b Intercept.

Once the measurement line is derived, the diesel contaminants in the soil can be calculated using n-hexane extraction, and the formula obtained from Eq. 31.1 can be brought into Formulas 31.2 and 31.3 for calculation:

$$CS = (Cc \times Vt \times D/WS) \times (1\ mg/1000\ \mu g) \tag{31.2}$$

$$WS = Wwet \times \left(100/\left(100 + W_{H_2O}\right)\right) \tag{31.3}$$

CS The concentration of TPH (aliphatic or aromatic hydrocarbon group or specific analyte) (mg/kg),

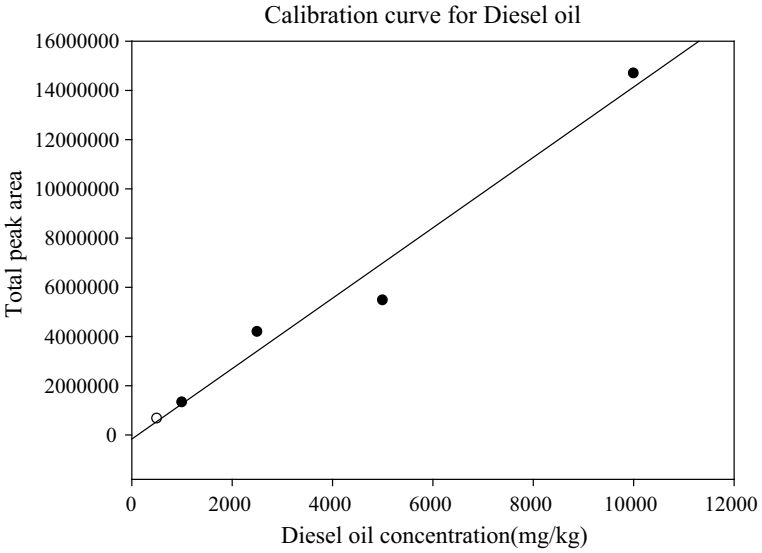

Fig. 31.3 The calibration curve of diesel standards

Cc The concentration of calibration line (μg/mL),
Vt Extraction volume (mL),
D Dilution factor,
WS Dry weight of extracted samples (kg),
Wwet Sample wet base weight (kg),
W_{H2O} Percentage of moisture content based on dry weight (m/m, %).

31.3 Results and Discussion

31.3.1 Effect of Soil Treatment Amount on Thermal Desorption

The smaller of contaminated soil entering the thermal desorption system, the faster the temperature of the contaminated soil will reach the boiling point of diesel, reducing the time required for diesel to desorb from the soil. In this study, the contaminated soil with different treatment amounts was placed in a high-temperature furnace that had been heated to 300 °C and continuously heated. The heating relationship of soil treatment amount was observed at different times and the results are shown in Fig. 31.4. Although the soil treatment amount is 10–20 times different, the soil with different treatment amounts reaches 250 °C at 5 min, and the temperature is closest to 300 °C when the treatment amount is 0.5 g. When the combustion time is extended to 30 min, the soil with different treatment amounts has reached 300 °C.

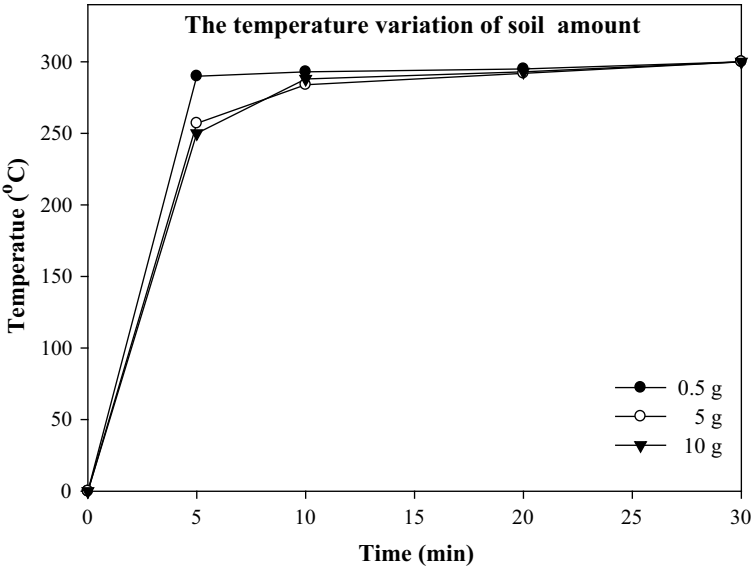

Fig. 31.4 The relationship between soil amount and temperature rise in the thermal desorption process

From the results, it is known that the time required to set the temperature of 300 °C will increase with the soil amount.

31.3.2 Effect of Operating Temperature on Thermal Desorption

This study performed thermal desorption of contaminated soil (2,000 mg/kg) at 200–300 °C and explored the removal efficiency of diesel from contaminated soil, and the results were shown in Fig. 31.5. At a treatment time of five minutes, the removal efficiency of diesel at low-temperature thermal desorption at 200 and 250 °C are about 20%. When the temperature is increased to 300 °C, the removal efficiency can be increased to 95%, and the concentration is reduced from 2,000 to 92 mg/kg. The main reason is that the boiling point of diesel is 167–367 °C, and at a temperature of 300 °C, the C_{14}–C_{18} has the most significant proportion of carbon in diesel that can be desorbed, the removal efficiency effectively improve. Although the required temperature for carbon number above C_{18} needs to be higher, it can also be desorbed by continuous heating. The diesel pollution can be removed entirely at a temperature of 300 °C at 30 min of treatment, while the removal efficiency at 200 and 250 °C can reach 39 and 53%, respectively.

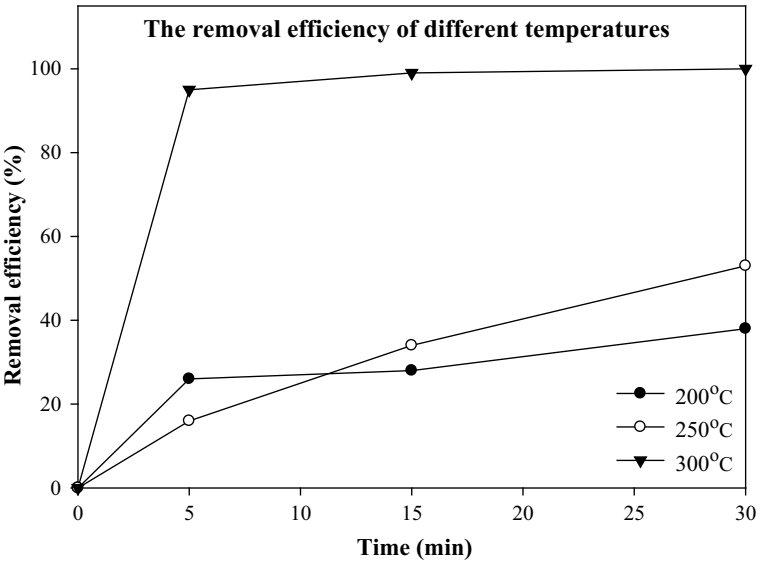

Fig. 31.5 The removal efficiency of diesel contaminated soil at different temperatures

31.3.3 Capture of Volatilization Gas During Thermal Desorption Treatment

In this study, the gas generated by the thermal desorption of diesel contaminated soil in the treatment system is recovery, and the collection efficiency is as shown in Table 31.1. This study uses grease traps to heat contaminated soil to 250 and 300 °C, the resulting gas is introduced into the extract and directly into n-hexane for collection. The prepared contaminated soil concentration was about 1,800 mg/kg, the removal efficiency was 20% at a temperature of 250 °C and 34% at a temperature of 300 °C, respectively, at 10 min of operation. Compared with high-temperature furnaces, there is a similar removal efficiency at 250 °C. However, there is a significant difference in the thermal desorption efficiency of the high-temperature furnace at a temperature of 300 °C, which may be due to the result of indirect heating of the soil and the difference in soil temperature. In addition, the exhaust gas collection part of the institute is concerned, and the exhaust gas collection efficiency can reach more than 70% at different temperatures, which confirms that the system can desorb diesel and achieve the goal of recovery. In the future, the efficiency of grease trap heating can be improved to increase the removal efficiency of diesel.

Table 31.1 The efficiency of exhaust gas collection

Temp (°C)	Raw soils (mg/kg)	Treated soils (mg/kg)	Recovery gas (mg/kg)
250	1,715	1,355	273 (75%)
300	1,776	1,157	433 (70%)

Fig. 31.6 The treatment system of real field thermal desorption

31.3.4 Remediation of Real Field Contaminated Soil

The thermal desorption experiment was further performed in the real field contaminated site, and the thermal desorption mold is shown in Fig. 31.6. The diesel contaminated concentration was reached 22,000 mg/kg before thermal desorption, and the removal efficiency of nearly 90% after thermal desorption operation was reached, and the higher the concentration of contaminated soil, the more obvious the treatment efficiency. The results show the feasibility of the thermal desorption technique of this study for the remediation of real field diesel contaminated soil.

31.4 Conclusion

Based on experimental results, several conclusions can be drawn:

1. The amount of soil treatment will affect the efficiency of thermal desorption treatment, causing resistance due to the volatilization of oil in the soil, resulting in the inability to fully heat up to the required temperature. The amount of soil treatment is related to the efficiency of thermal desorption.

2. The optimal conditions for thermal desorption in this study are 300 °C for more than 5 min of operation, the diesel removal efficiency can reach 95%, and the heat time varies with the amount of soil treatment.
3. In the concentration of the exhaust gas in the collection system, it is found that the recovery efficiency of diesel gas can reach more than 70%, which confirms that the mold of this study can effectively desorb diesel and achieve the recovery of exhaust gas.
4. This study applies appropriate operating conditions in the real field diesel contaminated soil for thermal desorption, and its removal efficiency can reach 90%. The result shows the feasibility of the thermal desorption technique to be treated in the real field with oil-contaminated soil in the future.

References

Falciglia PP, Giustra MG, Vagliasindi FGA (2011) Low-temperature thermal desorption of diesel polluted soil: influence of temperature and soil texture on contaminant removal kinetics. J Hazard Mater 185:392–400

Li M, Yu H, Zheng D, Kleměs JJ, Wang J (2021) Effects of salt and solidification treatment on the oil-contaminated soil: a case study in the coastal region of Tianjin, China. J Clean Prod 312:127619

Liang C, Yang SY (2021) Foam flushing with soil vapor extraction for enhanced treatment of diesel contaminated soils in a one-dimensional column. Chemosphere 285:131471

Liu PF, Yang ZH, Chen YL, Lo KH, Kao CM (2021) Remediation of weathered diesel-oil contaminated soils using biopile systems: an amendment selection and pilot-scale study. Sci Total Environ 786:147395

Yu Y, Liu L, Yang C, Kang W, Yan Z, Zhu Y, Wang J, Zhang H (2019) Removal kinetics of petroleum hydrocarbons from low-permeable soil by sand mixing and thermal enhancement of soil vapor extraction. Chemosphere 236:124319

Chapter 32
Experiment and Simulation of Mobile Underwater Dredger Fill in- Layers Technology in Open Water

Hui Sun, Jiaming Qu, Ran Tao, Qinze Chen, and Yuchi Hao

Abstract In the construction of artificial islands filled in open water along the Belt and Road, there are common engineering problems such as harsh construction environment and poor flatness. The prediction model of mobile underwater dredger fill construction was established by numerical simulation method. Aiming at the problems of uneven distributed flow velocity at outlets and poor filling flatness in conventional lifting pipe type filling device, the device structure was optimized by adding the splitter plate, and the influence of hydro environment conditions on filling effect was further analyzed. The results show that the outlet velocity and filling thickness uniformity of the optimized filling device is improved obviously. The device achieves effective promotion of the filling flatness, leading to a 20% reduction of filling thickness deviation comparing with Chinese current standard for mobile dredger fill in-layers. The results can provide technical support and theoretical basis for high-precision dredger fill construction of filled artificial island in open water.

Keywords Filled artificial island · Open water · Mobile dredger fill · Filling flatness

32.1 Introduction

With the expansion of urban scale and the increase of population, for countries and regions with abundant coastline resources along the Belt and Road, the construction of filled artificial island has become an effective way to solve the land supply problem and to meet the upgrading requirement of residential resources. However, with the advancement of the construction projects, the engineering restrictions have

H. Sun · J. Qu · Q. Chen · Y. Hao (✉)
CCCC National Engineering Research Center of Dredging Technology and Equipment Co. Ltd, Yangpu District, No. 1088 Yangshupu Road, Yangpu District, Shanghai, China
e-mail: haoyuchi@cccc-drc.com

R. Tao
China Harbour Engineering Company Ltd., No.9 Chunxiu Road, Dongcheng District, Beijing, China

H.-Y. Jeon (ed.), *Sustainable Development of Water and Environment*,
Environmental Science and Engineering,
https://doi.org/10.1007/978-3-031-07500-1_32

increased and the quality requirements have been continuously improved. For dredger fill construction subject to complex construction environment and high filling flatness requirement in open water, how to improve the quality and efficiency of dredger fill construction is still a great challenge.

At present, the layered dredger fill method is a most effective method for land reclamation, as shown in Fig. 32.1. Compared with the conventional direct-dredger-fill method, although the layered dredger fill method increases the difficulty of operation technology and the commitment of manpower, material resource and construction period, it can improve the foundation bearing capacity and reduce the difficulty and investment of later foundation treatment (Xianqing 2018). Due to the technical difficulty in construction and planning, there are relatively few projects using layered dredger fill method for construction at present, which is mainly applied to offshore projects and projects with good hydro environment (Zhiqiang et al. 2012; Enyao et al. 2008). On the basis of the layered dredger fill technology used in good hydro environment, how to form a high-precision layered dredger fill technology in complex hydro environment such as open water with deep water depth, abnormal flow velocity and wave conditions during the filled artificial island construction still needs further exploration and systematic study.

In this paper, based on the project environment and reclamation requirements of PASAY filled artificial island in Philippines along the Belt and Road, the method of physical model test and numerical simulation were used. Taking a conventional lifting pipe type filling device as the prototype, aiming at coarse sediment, the mobile underwater dredger fill in-layers construction prediction model in open water was established to explore the influence of different construction conditions on filling effect, so as to provide technical support and theoretical basis for high-precision dredger fill construction in open water affected by the construction hydro environment.

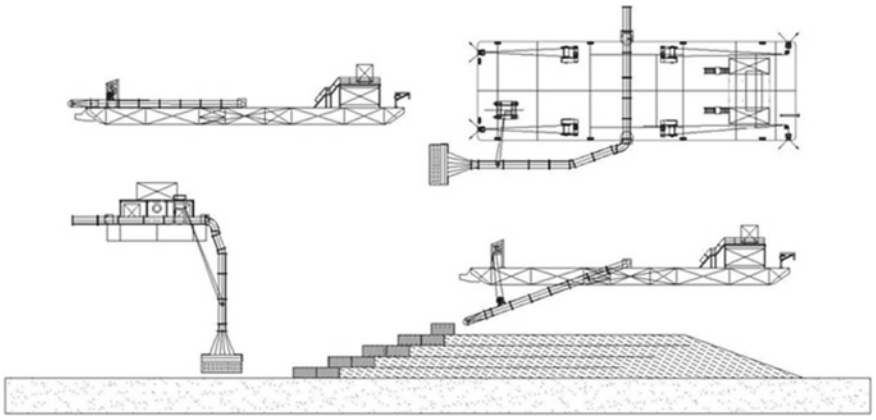

Fig. 32.1 Dredger fill in-layers construction schematic diagram

32.2 Numerical Model and Method

32.2.1 Theory Method

Basic equations of fluid mechanics. Assuming that the fluid is an incompressible viscous Newtonian fluid, the continuity equation and Navier–Stokes equation of incompressible viscous fluid motion are used as the governing equations of fluid motion in the numerical model.

The general mass continuity equation is

$$V_F \frac{\partial \rho}{\partial t} + \frac{\partial}{\partial x}(\rho u A_x) + R\frac{\partial}{\partial y}\left(\rho v A_y\right) + \frac{\partial}{\partial z}(\rho w A_z) + \xi \frac{\rho u A_x}{x} = R_{DIF} + R_{SOR} \tag{32.1}$$

The momentum equation is given as

$$\left\{\begin{array}{l} \dfrac{\partial u}{\partial t} + \dfrac{1}{V_F}\left(u A_x \dfrac{\partial u}{\partial x} + v A_y \dfrac{\partial u}{\partial y} + w A_z \dfrac{\partial u}{\partial z}\right) = -\dfrac{1}{\rho}\dfrac{\partial P}{\partial x} + G_x + f_x \\ \dfrac{\partial v}{\partial t} + \dfrac{1}{V_F}\left(u A_x \dfrac{\partial v}{\partial x} + v A_y \dfrac{\partial v}{\partial y} + w A_z \dfrac{\partial v}{\partial z}\right) = -\dfrac{1}{\rho}\dfrac{\partial P}{\partial y} + G_y + f_y \\ \dfrac{\partial w}{\partial t} + \dfrac{1}{V_F}\left(u A_x \dfrac{\partial w}{\partial x} + v A_y \dfrac{\partial w}{\partial y} + w A_z \dfrac{\partial w}{\partial z}\right) = -\dfrac{1}{\rho}\dfrac{\partial P}{\partial z} + G_z + f_z \end{array}\right\} \tag{32.2}$$

where V_F is the fractional volume open to flow, ρ is the fluid density, R_{DIF} is a turbulent diffusion term, and R_{SOR} is a mass source. The velocity components (u, v, w) are coordinate directions of Cartesian coordinates (x, y, z) or cylindrical coordinates (r, θ, z). A_x is the fractional area open to flow in the x-direction, $A_y$and A_z are similar area fractions for flow in the y and z directions, respectively. (G_x, G_y, G_z) are body accelerations, (f_x, f_y, f_z) are viscous accelerations, P is the pressure on the fluid element.

Basic equations of sediment movement. For the process of underwater mobile dredger fill, the sediment movements of suspension, erosion, advection and deposition are taken into account.

Suspended sediment is transported by advection along with the fluid. The concentration of suspended sediment is calculated by solving the following transport continuity equation for each particle.

$$\frac{\partial C_{s,i}}{\partial t} + \nabla \cdot \left(C_{s,i} u_{s,i}\right) = \nabla \cdot \nabla\left(D C_{s,i}\right) \tag{32.3}$$

$$u_{s,i} = \overline{u} + u_{settle,i} c_{s,i} \tag{32.4}$$

$$c_{s,i} = \frac{C_{s,i}}{\rho_i} \tag{32.5}$$

where $C_{s,i}$ is the mass concentration of the suspended sediment, $u_{s,i}$ is the velocity of the suspended sediment, D is the diffusion coefficient, $\bar{u}$ is the mean velocity of the fluid/sediment mixture, $c_{s,i}$ is the volume concentration of the suspended sediment.

Due to the complexity of sediment erosion, an empirical model is of prior consideration. The model used here is based on Mastbergen and Von den Berg (2010). The entrainment lift velocity of sediment is computed as

$$u_{lift} = \alpha n_s d_*^{0.3} (\theta - \theta_{cr})^{1.5} \sqrt{\frac{\|g\| d_s (\rho_s - \rho_f)}{\rho_f}} \tag{32.6}$$

$$d_* = d_s \left[\frac{\rho_f (\rho_s - \rho_f) \|g\|}{\mu^2} \right]^{\frac{1}{3}} \tag{32.7}$$

where α is the entrainment parameter, n_s is the outward pointing normal to the packed bed interface, θ is the local Shields number, θ_{cr} is the critical Shields parameter, g is the magnitude of the gravitational vector, μ is the fluid viscosity, d_s is the particle size of sediment, ρ_s is density of sediment material, ρ_f is the density of fluid.

The local Shields number is calculated as

$$\theta = \frac{\tau}{\|g\| d_s (\rho_s - \rho_f)} \tag{32.8}$$

where τ is the local shear stress.

The critical Shields parameter is the key parameter to accurately simulate the incipient motion and erosion of sediment. In general, it is best to determine the critical Shields parameter (θ_{cr}) according to the experiment. In the case of lack of experiment data, the critical Shields parameter of sediment whose particle size is greater than 170 μm can be computed using the Shields-Rouse equation (1998).

$$\theta_{cr} = \frac{0.3}{1 + 1.2 d_*} + 0.055 \left[1 - \exp(-0.02 d_*) \right] \tag{32.9}$$

where d_* is the dimensionless mean particle diameter $d_* = d_{50} \left[\frac{\rho_f (\rho_s - \rho_f) \|g\|}{\mu^2} \right]^{\frac{1}{3}}$.

The critical Shields parameter is further modified for sloping surface to consider the effect of sediment repose angle, the modification further alters $\theta_{cr,i}$'

$$\theta'_{cr} = \theta_{cr} \frac{\cos\psi \sin\kappa + \sqrt{\cos^2\kappa \tan^2\phi - \sin^2\psi \sin^2\kappa}}{\tan\phi} \tag{32.10}$$

where $\varkappa$ is the computed angle of the packed interface normal relative to the gravitational vector g, φ is the angle of repose for sediment species, and ψ is the angle between the flow and the upslope direction.

Bed-load transport is the mode of sediment transport due to rolling or bouncing over the surface of the packed bed of sediment. The equation from Meyer-Peter and Műller (1948) is used here.

$$\Phi = \beta\left(\theta - \theta'_{cr}\right)^{1.5} \tag{32.11}$$

where β is the transport coefficient of sediment in bed-load layer, Φ is the dimensionless bed-load transport rate, which is related to the volumetric bed-load transport rate per unit width q, by

$$q = \Phi\left[\|g\|\left(\frac{\rho_s - \rho_f}{\rho_f}\right)d_s^3\right]^{\frac{1}{2}} \tag{32.12}$$

The estimation of the thickness of the bed load sediment δ (Van Rijn 1984)

$$\frac{\delta}{d_s} = 0.3d_*^{0.7}\frac{\theta}{\theta'_{cr}} - 1^{0.5} \tag{32.13}$$

Therefore, the calculation formula of bed load transport velocity q_b is expressed as

$$u_b = \frac{q_b}{\delta f_b} \tag{32.14}$$

32.2.2 Modeling of Typical Lifting Pipe Type Filling Device

Taking one conventional lifting pipe type filling device as a prototype, a three-dimensional numerical model of typical filling device with a scale of 1:1 is established in this study. The size and measuring points of the model are shown in Fig. 32.2.

32.2.3 Sediment Characteristic

According to the particle size range of sediment used in Philippines PASAY filled artificial island construction, the experiment is set up with a medium diameter of coarse sediment (median particle diameter 0.96 mm, density 2650 kg/m^3, concentration 20–50%, critical Shields parameter 0.029).

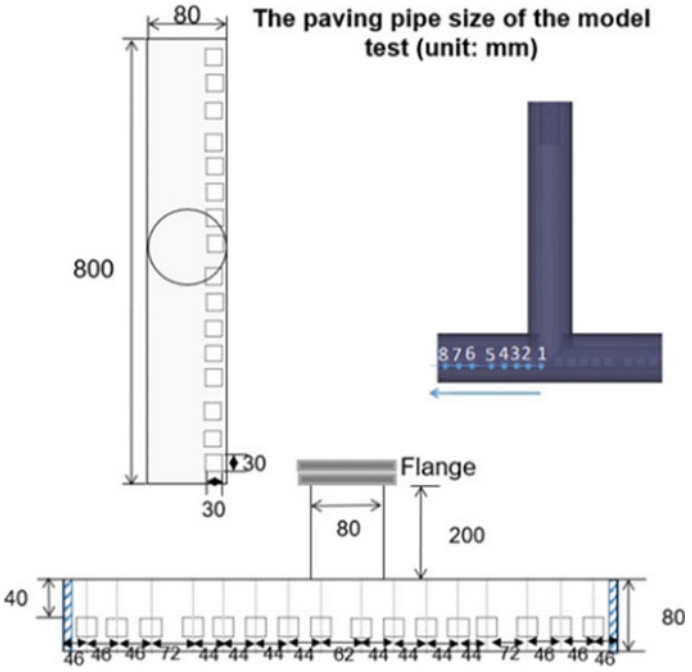

32.2 Model size of typical lifting pipe type filling device

32.2.4 Meshing

An orthogonal structural grid is used in the simulation, the mesh size of overall calculation area is set 0.1 m, and a more-refine element is meshed around the area below the horizontal pipe at the filling device, as well as outlets. There are approximately 2.02 million meshes in total.

32.2.5 Boundary Condition and Initial Condition

The initial water level is set as construction water depth. As shown in Fig. 32.3, the boundary conditions in model include setting the specified flow rate and sediment concentration at the inlets, the top with specified pressure, around the calculation area with the pressure boundary at a certain water depth, the bottom with the roughness wall consistent with the sediment median particle size.

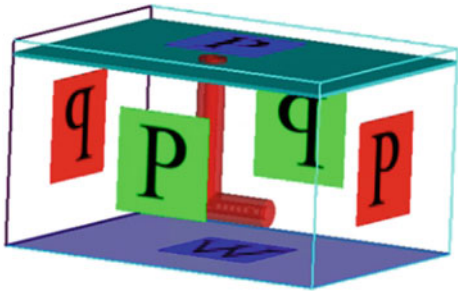

Fig. 32.3 Boundary conditions in the numerical model

32.3 Analysis of Results

32.3.1 Model Validation

In order to verify the feasibility of numerical simulation of layered dredger filling, a typical stratified mobile dredger filling device was used as a prototype, laboratory tests with a length scale of $\lambda = 1{:}10$ were carried out according to the principles of geometric similarity, gravity similarity and dynamic similarity. Numerical simulations of the same scale were also performed, and the results are compared as shown in Figs. 32.4 and 32.5.

The results show that the filling effect of the laboratory test and the numerical simulation is consistent on the whole, and the overall deviation of the calculated and simulated values of the filling thickness is within the allowable error range, indicating that the numerical model can simulate the filling device construction well.

In addition, by comparing the non-moving and 0.2 m/s moving speed conditions of the filling device, it is found that the sediment thickness of the mobile filling is significantly lower than that of the static filling, the sediment slope ratio is significantly reduced, and the flatness is improved.

32.3.2 Optimization of Model Structure

In order to improve the filling flatness, the structure of filling device is optimized by adding various distribution plates, which can effectively even the distribution of flow velocity and reduce the local backflow area. The established four optimized filling devices are shown in Fig. 32.6.

In order to analyze the filling characteristics of the 4 models, the flow velocity along the traveling direction and the filling thickness data of the measuring point 2 are extracted as shown in Fig. 32.7. The results show that, except for the optimized model 2, there is a local backflow phenomenon at the outlet of other models. And Model 2 has the smallest filling thickness difference.

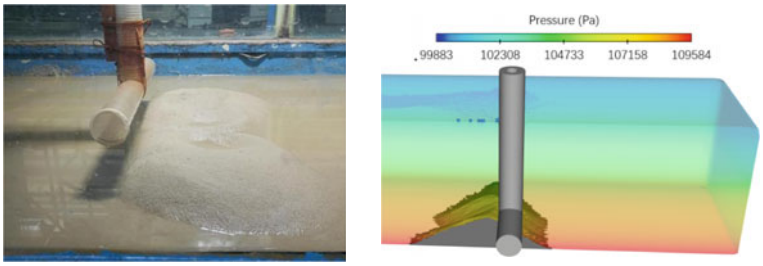

(1) v=0

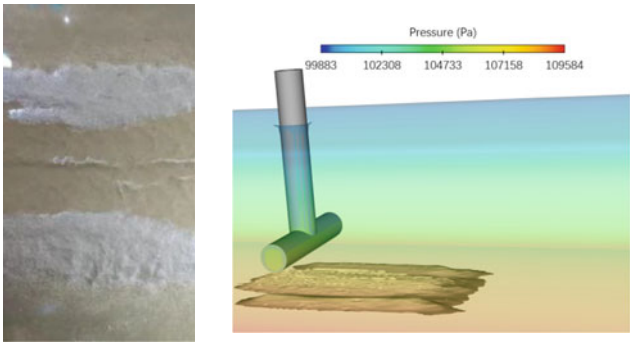

(2) v=0.2m/s

Fig. 32.4 Comparison of static and mobile conditions of typical dredger filling device

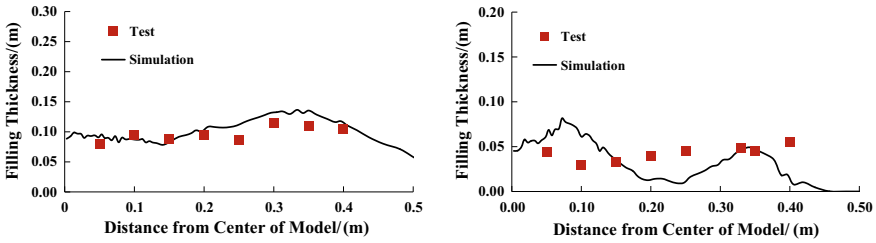

(1) v=0 (2) v=0.2m/s

Fig. 32.5 Filling thickness under stationary and moving conditions

In addition, the average, maximum, minimum and standard deviation of the filling thickness of different models are compared in Fig. 32.8. The results show that the standard deviation of the optimized model 2 is significantly lower than that of other models. Specifically, the standard deviation of the optimized model 2 is 19% lower than that of the original model.

According to the requirements of "Design Specifications for Dredging and Reclamation Engineering" (JTS181-5-2012), the allowable deviation between the average

(1) Model 1

(2) Model 2

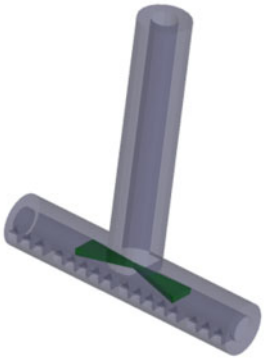

(3) Model 3

(4) Model 4

Fig. 32.6 Optimized structure of typical lifting pipe type filling device

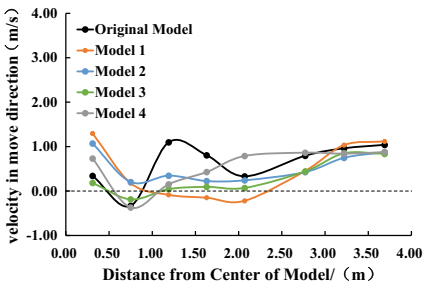

(1) Velocity in move direction

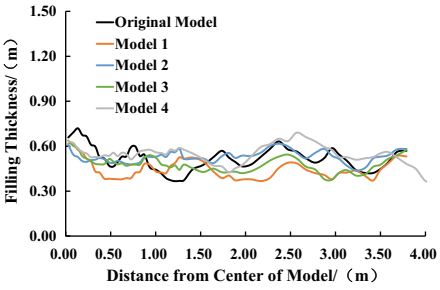

(2) Packed sediment height

Fig. 32.7 Velocity in move direction and packed sediment height in different model conditions

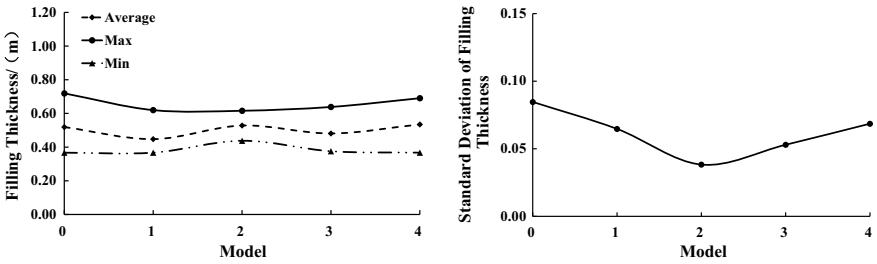

(1) Average Max Min (2) Standard Deviation

Fig. 32.8 Average, max and min values of filling thickness in different model conditions

elevation after completion and the design value is ±0.2 m, that is, from the perspective of flatness, the standard deviation of thickness is required not to exceed 0.2.

It can be seen that the filling thickness deviation of the optimized model 2 is greatly reduced. Therefore, optimized model 2 has the best filling effect compared to other models.

32.3.3 Analysis of the Characteristics of Dredger Fill Under Different Conditions

Based on the project of PASAY filled artificial island in Philippines along the Belt and Road, the generalized research cases are as follows. Table 32.1 shows that the variables include wave height, flow velocity and water depth, a total of 8 cases.

Wave Height. As shown in Figs. 32.9 and 32.10, the filling thickness under different wave conditions is compared, and the results show that the wave increase the filling thickness, but has little effect on the filling thickness flatness. The filling thickness shows a slight decreasing trend with the increase of wave height both along

Table 32.1 Generalized research cases

NO	Flow rate /(m^3/s)	Sediment concentration/%	Wave height/m	Fluid velocity/(m/s)	Water depth/m	Device move velocity/(m/s)
1	2	30	0	0	9.3	0.2
2	2	30	0.3	/	9.3	0.2
3	2	30	0.6	/	9.3	0.2
4	2	30	1.0	/	9.3	0.2
5	2	30	/	0.75	9.3	0.2
6	2	30	/	1.50	9.3	0.2
7	2	30	/	/	15.3	0.2
8	2	30	/	/	20.3	0.2

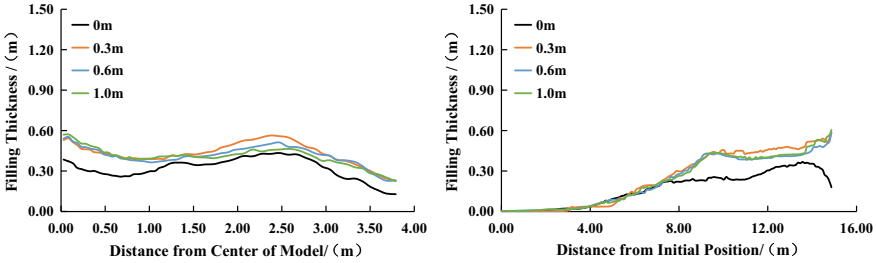

(1) Direction of Model (2) Direction of Movement

Fig. 32.9 Filling Thickness in different wave height conditions

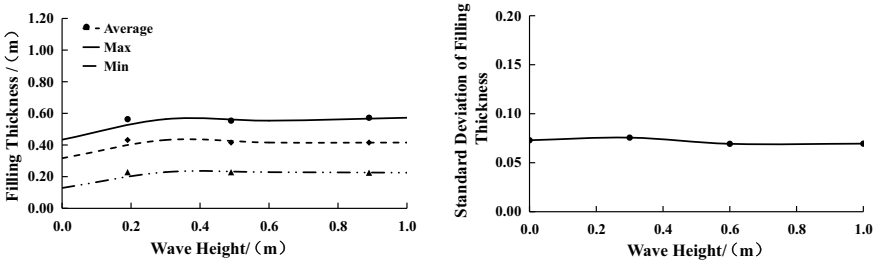

(1) Average Max Min (2) Standard Deviation

Fig. 32.10 Average, max and min values of filling thickness in different wave height conditions

the moving direction and the filling device direction. However, the filling thickness when there are waves is obviously larger than that under the condition of no wave.

By comparing the standard deviation of the filling thickness, it is found that along the filling device direction, the presence or absence of wave condition has little effect on the flatness of the filling surface, and the standard deviation can be kept within 0.11.

Water flow velocity. By comparing the filling thickness under different water flow velocity conditions, it is found that with the increase of the water flow velocity, the position of the maximum filling thickness keeps moving backwards, and the filling thickness decreases sharply after the filling distance exceeds this position, that is, as the flow rate increases, the filling range becomes smaller.

Figures 32.11 and 32.12 show the maximum, average, minimum and standard deviation data of the filling thickness within calculated area under different flow velocity conditions. The results indicate that there is little difference in the average thickness, which is about 0.32 m. The average thickness deviation can be controlled within 0.1, which is 33.3% smaller than that allowed by the engineering specification.

The water flow velocity has little effect on the thickness and flatness of the filling layer, but increasing the flow velocity will cause the position of the sediment to move significantly, increasing the risk of sediment loss.

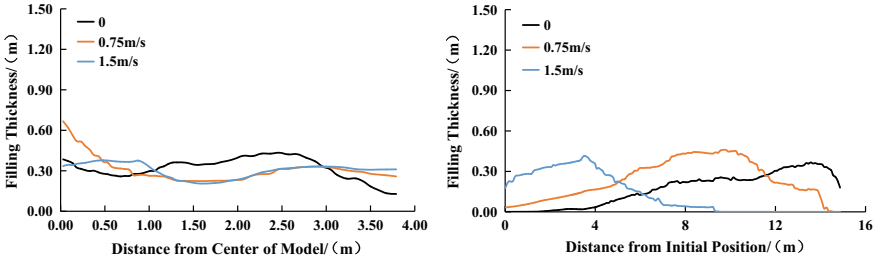

(1) Direction of Model (2) Direction of Movement

Fig. 32.11 Filling thickness in different fluid velocity conditions

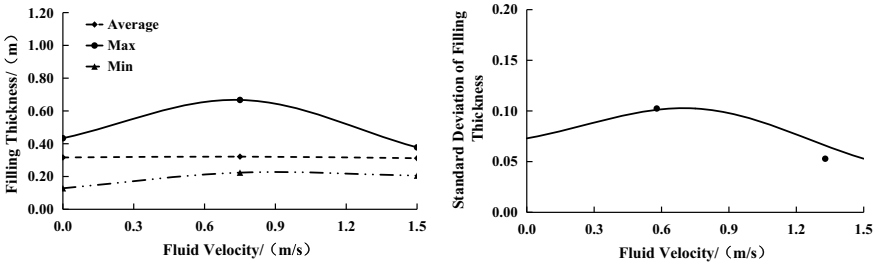

(1) Average Max Min (2) Standard Deviation

Fig. 32.12 Average, max and min values of filling thickness in different fluid velocity conditions

Fluid depth. By comparing the filling thickness under different fluid depth conditions, the thickness decreases obviously with the increase of fluid depth. In the case of fluid depths of 15.3 and 20.3 m, the thickness is similar, but the thickness fluctuation is smaller in the case of water depth of 20.3 m.

From the data in Figs. 32.13 and 32.14, it can be seen that the average deviation of the filling thickness is 0.12 under each working condition, which is within the allowable deviation range of the engineering specification.

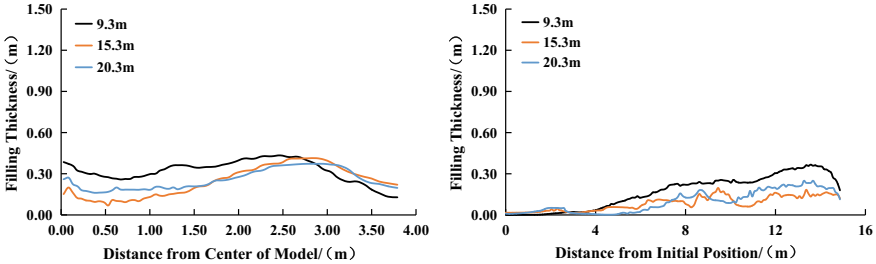

(1) Direction of Model (2) Direction of Movement

Fig. 32.13 Filling thickness in different flow depth conditions

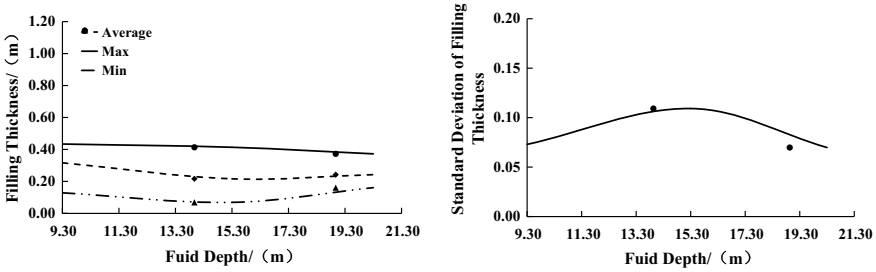

(1) Average Max Min (2) Standard Deviation

Fig. 32.14 Average, max and min values of filling thickness in different fluid depth conditions

The figures show that the average filling thickness is the largest when the fluid depth is 9.3 m. As the fluid depth increases, the filling thickness decreases, that is, a larger fluid depth will have an adverse effect on the filling effect.

The reason may be that the deep water has weak restriction on the vortex. Once the vortex is generated, the scale of the vortex can be maintained in a large range, and the diffusion coefficient of the fluid will increase, which will lead to the diffusion of sediment and the natural reduction of the deposition height.

32.4 Conclusions

(1) The average deviation of the filling thickness can be controlled at 0.12 m under various construction conditions by the use of optimized lifting pipe type dredger filling device for mobile underwater dredger fill construction, which is 20% lower than the average deviation allowed by the current Chinese norm. The research results can provide the basis and technical support for high-precision dredger fill construction of filled artificial island in open water.

(2) Model 2 of optimized lifting pipe type filling device can effectively homogenize the fluid velocity and flilling thickness of outlets and improve the filling flatness. The standard deviation of filling thickness is 19% lower than that of the prototype device.

(3) In general, the severe construction hydro environment is of negative impact on the underwater dredger fill construction in open water. The existence of wave will lead to a certain degree of fluctuation in the filling thickness, but the influence of different wave heights on the flatness is not obvious. The flow velocity has little effect on the thickness and flatness of dredger fill, but leads to the obvious movement of dredger fill location, which increases the risk of sediment loss. With the increase of water depth, the thickness of dredger fill decreases.

(4) Compared with conventional direct-dredger-fill method, the use of mobile underwater dredger fill in-layers method makes the dredger filling thickness

and sediment slope ratio reduced significantly, which can effectively improve the dredger fill flatness in the construction process.

References

Enyao Z, Jing yi L, Shean B (2008) Technology of layered back filling in coast reclamation project. Port Waterway Eng 418(8):148–152 (2008)

Mastbergen DR, Berg J (2010) Breaching in fine sands and the generation of sustained turbidity currents in submarine canyons. Sedimentology 50(4):625–637

Meyer PE, Müller R (1948) Formulas for bed-load transport. In: 2nd Proceeding of congress IAHR, pp39–64, Stockholm, Sweden

Soulsby R (1998) Dynamics of marine sands: a manual for practical applications. Thomas Telford, London

Van Rijn LC (1984) Sediment transport, Part I: bed load transport. J Hydraul Eng 110(10):1431–1456

Xianqing Y (2018) Application of stratified block fill in ultra-thick silt bottoming fill area. Port Waterway Eng 550(S1):62–65

Zhiqiang L, Xinqiang W, Jingrun L (2012) Application of dredger-fill in-layers in sea reclamation project. Port Eng Technol 49(2):62–64